Model-Independent Measurement of the Neutral-Current Interaction Rate of Solar ^{8}B Neutrinos with Deuterium in the Sudbury Neutrino Observatory

Karsten Miklas Heeger

A dissertation submitted in partial fulfillment
of the requirements for the degree of

Doctor of Philosophy

University of Washington

2002

Program Authorized to Offer Degree: Physics

University of Washington

Graduate School

This is to certify that I have examined this copy of a doctoral dissertation by

Karsten Miklas Heeger

and have found that it is complete and satisfactory in all respects,
and that any and all revisions required by the final
examining committee have been made.

Chair of Supervisory Committee:

R.G. Hamish Robertson

Reading Committee:

Wick C. Haxton

R.G. Hamish Robertson

David J. Thouless

Date:

In presenting this dissertation in partial fulfillment of the requirements for the Doctoral degree at the University of Washington, I agree that the Library shall make its copies freely available for inspection. I further agree that extensive copying of this dissertation is allowable only for scholarly purposes, consistent with "fair use" as prescribed in the U.S. Copyright Law. Requests for copying or reproduction of this dissertation may be referred to Bell and Howell Information and Learning, 300 North Zeeb Road, Ann Arbor, MI 48106-1346, to whom the author has granted "the right to reproduce and sell (a) copies of the manuscript in microform and/or (b) printed copies of the manuscript made from microform."

Signature_____

Date_____

University of Washington

Abstract

Model-Independent Measurement of the Neutral-Current Interaction Rate of Solar ^{8}B Neutrinos with Deuterium in the Sudbury Neutrino Observatory

by Karsten Miklas Heeger

Chair of Supervisory Committee:

Professor R.G. Hamish Robertson
Physics

With heavy water as a target medium the Sudbury Neutrino Observatory (SNO) is designed to study solar neutrinos by measuring both the total flux of ^{8}B neutrinos through the neutral-current interaction as well as the electron-type neutrino flux via charged-current dissociation of deuterium. Using data from the pure D_2O phase of SNO we determine the interaction rates of solar neutrinos with deuterium and characterize the backgrounds throughout the SNO detector volume. Without assumptions about the shape of the underlying ^{8}B spectrum a model-independent measurement of the total flux of active solar ^{8}B neutrinos is made. In addition, we determine the contribution of *hep* neutrinos to the SNO data and find evidence for low-energy elastic scattering events below 4 MeV. The measurement of the neutral-current and charged-current interaction rates provides direct evidence for the flavor transformation of solar neutrinos and indicates that neutrinos have mass. With the observation of massive neutrinos at the Sudbury Neutrino Observatory the long-standing solar neutrino problem is resolved.

In a future phase of the SNO experiment, the total flux of ^{8}B neutrinos will be measured by means of an array of ultra-clean ^{3}He-filled proportional counters. The design, construction, and background studies characterizing the performance of this novel neutral-current detection system are described.

TABLE OF CONTENTS

LIST OF FIGURES

LIST OF TABLES

GLOSSARY

BIG BANG NUCLEOSYNTHESIS: Big Bang Nucleosynthesis (BBN) is the synthesis of the light nuclei, deuterium, ^{3}He, ^{4}He and ^{7}Li during the first few minutes of the universe.

BIG BANG THEORY: The theory of an expanding universe that begins as an infinitely dense and hot medium. The initial instant is called the Big Bang.

BLIND DATA SET: Data set that is not analyzed or studied before all methods used in the data analysis have been finalized.

CHERENKOV LIGHT: Radiation which is emitted whenever charged particles pass through matter with a velocity exceeding the velocity of light in the medium.

CONSERVATION: When a quantity (e.g. electric charge, energy, or momentum) is conserved, it is the same after a reaction between particles as it was before.

CROSSTALK: PMT or electronics signal generated by a neighbouring channel.

ELECTROWEAK INTERACTION: In the Standard Model, electromagnetic and weak interactions are related (unified); physicists use the term electroweak to encompass both of them.

EVENT: An event occurs when two particles collide or interact, or a single particle decays. Every neutrino interaction with deuterium is called an event. It may or may not be observed through Čerenkov electrons or a γ signnature.

EVENT BUILDER: Program that combines event headers with PMT bundles to form events.

EVENT HEADER: Data bundle from detector containing information about an event.

FIDUCIAL VOLUME: Reference volume in a particle detector. All event candidates are detected in this volume.

GRAND UNIFIED THEORY: Theories that attempt to unify the strong, weak, and electromagnetic interactions.

INTERACTION: A process in which a particle decays or it responds to a force due to the presence of another particle (as in a collision). Also used to mean the underlying property of the theory that causes such effects.

LEPTON: A fundamental fermion that does not participate in strong interactions. The electrically-charged leptons are the electron (e), the muon (μ), the tau (τ), and their antiparticles. Electrically-neutral leptons are called neutrinos (ν).

NEUTRINO: A lepton with no electric charge. Neutrinos participate only in weak and gravitational interactions and are therefore difficult to detect. There are three known types of neutrinos, all of which are very light.

ORPHANS: A PMT bundle that has not been correctly combined with an event header results in events that are incorrectly assembled in the builder.

PARTICLE FLAVOR: The name used for the different quarks types (up, down, strange, charm, bottom, top) and for the different lepton types (electron, muon, tau). For each charged lepton flavor there is a corresponding neutrino flavor. In other words, flavor is the quantum number that distinguishes the different quark/lepton types. Each flavor of quark and charged lepton has a different mass.

PARTICLE GENERATION: A set of one of each charge type of quark and lepton, grouped by mass. The first generation contains the up and down quarks, the electron and the

electron neutrino.

PMT WET-END: Base connector of photomultiplier immersed in the water of the Čerenkov detector.

QUANTUM CHROMODYNAMICS: The quantum theory of the strong interaction.

QUANTUM ELECTRODYNAMICS: The quantum theory of the electromagnetic interaction.

SEESAW MECHANISM: Mechanism that describes the mass hierarchy of neutrinos. It is based on the assumption that the conservation of the total lepton number L is violated by the right-handed Majorana mass term at the scale M that is much larger than the scale of the electroweak symmetry breaking.

STANDARD MODEL: Theory of fundamental particles and their interactions. It is widely tested and is accepted as correct by particle physicists.

STANDARD SOLAR MODEL: Standard model of solar physics (SSM), based on the assumption of steady-state hydrogen burning in the Sun.

SUPERSYMMETRY: Class of Grand Unified Theories. Supersymmetric theories postulates that every particle has a massive "shadow" particle partner.

VECTRAN: Vectran is a high-performance thermoplastic multifilament yarn spun from Vectra^{TM} liquid crystal polymer (LCP). Vectran is the only commercially available melt spun LCP fiber in the world. Vectran fiber exhibits exceptional strength and rigidity. Pound for pound Vectran fiber is five times stronger than steel and ten times stronger than aluminum.

WEAK INTERACTION: The interaction responsible for all processes in which flavor changes, hence for the instability of heavy quarks and leptons, and particles that contain them. Weak interactions that do not change flavor (or charge) have also been observed.

Z BOSON: A carrier particle of the weak interactions. It is involved in all weak processes that do not change flavor and mediates the neutral-current interaction of neutrinos with deuterium.

ACRONYMS

ADC: Analogue to Digital Converter

ALEPH: Detector System at Large Electron Positron Collider (LEP).

AV: Acrylic Vessel of the SNO Detector

BUTT: Berkeley Underwater Test Tube

CC: Charged-Current

C.L.: Confidence Level

CERN: European Organization for Nuclear Research

CKM: Cabibbo-Kobayashi-Maskawa Weak Mixing Matrix

CHIME: Construction Hardware In-Situ Monitoring Experiment of the SNO NCD Project

CHOOZ: Reactor Neutrino Experiment in Chooz, France

CNO: Carbon-Nitrogen-Oxygen Nuclear Fusion Cycle

COSMO: Computer Program to Estimate Spallation Radioactivity

CVD: Chemical Vapor Deposition

DAMN: Data Analysis Mask Number (Used in SNO Data Reduction)

DAQ: Data Acquisition

DCR: Deck Clean Room

D/I: De-Ionized

DONUT: Direct Observation of the Nu Tau Experiment at Fermilab

DQXX: Detector Status

EC: Endcap of ^{3}He-filled Neutral Current Detector

EGS: Electron-Gamma Shower Particle Transport Code

ES: Electron Scattering

ESUM: Energy Sum (Total Integrated Charged in an Event)

FRÉJUS: Nucleon Decay Experiment in Fréjus, France

FTG: Event Reconstruction Algorithm (Based on the SNOMAN Grid Fitter)

GALLEX: Gallium Solar Neutrino Experiment at Gran Sasso, Italy

GEANT: Geometry and Tracking Monte-Carlo System

GNO: Gallium Neutrino Observatory

GPS: Global Positioning System

GTID: Global Trigger Identification

GUT: Grand Unified Theory

HCA: History Calibration of PMT Signals

HLC: High-Level Event Cuts

HV: High Voltage

ICPMS: Inductively Coupled Mass Spectroscopy

IMB: Irvine Michigan Brookhaven Experiment in the Morton Mine, Ohio

INCO: International Nickel Company, Ltd. in Ontario, Canada

ITR: In-Time Ratio

KAMIOKANDE: Kamioka Nucleon Decay Experiment

KARMEN: Karlsruhe Rutherford Medium Energy Neutrino Experiment

LAMPF: Los Alamos Meson Physics Facility

LED: Light Emitting Diode

LEP: Large Electron Positron Collider at CERN

LMA: Large Mixing Angle

LSND: Liquid Scintillating Neutrino Detector at Los Alamos

MACRO: Monopole Astrophysics and Cosmic Ray Observatory at Gran Sasso, Italy

MC: Monte Carlo Calculation

MCNP: A General Monte Carlo N-Transport Code

MINIBOONE: Mini-Booster Neutrino Experiment at Fermilab

MINUIT: A Function Minimization and Error Analysis Program

MNS: Maki-Nakagawa-Sakata Matrix

M.P.E.: Multiple Photon Electron

MSM: Minimum Standard Model

MSW: Mikheyev-Smirnov-Wolfenstein Matter Oscillation Effect

MUX: Multiplexer

MWE: Mean Water Equivalent

NC: Neutral-Current

NCD: ^{3}He-Filled Neutral Current Detector

NCD DAQ: Neutral Current Detector Data Acquisition

NECK PMT: PMT in the Neck of the Acrylic Vessel

NHIT: Number of Hit PMT's in an Event (With Anode Signal Above Threshold)

NUSEX: Nucleon Stability Experiment in Mont Blanc Tunnel, France

NUTEV: Experiment E815 at Fermilab

OWL: Outward Looking Phototube

PDG: Particle Data Group

PDF: Probability Distribution Function

PGT: Pulsed Global Trigger

PMT: Photomultiplier Tube

PSI: Paul Scherrer Institute

P.E.: Photo-Electron

PP: Proton-Proton Solar Fusion Chain

PSUP: Photomultiplier Support Structure

QA: Quality Assurance

QCD: Quantum Chromodynamics

QE: Quantum Efficiency

QED: Quantum Electrodynamics

RF: Radio Frequency

RNAA: Radiochemical Neutron Activation Analysis

ROV: Remotely Operated (Submersible) Vehicle

RSFP: Resonant Spin Flavor Precession

SAGE: Russian-American Gallium Solar Neutrino Experiment in Russia

SM: Standard Model of Particle Physics

SMA: Small Mixing Angle

SNO: Sudbury Neutrino Observatory

SNOMAN: SNO Monte Carlo and Analysis Software

SNP: Solar Neutrino Problem

SNU: Solar Neutrino Unit (10^{-36} interactions per target per second)

SOUDAN: Soudan Nucleon Decay Experiment in Tower-Soudan Mine, Minnesota

SSM: Standard Solar Model

STP: Standard Temperature and Pressure

STR: SNO Technical Report

SUSY: Super-Symmetry

SUPER-KAMIOKANDE: (Super-K) Neutrino Experiment in Kamioka, Japan

TAC: Time to Amplitude Converter. (TAC also describes the uncalibrated measurement of the PMT timing information.)

TSLH: Time Since Last Hit

U/G: Underground

UTC: Coordinated Universal Time (A worldwide standard for time)

VAC: Vacuum Oscillation of Neutrinos

WIMP: Weakly Interacting Massive Particle

XRF: X-Ray Fluorescence

XSNOED: X-windows based SNO Event Display

ACKNOWLEDGMENTS

My sincere appreciation and thanks goes to the many people who contributed to this work through their support, patience, and knowledge. First, I would like to acknowledge the faculty who accompanied me on this long endeavor and who made it possible for me to pursue this work. I am especially grateful for the role my advisor Hamish Robertson played in my graduate education. As a mentor and teacher he shaped much of my scientific work while working with me as a colleague at the same time. He encouraged me to pursue and believe in my own independent research and provided support when needed. I greatly appreciated the opportunity to work with him and owe a great deal to his role in both my professional and personal development. I would also like to thank the other faculty I closely worked with: John Wilkerson for teaching me efficiency in research and providing insight into how to manage science projects. Peter Doe for his cheerful spirit and for reminding me occasionally that there is life outside physics, and Steve Elliott for his support and many useful discussions and conversations.

As a member of the Sudbury Neutrino Observatory, I am grateful for the opportunity and the stimulating environment the collaboration has provided over many years. The work presented in this thesis would not have been possible without the collaborative effort of the Sudbury Neutrino Observatory and the results of this experiment.

I would like to especially thank Prof. Wick Haxton and Prof. David Thouless for reading a draft of this thesis. Your comments have been invaluable for the presentation of this work.

The Nuclear Physics Laboratory at the University of Washington, also known as the Center for Experimental Nuclear Physics and Astrophysics (CENPA), was my home for the past years. The staff at the laboratory was very helpful in teaching me the basics of technical work as well as helping me complete various hardware projects. In particular, I would like to thank John Amsbaugh who has provided invaluable technical support in

the design and realization of the CHIME project. Barb Fulton and Kate Higgins were a tremendous help in dealing with all my administrative questions and travel requests.

Lastly, this thesis would have never been completed without the long-lasting support and encouragement I received from my family. My special thanks goes to Reina Maruyama: *Für die Dinge, die unser gemeinsames Leben so besonders machen.*

Meinen Eltern in Dankbarkeit.

Für Reina.

CHAPTER 1

SUMMARY AND OUTLINE

Solving the Solar Neutrino Problem at SNO:
Evidence for Massive Neutrinos and Neutrino Flavor Transformation

1.1 Neutrino Mass and Oscillations

For more than 30 years, experiments have detected neutrinos produced in the thermonuclear fusion reactions which power the Sun. These reactions fuse protons into helium and release neutrinos with an energy of up to 15 MeV. Data from these solar neutrino experiments were found to be incompatible with the predictions of solar models. More precisely, the flux of neutrinos detected on Earth was less than expected, and the relative intensities of the sources of neutrinos in the sun was incompatible with those predicted by solar models. By the mid-1990s the data were beginning to suggest that one could not even in principle adjust solar models sufficiently to account for the effects. Novel properties of neutrinos seemed to be called for. With the recent measurements of the Sudbury Neutrino Observatory (SNO), it has finally become possible to test the solar model predictions and the particle properties of neutrinos independently.

Solar models that simulate the interior of the Sun and explain stellar evolution have been developed using experimental and theoretical inputs from nuclear physics, astrophysics, and particle physics. These models are based on the assumption of light element fusion in the Sun. As more and more astrophysical data have become available, solar models were tested through a variety of observables and found to be successful in many respects.

A variety of hypotheses that require new particle physics have been postulated to explain the discrepancy between the solar model expectations and the apparent deficit of solar

neutrinos detected on Earth. In the Standard Model, neutrinos belong to the family of leptons. Neutrinos were believed to be massless particles with three distinct flavors (electron, muon, and tau) depending on the weak interaction process that created them. One flavor could not transform into another. All three types of neutrinos have been directly detected experimentally, the tau neutrino only two years ago. In the light element fusion processes in the Sun, only electron type neutrinos are created.

As early as 1969, Bruno Pontecorvo proposed that neutrinos might oscillate between the electron and muon flavor states (the only ones known then). Like the mixing phenomenon, neutrino oscillations are a quantum effect. Oscillations can occur if the physical neutrinos are actually particles with different masses but not unique flavors. Neutrino mass and flavor mixing are not features of the Standard Model of particle physics. In quantum mechanics, an initially pure flavor (e.g. electron) can change as neutrinos propagate because the mass components that made up that pure flavor get out of phase. The probability for neutrino oscillations to occur may even be enhanced in the Sun in an energy-dependent and resonant manner as neutrinos emerge from the dense core of the Sun. This effect of matter-enhanced neutrino oscillations was suggested by Mikheyev, Smirnov, and Wolfenstein (MSW) and is one of the most promising explanations of the solar neutrino problem.

The measurements at the Sudbury Neutrino Observatory (SNO) show that the neutrino flux produced in the $^8\mathrm{B} \rightarrow {}^8\mathrm{Be}^* + \mathrm{e}^+ + \nu_e$ beta-decay reaction in the Sun contains a significant non-electron type component when measured on Earth. This measurement is the first direct evidence for the flavor transformation of solar neutrinos. Neutrino flavor conversion indicates that neutrinos have mass. Together with the oscillation signature in atmospheric neutrino studies, these results are strong evidence for mixing in the lepton sector and new physics beyond the Standard Model. It is also interesting that most theories that attempt to unify the description of all forces between elementary particles already permit non-zero neutrino masses. As for the cosmological implications, the measurements of SNO, combined with the results from other experiments, set upper and lower limits on the total mass of neutrinos in the Universe. Neutrinos account for as much matter as stars but they cannot explain the mystery of dark matter in the Universe.

1.2 Detecting Solar Neutrinos at the Sudbury Neutrino Observatory

Located 2 km underground in an active nickel mine in Sudbury, Ontario, the Sudbury Neutrino Observatory is a water Čerenkov detector specifically designed to measure the flux of solar ^{8}B neutrinos and to determine the shape of the solar neutrino spectrum. SNO consists of a spherical acrylic tank filled with 1000 tonnes of heavy water and surrounded by 7000 tonnes of light water to shield it from backgrounds. The choice of D_2O as a target material makes the SNO detector unique in comparison with other solar neutrino detectors. It allows SNO to measure both the total flux of solar neutrinos as well as the electron-type component of the ^{8}B neutrino flux produced in the Sun.

Solar neutrinos from the decay of ^{8}B are detected via the charged-current reaction on deuterium ($\nu_e + d \rightarrow p + p + e^-$) and by elastic scattering off electrons ($\nu_x + e^- \rightarrow \nu_x + e^-$). Some 9,500 photomultiplier tubes (PMT's) are used to record the Čerenkov signature of these neutrino interactions. The charged-current reaction is sensitive exclusively to ν_e while the elastic-scattering reaction also has a small sensitivity to ν_μ and ν_τ. Neutrinos also interact through the neutral-current reaction ($\nu_x + d \rightarrow p + n + \nu_x$). The neutron produced in the neutral-current (NC) interaction thermalizes in the heavy water and captures on deuterium, emitting a characteristic 6.25-MeV γ. All three interactions have been measured in SNO.

1.3 Measurement of the Neutrino Interaction Rates of ^{8}B Neutrinos

SNO has been online since November 1999 taking production data, calibration data, and background measurements. The results reported in this work are based on data taken between November 1, 1999 and January 15, 2001 and correspond to a live time of 241 days. Events are defined by a multiplicity trigger counting the number of hit PMT's above channel threshold. For every event trigger, the time and charge response of each participating PMT are recorded. Electronic pulsers and pulsed light sources are used for the calibration of the PMT timing and charge response. Optical calibration of the detector response is obtained using a diffuse source of pulsed laser light. The absolute energy scale and uncertainties are established with a tagged ^{16}N source (predominantly 6.13-MeV γ) deployed in the D_2O

and H_2O. The detector response is tested using neutrons from ^{252}Cf, the electron spectrum from ^{8}Li, and a 19.8-MeV γ calibration source. The energy of each neutrino event is determined based on the total number of triggered PMT's (which corresponds to the total light generated by the Čerenkov electron).

Instrumental backgrounds are eliminated from the raw data based on the timing and charge of hit PMT's in comparison with Čerenkov light. In addition, a set of high level cuts is applied to test the hypothesis that each neutrino event has the characteristics of single electron Čerenkov light.

Backgrounds from radioactivity in the D_2O and H_2O are measured by regular low-level radioassays of U and Th decay chain products and from a lower-threshold neutrino signal analysis. High-energy gamma rays from the cavity are attenuated by the H_2O shield. In this analysis the neutrino interactions as well as backgrounds are studied throughout the entire detector volume. Using the characteristic radial and solar angle distributions as well as the energy spectrum of γ's from neutron capture events on deuterium, the neutrino candidate event set is resolved into contributions from charged-current interactions, elastic scattering, and neutron events.

1.4 Results from the Pure D_2O Phase

In common with all previous solar neutrino experiments, SNO observes a reduced flux of ν_e from the Sun. The fraction of the SNO charged-current ^{8}B flux of the Standard Solar Model (SSM) predictions is 0.342 ± 0.024 (stat.) $^{+0.025}_{-0.022}$ (syst.) for a SSM prediction of 5.05×10^6 cm^{-2} s^{-1}. The elastic scattering flux measured by SNO is consistent with the high-precision measurement performed at Super–Kamiokande, a light water Čerenkov detector located in Kamioka, Japan. The total flux of active ^{8}B neutrinos is the sum of the electron and non-electron flavors and is measured to be 6.35 ± 1.35 (stat.) $^{+0.60}_{-0.60}$ (syst.) $\times 10^6$ cm^{-2} s^{-1} without assuming the standard shape of the ^{8}B spectrum.

A comparison of the charged-current and neutral-current interaction rates is used to test the hypothesis of neutrino flavor transformation. The charged-current reaction on deuterium is sensitive exclusively to ν_e while the neutral-current interaction rate is equally sensitive to

ν_μ and ν_τ, as well as ν_e. Under the assumption of no spectral distortions in the ^{8}B charged-current spectrum the difference between the CC and NC interaction rates is measured to be 4.8 σ. This is clear evidence for the non-electron flavor component of the solar neutrino flux. Without the constraint on the CC spectrum we make a model-independent determination of the ^{8}B flux. In this case, the difference between the solar ν_e and ν_x flux derived from the charged-current and neutral-current interaction rates is more than 3.1 σ. The measured total flux of solar ^{8}B neutrinos is in good agreement with solar model predictions. About 2/3 of the active solar neutrino flux consists of flavors other than ν_e. We note that the total ^{8}B neutrino flux deduced in June 2001 from SNO's measurement of the charged-current interaction and Super–Kamiokande's measurement of the elastic scattering of ^{8}B neutrinos is in excellent agreement with the neutral-current measurement obtained in this work. At present there is no evidence for a deviation of the ^{8}B CC spectral shape from the predicted shape but statistics of the measured CC energy spectrum in SNO are limited.

The difference between the elastic scattering and neutral-current interaction rate (normalized to the standard solar model predictions) disfavors the oscillations of ν_e to sterile neutrinos, which would lead to a reduced flux of electron neutrinos but equal charged-current and elastic scattering rates. Sterile neutrinos might be, for example, right-handed neutrinos or left-handed antineutrinos which do not interact through Standard Model interactions. On the other hand, the different interaction rates are consistent with oscillation of ν_e into active ν_μ and ν_τ. SNO's result is consistent with both the hypothesis that electron neutrinos from the Sun oscillate into other active flavors, and with the standard solar model prediction for the total number of neutrinos released in the solar fusion reactions.

1.5 Search for Solar hep Neutrinos

Neutrinos from the beta-decay of ^{8}B dominate the solar neutrino spectrum between 5-15 MeV. The shape of the neutrino energy spectrum from a single beta-decaying source is well known and independent of solar physics to an accuracy of 1 part in 10^6. A measurement of the shape of the solar neutrino energy spectrum is a direct test of the minimal electroweak model and can be used to constrain models of neutrino flavor transformation.

Near the ^{8}B endpoint the solar neutrino spectrum is very sensitive to any underlying background, including neutrinos with energies above 15 MeV from other sources than ^{8}B decay. In a rare branch of the pp-chain in the Sun, ^{3}He and proton fuse forming the reaction $^3\mathrm{He} + \mathrm{p} \rightarrow {}^4\mathrm{He} + \mathrm{e}^+ + \nu_e$. This *hep* process produces high energy solar neutrinos with an energy of up to 18.77 MeV.

In the past, the measurements of the energy distribution of recoil electrons created by ^{8}B and *hep* neutrinos scattering off electrons in the Super–Kamiokande detector raised significant experimental and theoretical interest in the observation and calculation of the *hep* neutrino flux. One possible interpretation of the Super–Kamiokande measurement suggested a flux of hep neutrinos ≥ 20 times larger than the best theoretical estimate at the time. Standard Solar Model (SSM) calculations for the flux of *hep* neutrinos predict a flux of 9.3×10^3 cm^{-2} s^{-1} compared to 5.05×10^{10} cm^{-2} s^{-1} for the much more abundant ^{8}B neutrinos. The SSM predictions of the *hep* flux are based on low-energy cross-section calculations with an S-factor of $S^{SSM}(hep) = (2.3 \pm 1.3) \times 10^{-20}$ keV-b. The rate of the *hep* reaction is so small that it does not affect solar modeling and other solar model predictions. The reliable estimation of the *hep* cross-section has been a long-standing challenge in nuclear physics. A measurement of the flux of *hep* neutrinos at the Sudbury Neutrino Observatory is of interest to astrophysics and nuclear physics alike. It is also an important part of a detailed shape analysis of the solar neutrino energy spectrum measured at SNO.

In the first phase of the experiment, SNO has measured the interaction rates of solar ^{8}B and *hep* neutrinos with pure D_2O. The total ^{8}B flux was found to be in good agreement with Standard Solar Model predictions. Low backgrounds and the efficient discrimination of instrumental effects have also allowed SNO to measure the energy spectrum of solar neutrinos and to perform a rare event study in the energy region between 15-30 MeV. Using analysis techniques similar to the ones developed for the measurement of the interaction rates of ^{8}B neutrinos with deuterium the flux of *hep* neutrinos in the Sudbury Neutrino Observatory has been determined to be less than 1.7×10^4 cm^{-2} s^{-1} at the 95% C.L..

1.6 Implications of the SNO Result

Phenomenological studies have analyzed the SNO result in terms of 2, 3, and even 4-flavor neutrino oscillation scenarios and determined the favored oscillation parameters, i.e. the most likely values for the mixing angle and the splitting of the neutrino mass eigenstates. A 2-flavor analysis finds that only the solutions with large mixing angles survive, with a preference for the one with the larger mass splitting. This is the so-called large mixing angle (LMA) solution. Global analyses with 3 and more neutrino species find that additional active and sterile neutrino oscillations solutions are currently allowed at $\sim 3\ \sigma$. Interestingly, all favored solutions involve large, but not necessarily maximal, mixing angles. In summary, the recent SNO results disfavor complete conversion of electron neutrinos into sterile neutrinos and appear to favor large mixing angles between active neutrino flavors.

Even without knowing the exact oscillation parameters this result already has theoretical implications for neutrino masses and high energy theories. Theoretical frameworks which invoke large extra dimensions with right-handed neutrinos in the bulk to explain the small neutrino masses tend to resemble neutrino oscillations into sterile neutrinos and also involve small-mixing angles. In contrast, some see-saw type mechanisms readily yield solutions with large mixing angles. A see-saw solution would imply a large mass scale in physics associated with right-handed neutrinos. This large mass scale may be the scale at which the forces (except gravity) are unified, and hence may affect our predictions for supersymmetry (SUSY).

The data from SNO have provided clear evidence for neutrino flavor conversion, and hence for new physics beyond the Standard Model. It is very likely that the conversion mechanism is neutrino oscillations, although other non-Standard-Model processes have also been suggested. Recent analyses have shown that small mixing angles are disfavored in solar neutrino oscillations. At present, it is not clear whether the oscillation occurs only between active neutrino species or with an admixture of a sterile component. Pure $\nu_e \rightarrow \nu_s$ oscillations, however, are ruled out by the current data.

1.7 Future Studies with SNO

At the beginning of June 2001, SNO started the second phase of its scientific operation. Using NaCl as an additive to the heavy water enhances the capture efficiency of neutrons produced in the neutral-current dissociation of deuterium. This enables SNO to make a precision measurement of the neutral-current interaction rate of ^{8}B neutrinos to confirm the first result from the pure D_2O phase. In a future phase of the SNO experiment, the total flux of ^{8}B neutrinos will be measured independently by means of an array of ultra-clean ^{3}He-filled proportional counters. This detection system will provide event-by-event identification of neutral-current interactions in real-time, sensitivity to supernova bursts, improved sensitivity to Day-Night variations in the solar neutrino flux and to spectral distortions in the energy spectrum of ^{8}B neutrinos. The array of ^{3}He-filled proportional counters will also feature completely different systematics than the previous phases of the SNO experiment.

The Sudbury Neutrino Observatory is a collaboration of about 100 scientists from 11 universities and laboratories in Canada, the US, and the UK.

1.8 Thesis Outline

In this thesis we present a complete analysis for the measurement of the interaction rates of solar ^{8}B and *hep* neutrinos with deuterium in the Sudbury Neutrino Observatory. The appendices to this work describe the design, construction, and background studies for a ^{3}He-filled Neutral Current Detector system which will be used in a future phase of SNO. Every chapter of this thesis is self-contained and can be read independently. Chapters 1 and 2 introduce the field of neutrino physics and motivate the search for physics beyond the Standard Model in solar neutrino experiments. The main results of this thesis analysis are contained in Chapter 9 and 11. Chapter 11 summarizes our conclusions and discusses the significance of this measurement for our understanding of neutrinos in particle physics, astrophysics, and cosmology. A short description of the content of each chapter is given at the end of this section.

A number of different analyses of the data from the D_2O phase have been performed by members of the SNO collaboration. These analyses have been performed independently using different analysis components and techniques in an effort to provide confirmation and verification of the final results. The efforts are documented in a number of Ph.D. theses [15, 150, 142] and internal analysis reports. The final results of this collaboration-wide analysis effort have been published [70, 106, 107]. A detailed description of the SNO data analysis of the data taken in the pure D_2O phase is forthcoming [108].

While the analyses mentioned above differ in many details some inputs and tools are common to all of them. All analyses make use of the same Monte-Carlo simulation code and share the calibration data. The high-level event-quality cuts are similar in all analyses. However, the treatment of radioactive backgrounds, however, is handled quite differently. Furthermore, the reconstruction of events, the choice of fiducial volume, the event energy estimation and the techniques used for the extraction of neutrino signals are developed and chosen independently.

To the existing body of SNO analyses we add the following:

• *Model-Independent Measurement of ^8B Flux:* The analysis techniques presented in this work allow one to determine the flux of solar ^{8}B without any assumptions on the shape of the ^{8}B spectrum. This approach provides a unique way of measuring the total active solar neutrino flux in the presence of neutrino oscillations and possible distortions in the shape of the charged-current spectrum. A model-independent measurement of the ^{8}B flux is used in our search for new neutrino properties. It also provides a direct test of solar model predictions.

• *Model-Independent Determination of Charged-Current Electron Spectrum:* The analysis approached developed for the model-independent signal decomposition allows one to determine the charged-current spectrum without assumptions or constraints on the shape of the ^{8}B spectrum. This allows us to measure the true CC spectrum in the presence of neutrino oscillations or spectral shape distortions.

• *Search for Solar hep Neutrinos:* The techniques developed in this thesis for the extraction and decomposition of the neutrino signals can be applied to the determination of the flux of solar *hep* neutrinos. A new upper limit on the flux of solar *hep* neutrinos is obtained.

• *Simultaneous Determination of Neutrino Signals and Backgrounds:* A combined fit to the neutrino signals and backgrounds is used to resolve the data set into its individual components and to determine the contributions from the charged-current and neutral-current interaction of neutrinos, as well as the elastic scattering. This approach allows one to study the data set for different fiducial volumes and investigate the correlation between detector distributions of signals and backgrounds.

• *Analysis in Variable Fiducial Volumes:* The simultaneous fit to signals and backgrounds is critical for the characterization of the neutrino signals and background distributions throughout the entire detector volume including both the D_2O and H_2O.

• *Calibration-Source Independent Analysis of ^8B Spectrum:* An analysis of the SNO charged-current β-spectrum without use of calibration data is used as an independent verification of the solar ν_e flux measurement. This approach also has the potential to reduce the uncertainty in the energy scale of the detector response which is the dominant systematic

error in the SNO charged-current flux measurement.

• *Total Light Energy Estimator:* An event energy estimator based on the total light observed for each event is used as a measure of the neutrino energy. The use of total light maximizes the energy resolution of the data. Techniques are developed to calculate the most likely event energy from the number of photomultiplier hits in an event.

• *Sensitivity to Optical Response Parameters:* The optical response parameters chosen in this analysis are a parameterization of a full 3-dimensional PMT simulation code available to the SNO collaboration. Agreement between this work and other analyses demonstrates our understanding of the optical properties of this complex detector.

• *Reconstruction Independent of Event Class:* The algorithm used for the reconstruction of the reduced data set is independent of the particle nature of the events. This allows one to reconstruct single-particle events, such as Čerenkov electrons, in the same way as multi-particle backgrounds. This is an important feature as neutrino signals are extracted by a combined fit to the neutrino and background components of the data set. Furthermore, it allows one to simultaneously reconstruct both solar *hep* and low-energy atmospheric neutrinos near the high-energy end of the ^{8}B spectrum without having to perform an event identification first.

• *Development and Verification of Data Reduction Techniques:* In the SNO solar neutrino analysis the raw data is first reduced to a neutrino candidate event set. This work describes some of the verification of the standard data reduction cuts and the contributions towards the development of an independent data reduction scheme.

• *Overview of the SNO Neutral Current Detector Project:* The construction of the ^{3}He-filled Neutral Current Detectors has been completed and commissioning efforts are underway. We give an overview of the design, construction, and background studies for the ^{3}He-filled proportional counters of this novel neutral-current detection system.

• *First Deployment of Neutral-Current Detectors into SNO:* As part of our background studies for the Neutral Current Detector array a background test source consisting of 7 Neutral Current Detectors was deployed into the central heavy water volume in SNO. This first *in-situ* background test verified the cleanliness of the NCD array after construction.

The contents of each chapter and the appendices of this thesis are outlined below:

Chapter 1 contains an executive summary of the solar neutrino measurements from the D_2O phase at SNO.

Chapter 2 gives an overview of the theoretical and experimental aspects of neutrino physics and describes the search for signatures of new physics in solar neutrino experiments. The key measurements for the study of solar neutrinos at the Sudbury Neutrino Observatory are described.

Chapter 3 gives a brief description of the SNO detector and outlines the analysis procedure used in our study of the SNO solar neutrino data. The reduction of the raw data set and the removal of instrumental backgrounds is discussed.

Chapter 4 describes and characterizes the algorithms used to reconstruct the vertex and direction of the original neutrino interaction from the PMT hit pattern produced by the characteristic Čerenkov electron or the γ signature of events.

Chapter 5 develops and characterizes the high-level event-quality cuts that are applied to the reduced data set to obtain the final event set of solar neutrino candidates.

Chapter 6 describes the energy response of the SNO detector during the period of data taking and studies temporal variations in the energy scale. A transformation function mapping the raw number of PMT hits to an effective event energy is developed.

Chapter 7 describes the generation of probability distribution functions for the neutrino signals and backgrounds in the SNO detector. The Monte-Carlo simulation of events in the SNO detector is discussed.

Chapter 8 describes the characteristic event distributions of the neutrino candidate event set and their use in the determination of the neutrino interaction rates. First estimates of the charged-current and elastic scattering interaction rate are obtained from the radial and solar angle distribution of events. In addition, evidence for low-energy elastic scattering events with energies below 4 MeV is presented.

Chapter 9 describes our measurement of the interaction rates of solar ^{8}B neutrinos with deuterium in SNO and presents the main results of this thesis. A technique for the model-independent spectral decomposition of the data into their neutrino signal and background

components is presented. This allows us to determine the neutrino interaction rates free of assumptions about the shape of the underlying ^{8}B spectrum. The total flux of active solar ^{8}B neutrinos is measured. The comparison of the charged-current and neutral-current interaction rate yields evidence for the flavor transformation of solar neutrinos.

Chapter 10 describes SNO's search for high-energy solar *hep* neutrinos from the rare $^3\mathrm{He} + \mathrm{p} \rightarrow {}^4\mathrm{He} + \mathrm{e}^+ + \nu_e$ process The contribution of *hep* neutrinos to the solar neutrino energy spectrum measured in SNO is determined.

Chapter 11 summarizes the evidence for the flavor transformation of massive neutrinos from the solar neutrino measurements at SNO and discusses the implications for particle physics, astrophysics, and cosmology.

In a future phase of the SNO experiment, the total flux of ^{8}B neutrinos will be measured by means of an array of ultra-clean ^{3}He-filled proportional counters. The design, construction, and background studies characterizing the performance of this novel neutral-current detection system are described in the appendices to this thesis.

Appendices A-D give an overview of the design characteristics, the background considerations, and the construction of SNO's ^{3}He-filled Neutral Current Detector (NCD) array.

Appendices E-F describes the design of a NCD background test source and background studies in preparation for the installation of the Neutral Current Detector array in SNO.

CHAPTER 2

SEARCH FOR SIGNATURES OF NEW PHYSICS IN SOLAR NEUTRINO EXPERIMENTS

Over the past fifty years research in particle physics has led to the Glashow-Weinberg-Salam theory of electroweak interactions, which, combined with the Quantum Chromo-Dynamics, is now called the Standard Model of elementary particle physics. The Standard Model is a theory of weak, electromagnetic, and strong interactions. Gravity is not included in the current Standard Model.

While the Standard Model predicted successfully the existence of charmed particles, b and t quarks, weak neutral currents, the existence of the vector $W^{\pm}$ and Z^0 bosons and their masses, it is generally accepted that the Standard Model is not a complete and final theory of particle physics. Not only does the Standard Model not predict over 20 fundamental constants such as quark masses, coupling constants, and mixing angles, it also does not explain why there exist only three generations of quarks and leptons. Nevertheless, predictions of the Standard Model have been confirmed by numerous experiments in the past and the theory behind the Standard Model describes almost all experimental data at present.

Efforts in experimental and theoretical particle physics are directed towards the search for a theory of elementary particles that could generalize the Standard Model and would solve some of its conceptual problems. Grand Unified Theories (GUT), models based on supersymmetry (SUSY), and superstring models predict the mass scale of the particles involved in a natural way and fit the low-energy data remarkably well. SUSY GUTs may provide a framework to reduce the number of free Standard Model parameters and explain some or all of the observations that seem to violate the Standard Model.

Several experiments have recently given indications of possible violations of the Standard Model and provided first signs of new physics beyond the Standard Model. At present

the strongest indications come from experiments studying the neutrino sector of the Standard Model. The zenith angle dependence of the atmospheric neutrino flux measured in the Super-Kamiokande experiment, the deficit in the observed flux of solar neutrinos, and NuTeV's measurement of the electroweak parameter $\sin^2\theta_W$ in neutrino-nucleon scattering show clear discrepancies between the Standard Model predictions and experimental observation. The evidence of neutrino oscillations as reported by the LSND beamstop neutrino oscillation experiment may be the first direct evidence for neutrino oscillations. The LSND results, however, need independent confirmation from other experiments and are partly in contradiction with results reported by the KARMEN experiment. A definitive answer will have to await new experiments.

Most of these observations can be explained by the oscillation of massive neutrinos. Besides the hypothesis of neutrino oscillations, any explanation involving neutrino flavor conversion requires physics beyond the Standard Model. While solar neutrino experiments were originally designed to test solar model predictions and measure the flux of neutrinos from the Sun, modern experiments have the potential and accuracy to study the unique particle properties of neutrinos. The observation of neutrino oscillations and measurement of their masses could potentially open a window to physic at very large energy scales and provide signs of new physics beyond the Standard Model.

2.1 Neutrinos Within the Standard Model

2.1.1 Discovery of the Neutrino

In 1930 Pauli postulated the neutrino as "a desperate remedy" to the energy crisis of that time - the continuous energy spectrum of electrons emitted in nuclear β-decay. Postulating the neutrino Pauli could account for the continuous spectrum by assuming that in nuclear β-decay a neutron is emitted together with the electron in such a way that the sum of the energies of neutron and electron is constant. Sensitive measurements of the energy and momentum of β-decay electrons and of their recoiling nuclei in cloud chambers indicated that substantial quantities of energy and momentum were missing. These single-process experiment left little doubt that a third particle had to be involved. As early as 1932

Enrico Fermi provided a theoretical framework for β-decay which included the neutrino and was inspired by the structure of electromagnetic interactions. However, it took almost two decades before the neutrino was detected experimentally.

In 1956 Frederick Reines and Clyde Cowan performed the first direct detection of neutrinos utilizing the flux of $\overline{\nu}_e$ from the Savannah river nuclear reactor. In this experiment tanks of organic scintillator were used in combination with a $H_2O + CdCl_2$ target. Electron antineutrinos were detected through the reaction $\overline{\nu}_e + n \rightarrow e^+ + n$. The signature of a $\overline{\nu}_e$ interaction was the coincidence signal of two 0.51 MeV γ's and a γ burst 10 μs later from positron annihilation and neutron capture on Cd respectively.

By the end of the fifties, measurements of positron, electron, and neutron polarization in β-decays and muon decay seemed to indicate both of these reactions proceeded through a combination of vector and axial-vector couplings, an indication that these interactions might be the same. The experimental limit on the branching ratio of $\frac{R(\mu \rightarrow e+\gamma)}{R(\mu \rightarrow e+\nu+\overline{\nu})}$ was found to be smaller than the predictions from the universality of Fermi interactions. Now if the neutrinos associated with muons are different from neutrinos associated with electrons, then the branching ratio will be proportional to $|V_{\mu\nu_e} + V_{\nu_\mu\, e}|^2$, where $V_{\alpha\beta}$ are lepton family mixing coefficients. The muon neutrino was finally detected by Schwartz, Lederman, and Steinberger in 1961. Using a proton beam at Brookhaven Laboratory pions and kaons were produced in a beamstop experiment. Neutrinos from pion and kaon decays had energies ranging from hundreds of MeV to several GeV. Their interaction was detected in a 10 ton spark chamber built from aluminum plates. If the neutrinos produced in reactions such as $\pi \rightarrow \mu + \nu$ are distinct from those produced in β-decays they expected to see only the tracks of muons generated by neutrinos that interacted in the aluminum. Otherwise, there should have been as many e-type as μ-type events.

While there was little doubt about its existence the tau neutrino was the last active neutrino to be discovered. A wealth of indirect evidence points to the existence of ν_τ . Most of it comes from data suggesting the tau has a neutral, spin 1/2, weak isospin partner. If the tau neutrino were the muon or electron neutrino, then 50% of the muon (electron) neutrino-induced charged-current reactions would produce a tau. The current experimental limit on this process is $\Gamma(\tau^- \rightarrow l^- \overline{\nu_l} \nu_\tau) = 4.18 \times 10^{-10}$ MeV [53] which clearly demonstrates

that ν_τ is not ν_μ or ν_e assuming Standard Model weak interactions. By measuring the spin alignment of the ρ in $\tau^- \rightarrow \rho^- \nu_\tau$ decays it has been demonstrated that the ν_τ spin is 1/2 [56]. While there have been attempts to confirm the V-A structure of the $\tau - \nu_\tau$ vertex the present experimental limits still leave room for non-standard couplings. Confirmation of the V-A nature of the interaction would be an indication for the existence of ν_τ based on the similarity of the $\tau - \nu_\tau$ vertex to $e - \nu_e$ and $\mu - \nu_\mu$. Measurement of e^+e^- collisions at LEP indicate that the tau has a weak isospin -1/2 and that the τ, μ, and e couplings to the weak neutral current are identical to within 1%. This strongly suggests lepton universality. The experimental challenge in detecting the tau neutrino comes from the difficulty of making an intense ν_τ beam and from unambiguous identification of ν_τ in τ decays. In 2000 the existence of ν_τ was confirmed by the Fermilab DONUT experiment [82]. This experiment utilizes emulsion techniques to image and reconstruct the decay of τ leptons. They observe ν_τ-induced charged-current interactions through the identification of the produced tau lepton.

2.1.2 Properties of Massless Neutrinos

In the Standard Model, fermions are matter constituents with half-integer spin. They are grouped into two classes. Leptons and quarks are regarded as elementary, point-like entities which come in pairs. Quarks and leptons can be grouped into three different generations. A generation is a set of one of each charge type of quark and lepton, grouped by mass. The first generation contains the up and down quarks, the electron and the electron neutrino.

$$\overbrace{\begin{pmatrix} u \\ d \end{pmatrix}, \begin{pmatrix} c \\ s \end{pmatrix}, \begin{pmatrix} t \\ b \end{pmatrix}}^{Quarks} \qquad \overbrace{\begin{pmatrix} \nu_e \\ e \end{pmatrix}, \begin{pmatrix} \nu_\mu \\ \mu \end{pmatrix}, \begin{pmatrix} \nu_\tau \\ \tau \end{pmatrix}}^{Leptons} \tag{2.1}$$

The Standard Model unifies the electromagnetic and weak interaction in the electroweak interaction. In the Standard Model the three left handed neutrinos are represented by two-component spinors ν_i, with i=e,μ,τ, each describing a left-handed fermion. They are lower components of weak isodoublets L_i, they have I_{3W}=1/2, and an unit of the global i^{th} lepton

number. Right-handed singlets have electric charge and are active under $U(1)$. Standard Model neutrinos are the weak isospin partners of the charged leptons: the electron neutrino forms a weak isospin doublet with the electron, the muon neutrino with the muon, and the tau neutrino with the tau. These standard model neutrinos are strictly massless.

Apart from the mass aspect, neutrinos are very well behaved particles within the framework of the Standard Model and some of their properties have been confirmed with great accuracy in collider experiments. The number of light neutrino types, N_ν, has been deduced from the studies of Z production in e^+e^- collisions. From a precise determination of the mass and total width of the Z boson, combined with the hadronic pole cross-section and the ratios of the hadronic and leptonic partial decay widths of the Z, the number of light neutrinos ($m_\nu \leq 45$ GeV) with standard coupling to the Z can be derived. Assuming that the invisible partial decay width of a Z is due to light neutrino species with partial width Γ_ν the total number of active, light neutrino species is:

$$N_\nu = \frac{\Gamma_{inv}}{\Gamma_l}\left(\frac{\Gamma_l}{\Gamma_\nu}\right) = 2.994 \pm 0.012 \tag{2.2}$$

The LEP lineshape measurement of Z bosons at CERN implies that the number of active neutrino flavors is equal to three. The error in N_ν accounts for the measurement errors as well as uncertainties in the top mass ($m_t = 175 \pm 6$ GeV) and the Higgs mass (60 GeV $\leq m_H \leq$ 1000 GeV).

All the existing data on weak interaction processes in which neutrinos take part are perfectly described by the Standard Model charged-current and neutral-current Lagrangian.

$$j_\alpha^{W,CC} = \sum_i (\overline{\psi_f}\gamma_\alpha(1-\gamma_5)\psi_i) \tag{2.3}$$

$$j_\alpha^{W,NC} = \sum_i (\overline{\psi_f}\gamma_\alpha(g_{Vi} - g_{Ai}\gamma_5)\psi_i) \tag{2.4}$$

The CC and NC interaction Lagrangians conserve the three lepton numbers $L_{e,\mu,\tau}$ while CC interactions determine the notion of flavor neutrinos $\nu_{e,\mu,\tau}$. There are no indications in favor of violation of lepton numbers in weak processes. From the existing experiments very

strong bounds on branching ratios of rare, lepton-number-violating processes are obtained [53] [1].

2.1.3 Direct Neutrino Mass Limits

Over the past decades there has been steady progress in probing neutrino masses through direct measurements of decay kinematics. Direct kinematical measurements of neutrino masses give values consistent with zero. Techniques for measuring the mass of the electron (anti)neutrino involve the search for a distortion in the shape of the β-spectrum in the endpoint region. Tritium decay is commonly used for this measurement because of its low endpoint energy and simple nuclear and atomic structure. Tritium β-decay experiments use electromagnetic or magnetic spectrometers to analyze the momentum of the electrons and to infer the endpoint energy of the spectrum. The direct limits on both the muon and the tau neutrino masses are based on kinematic measurements using semileptonic, weak particle decays. The observables in these measurements are either invariant mass or the decay particle momentum. As these measurements rely on knowing the particle mass and momentum the sensitivity of these measurements to neutrino mass is limited. Limits obtained from cosmology and nucleosynthesis, as well as from supernovae SN1987A, set limits far lower then those placed by direct mass measurements. The direct experimental limits on neutrino mass as reported by the Particle Data Group in 2000 [53] are summarized in Table 2.1. The neutrino mass limits and the masses of other fermions are compared in Figure 2.1.

Since stable neutrinos with masses as large as the limits from direct kinematic measurements would certainly overclose the Universe (i.e. contribute such a large cosmological density that the Universe could have never attained its present age.), cosmology implies a much lower upper limit on these neutrino masses. Considering the freezeout of neutrinos in the early Universe it can be shown [10] that the mass density and the sum of the neutrino masses are related.

---

[1] In principle, nothing in the Standard Model forbids the kind of flavor mixing for neutrinos that you get for quarks. Only massive neutrinos are ruled out but the Standard Model.

Table 2.1: Experimental limits on neutrino masses from direct mass measurements.

Neutrino Mass	Mass Limit	Decay Mode	Experiment	Ref.
m_{ν_e}	< 3 eV	$^3\mathrm{H} \rightarrow {}^3\mathrm{He} + \mathrm{e}^- + \overline{\nu}_e$	Mainz 2000	[53]
m_{ν_μ}	< 190 keV	$\pi^+ \rightarrow \mu^+ + \nu_\mu$	PSI 1996	[53]
m_{ν_τ}	< 18.2 MeV	$\tau^- \rightarrow 2\pi^-\pi^+\nu_\tau$	ALEPH 1998	[53]
		$\tau^- \rightarrow 3\pi^-2\pi^+\nu_\tau$	[53]	

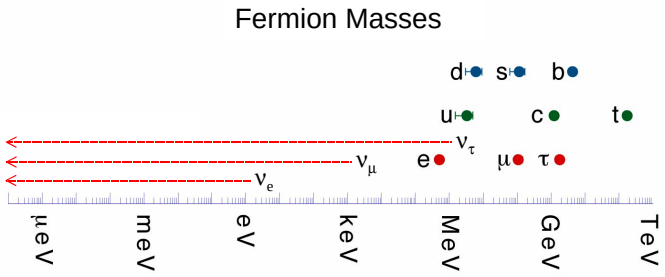

Figure 2.1: The masses of the fermions, showing current limits on neutrino masses.

$$\Sigma m_{\nu_x} = 93\ \Omega_m h^2 \mathrm{eV} \tag{2.5}$$

where Ω_m is the mass contribution to the cosmological constant. With $\Omega_m h^2 \leq 0.25$ we obtain an upper limit on the sum of the neutrino masses for light neutrinos of $\Sigma m_{\nu_x} \leq 24$ eV and a limit for single high-mass neutrinos $m_\nu \geq 1$ MeV. Big Bang Nucleosynthesis constrains the parameters of possible sterile neutrinos which do not interact and are produced only by mixing. The current limit on the total number of neutrinos from Big Bang Nucleosynthesis is $1.7 \leq N_\nu \leq 4.3$ at 95% C.L.. In conclusion, direct kinematic methods have not yet measured a non-zero neutrino mass. At present, there is no direct indication from these experiments for new physics beyond the Standard Model and other searches for signatures of massive neutrinos are needed.

2.2 Physics of Massive Neutrinos

In the Standard Model neutrinos are kept massless by global chiral lepton number symmetry which includes the absence of right-handed fields, and more general properties such as renormalizability of the theory. However, this is only a formal argument in favor of such a symmetry and there is no reason why this symmetry needs to be intact. In contrast, in most of the grand unified theories that unify the strong, electromagnetic, and weak interaction, a given neutrino belongs to a multiplet consisting of a charged lepton, l, positively and negatively charged quarks, q^+ and q^-, and a neutrino. Symmetry considerations suggest that a neutrino in the context of grand unified theories would not be massless but related to the components of this multiplet.

$$\left[\nu, l, q^+, q^-\right] \tag{2.6}$$

Below we summarize the physics of massive neutrinos and describe the unique signatures of massive neutrinos, including neutrino oscillation, lepton number violation, and magnetic moments.

2.2.1 Neutrino Fields

The Standard Model coupling between neutrinos, charged leptons, and the W boson is given by

$$L_{l_{\nu W}} = -\frac{g}{\sqrt{2}}\overline{l^0}_L\gamma_\lambda\nu_L^0 W^\lambda + H.C. \tag{2.7}$$

In general, particles which have a simple weak coupling do not have definite mass. Each of them is a coherent superposition of particles with definite mass. For charged leptons, we have a mass term

$$L_{m_l} = -\overline{l_R^0}M_l l_L^0 + H.C. \tag{2.8}$$

with M_l as the charged-lepton mass matrix.

The Standard Model weak interaction will only absorb a neutrino to make a negatively charged lepton or absorb an $\overline{\nu}$ to make a positively charged lepton. This interaction conserves the lepton number L as it distinguishes particles and antiparticles. The Standard Model couplings of the Z boson are also L-conserving. To generate neutrino masses without new fermions, lepton number symmetry must be broken by adding Higgs fields carrying lepton numbers to the Standard Model. One can then arrange to break lepton number symmetry explicitly or spontaneously through their interactions.

Any satisfactory model that generates neutrino masses must contain a natural mechanism that explains their small value relative to those of their charged partners. Given the latest experimental indications it would also be desirable to include justification for near maximal mixing and possibly light sterile species. The most familiar approach to give neutrino masses is, however, to introduce for each one an electroweak neutral singlet ψ_R. This happens naturally in left-right symmetric models where the origin of SM parity violation is ascribed to spontaneous symmetry breaking. According to the scale where they have relevant effects unification models, such as SO(10) GUT, and weak-scale approaches, e.g. radiative models, can be distinguished.

Phenomenologically, mass terms can be viewed as describing transitions between right- and left-handed states. For neutrinos, there can be both Dirac and Majorana masses. If a neutrino is distinct from its antiparticle, four states are possible and the particle is called a Dirac particle. However, if a neutrino is identical to its antiparticle it consists of just two mass-degenerate states with different spins and is called a Majorana neutrino.

In general a spin half particle is said to be a Majorana particle if the spinor field satisfies the following condition:

$$\psi = \psi^C = C\overline{\psi}^T \tag{2.9}$$

The Dirac or Majorana particle are limiting cases where either all Majorana or the Dirac mass terms are zero.

In the absence of right-handed singlets the only Lorentz scalar made out of neutrinos is the Majorana mass. It has the form $\nu_i^\dagger \nu_i$ and has the quantum number of a weak isotriplet

with I_{3W} =1 as well as two units of total lepton number. Thus the most general neutrino mass term is

$$L_{M_\nu} = -\frac{1}{2}[\overline{(\nu_L^0)^C}, \overline{\nu_R^0}] M_\nu \begin{bmatrix} \nu_L^0 \\ (\nu_R^0)^C \end{bmatrix} + H.C. \tag{2.10}$$

The M_ν may be decomposed as

$$M_\nu = \begin{bmatrix} M_L & M_D^T \\ M_D & M_R \end{bmatrix} \tag{2.11}$$

where M_L and M_R contain left-handed and right-handed Majorana mass terms while M_D contains Dirac mass terms. In the case of 3 neutrino flavors each mass is a 3×3 matrix, and each field is a column vector in flavor space. Thus, the vector space is of dimension 12.

If all Majorana terms are zero one obtains three four-component solutions, and three right-handed ones. If the Dirac masses are zero, we obtain six two-component solutions. In this limit, the right-handed and left-handed field decouple completely and one obtains the three familiar left-handed 2-component solutions and three right-handed ones. The number of light neutrinos with definite mass can now vary from three to six. If the total lepton number is conserved, massive neutrinos are Dirac particles and the number of massive neutrinos is equal to three.

Diagonalizing the new neutrino mass matrix one finds that the physics particle content is given by two Majorana mass eigenstates: The inclusion of the Majorana mass splits the four degenerate states of the Dirac field into two non-degenerate Majorana pairs. If we assume that the states ν, N are respectively active and sterile, the Majorana masses m_L and m_R transform as weak triplets and singlets respectively. m_D is a standard Dirac mass term. The neutrino mass matrix can be generalized to three or more families, in which case the masses become matrices themselves.

The Lagrangian with the neutrino mass matrix becomes:

$$-L = (\overline{\nu}, \overline{N}) \begin{pmatrix} m_L & m_D \\ m_D & m_R \end{pmatrix} \begin{pmatrix} \nu \\ N \end{pmatrix} \tag{2.12}$$

The weak interaction can be expressed in terms of neutrinos which do have definite mass as

$$\begin{aligned} L_{l_\nu W} &= -\frac{g}{\sqrt{2}}\overline{l^0}_L\gamma_\lambda\nu_L^0 W^\lambda + H.C. \\ &= \frac{g}{\sqrt{2}}\overline{l_L}\gamma_\lambda U\nu_L W^\lambda + H.C. \end{aligned} \tag{2.13}$$

where $U = V_{Ll}^\dagger V_\nu$ is called the leptonic mixing matrix.

The leptonic mixing matrix is also known as the "Maki-Nakagawa-Sakata-Pontecorvo" (MNSP) matrix. If all the Majorana mass terms in M_ν vanish, the Majorana mass eigenstates of M_ν pair up to make Dirac neutrinos. Dirac mass terms conserve L. However, Majorana mass terms such as $\overline{(\nu_L^0)^C}\nu_L^0$ or $\overline{\nu_R^0}(\nu_R^0)^C$ which convert a neutrino into an antineutrino and vice versa break L conservation.

If neutrinos are massive a number of interesting effects can occur. Some of the most interesting effects are discussed in the sections below. Discovery of any of these effects would establish the existence of massive neutrinos and open the window to an unexplored area of fundamental particle physics.

2.2.2 Seesaw Mechanism

The Seesaw model is a mechanism that can be used to give a natural, qualitative explanation of the smallness of neutrino masses. In a gauge field theory of electroweak interactions two distinct types of neutrino mass terms can appear. Dirac mass terms are of the form

$$-m_D(\overline{\nu_L}\nu_R + \overline{\nu_R}\nu_L) \tag{2.14}$$

and Majorana mass terms are of the form

$$-\frac{1}{2}m_M^L(\overline{\nu_L}\nu_L^c + \overline{(\nu_L)^c}(\nu_L)) - \frac{1}{2}m_M^R(\overline{\nu_R}\nu_R^c + \overline{(\nu_R)^c}(\nu_R)) \tag{2.15}$$

Here ν represents a neutrino field, the subscript L or R denotes the helicity and ν^c is the charged-conjugated field.

$$\nu^c = C\overline{\nu}^T \; C\gamma_0\nu^* \tag{2.16}$$

Note that $(\nu_L)^c = (\nu^c)_R$. The charge-conjugation operation and helicity projection do not commute. This implies that an interaction containing only left-handed fields must violate the charge-conjugation maximally. It was pointed out by Gell-Mann, Ramond, and Slansky [117] and independently by Yanagida [184] that smallness of neutrino masses could be caused by the extremely large value of the Grand Unification Scale M_{GUT}. If both terms are present in the Lagrangian then these terms can be combined such that

$$L_{Mass} = -\frac{1}{2}(\overline{\nu_L}\overline{(\nu_R)^c})M \begin{pmatrix} (\nu_L)^c \\ \nu_R \end{pmatrix} + H.C. \tag{2.17}$$

where M is the seesaw matrix

$$M = \begin{pmatrix} m_M^L & m_D \\ m_D & m_M^R \end{pmatrix} \tag{2.18}$$

Assuming a hierarchy in the values of the elements of M

$$m_M^R = M \gg m_D \gg m_M^L = \mu \tag{2.19}$$

with μ negligible or zero then one set of particles becomes light while another becomes heavy (a "seesaw" effect). In the case of one generation the "seesaw" mass matrix 2.18 has one heavy eigenvector

$$N \approx [\nu_R + (\nu_R)^c] + (m_D/M)\,[\nu_L + (\nu_L)^c] \tag{2.20}$$

which consists mainly of the sterile ν_R, and light eigenvector

$$\nu \approx [\nu_L - (\nu_L)^c] + (m_D/M)\,[\nu_R - (\nu_R)^c] \tag{2.21}$$

which consists mainly of the active ν_L. Their masses are the eigenvalues of the matrix:

$$m_N \approx M, m_\nu \approx \left| \mu - \frac{m_D^2}{M} \right| \tag{2.22}$$

In the case of three generations, the neutrinos in 2.17 become vectors and M, m_D, and μ are matrices. The heavy and light eigenvectors are found diagonalizing the matrices

$$m_N = M, m_\nu = \mu - m_D M^{-1} m_D^T \tag{2.23}$$

In the simple seesaw model there are as many right- as left-handed neutrinos such that we have three light and three heavy neutrinos with masses

$$\frac{m_{D1}^2}{M_1}, \frac{m_{D2}^2}{M_2}, \frac{m_{D3}^2}{M_3}, M_1, M_2, M_3 \tag{2.24}$$

where M_i and m_{Di} are the eigenvalues of matrix M and m_D respectively. The Dirac masses m_{Di} could be similar to the up-quark masses or the charged lepton masses, and the heavy masses M_i could just be similar $M_i \approx M$ (quadratic seesaw mechanism) or follow the same hierarchy as the m_{Di} (linear seesaw mechanism).

An illustration of the seesaw mechanism and other fundamental mass-generating interactions is shown in Figure 2.2.

2.2.3 Flavor Mixing and Neutrino Oscillations

One of the most interesting consequences of neutrino mass and mixing is the phenomenon of "neutrino oscillations". This describes the flavor conversion of neutrinos in which a neutrino born in association with a charged lepton of one flavor interacts to make a charged lepton of a different flavor. As early as 1969, Bruno Pontecorvo proposed that neutrinos might oscillate between the electron and muon flavor states (the only ones known then). The notation $\nu_e \rightarrow \nu_\mu$ usually describes this sequence of events that lead to an effective flavor transformation between the creation and the detection of neutrinos. Flavor transformation is a clear signature of neutrino oscillations.

If neutrinos have mass the neutrino mass and weak (or flavor) eigenstates are not necessarily identical. The flavor eigenstates ν_f are linear combinations of the projections of the neutrino mass eigenstates ν_m.

$$|\nu_f\rangle = \sum_m U_{fm}|\nu_m\rangle \tag{2.25}$$

with U as an orthonormal mixing matrix. In the case of 3 different neutrino flavors and in the absence of new interactions or sterile states, the flavor neutrino states $\nu_f = (\nu_e\,, \nu_\mu\,, \nu_\tau\,)$ and the mass eigenstates $\nu_{mass} = (\nu_1, \nu_2, \nu_3)$ are related by the unitary neutrino mixing matrix U_{MNSP}. It is a standard parameterization of mixing among neutrinos and its element describe the mixing angles.

$$U_{MNSP} \;=\; \begin{pmatrix} U_{e1} & U_{e2} & U_{e3} \\ U_{\mu 1} & U_{\mu 2} & U_{\mu 3} \\ U_{\tau 1} & U_{\tau 2} & U_{\tau 3} \end{pmatrix} \tag{2.26}$$

The complete flavor mixing comes from two different parts, the diagonalization of the charged-lepton Yukawa couplings and that of the neutrino masses. In most simple extensions of the Standard Models, the elements of U_{MNSP}, this CKM-like leptonic mixing matrix, are totally arbitrary with parameters only to be determined by experiment.

Note, in a 3-ν scheme with Dirac neutrinos the elements of U_{MNSP} can be factorized and separated into three individual mixing matrices that are constrained by the solar, atmospheric, or reactor and accelerator neutrino experiments. U_{MNSP} is written as a product of three matrices with s_{ij}=sinθ_{ij}, c_{ij}=cosθ_{ij}, and δ_D as a CP-violating phase.

$$U_{MNSP} \;=\; \overbrace{\begin{pmatrix} 1 & 0 & 0 \\ 0 & c_{23} & s_{23} \\ 0 & -s_{23} & c_{23} \end{pmatrix}}^{\text{atmospheric } \nu} \overbrace{\begin{pmatrix} c_{13} & 0 & s_{13}e^{-i\delta_D} \\ 0 & 1 & 0 \\ -s_{13}e^{i\delta_D} & 0 & c_{13} \end{pmatrix}}^{\text{reactor/accelerator } \nu} \overbrace{\begin{pmatrix} c_{12} & s_{12} & 0 \\ -s_{12} & c_{12} & 0 \\ 0 & 0 & 1 \end{pmatrix}}^{\text{solar } \nu} \tag{2.27}$$

The time evolution of a flavor state produced in association with a lepton flavor f is given by

$$
\begin{aligned}
|\nu_f(t)\rangle &= \sum_m U_{fm}|\nu_m\rangle e^{-iE_m t} \\
&\approx e^{-ipt}\sum_m U_{fm}|\nu_m\rangle e^{-i(M_m^2/2p)t}
\end{aligned}
\tag{2.28}
$$

where $|\nu_f\rangle$ is a superposition of states $|\nu_m\rangle$ of energy $E_m = \sqrt{p^2 + M_m^2} \approx p + \frac{M_m^2}{2p}$ assuming $M_m \ll p$. M_m is the mass of ν_m. Using the unitarity of U we have

$$
|\nu_m\rangle = \sum_{f'} U^*_{f'm}|\nu_{f'}\rangle \tag{2.29}
$$

Strictly speaking, the unitarity constraint $\sum_f U^*_{fm}U_{fm'} = \delta_{mm'}$ does not necessarily hold if neutrinos are Majorana particles. However, unitarity of U is a reasonable assumption if right-handed neutrinos are heavier than 45 GeV and are only negligible admixtures of the three usual flavor eigenstates. Under the assumption of unitarity we find

$$
|\nu_f(t)\rangle \approx e^{-ipt}\sum_{f'}\left[\sum_{m=1}^{3} U_{fm}e^{-i(M_m^2/2pt)t}U^*_{f'm}\right]|\nu_{f'}\rangle \tag{2.30}
$$

If lepton flavor is not conserved, the neutrino state $|\nu_f\rangle$ will evolve into a superposition of all the flavors after a time t. One can evaluate the probability that the neutrino born with flavor f will be found with flavor f' at a distance L.

$$
P(\nu_f \to \nu_{f'}; L) \approx \left|\sum_m U_{fm}e^{-i(M_m^2/2E_\nu)L}U^*_{f'm}\right|^2 \tag{2.31}
$$

This approximation holds for relativistic neutrinos. More rigorous quantum mechanical wave packet treatments of neutrino oscillations have been performed [119, 120, 118] and they yield the same result.

As an example, we consider the oscillation between the flavor and mass eigenstates of two neutrino flavors.

$$\begin{aligned} |\nu_e\rangle &= cos\theta|\nu_1\rangle + sin\theta|\nu_2\rangle \\ |\nu_\mu\rangle &= -sin\theta|\nu_1\rangle + cos\theta|\nu_2\rangle \end{aligned} \tag{2.32}$$

After time t they have evolved such that

$$\begin{aligned} |\nu_e\rangle &= cos\theta e^{-iE_1 t}|\nu_1\rangle + sin\theta e^{-iE_2 t}|\nu_2\rangle \\ |\nu_\mu\rangle &= -sin\theta e^{-iE_1 t}|\nu_1\rangle + cos\theta e^{-iE_2 t}|\nu_2\rangle \end{aligned} \tag{2.33}$$

The probability that an electron neutrino generated at t=0 remains an electron neutrino after travelling a distance L in time is given by:

$$\begin{aligned} P(\nu_e \rightarrow \nu_\mu) &= |\langle \nu_\mu | \nu_e(t)\rangle|^2 = sin^2 2\theta sin^2 \frac{\Delta m^2 L}{4E} \\ P(\nu_e \rightarrow \nu_e) &= |\langle \nu_e | \nu_e(t)\rangle|^2 = 1 - P(\nu_e \rightarrow \nu_\mu) \end{aligned} \tag{2.34}$$

$\Delta m^2 = |m_2^2 - m_1^2|$ is the difference between the squares of the masses of the two mass eigenstates. L is the length between the point of neutrino production and detection. E is the energy. One can define an oscillation length $L_{osc} = \frac{4\pi E}{\Delta m^2}$ which is the length needed to go from ν_e to ν_μ and back to ν_e. We note that the sensitivity of an experiment to Δm^2 is determined by its value of L/E, i.e. low energy, long baseline experiments (such as solar neutrino experiments) are sensitive to lower values of Δm^2. At large Δm^2, the oscillation probability becomes

$$P(\nu_e \rightarrow \nu_\mu) = \frac{1}{2} \times sin^2 2\theta \tag{2.35}$$

Sterile neutrinos are defined as right-handed fields that do not interact with matter through standard electroweak interaction. Sterile neutrinos can be final states of neutrino oscillations. If all the Majorana masses are small, active neutrinos can oscillate into sterile right-handed fields. Light sterile neutrinos can appear in particular *Seesaw* mechanisms

if additional assumptions are considered with some fine tuning. Alternatively, one can invoke new unknown interactions that produce sterile neutrinos. This, however, requires substantial additions to the Standard Model.

2.2.4 Neutrino Oscillations in Matter: MSW Effect

The fundamentals of neutrino oscillations in vacuum are discussed in the previous section where it was shown that neutrino oscillations are energy- dependent. When neutrinos propagate through matter the effect of coherent forward scattering must be taken into account. Neutrino propagation through matter differentiates neutrino flavors because matter is nearly exclusively composed of first generation quarks and leptons. This effect was first observed by L. Wolfenstein in 1978 [183]. Wolfenstein observed that if there exists an interaction through which neutrinos can change flavor, this flavor change can be enhanced if neutrinos travel through matter. In 1984 S.P. Mikheyev and A.Yu. Smirnov noticed that for specific oscillation and matter density parameters this enhancement could develop a resonance behavior [145]. This effect is now known as the Mikheyev-Smirnov-Wolfenstein (MSW) matter oscillation effect.

When electron neutrinos propagate through matter they interact through both the charged-current interaction and the neutral-current interaction. Due to those charged-current interactions electron neutrinos acquire a potential energy

$$V_{\nu_e} = \sqrt{2} G_F N_e \tag{2.36}$$

where N_e is the electron density of the medium. We assume that the medium is unpolarized and at rest. In the two-neutrino mixing case, the evolution of flavor content as a function of propagation can be described by

$$i\frac{d}{dx}\begin{pmatrix}\nu_e \\ \nu_x\end{pmatrix} = \frac{1}{2E} M^2 \begin{pmatrix}\nu_e \\ \nu_x\end{pmatrix} \tag{2.37}$$

The matrix M^2 can be written as

$$M^2 = \frac{1}{2}\left[R\begin{pmatrix}-\Delta m^2 & 0\\ 0 & \Delta m^2\end{pmatrix}R^T + 2E\begin{pmatrix}\sqrt{2}G_F N_e & 0\\ 0 & -\sqrt{2}G_F N_e\end{pmatrix}\right] \tag{2.38}$$

where R is defined by the relation of the local mass eigenstates, ν_1 and ν_2, and the flavor states, ν_e and ν_x. These states are only true eigenstates if the density is constant.

$$\begin{pmatrix}\nu_e\\ \nu_x\end{pmatrix} = R\begin{pmatrix}\nu_1\\ \nu_2\end{pmatrix}, \begin{pmatrix}\nu_1\\ \nu_2\end{pmatrix} = R^T\begin{pmatrix}\nu_e\\ \nu_x\end{pmatrix} \tag{2.39}$$

The mass eigenstates can be obtained by diagonalizing M^2.

$$R^T M^2 R = \frac{1}{2}\begin{pmatrix}-\Delta_m & 0\\ 0 & \Delta_m\end{pmatrix} \tag{2.40}$$

where $\Delta_M = \Delta m^2\sqrt{(a - cos2\theta)^2 + sin^2 2\theta}$ and $a = 2\sqrt{2}EG_F N_e/\Delta m^2$. Maximal mixing occurs if $a = cos2\theta$.

2.2.5 CP-Violation in the Lepton Sector

Quark mixing is a well established feature of the Standard Model. The elements of the quark mixing matrix, the CKM matrix have been measured with great precision. CP-violation has been found in many systems and is related to the mixing of quarks through the unitarity triangle. The area of the unitarity triangle is a measure of CP-violation.

Measurement of CP-violation in the lepton sector is one of the main challenges in particle physics. For three neutrinos there is a unique complex phase in the lepton matrix, δ_D, which produces observable CP-violating effects. If neutrinos are Majorana particles, two additional CP-violating phases exist. The phase δ_D leads to CP-asymmetry as well as T-asymmetry.

$$\text{CP} - \text{Asymmetry}: \qquad P(\nu_\alpha \to \nu_\beta) \neq P(\overline{\nu}_\alpha \to \overline{\nu}_\beta) \tag{2.41}$$

$$\text{T} - \text{Asymmetry}: \qquad P(\nu_\alpha \to \nu_\beta) \neq P(\nu_\beta \to \nu_\alpha) \tag{2.42}$$

$$\tag{2.43}$$

From the measurements of CP-conserving quantities one can determine the asymmetry as well as the phase δ_D. Alternatively, one can measure the area of the unitarity triangle. In the 3-ν scheme the flavor eigenstates ν_f and the mass eigenstates ν_m are related by the Maki-Nakagawa-Sakata neutrino mixing matrix, U_{MNSP}. Unitarity implies

$$U_{e1}U^*_{\mu 1} + U_{e2}U^*_{\mu 2} + U_{e3}U^*_{\mu 3} = 0 \tag{2.44}$$

$$U_{e1}U^*_{\tau 1} + U_{e2}U^*_{\tau 2} + U_{e3}U^*_{\tau 3} = 0 \tag{2.45}$$

$$U_{\tau 1}U^*_{\mu 1} + U_{\tau 2}U^*_{\mu 2} + U_{\tau 3}U^*_{\mu 3} = 0 \tag{2.46}$$

At present we cannot construct the unitarity triangle. Knowledge of the mixing matrix is limited to a few elements of U_{MNSP}. Reconstruction of the unitarity triangle will require a series of measurements which differ from direct measurements of CP- and T-asymmetries [115]. Under certain conditions one might be able to establish CP-violation in the lepton sector with precise measurements of neutrino oscillation parameters. As a measure of CP-violation we can consider the quantity $\Delta P = P(\nu_e \rightarrow \nu_\mu) - P(\overline{\nu}_e \rightarrow \overline{\nu}_\mu)$.

$$\begin{aligned}\Delta P &= P(\nu_e \rightarrow \nu_\mu) - P(\overline{\nu}_e \rightarrow \overline{\nu}_\mu) \\ &= 16 \sin\theta_{12}\cos\theta_{12}\sin\theta_{13}\cos\theta^2_{13}\sin\theta_{23}\cos\theta_{23} \\ &\quad \sin\delta \ \sin\left(\frac{\Delta m^2_{12}}{4E}L\right)\sin\left(\frac{\Delta m^2_{13}}{4E}L\right)\sin\left(\frac{\Delta m^2_{23}}{4E}L\right)\end{aligned} \tag{2.47}$$

One finds that observation of CP-violation in neutrino oscillations is only possible if Δm^2_{12}, $\sin\theta_{12}$, as well as θ_{13} are large enough.

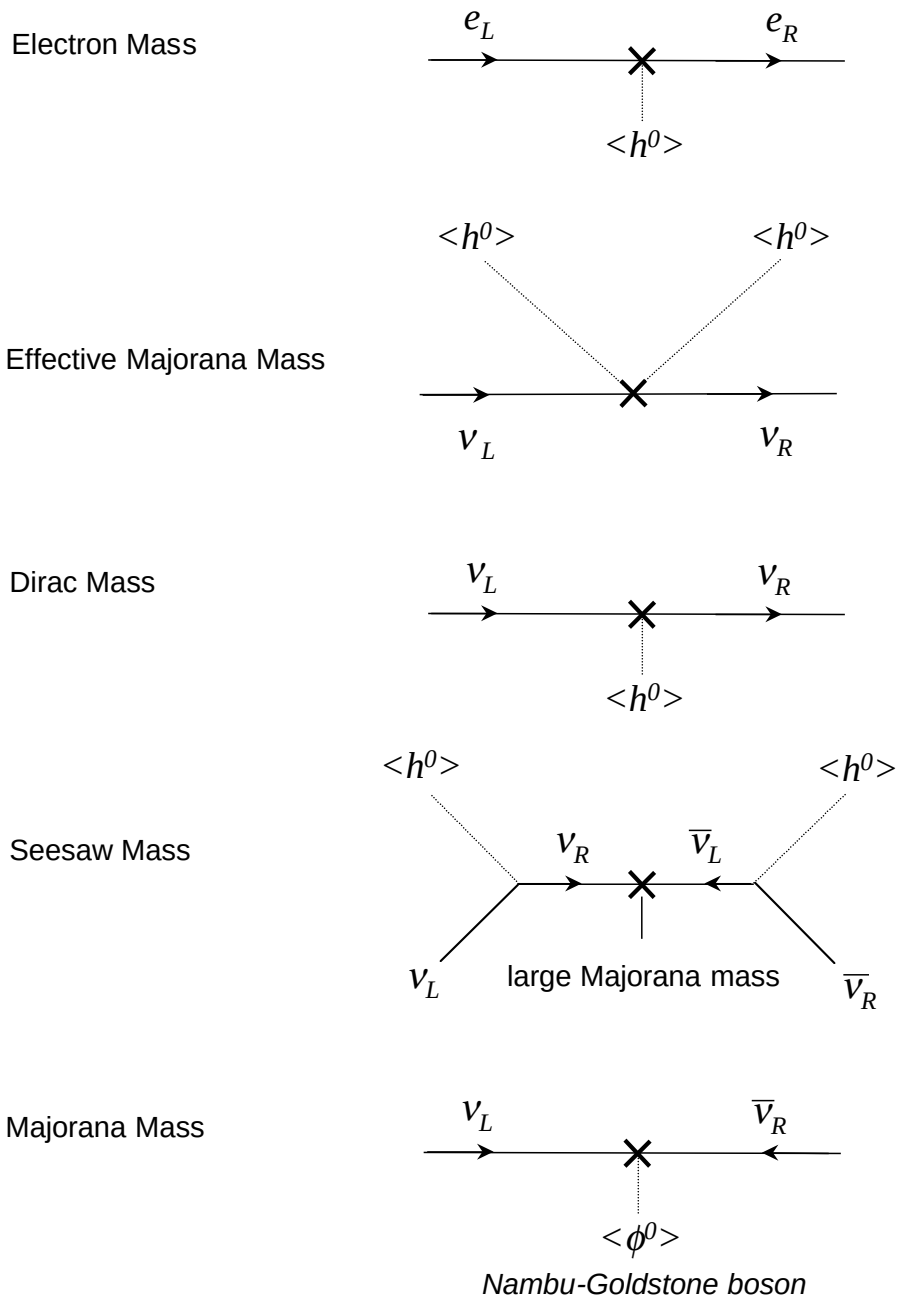

Figure 2.2: Neutrino and lepton mass terms. Illustration of the fundamental mass-generating interactions.

2.2.6 Neutrinoless Double Beta-Decay

Another unique signature of massive neutrinos is neutrinoless double β-decay, also known as $\beta\beta(0\nu)$.

$$(A, Z) \rightarrow (A, Z+2) + 2e^{-} \tag{2.48}$$

This requires the transition $(\overline{\nu}_e)_R \rightarrow \nu_{eL}$ which is a second-order weak process with a suppression factor m_M/E in the amplitude due to the change of spin and an amplitude proportional to the mass m_M. The process is suppressed by the square of this. For neutrinoless double β-decays to occur the required L violation can only come from the neutrino mass. See Figure 2.3 for an illustration of this process. Thus, neutrinoless double β-decay distinguishes between Majorana and Dirac masses. The L violation which is necessary to make this process happen can only occur if the Majorana mass term is non-zero. Therefore, the observation of neutrinoless double β-decay would be evidence for new physics, and possibly a signature of massive neutrinos. In principle, double β-decay can occur by various mechanisms that do not involve mass, such as right-handed currents and Higgs exchanges. The existence of right-handed currents would still allow Majorana neutrinos to be massless. However, as long as the weak interactions are described by a gauge theory right-handed currents imply the existence of massive Majorana neutrinos.

The experimental signature of neutrinoless double β-decay is a peak in the combined electron spectrum at the Q-value of the reaction. The lifetime measurement is translated into an effective Majorana mass using nuclear structure calculations which in turn can be used to set upper limits on the neutrino mass. Currently the best limit comes from the ^{76}Ge experiments and they indicate that $\langle m_\nu \rangle < 0.3 - 1$ eV [42]. Recent claims of the observation of neutrinoless double β-decay are controversial [130, 51].

2.2.7 Neutrino Magnetic Moments

Besides neutrino oscillations and lepton-number violating processes the magnetic dipole moment is another probe of possible new interactions. A spin-1/2 particle can have four

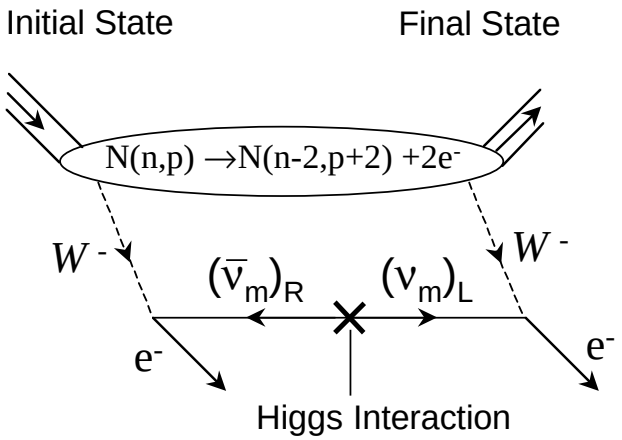

Figure 2.3: Neutrinoless double β-decay, $\beta\beta(0\nu)$.

moments, a J=0 charge moment and three J=1 moments. The magnetic moment, the electric dipole moment (P and CP violating), and the anapole moment are the J=1 moments. Neutrinos are chargeless. Dirac neutrinos can have all three diagonal J=1 moments. Majorana neutrinos have identically zero magnetic and electric dipole moments but they have a toroid dipole moment which is very similar to a nuclear anapole moment [35]. Flavor transition magnetic moments are allowed, however, in general for both Dirac and Majorana neutrinos. In the Standard Model electroweak theory, extended to allow for Dirac neutrino masses, the neutrino magnetic dipole moment is nonzero.

$$\mu_\nu = \frac{3eG_F m_\nu}{8\pi^2\sqrt{2}} = 3 \times 10^{-19}(m_\nu/1 \text{ eV})\mu_B \tag{2.49}$$

where μ_B is the Bohr magneton. The proportionality of μ_ν to the neutrino mass is due to the absence of any interaction of ν_R other than the Yukawa coupling which generates its mass. In the absence of additional symmetries a large magnetic moment is incompatible with a small neutrino mass. In left-right symmetric theories μ_ν is proportional to the charged-lepton mass. Neutrino magnetic moments with values of 10^{-13}-10^{-14} μ_{uB} are still too small to have significant astrophysical consequences.

For Dirac neutrinos, the magnetic moment is diagonal. If the lepton flavor L_f is conserved the matrix describing the neutrinos' magnetic moment does not have any non-zero off-diagonal elements which would connect neutrinos of different flavor. In an interaction with a transverse magnetic field there can only be a spin-flip interaction of type $\nu_{x,L} \rightarrow \nu_{x,R}$ but not any neutrino flavor transition. In the case of Majorana neutrinos, the neutrinos' magnetic moment can have non-zero off-diagonal elements which connect neutrinos of different flavors and spin-flavor transitions of type $\nu_{x,L} \rightarrow \overline{\nu}_{y,R}$ result.

2.2.8 Lepton Mixing and Non-Conservation

In the Standard Model lepton number L is a conserved quantity. If neutrinos are massive and have a mass-generating interaction, such as coupling to the Higgs field or a new type of Nambu-Goldstone boson, the neutrino flavor can change. As a result, lepton mixing can occur in which a lepton of flavor l transforms into a lepton of different flavor i, where $l \neq i$. Also, it becomes possible for electron capture and inverse β-decay to proceed such that lepton number is not conserved.

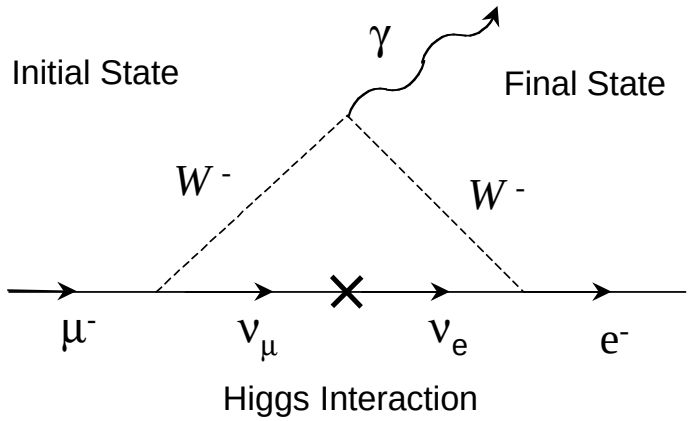

Figure 2.4: Lepton mixing.

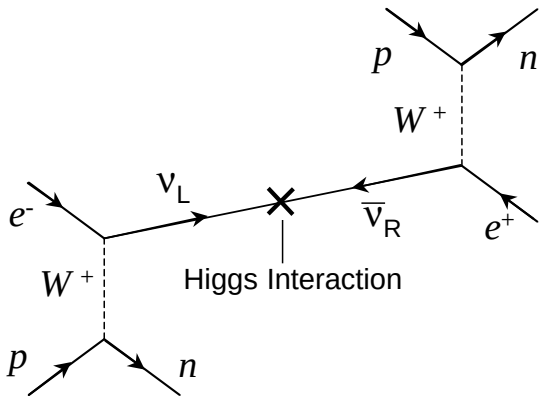

Figure 2.5: Lepton non-conservation.

2.2.9 Indications of Neutrino Oscillations in Atmospheric and Terrestrial Oscillation Experiments

A variety of experiments have measured the particle properties of neutrinos and searched for signatures of neutrino oscillations, or other signs of massive neutrinos. Kinematical searches have mostly been able to set limits on the Dirac or Majorana mass of neutrinos [53]. With one exception reactor and accelerator experiments have been null experiments and only constrained the entries in the generalized neutrino mixing matrix. There are strong indications for the oscillation of atmospheric neutrinos from the proton-decay experiments. Below we will discuss the indications for neutrino oscillations from atmospheric and beamstop neutrinos.

Atmospheric Neutrinos: Strong indication for neutrino oscillations comes from observation of atmospheric neutrinos. These neutrinos are the decay products of hadronic showers produced by cosmic ray interactions in the atmosphere. The pion production in the atmosphere determines the flux of atmospheric neutrinos incident on Earth. Around 1 GeV, where the product of flux and neutrino charged-current interaction cross-section reaches a maximum, the atmospheric neutrino flux is about 1 $\mathrm{cm}^{-2}\mathrm{s}^{-1}$. Supposing all the pions and muons decay we then expect to observe about two μ-like neutrinos for each e-like neutrino. The ratio $\nu_e\,/\overline{\nu}_e$ is expected to be close to μ^+/μ^-, about 1.2 at 1 GeV.

$$\begin{aligned} \pi^{\pm} \rightarrow \quad & \mu^{\pm} + \nu_{\mu}\,(\overline{\nu}_{\mu}\,) \\ & \downarrow \\ & \mu^{\pm} \rightarrow e^{\pm} + \nu_e\,(\overline{\nu}_e\,) + \overline{\nu}_{\mu}\,(\nu_{\mu}\,) \end{aligned} \tag{2.50}$$

Several effects influence this prediction. They include the muon decay length at high energies above 2.5 GeV, the muon energy loss, the geomagnetic cut-off, and the variations of the cosmic ray flux with the solar cycle. Experiments measure the flux of atmospheric neutrinos as well as the zenith-angle distribution. To compare between various experiments while taking into account the different detection efficiencies, the measurement of the flux of atmospheric neutrinos is usually expressed in the experimental "ratio of ratios", R_{atm}.

$$R_{atm} = \frac{(\nu_\mu + \overline{\nu}_\mu)/(\nu_e + \overline{\nu}_e)_{Data}}{(\nu_\mu + \overline{\nu}_\mu)/(\nu_e + \overline{\nu}_e)_{MC}} \tag{2.51}$$

where $(\nu_\mu + \overline{\nu}_\mu)/(\nu_e + \overline{\nu}_e)$ denotes the ratio of the numbers of μ-like to e-like neutrino interactions observed in the data or predicted by simulations. R_{atm} is an estimator of the atmospheric neutrino flavor ratio. Statistically significant, low values of the ratio R_{atm} have been obtained in the first generation detectors Kamiokande [92], IMB-3 [88], Soudan-2 [109], and MACRO [97]. The NUSEX [102] and Frejus experiments [83] have reported results consistent with no deviation from unity but also consistent with other experiments. The results of the modern Super-Kamiokande experiment [168] are completely consistent with the data from IMB and Soudan but have much higher accuracy. Super-Kamiokande has been able to confirm that the flux of muon neutrinos going up is smaller than that of downgoing neutrinos. The results of the neutrino flux measurements at the atmospheric neutrino experiments are summarized in Table 2.2.

Table 2.2: Results from the atmospheric neutrino experiments.

Experiment	$R_{atm} \pm$ (stat.) $\pm$ (syst.)	Ref.
Frejus	$0.99 \pm 0.13 \pm 0.08$	[84]
IMB-3	$0.54 \pm 0.05 \pm 0.11$	[87, 89, 90]
Kamiokande (sub-GeV)	$0.60^{+0.06}_{-0.05} \pm 0.05$	[93, 95, 94]
Kamiokande (multi-GeV)	$0.57^{+0.08}_{-0.07} \pm 0.08$	[93, 95, 94]
Macro	$0.73 \pm 0.05 \pm 0.12$	[98, 100, 99]
NUSEX	1.00 ± 0.3 (stat + syst)	[103]
Soudan-2	$0.68 \pm 0.11^{+0.05}_{-0.07}$	[111, 110]
Super-Kamiokande (sub-GeV)	$0.65 \pm 0.02 \pm 0.05$	[112, 114, 168]
Super-Kamiokande (multi-GeV)	$0.67 \pm 0.03 \pm 0.08$	[112, 114, 168]

The strongest evidence for the oscillation comes from the zenith angle distribution of the atmospheric neutrino flux and the up-down asymmetry of atmospheric ν_μ flux. The

measured distribution of muon neutrinos differs significantly from the distribution expected for massless neutrinos and the downward flux of atmospheric muon neutrinos is much larger. Only a zenith-angle dependent transformation of neutrino flavors can explain this result. Upgoing neutrinos traverse a much longer distance and have time to oscillate, whereas downward going neutrinos do not. For electron neutrinos the event rate is independent of direction and the solid angle.

Since no asymmetry is seen for electron neutrinos, the result cannot be explained by $\nu_e \rightarrow \nu_\mu$ oscillations but is more likely $\nu_\mu \rightarrow \nu_\tau$ or $\nu_\mu \rightarrow \nu_s$, where ν_s is some sterile state. There are three arguments against sterile solutions in a 2-ν scheme: Matter effects are absent, as they would be for $\nu_\mu \rightarrow \nu_\tau$. Oscillations into sterile species is disfavored because of the lack of sterile neutrino matter potential in the Earth. The π_0 production in the neutral-current channel agrees with $\nu_\mu \rightarrow \nu_\tau$ to about 25%, and there is some (statistically weak) indication for reconstructed τ's in the Super-Kamiokande experiment. The hypothesis of $\nu_\mu \rightarrow \nu_\tau$ oscillations fits well the angular distribution of the atmospheric neutrino flux. Apart from neutrino oscillation and neutrino decay, no other consistent particle physics explanation has been proposed to explain the atmospheric neutrino result.

Reactor and Accelerator Neutrinos: In 1994 the Liquid Scintillator Neutrino Detector (LSND) beamstop experiment at Los Alamos reported indications of possible $\overline{\nu}_\mu \rightarrow \overline{\nu}_e$ oscillations. LSND detects neutrinos produced in a proton target and a beam stop at the Los Alamos Meson Physics Facility LAMPF. Both the $\overline{\nu}_\mu \rightarrow \overline{\nu}_e$ and the $\nu_\mu \rightarrow \nu_e$ channels are accessible in the search for oscillations. An intense flux of 800 MeV protons produces pions in a water target with a ratio $\pi^+/\pi^- = 8$. Most of the positive pions decay at rest through the chain

$$\pi^+ \rightarrow \quad \mu^+ + \nu_\mu \tag{2.52}$$

$$\downarrow \tag{2.53}$$

$$e^+ + \nu_e + \overline{\nu}_\mu \tag{2.54}$$

generating a flux of $\overline{\nu}_\mu$ with a maximum energy of 52.8 MeV. Electron anti-neutrinos are produced in the π^- decay sequence but most of the π^- are captured before they decay. Only

5% decay in flight. The relative yield of $\overline{\nu}_e$ is estimated at 7.8×10^{-4}. The results of the LSND experiment [96], however, need independent confirmation from other experiments. Large portions of the region of mass differences and mixing angles indicated by LSND have been excluded by the KARMEN Experiment [27, 47]. A definitive answer will have to await new experiments such as MiniBooNE [101] at Fermilab.

Other reactor or accelerator experiments have found no unambiguous indications of neutrino oscillations. Amongst all other experiments, the CHOOZ experiment is of particular interest as it has studied $\overline{\nu}_e \rightarrow \nu_x$ in disappearance mode and set the best constraints for $\nu_e \rightarrow \nu_\mu$ oscillations of atmospheric neutrinos. Based on the CHOOZ results [65] one obtains $\sin\theta_{13} \leq 0.16$ for $\Delta m^2 = 3 \times 10^{-3}$ eV^2 which corresponds to the region that fits the oscillation of atmospheric neutrinos.

2.2.10 Summary

Neutrino experiments have provided valuable results for the understanding of the weak interaction. The existence of three flavors of light, standard-model neutrinos is well established. While neutrinos are massless in the Standard Model we have seen that neutrinos are likely to have mass in the context of higher-energy Grand Unified Theories. The propagation of massive neutrinos leads to flavor conversion or the "oscillation" between neutrino flavor states. The search for neutrino oscillation is a sensitive and powerful technique to search for massive neutrinos and non-standard neutrino properties. Many experimental results are compatible with massive, oscillating neutrinos and give an indication for the possible flavor conversion. Measurements of the atmospheric neutrino flux have provided strong indication for neutrino oscillation. Model-independent evidence for neutrino flavor conversion and mixing in the lepton sector can be obtained by measuring directly the original and the oscillated component of neutrinos produced in reactors, at beamstops, in the atmosphere, or in the Sun. Modern solar neutrino experiments, such as the Sudbury Neutrino Observatory, may hold the key to discovering the flavor conversion of neutrinos by measuring the flux of electron and non-electron solar neutrinos on Earth.

2.3 Solar Neutrinos as a Probe of Neutrino Oscillations

Solar Neutrinos are produced in the light element fusion reactions that power the Sun. Using input from astronomical observation, nuclear physics and astrophysics, models have been developed that allow us to make detailed predictions of the life cycle of stars. Solar models trace the evolution of the Sun over the past 4.7 billion years of main sequence burning, thereby predicting the present-day temperature and composition profiles of the solar core. It is believed that thermonuclear reaction chains generate the solar energy. Standard Solar Models (SSM) predict that over 98% of the solar energy is produced from the *pp* chain conversion of four protons into ^{4}He, $4p \rightarrow {}^4\mathrm{He} + 2\mathrm{e}^+ + 2\nu_e$, while the proton burning through the CNO cycle contributes the remaining 2%. The sequence of light element fusion reactions is shown in Figures 2.7 and Figure 2.8

Solar models are constrained to produce today's solar radius, mass, and luminosity. The predictions of these models are in good agreement with recent observations from helioseismology and other observables.

The principal neutrino-producing reactions of the *pp* chain are summarized in Table 2.3. Solar neutrinos are either produced in β-decays or in electron capture processes. The endpoint energy of the β-spectra or the energy of the lines are given as E_ν^{max}. In the main CNO cycle, neutrinos are produced in the β^+-decay of $^{13}\mathrm{N} \rightarrow {}^{13}\mathrm{C} + e^+ + \nu_e$ and $^{15}\mathrm{O} \rightarrow {}^{15}\mathrm{N} + e^+ + \nu_e$ with energies of $E_\nu \leq 1.199$ MeV and ≤ 1.732 MeV respectively.

According to Standard Solar Models only 0.01% of the total solar neutrino emission is produced in the β^+-decay of $^8\mathrm{B} \rightarrow {}^8\mathrm{Be}^* + \mathrm{e}^+ + \nu_e$. Figure 2.6 shows the decay scheme of ^{8}B. Creation of ^{8}B is driven by the ^{7}Be(p,γ)^{8}B reaction. Flux predictions for solar neutrinos have reached an accuracy of up to 1% for *pp* neutrinos and $\sim$ 20% for ^{8}B neutrinos. The uncertainty in the ^{8}B flux prediction is driven by the experimental uncertainty in the cross-section for the ^{7}Be(p,γ) process.

Neutrinos from the beta decay of ^{8}B dominate the solar neutrino spectrum between 5-15 MeV. The shape of the neutrino energy spectrum from a single beta-decaying source is well known and independent of solar physics to an accuracy of 1 part in 10^6. In a rare branch of the pp-chain in the Sun, ^{3}He and proton fuse forming the reaction $^3\mathrm{He} + \mathrm{p} \rightarrow {}^4\mathrm{He}$

Table 2.3: Solar neutrino-producing reactions and Standard Solar Model (SSM) flux predictions in units of cm^{-2} s^{-1}. The predictions listed in this table are from BPB00 [11].

Source	Termination (%)	τ (yr)	E_ν^{max} (MeV)	SSM (BPB00)
$p + p \rightarrow {}^2\mathrm{H} + e^+ + \nu_e$	99.75	10^{10}	0.42	5.95×10^{10}
${}^7\mathrm{Be} + e^- \rightarrow {}^7\mathrm{Li} + e^+ + \nu_e$	13.5	0.11	0.863 (90%)	4.34×10^9
	1.5	1	0.385 (10%)	0.48×10^9
${}^{13}\mathrm{N} \rightarrow {}^{13}\mathrm{C} + e^+ + \nu_e$		10^5	1.20	5.48×10^8
$p + \mathrm{e}^- + p \rightarrow {}^2\mathrm{H} + \nu_e$	0.25	10^{12}	1.44	1.4×10^8
${}^{15}\mathrm{O} \rightarrow {}^{15}\mathrm{N} + e^+ + \nu_e$		10^{-1}	1.73	4.80×10^8
${}^{17}\mathrm{F} \rightarrow {}^{17}\mathrm{O} + e^+ + \nu_e$		10^{-5}	1.74	5.63×10^3
${}^8\mathrm{B} \rightarrow {}^8\mathrm{Be} + e^+ + \nu_e$	0.02	10^{-8}	$\sim$15	5.05×10^6
${}^3\mathrm{He} + p \rightarrow {}^4\mathrm{He} + e^+ + \nu_e$	0.00003	10^{12}	18.77	9.30×10^3

$+ \mathrm{e}^+ + \nu_e$. This *hep* process produces high-energy solar neutrinos with an energy of up to 18.77 MeV [2]. The contribution of *hep* neutrinos to the total solar neutrino flux is negligible.

The reliable estimation of the *hep* cross-section has been a long-standing challenge in nuclear physics and a direct measurement of the flux of solar *hep* neutrinos has not been performed yet. Therefore, a measurement of the flux of *hep* neutrinos at the Sudbury Neutrino Observatory is of interest to astrophysics and nuclear physics alike. SNO is able to detect *hep* neutrinos by searching for events beyond the endpoint of the ${}^8\mathrm{B}$ spectrum.

Over the past 30 years the flux of electron neutrinos from the Sun has been detected and measured in a number of experiments using a variety of experimental techniques and approaches. A summary of the detection methods and the experimental results obtained prior to SNO is tabulated in Table 2.4. All solar neutrino experiments found indications for a suppression of the solar neutrino flux. Because of the different detection thresholds of the experiments data from five experiments provided information across the entire solar neutrino

[2]The highest-energy solar neutrinos are produced in the reaction ${}^3\mathrm{He} + e^- + p \rightarrow {}^4\mathrm{He} + \nu_e$ which emits monenergetic neutrinos with an energy of 19.79 MeV

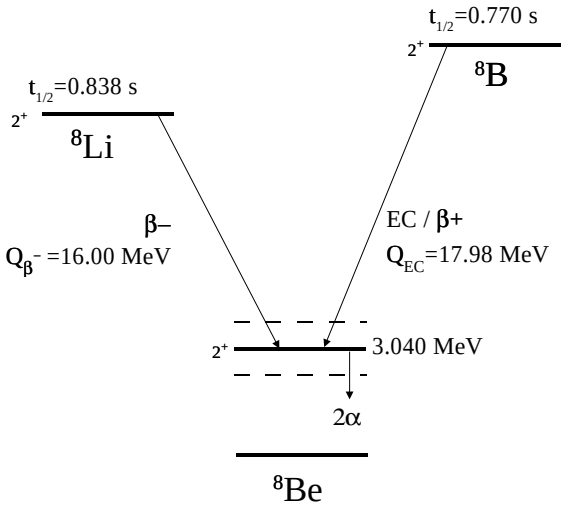

Figure 2.6: Decay scheme of ^{8}B and ^{8}Li.

spectrum. In all cases the experimental results fall significantly below the predictions of the standard solar model. These results can be combined to limit the principal solar neutrino fluxes under the assumption that no new particle physics distorts the spectral shape of the *pp* and ^{8}B neutrinos. Because each experiment is sensitive to different but overlapping regions of the solar neutrino spectrum, a coarse neutrino spectroscopy of the Sun has been made. The individual contributions to the total neutrino flux of the pp, ^{7}Be, and ^{8}B neutrinos can be estimated. One finds the following results for the measured fluxes Φ^{Exp}:

$$\Phi_{pp}^{Exp} \sim 0.9\Phi_{pp}^{SSM} \tag{2.55}$$

$$\Phi_{7Be}^{Exp} \sim 0 \tag{2.56}$$

$$\Phi_{8B}^{Exp} \sim 0.47\Phi_{8B}^{SSM} \tag{2.57}$$

These observations seem difficult to reconcile with plausible solar models. We also notice that the individual fluxes show an energy dependent suppression of the solar neutrino spectrum.

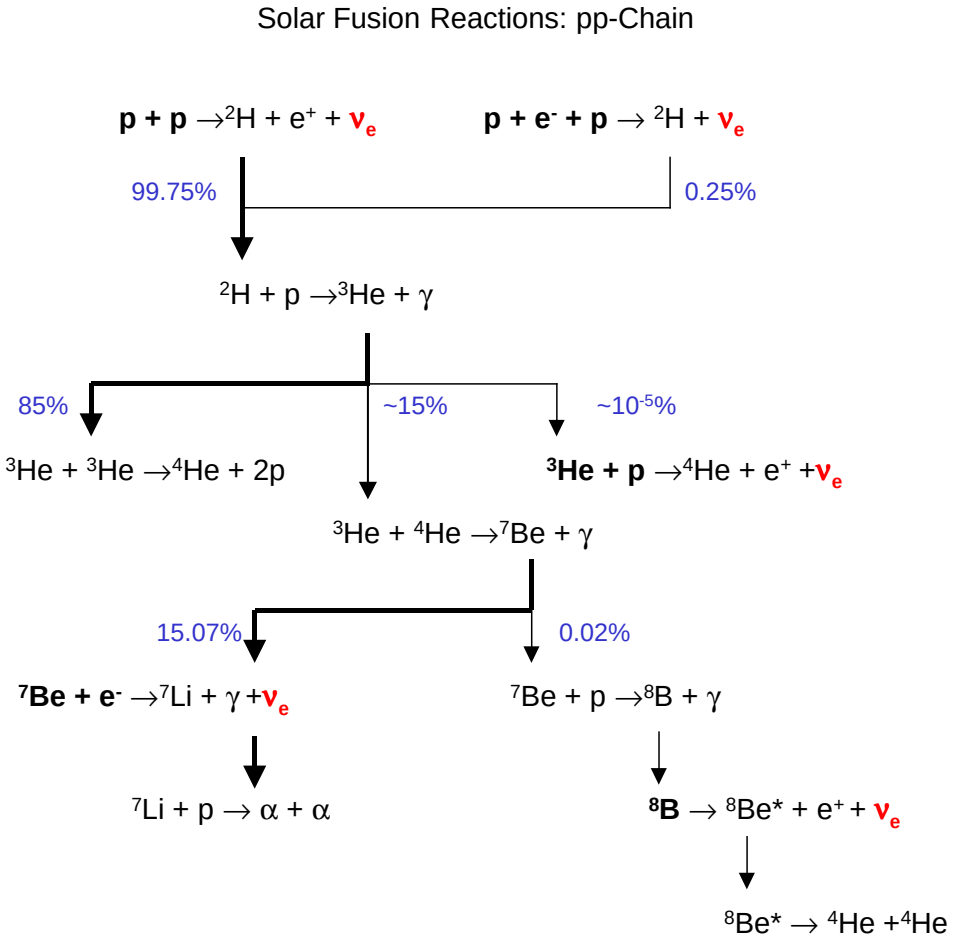

Figure 2.7: Light element fusion reactions in the Sun. The solar pp-chain.

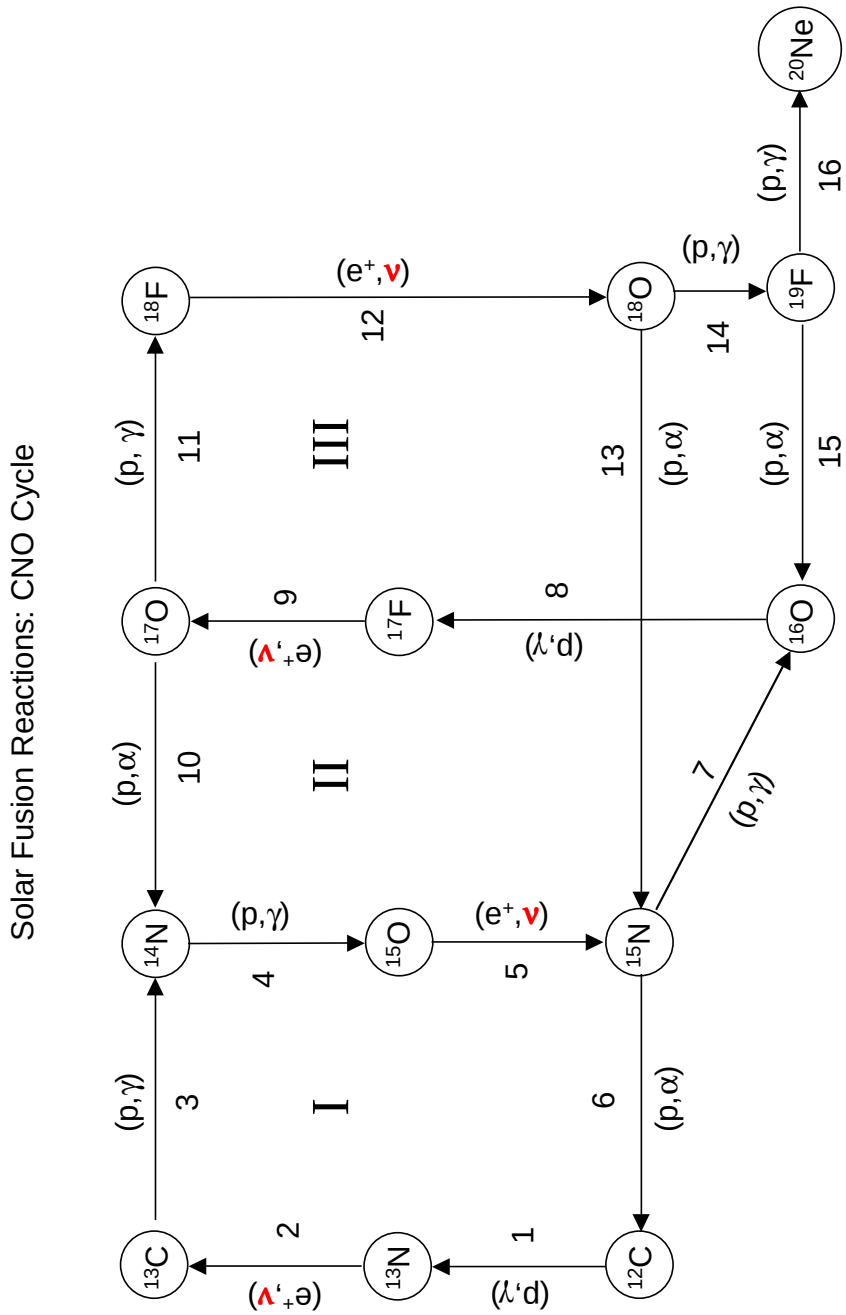

Figure 2.8: Light element fusion reactions in the Sun. The solar CNO-cycle.

Table 2.4: Solar Neutrino Experiments in 2001 before SNO: The capture rates for the Cl-Ar and Ga experiments are given in SNU while the flux from the Kamiokande and Super-Kamiokande experiments is reported in 10^6 cm^{-2} s^{-1}. For all values tabulated here the first error is the statistical uncertainty and the second error gives the systematic error.

Detector	Experiment	Result	SSM BPB00	Ref.
Chlorine-Argon	Homestake	$2.56 \pm 0.16 \pm 0.16$	$7.6^{+1.3}_{-1.1}$	[48]
$^{37}Cl + \nu_e \rightarrow {}^{37}Ar + e^-$				
Water	Kamiokande	$2.80 \pm 0.19 \pm 0.33$	$5.19^{+0.93}_{-0.73}$	[91]
$\nu_e + e^- \rightarrow \nu_e + e^-$	Super-Kamiokande	$2.32 \pm 0.03^{+0.08}_{-0.07}$	$5.19^{+0.93}_{-0.73}$	[113]
Gallium	SAGE	$70.8^{+5.3+3.7}_{-5.2-3.2}$	128^{+9}_{-7}	[104]
$^{71}Ga + \nu_e \rightarrow {}^{71}Ge + e^-$	GALLEX I-IV	$77.5 \pm 6.2^{+4.3}_{-4.7}$	128^{+9}_{-7}	[85]
	GNO I	$65.8^{+10.2+3.4}_{-9.6-3.6}$	128^{+9}_{-7}	[86]
	GALLEX+GNO	$77.5 \pm 6.2^{+4.3}_{-4.7}$	128^{+9}_{-7}	[86]

Unless the experiments are seriously in error, there must be some problem with either our understanding of the Sun or neutrino properties in the Standard Model of particle physics. Standard Solar Models [11] cannot account for the data and possible non-standard solar models are constrained by helioseismological studies. The incompatibility of the current experimental results can be demonstrated in a model-independent analysis of the Solar Neutrino Problem [124, 125, 126] which illustrates that no SSM change can completely remove the discrepancy with experiment. If one assumes undistorted neutrino spectra no combination of *pp*, ^{7}Be, and ^{8}B neutrino fluxes fits the experimental results well. Tests, independent of any solar model, can be made of whether solar neutrino experiments are consistent with the minimal standard model of stable, massless neutrinos. If the experimental uncertainties are correctly estimated and the Sun is generating energy by light-element fusion in quasistatic equilibrium, the probability of a standard-physics solutions is less than 2%. Even when the luminosity constrained is abandoned, the probability is not more than 4%. In summary, the long-standing solar neutrino problem states states that either Standard Solar Models are incorrect and do not predict correctly the neutrino production and

emission from the Sun (in which case the current experimental results are inconsistent at the 96% level) or solar neutrinos undergo a flavor changing transformation on their way from the Sun to Earth, and the electron solar neutrino flux detected in all solar neutrino experiments before SNO is only a component of the total solar neutrino flux.

These observations suggest that the solution to the solar neutrino problem may involve new physics beyond the Standard Model. Particle physics explanations involving neutrino oscillations, neutrino decay, and neutrino magnetic moments can account for the suppression of intermediate energy neutrinos in the solar neutrino spectrum. If neutrinos are massive they can undergo flavor transformation which would could reduce the observed flux of solar electron neutrinos on Earth. In case of mixing between 2 neutrinos, neutrino oscillations in vacuum require a large mixing angle and a seemingly unnatural fine tuning of neutrino oscillation length with the Sun-Earth distance for intermediate energy neutrinos. Vacuum mixing between 3 neutrino states is not ruled out by the current solar neutrino data and can explain the experimental observations. Oscillations based on level-crossing effects, such as Mikheyev-Smirnov-Wolfenstein (MSW) and general Resonant Spin Flavor Precession (RSFP) effects require no fine tuning of either the mixing parameters or the neutrino mass differences. Resonance Spin Flavor Precession can occur in the presence of solar matter and magnetic fields. The MSW mechanism explains naturally the suppression of intermediate energy neutrinos, leaving the low energy pp neutrino flux intact and high energy ^{8}B neutrinos only weakly suppressed.

Based on the data from solar neutrino experiments prior to SNO we can only conclude that neutrino oscillations is a plausible mechanism to explain the observed suppression of the solar electron neutrino flux. The combined results from different experiments make it very likely that a possible solution within the minimal Standard Model cannot be found. However, none of the experiments by itself requires solar neutrinos to have new properties. It is the goal of the Sudbury Neutrino Observatory to resolve this long-standing puzzle and probe in a model-independent way the particle properties of solar neutrinos.

It should be mentioned that the anomalies observed in the solar neutrino flux, atmospheric flux, and low energy accelerator experiments cannot all be explained consistently with neutrino oscillations without introducing a new light, sterile species. The observation

of these different experiments lead to 3 different mass differences between neutrino mass states, Δm^2, that cannot be accommodated by 3 neutrinos in general. In a 3-ν scheme the positive evidence for the oscillation of beamstop neutrinos in the LSND experiment is incompatible with the neutrino oscillation parameters required to explain the atmospheric neutrino anomaly and the solar neutrino problem. While efforts are underway to confirm directly the results from the LSND experiment with the MiniBooNE experiment the Sudbury Neutrino Observatory may have the potential to shed light on the question of sterile neutrinos through possible diurnal variations in its measurement of the neutral-current interaction rate.

2.4 Search for Signatures of New Physics in the Sudbury Neutrino Observatory

The Sudbury Neutrino Observatory (SNO) is a water Čerenkov detector using a 1000 t of ultra-pure heavy water as its primary target medium. The D_2O is contained in a central acrylic vessel surrounded by some 9456 photomultipliers (PMT). The acrylic vessel and the PMT array are submerged in an underground cavity filled with 7.5 kilotons of light water. The light water provides additional support to the freely suspended acrylic vessel as well as shielding from radioactive backgrounds from the PMT array and the rockwall. The experiment is located 2 km underground in the Creighton Mine of Inco, Ltd. in Sudbury, Ontario, Canada. A description of the experiment and technical details are given in [105].

A unique set of interactions allows the SNO experiment to study the particle properties of solar neutrinos as well as test predictions of Standard Solar Models. The results from this experiment are of interest for particle physics and astrophysics alike. The results from the SNO experiment may give first conclusive evidence for the non-standard properties of solar neutrinos and resolve the long-standing Solar Neutrino Problem.

2.4.1 Detection of Solar Neutrinos in SNO

Solar neutrinos produced in the ^{8}B-decay $^8\mathrm{B} \rightarrow {}^8\mathrm{Be} + e^+ + \nu_e$ or in the *hep* process $^3\mathrm{He} + p \rightarrow {}^4\mathrm{He} + e^+ + \nu_e$ reaction interact in three different reactions with the heavy and light water in SNO. Neutrinos can dissociate the deuterium in the heavy water target via the charged-current (CC) reaction which is only sensitive to electron-type neutrinos, ν_e, or through the neutral-current (NC) interaction. In addition, electron neutrinos can scatter elastically off the electrons in both the D_2O and H_2O. The Čerenkov electrons produced in the charged-current interaction or the elastic scattering are detected in the spherical array of photomultipliers that surround the acrylic vessel. The signature of the neutral-current interaction of neutrinos is a neutron which thermalizes in the heavy water. In pure D_2O, the neutron will capture with $\sim 29\%$ probability on deuterium in the heavy water and release a 6.25-MeV γ signal. In future phases of the SNO experiment, the neutron will be detected indirectly through the capture on ^{35}Cl or by means of a specially designed discrete array of ^{3}He-filled neutron detectors.

With heavy water as its target medium the Sudbury Neutrino Observatory has the unique capability to perform a variety of measurements that allow it to determine particle properties of solar ^{8}B and *hep* neutrinos and measure the neutrino flavor components of the solar neutrino flux. Table 2.5 summarizes the characteristics of different neutrino interactions and the main observables we can determine from the various interactions. The charged-current interaction rate, $[CC]$, allows one to determine unambiguously the flux of electron-type neutrinos. The strong energy dependence of the charged-current cross-section yields a good measurement of the energy spectrum of Čerenkov electrons produced in the charged-current reaction. The neutrino elastic scattering off electrons, $[ES]$, provides good directional sensitivity and can be used to determine the origin of the detected neutrinos. The solar angle distribution of elastically scattered neutrinos peaks away from the Sun and is a clear indication of the solar origin of the neutrinos observed in SNO. The neutral-current interaction rate, $[NC]$, is a measure of the total flux of active neutrinos from the Sun.

The flux of solar neutrinos and their respective interaction rates in the SNO detector are related through the cross-section of the target medium. The quantities $[CC]$, $[NC]$, and $[ES]$ are the interaction rates as measured in the SNO detector. Although all flavors of neutrinos scatter elastically the cross-section for neutrino-elastic scattering depends on the neutrino flavor. Neutrino-elastic scattering for ν_e involves both a charged-current as well as a neutral-current contribution while ν_μ and ν_τ can only scatter elastically through the exchange of a Z boson. The elastic-scattering cross-section of ν_μ and ν_τ is about 7 times smaller than the elastic scattering cross-section of ν_e in water [174]. The elastic scattering interaction rate is energy dependent and $[ES] \approx \sigma_{ES} \left[\Phi_{\nu_e} + \eta \left(\Phi_{\nu_\mu} + \Phi_{\nu_\tau}\right)\right]$ with $0.14 < \eta < 0.156$ for $5 < E < 15$ MeV. For a fiducial volume of $R_{fit} \leq 550$ cm and an energy threshold of $E \geq 6.75$ MeV one obtains $\eta = 0.154$.

$$[CC] = \sigma_{CC}\ \Phi_{\nu_e} \tag{2.58}$$

$$[NC] = \sigma_{NC}\ \left(\Phi_{\nu_e} + \Phi_{\nu_\mu} + \Phi_{\nu_\tau}\right) \tag{2.59}$$

$$[ES] \approx \sigma_{ES}\ \left[\Phi_{\nu_e} + 0.154\ \left(\Phi_{\nu_\mu} + \Phi_{\nu_\tau}\right)\right] \tag{2.60}$$

The SNO experiment can perform an absolute measurement of the flux of ^{8}B neutrinos as

Table 2.5: Neutrino interactions with D_2O and H_2O in the Sudbury Neutrino Observatory.

Interaction	Target Medium	Flavor Sensitivity	Physical Quantity
Charged-Current (CC)	D_2O	ν_e only	Solar ν_e flux
$\nu_e + d \rightarrow e^- + p + p$			Čerenkov e^- Energy Spectrum
$E_{thresh} = 1.44$ MeV			
Elastic Scattering (ES)	D_2O and H_2O	ν_x, enhanced for ν_e	Directional Sensitivity
$\nu_x + e^- \rightarrow \nu_x + e^-$			
Neutral-Current (NC)	D_2O	ν_x	Solar ν_x flux
$\nu_x + d \rightarrow \nu_x + n + p$			
$E_{thresh} = 2.22$ MeV			

well as a determination of the non-electron component of the solar neutrino flux. This allows SNO both to search for neutrino flavor changes, in particular neutrino oscillations, and to test solar models. The conclusions SNO can draw on the possible flavor transformation of solar neutrinos is model-independent and free of any solar model uncertainties.

2.4.2 Signatures of New Physics in the Neutral-Current Interaction Rate

The Sudbury Neutrino Observatory has a broad and diverse physics program including the study of solar neutrinos, atmospheric neutrinos, muons, and search for supernovae. However, its main goal is to determine the particle properties of solar neutrinos and test the predictions of solar models. With its capability to measure the total flux of active neutrinos through the neutral-current interaction rate as well as the electron neutrino flux, SNO has unique sensitivity to determine both the electron and the non-electron component of the solar neutrino flux and search for signatures of neutrino oscillations. The flux of electron neutrinos and the total flux of all active flavors are obtained directly from the neutral-current and charged-current interaction rate. By definition of the properties of sterile species, SNO can only determine the total flux of active solar neutrinos. The cross-sections that relate the

rates of deuterium dissociation to the neutrino fluxes are based on theoretical calculations.

The flavor composition of the solar neutrino flux can be determined by comparing the different interaction rates in SNO. Because of their unique flavor sensitivity the ratio of the neutral-current interaction rate, $[NC]$, to the charged-current interaction rate, $[CC]$, normalized by their respective cross-sections is a direct test of neutrino flavor transformation. The neutral-current interaction rate, $[NC]$, is equally sensitive to all active neutrino flavors and hence is directly related to the total flux of active ^{8}B neutrinos, Φ_{8B}^{SNO}, while the charged-current interaction rate determines the electron component of the solar neutrino flux.

$$\frac{[CC]'}{[NC]'} = \frac{[CC]\,\backslash\sigma_{CC}}{[NC]\,\backslash\sigma_{NC}} = \frac{\Phi_{\nu_e}}{\Phi_{\nu_e} + \Phi_{\nu_\mu} + \Phi_{\nu_\tau}} \tag{2.61}$$

The ratio of $[CC]'\,/\,[ES]'$ shows the same effect. The elastic scattering of neutrinos also involves all neutrino flavors although its significance is reduced due to the smaller elastic-scattering cross-section of ν_μ and ν_τ. The comparison of the charged-current rate, $[CC]$, to the elastic scattering rate, $[ES]$, allows one to determine the non-electron component in the solar neutrino flux without using the measurement of the neutral-current interaction rate.

$$\frac{[CC]'}{[ES]'} = \frac{[CC]\,\backslash\sigma_{CC}}{[ES]\,\backslash\sigma_{ES}} = \frac{\Phi_{\nu_e}}{\Phi_{\nu_e} + 0.154(\Phi_{\nu_\mu} + \Phi_{\nu_\tau})} \tag{2.62}$$

If these ratios differ from unity we have evidence that the solar neutrino flux contains a non-electron neutrino component. This would be the first direct and *solar model-independent* evidence for the flavor transformation of solar neutrinos. For massless Standard Model neutrinos we expect $\frac{[CC]'}{[NC]'}=\frac{[CC]'}{[ES]'}=1$.

Standard Solar Model (SSM) predictions can be tested in SNO by comparing the measured solar neutrino flux of ^{8}B and *hep* neutrinos, Φ_{8B}^{SNO} and Φ_{hep}^{SNO}, to the solar model predictions, Φ_{8B}^{SSM} and Φ_{hep}^{SSM}. In principle, solar model predictions can be tested in SNO through both the measurement of the neutral-current interaction rate alone as well as the simultaneous measurement of the charged-current and elastic scattering interaction rates. As explained above, the total active neutrino flux measured in SNO is given by:

$$\Phi_{\nu_x} = \Phi_{\nu_e} + \Phi_{\nu_\mu} + \Phi_{\nu_\tau} \quad (2.63)$$

$$= \frac{[CC]}{\sigma_{CC}} + \frac{1}{0.154}\left(\frac{[ES]}{\sigma_{ES}} - \frac{[CC]}{\sigma_{CC}}\right) \quad (2.64)$$

Under the assumption that the contribution of *hep* neutrinos to the total solar neutrino flux measured in SNO is negligible, agreement between the total ^{8}B solar neutrino flux measured in SNO and the SSM predictions implies:

$$\Phi_{8B}^{SSM} = \frac{[NC]}{\sigma_{NC}} = \frac{[CC]}{\sigma_{CC}} + \frac{1}{0.154}\left(\frac{[ES]}{\sigma_{ES}} - \frac{[CC]}{\sigma_{CC}}\right) \quad (2.65)$$

In addition, SNO measures the total energy spectrum of all neutrino interactions in SNO. A spectral decomposition of the data allows one to deduce the energy spectrum of Čerenkov electrons produced in the charged-current interaction rate. The hardness of the electron spectrum and the relatively small fraction of the ν_e energy that goes into the invisible final-state distribution make reconstruction of the energy of ν_e easier than in the case of neutrino-elastic scattering. Thus, SNO may be able to detect distortions of the neutrino spectrum resulting from the MSW effect.

In summary, the measurement of the neutral-current interaction rate allows one to address three main topics: (i) The comparison of the total solar ^{8}B flux to the electron neutrino flux deduced from the charged-current reaction is a direct test of neutrino flavor change. If observed, this would provide unambiguous evidence for physics beyond the Standard Model. (ii) With the measurement of the total active solar ^{8}B neutrino flux in SNO the flux prediction of Standard Solar Models can be tested. Under the assumption that solar neutrinos do not change into sterile species the NC flux gives us a measure of the total neutrino production rate in the Sun. (iii) With the measurement of the NC flux and the spectral decomposition of the data we have a unique opportunity to measure the electron neutrino energy spectrum and to look for spectral distortions as a signature of neutrino oscillations.

Furthermore, if neutrinos oscillate due to a matter-enhanced (MSW) resonance effect there could be a significant difference in the number of electron neutrinos observed during

the day or night. Certain neutrino oscillation models predict neutrino regeneration in the Earth. Electron neutrinos produced in the ^{8}B decay in the Sun could undergo a flavor transformation on their passage through the core of the Earth, resulting in a different charged-current interaction rate during day and night $\frac{[CC]_{Day}}{[CC]_{Night}}=\frac{[\nu_e]_{Day}}{[\nu_e]_{Night}} \neq 1$. Similarly, if there are sterile neutrinos the neutral-current interaction rates could differ between day and night as more active neutrinos oscillate into sterile species on their way through the Earth. In the presence of sterile neutrinos we would find $\frac{[NC]_{Day}}{[NC]_{Night}}=\frac{[\nu_x]_{Day}}{[\nu_x]_{Night}} \neq 1$. Based on the current results from solar neutrino experiments a number of authors have made predictions for the temporal variation of the neutrino signal in SNO [140]. The study of diurnal variations of the measured neutrino interaction rates in SNO is reported in [107] and described in detail in [172].

It is also of interest to observe the temporal variations of the measured solar neutrino flux. Because of the eccentricity in the Earth's orbit one expects to observe a 7% change in the solar neutrino flux over the period of one year.

2.4.3 Multiple Measurements of the Neutral-Current Interaction Rate: The Three Phases of the SNO Experiment

The SNO experiment is run in three distinct phases using different detector configurations. This allows SNO to measure the neutral-current interaction rate with different techniques and systematics. In the first phase of the experiment pure D_2O is used as the target medium. In this configuration the CC and ES interactions of solar neutrinos produce Čerenkov electrons which can be detected with the PMT array. The neutron produced in the NC interaction captures on deuterium and produces a γ with a characteristic energy of E_γ=6.25 MeV. In the second phase of the SNO experiment 2 t of NaCl are added to the heavy water to enhance the capture efficiency of the neutron produced in the NC dissociation of deuterium. The neutron now captures predominantly on ^{35}Cl and a cascade of γ's with a total energy of 8.6 MeV is released. The final configuration of SNO will consist of purified heavy water and a discrete array of ^{3}He-filled proportional counters. The neutrons from the NC interaction of solar neutrinos can then be detected on an event-by-event basis

Table 2.6: The three operational and experimental phases of the SNO experiment.

Phase	Detector Configuration	Sensitivity to ν Interactions	NC Signature
I	Pure D_2O	CC, ES	
		some NC	n+d $\rightarrow$ t+ γ
			E_γ= 6.25 MeV, ϵ_n=24%
II	D_2O	CC, ES	
	+ NaCl	enhanced NC	$n + {}^{35}Cl \rightarrow {}^{36}Cl + \Sigma\gamma$
			$E_{\Sigma\gamma}$ = 8.6 MeV, ϵ_n=45%
III	D_2O	CC, ES	
	+ ^{3}He counters	NC event-by-event separation	n+^{3}He $\rightarrow$ p+t, ϵ_n=37%

through the ^{3}He(n,p)^{3}H reaction. In this configuration, two detection systems are used: a light-sensitive array of some 9456 photomultipliers and a discrete array of neutron-sensitive proportional counters. The three phases of the SNO experiment and their characteristics are summarized in Table 2.6.

This work reports on the measurement of the solar neutrino interaction rates from the pure D_2O phase. The data for this study were obtained between November 2, 1999, and January 15, 2001.

CHAPTER 3

OBSERVING SOLAR NEUTRINO INTERACTIONS WITH HEAVY WATER: DATA FROM THE FIRST PHASE OF SNO

3.1 The SNO Detector

The Sudbury Neutrino Observatory (SNO) is an imaging water Čerenkov detector located in the Creighton mine of the International Nickel Company (INCO) near Sudbury, Ontario, Canada. A barrel-shaped cavity with a height of 34 m and a diameter of 22 m at a depth of 2092 m, or 6010 m mean water equivalent (mwe), houses the detector. Figure 3.1 shows a cross-sectional view of the detector. The neutrino detection medium is 1000 t of 99.92% isotopically pure D_2O. The heavy water is contained a 12-m diameter transparent acrylic vessel, and is surrounded by 2 kt of ultra-pure light water shielding. The acrylic vessel is constructed from 122 ultraviolet transmitting acrylic panels. The Čerenkov light produced by neutrinos and radioactive backgrounds is detected by an array of photomultiplier tubes (PMT's). A 17.8-m diameter stainless steel structure supports 9456 20-cm inward-facing photomultiplier tubes (PMT's). A non-imaging light concentrator is mounted on each PMT, which increases the total photocathode coverage to $\sim 55\%$. An additional 91 PMT's are mounted facing outward on the support structure to serve as cosmic veto. Outside the PMT support sphere is another 7 ktons of light water shielding to shield the detector from high energy γ rays and neutrons originating from the cavity wall. A detailed description of the SNO detector is given in [105].

The gain characteristics and photon-detection efficiency of the PMT's are influenced by the Earth's magnetic field. To cancel the vertical components of the terrestrial magnetic field, 14 horizontal magnetic compensation coils were built into the cavity wall. The maximum residual field at the PMT array is < 19 μT, and the reduction in photo-detection efficiency is about 2.5% from the zero-field value.

With D_2O as its target medium the SNO detector is uniquely suited to make a simulta-

neous measurement of the solar ν_e flux and the total flux of all active ^{8}B neutrinos. In SNO, solar ^{8}B neutrinos interact with deuterium in three different reactions: The charged-current interaction of electron neutrinos with deuterium (CC), the neutral-current dissociation of deuterium through the interaction with active neutrino flavors, and the elastic scattering off electrons. Only the charged-current reaction is exclusively sensitive to ν_e.

$$\begin{aligned}
&\text{(CC)} \qquad \nu_e + d \rightarrow p + p + e^-, \qquad \mathrm{E}_{thresh} \geq 1.44 \text{ MeV} \\
&\text{(NC)} \qquad \nu_x + d \rightarrow p + n + \nu_x, \qquad \mathrm{E}_{thresh} \geq 2.22 \text{ MeV} \\
&\text{(ES)} \qquad \nu_x + e^- \rightarrow \nu_x + e^-
\end{aligned}$$

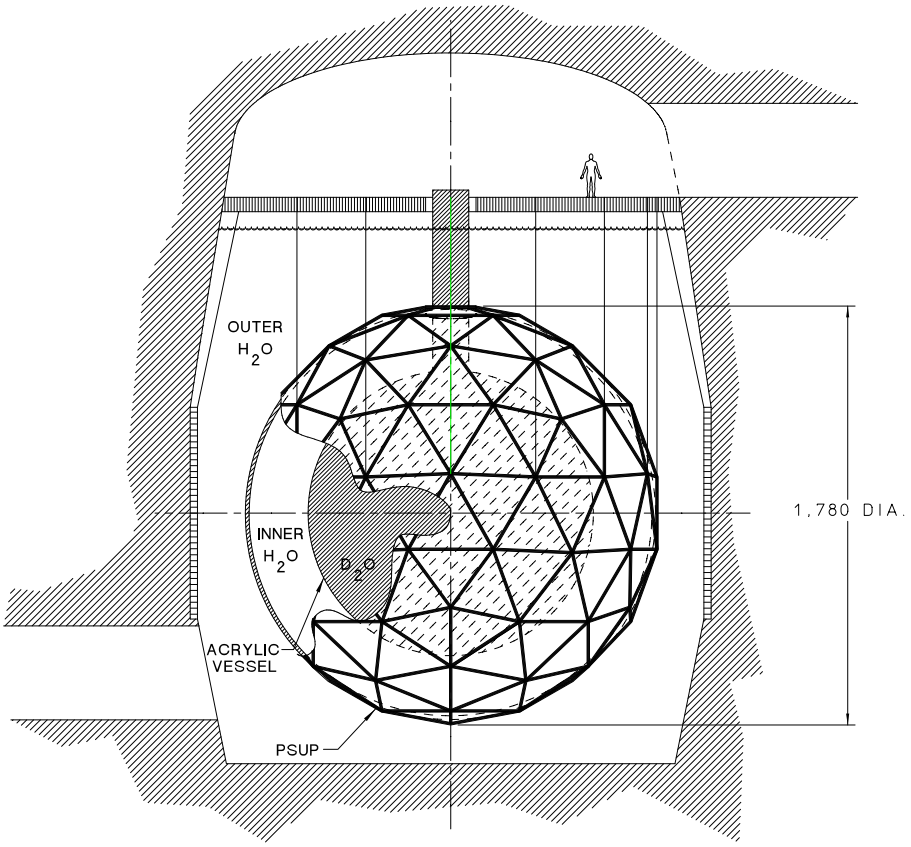

Figure 3.1: Schematic view of the SNO detector. The PMT support structure (PSUP) shown inside the SNO cavity, surrounding the acrylic vessel, with light- and heavy-water volumes located as indicated.

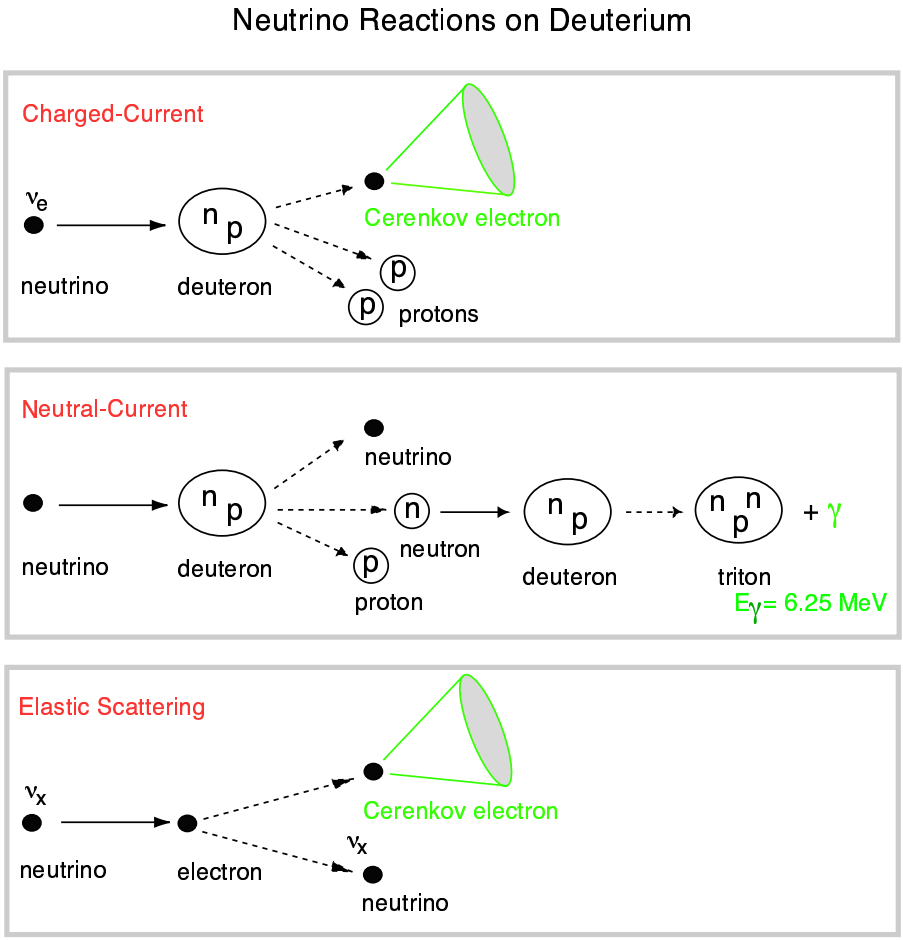

Figure 3.2: Illustration of the neutrino interactions in the SNO detector and the characteristic signatures of the charged-current, neutral-current, and elastic scattering interaction. The characteristic signatures of the neutrino interaction are shown in green. Čerenkov electrons are the signature of charged-current and elastic scattering events while the neutron from the neutral-current interaction is identified through the 6.25-MeV γ from its capture on deuterium.

3.2 Analysis Process

This thesis describes the entire analysis chain in the SNO solar neutrino analysis, from data selection to the extraction and interpretation of the neutrino signal. The chain of analysis components that will be discussed in this and the subsequent chapters is shown in Figure 3.3.

3.3 Detector Conditions and Performance

The general detector configuration for the D_2O phase of the SNO experiment was established and optimized before the start of production running. This includes the high voltage settings, trigger mask and thresholds, and a majority of the channel thresholds. As of November, 1999, the desired detector specifications had been met, the detector parameters were frozen and accumulation of production data was started on November 2, 1999, interspersed with a variety of calibration measurements. During production data taking the detector performance was very good, with more than 98.5% of all channels operational. The total event rate was less than 5 Hz above a threshold of about 20 hit PMT's. The individual PMT noise rates are $\sim$ 500 Hz for a threshold of about 0.3 photoelectrons, providing fewer than 2 noise hits per event.

The default configuration including the physics triggers and their thresholds for this data set are summarized in Table 3.1. Technical details of the SNO detector, its electronics, and water systems can be found in [105]. A detailed description of the SNO trigger system is given in [131].

3.3.1 Event Trigger

The SNO trigger system is a multiplicity trigger based on the number of hit PMT's, NHIT, in a chosen time window. If a pre-determined number of PMT's signals are received in coincidence the data are collected by the front-end electronics, read-out by the data acquisition system, and built into events. A detailed description of the SNO electronics is given in [105, 54, 131, 151]. In this context we briefly describe the conditions that lead to a trigger in case of a neutrino candidate event. Different trigger conditions are used for calibration

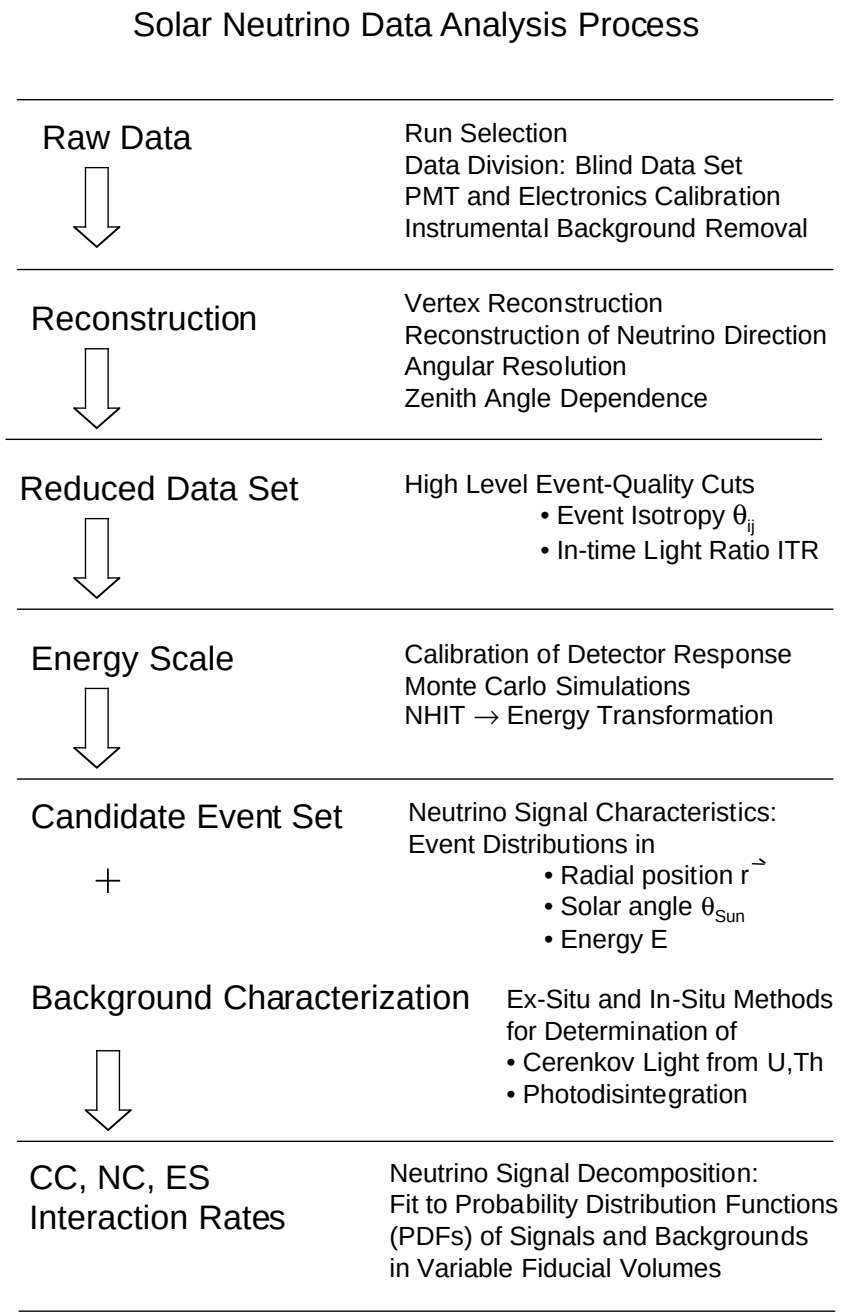

Figure 3.3: Steps in the SNO solar neutrino analysis.

Table 3.1: Detector configuration for neutrino data taking during the D_2O first phase of SNO.

Detector Configuration	
Electronics Configuration	All crates online.
	Valid electronic calibration constants.
	Time synchronization.
Trigger Setup (OR)	Pulsed Trigger at 5 Hz
	100 ns coincidence: 16 PMT's
	20 ns coincidence: 16 PMT's
	Energy sum $\geq$ 150 photoelectrons
	Prescaled (1:1000): 11 PMT's
Water Systems	No D_2O assays
	D_2O circulation without light production
Run Selection	No changes to configuration during run.
	Set of standard data selection criteria.

data and other data-taking modes. The global trigger is derived from a variety of candidate trigger pulses that can be individually masked into the trigger for a run. The basic trigger used for neutrino data is $NHIT100med$ (or NHIT100M), a medium-threshold 100-ns trigger. A physics event trigger is generated in the detector when there are 18 or more PMT's exceeding a threshold of ~ 0.25 photoelectrons within a coincidence time window of 93 ns. All the PMT's in the ~ 420 ns window after the start of the coincidence time window are recorded in the data stream. This 420-ns time window allows scattered and reflected Čerenkov photons to be included in the event. This multiplicity trigger becomes 100% efficient at NHIT$\sim$ 25 [151]. With a channel threshold of about 0.25 photo-electrons (p.e.) this corresponds to a hardware threshold of about $\sim$ 2 MeV and 100% trigger efficiency threshold at ~ 3 MeV. The complete trigger mask for neutrino data taking is described in Table 3.1. Generation of global triggers is synchronous to the master 50 MHz clock. The status of each trigger type is saved with each event in the trigger word. A GPS interface keeps the time with a resolution of 100 ns and an accuracy of ~ 300 ns. The time between events is kept by a synchronous master 50 MHz clock whose count is saved with each event.

In standard run conditions the instantaneous trigger rate of the detector is about $\sim$ 15-18 Hz, of which only $\sim$ 6-8 Hz correspond to the data trigger rate. The rest of the triggers are due to online monitoring tools and diagnostics.

3.4 Data Set

The data set used in this analysis was taken between November 2, 2001, to January 15, 2001. These data correspond to roughly 2/3 of the D_2O phase of the SNO experiment. The D_2O phase was concluded on May 28, 2001. At this time NaCl was introduced into the heavy water to increase its sensitivity to neutron capture events. A complete analysis of all the D_2O data from the first phase of the SNO experiment is presented in [106].

3.4.1 Data Taking and Selection

Data in the SNO detector is taken in runs of variable lengths. The runs can be started and stopped manually by the shift operator but are automatically restarted once they exceed a

certain maximum run length. The data for the solar neutrino analysis are selected based on stringent criteria to assure quality. The selection is based on information contained in the run header, the crate mask, the run length, and external information such as shift reports. Several run types are defined in the operation of the SNO detector. The selected runs are required to be neutrino runs and not maintenance, diagnostic, calibration, or experimental setup runs. These run information bits were defined to denote potential problems with certain runs. Some of the bits are set automatically, some of them are set by the shift operator, and some are generated by inspecting the shift logs. Furthermore, it is required to have all crates online, to have the compensation coils online and stable and to have a duration of at least 30 minutes. These criteria are chosen to assure the stability of all detector components during data taking. Runs are discarded if there were significant hardware problems or unusual conditions. These include D_2O water assays, extensive electronic pickup, inconsistencies between the clocks (in particular the 10 MHz clock) and the GPS, activity in the deck clean room, and D_2O circulation with light production noted by operator. In the data selection process the reports from every detector shift between November 2, 1999, and January 15, 2001, are read and examined for unusual occurrences. In terms of bits set in the SNO data stream the data selection criteria are summarized in Table 3.2. Of all neutrino runs, the additional run selection criteria removed $\sim 12\%$ of the data set.

The total livetime of the detector as well as the neutrino livetime are shown in Figure 3.4. The difference between the total livetime for this period and the neutrino livetime is due to detector maintenance and calibrations. While SNO is live and taking data during nearly all calibrations, data taken during these periods is considered to be non-standard and not used for the solar neutrino analysis. Figure 3.4 also illustrates how the SNO detector depends on the infrastructure and environment in the mine. Power outages and other emergencies require occasionally that the SNO experiment be shut down. Hence the total livetime is affected by any underground system failures. The livetime corresponding to the final neutrino candidate event set is calculated after reduction of the raw data to a candidate event set. The average neutrino livetime of the SNO detector between November 2, 1999, and January, 15, 2001, is about 73.5%.

Table 3.2: SNO D_2O run selection criteria. A run is selected if the logical AND of these tests is true.

Run Information	Source	Condition
Neutrino	Run Header	ON
D2O	Run Header	ON
Magnetic Compensation Coils	Run Header	ON
Number of Crates	Crate Mask	ALL ON
Run Length	10 MHz clock	>1800 s
Transitional	Run Header	OFF
Experimental	Run Header	OFF
Diagnostic	Run Header	OFF
Maintenance	Run Header	OFF
Bubblers	Run Header	OFF
Electronics Calibration (ECA)	Run Header	OFF
Pedestal Calibration (PCA)	Run Header	OFF
Other Calibration	Run Header	OFF
Source Moving	Run Header	OFF
Source	Run Header	OFF
DCR Activity	Run Header	OFF

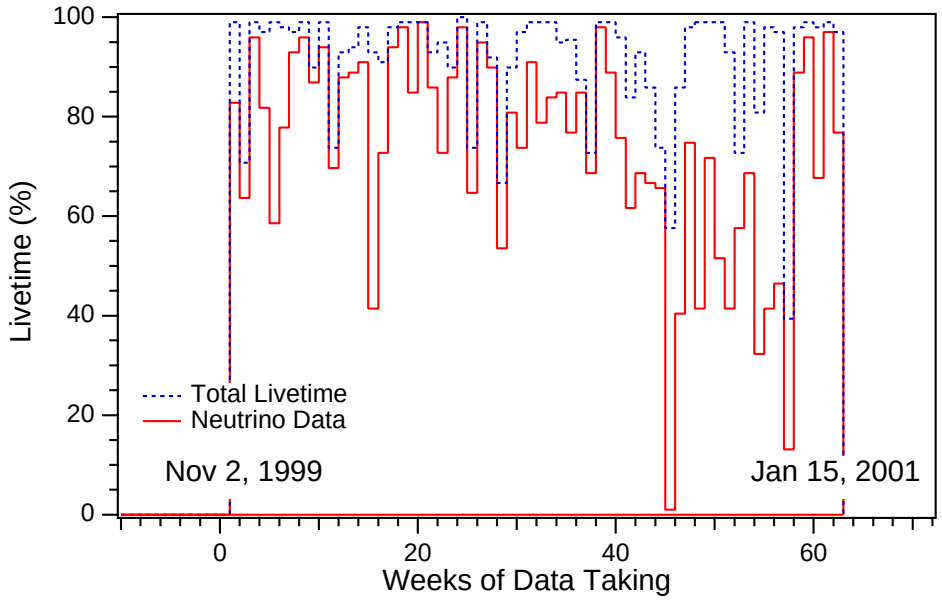

Figure 3.4: Livetime per week during the period of data taking.

3.4.2 Blindness and Data Division

In the first analysis of the solar neutrino signals from the D_2O phase in SNO a scheme of blindness and data division was adopted. Each run was divided into 3 contiguous blocks, equal in time duration. Each block was then pseudo-randomly assigned to one of 3 data sets: A, B, or C. The analysis was completely developed on an open data set before the finalized cuts and tools were applied to the blind data set. The cuts used in data reduction were developed and optimized on data set A, and then verified on data set B. Data set B was also used for systematic studies of all cuts and the evaluation of contamination levels. Set C was kept completely blind until the analysis was completely finalized. This scheme allowed a final check against both statistical and systematic biases. No significant difference was found between the data sets and the results from the combined data set A+B+C are reported here.

3.5 Data Reduction

The first step in the analysis process is the reduction of the raw data to a candidate event set which can be used for subsequent higher-order analyses. This data reduction consists of the removal of instrumental and detector effects and the application of high-level cuts which are used to test the physics nature of the recorded events. The livetime calculation for the data set under consideration is presented.

3.5.1 Components of Raw SNO Data

All events satisfying a simple multiplicity trigger of PMT hits are recorded in the SNO data stream. In this raw data we can distinguish between instrumental backgrounds due to detector effects and physics events. As illustrated in Figure 3.5, a majority of the raw data consists of instrumental backgrounds which will be removed before the neutrino data analysis using a set of cuts specifically designed to discard them. Numerous effects can cause these events and a few of them are discussed below. Physics events include a variety of event classes such as radioactive backgrounds, muons, muon-induced spallation products and, of course, interactions of solar neutrinos and atmospheric neutrinos. The different event types that can be identified in the raw SNO data are listed in Table 3.3.

In this chapter we will discuss the removal of instrumental backgrounds and the reduction of the data set that we perform to obtain a candidate event set of neutrino and physics background events. The analysis of solar neutrino candidate events is described in subsequent chapters.

3.5.2 Characteristics of Instrumental Backgrounds

Numerous effects in the detector can cause instrumental backgrounds and trigger the detector. All of the instrumental effects, however, have very distinct signatures that make it easy to uniquely identify them and remove these events from the data. When the detector is triggered the data stream records three basic quantities in various forms:

1. Absolute and relative timing of PMT hits.
2. Charge deposited in each hit PMT.

3. Unique location of each hit PMT.

These basic event characteristics allow one to derive for every event characteristic timing and spatial distributions of PMT hits as well as measures of the total charge. In addition to the 9456 inward looking photomultipliers SNO has 91 outward-looking PMT's and 4 PMT's in the neck of the acrylic vessel that allow further discrimination of muons and backgrounds. These tubes are usually referred to as "Neck PMT's". Information from the "Neck PMT's" is also used to remove instrumental background effects. Instrumental backgrounds are discriminated based on five different characteristics:

1. *Charge:* Most of the instrumental effects have unusual charge distributions.

2. *Time:* The Čerenkov light from charged-current and elastic scattering interactions of neutrinos produces a prompt peak in the timing distribution of PMT hits in an event. Usually the timing distribution of instrumental background events does not show the same characteristic structure.

3. *Geometry:* Patterns of hit PMT's can be very distinctive both in the geometry space of the PMT structure as well as in electronic space. Instrumental background events do not show a Čerenkov ring in their PMT hit pattern. Instead they may show some clustering in electronics space.

4. *Event Rate:* Many instrumental backgrounds in the SNO detector occur in bursts and are sometime correlated with external events, such as blasting in the mine. These events can be removed using a burst cut. While most of these instrumentals are also removed by other cut criteria, burst cuts provide additional safety against leakage through cuts.

5. *Veto Tubes:* External backgrounds fire veto tubes and hence give a clear signal for discrimination. The classes of PMT's that are used in the rejection of instrumentals and external backgrounds are PMT's that are installed in the neck of the AV (Neck PMT's), the outward-looking tubes (OWL's), and the "Berkeley Underwater Test Tubes" (BUTT's). For example, the four additional PMT's that are installed in the neck of the acrylic vessel provide a clear indication of instrumental light emitted in this region, probably from static discharges of insulating materials.

Table 3.3: Event classes in the raw SNO data. A description of the different event classes is given in the text below.

Neutrino Events	Solar ^{8}B Neutrinos
	Solar *hep* Neutrinos
	Atmospheric Neutrinos
Low-Energy Backgrounds	Photodisintegration from internal D_2O backgrounds
	Čerenkov light from U, Th in the D_2O
	PMT $\beta - \gamma$
	Backgrounds from PMT support structure and cavity
	Acrylic vessel background
High Energy Backgrounds	Backgrounds from PSUP and cavity
	Muons
	Muon-induced spallation
Instrumental Effects	PMT flashers
	PMT Wet-end HV breakdown
	Bubbler events
	Electronic pickup
	Retrigger events
	Neck events
	Isotropic ("Leslie/Heeger") Events
	And possibly other instrumental event classes

Figure 3.5 shows the NHIT spectrum of the selected, but otherwise raw data set compared to the expected spectrum of charged-current neutrino interactions in the SNO detector. The charged-current spectrum is normalized according to the standard solar model predictions from BPB00 [11]. The expected number of events from solar neutrino interactions is more than 5 orders of magnitudes less than the number of recorded events in the raw data set.

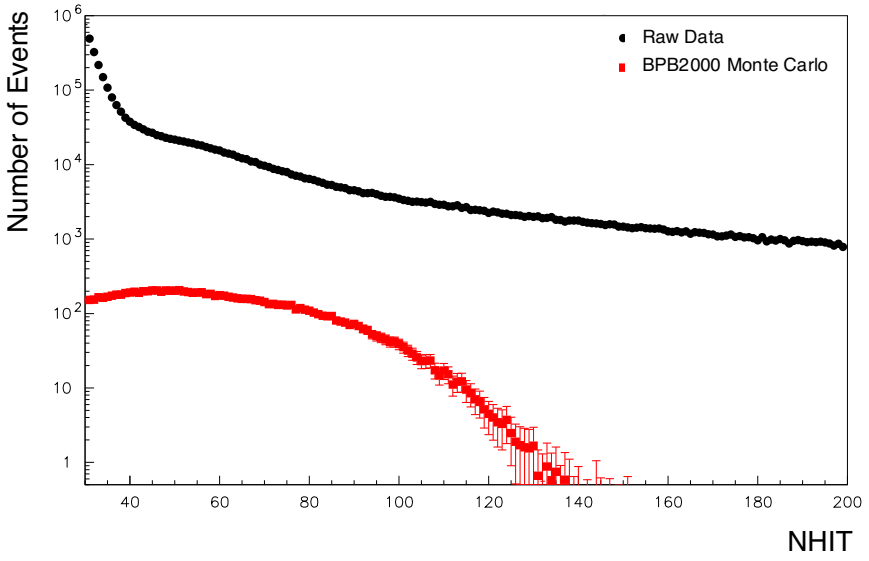

Figure 3.5: NHIT spectrum of raw SNO data compared to the expected spectrum of charged-current neutrino interactions in the SNO detector. Figure courtesy of N. McCauley, Oxford University, UK.

A few examples of instrumental effects in the SNO detector are described and shown below. For comparison, we also show ^{16}N and ^{8}Li calibration events as well as neutrino candidates. In our discussion of the different event classes we focus on four event characteristics: The PMT hit pattern, the TAC timing distribution, the charge distribution, and the channels geometry in crate space. These characteristics illustrate very clearly the difference between γ and Čerenkov electron signatures of neutrinos and calibration events, and instrumental effects.

PMT Flashers: It is well known that PMT's can occasionally emit light, perhaps through internal electrical discharges. Light from this source has very different characteristics from the typical patterns observed for Čerenkov light at solar neutrino energies. The light from a flashing PMT shows an early trigger for the flashing PMT, followed by light observed across the detector some 70 ns later. The characteristic 70 ns time signature shows in the double-peaked timing distribution (TAC) of the event. For SNO, six or more electronic channels surrounding the flashing PMT typically show pickup signals, distinguishing the events further from Čerenkov events. The flasher rate of PMT's are correlated with vibrations in the SNO detector system induced by blasting in the mine or other effects. Flashers can usually be removed based on their high and early charge, the high energy sum, and the hit pattern.

Bubbler Events: During the circulation and purification of the heavy water in the SNO detector water is introduced into and removed from the inner volume of the SNO detector through a set of acrylic pipes. It has been observed that bubbles generated at the end of the pipe from the water flow emit light that is detected in the PMT array. Runs during which the water was circulated have been excluded from the data set.

Wet-end High Voltage Breakdown: During the commissioning phase of the SNO detector it was found that degassing the light water, which was done to prevent biological growth, had also removed any gases in the gel base of the PMT's and created microscopic voids. These voids can lead to high-voltage breakdown. The problem was rectified by re-gassing the purified H_2O with nitrogen. However, wet-end high voltage breakdowns still occur occasionally and are easily identified by their spectacularly high charge and NHIT. The triggers caused in such an event need to be removed from the data stream.

Electronic Pickup: Neighboring channels in electronic space are susceptible to cross-talk and pickup. The pickup signal is usually bipolar because it is coupled in via stray capacitance and the charge integrates to zero for pickup events.

Retrigger Events: Triggers that follow high-charge or high-NHIT events in the SNO detector are usually referred to as retrigger events. A combination of burst cuts and event-follower cuts are used to remove these retrigger events but not the original first event in the detector. Retrigger events often follow muons.

Flat TAC Events: The TAC distribution of an event refers to the uncalibrated measurement of the PMT timing information. It has been observed that some events exhibit an unusually flat TAC spectrum. For an example of such an event see Fig 3.9. Flat TAC events occur frequently after wet-end high voltage breakdowns.

Neck Events: These events may arise from static discharges of insulating materials in the neck region of the detector. In September 1999, four additional PMT's were installed in the neck region of the detector to detect this light. The PMT's are specifically oriented to identify these events. They are insensitive to light generated in the detector itself, as determined from calibration sources.

Isotropic Events: Isotropic events have no discernible pattern to their PMT hits but they show no anomalous signatures in their timing distribution (TAC) or charge. They are a component of ^{16}N and ^{8}Li calibration data but their distribution in the raw SNO data suggests that they might also come from instrumental light production in the SNO detector or external γ backgrounds.

Table 3.4: List of sample events shown below. The event identification (GTID and Run Number) as well as the characteristic number of photomultiplier hits (NHIT) are given for each event.

Event Type	Photomultiplier Hits (NHIT)	Run Number	Global Trigger ID (GTID)
Neutrino Candidate	102	10038	2045334
Neutrino Candidate	90	10700	327384
^{8}Li	79	14329	39591
^{16}N	60	10353	4416566
Flasher	67	1000	15662
Flat TAC	52	10655	1888297
Isotropic Event *(from calibration data)*	71	10298	873735
Isotropic Event *(from reduced neutrino data)*	66	10035	1239551

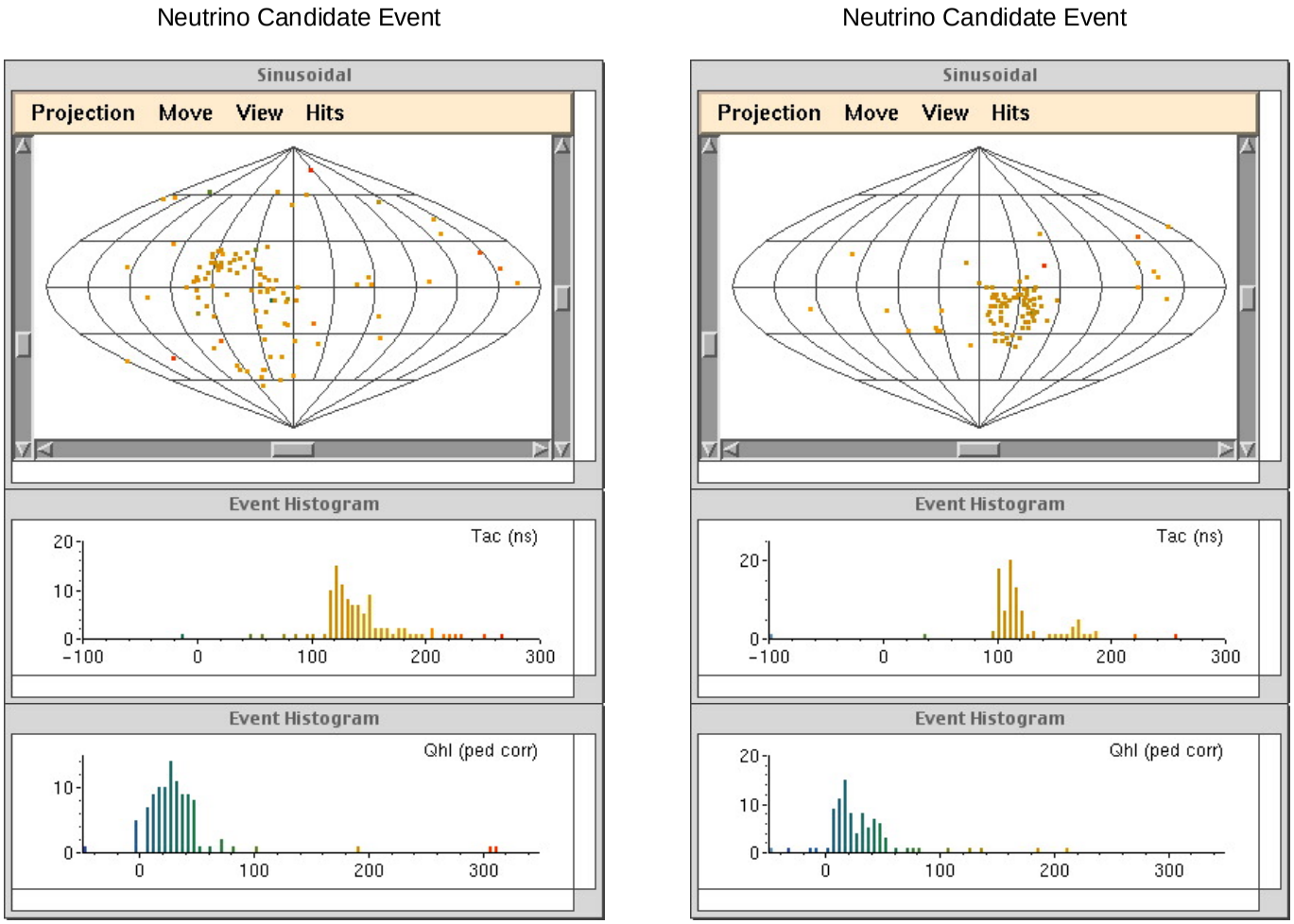

Figure 3.6: Event display of neutrino candidate events. Both events show clearly the Čerenkov pattern. The characteristic number of photomultiplier hits (NHIT) and identification (GTID and run number) of these events are listed in Table 3.4

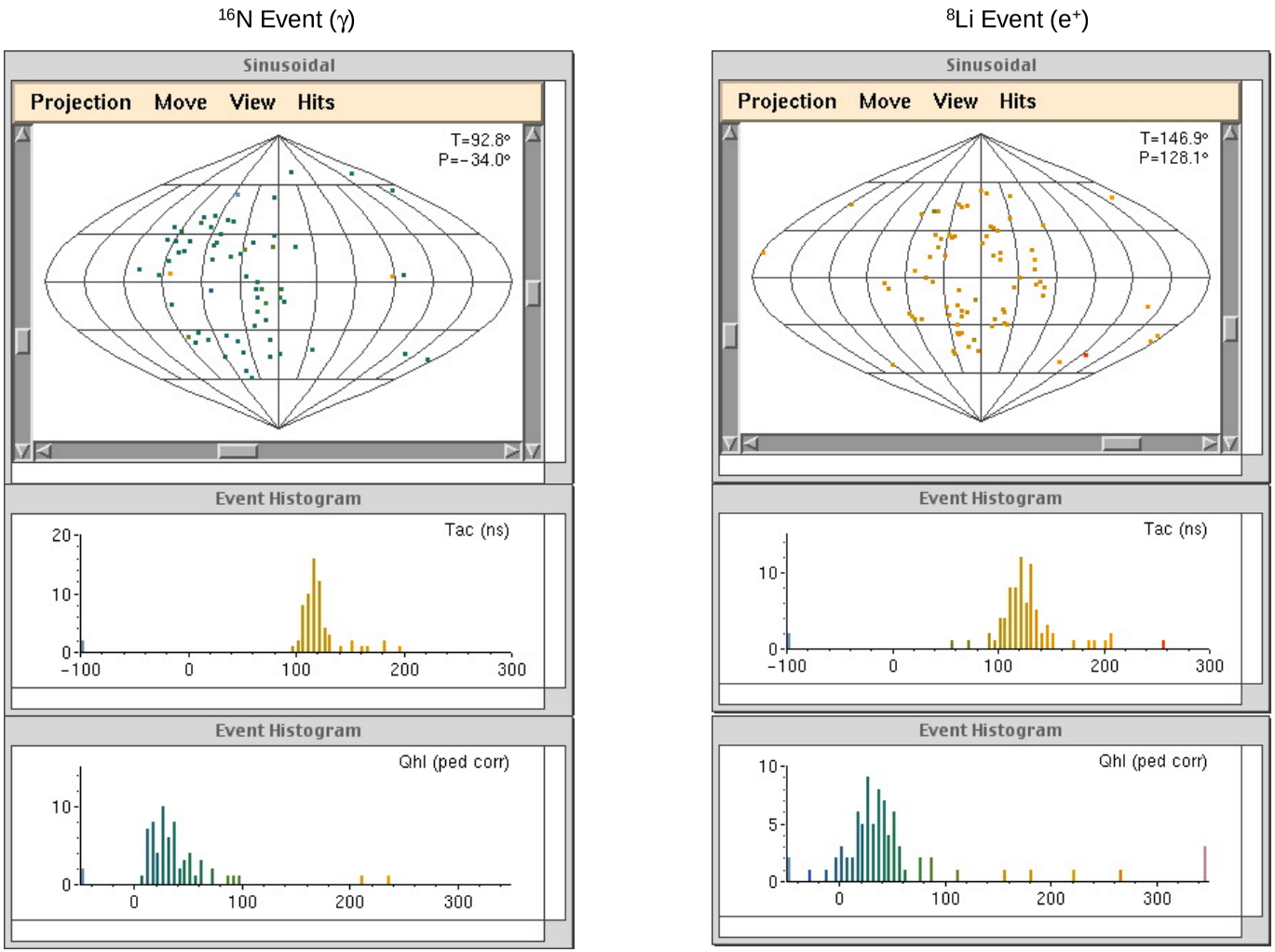

Figure 3.7: Event display of ^{16}N and ^{8}Li calibration data. The event characteristics and identification are listed in Table 3.4

Isotropic Physics Event (^{16}N or Muon Follower)

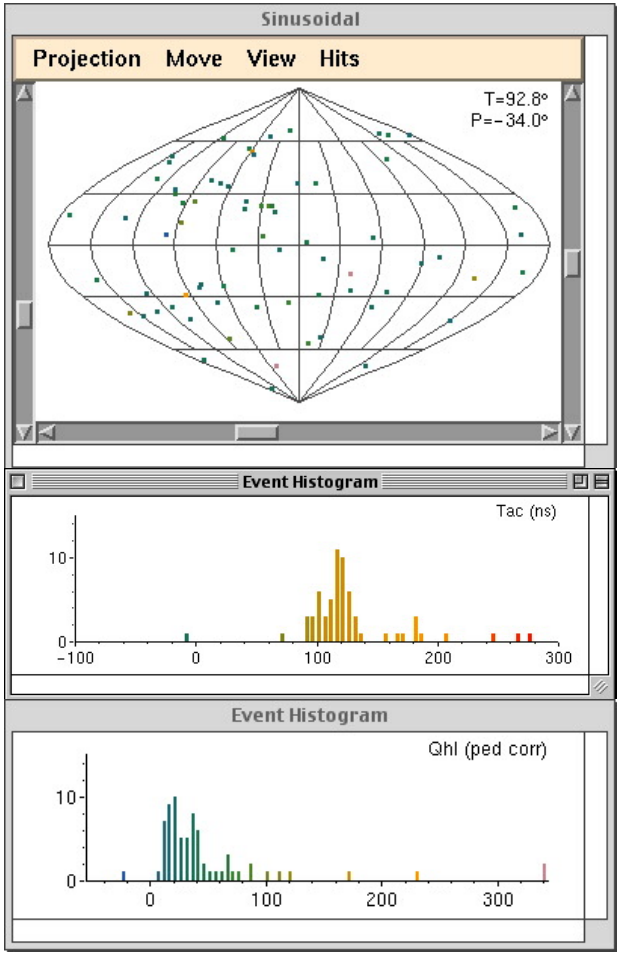

Isotropic Event in Reduced Data Set

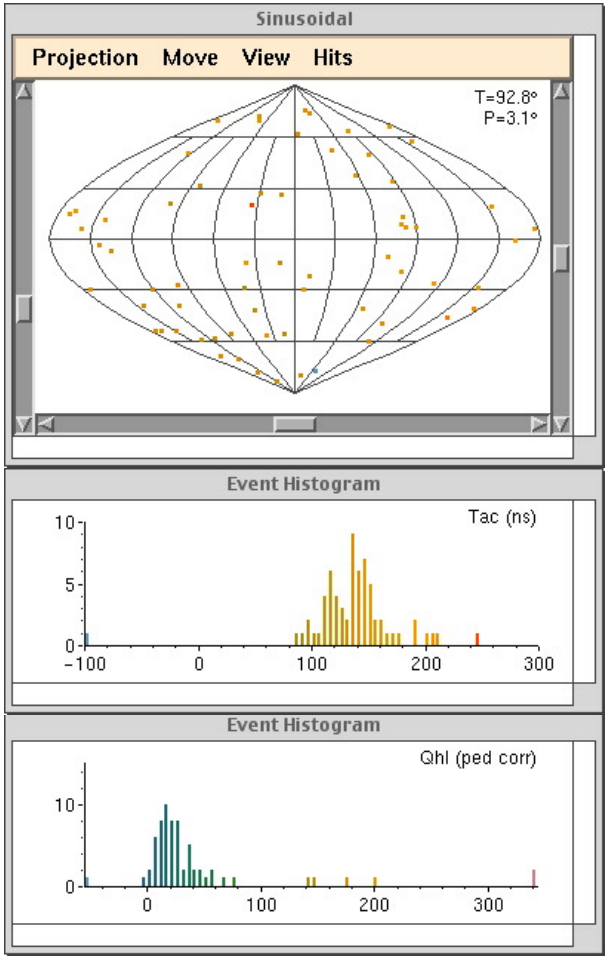

Figure 3.8: Event display of isotropic events from the reduced data set and from calibration data show similar characteristics. However, the fraction of isotropic events was found to be significantly higher in the reduced data set compared to calibration data.

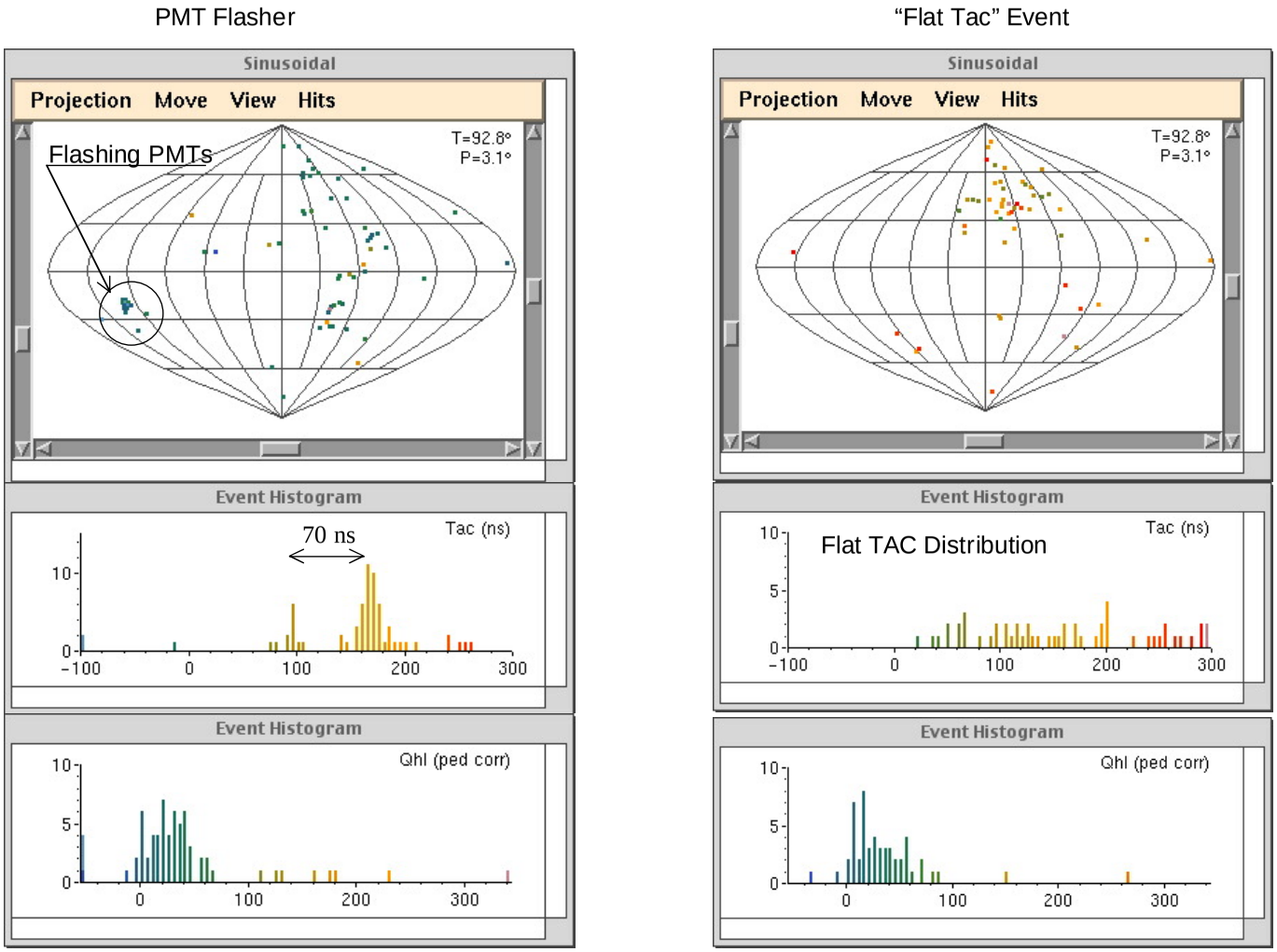

Figure 3.9: Event display of PMT flashers and flat-TAC events. The left panel illustrates nicely the characteristics of PMT flashers. A time difference of 70 ns corresponds to the transit time of light across the detector.

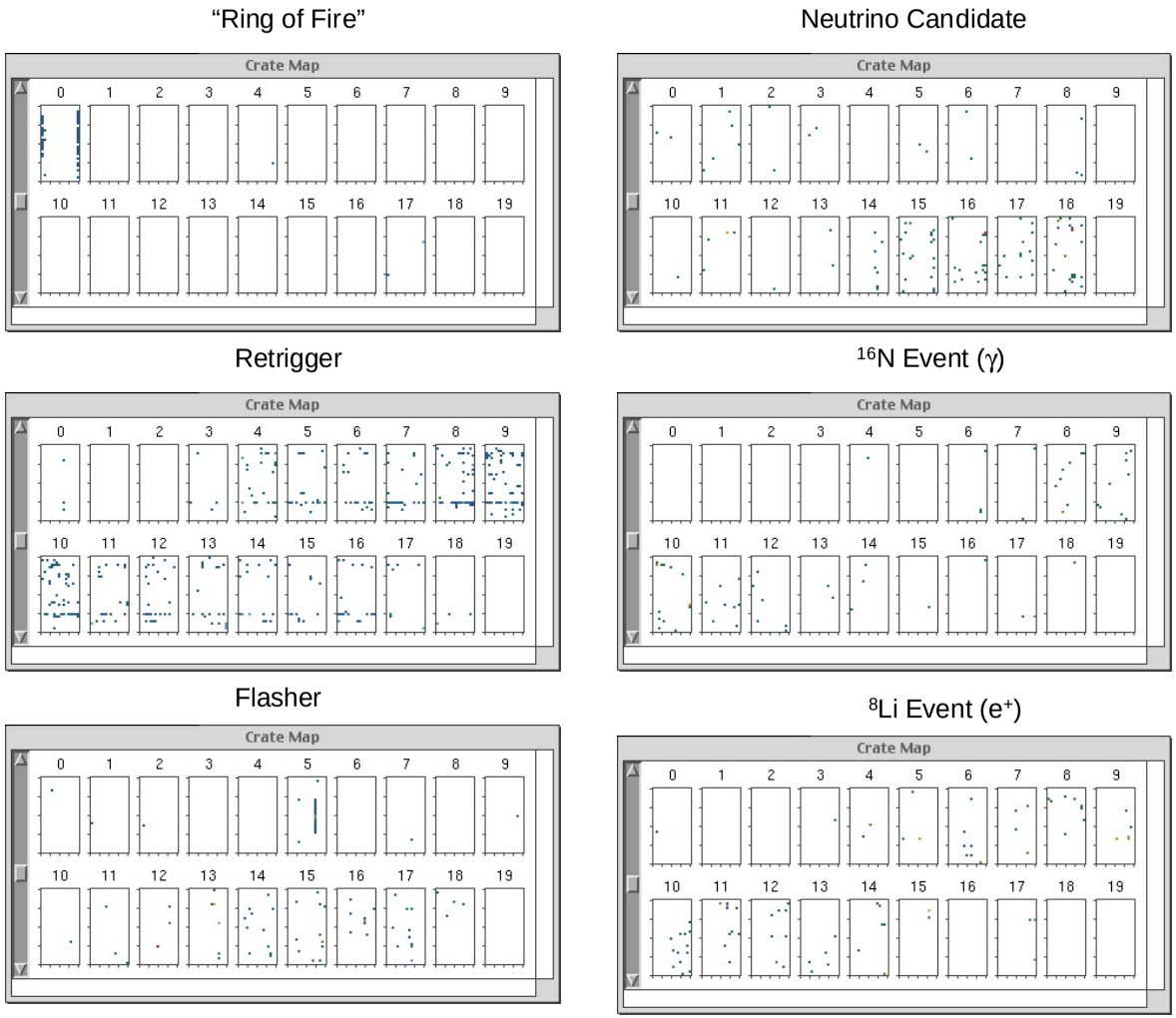

Figure 3.10: Crate topology of different event classes. The "random" distribution of channels in neutrino or calibration events is clearly visible compared to the pathological distribution of retrigger events or "rings of fire".

Instrumental backgrounds are discriminated based on a variety of event signatures. The TAC time distribution of events is an example of a powerful 1-dimensional distribution that is used in the identification and discrimination of events. TAC time is the relative time between PMT hits in an event. It is derived from the TAC, Time-to-Amplitude conversion, of the PMT. Figure 3.11 shows the TAC distributions of a number of different classes of instrumental events in the SNO detector compared to neutrino candidate events. These events are obtained from benchmarking data [73] which were compiled by handscanning a raw data sample. Figure 3.12 compares the TAC distribution of ^{16}N calibration data to neutrino candidate events. Some of the event classes shown in Figure 3.11 are discussed in more detail in Section 3.6.

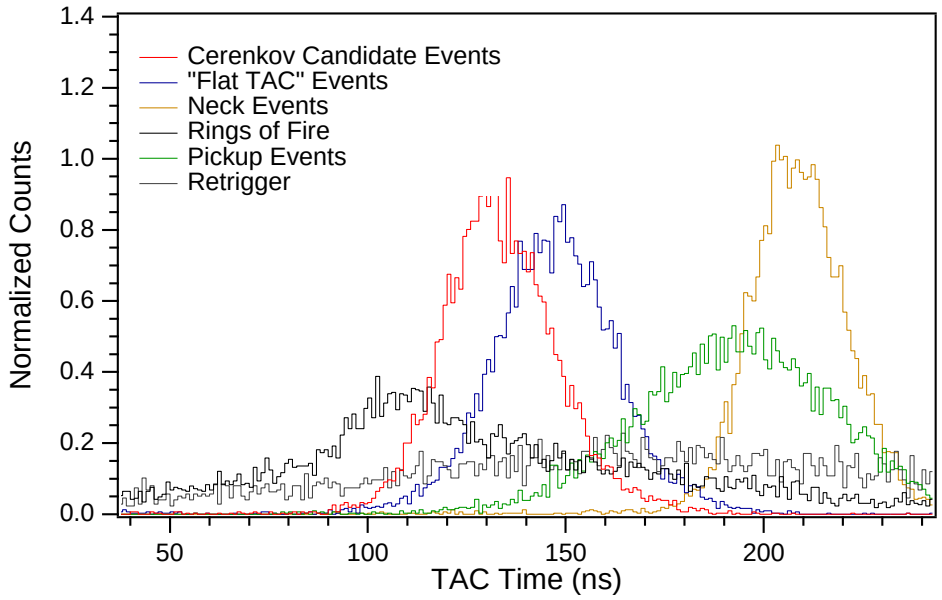

Figure 3.11: TAC distributions of Čerenkov candidate events and various instrumental backgrounds. All distributions are normalized to unit area.

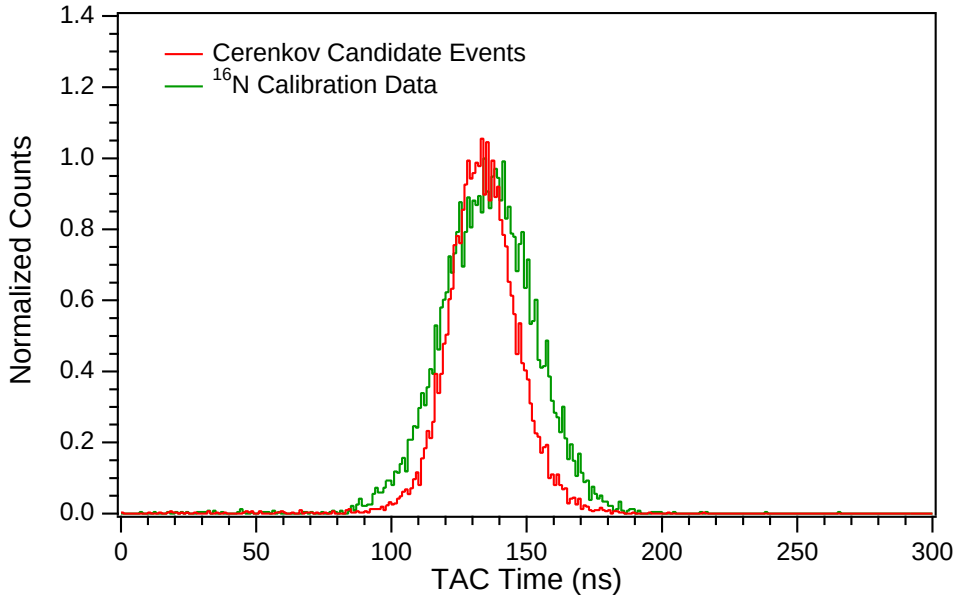

Figure 3.12: TAC distributions of Čerenkov candidate events and ^{16}N calibration data.

3.5.3 Cuts for the Removal of Instrumental Backgrounds

Two entirely independent schemes have been developed to remove instrumental backgrounds in the raw SNO data set: The Data Analysis Mask Number (DAMN) and the First, Second, and Third data reduction (FiST) [1]. Following the SNO data division and blindness scheme all cuts were developed and tested only on one third of the data set. In this data division scheme each run is divided into 3 contiguous blocks equal in time duration. Each block is then pseudo-randomly assigned to one of 3 data sets: A, B, or C. Cuts to remove instrumental backgrounds were developed and optimized on data set A. The suite of standard SNO cuts that has been developed to remove various types of backgrounds are listed in Table 3.5 and 3.6. The data reduction mask used in this analysis consists of the cuts indicated in this table. This corresponds to DAMN mask 15822821 (x00F16FE5) in the SNO Monte Carlo and analysis code. Short descriptions of the individual cuts are given in Tables 3.5 and 3.6. For a detailed discussion of these cuts we refer to [142] and the forthcoming detailed paper on the analysis of the solar neutrino data from the pure D_2O phase at SNO [108]. The FiST data reduction scheme has been described in a number of internal SNO analysis reports [45, 46].

Figures 3.13 illustrates the change in the NHIT spectrum with the sequence of some of the data reduction cuts that are applied to remove instrumental backgrounds from the raw data.

For the purpose of verification a second data reduction scheme was developed using some of the experience from the cuts described above and combining it with the flexibility of a multi-level system and input from hand-scanned data sets. This data reduction scheme consists of a first and and second pass filter. In the first pass, the raw data file is examined and some very simple filters are applied to identify pathological events. This first pass filter allows one to monitor the general stability of the detector. At this stage no events are removed from the data set. The information from the first pass filter is then passed on to the second pass filter. The actual data reduction is done only in the second pass filter

[1] These two independent data reduction schemes were developed by the independent SNO analysis groups that were maintained for the first analysis of the SNO solar neutrino data.

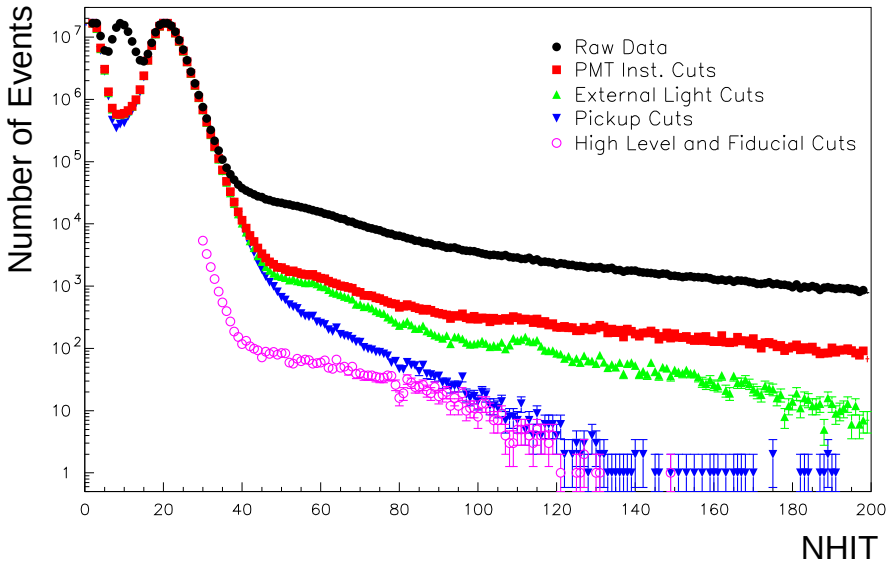

Figure 3.13: Reduction of the raw NHIT spectrum through a sequence of cuts. These cuts are designed to remove instrumental backgrounds. Figure courtesy of N. McCauley, Oxford University, UK.

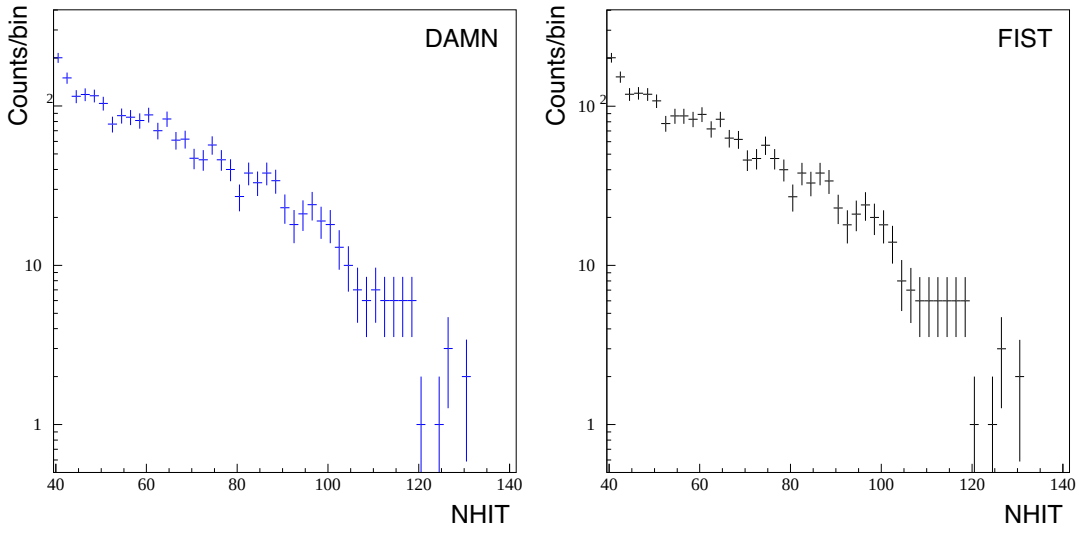

Figure 3.14: Comparison of the NHIT spectra of the reduced data sets obtained with the two independent data reduction schemes, DAMN and FIST.

because statistical information on bad electronics channels from the first level analysis are used in the second pass filter. Based on the characteristics of pathological events observed during hand-scanning of raw data (see section 3.6) a third data reduction level with four more data reduction cuts was established. In hand-scanning the raw events the spatial and timing distribution of PMT hits as well as their clustering in crate and electronics space was inspected visually and compared to standard calibration data. The application of a multi-level data reduction system allows for a feedback-driven application of data reduction cuts. The cuts used in the first, second, and third pass filter are listed and described in Table 3.7.

Excellent agreement was found between the data sets produced by these two data reduction schemes. The NHIT spectra of the reduced data sets obtained with the 2 data reduction schemes are almost identical (Figure 3.15). Once this independent agreement was obtained the first data reduction scheme was used in all of the subsequent analysis.

In addition to the cuts described above, the raw data selected for analysis must satisfy

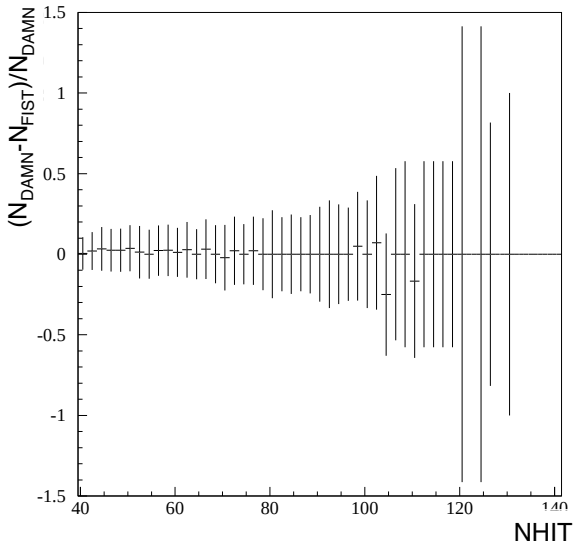

Figure 3.15: Fractional difference between the DAMN- and FIST-reduced data sets. The agreement is very good over the NHIT range of interest for a solar neutrino analysis.

two cuts based on the number of PMT hits, i.e. NHIT. All events are required to have greater than or equal 30 PMT hits and less than 1000 NHIT. The upper boundary represents some limit in the reconstruction algorithm.

While muon followers are not removed in the initial data reduction process a short muon follower cut is applied after the first data reduction to remove any events correlated with muons in the detector.

The standard data reduction cuts are usually not applied to calibration data. To guarantee good event samples from calibration data the following selection criteria are used for calibration data.

^{16}N *Calibration Data:* Trigger from the scintillator PMT of the tagged ^{16}N source.

^{8}Li *Calibration Data:* Tag from ^{8}Li PMT should be present and have sufficient charge.

pT *Calibration Data:* $100 \leq$ NHIT ≤ 500 to reduce signals from neutrons and umbilical.

Table 3.5: Definition of the principal SNO data reduction cuts (DAMN). A complete discussion and detailed description can be found in [28, 142]. The items marked with X are used in this analysis for the data reduction and removal of instrumental backgrounds.

Mask	Cut ID	Cut Name	Description of Cut
X	0	Retrigger	Event within 5 μs of a previous event.
	1	First Event	First event of a retrigger burst (see tag 0).
X	2	Burst	3 or more events occur within 1 ms.
	3	Charge	Calibrated channel has any pedestal subtracted charge less than -80.
	4	Cluster	More than 6 hits in a paddle card or more than 200 hits in a crate.
X	5	QvT	High charge tube is between 60 and 250 ns before the median tube time in the event.
X	6	Pe/NHIT	Pe/NHIT ratio is below 0.35.
X	7	Crate Isotropy	More than 70% of the hits occur on one crate and more than 80% of those hits occur on $\leq$ 2 adjacent cards.
X	8	AMB	Cuts events based on the value of the integral NHIT distribution of their ESUMHI pulse AND/OR the Peak/NHIT distribution.
X	9	FTS	Median time difference between tubes closer than 3 m is $\leq$ 10 ns.
X	10	OWL	Number of OWL and BUTT tubes is 5 or more.
X	11	Junk	Removes orphans and event containing the same PMT more than once.
	12	Ring of Fire	More than 70% of the hits occur on a crate and more than 80% of those occur in a ring around the edge of the crate.
X	13	Neck	Cuts events containing $\geq$ 2 neck veto tubes.

Table 3.6: Definition of the principal SNO data reduction cuts (DAMN) continued. A complete discussion and detailed description can be found in [28, 142]. The items marked with X are used in this analysis for the data reduction and removal of instrumental backgrounds.

Mask	Cut ID	Cut Name	Description of Cut
X	14	ESUM	ESUMLO trigger but no NHIT trigger.
	15	HIB	Cuts events occurring in a time window 0.1 s before and 0.6 s after a hydrophon trigger.
X	16	Qcluster	Charge and cluster cut.
	17	Muon	Cuts muons by using OWL tubes.
X	18	μ Follower Short	Events in time window of 100 ms following a muon.
	19	μ Follower Long	Events in time window of 20 s following a muon.
X	20, 21, 23	ITC, FGC, OWLEHI	See [142].
X	22	NHIT burst	See [28, 142].
	24	Subrun boundary	See [28, 142].

Table 3.7: Definition of cuts developed for an independent, multi-level data reduction scheme (FiST) [45, 46].

Level				
1	2	3	Cut Name	Description of Cut
X	X	X	Burst	Removes bursts if a global trigger occurs 10^{-6} s after the last global trigger.
X	X	X	Orphan	Identifies and removes event orphans.
X	X	X	SoftGT	Identifies SoftGT triggers.
X	X		Prescale	Identifies prescale triggers.
X	X	X	PGT	Removes Pulsed Global Trigger events.
X			Cluster Density	Identifies clustering behavior of fired channels in crate space for flashers and other instrumentals.
X			Charge	Identifies railed charges
	X	X	QTC	Uses clustering, charge, and timing information. Reduces bias of cluster density cut.
	X	X	TRMS	Removes flat-TAC events with large spread in time spectrum.
	X	X	N100HM	Requires NHIT100high or NHIT100med in trigger word. Ensures that event triggered by in-time hits.
	X	X	Neck	Cuts events containing ≥ 2 neck veto tubes.
	X	X	QBC	Identifies channels with bad charge.
	X	X	FGC	Flasher geometry cut looks for geometric clustering. and reduces the contamination from flashing PMT's.
		X	TKUR	TRMS and TKUR cuts eliminate classes of flat-TAC events.
		X	BONe	OWL and BUTT PMT's used to reject muon background. and some classes of non-physics backgrounds.
		X	QQP	Uses integrated charge of channel and ESUMHI pulse to discriminate events with atypical charge behavior.
		X	SoFA	Inspects event topology in crate space. Identifies events that show most channels in neighboring slots firing.

3.6 Event Verification: Observation of Isotropic and Flat-TAC Events

As an independent check of the removal of instrumentals a subset of the reduced data was verified visually on an event-by-event basis. Using XSNOED, a X-windows based event display written for SNO, all data above NHIT ≥ 50 from runs 10000-10976 (about ~ 1700 events) that passed the run selection criteria were hand-scanned to assess the performance of the data reduction cuts. The goal was to understand qualitatively the residual contamination of the data set. The events were categorized into different categories of accepted and rejected events. The data set was scanned by several people. Their results were calibrated against each other using a standard set of benchmarking runs.

In the verification of the reduced data set two characteristic event classes were found. These events are described by either a fairly isotropic light distribution or a flat TAC distribution. Isotropic events have no discernible pattern to their PMT hits but they show no anomalous signatures in their timing distribution (TAC) or charge. Some of these isotropic events do appear to have a broader time distribution than neutrino events and two populations of isotropic events, one with a good timing distribution and one with a poor "in-time" light ratio, have been identified [159, 139]. To determine the nature of isotropic events a search for physics events with an isotropic hit pattern was performed. There are two sources of low-energy events that are due to real interactions in the detector: bursts of muon followers and ^{16}N calibration data. Studies of Čerenkov events and γ's from calibration data show that real physics interactions can produce isotropic events and there is no intrinsic reason to remove isotropic events from the data sample. However, the fraction of isotropic events in the reduced neutrino data set was significantly higher than the fraction of isotropic events found in calibration data. Furthermore, the isotropic events in the reduced data set have a very different reconstructed radial distribution than the isotropic events from known physics interactions, and they comprise a much larger fraction of the data set. To be free from any bias in the hand-scanning procedure calibration data and events from the reduced data set were randomly mixed in one file so that the person performing the event verification had no prior knowledge of the source of the event. The results of this event verification are summarized in Table 3.8.

Table 3.8: Percentage of isotropic events in the hand-scanned data sets.

Data Set	Fraction of Isotropic Events	Fraction of Isotropic Events with R_{fit} ≤600 cm
Muon Followers	6.9%	90%
^{16}N Calibration Data	7.4%	91%
Reduced SNO Data (without high level cut)	20%	6%

From the sample of reconstructed isotropic events from ^{16}N or muon follower data or from the reduced data set we find that virtually all (91%) of the physics events reconstruct within the AV, but almost none (6%) of the scanned events from the reduced data set do. See Table 3.8. The NHIT (or energy) distribution of these events exhibits a significant tail extending up to an NHIT of 150 and higher. This is a clear indication that these events are not due to radioactive backgrounds, such as ^{214}Bi and ^{208}Tl. The high NHIT of the isotropic events makes them possibly a worrisome background to neutrino signal. For comparison, the NHIT spectrum of Čerenkov electrons from charged-current neutrino interactions extends to an NHIT of ~ 140.

To understand the nature of these events the detector distributions of the selected isotropic events were studied. A threshold of NHIT = 50 was applied to the reduced data set. It was found that isotropic events reconstruct primarily around the equator of the detector in the H_2O region or on the AV in the neck region of the acrylic vessel [159] [2]. It is believed that crazing of the acrylic vessel and high-energy γ's coming from the rock can explain these two classes of isotropic events.

Figure 3.17 shows the distribution of reconstructed event coordinates and the radial distribution of events normalized to the position of the AV. The isotropic events do appear to have some clusters near the top of the detector at $R_{fit} \approx 600$ cm. This is the point where

[2]The reconstruction of events is discussed in detail in Chapter 4.

the neck joins the main body of the acrylic vessel. It has been shown by A.W.P. Poon [159] that crazing of acrylic generates light. One can imagine that the stress in the acrylic vessel generates some light that is observed in the PMT array.

The equator is unique in several ways: It is the location of the belly band and rope grooves that support the AV, it is closest to the rock of the cavity walls, and it is the location at which clean light water is introduced. Since reconstruction places them in the light water, the isotropic nature of the events implies that they are inward-going. This is clearly illustrated in Figure 3.21, where the angle between the reconstructed radial vector and the fitted event direction is plotted. The parameter $\vec{u}.\vec{r} = -1$ points clearly towards the center of the detector. The $\vec{u}.\vec{r}$ distributions is not quite as pronounced for lower NHIT thresholds. The concentration of inward-going events suggests that the isotropic events originate from the photomultiplier support structure (PSUP) or the rock wall. The anisotropy in $\vec{u}.\vec{r}$ could be an indication of unidentified backgrounds in the light water region outside the AV. It is also possible that they originate from the Vectran ropes that suspend the AV. This hypothesis could possibly explain the symmetric TAC distribution that has been observed with many isotropic events. The apparent inward-going nature of the events argues against them being due to the AV. Some of the inward-going events are likely due to high-energy γ backgrounds leaking into the detector near the equator. Monte Carlo simulations confirm that high-energy γ's from the rock can produce isotropic-looking event patterns that reconstruct primarily around the equator of the detector.

As a systematic check, we considered the temporal behavior and other variables of the selected isotropic data. The isotropic events from the reduced data set were checked for correlations in their distribution with run number, GTID, Julian days (since 1975), and the time of day. Figure 3.18 shows the livetime-normalized distribution of isotropic events for the first 100 days of data taking since November 2, 1999, and for the hour of day. When we take into account that some of the isotropic events occur in bursts no significant variation of event rate with time of day is observed. This shows that these events are not due to reoccurring interference with daily detector operations or operations in the Creighton mine. However, it has been demonstrated that the rates of isotropic events at particular reconstructed locations on the AV may change abruptly after week-long periods of stable

event rates [159]. This is consistent with the hypothesis that some of the isotropic events are due to the crazing of acrylic.

The plot on the right hand side in Figure 3.18 shows the time distributions of isotropic events for 9070 $\leq$ Julian Day (JDY) $\leq$ 9120 and 9120 $\leq$ JDY $\leq$ 9170, as well as the combined distribution (solid line) for the first 100 days of data taking. Occupancy plots in TAC and hit tubes indicate that the isotropic events are distributed uniformly within the limited statistics of the selected data set. The TAC distribution of isotropic events is also an indication that some of these PMT hit patterns are not from signal events with a γ or a Čerenkov electron. Alternatively, the isotropy of the events could just be due to them being in the H_2O. In Figure 3.19 two sets of isotropic events are compared, one from the reduced data set and one from a collection of known physics events, such as muon followers and ^{16}N calibration data. The centroid of their summed-TAC distributions differs by 10-15 ns.

Flat-TAC events do not exhibit the characteristic time spectrum of Čerenkov events. It was observed that flat-TAC events often follow large events in the SNO detector. Flat-TAC events can be isotropic in distribution or have a distribution similar to the original event. They can also show a charge distribution peaked at zero in which case they are associated with electronics ringing. Usually, flat-TAC events do not reconstruct well with any of the fit algorithms used in SNO and hence are discarded after the reconstruction process.

Isotropic and flat-TAC events are potentially a worrisome background but it turns out that they can be removed fairly effectively using high-level data cuts. These are cuts designed to test the Čerenkov nature of events. Flat-TAC events are identified effectively based on the ratio of "in-time" to total light, their charge distribution, and by applying a reconstruction cut. As they are often following large events in the SNO detector, they are also removed by burst cuts. In addition, an isotropy parameter, called θ_{ij}, has been developed that is related to the average angle between hit PMT's and is a measure of the Čerenkov nature of the PMT hit pattern. It allows one to distinguish statistically between events with a single vertex or multiple vertices. The origin of isotropic events is unknown, however, they are characterized by possessing a large value of θ_{ij}. The high level cuts applied to the SNO data set are discussed in detail in Chapter 5.

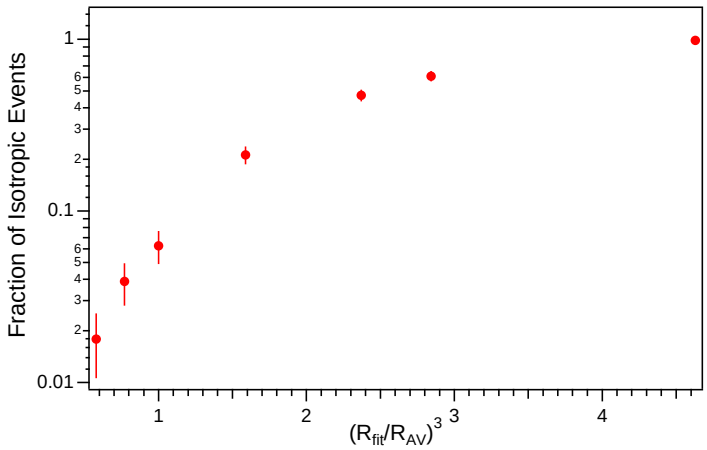

Figure 3.16: Fraction of reconstructed isotropic events with $R_{fit} \leq R$ as function of $(R_{fit}/R_{AV})^3$. The error bars are statistical. The data were reconstructed using the grid fitter.

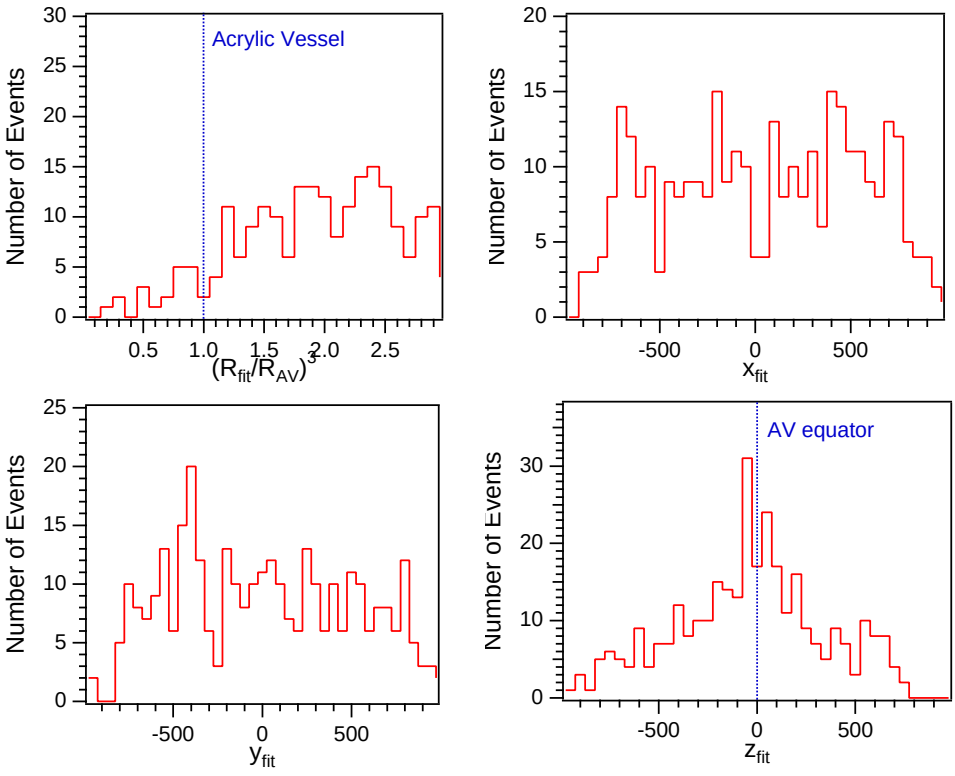

Figure 3.17: Reconstructed position of the isotropic events in the reduced data set.

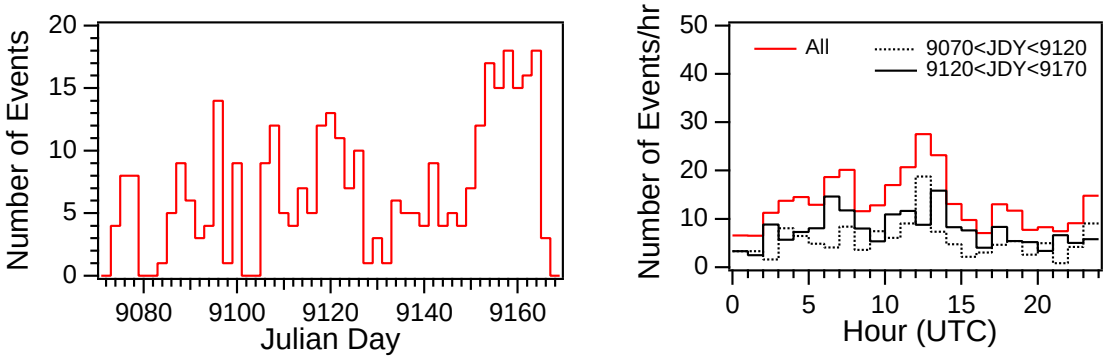

Figure 3.18: Normalized time distribution of isotropic events per day since the beginning of data taking (Nov 2, 1999) and per hour of day (UTC).

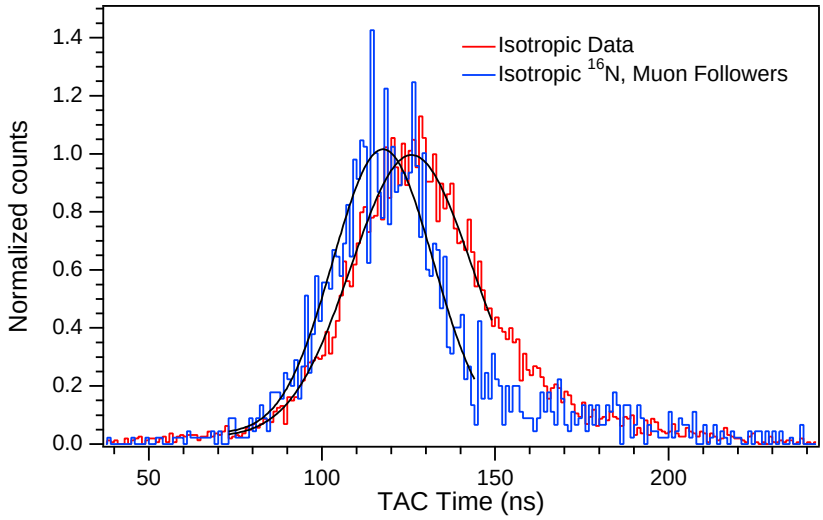

Figure 3.19: TAC spectra for isotropic events obtained from physics events (muon followers and ^{16}N) compared to isotropic events from the reduced data set.

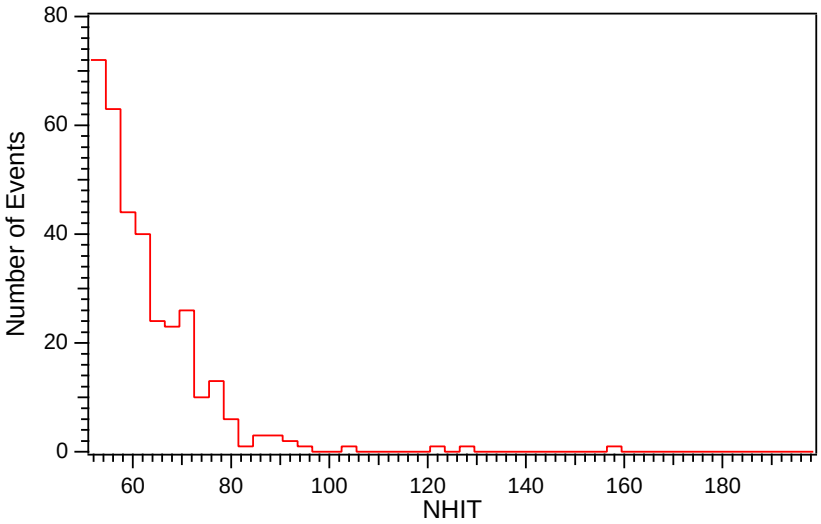

Figure 3.20: NHIT distribution of isotropic events in the reduced data set.

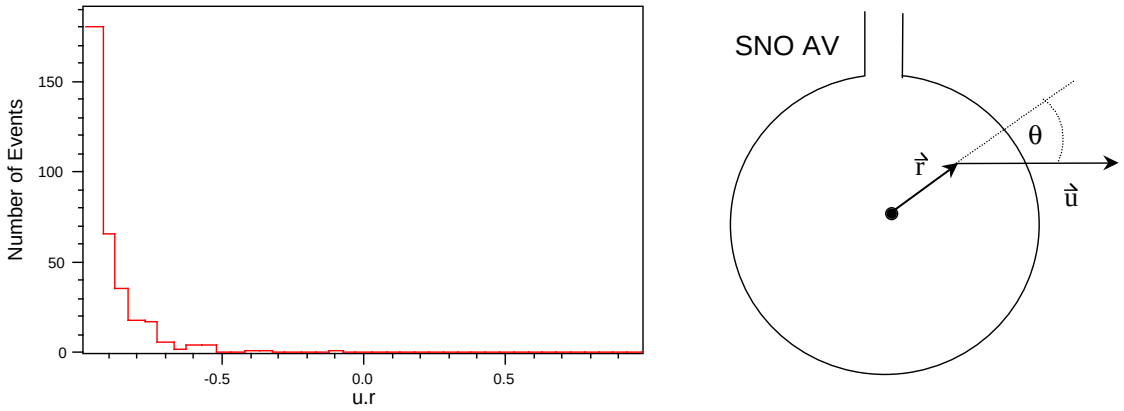

Figure 3.21: $\vec{u}.\vec{r}$ distribution of isotropic events with NHIT ≥ 50. This distribution from a set of isotropic events selected from the reduced data set.

3.7 Neutrino Signal Loss and Residual Background Contamination in the Reduced Data set

The data reduction cuts described in the previous sections allow us to eliminate the instrumental background in the raw data set. An obvious concern is that these data reduction cuts may also remove some of the neutrino signal and introduce a bias into the data sample. A second issue is the residual contamination of the data set. It is important to verify that after application of these cuts no further instrumental backgrounds are left in the data sample that could mimic a neutrino signal. Therefore, it is important to determine two quantities:

- Neutrino signal loss due to the application of data reduction cuts.
- Residual contamination of the reduced data set with instrumental backgrounds .

The characteristics of the data cleaning cuts have been studied in great detail in [142]. The signal loss has been measured in the SNO detector using different types of event from tagged calibration sources: 6.13-MeV γ-rays from ^{16}N, electrons from ^{8}Li, and photons from a diffuse laserball source. The contamination of the data set can be estimated using a bifurcated analysis method [13]. Based on the event verification described above, the contamination level in the reduced data set was estimated to be of the order of 1% or less.

In the solar neutrino analysis a second set of high-level event-quality cuts are applied to characterize the Čerenkov nature of events. The development and application of these cuts are described in the following Chapter 5. At the end of that chapter we will summarize our studies of neutrino signal loss in the final neutrino candidate event set.

3.8 Livetime Calculation

The SNO experiment is designed to measure the flux of solar neutrinos as well as their energy spectrum. For an accurate determination of the neutrino flux the interaction rates of solar neutrinos need to be calculated. This requires knowledge of the livetime of the detector over the period of data taking. The livetime of the candidate event set is calculated after instrumental backgrounds have been removed from the data set and the reduced data only consists of physics backgrounds and neutrino candidate events.

Two clock systems are used in the SNO electronics system to determine the absolute and relative time of each event. A 10 MHz clock coupled to the Global Positioning System (GPS) provides the primary time calibration. It is used to control most timing aspects of the raw SNO data stream and is continuously checked against the external GPS reference. A more precise 50 MHz clock with a 2-day roll-over time is used to measure accurately the timing between events. The signal for the 50 MHz clock comes from an external oscillator into the trigger system and is not tied to the GPS. The 50 MHz clock can replace the 10 MHz one in case of failure or be used as an independent check.

The raw livetime for each run is calculated by using the time stamps from the 10 MHz clock for the earliest and latest event. These times are verified by comparing to the 50 MHz clock and they are found to be in agreement to within 0.004% [142]. The livetime calculation can be verified using the Pulsed Global Trigger (PGT) or PulseGT. PulseGT triggers at 5 Hz and accompanies usual data taking. This trigger allows one to take a reading of the state of the detector, and to measure the noise rate of PMT's. It can also be used to verify the livetime. The livetime of the data set can be determined by counting the total number of PulseGT triggers. In comparison with the livetime calculation from the 10 and 50 MHz clock it is found that the livetime from PulseGT is about 8.9 hrs less than the 10 MHz livetime. This is due to a problem with the NHIT monitor.

The NHIT monitor is a tool that is used to monitor the NHIT trigger. This monitoring task is carried out by causing artificial triggers on channels of one specific crate. These triggers cause the NHIT trigger to fire, and the NHIT monitor checks that this takes place. The artificial events used in this process are called pedestals. In this process the NHIT

monitor prevents a fraction of PulseGT triggers from being recorded and they are lost from the analysis. These events be recovered by the use of the pedestal trigger in NHIT monitor events and the hit pattern of the pedestals. With these events we recover 8.6 hours of livetime. This leaves a residual discrepancy of 19 minutes between the livetimes derived from the 10 MHz clock and PulseGT. One should note that the 50 MHz clock which provides timing for the PGT actually runs at 49.9995 MHz. This accounts for 12.8 of the 19 minutes. The remaining difference is thought to be due to PGT triggers overlapping with real events or by a drifting 10 MHz clock.

In the removal of instrumental backgrounds several cuts are applied. Four of these cuts are time sensitive and affect the livetime of the neutrino run. These include the muon follower short, retrigger, burst, and NHIT burst cut. The muon follower and NHIT burst cut are the most significant ones. The error on the combined cut is primarily due to systematic errors in the NHIT burst cut. The associated livetime correction was calculated by adding the NHIT burst and Muon follower short corrections. The final livetime correction due to these cuts has been calculated and is listed in Table 3.9.

An additional correction to the livetime of the data set comes from dead time due to detector inefficiencies. At very high data rates in case of event bursts the PMT information sent to the event builder can exceed its capacities and the builder memory can become full. This results in events being flushed from the buffer. In this process events can lose all or part of their PMT information. Events that are not correctly assembled in the builder are called orphans. They represent PMT hit information that was not correctly built into regular events or events that lost a significant fraction of their PMT hits. Orphans can affect the livetime of the data set, the measured effective energy of events, and possibly the reconstructed direction. Orphans affect livetime in that there are periods when the throughput drops out in correlation with orphan bursts. The throughput is defined as the total number of hits assigned to non-orphan events. The periods of dropout were estimated by measuring the median throughput of each run and seeing where the throughput drops below 50% of the median. It is estimated that 3.078 hrs of data are lost in orphans. The orphan related deadtime is to be taken as an upper limit as the overlap between orphans and burst or muon related deadtime has not been studied. While orphans are effectively a loss

of PMT hits from events, it is also possible for PMT hits to be built into the wrong event. Some events can have duplicate hits recorded for one or more PMT. This type of event is discarded through the "Junk Cut" used in the removal of instrumental backgrounds.

The final livetime is calculated by subtracting off the corrections from the cuts and half of the estimated orphan deadtime. The uncertainty in the instrumental cut-related deadtime is taken to be $\pm 0.1\%$. As the uncertainties from the orphan deadtime and the instrumental cuts are not normal errors they are added linearly in the final error analysis. The uncertainty in the livetime calculation is mostly due to the livetime corrections and the associated systematics. The livetime calculation for the data set under consideration is summarized in Table 3.9.

Table 3.9: Calculation of the total livetime of the D_2O neutrino data set used in this analysis.

Measurement	Livetime /Deadtime	% of Raw Livetime
Raw 10 MHz clock	5894.78 hrs	100.00%
Retrigger	13.3 s	0.000063%
Burst	15.8 min	0.0045%
NHIT Burst	8.4 hrs	0.14%
Muon Follower	102.1 hrs	1.73%
Combined Instrumental Cuts	110.47 hrs	1.86%
Orphans	≤ 3.08 hrs	$0.026 \pm 0.026\%$
Corrected livetime	5782.8 ± 7.3	

A month-by-month livetime calculation is summarized in Table 3.10. In addition to miscellaneous deadtime corrections a month-by-month estimate of the orphan deadtime was obtained. This estimate was obtained by measuring the median throughput of each run and seeing where the throughput drops below 50% of the median. The throughput is defined as the total number of hits assigned to non-orphan events, binned into 10 second intervals. In addition, the two bins before and the bin after the drop are tagged. To ensure that the dropout is real, it is required that at least 10 orphans are observed in this time window.

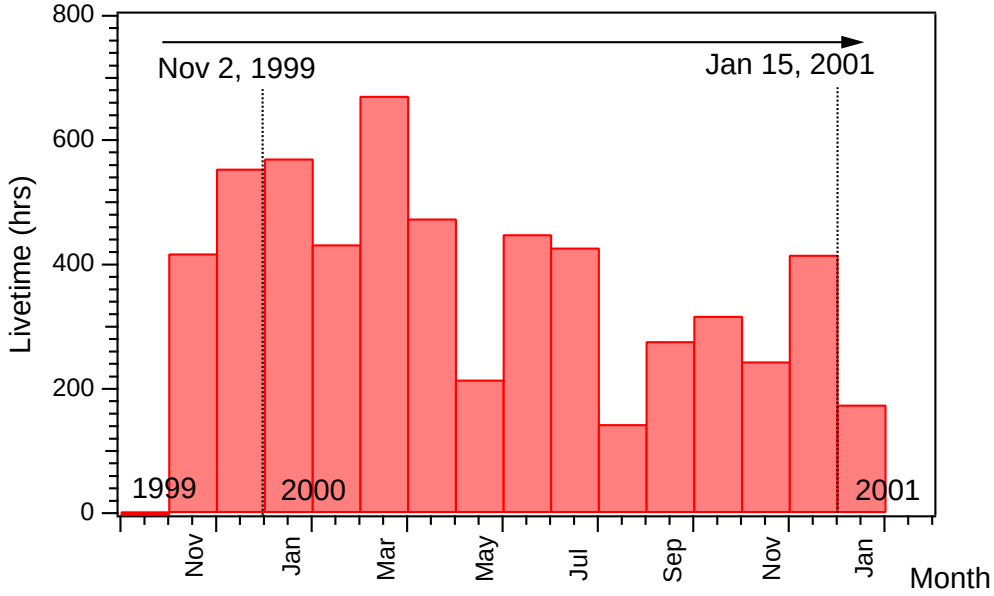

Figure 3.22: Monthly livetime during the period of data taking.

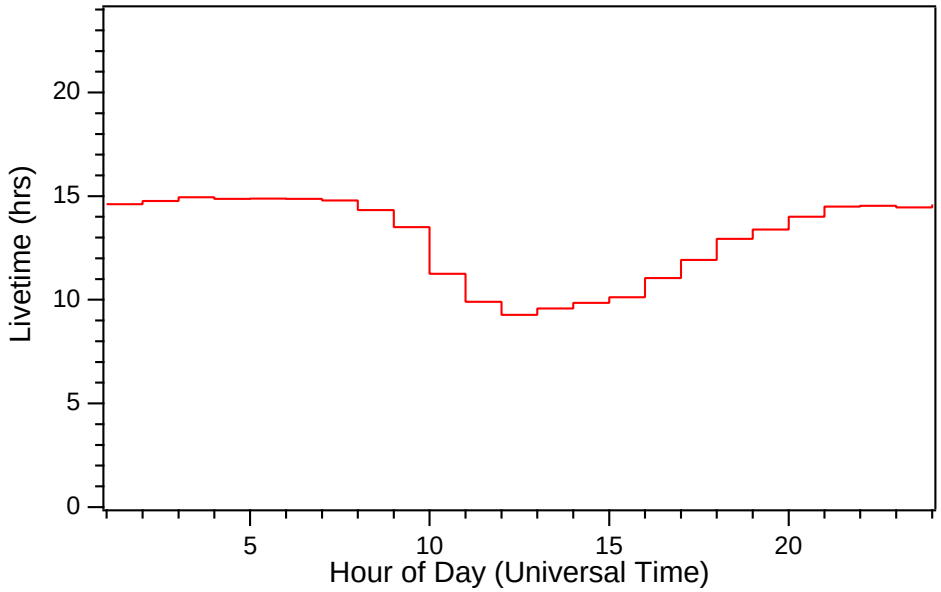

Figure 3.23: Livetime distribution of per day averaged over the period of data taking.

Table 3.10: Month-by-month livetime calculation for the D_2O neutrino data set. All times are in hrs.

Month	Number of Runs	Run Number	Raw Livetime 10 MHz Clock (hrs)	Misc. Corrections (hrs)	Orphan Deadtime (hrs)	Total Livetime (hrs)
Nov99	41	10000 - 10237	426.26	8.64	0.05	417.6 ± 0.5
Dec99	44	10534 - 10770	565.69	11.67	0.26	553.9 ± 0.7
Jan00	61	10773 - 10956	581.75	11.06	0.35	570.5 ± 0.8
Feb00	28	10959 - 11389	440.55	8.02	0.01	432.5 ± 0.4
Mar00	32	11390 - 11510	683.98	12.24	0.48	671.5 ± 0.9
Apr00	30	11512 - 11681	483.25	9.09	0.24	474.0 ± 0.6
May00	21	11682 - 11899	219.56	4.72	0.08	214.8 ± 0.3
Jun00	24	11901 - 12168	457.12	8.48	0.14	448.6 ± 0.5
Jul00	22	12172 - 12289	436.47	8.67	0.54	427.5 ± 0.7
Aug00	12	12290 - 12614	146.24	2.65	0.03	143.6 ± 0.2
Sep00	16	12615 - 13401	282.00	5.21	0.14	276.7 ± 0.4
Oct00	15	13405 - 13746	322.36	5.27	0.00	317.1 ± 0.3
Nov00	19	13811 - 14196	248.36	4.25	0.10	244.1 ± 0.3
Dec00	30	14252 - 14417	423.31	7.37	0.51	415.7 ± 0.7
Jan01	15	14422 - 14685	177.87	3.11	0.16	174.7 ± 0.3
All runs	410	10000-14685	5894.78	110.47	3.08	5782.8 ± 7.3

CHAPTER 4

EVENT RECONSTRUCTION WITH THE SNO GRID FITTER

The aim of fitters is to reconstruct the vertex and direction of any given event, including Čerenkov electrons from neutrino interactions, $\beta - \gamma$ backgrounds, and γ's from calibration data or other backgrounds. Reconstruction of an event vertex and direction is arguably one of the key steps in the analysis of data recorded in the SNO detector. Accurate vertex reconstruction enables us to correlate the event with different detector regions and allows us to determine the likelihood for an event to come from a distribution of backgrounds or neutrino signals. In particular, the characteristic spatial distributions of event classes play a significant role in distinguishing and separating event classes. It is also important to avoid misreconstruction and to reduce the tail in the spatial distributions of the fitted vertices. This minimize the number of external backgrounds leaking into the central volume of the SNO detector. Of particular concern are PMT, AV, and H_2O $\beta - \gamma$s which are found to reconstruct sometimes inside the central D_2O volume. Directional information is important as it allows us to correlate the event direction with the solar position. For a neutrino candidate event, the reconstructed direction of the event is expected to point away from the Sun.

Furthermore, it is desirable that the fitter used for the reconstruction of the reduced data set not be optimized for any one particular event class. This would make it impossible to simultaneously fit neutrino signals and background events in the raw data set. The fitter chosen in this analysis is designed to handle various classes of events without making specific assumptions on their origin.

Reconstruction is a critical component of the analysis as the uncertainty in reconstruction does affect the uncertainties in our flux measurement. Some of the general considerations that drive the accurate reconstruction of both neutrino signals and backgrounds are summarized below.

- *Definition of the Fiducial Volume:* The fiducial volume describes the detector region that is used in the selection of candidate neutrino events. The number of neutrino interactions in the fiducial volume is determined from the number of reconstructed interactions in that volume. Therefore, it is critical that the reconstructed positions match the actual event positions. The systematic error on the absolute number of events in the fiducial volume depends directly on the vertex reconstruction uncertainty of events.

- *Separation of Neutrino Signal and Background Events:* Neutrino signals and backgrounds exhibit very different detector distributions. For a detailed discussion of the characteristic event distributions see Chapter 8. The reconstructed detector distributions can be used in the separation of signals and backgrounds. The goal of reconstruction is to match the underlying event distributions that are determined from the fundamental physics of the interaction and the propagation of the resulting particles. An error in the response function used to model the detector will alter the number of events we fit out from the data. Both the reconstructed position and direction are important quantities in the separation of event classes.

- *Reconstruction Independent of Event Type:* The reduced data set which we obtain after removal of all instrumental backgrounds contains events from radioactive backgrounds as well as signatures of neutrino interactions. In an unbiased analysis of the event set it is important that the reconstruction algorithm has the ability to reconstruct different event classes, including Čerenkov electrons, γ's from ^{2}H(n,γ)^{3}H reactions, and background events, such as $\beta - \gamma$'s from ^{208}Tl and ^{214}Bi decays. If the fitter is optimized to one particular event class one can end up with good performance for the optimized class but poor performance for other classes.

The performance of fit algorithms is characterized by comparing Monte Carlo and calibration data. The scale of the systematic uncertainties on reconstruction is determined through comparison of Monte Carlo prediction of fitter performance with that determined from calibration sources. The dependence on event position is explored through position

scans with calibration devices and the dependence on energy by using Monte Carlo as well as sources producing varying particle energies. The difference between the reconstructed distributions obtained from calibration data and Monte Carlo represents the accuracy in the Monte Carlo generation of spatial distributions for neutrino events as well as backgrounds.

4.1 Reconstruction with the Grid Fitter

The grid fitter (FTG) is a maximum likelihood fitter which uses a normalized distribution of PMT hit time residuals derived from Monte Carlo as a PDF. The vertex and direction are fit independently, using only time information. The angular information of the hit PMT's is ignored. This makes the fitter as general as possible and capable of fitting simultaneously different classes of events which can have very different angular distributions.

The grid fitter likelihood is maximized in two steps. The fitter operates by finding places in the detector where photons could have originated from. First, the function is maximized at each point in a 3-dimensional position grid of ∼1 m spacing within the detector volume. At each gridpoint a log-likelihood function is minimized with respect to time, the only remaining free parameter of the vertex. This is a set of N_{grid} 1-dimensional minimizations in the fit time, where N_{grid} is the total number of grid points. After the grid search has been completed, the r_{fit} and t_{fit} corresponding to the grid point with the lowest log-likelihood is used as a start point for minimizing the complete likelihood function in 4 dimensions with respect to x, y, z, and t. The PDF is derived from fitting t_{fit} while keeping r_{hit} at the true vertex. The minimization is done with the CERN routine MINUIT [55] [1].

The log-likelihood function is calculated in the dimension of residual time, t_{res}, which for each hit tube is defined as:

$$t_{res} = t_{hit} - t_{fit} - |r_{fit} - r_{PMT}| \frac{n}{c} \tag{4.1}$$

Figure 4.1 shows typical timing residuals for an event inside the detector. The peak of

[1] MINUIT is a function minimization and error analysis program. It is a tool to find the minimum value of a multi-parameter function and analyze the shape of the function around the minimum. Its principal application is in statistical analysis. For more information see http://wwwinfo.cern.ch/asdoc/minuit/.

prompt light is clearly visible. The distribution of timing residuals has large tails which can be different for different classes of events. The tail on the early side ($t_{res} \leq 0$) is entirely due to PMT noise as all scattered and reflected light can only arrive later compared to the arrival time of photons from the true vertex. The small early peak is due to direct photoemission from the first dynode. The relative probability for getting noise events hits is inversely proportional to the total number of hits per event, the NHIT of an event. The late side of the timing distribution is mainly characterized by the effects of reflection and scattering which are dependent on the location of the event vertex. Reflections from the photomultiplier support structure (PSUP) show the characteristic time difference of 70 ns (the photon transit time across the detector) relative to the prompt peak in the timing distribution.

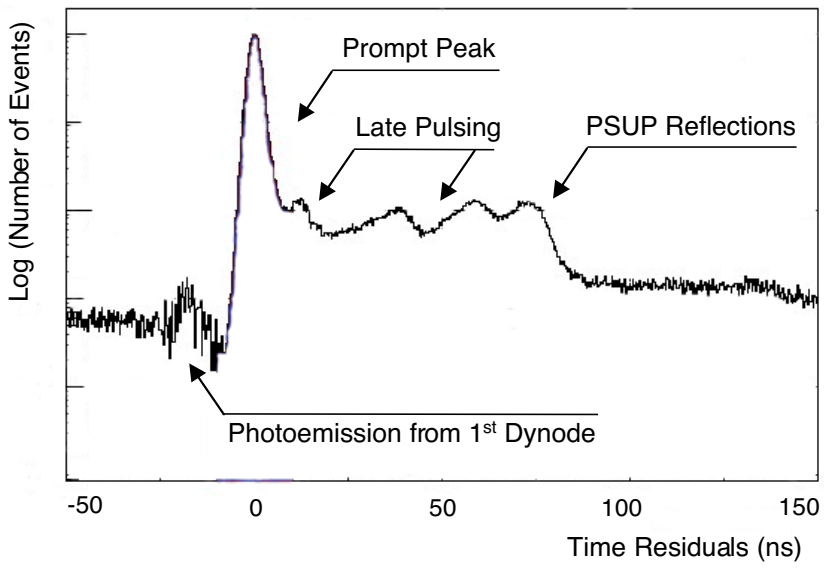

Figure 4.1: Timing residuals of ^{16}N calibration events.

Fully multidimensional probability distribution functions (PDF) of tubes that take into account the correlation between the time and the angular distribution are difficult to deal with as they are functionally discrete. The grid fitter uses averaged t_{res} distributions that

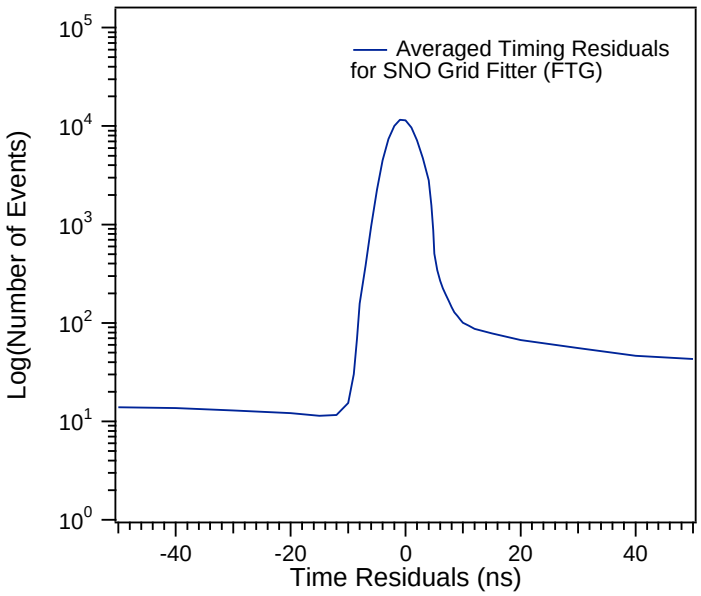

Figure 4.2: Functional form $P(t_{res})$ for an averaged distribution of timing residuals t_{res} in the grid fitter.

are fitted to a smooth functional form with six parameters. The Monte Carlo events used to generate the PDF were ^{208}Tl decays in the D_2O, AV, and PMT regions, and the final PDF is a fit to the average of the resulting t_{res} distributions from these simulations. An example of such a PDF is shown in Figure 4.2.

In this PDF the PMT noise component is a flat background across the entire distribution. It is inversely proportional to the NHIT values of the fitted event. Having obtained a functional form for the probability distribution $P(t_{res})$ one can fit t_{fit} in 1 dimension keeping r_{fit} fixed or fit t_{fit} and r_{fit} simultaneously in 4 dimensions by minimizing the log-likelihood function

$$\log - \text{likelihood} = \sum_{i=1}^{NHIT} -log(P(t_{res}(i))) \tag{4.2}$$

where t_{res} is given by 4.1 and $P(t_{res})$ is the function shown in Figure 4.2.

With this method the long non-gaussian tails that occur in the vertex reconstruction

Table 4.1: Efficiency of grid fitter on Monte Carlo events with NHIT ≥ 30.

Particle/Decay	Reconstructed Events	Failed Reconstruction	Efficiency
5 MeV electron	4717	1	>99.97%
6.13-MeV γ from ^{16}N	40802	0	>99.99%
^{208}Tl decays	32517	1	>99.99%
^{214}Bi decays	25061	2	>99.99%
PMT $\beta - \gamma$	1172	14	>98.9%

based on a time residual alone are eliminated. The time difference in hit PMT's due to scattering, reflections, and PMT noise is no longer of concern. The efficiency of the grid fitter is $\geq 99.9\%$ for all events with NHIT ≥ 30 except for PMT $\beta-\gamma$'s. The fitter efficiency was determined using Monte Carlo simulations for charged-current (CC), neutral-current (NC), and elastic scattering (ES) events, as well as ^{208}Tl and ^{214}Bi backgrounds, and ^{16}N calibration data. For a detailed summary see Table 4.1.

In all of the subsequent analysis we use the event vertex and the maximum likelihood direction from the grid fitter. The fitter has been characterized using ^{16}N, ^{8}Li, Monte Carlo simulations, and benchmarking data sets of various event types and classes. Uncertainties related to the reconstruction with this fitter are included in the evaluation of systematics.

The refractive indices of the different materials and detector regions in SNO affect the reconstruction of events. The specific values used in this analysis are listed in Table 4.2. The speed of light used in the propagation of Čerenkov photons in heavy water is 21.75 cm/ns corresponding to an effective refractive index of 1.378 in heavy water.

4.1.1 Position Fit

All SNO position fitters are based on the same principle. If $\vec{r}_i$ and t_i are the position and time of a PMT hit, and $\vec{r}_{ev}$ and t_{ev} are the creation position and time of the photon that caused the hit, and v is the group speed light in water then

Table 4.2: Effective refractive indices of optical detector media and speed of light used in the calculation of propagation of Čerenkov photons.

Medium	Index of Refraction	Speed of Light (cm/ns)
Heavy Water	1.378	21.75
Light water	1.342	22.33
Acrylic	1.5	19.98

$$R_i = |\vec{r}_i - \vec{r}_{ev}| - v(t_i - t_{ev}) = 0 \tag{4.3}$$

All position fitters to date are based on minimizing the PMT timing residuals, R_i. In fitting the same $\vec{r}_{fit}$ and t_{fit} to all residuals of an event the implicit assumption is being made that all the light originates from a single point in space and at a single time. This is a reasonable assumption for Čerenkov electrons. The time over which Čerenkov light is emitted by a 10 MeV electron is smaller than the timing resolution of the PMT's and the region over which it is emitted is smaller than v times the timing resolution, even when considering Compton scatters from most γ cascades.

In principle, the cone of an event could also be used to fit an event position by simply placing a cone of the correct opening angle in the position and direction that best accounts for the observed hit positions and times. In SNO this method does not yield any improvement since the Čerenkov cone of events is smeared by electron scattering. A hybrid method using a combination of a cone fit and a reconstruction based on PMT residuals has been pursued and is used in a different SNO analysis [150].

4.1.2 Direction Fit

Fitting a direction to an event only makes sense if the hits originate from a single Čerenkov electron. A direction fit makes the intrinsic assumption that the event is a single electron produced in a neutrino interaction. The aim of the direction fit is to infer the mean electron

direction. However, in the reduced data set it is not known *a priori* whether an event stems from one electron or a multi-particle event. All direction fits are also based on one principle: The axis of the Čerenkov cone as the electron propagates is given by the instantaneous direction and so the directions of the PMT hits from a fitted event position can be used to infer a single electron direction. Electrons between 5 and 10 MeV will undergo considerable direction changes as they propagate and multiply scatter in the electric field of the surrounding atoms. Because the time between the creation of a Čerenkov electron and its energy loss below the Čerenkov threshold is smaller than the intrinsic time resolution of the PMT's the creation order of the photons which cause the PMT hits cannot be inferred and so the direction fit reflects some average electron direction which may be very different from the initial direction one is usually interested in.

Event reconstruction based on the time residuals, t_{res}, does not make use of the fact that many Čerenkov photons produced by an electron are emitted along a Čerenkov cone. As the definition of direction is only meaningful for a single-particle event the Čerenkov cone information can be used in the reconstruction of the event direction without losing generality with respect to the different event classes.

For this work, a probability distribution function of Čerenkov photon hits was derived from Monte Carlo simulations. The result of a Monte Carlo simulation of $\sim 30,000$ photons is shown in Figure 4.3. The probability distribution function, $Prob(\theta)$, can be parameterized in form of a discrete polynomial function for $\theta < 0.733$ and $\theta > 0.733$:

$$Prob(\theta) = \alpha_0 + \alpha_1\theta + \alpha_2\theta^2 + \alpha_3\theta^3 + \alpha_4\theta^4 \tag{4.4}$$

where θ is the angle between the photon direction and the electron direction. The fit parameters of this function are tabulated in Table 4.3.

The event direction is reconstructed by maximizing the likelihood function.

$$P(\theta)_{Likelihood} = \sum_i Log(Prob(\theta_i)) \tag{4.5}$$

Table 4.3: Čerenkov photon angle parameterization. Coefficient of the polynomial probability distribution function that parameterizes the Čerenkov photon angle.

Parameter	$\theta < 0.733$	$\theta > 0.733$
α_0	-7.48	4742.3
α_1	1354.2	-6657.1
α_2	-1617.6	3674.4
α_3	3611.6	-925.23
α_4	0	88.222

The hits discarded by the vertex reconstruction are not used in the direction reconstruction. The direction fit turns out to be fairly insensitive to the energy dependence and the exact functional form of the probability distribution function, $Prob(\theta)$. Instead of the polynomial given above a truncated Gaussian can be used to describe the peak at the Čerenkov angle.

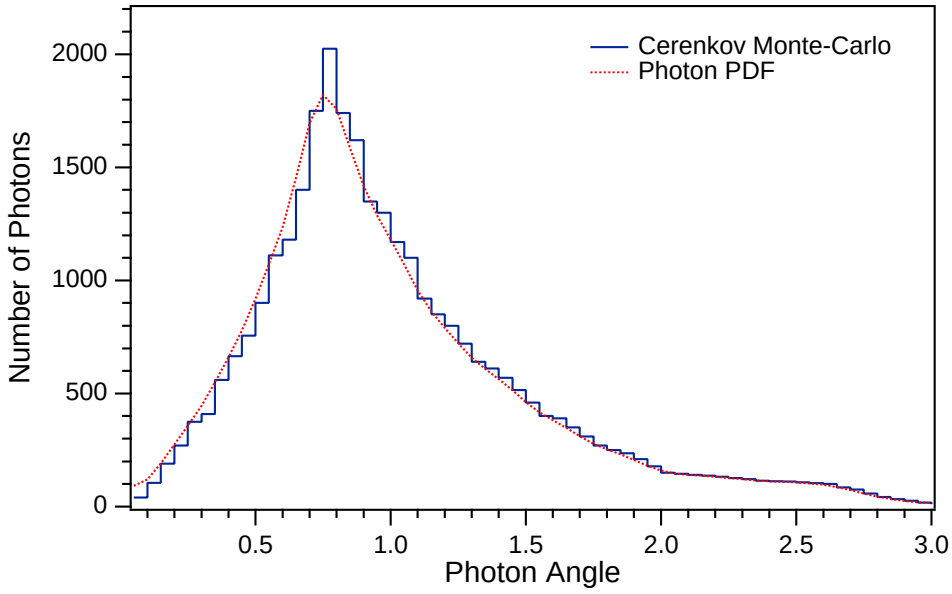

Figure 4.3: Angular distribution of Čerenkov photons produced by $\sim$ 30,000 5 MeV electrons uniformly generated in the D_2O region. The dotted line is the probability distribution function used to fit the distribution.

4.2 Systematic Effects in Reconstruction

Both the reconstructed position and direction of an event are critical in the analysis and decomposition of the reduced data set. The location of an event in space and its directionality are used in determining the likelihood of a particular event class.

The position of an event will also determine whether it is included in the fiducial volume chosen for the final analysis of the data set.

4.2.1 Misreconstruction of Event Positions: Fitter Tail

In the Monte Carlo study of the reconstruction algorithms used in SNO it was found that there are events that are reconstructed far from their event vertex. This leads to backgrounds in the reconstructed data set that appear to have originated in the fiducial volume while they actually come from detector regions outside the central D_2O volume. Misreconstructed events include $\beta - \gamma$ backgrounds from the PMT's, the H_2O, and the acrylic vessel. The following issues motivate the reduction of these tails with an appropriate reconstruction algorithm.

• The number of PMT $\beta - \gamma$'s which reconstruct inside the D_2O is a direct background to the low-energy neutrino signal. The goal is to eliminate these events so that the analysis threshold is determined by the intrinsic background from D_2O $\beta - \gamma$'s. The high number of PMT backgrounds events makes this difficult. The ratio of background events from the PMT's and the D_2O is about $N_{PMT\beta-\gamma}/N_{D2O\beta-\gamma} \sim 10^6$.

• The inner volume of the SNO detector with R$\leq$400 cm is the cleanest part of the SNO experiment and furthest away from any external backgrounds. This central volume can be used for an *in-situ* monitoring of the D_2O-internal Čerenkov backgrounds [26]. It allows one to measure the concentrations of ^{208}Tl and ^{214}Bi in the D_2O. For this method to be useful the reconstructed data set from the central volume of the SNO detector must be free from any events other than D_2O $\beta - \gamma$'s. The contamination with misreconstructed, external backgrounds is to be minimized.

Figure 4.4 shows the distribution of misreconstruction for different Monte Carlo event classes. For this Monte Carlo study the CC and NC events were generated uniformly in the

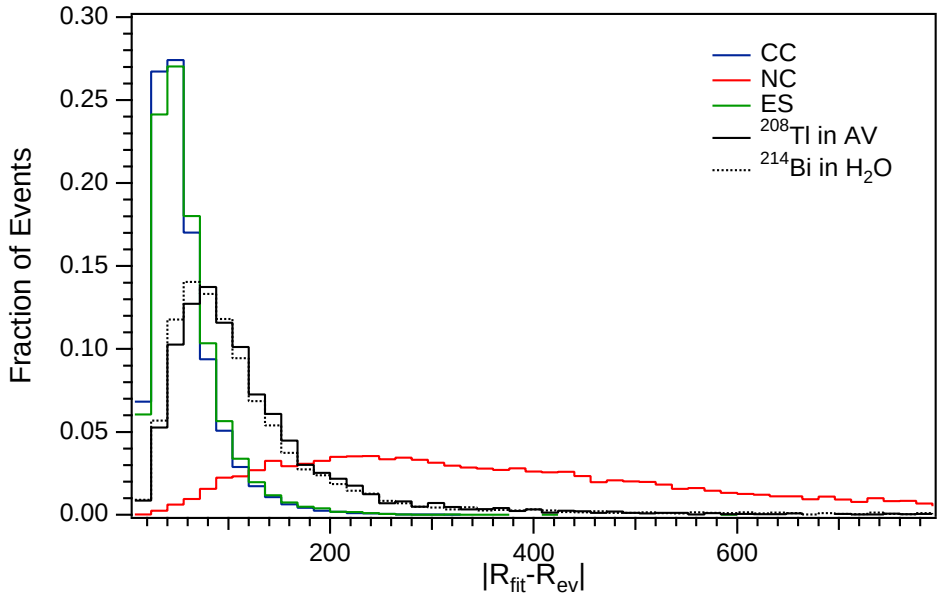

Figure 4.4: Distribution of misreconstruction, defined as $|R_{fit} - R_{ev}|$, for different Monte Carlo event classes.

D_2O while ES events are generated in both the D_2O and H_2O. The H_2O background is a uniform distribution of ^{214}Bi in the light water. In general, the AV and H_2O backgrounds show a much longer tail than the neutrino signals in the D_2O. The wide distribution of $|R_{fit} - R_{ev}|$ for neutral-current events is striking. The neutron produced in the neutral-current interaction thermalizes in the D_2O before it capture on deuterium or hydrogen. In reconstruction, the point of neutron capture is identified. This, however, can differ significantly from the original vertex of neutrino interaction.

For comparison, Figure 4.5 shows the radial distributions of various interactions and reconstructed events. The reconstructed distributions of the AV and H_2O backgrounds illustrate nicely how misreconstructed events from the AV and H_2O can contaminate the central D_2O volume.

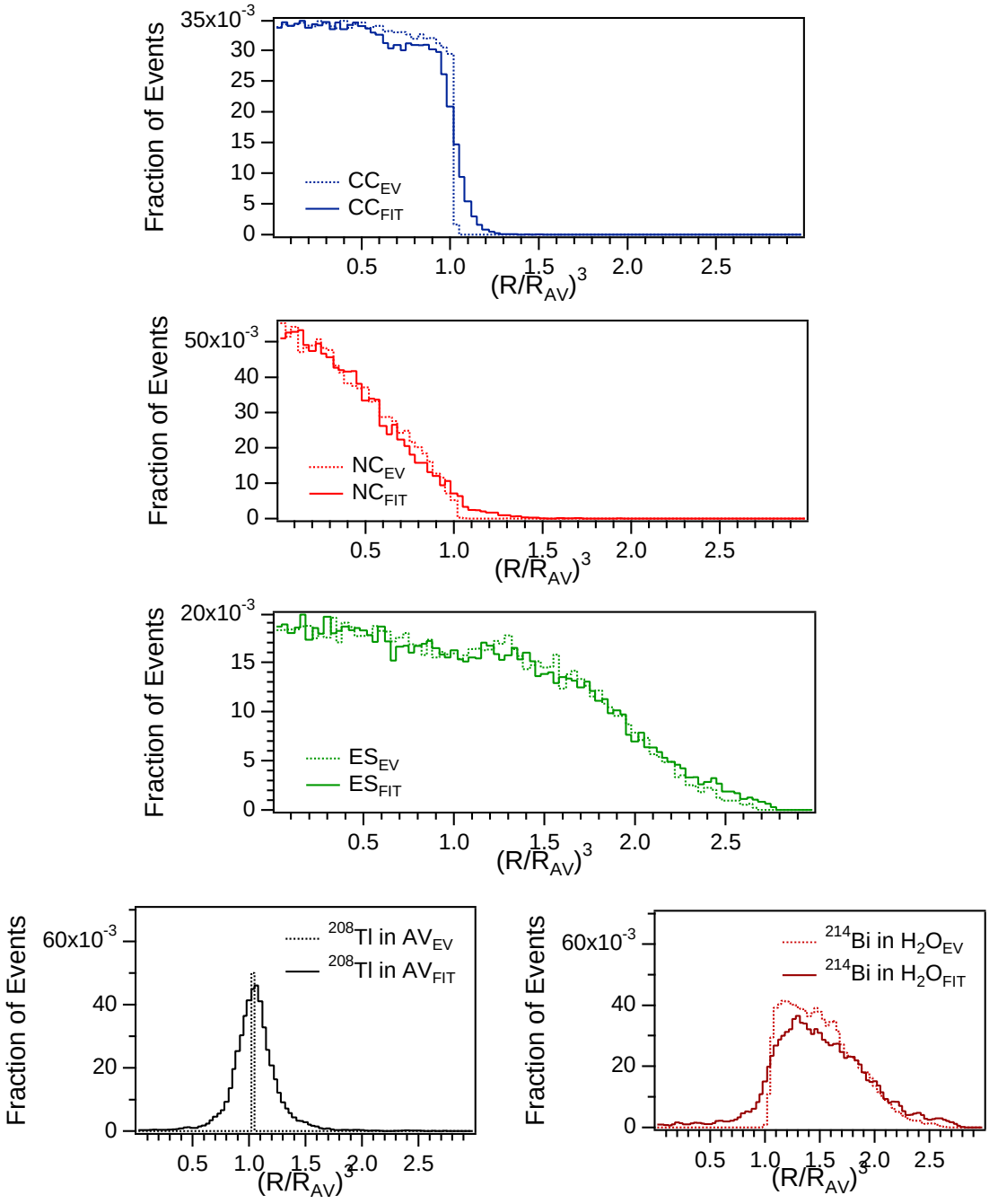

Figure 4.5: Distributions of $(R/R_{AV})^3$ for the different neutrino signals with NHIT $\geq$ 45 and the main AV and H_2O backgrounds for NHIT $\geq$ 20. The H_2O background assumes a uniform distribution of ^{214}Bi in the light water. The actual distributions of Monte Carlo events are indicated by the dashed lines. The solid lines show the reconstructed event distributions.

4.2.2 Directional Fitter Pull

In the characterization of fit algorithms it is found that the hit time information alone is not sufficient. It leads to the so-called "fitter drive", which tends to push an electron along its direction of motion. In this effect late PMT's inside the Čerenkov ring tend to move the electron backwards, late tubes outside move the electron forward. All fitters that are based on the minimizing PMT residuals are subject to a systematic shift of the fitter position away from the true vertex and along the electron direction. This shift is known as fitter drive. This effect is mostly due to the fact that photons do scatter or reflect on their way from the event vertex to the PMT and the fact that late hits are more likely to occur outside the Čerenkov cone. These effects combine to produce a systematic shift in the fitted position away from the true position and along the electron's direction. It can be parameterized in the form

$$\frac{(\vec{r}_{fit} - \vec{r}_{ev}).\vec{u}}{|\vec{r}_{fit} - \vec{r}_{ev}|} \tag{4.6}$$

Figure 4.6 shows the effect of fitter drive for Monte Carlo simulations of the different neutrino signals and ^{16}N data. We find that $\vec{r}_{fit}$ is usually pulled away from the true position $\vec{r}_{ev}$ and along the direction $\vec{u}$. The large peak at +1 indicates a string tendency for the fitted position $\vec{r}_{fit}$ to be pulled away from the true position $\vec{r}_{ev}$ and along the direction $\vec{u}$. The smaller peak at -1 shows a weaker tendency for the pull to be against the electron direction.

It is well known that late hits within the Čerenkov cone tend to push the fit position back along the track direction and such hits outside the cone pull it along the track direction. With more phase space outside the Čerenkov cone then the usual effect of such fitter drive is to push the fit position along the direction of the Čerenkov electron.

This effect can explained as follows: An electron travelling radially with direction $\vec{u}$ will produce a Čerenkov cone that intersects the PMT sphere in a perfect circle. If the detector had an infinite spatial resolution and if none of the photons scattered away the photons would form a perfect circular hit pattern. Each photon would have the same arrival time t_a. A residual based fitter applied to this pattern will be able to determine

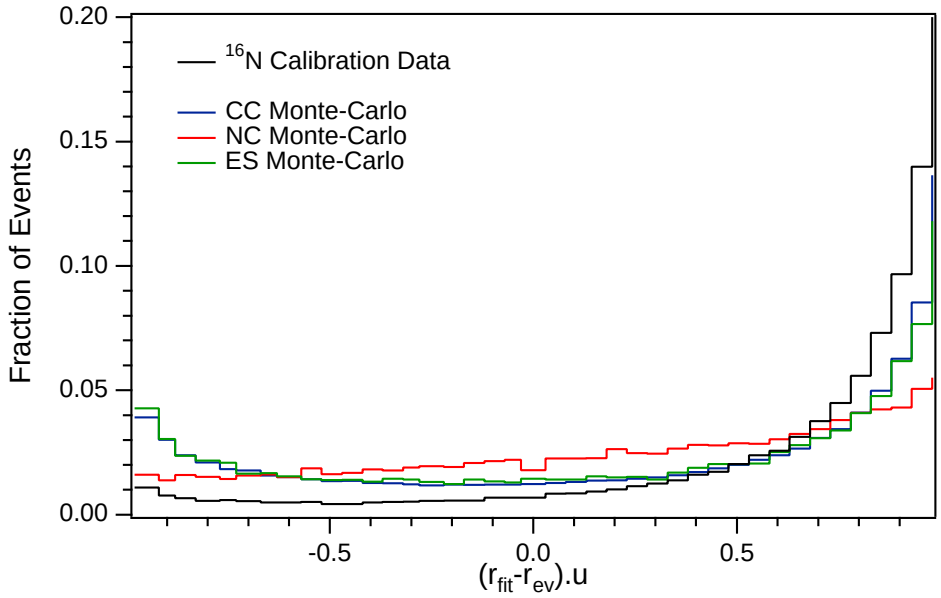

Figure 4.6: The effect of fitter drive on the reconstructed direction of neutrino signals and ^{16}N calibration data.

that the event lies along the dashed line but its position along the line will be completely undetermined. A single additional hit off the circle would enable the fitter to pin down an event position along the line of direction. Scattered light is always late with respect to the prompt Čerenkov photons. With the assumption that hits from scattered and reflected light have equal probability to show up anywhere on the PMT sphere the Čerenkov angle ensures that they are more likely to occur outside the Čerenkov cone than inside. Therefore, the fitter drive will be along the electron's direction of motion.

4.3 Rate Dependence of Event Reconstruction

In the calibration of the SNO detector it was found that the timing of a particular channel depends on the time since its last valid event. This effect is due to a variation in the ADC pedestal and ADC slope with time since last hit (TSLH), an unanticipated and not completely understood feature of the electronics. It was observed that the fitter time residuals depend on the data rate. Low rate calibration data which was taken at a frequency of < 0.5 Hz exhibits a fairly large tail on the early side and shows this effect very clearly. This "Time-Since-Last-Hit-Dependence" (TSLH) affects the reconstruction of events as it is based on the timing residuals of the event. As a result, the spatial distribution of events is different for low- and high-rate data. A software solution performing a "History Calibration" (HCA) was applied to correct for this effect. After recording the raw data the time between valid event hits on a given channel is determined offline and a correction function applied. The HCA correction eliminates nearly all of the early-side tail in the timing residuals. The difference in the spatial distribution of reconstructed events with and without the HCA correction applied is shown in Figure 4.7.

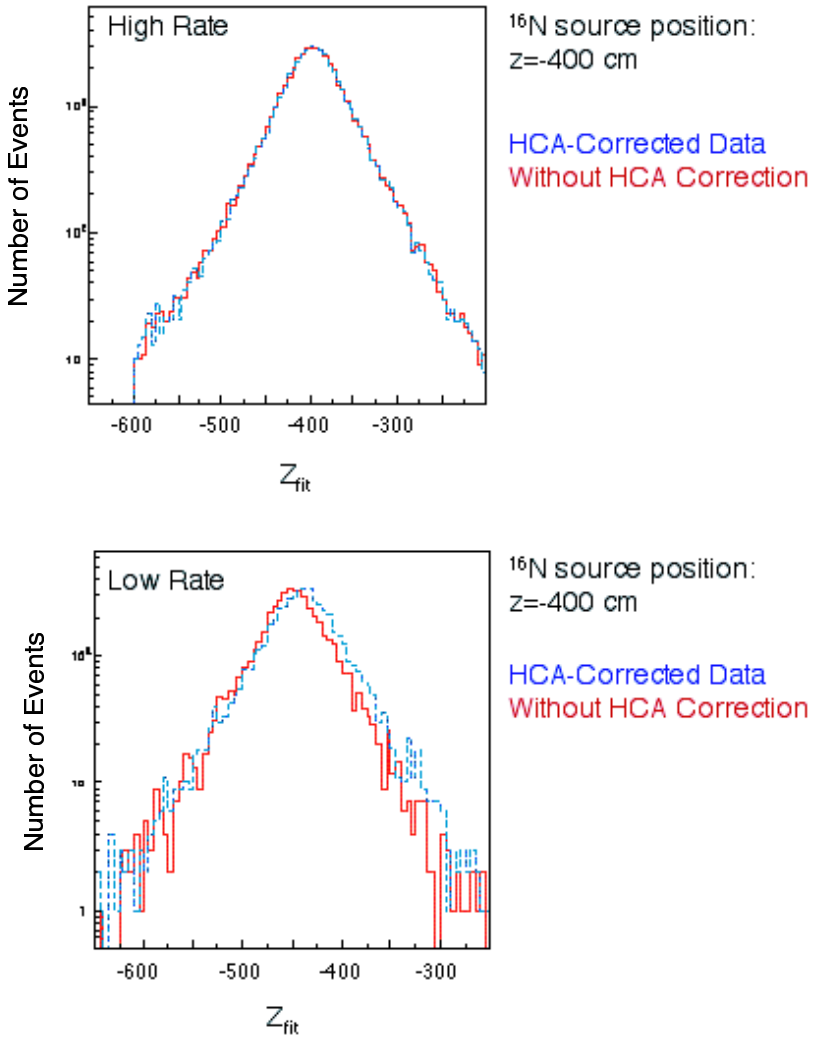

Figure 4.7: Event rate correction in ^{16}N reconstruction. Reconstructed z_{fit} distributions of ^{16}N calibration data taken at low and high rate with and without the HCA timing correction. The comparison illustrates the need for a timing correction based on the channel history.

4.4 Fitter Performance

Data from ^{16}N calibrations were used to evaluate the performance of the grid fitter quantitatively. Both the vertex shift and resolution as well as the fitter drive were studied. In addition, fits of the characteristic radial and angular distribution of ^{16}N data to Monte Carlo were made to evaluate the overall agreement between the detector response and Monte Carlo predictions. This is of particular interest to the neutrino signal extraction described in Chapter 9 as it allows us to quantify the goodness of fit of the calibration data and Monte Carlo predictions.

4.4.1 Vertex Shift and Resolution

The performance indicator of a vertex fitter is the spatial difference between the true event vertex and the fitted vertex. This difference is described by the difference between the individual cartesian coordinates of the reconstructed vertex and the location event. As the SNO detector is approximately spherical, the difference in the radial position is of particular interest.

$$\begin{aligned} \Delta x &= x_{fit} - x_{ev} \\ \Delta y &= y_{fit} - x_{ev} \\ \Delta z &= z_{fit} - x_{ev} \end{aligned} \tag{4.7}$$

$$R_{dev} = |\vec{r}_{fit} - \vec{r}_{ev}| = \left| \sqrt{(x_{fit} - x_{ev})^2 + (y_{fit} - y_{ev})^2 + (z_{fit} - z_{ev})^2} \right| \tag{4.8}$$

The absolute vertex resolution as well as systematic shifts in the vertex reconstruction are of concern to the solar neutrino flux analysis. Misreconstructed vertices are (presumably) symmetrically distributed around the true event vertex and their effects on the fiducial volume of the solar neutrino data set may cancel out. Systematic shifts in the reconstructed vertex, however, will directly affect the selected neutrino candidate event set.

Distributions in these variables have been generated in Monte Carlo simulations for all important classes of neutrino signals and backgrounds events using the grid fitter. The

vertex shift and angular resolution have also been studied using calibration data. The position resolution of the fitter is determined by comparison of HCA-corrected ^{16}N source data with the actual source position. Parameters have been extracted that describe the deviation from the source position in radius, and individual coordinates. The plots below illustrate the reconstruction properties of the grid fitter for HCA-corrected ^{16}N data.

The reconstructed detector distributions are a convolution of the true event distribution, $S(X_{ev})$, the detector response, and the reconstruction function.

$$D(x_{fit}, \sigma, \mu) = \int_{-\infty}^{\infty} F(x_{fit}, \sigma_{x,fit}, \mu, x_{ev}) S(x_{ev}) dx_{ev} \tag{4.9}$$

The reconstruction accuracy is determined by a Gaussian fit to the peak of the reconstructed distribution of ^{16}N events. The reconstruction response function can be defined as follows:

$$F_x(x_{fit}, \sigma_{x,fit}, \mu, x_{ev}) = \frac{1}{\sqrt{2\pi}\sigma} e^{\frac{[(x_{fit} - x_{ev}) - \mu]^2}{2\sigma^2}} \tag{4.10}$$

The response function F depends on the vertex resolution, σ, and the mean shift, μ.

Figures 4.8 and 4.9 show the calibration positions inside the D_2O detector volume used to characterize the grid fitter. An example of the reconstructed distribution of ^{16}N events in x, y, and z, as well as the Gaussian fit (dotted line) to the distributions is shown in Figure 4.10. Figure 4.11 shows the mean of the peak in the reconstructed radius, R_{fit}, and the standard error of the fit, σ_{Rfit}. The error estimates obtained from the radial reconstruction are consistent with the variation of the reconstructed event position in x, y, and z (Figure 4.12).

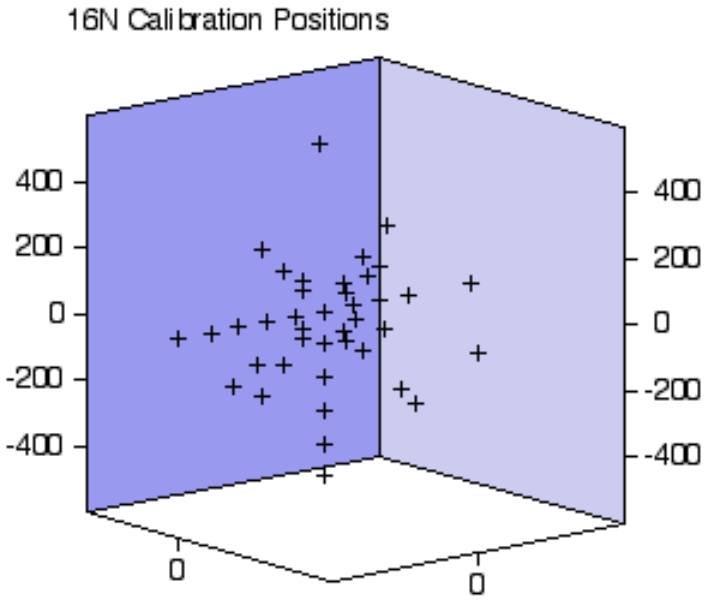

Figure 4.8: Calibration positions of the ^{16}N calibration source inside the D_2O during the ^{16}N scan in November 1999.

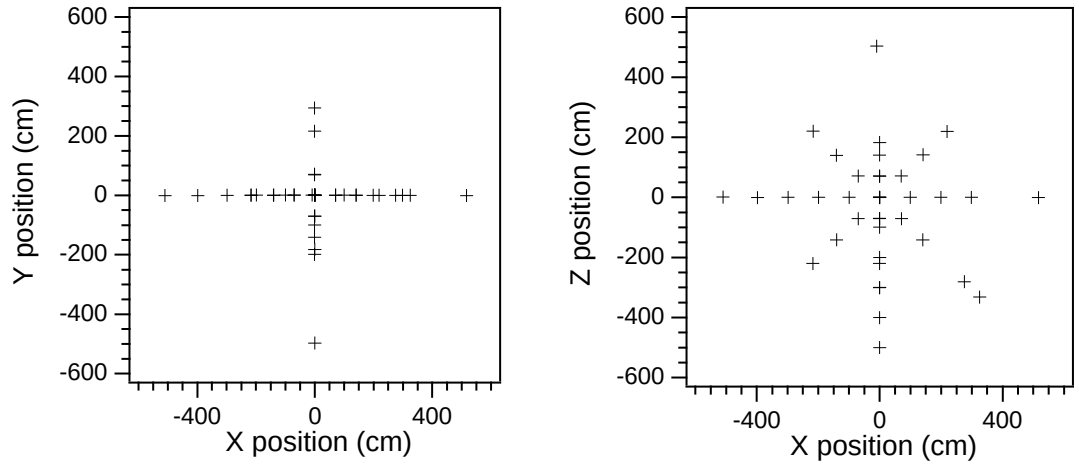

Figure 4.9: ^{16}N calibration positions in the x-y and x-z detector plane.

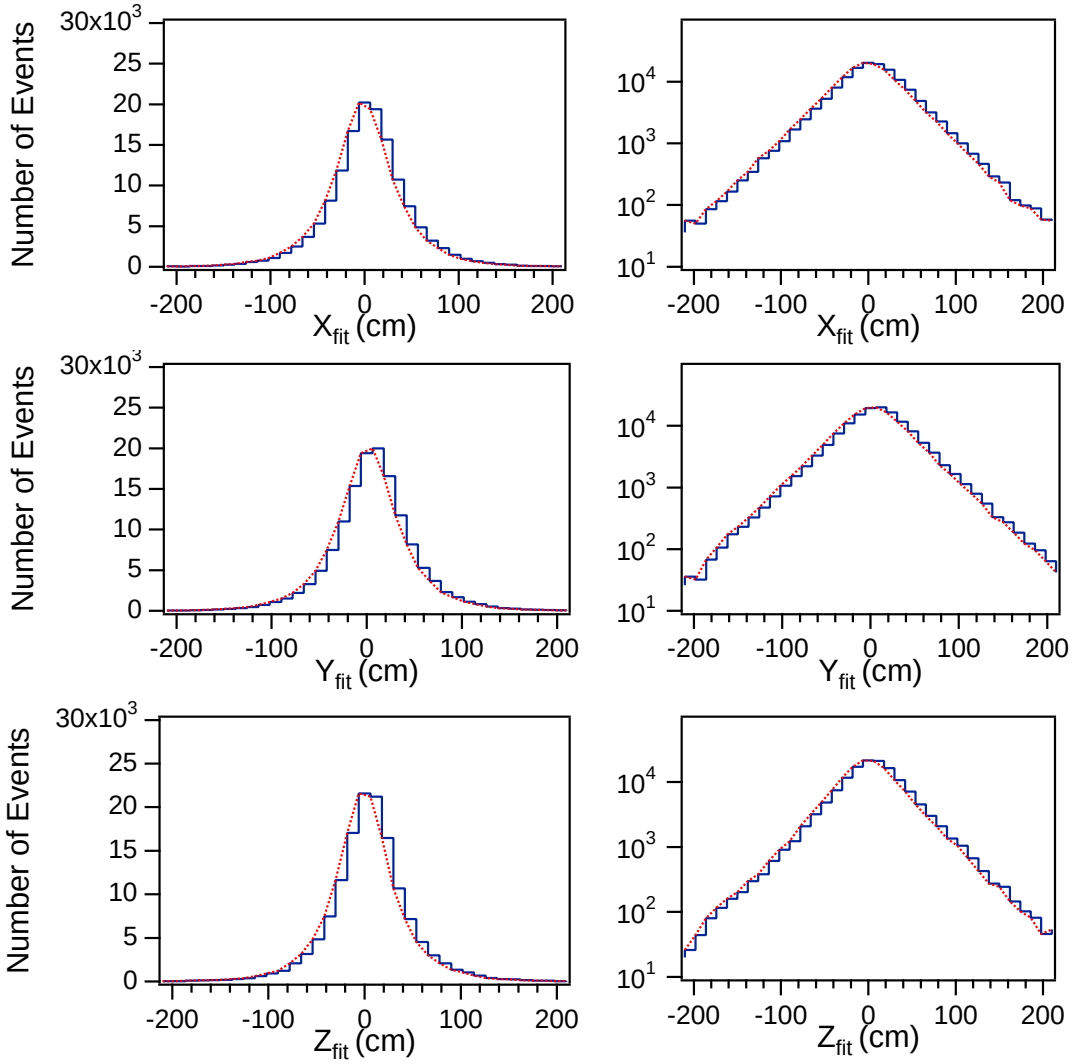

Figure 4.10: Example of the reconstructed distribution of ^{16}N events in x, y, and z, as well as the Gaussian fit (dotted line) to the distributions. These particular distributions are from run 10278 taken at the center of the detector. The left and right panels of the figure show the same data in linear and logarithmic representation.

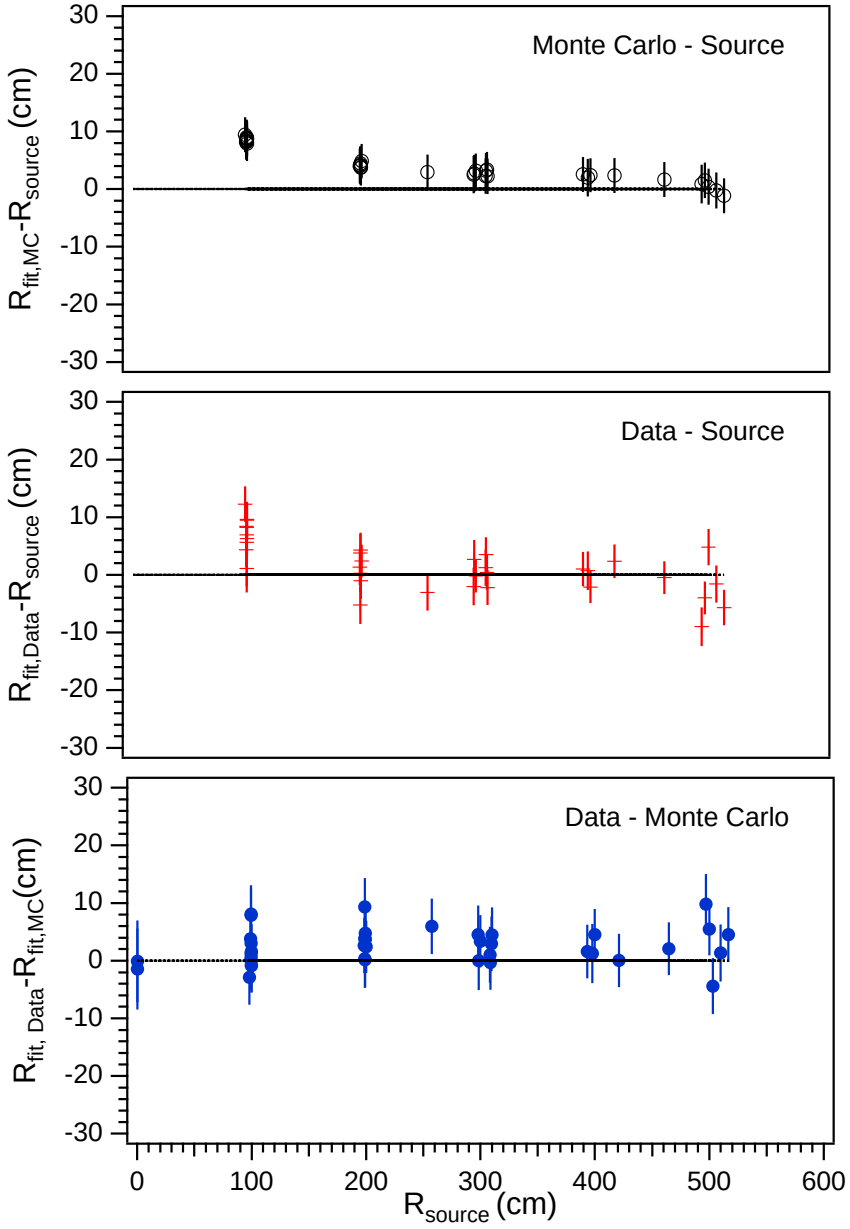

Figure 4.11: Radial position accuracy and resolution of the ^{16}N source as a function of source position. For a fiducial volume smaller than the acrylic vessel, the uncertainty in the radial reconstruction of the ^{16}N source determines the possible systematic error in the fiducial volume.

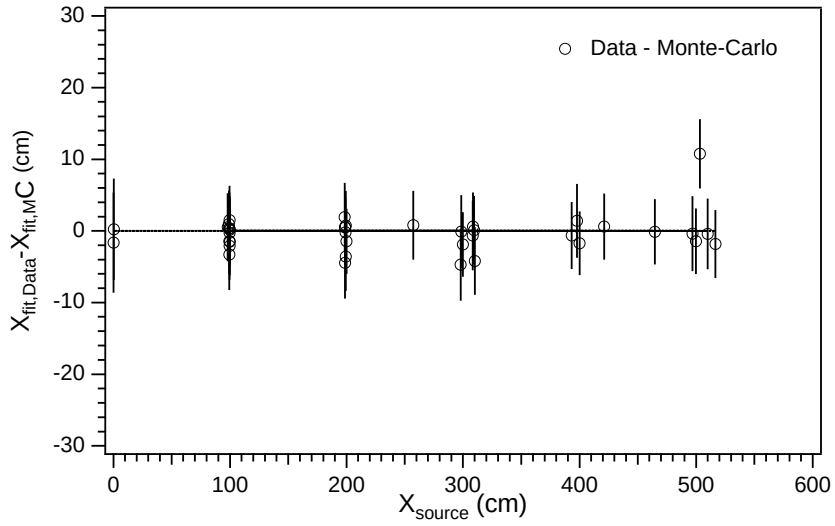

Figure 4.12: Position accuracy and resolution of the ^{16}N source as a function of source position in x.

In general good agreement between the reconstructed positions in Monte Carlo and data is found. The systematic error on the vertex shift is derived from the mean difference between the reconstructed data and source positions.

$$\Delta\mu = \frac{1}{N}\sum_i \left| R_i^{fit} - R_i^{source} \right| \tag{4.11}$$

The mean vertex resolution, $\overline{\sigma}$, is derived from the mean of the uncertainties in N reconstructed positions of the source at different source positions R_i.

$$\overline{\sigma} = \frac{1}{N}\sum_i \sigma_i(R_i) \tag{4.12}$$

From this study we find $\Delta\mu = 3.6$ cm and $\overline{\sigma} = 17.4$ cm. (Looking ahead to Chapter 9, one should note that these parameters are used in the perturbation of event variables to evaluate the systematic errors due to reconstruction in the spectral decomposition.)

4.4.2 Reconstruction of Event Distributions

A different type of evaluation of the reconstruction algorithm can be performed by comparing the characteristic R^3 and $\cos\theta_\odot$ event distributions of data and Monte Carlo [29]. These distributions are of particular interest as they will be used in the determination of the neutrino signal and the decomposition of the data set.

In this test, ^{16}N data with normalization N_{Data} is fit to Monte Carlo data, N_{MC}, with variable energy scale, α. The Monte Carlo data is generated at the same source positions. The fit equation is of the form

$$S_{\mathcal{D}} = N_{Data}/(\alpha_{\mathcal{D}} \times N_{MC}) \tag{4.13}$$

where $S_{\mathcal{D}}$ is the fit parameter for a particular event distribution $\mathcal{D}$. The fit results from the individual runs are shown in Figure 4.13. They can be combined by weighting the individual results by an appropriate amount to account for the relative volumes sampled by the ^{16}N runs. The results of the volume weighting are summarized below in Table 4.4.

Table 4.4: Volume-averaged differences between ^{16}N data and Monte Carlo. $\alpha_{\mathcal{D}}$ is a free parameter in this fit.

Fit Parameter	Results
$S_{r^3} = N_{Data}/(\alpha_{r^3} \times N_{MC})$	1.1053
$S_{\cos\theta} = N_{Data}/(\alpha_{\cos\theta} \times N_{MC})$	1.1855
$S_{r^3,\cos\theta} = N_{Data}/(\alpha_{r^3,\cos\theta} \times N_{MC})$	1.1081

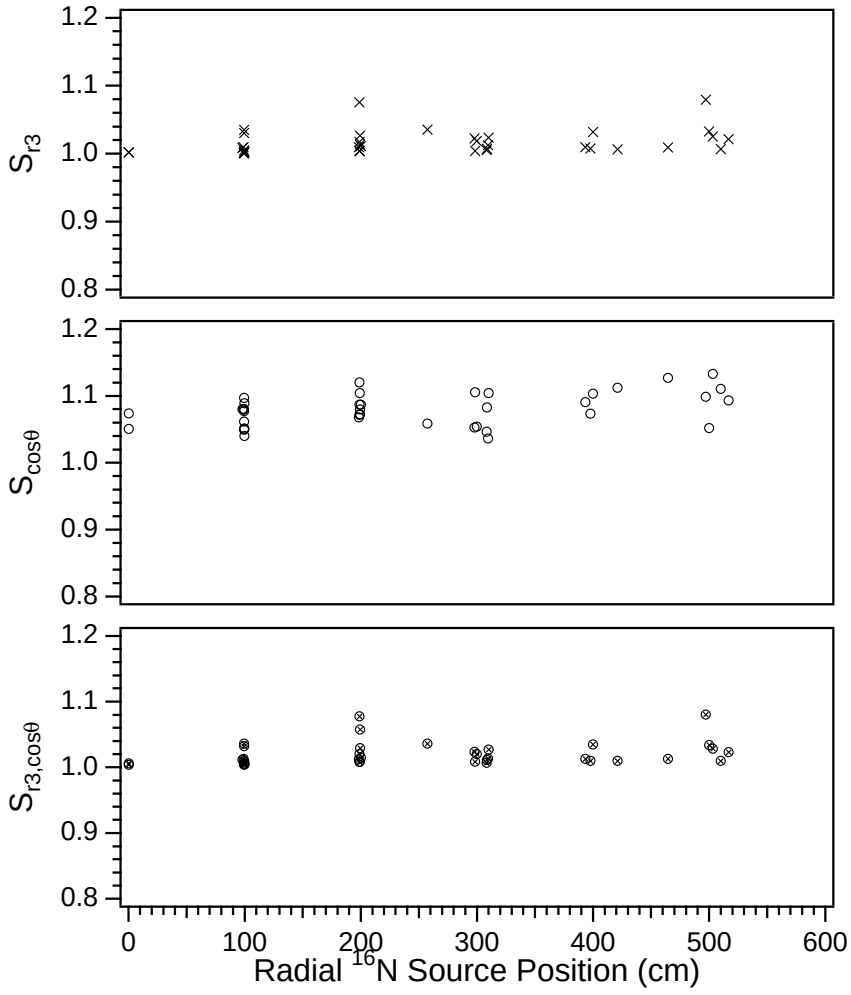

Figure 4.13: Results of the fits of the radial distribution, the angular distribution, and the combination of both of the data to the Monte Carlo. The fit parameters S parameterize the difference between the data and Monte Carlo distributions.

4.4.3 Angular Resolution

The angular resolution describes our ability to reconstruct the event direction. For a given position, direction, and energy, the angular resolution function is determined by the fraction of events reconstructing within an interval $[\theta, \theta + \delta\theta]$, where θ is the angle between the reconstructed and known initial direction. Data from the ^{16}N calibration source can be used for determining the angular resolution by using the natural colinearity of the Compton scattered electron with the γ direction. The angular resolution can be determined from ^{16}N by parameterizing the opening angle of the reconstructed direction with the vector from the source to the reconstructed position. If the scattering vertex, r_{ev}, is known then the γ-ray direction is related to the ^{16}N source position, r_s. The angle between the γ-ray direction and the reconstructed direction gives the angle between these two vectors. The fit vertex, $\vec{r}_{fit}$, can be used as an estimator of the true Compton scattering vertex ($r_{fit} \approx r_{ev}$).

$$\cos\theta = \frac{(\vec{r}_{fit} - \vec{r}_{ev}).\vec{u}_{fit}}{|(\vec{r}_{fit} - \vec{r}_{ev}|} \tag{4.14}$$

Figure 4.14 illustrates the approach. The method of determining the angular resolution is described in detail in [128, 15, 150]. In order to minimize the effect of finite vertex resolution on the angular resolution measurement, only events reconstructing at a distance from the ^{16}N source that is large compared to the vertex resolution are considered. A radial cut of $R_{fit} \geq 120$ cm is applied to ^{16}N calibration data for this purpose.

The angular resolution is usually determined by fitting the angular resolution distribution to a double exponential function.

$$F_{\cos\theta}(A_0, A_1, B_0, B_1, \theta) = e^{A_0 + A_1 \cos\theta} + e^{B_0 + B_1 \cos\theta} \tag{4.15}$$

The results of the fit to a double exponential function are given in Figure 4.16. The variation of these fit parameters is used as an estimate of the systematic error on the reconstructed direction and the angular resolution of events. (In the error estimates in Chapter 9 we perturb the reconstructed event direction by an amount that is consistent with the scatter of these fit results.)

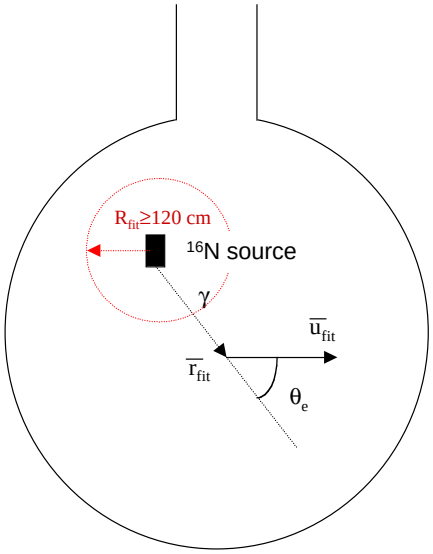

Figure 4.14: Schematic of the determination of the angular resolution with ^{16}N data.

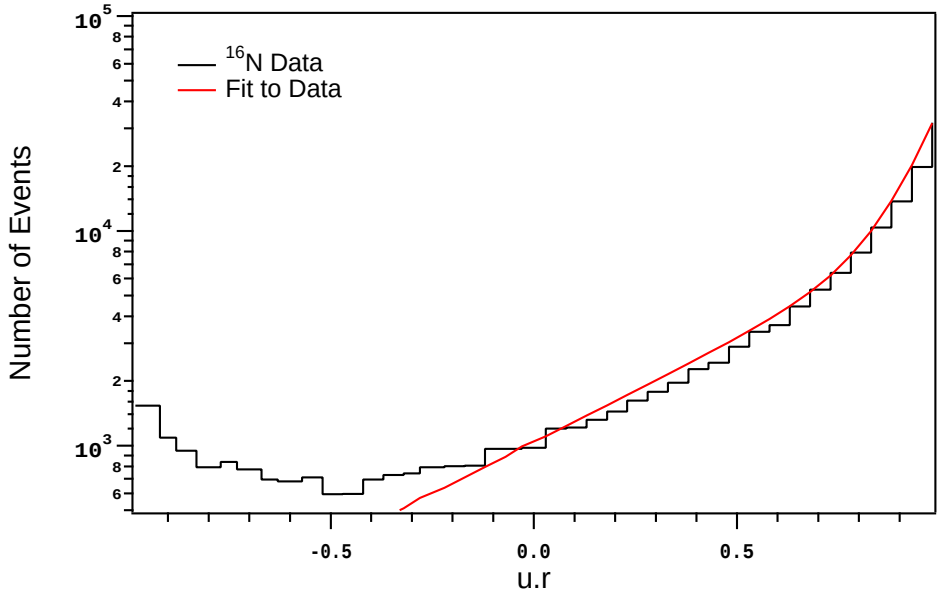

Figure 4.15: Example of the fit of the angular resolution distribution to two exponential functions in the range $0 \leq \vec{u}.\vec{r} \leq 1$.

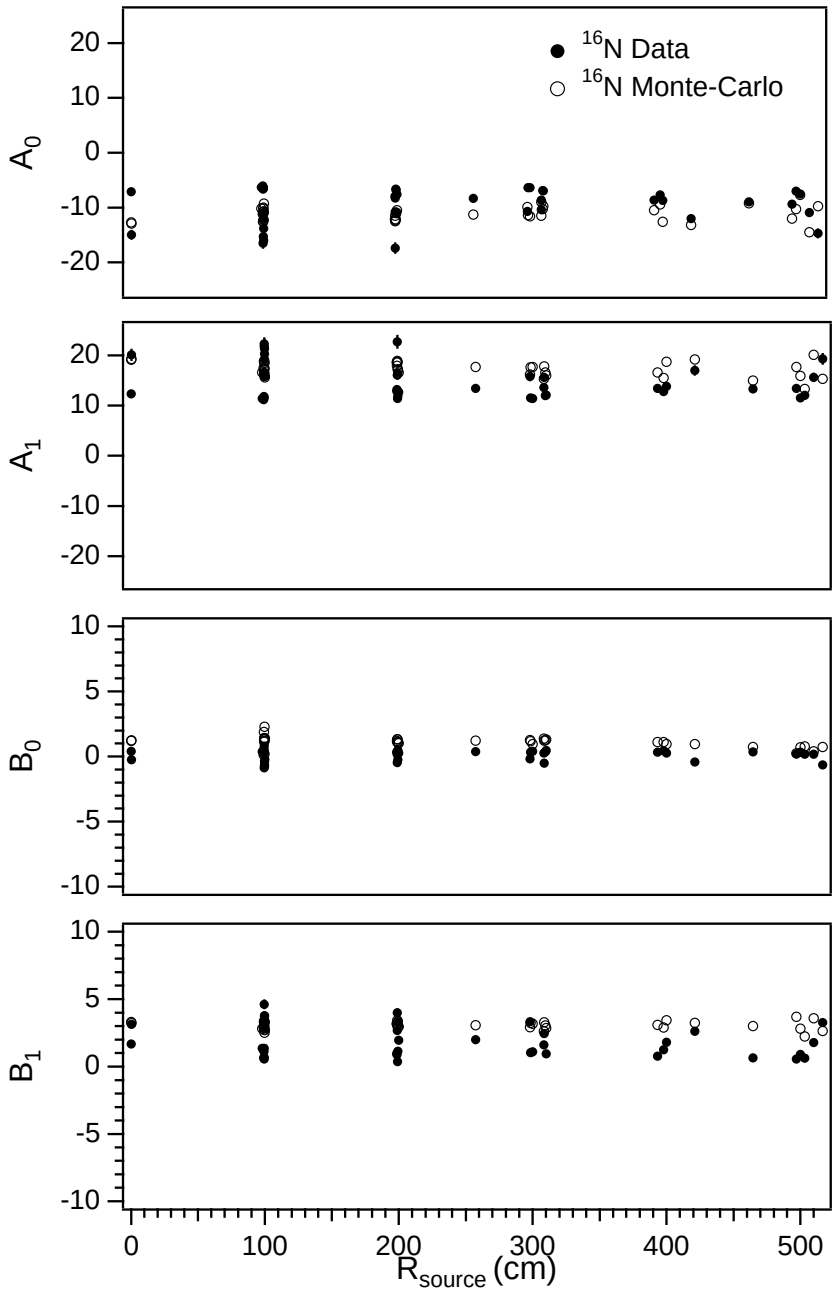

Figure 4.16: Comparison of the angular resolution parameters for ^{16}N calibration data and Monte Carlo results.

CHAPTER 5

HIGH LEVEL DATA CUTS

A series of cuts are applied to the data to remove a variety of different backgrounds and to obtain the neutrino candidate event set. Three different types of cuts are used in the solar neutrino analysis at SNO:

1. Data Reduction and Removal of Instrumental Backgrounds: These cuts are specifically designed to remove pathological instrumental backgrounds in the data set. Two independent data reduction schemes, called DAMN and FiST, have been designed and are described in Chapter 3.

2. Reconstruction of Events: The current reconstruction algorithm has a very high efficiency ($\geq 99.9\%$) of reconstructing events and determining an event location. While the event reconstruction chosen in this analysis does not make any specific assumptions on the event class the fit algorithm does test basic properties of the events. Pathological time distributions of PMT hits will fail reconstruction or lead to misreconstructed events. All events that are not reconstructed are lost to the analysis and not included in the candidate event set. Some events are misreconstructed into detector regions that are outside the fiducial volume selected for the solar neutrino analysis. In this case the events are included in the candidate event set but not selected in the final analysis once a radial fiducial volume cut is applied. The details of event reconstruction are described in Chapter 4.

3. High Level Event Cuts (HLC): These cuts are designed to test the Čerenkov nature of events and help discriminate instrumental and radioactive backgrounds from neutrino signals. Details of the high-level event cuts are described below.

Neutrino interactions in the D_2O and H_2O produce characteristic Čerenkov electrons that are detected with an array of light-sensitive photomultipliers. Two high-level cuts have been developed that make use of the characteristic Čerenkov hit pattern and the prompt peak in the time distribution of Čerenkov light to distinguish single-particle Čerenkov events

from multi-particle backgrounds and instrumental events. High level cuts (HLC) are designed to test the Čerenkov nature of events and discriminate various types of physics backgrounds. They also reduce further the residual instrumental contamination in the data set. These cuts are based on the event isotropy and the prompt, in-time window. Their performance is characterized using calibration data from electron and γ sources. In this chapter we study the event topologies of both neutrino signals and backgrounds. We also show that these cuts do not affect our ability to identify the 6.25 MeV γ signature of the neutral-current interaction.

5.1 Event Isotropy

The isotropy of the PMT hit pattern of an event can be used to describe its Čerenkov nature. The parameter $\overline{\theta}_{ij}$, or for short, θ_{ij}, is the mean angle between hit PMT's from the reconstructed event vertex. It describes the isotropy of both single and multi-particle events.

$$\overline{\theta}_{ij} = \frac{1}{(N_{hit})^2} \sum_{i,j<i} \theta_{ij} \tag{5.1}$$

where θ_{ij} describes the angle between the i^{th} and j^{th} photomultiplier and N_{hit} is the total number of PMT hits. Figure 5.1 illustrates the definition of θ_{ij}. Originally, the θ_{ij} parameter was introduced to distinguish different types of background events [26, 16]. In general, the direction of the Čerenkov photons is correlated with the direction of the original charged particle. There is little correlation among the directions of multiple particles produced by the decay of radioactive backgrounds, such as ^{208}Tl. However, θ_{ij} can be used to describe the degree of isotropy of multi-particle background events. For example, it is expected that for more than 30 hits the PMT hits produced by ^{208}Tl are distributed more isotropically than those of ^{214}Bi decay events. The θ_{ij} parameter has been used successfully for the statistical separation of these background events. The θ_{ij} parameter can be used to classify different types of background events as well as eliminate backgrounds near the AV and in the H_2O. A cut on θ_{ij} will eliminate most backgrounds and remove a very small fraction

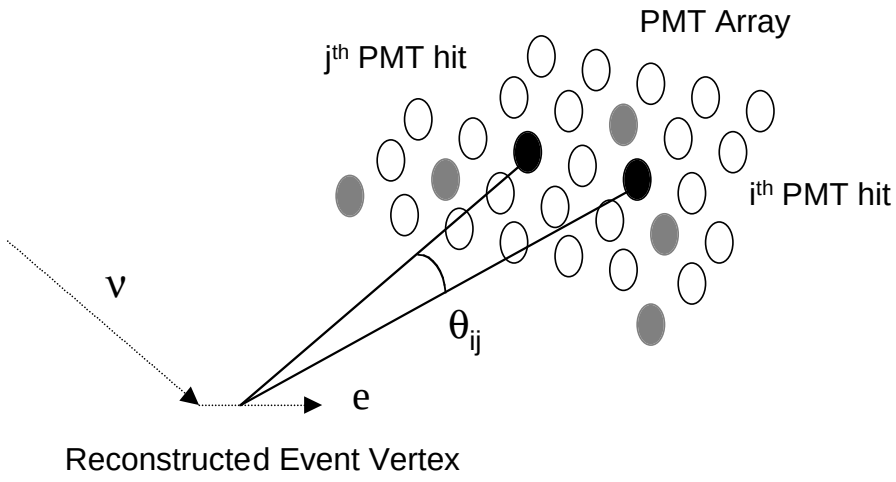

Figure 5.1: Definition of the θ_{ij} parameter with an illustration of the PMT hit pattern of Čerenkov electrons.

of good neutrino events. A detailed characterization of this signal loss is an integral of our studies of data reduction cuts.

The different nature of single-particle neutrino interactions and $\beta-\gamma$ backgrounds leads to characteristic θ_{ij} distributions. Figures 5.2 and 5.3 show Monte Carlo simulations for the θ_{ij} distributions of CC, ES, and NC neutrino interactions and $\beta-\gamma$ events in the ^{208}Tl and ^{214}Bi in the AV and H_2O respectively. A cut on θ_{ij} will remove some of the backgrounds but cannot eliminate them completely as significant parts of the θ_{ij} spectra overlap.

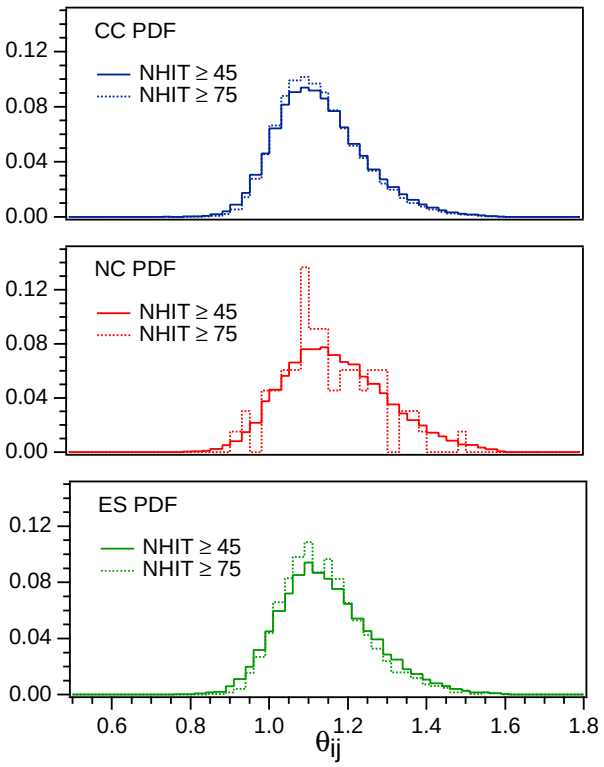

Figure 5.2: Normalized θ_{ij} distributions for Monte Carlo CC, ES, and NC neutrino interactions for different NHIT thresholds. A radial cut of $R_{fit} \leq 650$ cm is applied.

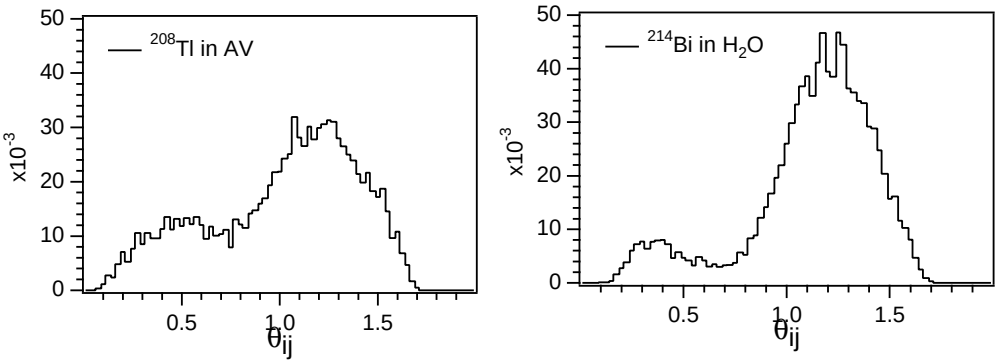

Figure 5.3: Normalized θ_{ij} distributions obtained from Monte Carlo of ^{208}Tl in the acrylic vessel and ^{214}Bi in the H_2O, some of the principal radioactive backgrounds. A radial cut of $R_{fit} \leq 650$ cm is applied.

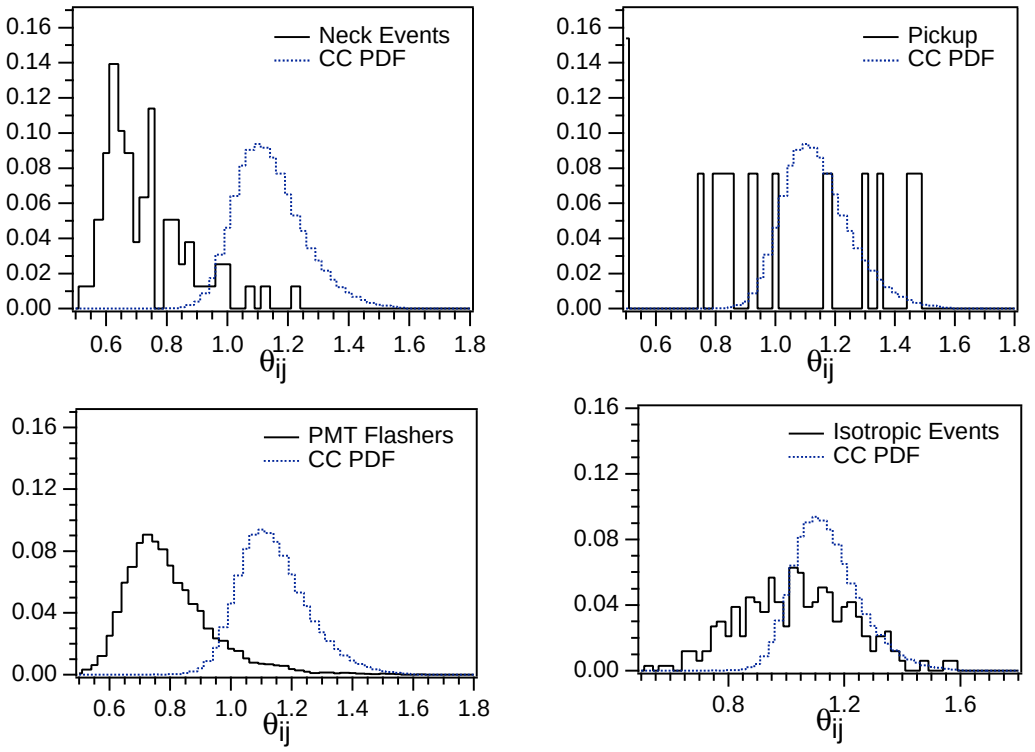

Figure 5.4: θ_{ij} distributions of instrumental backgrounds and the charged-current PDF for comparison. While most background events have a fairly distinctive θ_{ij} distribution a simple cut on θ_{ij} will not be able to remove them completely. A threshold of NHIT $\geq$ 45 and a radial cut of $R_{fit} \leq 650$ cm are applied.

Application of high-level cuts such as θ_{ij} also greatly reduces the residual contamination of instrumental backgrounds. Figure 5.4 compares the θ_{ij} distribution of CC events with some of the most prominent instrumental backgrounds. For example, PMT flashers are characterized by a θ_{ij} distribution that peaks at small θ_{ij}. This is consistent with the clustering of PMT hits expected in this type of event class. Other instrumental backgrounds that are not characterized by a unique PMT hit pattern, such as pickup, cannot be described well by θ_{ij}. Their distribution of θ_{ij} values is flat. The sample distributions of instrumental backgrounds shown in Figure 5.4 are obtained by handscanning the raw data set.

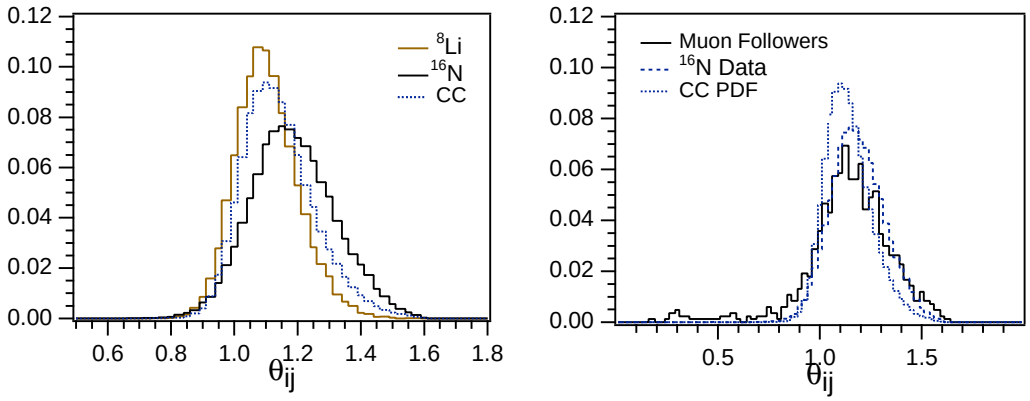

Figure 5.5: θ_{ij} distributions for calibration data, muon followers, and the CC PDF. All distributions are found to be in reasonable agreement. As expected, the θ_{ij} distribution of the ^{8}Li calibration data resembles more the CC PDF than the ^{16}N calibration data. The ^{16}N distribution is in closer agreement with the muon followers which are neutron capture events on deuterium.

The robustness of a cut on θ_{ij} can be tested by comparing the signal from different calibration devices. Figure 5.5 shows the θ_{ij} distribution for ^{8}Li, ^{16}N, and muon followers. All distributions are found to be in reasonable agreement. As expected, the θ_{ij} distribution of the ^{8}Li calibration data resembles more the Monte Carlo simulation of CC events (CC PDF) than the ^{16}N calibration data. The ^{16}N distribution is in closer agreement with the muon followers. The term muon followers refers to neutrons that are produced in the spallation products of muons in the SNO detector. The neutrons thermalize and capture on deuterium with emission of a 6.25-MeV γ. Their signature is identical to the signature of neutral-current neutrino interactions in SNO. The sample of muon followers is obtained from the muon analysis presented in [3]. We find that the θ_{ij} distributions of none of the calibration signals extends beyond $\theta_{ij} \sim 1.5$. The lower end of the θ_{ij} spectrum is at $\theta_{ij} \sim 0.7$ although some of the muon followers have θ_{ij} values as low as 0.2. As the high-level cuts are globally applied to the reduced data set it is important to understand possible variations of θ_{ij} with the energy and position of an event.

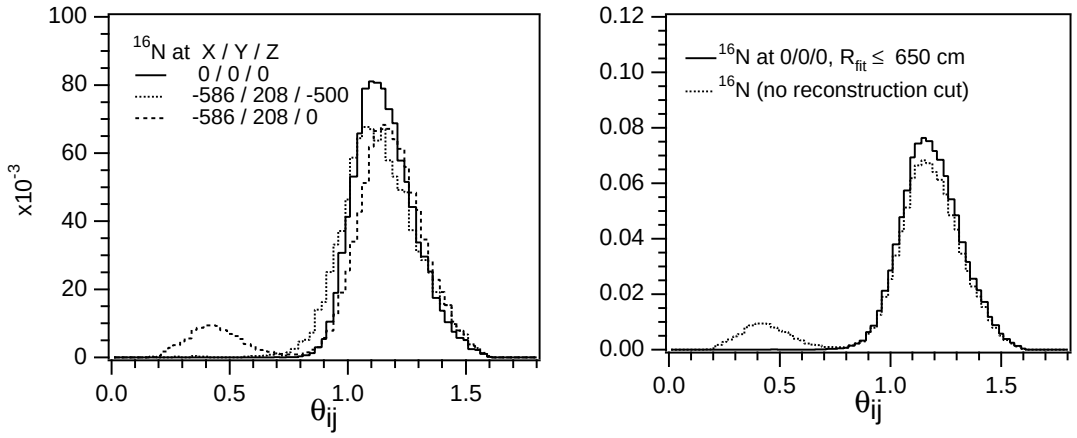

Figure 5.6: Position dependence of the ^{16}N θ_{ij} distribution. We find some variation of the ^{16}N θ_{ij} distribution with source position. A threshold of NHIT ≥ 45 is applied. Low-θ_{ij} events appear predominantly in data taken near the acrylic vessel and in the H_2O. A reconstruction cut of $R_{fit} \leq 650$ cm removes these events. This suggests that the low-θ_{ij} events are most likely due to misreconstruction.

As indicated in Figure 5.2, the NHIT dependence of θ_{ij} is expected to be small. The radial dependence can be determined from calibration data taken at various positions in the detector. The left panel in Figure 5.6 compares the θ_{ij} distributions of ^{16}N data taken at three different locations, in the center of the detector as well as near the acrylic vessel. There are only small variations in the peak of the normalized θ_{ij} distribution. However, calibration data taken near the AV shows some low-θ_{ij} events. It is expected that optical effects from the acrylic alter the event pattern and lead to a high fraction of misreconstructed events that occur near the AV. This excess of low-θ_{ij} events is eliminated when a general radial cut of $R_{fit} \leq 650$ cm is applied. For all analyses of events within $R_{fit} \leq 650$ cm the θ_{ij} distribution of ^{16}N signals is essentially independent of position and well described by the central peak between $0.7 \leq \theta_{ij} \leq 1.6$. The comparison of θ_{ij} distributions of calibration data, instrumental backgrounds, and Monte Carlo simulations of neutrino signals shows that an acceptance window of $0.7 \leq \theta_{ij} \leq 1.5$ includes all signals of interest.

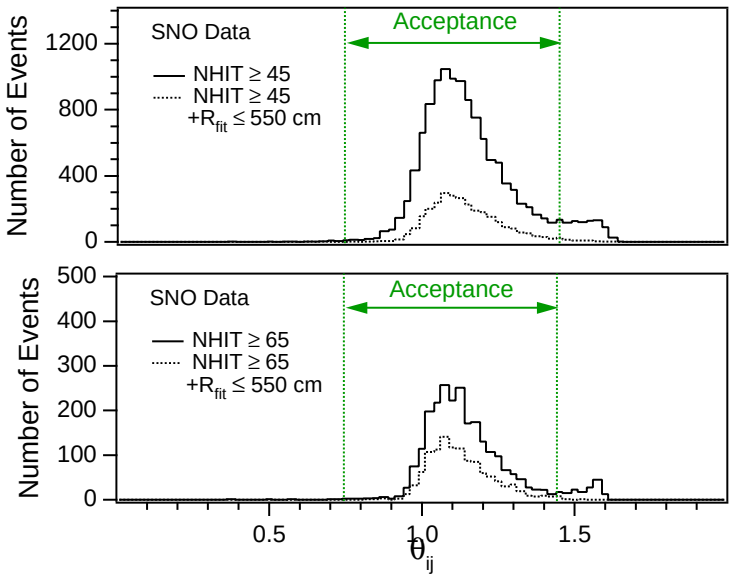

Figure 5.7: θ_{ij} distribution of SNO data for various NHIT thresholds and radial cuts. The acceptance of the θ_{ij} cut is indicated. The data shows some indication for high-θ_{ij} events. These could be the "isotropic events". They are the only known event class with $\theta_{ij} \geq 1.5$.

It was noticed, however, that the isotropic events which we found in the data set (see Chapter 3) are characterized by anomalously high values of θ_{ij}. The reduced SNO data set shown in Figure 5.7 clearly shows a peak at $\theta_{ij} \sim 1.58$ and raises concern about contamination of the data with this class of background events. A tighter cut on high θ_{ij} events will only slightly increase the neutrino signal loss but discriminate this background. The θ_{ij} cut values chosen in this analysis are:

$$0.75 \leq \theta_{ij} \leq 1.45 \tag{5.2}$$

This range of parameters minimizes the signal loss while providing efficient discrimination of backgrounds at the same time. As the θ_{ij} distributions for signals and backgrounds overlap no θ_{ij} cut will provide a complete removal of background events. A second cut based on the timing of Čerenkov events is needed to discriminate events that have a similar PMT hit pattern (or θ_{ij} distribution) but do not originate from prompt Čerenkov light.

5.2 In-Time Ratio of Prompt to Total Light

The in-time ratio (ITR) cut calculates the ratio of hits within a prompt time window of [-2.5 ns,+5 ns] relative to the total number of hits which pass the calibration of all electronics channels. Čerenkov light comes from a fast pulse of light. This is not true for some backgrounds. The ITR parameter compares in-time light to total light.

The results of this study are fairly independent of the parameterization of the in-time window. Presently adapted in SNO is the ITR definition which is based on a [-2.5 ns,+5 ns] timing window.

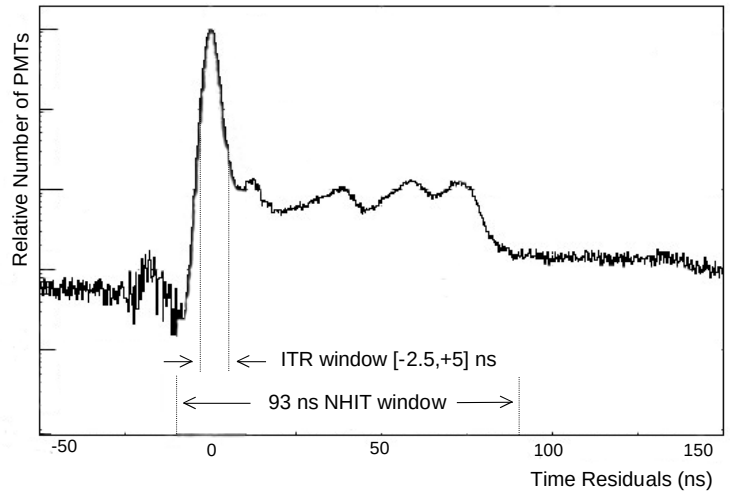

Figure 5.8: ITR time window: In-time ratio of prompt light to total light in an event. The structure of the timing residuals is described in detail in Figure 4.1.

Monte Carlo simulations of the ITR distributions of neutrino signals and of ^{208}Tl and ^{214}Bi backgrounds are shown in Figures 5.9 and 5.10. Similiar to what we observed in the θ_{ij} distributions the normalized ITR distribution for radioactive backgrounds and neutrinos is quite different. This may only be due to the position-dependence of the radioactive backgrounds and neutrino signals. For backgrounds the ITR distribution peaks at ITR ~ 0.7 and extends down to ITR ~ 0.4. For events in the central D_2O volume we do not expect to see any neutrino signals with ITR values below ITR ~ 0.5.

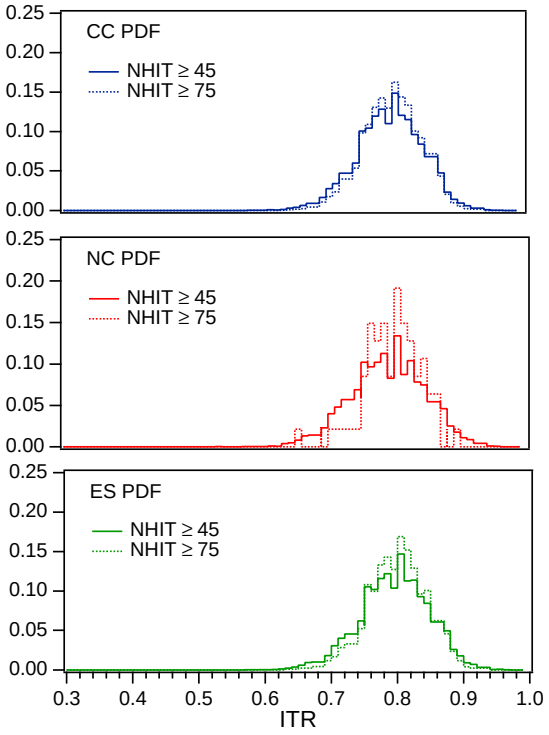

Figure 5.9: Normalized ITR distributions for Monte Carlo CC, ES, and NC neutrino interactions for different NHIT thresholds and radial cuts. A radial cut of $R_{fit} \leq 650$ cm is applied.

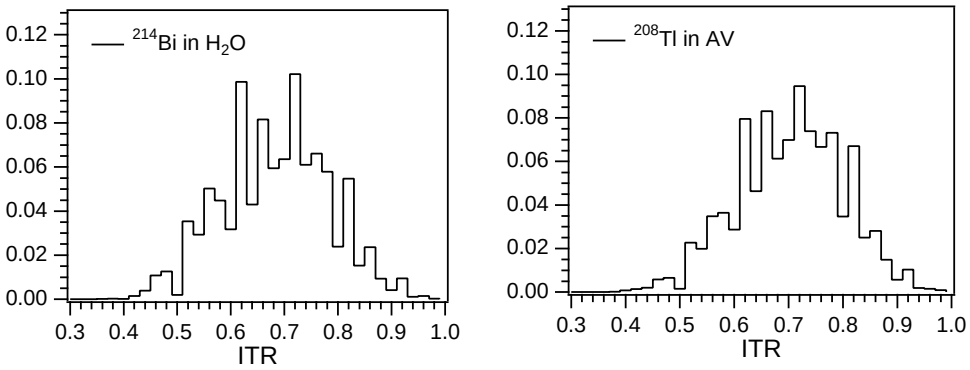

Figure 5.10: Normalized ITR distributions obtained from Monte Carlo of ^{208}Tl in the acrylic vessel and ^{214}Bi in the H_2O, some of the principal radioactive backgrounds. A radial cut of $R_{fit} \leq 650$ cm is applied.

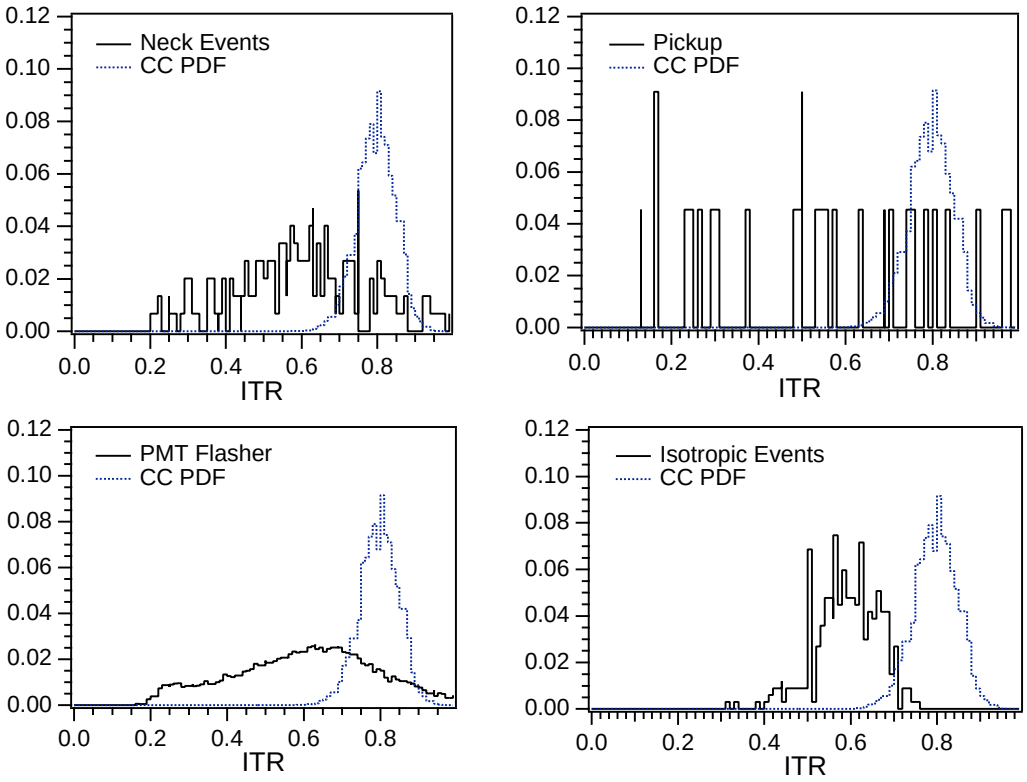

Figure 5.11: Comparison of the ITR distribution of instrumental background events to the CC PDF. While most background events have a fairly distinctive ITR distribution a simple cut on ITR will not be able to remove them completely. A threshold of NHIT ≥ 45 and a radial cut of $R_{fit} \leq 650$ cm are applied.

For illustration, we compare the characteristic ITR distributions of instrumental backgrounds with the ITR distribution of CC neutrino interactions. Both PMT flashers and neck events show again distinctive signatures in this event distribution. Interestingly, the class of isotropic events can be distinguished quite clearly with the ITR parameter. While isotropic events resemble more closely the peak of the ITR distribution of neutrino signals their ITR distributions only overlap marginally. Isotropic events are peaked at ITR ~ 0.6. Again, this difference may only be due to a position-dependence in the ITR distribution.

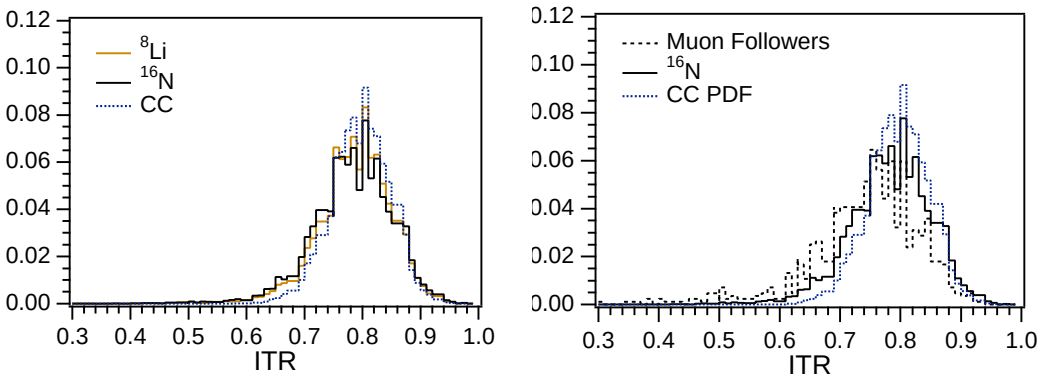

Figure 5.12: ITR distributions for calibration data, muon followers, and CC Monte Carlo events. A threshold of NHIT ≥ 45 is applied. All distributions are found to be in reasonable agreement. The muon followers exhibit a slightly wider distribution extending to lower values of ITR.

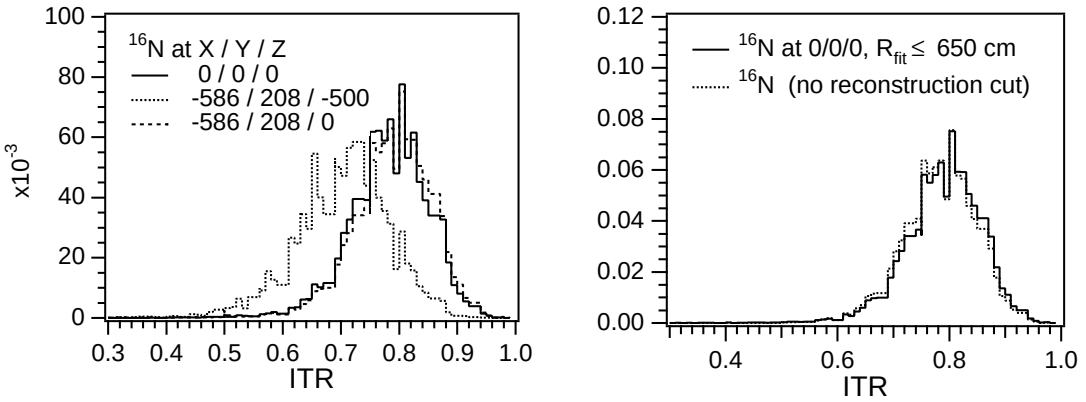

Figure 5.13: Position dependence of the ^{16}N ITR distribution. We find some variation of the ^{16}N ITR distribution with source position. Moving close to the acrylic vessel appears to shift the ITR distribution to lower values of ITR. Nevertheless, all ^{16}N events are contained in the window $0.5 \leq \text{ITR} \leq 1.0$. A threshold of NHIT ≥ 45 is applied.

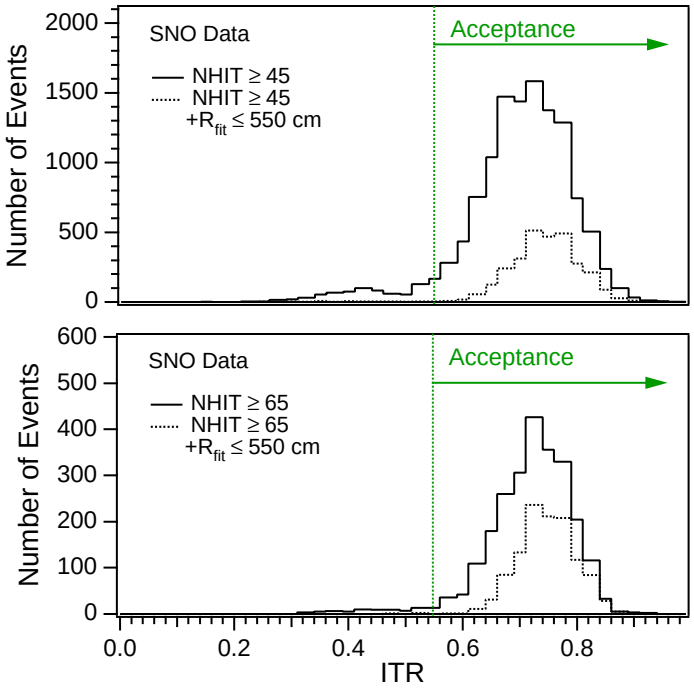

Figure 5.14: ITR distribution of SNO data for various NHIT thresholds and radial cuts. The acceptance of the ITR cut is indicated. The data shows some indication for low-ITR events at low thresholds. These event are most likely due to radioactive background or residual instrumental backgrounds.

Based on studies of selected instrumental backgrounds as well as calibration data from ^{8}Li and ^{16}N the acceptance region of the in-time light ratio, ITR, for neutrino signals is:

$$0.55 \leq \mathrm{ITR} \leq 1 \tag{5.3}$$

5.3 Correlation of θ_{ij} and ITR: 2-Dimensional Cuts

The ITR and θ_{ij} parameters used to describe the Čerenkov nature of events are not completely independent. Their orthogonality depends very much on the event class. Variations in ITR do not change much the θ_{ij} distribution of neutrino events but may affect the θ_{ij} distributions of the some of the backgrounds. Better discrimination of backgrounds with less residual contamination and improved identification of neutrino signals can be achieved by considering the 2-dimensional representation of events in ITR and θ_{ij}. We find that a circular or elliptical cut seems more appropriate and could be used in an improved analysis.

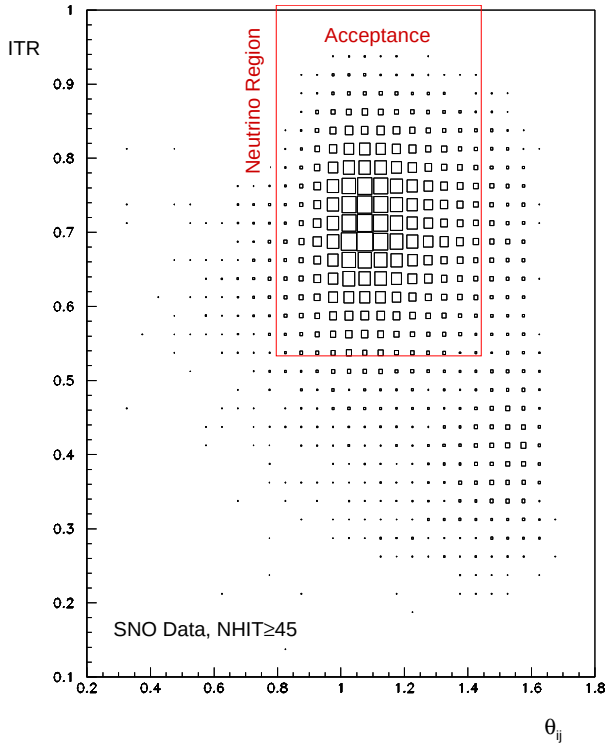

Figure 5.15: Region of accepted neutrino candidate events in the ITR versus θ_{ij} plane. The box plot shows the selected and reduced SNO data set.

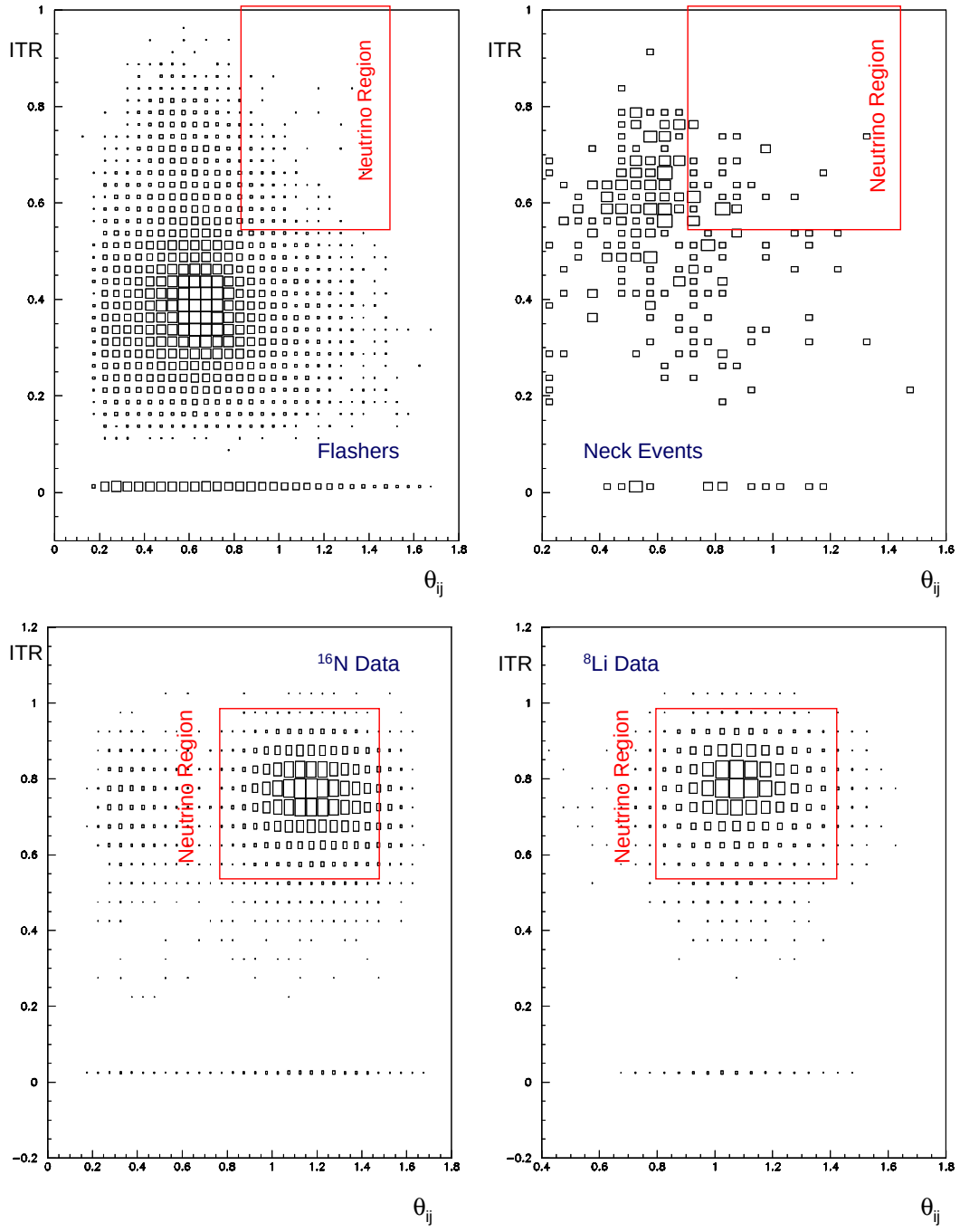

Figure 5.16: 2-dimensional distribution in the ITR versus θ_{ij} plane for instrumental backgrounds and ^{16}N and ^{8}Li calibration data . The region of acceptance as defined by the current set of ITR and θ_{ij} cut values is indicated.

5.4 Orthogonality of High Level Cuts

The standard high-level cuts used in this analysis are defined by the following parameters:

$$\mathrm{CUT}_1: \quad 0.55 \leq \mathrm{ITR} \leq 1 \tag{5.4}$$

$$\mathrm{CUT}_2: \quad 0.75 \leq \theta_{ij} \leq 1.45 \tag{5.5}$$

The combination $CUT_1 \otimes CUT_2$ is usually referred to as the high-level cuts (HLC). In addition to the HLC, a muon follower cut is applied which cuts 20 s of livetime subsequent to an identified through-going muon.

As we will see in later chapters of this thesis, characteristic event distributions such as the radial distribution, the solar angle distribution, and the energy spectrum are used in the determination of the neutrino signals. ITR and θ_{ij} can only be applied as high-level cuts on the raw data if they are orthogonal to the parameters used in the signal decomposition. We require the fraction of events cut by θ_{ij} and ITR to be independent of R^3, $\cos\theta_\odot$, and NHIT. In addition, the high-level event cuts need to be stable over the period of data taking. To avoid correlations and distortions of the characteristic event distributions we require:

$$N(\cos\theta_\odot|ITR,\theta_{ij}) = N(\cos\theta_\odot) \tag{5.6}$$

$$N(R|ITR,\theta_{ij}) = \epsilon_{ITR}\ \epsilon_{\theta_{ij}}\ N(R) \tag{5.7}$$

$$N(NHIT|ITR,\theta_{ij}) = \epsilon_{ITR}\ \epsilon_{\theta_{ij}}\ N(NHIT) \tag{5.8}$$

$$\tag{5.9}$$

The following sections investigate the orthogonality of the high level cuts using Monte Carlo simulations and the neutrino candidate event set. More detailed studies including determination of the systematics using calibration data can be found in [142]. We also consider the time variations in θ_{ij} and ITR over the period of data taking.

5.4.1 Radial Dependence of ITR and θ_{ij}

A study of Monte Carlo data shows that there is very little radial dependence in the fraction of Monte Carlo neutrino events cut by the θ_{ij} parameter. Comparing the means of ITR and θ_{ij} for different radial bins we find consistency between the signal loss in the data and Monte Carlo predictions. The sacrifice of neutrino events is well characterized and can be corrected for in the determination of the neutrino interaction rates.

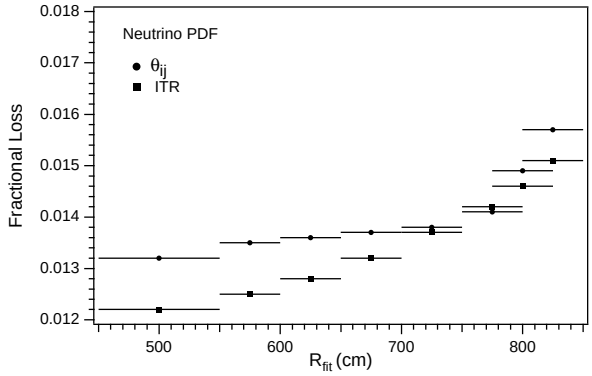

Figure 5.17: Fractional loss of neutrino signal as a function of radius due to the high level cuts. The signal loss is small and fairly constant in the radial region of interest $R_{fit} \leq 650$ cm.

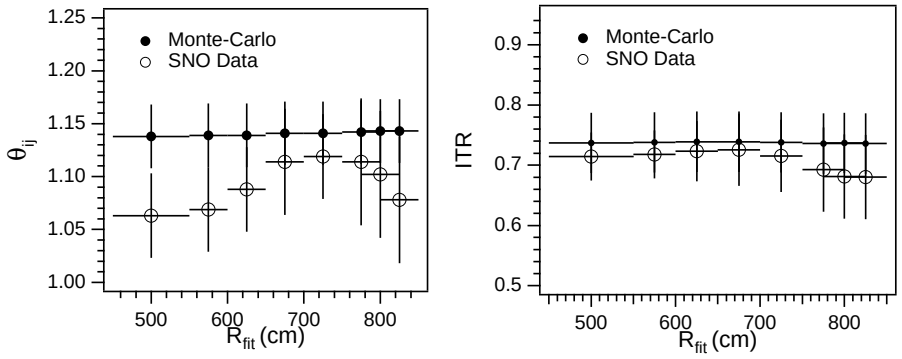

Figure 5.18: Mean of θ_{ij} and ITR as a function of radius for data and Monte Carlo. The signal loss is small and fairly constant in the radial region of interest $R_{fit} \leq 650$ cm.

5.4.2 Solar Angle Dependence of ITR and θ_{ij}

Monte Carlo simulations of the solar angle distribution can be used to study the effect of θ_{ij} and ITR on the shape of the $\cos\theta_{\odot}$ distribution of the neutrino signal. We find that the thetaij and ITR cuts lead to an overall reduction in the event set but do not significantly affect the shape of the $\cos\theta_{\odot}$ distribution. Figure 5.19 shows the normalized $\cos\theta_{\odot}$ distributions and the residuals in the data set. Cuts on θ_{ij} and ITR will not distort the $\cos\theta_{\odot}$ distributions which we will use to extract the elastic scattering component of the neutrino signal.

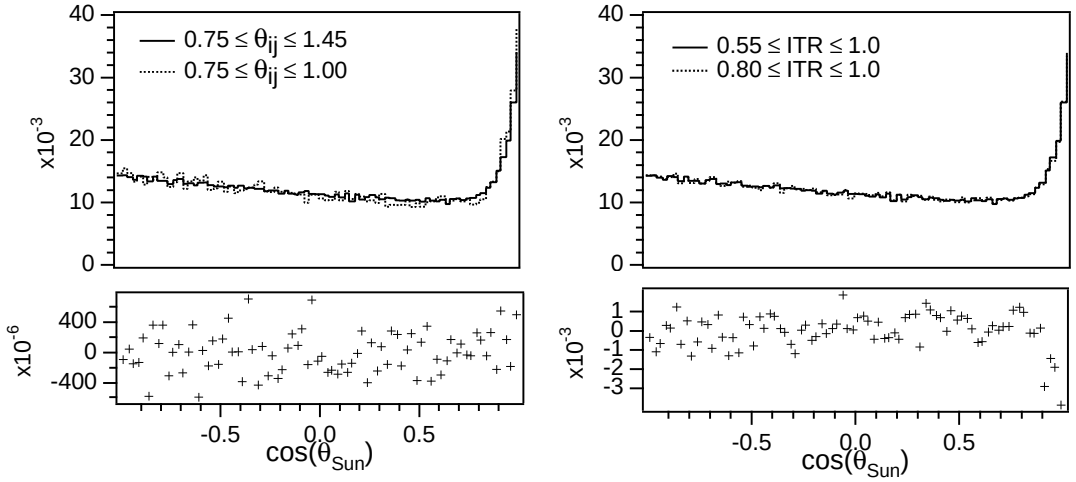

Figure 5.19: Normalized $\cos\theta_{\odot}$ distributions and residuals for the neutrino signal with various high level cuts applied. The application of θ_{ij} and ITR does not change the shape of the solar angle distribution.

5.4.3 Stability of ITR and θ_{ij} with Time

As a check of the stability of ITR and θ_{ij} with time we can monitor the respective distributions of the reduced but otherwise raw data set. The stability of the detector response to electrons and γ's is already checked periodically for the purpose of energy calibration. The energy response of the detector and its stability are discussed in Chapter 6. Monitoring the stability of the raw data set has the advantage that it takes into account all time varying phenomena. Under the assumption that the neutrino signal composition and its characteristics do not change significantly with time, stability of the θ_{ij} and ITR distributions of the data set implies that signal loss of these cuts is constant over time. Backgrounds or instrumental effects with a long term variation in time would change the mean and the uncertainty of the ITR and θ_{ij} distributions. Event bursts or other short term effects are detected in the low-level data reduction methods and monitoring techniques. It is unlikely that they would escape observation.

Figure 5.20 shows the peaks of θ_{ij} and ITR distribution as a function of time for selected SNO neutrino data. The peak position is obtained by a gaussian fit to the distributions within the RMS range of the mean. The central values of θ_{ij} and ITR vary by less than 3% and 5% respectively.

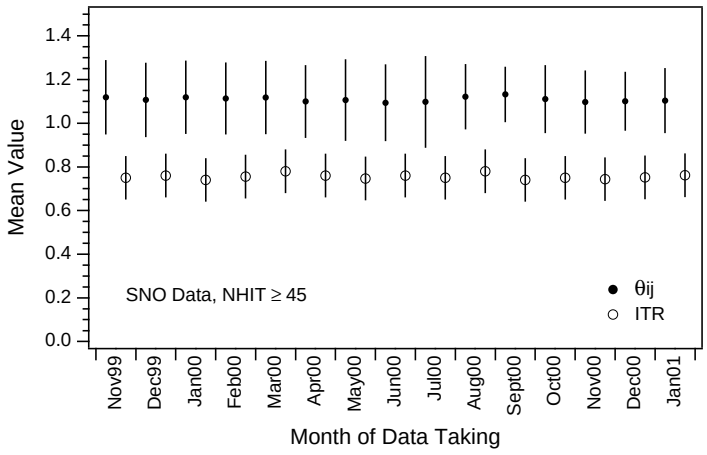

Figure 5.20: Mean of θ_{ij} and ITR distribution as a function of time for selected SNO neutrino data.

5.5 Signal Loss in The Reduced Data Set

The data cuts described above remove some fraction of neutrino signal. This acceptance loss must be measured and accounted for in the data set and the final calculation of signal rates in the detector. It is also necessary to account for any biases the cuts may produce in the data. To obtain a candidate event set all of the above described event cuts are applied to the raw data. Formally, we can write this combination of cuts as follows:

$$\begin{aligned} \mathrm{CUTS_A} &= DAMN \otimes FTG \otimes HLC \\ \mathrm{CUTS_B} &= FiST \otimes FTG \otimes HLC \end{aligned}$$

DAMN and FiST are the two independent data reduction schemes used for the removal of instrumental backgrounds. FTG denotes the grid fitter reconstruction algorithm and HLC is the acronym for the high level event cuts, including θ_{ij} and ITR.

The neutrino signal loss can be inferred from the signal loss of calibration data that is subject to (mostly) the same cuts and data reduction mechanism. In the context of this analysis we have studied the signal loss of ^{16}N calibration data taken at different positions throughout the entire detector region near the energy of the neutral-current signal. The calibration source positions used in this analysis are shown in Figure 5.25.

Figures 5.21 and 5.22 illustrate the radial and NHIT dependence of the signal loss in the removal of instrumental backgrounds. The signal loss due to $CUTS_A$ and $CUTS_B$ is found to be in good agreement.

The total signal loss of ^{16}N data in $CUTS_A$ (after data reduction, reconstruction, and high-level event cuts) is determined to be $\eta_{HLC} \sim 0.4 - 0.6\%$ for all NHIT of interest in the solar neutrino analysis. η_{HLC} is constant for all fiducial volumes with $(R_{fit}/R_{AV})^3 \leq 0.8$. For $0.8 \leq (R_{fit}/R_{AV})^3 \leq 1.0$, η_{HLC} increases from 0.5% to about 1.7%.

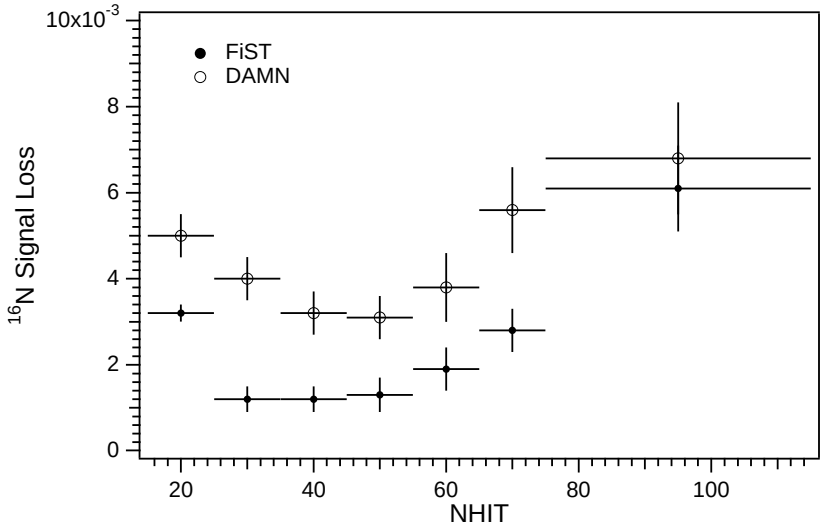

Figure 5.21: ^{16}N signal loss in data reduction with the FiST and DAMN data reduction schemes as a function of NHIT. Overall the signal loss of both schemes is comparable. The signal loss is slightly lower in the FiST method due to a looser selection of data cuts.

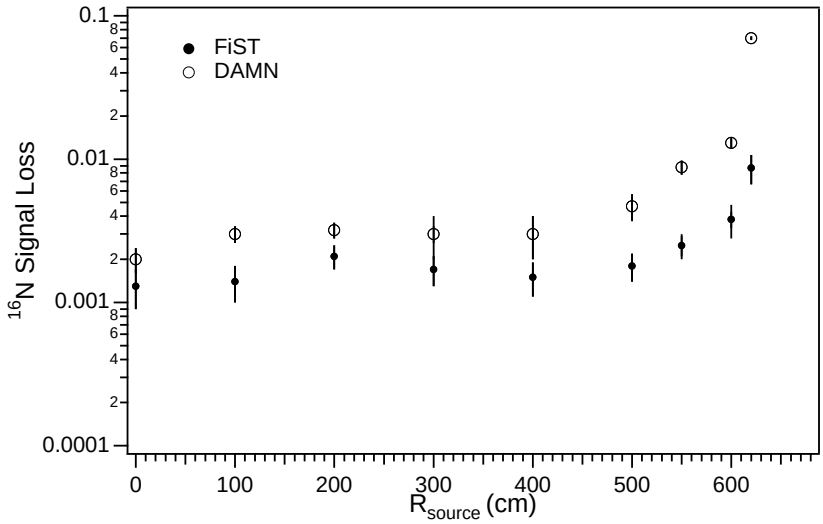

Figure 5.22: ^{16}N signal loss in data reduction with the FiST and DAMN data reduction schemes as a function of radius.

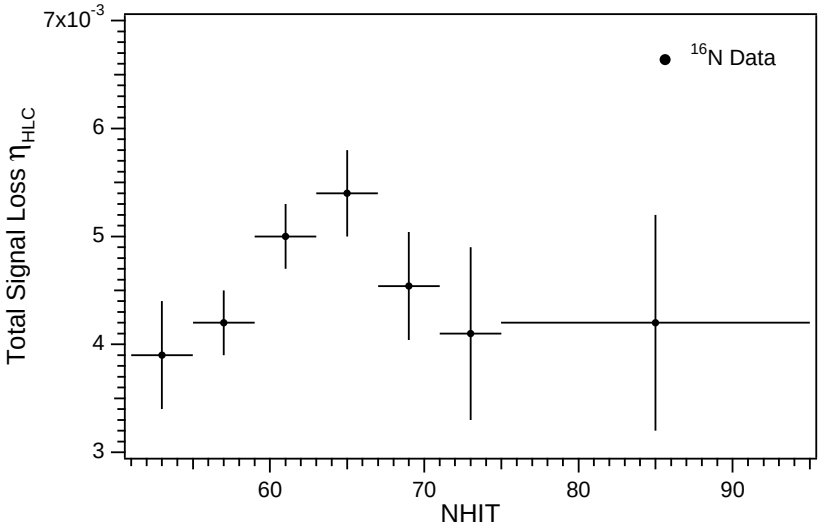

Figure 5.23: Total ^{16}N signal loss in $CUTS_A$ as a function of NHIT.

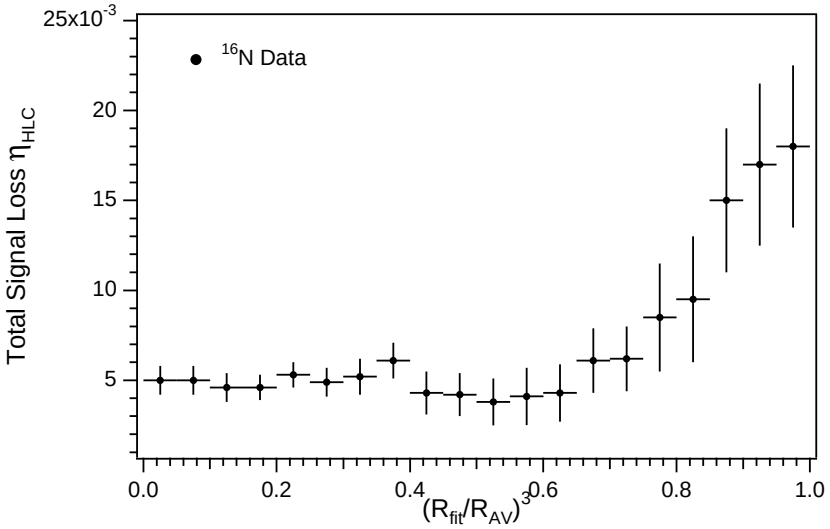

Figure 5.24: Total ^{16}N signal loss in $CUTS_A$ as a function of $(R_{fit/}R_{AV})^3$.

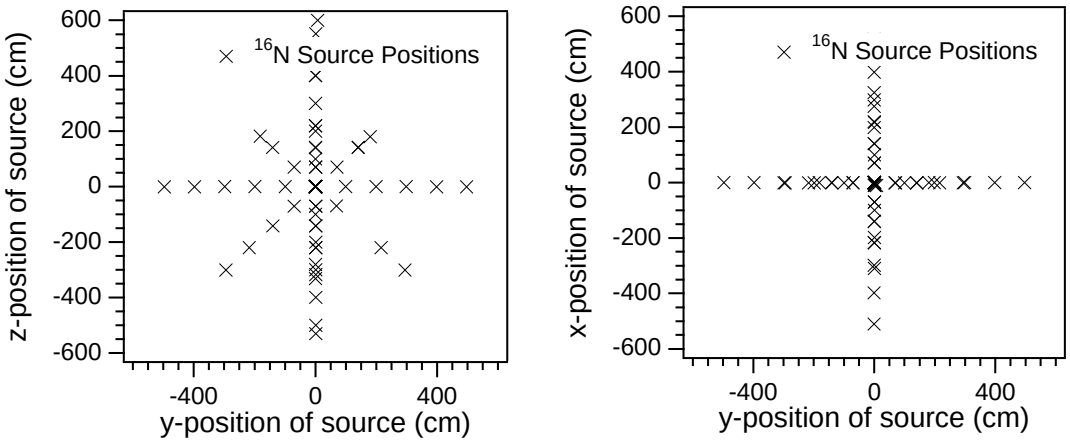

Figure 5.25: Positions of the ^{16}N calibration source that are used for the study of neutrino signal loss in data reduction.

The aspect of signal loss and the residual contamination in the data set has been studied in great detail in [142]. This includes signal loss studies on γ and electron calibration data. For reference, we reproduce the final estimates for the signal loss after application of all data reduction and high-level event cuts developed in [142]. The total signal loss due to all cuts for data within $R_{fit} \leq 550$ cm and above NHIT ≥ 65 is listed in Table 10.5.

Table 5.1: Total signal loss due to all cuts for data inside $R_{fit} \leq 550$ cm and with NHIT ≥ 65 as determined in [142].

Signal	Signal Loss (%)	Fractional Loss (η_{HLC})
^{8}B CC	$1.33^{+0.73}_{-0.63}$	$\eta_{CC} = 0.0133^{+0.73}_{-0.63}$
^{8}B NC	$1.33^{+0.78}_{-0.68}$	$\eta_{NC} = 0.0133^{+0.78}_{-0.68}$
^{8}B ES	$1.52^{+0.74}_{-0.64}$	$\eta_{ES} = 0.0152^{+0.74}_{-0.64}$
hep CC+ES	$1.74^{+0.73}_{-0.63}$	$\eta_{hep} = 0.0174^{+0.73}_{-0.63}$

CHAPTER 6

ENERGY RESPONSE AND SCALE OF THE SNO DETECTOR

6.1 Calibrations of the SNO PMT Array

The SNO detector is calibrated using a variety of sources, including an isotropic light source, γ-rays, neutrons, and β-particles. SNO's extensive calibration program addresses a multitude of questions associated with its complex detection system for Čerenkov light. This includes the issues of photon transport and detection and the detector response to a variety of different electron and γ signals.

Čerenkov light measurements in SNO are based upon coincident phototube signals registered within the ~ 400 ns time window of an event. Energy information is largely associated with the number of tube hits, NHIT, and the event position can be reconstructed using the relative phototube timings within the event. The hit pattern can be used to determine direction information and discriminate against instrumental backgrounds. NHIT and the associated hit patterns are dependent not only on the amount of light, that is the number of photons, but also on the details of the detector optics and the response of the individual photomultiplier tubes. Understanding the light production, propagation, and detection is critical for an accurate simulation and interpretation of event signals in SNO. The main issues that are addressed in the SNO calibration program are summarized below.

Photon Transport: The SNO detector consists of three primary optical media: D_2O, acrylic, and H_2O. Additional material in the PMT's, such as the glass of the phototube, as well as the geometry of the PMT array itself affect the response of the detector to light producing interactions. Attenuation, reflection, and scattering are the properties that need to be understood in the various media of the SNO detector.

Photon Detection: Photons from light producing interactions are detected in SNO by means of 9456 inward facing 8"-diameter PMT's from Hamamatsu. The response of these devices is calibrated as a function of event position and time.

Detector Geometry: Optical calibrations are a sensitive tool to study the *as-built* detector geometry of the SNO detector. These calibrations are needed as an input to the SNO Monte Carlo simulations.

Detector Status and Conditions: Using optical calibrations we can also monitor the status and the conditions of the SNO detector and determine changes in the PMT response over time. Changes in the attenuation of the light and heavy water as well as in the (a)symmetry of the detector response can be detected.

Various techniques are used to calibrate and monitor the performance of the PMT array. These include optical, electronics, and energy calibrations.

1. Calibration of Optical Response: The optical calibrations are performed using a pulsed laser with ∼2 ns time resolution. The optical constants are derived from a global fit to the laserball data at wavelengths of λ=337, 365, 386, 420, 500, 620 nm. The work presented in this thesis is based on optical constants from March 16, 2001. Details of the optical calibration are described in [146]. The optical analysis is done using the "grey disk" PMT model in the SNO Monte Carlo code. This particular PMT model is a parameterization of the full 3-dimensional PMT that is used in other SNO analyses. The optics constants derived in [146] are verified against ^{16}N and ^{8}Li in the energy calibration of the detector.

2. Calibration of Electronics: The front-end electronics and the PMT readout system is calibrated using both electronic pulsers as well as pulsed light sources, such as a sonoluminescent calibration device [143].

3. Energy Calibration: SNO's energy calibration is based on a number of different electron and γ sources that cover the entire energy range of the ^{8}B spectrum. Details of the energy calibration are given below.

6.1.1 Energy Calibration

The energy response of the SNO detector is calibrated using a variety of calibration sources that probe the energy response from about 6-20 MeV, over the entire range of the solar neutrino spectrum. The primary energy calibration in the SNO detector is established with a tagged ^{16}N source. The calibration obtained with this source is then tested against ^{8}Li,

^{252}Cf, and the higher-energy pT source. The characteristics of these sources are summarized in Table 6.1. Figure 6.1 shows the comparison of data and Monte Carlo for the energy calibration of the SNO detector. A calibration of the energy scale can also be obtained from a calibration source-independent study of the neutrino data alone, by fitting the spectrum of charged-current interactions to a ^{8}B β-spectrum.

Table 6.1: Energy calibration sources in the SNO detector.

Isotope	Energy	Tag	Source	Ref.
^{16}N	6.13 MeV	β	^{16}O(n,p)^{16}N	[67]
^{8}Li	13 MeV endpoint	α	^{11}B(n,α)^{8}Li	[68]
pT	E_γ = 19.8 MeV	None	^{3}H(p,γ)^{4}He	[44]
^{252}Cf	E_γ = 6.25 MeV	None	^{2}H(n,γ)^{3}H	[66]
^{8}B	15 MeV endpoint	None	$^{8}\mathrm{B} \rightarrow {}^{8}\mathrm{Be}^{*} + e + \nu_e$	Chapter 8

Primary calibration of the energy scale is obtained through γ-rays from ^{16}N β-decay [67]. The ^{16}N ($t_{1/2}$ = 7.13 s) is produced via the (n,p) reaction on ^{16}O in the form of CO_2 gas using 14-MeV neutrons from a commercially available Deuterium-Tritium (DT) generator. The ^{16}N is produced in a shielding pit in a utility room near the SNO cavity and transferred to the detector in a CO_2 gas stream via small diameter capillary tubing. The bulk of the activity decays in a decay/trigger chamber designed to block the energetic β-particles yet permit the primary branch 6.13 MeV γ-rays to exist. Detection of the coincident β-particles with plastic scintillator lining the walls of the decay chamber volume provides a tag for the SNO electronics. With an energy of 6.13 MeV this calibration device is ideally suited to probe the energy response of the SNO detector near the peak of the γ energy of the d(n,p)γ peak. This is particularly important for a precise measurement of the NC signal in pure D_2O. Calibrations with the ^{16}N source are used for a number of tasks including calibration of the energy scale and resolution, and verification of reconstruction and data-reduction algorithms.

The response of the SNO detector to electrons is probed with the ^{8}Li calibration source

[68]. This source is used to assist in energy calibrations, position reconstruction studies, and evaluation of instrumental background discrimination. It creates a spectrum of β particles with an energy range similar to that of the solar ^{8}B spectrum. The isotope decays with a Q-value of 16.003 MeV and the main β-decay branch is an allowed decay with a central end-point energy of 12.96 MeV. The energy spectrum it produces is similar to that of the ^{8}B charged-current neutrino interactions. Both isotopes decay to an excited state of ^{8}Be which in turn decays to α-particles that are used to tag events in the ^{8}Li source. The ^{8}Li isotope is created using a DT generator in conjunction with a ^{11}B target, and is carried to a decay chamber using a ^{4}He + 1% N_2 gas/aerosol system. The decay chamber detects prompt α particles by gas scintillation in coincidence with the β particles which exit through a thin stainless-steel wall.

A compact, self-contained ^{3}H(p,γ)^{4}He γ-ray source is used to calibrate the response of the SNO detector beyond the ^{8}B endpoint of 15 MeV [44]. An ion source generates and accelerates protons up to 30 keV incident on a high-purity scandium tritide target. The ^{3}H(p,γ)^{4}He reaction (pT) generates monoenergetic gamma rays at energies of E_γ = 19.8 MeV. Since ^{4}He does not have a bound excited state, the γ-ray emitted in this reaction is monoenergetic. The pT source has the highest energy of all calibration devices in SNO. The pT source is essentially free of neutrons if the proton energy is below the Q-value of ^{3}H(p,n)^{3}He. However, isotopic impurities and the isotopic exchange between the beam and the target can give rise to neutrons through the ^{2}H(t,n)^{4}He, ^{2}H(d,n)^{3}He and ^{3}H(t,2n)^{4}He reactions. The neutron background is low enough so that it does not mask the γ-ray signal during calibration.

Neutrons from ^{252}Cf are used to calibrate the detector with the ^{2}H(n,γ)^{3}H reaction. As the neutrons diffuse in the D_2O they probe the entire detector volume and are not localized to a calibration position.

The main results from the calibration of the SNO detector are summarized below. Figure 6.1 illustrates the good overall agreement between calibration data from the various calibration sources and the Monte Carlo predictions. For reference, the mean NHIT values for the ^{16}N and pT source are tabulated in Table 6.2.

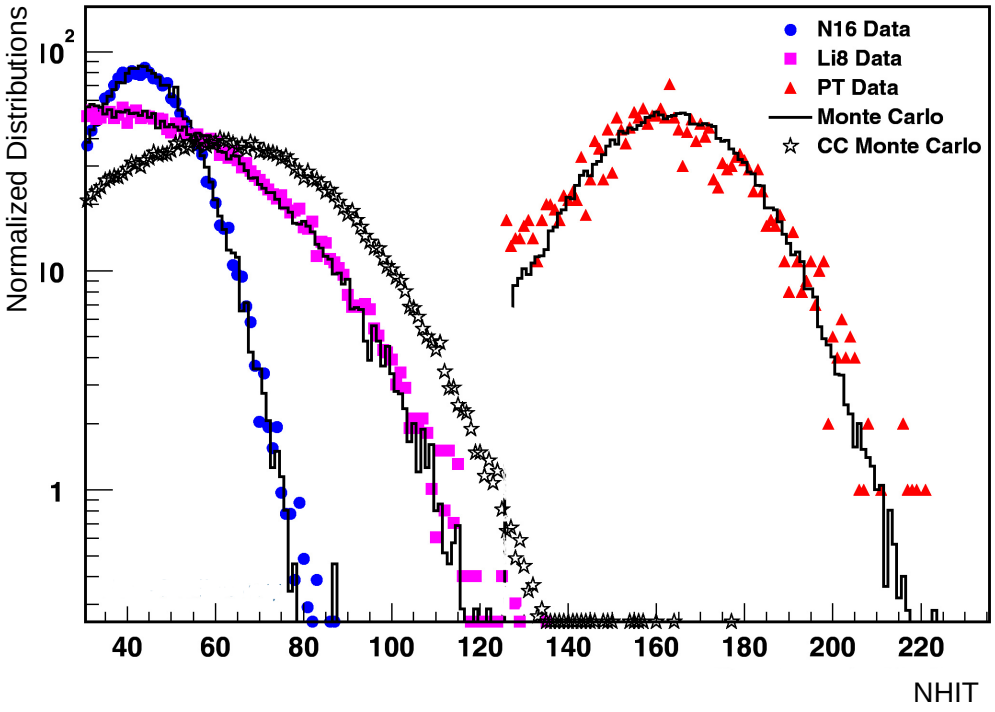

Figure 6.1: Energy calibration during the D_2O phase. Figure courtesy of A. Hamer, Los Alamos National Laboratory.

Table 6.2: Mean NHIT values, μ_{NHIT}, and resolution, σ_{NHIT}, of data taken with the ^{16}N and pT sources at the center of the detector.

Source	μ_{NHIT}	σ_{NHIT}	Ref.
pT Data	161.56 ± 0.59	16.79 ± 0.85	[28]
pT Monte Carlo	162.84 ± 0.10	16.92 ± 0.12	[28]
^{16}N Data	43.59 ± 0.05	4.42 ± 0.21	[this work]
^{16}N Monte Carlo	43.43 ± 0.04	4.39 ± 0.03	[this work]

6.2 Energy Estimators

The energy of a Čerenkov electron or a γ observed in the SNO detector is related to the number of PMT hits, NHIT, and the charge recorded in each PMT. It turns out that good energy estimators can be derived from the number of PMT hits alone. The charge resolution is not sufficient to be of additional value in the event energy estimation. Every energy event estimator in SNO is based on some measure of the number of hit PMT's. In using the raw number of PMT hits, NHIT, as an event energy estimator we assign a most likely hit pattern to an event of known energy.

In calibrating the optical response of the detector with the laserball source, detailed timing distributions of the PMT's are determined. One interesting quantity to study is the timing residuals of calibration events. Timing residuals are the difference in time between hit and direct flight time from vertex. Figure 6.2 shows a plot of the timing residuals. It illustrates the prompt and late light in an event. The late pulsing is believed to be soft X-ray production at the first dynode liberating another photoelectron from the cathode. The peak of the prompt light varies in Čerenkov events with the position and direction of an event. The timing residuals vary themselves depending on the event type.

One can think of two basis event energy estimators: It is possible to use the prompt light of an event within the first 20 ns and apply a position and direction correction on an event-by-event basis. In this case, one calculates an effective NHIT which adjusts the expected energy of an event based on its position and direction in the detector. This energy estimator uses a particular distribution of the timing residuals in estimating the energy of an event and hence assumes that the event in question is a single Čerenkov electron. As we do not know *a priori* whether a particular event is a neutrino event or a background this event energy estimator works primarily in the neutrino signal window but may not accurately describe low-energy backgrounds. The uncertainties on the energy scale and resolution are calculated by propagating in detail the uncertainties on the optical properties of the detector through the response function.

Alternatively, one can use the total light in an event given by the total number of PMT hits within 93 ns. To first order, this approach does not require a position and direction-

dependent correction. Furthermore, by using the total light in an event one collects about 30% more light per event and can ultimately achieve the best energy resolution. Using the total as an event energy estimator does not make any assumptions on the origin of the event and, hence, is applicable to both backgrounds and neutrino events. To combine the advantages of both approaches one can think of creating a total light version of an energy estimator which includes position and direction-dependent corrections to account for any detector asymmetries and variations. This has not yet been done.

Using NHIT as an energy estimator has the advantage that it is simple and robust. It uses no additional cuts to determine the good and bad hits in an event, it integrates over the uncertainties in the late light distribution, and it applies no correction to the data itself. On the other hand, it varies with position, event direction, changes in the detector hardware, such as discriminator thresholds, and the rate of correlated non-photon noise. These effects have to be taken into account when evaluating the overall energy scale of the detector.

In this chapter we study the energy scale and response of the detector during the time of data taking and develop a parameterized response function that describes the gain of the detector at any point in time. All subsequent Monte Carlo simulations make use of the exact, time-dependent detector properties and response described below. In addition, a $NHIT \rightarrow E$ transformation is given that relates the number of PMT hits in an event with its most likely energy, E.

The optical properties which dominantly affect the number of hit phototubes for a given energy event are the variation of phototube efficiency with photon incident angle and photon attenuation in the inner detector materials, that is the D_2O, acrylic, and the H_2O. These parameters are measured at various time intervals with extensive optical calibrations at various photon wavelengths.

The absolute photon collection efficiency is determined by comparing the number of phototubes hit in a Monte Carlo calculation with the measured optical parameters to data from an ^{16}N calibration source. Extensive scans with the ^{16}N source are taken at many points throughout the detector volume. The deviations between the measured detector gain and the Monte Carlo prediction are used as an estimate of the systematic uncertainty in the absolute energy calibration.

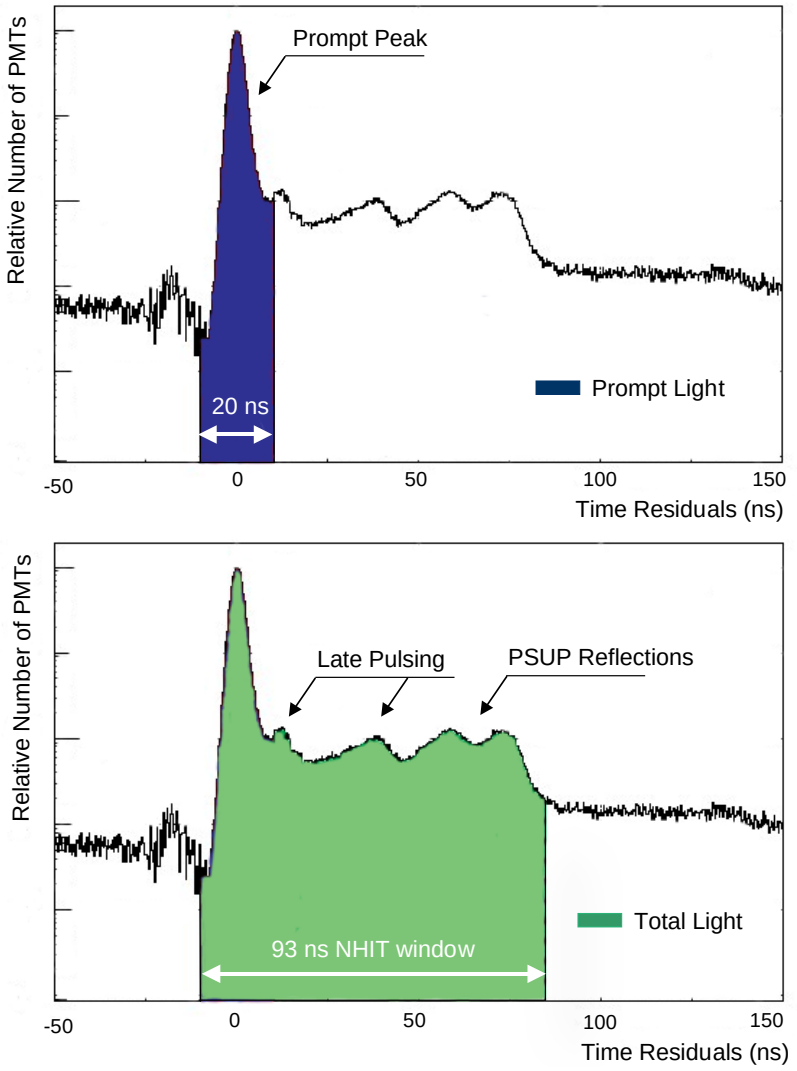

Figure 6.2: Prompt and total light energy estimators: Distribution of timing residuals from ^{16}N calibration data taken at the center of the detector. The energy of an event can be estimated by either using only the prompt light of the Čerenkov event and making a position and direction-dependent correction or by using the total light (NHIT). In the latter approach all PMT hits within 93 ns are counted and used to estimate the effective energy of an event. The exact distribution of the timing residuals depends on the position of the calibration source inside the detector.

6.3 Temporal Dependence of Detector Response and Energy Scale

The temporal stability of the detector response and energy scale is monitored with various calibration devices and online monitoring tools. Three basic quantities describe the state of the detector and its PMT detection system:

1. Number of Online PMT's: The number of working channels is determined by the number of online PMT's, the state of the electronics, and other criteria. For an exact definition see Table 6.3. The number of working channels in the SNO detector can be determined from the DQXX database file.

2. PMT Noise Rate: The PMT noise rate varies with temperature, high voltage, and variables. The PMT dark noise rate is usually determined from the PulsedGT which probes the detector at a rate of 5 Hz.

3. Mean Response to ^{16}N: As the ^{16}N calibration source is essentially a monoenergetic calibration device with an energy of $E_\gamma = 6.13$ MeV it is well suited to track the overall detector response at energies close to the signal from the neutral-current interaction ($E_{\gamma,NC} = 6.25$ MeV.)

A tube is online and taking data if a number if hardware and software requirements are met. The conditions for a PMT tube to be considered operational are summarized in Table 6.3. The number of working PMT's and the PMT noise rate are two basic detector properties that reflect the overall state of the detector. Figure 6.4 shows the temporal variation in noise rate since November 1, 1999. The absolute noise rate has decreased but the average value has been constant for most of the D_2O phase. Due to PMT failures and other problems the number of working channels also decreased continuously since the beginning of data taking (Figure 6.3).

The energy scale of the SNO detector is tested regularly using the ^{16}N source. The calibration data is compared to the Monte Carlo prediction for that time. The primary runs used to measure the temporal variation in the NHIT energy scale are ^{16}N high voltage stability runs taken at the center of the detector. The mean NHIT of the ^{16}N distributions is used as a measure of the energy scale. To make the comparison as a function of time the mean NHIT is corrected for the number of operational tubes and the detector noise

Table 6.3: Requirements for operational PMT's to be counted in occupancy correction. For reference, details of the SNO PMT and electronics system are described in [105].

Status Condition for Valid PMT's	OK
The PMT has an ID.	X
No problem bits for PMT's set.	X
Crate present and alive.	X
Card present and online.	X
PMTic (PMT interface card) present.	X
Daughter Card present.	X
HV to PMT is on	X
Sequencer on.	X

rate. The number of operational tubes, the occupancy of the detector, is determined from run-specific detector status records, the DQXX SNO database files. These files contain information on the state of the detector during each run and are written and recorded by the SNO data acquisition system. The status of the detector, that is the number of working PMT's and electronics channels, their state and calibration, and other information is stored in database files for the detector status. These DQXX files are written out for every run and allow us to reconstruct the state of the detector at any point in time.

Much of the work presented in this chapter builds on the techniques developed in [28]. However, all Monte Carlo simulations are based on our particular choice of optics and detector response models. In particular, the "grey disk" PMT model has been used throughout this work.

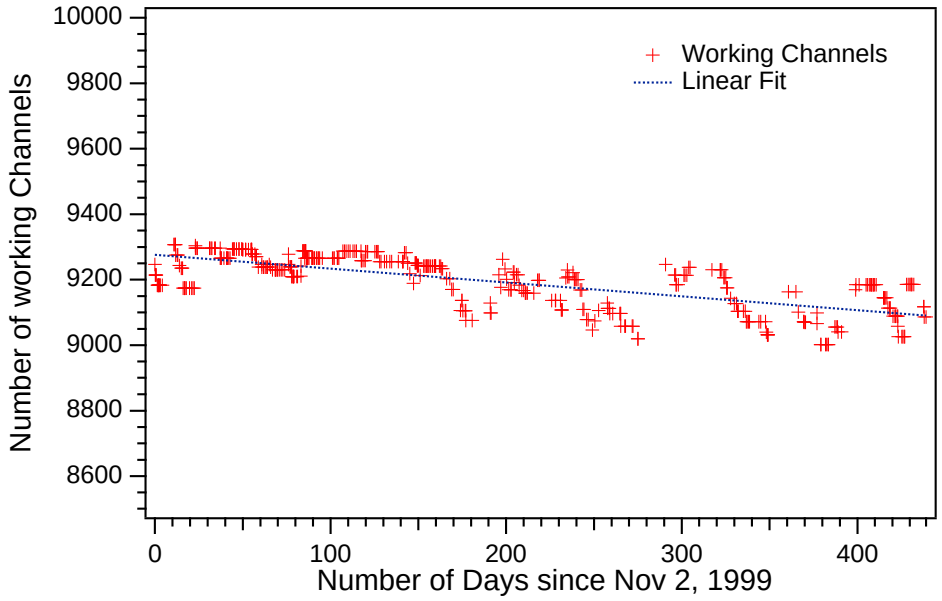

Figure 6.3: Number of working channels during the D_2O phase as a function of time.

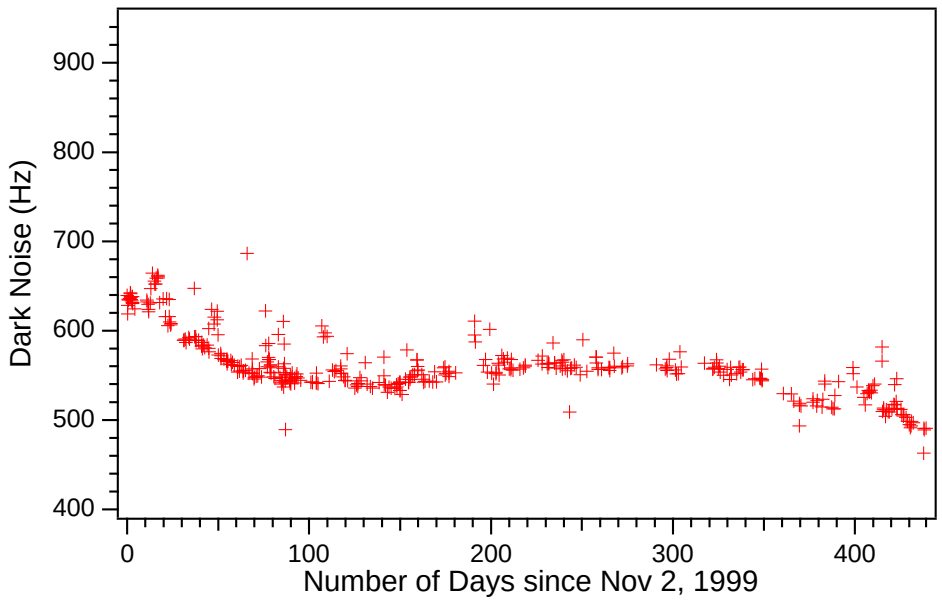

Figure 6.4: PMT dark noise during the D_2O phase as a function of time.

6.3.1 Monitoring the Detector Gain with ^{16}N Calibrations

The temporal dependence of the energy scale is determined by probing the detector with mononenergetic γs from the ^{16}N calibration source. In this analysis NHIT distributions from ^{16}N data taken at regular intervals at the center of the detector is compared to the distributions of the corresponding Monte-Carlo simulations over the time period of data taking. By correcting for time-varying variables such as the number of online channels and the PMT noise rate one can also compare individual ^{16}N calibration runs independent of Monte Carlo. The difference between ^{16}N calibration data and Monte Carlo simulations is taken as an estimate of systematic error.

For the study of the temporal dependence of the detector response we use ^{16}N data taken at the center of the detector. The center of the detector has some intrinsic advantages and is the location of choice for these detector stability checks. The center position is believed to be least sensitive to optics variation.

Calibration of the detector gain with ^{16}N data also accounts for the noise rate of the PMT's which can be deduced from the mean NHIT value of the PulsedGT for a particular run. Table 6.4 summarizes the results from nine HV stability runs. Given are the run number, the date of the run, the PGT mean, the NHIT mean, the number of operational tubes, and μ'_{NHIT} which is the NHIT mean corrected for noise and the occupancy. The determination of the relative NHIT means corrects for the detector configuration. This includes a noise correction based on PGT data and an occupancy correction.

The dark noise, R_{PMT}, in a PMT is related to the mean Pulsed Global Trigger (PGT) and the 420 ns-long NHIT trigger window. In the calculation of the PMT dark noise an effective 390 ns window is used to account for trigger inefficiencies. The mean PGT, μ_{PGT}, is measured after cutting out PED trigger from the PGT signal.

$$R_{PMT} = \frac{\mu_{NHIT}^{PGT}}{390\text{ns} \times N_{PMT,online}} \tag{6.1}$$

The mean detector response to ^{16}N calibrations corrected for all known time variations is usually described by μ'_{NHIT} which is defined as:

$$\mu'_{NHIT} = (\mu^{N16}_{NHIT} - \mu^{PGT}_{NHIT}) \times \frac{N_{PMT,total}}{N_{PMT,online}} \tag{6.2}$$

μ^{N16}_{NHIT} = Mean NHIT of ^{16}N
μ^{PGT}_{NHIT} = Mean number of PGT hits
$N_{PMT,total}$ = Total number of inward facing PMT's = 9456
$N_{PMT,online}$ = Estimated number of working tubes from DQXX

The mean NHIT of the ^{16}N calibration data, μ, is determined from a Gaussian fit to the centroid. A fit range of approximately $\mu \pm \sigma$ is used to determine μ.

Deviations from Gaussian in the tails of the distributions due to Compton interactions with the source chamber material and contributions from the 7.1 MeV γ-ray at higher NHIT cause deviations from the Gaussian tails in the distributions and limit the fit range. A narrower fit range permits a better fit of the peak centroid. Figure 6.5 illustrates the fit to the ^{16}N distribution.

From the detector stability calibration we find that the gain shift over the period of data taking is about 2.2%. A weighted linear time-dependent correction function is used to describe the detector response and correct the time-varying gain. Using this time-dependent correction in the SNOMAN Monte Carlo simulation of each run we find that the remaining difference between Monte Carlo and data was less that 0.4%. In this run-by-run corrected Monte Carlo simulation the DQXX information was read in explicitly as well as the correct run start date and time for the occupancy correction. The Monte Carlo simulations also used the noise rates as determined via the analysis of PGT events in the data. The cause of the gain drift is currently not understood and under investigation.

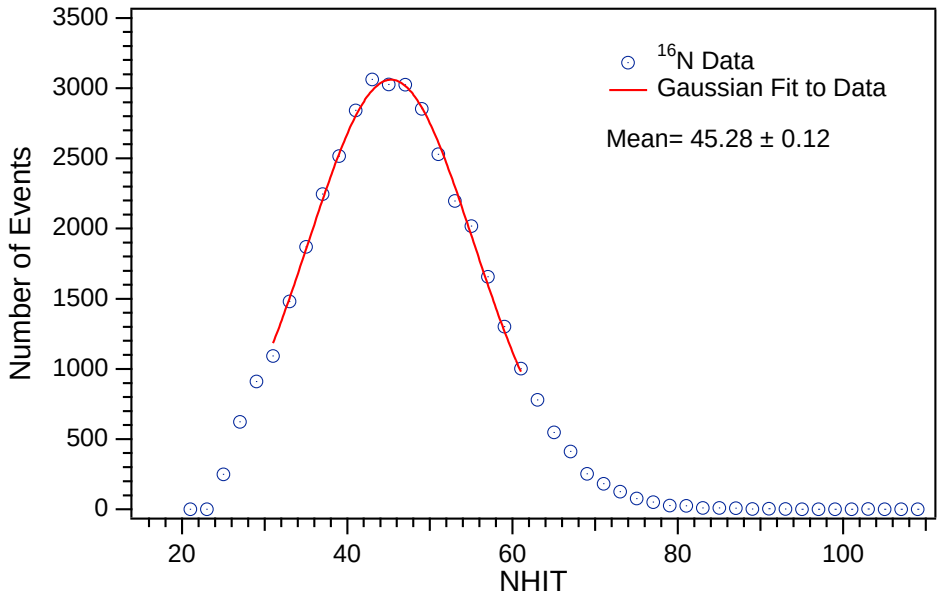

Figure 6.5: NHIT distribution of ^{16}N data and Gaussian fit. A limited fit range is used to determine mean detector response to 6.13-MeV γs from ^{16}N.

Table 6.4: Results from the detector stability analysis using ^{16}N data.

Run	Date	μ_{PGT}	μ_{NHIT}	$N_{PMT,online}$	μ'_{NHIT}	μ^{MC}_{NHIT}
10278	11/29/99	2.199± 0.079	44.90	9296	42.71	43.953 ± 0.063
11601	04/20/00	1.954± 0.079	43.93	9170	42.56	43.181 ± 0.063
12144	06/27/00	2.055± 0.084	43.99	9221	42.28	43.581 ± 0.061
12262	07/28/00	2.000± 0.065	43.02	9058	42.10	42.871 ± 0.064
12498	08/19/00	2.070± 0.076	43.90	9247	42.06	43.708 ± 0.062
13381	09/27/00	2.018 ± 0.063	43.22	9127	41.96	43.151 ± 0.063
13467	10/17/00	1.960± 0.110	42.70	9030	41.94	42.647 ± 0.082
14273	12/11/00	1.936± 0.077	43.44	9184	42.00	43.330 ± 0.060
14501	01/08/01	1.839± 0.064	43.21	9185	41.87	43.149 ± 0.067

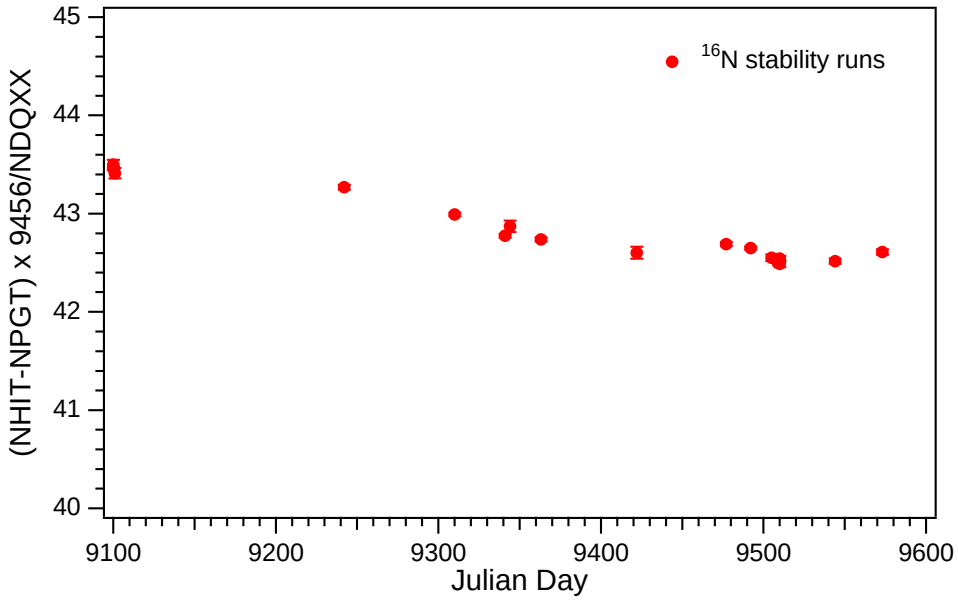

Figure 6.6: Energy stability during the D_2O phase. This figure shows the mean NHIT as a function of time for the HV stability runs corrected for the number of working channels and the noise rate.

In SNOMAN Monte Carlo simulations the energy scale is adjusted by scaling the PMT collection efficiency. The PMT collection efficiency is determined by comparison with ^{16}N calibration data taken at the center of the detector.

In SNOMAN, the energy scale is specified by the PMT collection efficiency PMT_{eff}. $NHIT'$ and PMT_{eff} are related as follows:

$$PMT_{eff} = \frac{0.5834}{40.669} \times \mu'_{NHIT} \tag{6.3}$$

6.3.2 Detector Stability Checks with Muons

The status of the detector, the number of working channels, and the energy scale can be checked with physics events that saturate the 9456 inward looking PMT's of the SNO detector. Muons that enter the detector deposit significantly more energy in the detector than solar neutrinos. They can be easily identified by the large number of PMT hits per event. On average about 75-85% of all PMT's get hit during a muon event. The average number of PMT hits in a muon event, μ_{NHIT}, can be used to determine the relative change in the number of working PMT's and electronics channels in the SNO detector. Muons and muon followers in the SNO detector have been studied in great detail in [3]. The analysis presented here uses the muon identification code developed in [3].

Muons that occur during the data taking for solar neutrinos are selected and classified according to their event characteristics. AV-going muons are events that pass through the acrylic vessel. In contrast, non-AV-going events miss the acrylic vessel and only pass through the light water region of the detector. Their light output can be much less. Only the class of AV-going events is used to check the detector status and stability.

Using a muon identification algorithm developed by [3] muons are selected and the path of a muon event identified. Muons that enter and exit the detector are called through-going muons. Based on the techniques developed in [3] any muon with a path length $L_\mu \geq 1179$ cm is identified as an AV-going event. The critical path length that defines a muon to be AV-going is largely determined by the geometry and optical response of the detector.

The NHIT of every selected muon event is corrected for the variation in the detector configuration based on PulsedGT and the channel status using the DQXX banks. The results of this analysis are shown in Figure 6.7 which illustrates the relative gain change of the detector response to AV-going muons over 13 months of data taking. For AV-going muons, the mean number of PMT hits, μ_{NHIT}, changes by ~ 1.9 %. Over the same period of time the mean number of working channels decreases by ~ 2 %. The low muon statistics in the SNO detector and systematics associated with the reconstruction of the muon path length make this technique less precise than calibration of the energy scale with the tagged, high-statistics ^{16}N source.

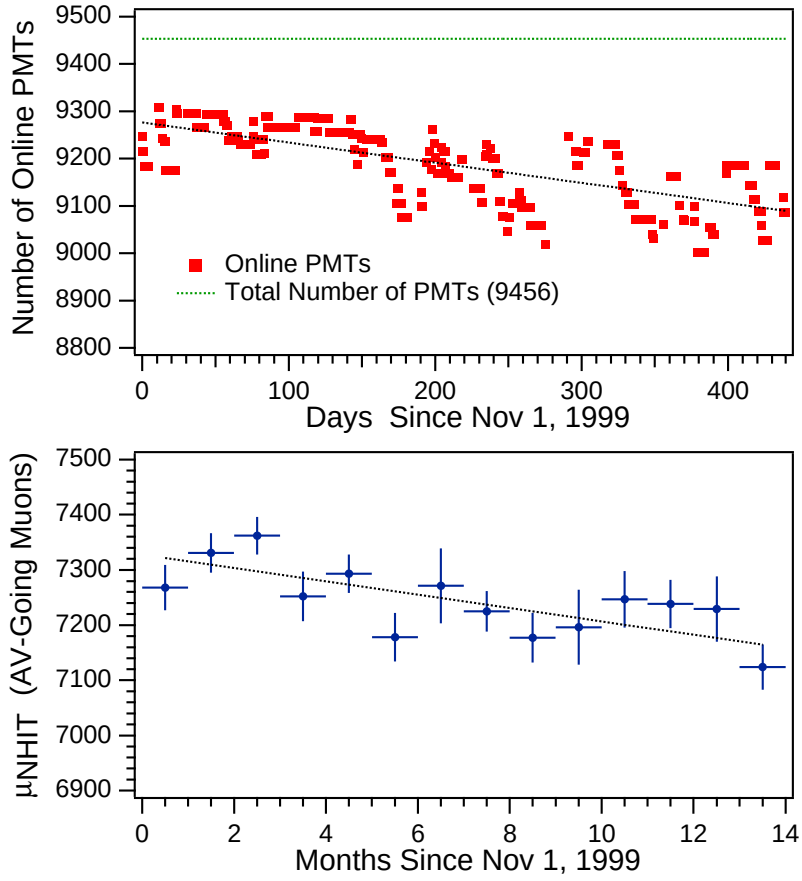

Figure 6.7: Comparison of the number of working channels during the D_2O phase and the mean NHIT, μ_{NHIT} of AV-going muons for the same data period. The lines are weighted least-square fits to the number of online channels and the mean NHIT of AV-going muons. The green horizontal line indicates the total number of channels in the SNO detector.

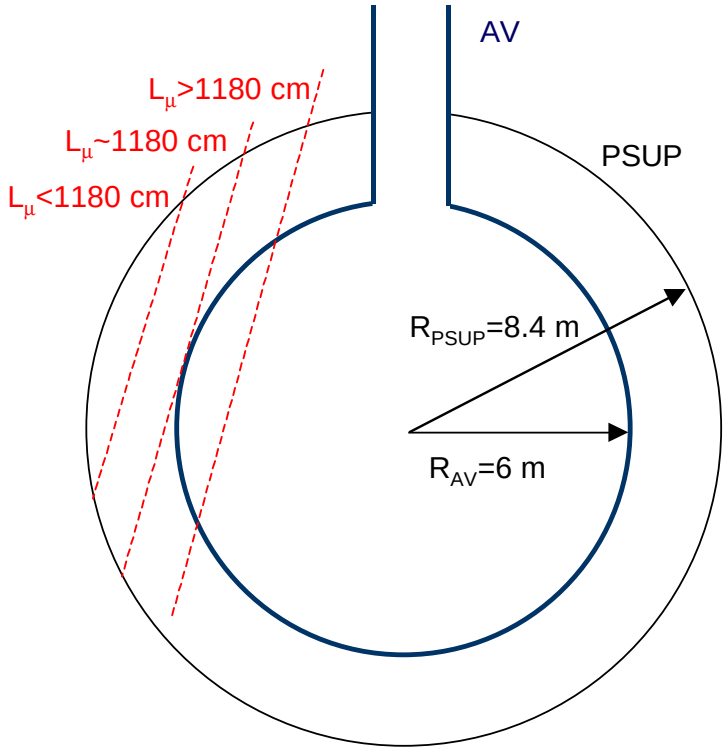

Figure 6.8: Illustration of the path length criterion L_μ for AV- and non-AV-going muons.

6.3.3 NHIT Energy Scale Uncertainties

A variety of systematic effects and errors can contribute to the energy scale uncertainty. Ideally, the energy scale uncertainty would be evaluated at every point in the energy or NHIT region of interest to solar neutrinos. Practically, this is impossible. Therefore, we distinguish between absolute uncertainties in the energy scale and differential uncertainties. A list of various issues to be considered in this context is given below:

1. Uncertainties in the Absolute (Overall) Energy Scale:

    - Calibration Source-Related Systematics
    - Trigger Threshold
    - Detector Properties

2. Differential energy Scale Uncertainties:

    - Cross-Talk

The ideal calibration source for SNO would be a monoenergetic point electron source with variable energy. Instead, SNO uses the ^{16}N γ-ray source at 6.13 MeV to derive its primary calibration. This energy scale is verified with the 19.8 MeV pT source and with electrons from ^{8}Li. The energy scale is essentially an extrapolation from the energy of neutron capture on deuterium to an energy beyond the endpoint of the solar ^{8}B spectrum. That extrapolation is then checked against the pT source, and any difference is used to estimate the uncertainties. The uncertainty in the energy scale of the CC spectrum measured in SNO is therefore largely dependent on the systematics and uncertainties from the ^{16}N source.

The ^{16}N source is not purely monoenergetic and has a decay chamber whose geometry blocks some of the backward light. The overall uncertainties related with the ^{16}N source have been evaluated by Monte Carlo simulations and are summarized in Table 6.5. The polar angle distribution of emitted γ-rays is a negligible contribution to the energy uncertainty.

Uncertainty in the energy scale calibration may also arise from the properties of the detector. While the detector status is recorded for every run in the DQXX database files there are uncertainties associated with channel counting and the rate dependence. The latter effect was discussed in Chapter 4. An estimate of the uncertainty due to the rate dependence yields 0.4%. This estimate is limited by the statistics of the ^{16}N data.

The threshold and charge stability of the detector have been studied in great detail and yield a 1% uncertainty in the energy scale. The number of online channels was determined using a variety of different schemes. Depending on whether occupancy tests for individual channels are taken into account or not the number of working and online PMT's is uncertain to 0.2%.

The PMT noise rate has been determined for every run over the entire period of data taking. Uncertainties in the noise rate averaged over a run are $\ll 1\%$. The short-term stability of the noise rates is estimated to be 0.1%.

Cross-talk can be described as the noise incurred by charge on one channel causing other channels to trigger. Cross-talk affects the NHIT of an event and hence translates directly into the energy scale uncertainty. It is differential and we expect it to vary with NHIT or energy of an event. The amount of cross-talk can be identified by low-charge hits accompanying hits with a large charge. Using a criterion developed in [122, 28] we count the number of cross-talk hits as the number of hits with $Q_{hs} \leq 8$ on a card with at least one hit of $Q_{hs} \geq 200$. The neutrino data set down to a NHIT= 35 was analyzed for cross-talk. Figure 6.9 shows the number of cross-talk hits against NHIT. Fitting the number of cross-talk hits we find that the cross-talk contribution to the total NHIT is:

$$\mathrm{NHIT}_{Xtalk} = -(0.037 \pm 0.044) + (0.01 \pm 0.001) \times \mathrm{NHIT} \tag{6.4}$$

One can use this model for the cross-talk contribution to the total NHIT and to estimate the resulting energy-scale uncertainty. Assuming that the cross-talk contribution is absorbed into the calibration at the ^{16}N calibration point the resulting energy scale uncertainty is zero at 6.13 MeV and increases with energy. At $\sim$ 20 MeV, the energy of the pT source, the uncertainty is about 0.9%.

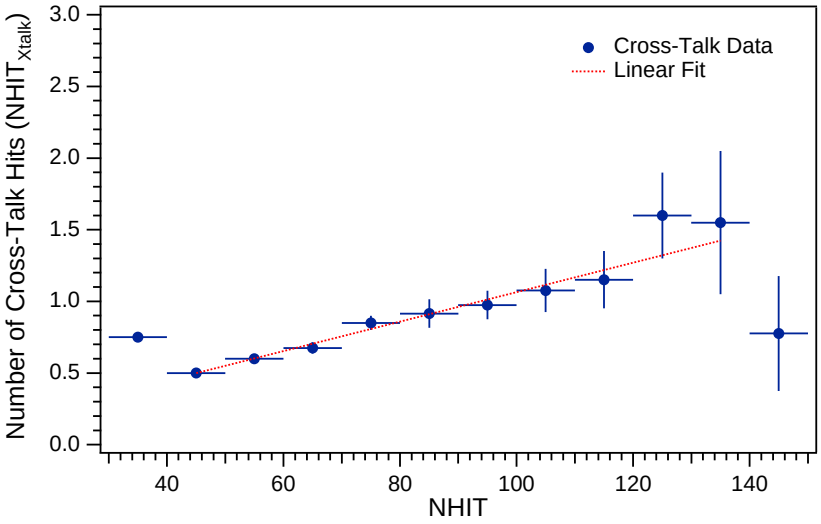

Figure 6.9: Cross-talk contribution to NHIT. Number of hits from cross-talk versus NHIT.

Table 6.5: Overall energy scale uncertainty for NHIT. The uncertainties in the differential energy scale are estimated from the cross-talk contribution. A breakdown of ^{16}N source-related uncertainties is given.

Systematic Effect	Contribution	Estimate
Temporal		0.34%
Position		1.03%
^{16}N Source (Total)		0.44%
	^{16}N Decay Scheme	0.1%
	^{16}N Source Geometry	0.3%
	EGS4 Code	0.3%
	β Trigger Efficiency	0.05%
PMT Threshold/Rate		1.0%
Channel Accounting		0.2%
Noise		0.1%
CrossTalk		0.9%
Total		1.56%

6.4 NHIT → Energy Scale Transformation: A Functional Parameterization of the SNO Detector Response

In this analysis NHIT is the chosen measure of energy:

- NHIT is an energy measure that is independent of the type of interaction. While the prompt light is different for Čerenkov electrons and multi-particle backgrounds NHIT does not distinguish between the nature of events.

- An event-independent energy measure allows us to generate an energy scale that is valid for both signal and background events. It effectively decouples the $NHIT \rightarrow E$ transformation from the signal extraction.

One of the results we obtain in the decomposition of the data set (see Chapter 9) is the energy spectrum of the recoil electrons produced in the charged-current (CC) reaction of neutrinos on deuterium. While the energy spectrum of NC events is well defined the shape of the CC spectrum is not. The underlying ^{8}B spectrum has been measured precisely but the observed spectrum of ^{8}B neutrinos can be distorted by neutrino oscillations. We have no *a priori* knowledge of the true shape of the CC NHIT spectrum.

For a physical interpretation of the decomposed CC NHIT spectrum it is desirable to convert the detector response measure, NHIT, into an energy scale. To determine the gain function that describes the scale transformation, the detector response to monoenergetic electrons is simulated using the SNO Monte Carlo code. The Monte Carlo simulation produces NHIT distributions centered at the NHIT value which is the most probable detector response to a monoenergetic electron of that specific energy. Inversely, it is impossible to assign a unique energy value to every NHIT, and a distribution of likelihood is obtained.

To first order, we assume that the distribution of CC neutrino interactions is uniform in the detector volume. In reality this is not quite true. The distribution of events is not truly isotropic since the Sun illuminates a band around the equator of the detector and the electrons are produced in a $1 - \frac{1}{3}\cos\theta_{\odot}$ distribution. This effect, however, is negligible for the electrons from the CC reaction but might be more significant for the ES interaction which is sharply peaked in the angle with respect to the Sun.

In principle, a simple transfer function between NHIT and E can be derived by taking the peak position of the Monte Carlo NHIT distributions generated for monoenergetic electrons. However, the statistical power of such a procedure is limited. It also does not take into account correctly systematic shifts in the peak position. Instead, a general maximum likelihood procedure (ML) is used to determine the most probable scale transformation from NHIT to energy ($NHIT \rightarrow E$).

The final result is a CC spectrum with a scale of most probable energy values. The maximum likelihood estimator is used to determine the uncertainty in the NHIT peak position corresponding to a particular electron energy. Through the required interpolation between the energy values simulated in Monte Carlo this error translates into an uncertainty on the derived energy scale.

6.4.1 Maximum Likelihood Method

The principle of maximum likelihood (ML) is a method for estimation [12]. For a data sample $\{x_1,.....,x_N\}$, the maximum likelihood estimator is the value for a for which the likelihood in the following equation is a maximum:

$$\mathcal{L}(x_1, ..., x_N; a) = \Pi(x_i, a) \tag{6.5}$$

In general, the principle of maximum likelihood determines the value of a that makes the probability of the actual result obtained, $\{x_1,...,x_N\}$, as large as possible.

In this particular problem, the objective is to construct a gain function that describes the $NHIT \rightarrow E$ scale transformation. The data sample consists of NHIT histograms generated by Monte Carlo for specific electron energies E. These histograms represent the NHIT probability distribution for monoenergetic electrons at a particular energy.

$$P_{NHIT,E} = P(NHIT) \tag{6.6}$$

The analytical shape of these distributions is not known and may vary with electron energy E. A fit to these distributions can be used to extract the most probable NHIT

corresponding to a certain electron energy.

Using the maximum likelihood approach, the goal is to determine the most probable NHIT values with uncertainties corresponding to every distribution. Fitting these distributions individually would overestimate the error on the most probable NHIT value. However, a global fit to all NHIT distributions takes into account that the detector response is known (or can be simulated) at a number of different energies. The uncertainty in the most probable NHIT value will be less than for a fit to the individual NHIT distributions. The number of available NHIT probability distributions for discrete electron energies is only limited by computational time.

Formally, we can write these probability distribution functions as a function of the independent variable $NHIT$. If their shapes do not vary significantly over the energy region of interest (or if they can be parameterized in E) one can write the probability distributions

$$P_{NHIT} = P(NHIT, E) \tag{6.7}$$

The NHIT of any event is drawn from $P(NHIT, E)$. For an event with given NHIT, $P(NHIT, E)$ measures the probability of this event to correspond to an electron of energy E.

As the analytical shape of the individual probability distributions $P_{NHIT,E}$ is unknown we may use a number of different fit functions with parameters k_i to describe these distributions for different electron energies. E can then be a function of several fit variables used to parameterize the probability distributions. As $P = P(NHIT, E)$ can only be generated for discrete values of E, we interpolate in the parameterization of E to derive a continuous function P':

$$P'_{NHIT} = P(NHIT, E|k_i) \tag{6.8}$$

For every discrete $NHIT$ value of the decomposed CC spectrum, one can then determine the value of the parameter E that makes the probability of the actual result, $NHIT$, as large as possible. There will be an uncertainty associated with this energy value which

is derived from a maximum likelihood estimator. This uncertainty takes into account the error introduced by fitting a combination of analytical functions to probability density distributions with unknown shape.

This scale transformation is based on the assumption that the SNO Monte Carlo code generates true probability density functions describing the detector response for any given electron energy E. For the purpose of this scale transformation, the procedure outlined above is sufficient. Our only objective is to *assign values of the most probable electron energy* to an NHIT scale. The question of what the probability to observe an event of certain NHIT is in the detector is different. This question requires taking into account the detector response function and the energy distribution of the original particles.

6.4.2 Determining the Centroid of the NHIT Probability Distributions

The analytical shape of the NHIT probability distributions for monoenergetic electrons is not known and may vary with electron energy E. A fit to these distributions is used to extract the most probable NHIT corresponding to a certain electron energy. Monte Carlo simulations show that the NHIT distributions of monoenergetic electrons can be described fairly well by Gaussian distributions. A Gaussian fit to the NHIT distribution determines the peak position and its uncertainty very well although it seems to overestimate the width of the Monte Carlo distribution at lower NHIT below the peak position (see Figure 6.10). Monte Carlo simulations indicate that the Gaussian fit introduces a small but systematic bias.

Alternatively, one could use the centroid or any other statistical measure that describes the peak of these distributions. On the other hand, it is useful to know that the detector resolution at each point can be simulated and fitted with a Gaussian distribution, centered at the right energy. Monte Carlo simulations show that the error introduced by a Gaussian fit to the NHIT probability distributions is $\leq 1\%$.

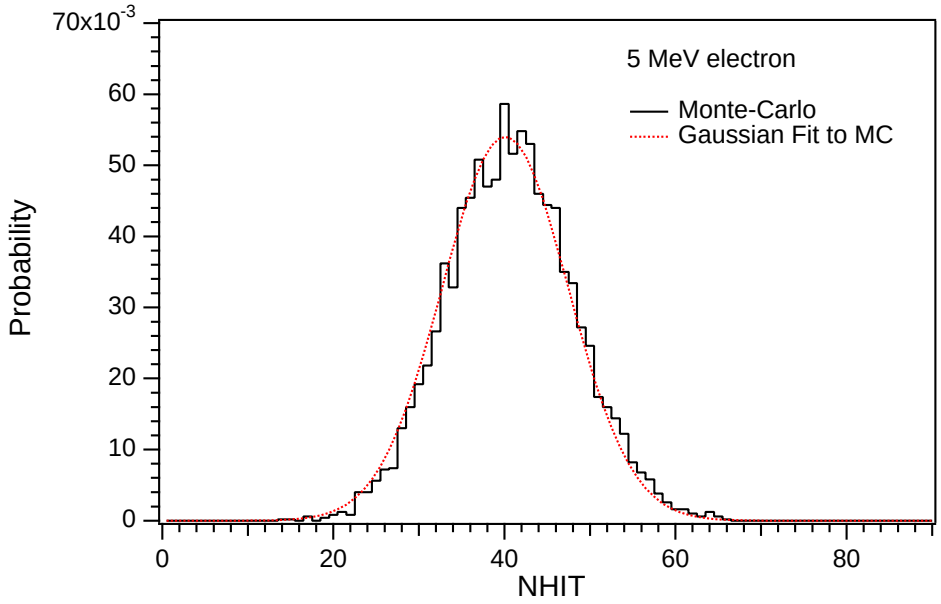

Figure 6.10: Gaussian fit to the NHIT distribution of a 5 MeV electron. The error introduced by the Gaussian fit is of the order of 1%. A radial cut of $R_{fit} \leq 840$ cm is applied.

6.4.3 Interpretation of the Energy Scale

The NHIT to energy scale transformation is dependent on the definition of the centroid or the peak position of the NHIT probability distributions for monoenergetic electrons. It is therefore necessary to state explicitly how to interpret the energy scale of the final CC spectrum. In the case described above, the energy values are derived for every NHIT by determining the likelihood of a Gaussian fit to every simulated NHIT probability distribution. The maximum likelihood estimator for the peak position gives the error in the NHIT corresponding to a particular electron energy. Through the required interpolation this error translates into an uncertainty on the derived energy scale.

Figure 6.11 illustrates the method we use to generate a $NHIT \rightarrow E$ scale transformation function. The NHIT spectra for monoenergetic electrons with energies between 5-15 MeV are shown in Figure 6.12. With increasing energy the CC NHIT spectrum broadens and increases the spread in the probable electron energies.

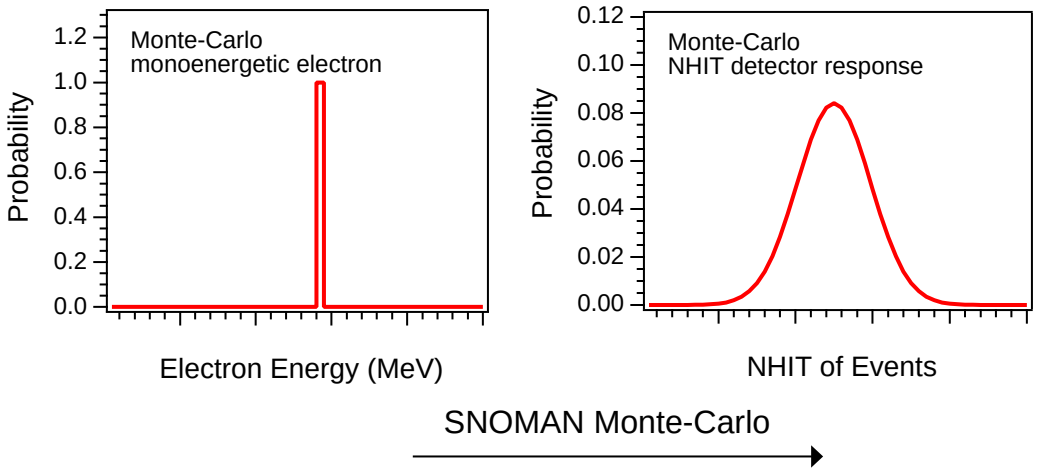

For every E_e, we obtain a probability distribution: $P_{NHIT,\,E}$ = *P(NHIT) at* E_e

E_e parameterizes the global probability density function: $P_{NHIT} = P(NHIT, E_e)$

Maximum Likelihood finds most probable NHIT $L(NHIT_{1,}.....NHIT_i, E_e) = \Pi\ P_{NHIT}(NHIT, E_e)$ *for every* E_e

Interpolation to form continuous P': $P' = P(NHIT, E)$

Determine most probable E for every NHIT: NHIT-> E scale transformation

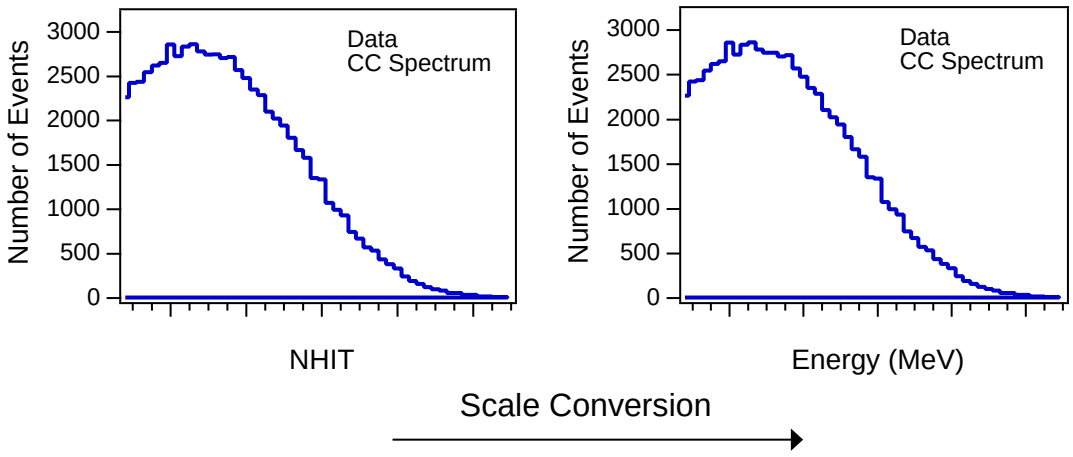

Figure 6.11: $NHIT \rightarrow E$ scale transformation method in our solar neutrino analysis.

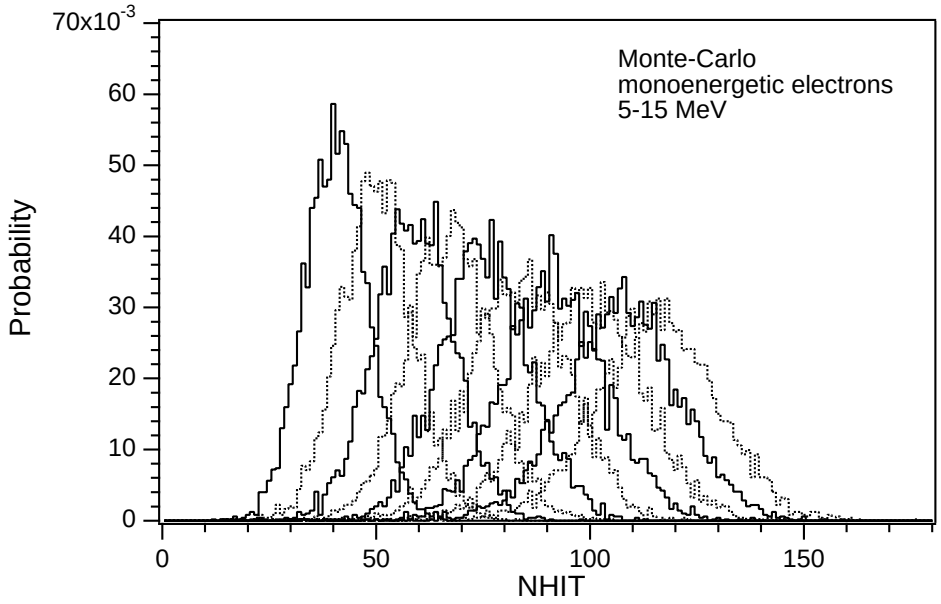

Figure 6.12: Monte Carlo NHIT distributions of monoenenergetic electrons in the range [5,15] MeV. A radial cut of $R_{fit} \leq$840 cm is applied to all these reconstructed data sets.

6.4.4 A NHIT→E Transformation Function

SNOMAN Monte Carlo simulations are used to generate NHIT spectra for monoenergetic electrons in the SNO detector. A reconstruction cut of $R_{fit} \leq$840 cm is applied to all data sets. Using the maximum likelihood (ML) procedure described above a global fit is made to all simulated NHIT spectra and a discrete $NHIT \rightarrow E$ transformation is obtained. In this transformation, E is the most probable energy corresponding to the peak, μ_{NHIT}, of the Gaussian which we fit to the NHIT distribution. The step size of this transformation is based on the simulated Monte Carlo electron energies. A continuos transformation function can be determined by performing a weighted fit to the NHIT centroids obtained from the ML method. A 3-term polynomial is chosen for this fit. The spread, σ, of the NHIT distributions can be described in the same way.

$$\mu_{NHIT}(E_e|k) = k_0 + k_1 E_e + k_2 E_e^2 \tag{6.9}$$

$$\sigma_{NHIT}(E_e|k) = k_0 + k_1 E_e + k_2 E_e^2 \tag{6.10}$$

A weighted fit yields the results shown in Table 6.6. E_e is the electron energy of the event in the detector. The centroid and σ are parameters derived from the Gaussian fit functions. Within the errors given in Table 6.6, the detector response to charged-current electrons distributed uniformly in the detector volume is well described by 6.9.

Table 6.6: Parameterization of the discrete $NHIT \rightarrow E$ transformation.

	μ_{NHIT}	σ_{NHIT}
k_0	-3.401 ± 0.001	3.006 ± 0.120
k_1	9.061 ± 0.001	0.954 ± 0.028
k_2	-0.043 ± 0.001	-0.013 ± 0.002

Figure 6.13 shows the global gaussian fit to the NHIT distributions with μ and σ as a function of NHIT. The residuals from the 3-parameter fit to the discrete transformation are shown for completeness. All detector related effects such as the position dependent resolution of the detector and the broadening of the NHIT distributions due to the detector response are included in the Monte Carlo simulation. The uncertainty on the above given NHIT function is the total error. It is derived from the fit to the discrete $NHIT \rightarrow E$ transformation.

6.4.5 Linearity of Energy Scale

This procedure produces an energy scale which is non-linear in NHIT. The deviation of this energy scale from a linear scale can be estimated from the quadratic term in the fit function. For example, at a Monte Carlo electron energy of 10 MeV the contribution of the quadratic term to the fitted μ_{NHIT} is 0.4% and to σ_{NHIT} is 0.01%.

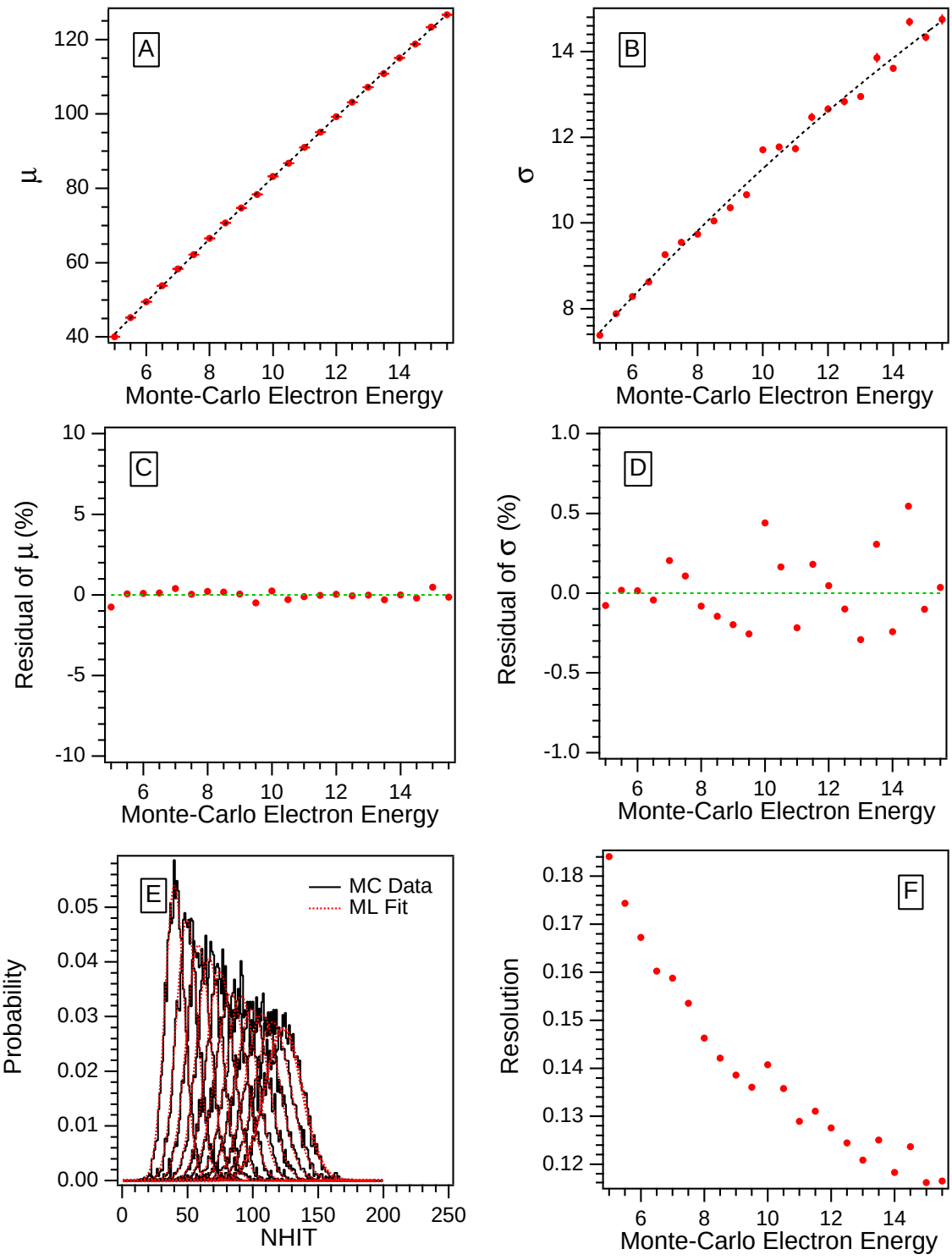

Figure 6.13: Characteristics of the NHIT→E transformation function. The plots of σ and the centroids contain error bars which are too small to be seen.

6.4.6 Resolution as a Function of Energy

The spread of the Monte Carlo NHIT distributions changes with NHIT. The intrinsic width of a NHIT distribution is the sum of the statistical width, $\sqrt{NHIT}$, and the spread due to the detector response.

$$\sigma_{tot}(E) = \sigma_{NHIT}(E) + \sigma_{detector}(E) \tag{6.11}$$

The parameter σ_{tot} is determined from fitting a Gaussian to the simulated Monte Carlo NHIT distribution.

6.4.7 Resolution as a Function of Radius

Simulating a point source of monoenergetic electrons at different radii we can study the change in resolution as a function of radius. Figure 6.16 shows that for 5 MeV electrons the resolution varies by 5% without showing a clear trend as a function of radius. The variation in resolution improves significantly with statistics of the underlying Monte Carlo electron spectra. However, μ and σ change systematically with radius. Their values as a function of radius can be described by a 4-term polynomial of the following form. In this particular case, the polynomial is not as much a fit as a guide to the eye.

$$\mu_{NHIT}[R|n] = n_0 + n_1 R + n_2 R^2 + n_3 R^3 \tag{6.12}$$

$$\sigma_{NHIT}[R|n] = n_0 + n_1 R + n_2 R^2 + n_3 R^3 \tag{6.13}$$

6.4.8 Volume-Averaged Detector Response

For every neutrino event the detector response is different. The response of the SNO detector varies with event position and energy and a number of other parameters, such as the event direction. The charged-current NHIT spectrum obtained from the decomposition analysis is a convolution of the charged-current electron energy spectrum and the detector response over the period of data taking. The $NHIT \rightarrow E$ transformation derived above is based on

Table 6.7: Variation of the $NHIT \rightarrow E$ transformation function with radius.

	μ_{NHIT}	σ_{NHIT}
n_0	44.01 ± 0.01	7.70 ± 0.02
n_1	$-0.05 \pm 3.33 \times 10^{-6}$	$-3.87 \pm 0.38 \times 10^{-3}$
n_2	$0.00 \pm 1.54 \times 10^{-8}$	$1.48 \pm 0.17 \times 10^{-5}$
n_3	$-2.34 \pm 0.01 \times 10^{-7}$	$1.71 \pm 0.20 \times 10^{-8}$

a volume-averaged detector response. To estimate the broadening of the NHIT distribution of monoenergetic electrons we can compare the detector's NHIT response for point sources of monoenergetic electrons at different positions in the detector. Figure 6.14 shows the NHIT distributions for 5 MeV electrons generated at (0/0/0), (500/0/0), and uniformly distributed in the detector. The resolution of 5 MeV electrons varies by about 5% over the entire range of the detector. The resolution of uniformly distributed electrons corresponds to the volume-weighted average of the resolution in the different regions of the detector.

6.4.9 Summary: $NHIT \rightarrow E$ Scale Transformation

The detector's NHIT response to monoenergetic electrons distributed uniformly in the D_2O with an isotropic direction has been simulated and a technique for assigning a most probable energy scale to a pure spectrum of electron Čerenkov events is developed. Using the best available Monte Carlo input parameters the following $NHIT \rightarrow E$ transformation function was determined. The continuous μ_{NHIT} is the most probable NHIT corresponding to the electron energy E_e.

$$\mu_{NHIT}[E_e] = -3.401 + 9.061 \times E_e - 0.043 \times E_e^2 \tag{6.14}$$

Figure 6.17 shows the energy scale transformation between monoenergetic electrons and NHIT as well as NHIT and the most probable electron energy.

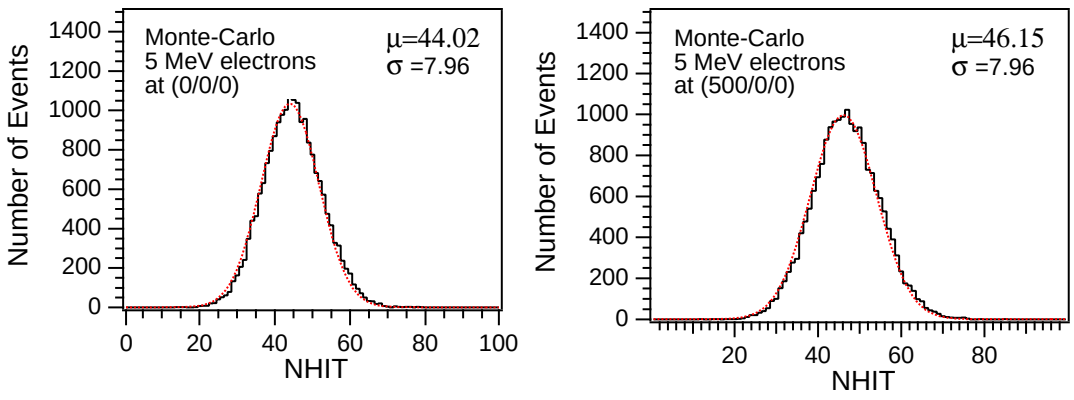

Figure 6.14: Detector response for different event positions.

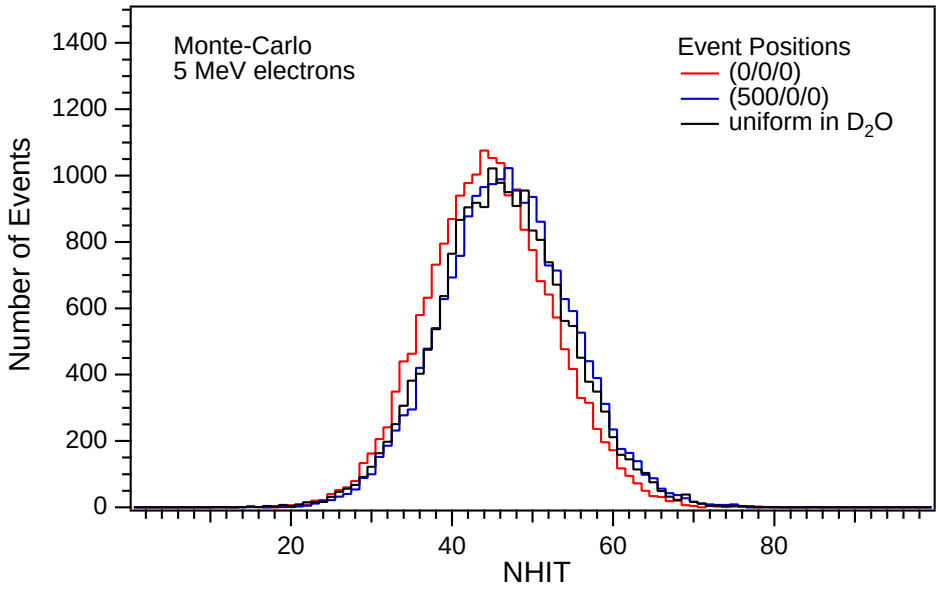

Figure 6.15: Volume-averaged detector response for events uniformly distributed throughout the detector compared to events in the center and near the acrylic vessel.

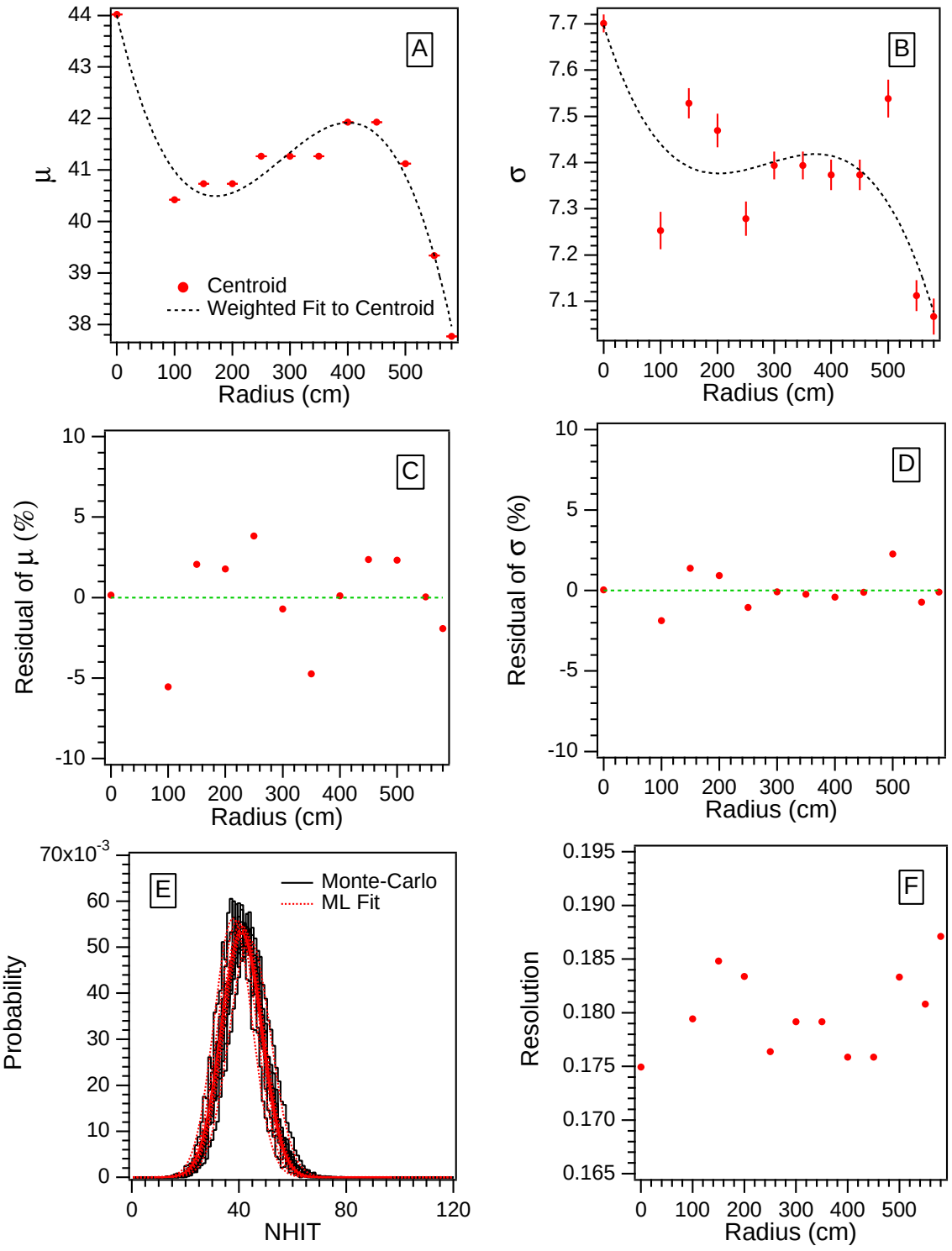

Figure 6.16: Characteristics of the NHIT→E transformation function for different radii. Panel E shows the Monte Carlo NHIT distributions for different radii.

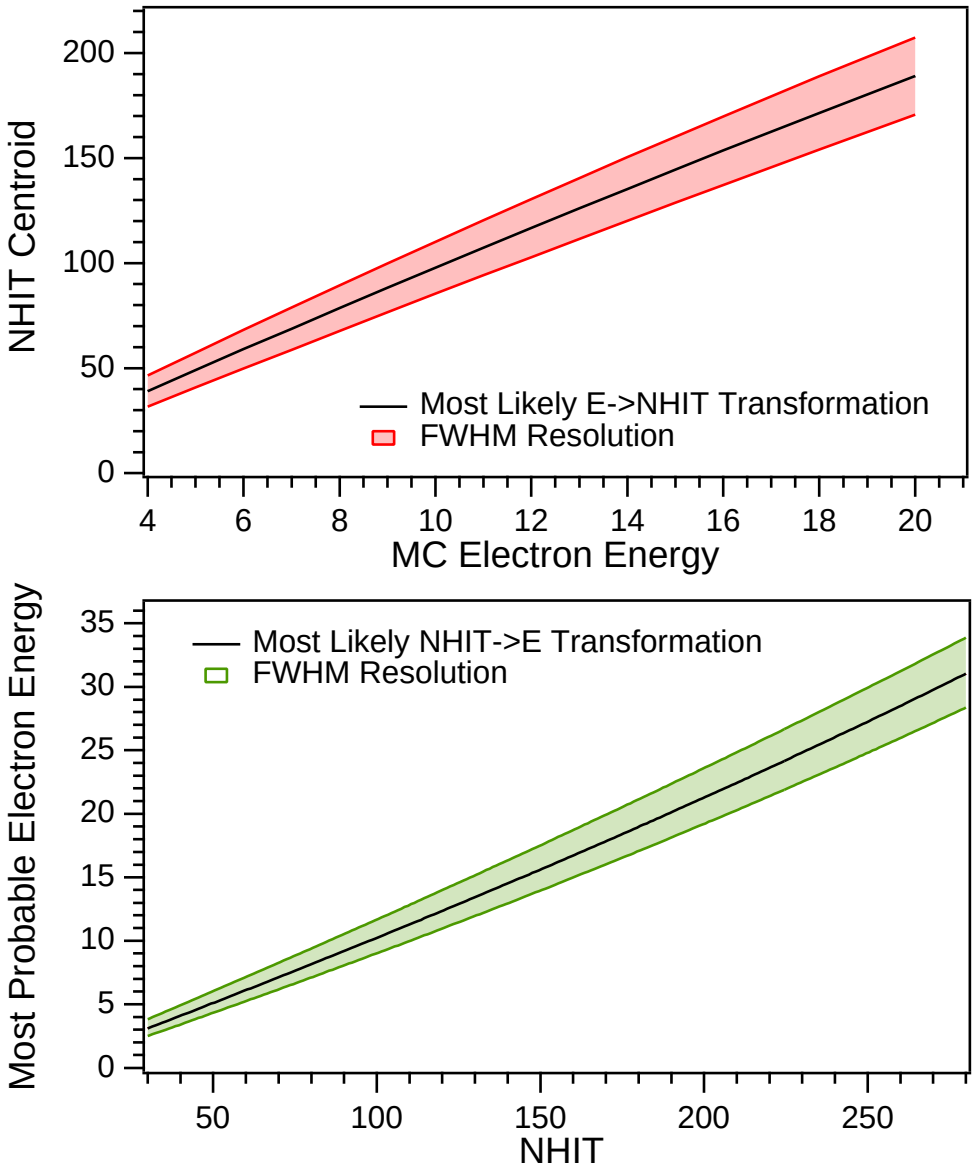

Figure 6.17: NHIT → E transformation function (based on a PMT collection efficiency of 0.59404).

6.5 Calibrations and NHIT → Energy Scale Transformation

The $NHIT \rightarrow E$ scale transformation is based on Monte Carlo simulations of the detector response to monoenergetic electrons. The PMT collection efficiency in the Monte Carlo is scaled to agree with the optical calibrations of the detector and the ^{16}N calibrations. No other calibration data are input to the Monte Carlo.

Figure 6.18 shows the calculated $NHIT \rightarrow E$ transformation function as well as the ^{16}N and pT calibration points. For comparison, the energy calibration of the ^{8}B spectrum analysis (Chapter 8) is shown. In general, there is reasonable agreement between the $NHIT \rightarrow E$ function and the various calibration points.

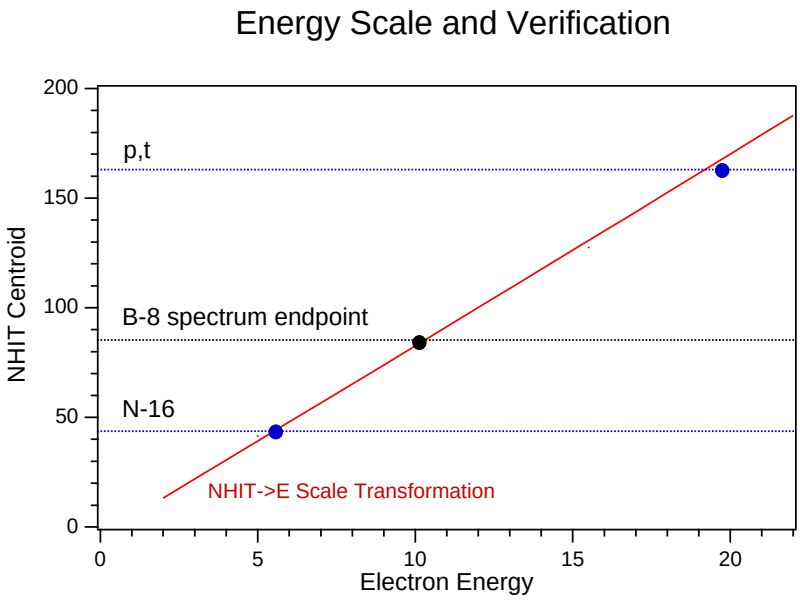

Figure 6.18: Comparison of the derived $NHIT \rightarrow E$ transformation function with calibration data from ^{16}N and the pT source.

CHAPTER 7

SIMULATION OF NEUTRINO SIGNALS AND BACKGROUNDS: GENERATION OF PROBABILITY DISTRIBUTION FUNCTIONS

Monte Carlo simulations of neutrino signals and background interactions are a critical part of the SNO solar neutrino analysis. Results from simulations are used as an input to all techniques that identify neutrino interactions in SNO. Monte Carlo techniques allow us to generate probability distribution functions (PDF) of the characteristic event distributions that are used in the decomposition of the data set and the extraction of the neutrino signal. These include among others the radial distribution of events in the detector, the angular distribution with respect to the Sun, and the energy spectrum. Therefore, it is important to review and characterize the main inputs to the Monte Carlo simulations. Standard solar model neutrino flux predictions, modern theoretical evaluations of the neutrino deuteron cross-sections, and detailed simulations of particle interactions and propagation in water are used to understand events occurring in the SNO detector.

The main inputs to the generation of probability distribution functions for the solar neutrino signal are:

• Solar Neutrino Flux Predictions: With input from the latest standard solar model calculations the flux of solar ^{8}B and *hep* neutrinos at the SNO detector is calculated, taking into account the Earth eccentricity variations. While the solar model predictions for the flux and energy spectrum are an input to our Monte Carlo simulations they are not used in our measurement of the ν_e flux or the total flux of active ^{8}B neutrinos. As we will show in the following chapters, the measurement of the CC interaction rate can be performed without assumptions on the shape of the ^{8}B energy spectrum. The ν_e flux is simply determined from the number of interactions with the heavy water target and an evaluation of the theoretical neutrino cross-sections. Hence, the analysis presented in this thesis is independent of solar models and from predictions of the energy spectrum of neutrinos produced in the β-decay

of ^{8}B $\rightarrow^8$ Be* + e^+ + ν_e . With this analysis we provide the first solar model-independent measurement of the CC interaction rate and a verification of the flux predictions of Standard Solar Models.

• Target Systematics: Critical to our measurement of neutrino interaction rates are, however, the systematics of the D_2O target and the neutrino cross-sections. An almost spherical volume of a 1000 t of heavy water contained in an acrylic vessel and surrounded by several thousand tonnes of light water is the neutrino target of the Sudbury Neutrino Detector. The measurement of the solar neutrino flux scales directly with the number of target atoms. The geometry and orientation of the SNO detector are also critical inputs to the analysis as they can affect the reconstruction of the event direction and the angular distribution of neutrino events with respect to the Sun.

• Neutrino Cross-Sections: While the measurement of the total ^{8}B flux can be performed independent of solar models and without assumptions on the underlying neutrino energy spectrum it does depend, however, on the theoretical neutrino cross-sections. The theoretical situation of neutrino-deuteron and neutrino-electron cross-section is reviewed and the uncertainties evaluated.

For the simulation of backgrounds and neutrino events the propagation of particles following the initial interaction is critical. The SNO Monte Carlo simulations allow detailed tracking of Čerenkov electrons, neutrons, and gammas and provide tools to evaluate the PMT signature of backgrounds and neutrinos. The generation of the signal and background probability distribution functions is done using the best available Monte Carlo input parameters and the most accurate representation of the detector run conditions as a function of time.

• Run-by-Run Simulation of Signals and Backgrounds: For every selected run neutrino interactions and backgrounds are simulated using the exact start and stop times as well as the dates of the run. The detector configuration used in the Monte Carlo simulations is read in from DQXX detector database files which were recorded during data taking. Run-specific parameters recorded during data taking and used in the Monte Carlo simulations include the PMT noise rate, PMT collection efficiency, and the number of working channels.

7.1 SNO Monte Carlo and Analysis Software: SNOMAN

The response of the SNO detector to Čerenkov electrons or γ's from neutrino interactions or radioactive backgrounds is simulated using SNOMAN, the SNO Monte Carlo Analyzer. This code allows detailed Monte Carlo simulations as well as processing of the data. The details of SNOMAN are described in [28] and references therein. In this analysis SNOMAN is used to generate probability distribution function of the characteristic distributions of solar neutrino interactions. These include the energy response of the detector in NHIT, the radial distribution of events, and the solar angle distribution. Information from the various calibration sources is used to optimize the Monte Carlo and its predictions. As with any simulation, SNOMAN is not perfect. Any remaining difference between SNOMAN and the calibration data is treated as a systematic error and propagated through the analysis. SNOMAN simulations also take into account the time-dependent variations of the detector response as measured with calibration sources. Specifically, the 2% change in energy scale over the period of data taking is simulated in all neutrino and background Monte Carlo simulations. For every run taken at SNO we simulate the neutrino signals and backgrounds at the same time and date but with sufficient statistics for a meaningful comparison.

All SNOMAN simulations described in this work were done using SNOMAN version 4_0186, the optics "titles" (that describe the optical properties of the detector) from March 16, 2001, and the time-dependent energy or NHIT scaling derived in Chapter 6.

7.1.1 Particle Propagation

As a water Čerenkov detector SNO depends critically on the distribution of Čerenkov photons with respect to the direction of Čerenkov electrons produced in the charged-current reaction or in elastic scattering. Electrons undergo multiple Coulomb scattering as they propagate. Correct modelling of the propagation of electrons and gammas is critical to the successful simulation of the detector response. In SNOMAN the propagation of electrons and gammas in SNOMAN is handled by EGS4, an electron gamma shower code [149] [1].

[1]The EGS computer code system is a general purpose package for the Monte Carlo simulation of the coupled transport of electrons and photons in an arbitrary geometry for particles with energies from a few

This code includes effects of Compton scattering, photoelectric conversion, pair production, positron annihilation, and bremsstrahlung radiation. ESG4 generates individual tracks in segments. The Čerenkov radiation from each segment of the scattered electron path is determined from the asymptotic formula for light yield [136]. The number of photons emitted is then sampled from a Poisson distribution and the creation points of these photons are positioned randomly along the segment. All photons are emitted at an angle θ_c to the electron track direction. For a straight section of an electron track the light yield, I, is described by Equation 7.1. I is proportional to the path length, L.

$$\frac{dI}{d\omega} = \frac{\omega e^2 L \sin^2 \theta_c}{c^2} \tag{7.1}$$

Besides the propagation of Čerenkov photons, neutron transport is an important component of the SNO Monte Carlo simulations. The neutral-current interaction of solar neutrinos dissociates deuterium and liberates a neutron. Neutrons can also be produced in the SNO detector through the photodisintegration of deuterium by gammas with an energy of 2.2 MeV or higher. Some neutrons enter the D_2O from the external regions of the detector. Free neutrons in the SNO detector thermalize quickly before they capture on deuterium or hydrogen. The capture ^{2}H(n,γ)^{3}H reaction produces γ's with an energy of 6.25 MeV. Neutron transport code is required to calculate the neutron's mean free path in the media of the SNO detector and to choose and resolve any interactions that might occur. The MCNP neutron transport code [58] [2], originally developed at Los Alamos National Laboratory, is used in SNOMAN. The SNO Monte Carlo code only transports photons (gammas), electrons, positrons, muons and neutrons. Any other particles generated by a neutron interaction, such as α's, are not transported.

---

keV up to several TeV. For further information see http://www.slac.stanford.edu/egs/.

[2]MCNP is a general-purpose Monte Carlo N-Particle code that can be used for neutron, photon, electron, or coupled neutron/photon/electron transport. It includes the capability to calculate eigenvalues for critical systems. For further information see http://laws.lanl.gov/x5/MCNP/index.html.

7.1.2 Optical Parameters

The optical calibration of the SNO detector is critical in understanding the transport, propagation, and detection of Čerenkov photons and light from radioactive backgrounds in the detector. They affect the modeling of the detector response and the Čerenkov signal we observe in SNO. In an analysis in which one fits data using Monte Carlo generated probability distribution functions (PDF's), the uncertainty in the optics leads to uncertainties in the energy scale and resolution as well as the fiducial-volume acceptance through reconstruction.

The optical constants used in this analysis were derived in [146] on March 16, 2001. The measurement of the optical properties was done using data from the laserball source at several different wavelengths and positions inside the detector. The optical parameters are obtained from a global fit to the laserball data at wavelengths of 337, 365, 386, 420, 500, and 620 nm. The optical analysis was performed with the "grey disk" PMT model in SNOMAN. The "grey disk" model uses an average angular and wavelength response combined with simulation of reflections. Simulations of the predicted event distributions in the detector based on this model and set of constants show good agreement with Monte Carlo simulations that use a more complete and complex PMT geometry. The exact distribution of the timing residuals, however, is not modelled very well. As the total number of PMT hits, NHIT, is used as the event energy estimator the disagreement in the simulated late-light distribution is not a concern in this analysis.

The optical constants are verified against ^{16}N and ^{8}Li in the inner volume of the detector. In our evaluation of the energy scale and reconstruction we take the difference between calibration data and the Monte Carlo simulations as an estimate of the systematic error. This takes into account possible variations and uncertainties in the optical parameters.

7.1.3 Generation and Propagation of Solar Neutrinos

Using input from solar models, theoretical cross-section calculations, and calibration data, the SNOMAN Monte Carlo can be used to calculate the predicted spectrum and number of solar neutrino interactions. Standard solar models describe the nuclear fusion of light nuclei and hydrodynamical processes in the Sun and make predictions for the flux and spectra of

Table 7.1: Solar neutrino flux predictions of standard solar model calculations in units of $cm^{-2}s^{-2}$ as given by Bahcall et al. Alternative calculations by Turck-Chièze et al. [18] yield similar results. The fractional uncertainty on the flux predictions is given.

	BTCM98	BPB98	BPB00
pp	5.98×10^{10}	5.94×10^{10}	5.96×10^{10} $(1.00^{+0.01}_{-0.01})$
pep	1.41×10^{8}	1.39×10^{8}	1.40×10^{8} $(1.00^{+0.015}_{-0.015})$
hep		2.10×10^{3}	9.30×10^{3}
^{7}Be	4.70×10^{9}	4.80×10^{9}	4.82×10^{9} $(1.00^{+0.10}_{-0.10})$
^{8}B	4.82×10^{6}	5.15×10^{6}	5.05×10^{6} $(1.00^{+0.20}_{-0.16})$
^{13}N	4.66×10^{8}	6.05×10^{8}	5.56×10^{8} $(1.00^{+0.21}_{-0.17})$
^{15}O	3.97×10^{8}	5.32×10^{8}	4.88×10^{8} $(1.00^{+0.25}_{-0.19})$
^{17}F		6.33×10^{3}	5.73×10^{3} $(1.00^{+0.25}_{-0.25})$

solar neutrinos. These models predict that more than 98% of the solar energy is generated by a series of nuclear reactions that fuse 4 protons into helium, generally called the p-p chain. The neutrino spectrum predicted by standard solar models is shown in Figure 7.1.

The Standard Solar Model parameters used in SNOMAN are based on the BPB00 model [11]. This particular model is the latest published version of solar model calculations prepared by Bahcall et al.. Their predictions are in good agreement with the standard solar model calculations performed by Turck-Chièze et al. [18, 19, 75].

The absolute flux values for the different neutrino-generating processes are listed in Table 7.1. With an energy threshold of 1.44 MeV from the charged-current and 2.22 MeV from the neutral-current interactions, SNO is mainly sensitive to ^{8}B and *hep* neutrinos. Standard solar models have been revised on a regular basis. The *hep* flux predicted in BPB00 is much higher than previous calculations due to new calculations of the cross-section factor S_0, which is 4.4 times larger than the previous best estimate.

In the Monte Carlo simulations used in this analysis the ^{8}B spectrum measured by Ortiz et al. [49] is chosen as the default. However, as our technique for the determination of

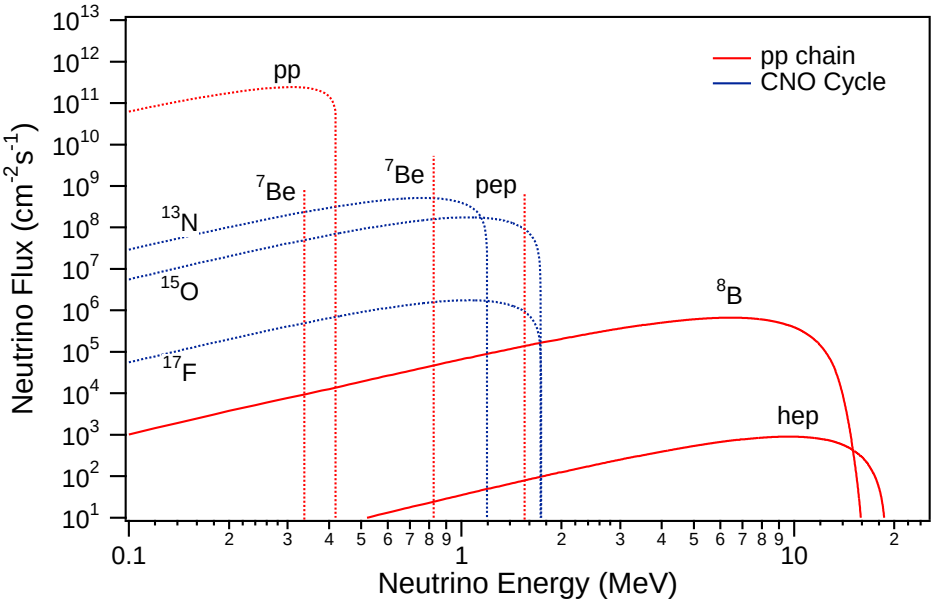

Figure 7.1: Solar neutrino spectrum as predicted by Bahcall et al. [11]. The solid lines indicate the neutrinos that can be detected in SNO. Low-energy neutrinos (dashed lines) are below SNO's energy threshold.

the neutrino interaction rate is independent of the shape of the ^{8}B energy spectrum the uncertainties related to this spectrum do not enter our analysis. As we will show in Chapters 8 and 9, the flux of ν_e solar neutrinos can be determined from the event distributions in the detector without making any assumptions on the shape of the ^{8}B spectrum. For an illustration of the possible systematic uncertainties associated with the ^{8}B spectrum we compare in Figure 7.2 the ^{8}B spectrum from Ortiz et al. to the one provided by Bahcall et al. [9]. It has been shown that all other characteristic distributions of the neutrino signal in the detector, such as the angular distribution with respect to the Sun and the radial distribution in the detector, are independent of the shape of the ^{8}B spectrum. The energy dependence of the characteristic event distributions in the SNO detector is negligible under reasonable assumptions on the possible variations in the ^{8}B spectrum.

The seasonal effects in the solar neutrino flux at SNO due to the Earth's orbital eccentricity are taken into account and modeled in SNOMAN. With an orbital eccentricity of

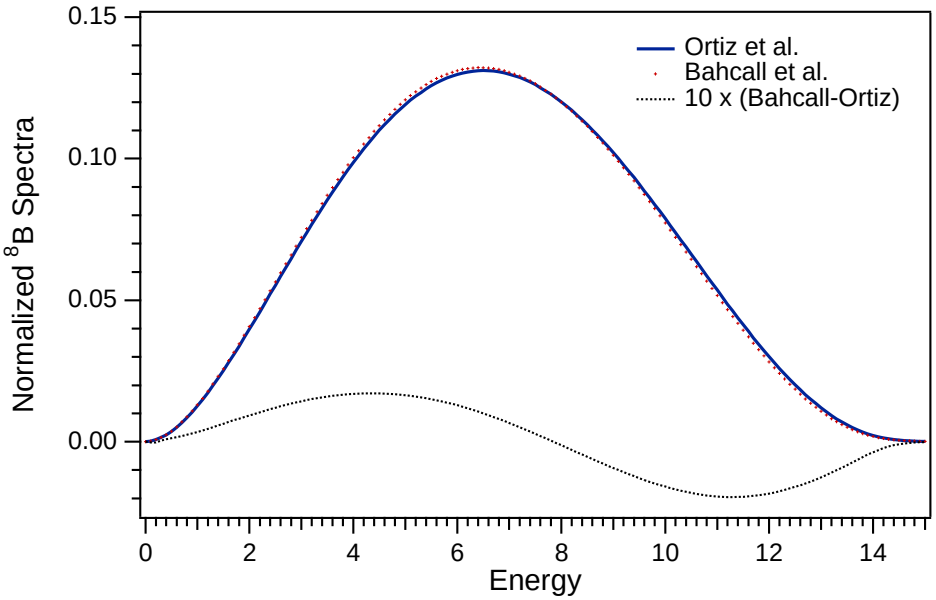

Figure 7.2: Comparison of the ^{8}B spectrum as measured by Ortiz et al. [49] and Bahcall et al. [9].

$\epsilon_{orbit} = 0.0167$ at a distance $a_0 = 1$ AU and a period τ of 365.25 days the flux variations are of the order of 7%. The predicted seasonal variations of the solar neutrino flux at SNO are given in Equation 7.2 and illustrated in Figure 7.3.

$$\phi(t) = \phi_0 \frac{1}{a_0(1 - \epsilon^2_{orbit} cos(2\pi(t - t_0)/\tau)} \tag{7.2}$$

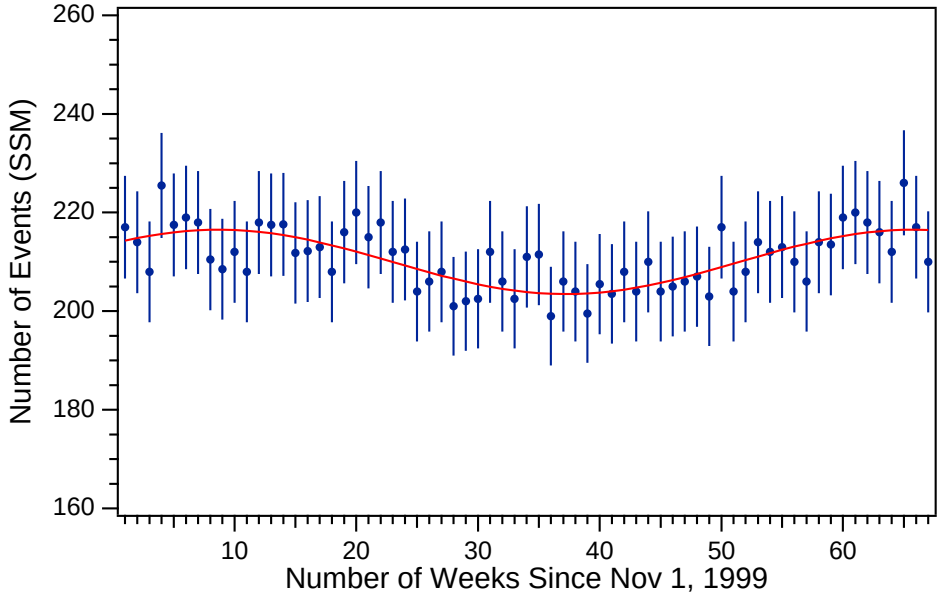

Figure 7.3: Expected seasonal variations of the neutrino interaction rate during the time of data taking at the Sudbury Neutrino Observatory as predicted by SNOMAN Monte Carlo simulations. A fit to the Monte Carlo data illustrates the expected 7% seasonal variation.

7.1.4 Simulation of Backgrounds

Besides the simulation of neutrino interactions the SNO Monte Carlo Code can also be used for the generation and propagation of particles from nuclear decays. The radioactive decay of a number of nuclei including ^{238}U, ^{232}Th, ^{40}K, and ^{56}Co is simulated.

The decay schemes for the $\beta - \gamma$ decays are mostly based on recommendations from the Isotope Project [169] . A minimum kinetic energy threshold is set for the generation of β's and γ's to stop the production of particles that are unlikely to produce Čerenkov light. Only the β-decay mode and not the α-decay mode is modelled for the decays of ^{212}Bi and ^{214}Bi. Calculations of the energy of the positron or electron take into account corrections for screening by simple atomic electrons, the exact Fermi function for a point source nucleus, and shape factors for first, second, and third unique forbidden decays. Decays to broad states, such as ^{8}Li or ^{8}B are approximated using many narrow states with the proper branching ratios.

Neutrons produced in the neutral-current dissociation or photodisintegration of deuterium capture on a variety of nuclei in the detector. The SNOMAN Monte Carlo simulations include the γ's that result from neutron capture on H, D, ^{23}Na, ^{24,25,25}Mg, ^{27}Al, ^{28,29,30}Si, ^{32,34}S, ^{35,37}Cl, ^{39,40,41}K, ^{40,42,44,46,48}Ca, ^{54,56,57,58}Fe, ^{58,60,62}Ni.

7.1.5 Statistics of Probability Distribution Functions

The statistics of the Monte Carlo simulations used in the generation of probability distribution functions for this analysis is 25× SSM BPB00 predictions for ^{8}B neutrinos and 2000× SSM BPB00 for *hep* neutrinos. Charged-current and neutral-current interactions are generated in the D_2O while elastic scattering of neutrinos is simulated in the D_2O, AV, and H_2O.

For the analysis presented in this thesis we have also simulated the principal backgrounds in the SNO detector, that is ^{208}Tl and ^{214}Bi in the D_2O, AV, and H_2O. The specific event rates for the Monte Carlo simulations used in this analysis are summarized in Table 7.2.

Table 7.2: Event rates used in the Monte Carlo simulation of the neutrino signals and principal backgrounds.

Source	Interaction	Medium	Rate
^{8}B	ν_e CC	D_2O	$25 \times$ BPB00
^{8}B	ν_x NC	D_2O	$25 \times$ BPB00
^{8}B	ν_x ES	D_2O	$25 \times$ BPB00
^{8}B	ν_x ES	AV	$25 \times$ BPB00
^{8}B	ν_x ES	H_2O	$25 \times$ BPB00
hep	ν_e CC	D_2O	$2000 \times$ BPB00
hep	ν_x NC	D_2O	$2000 \times$ BPB00
hep	ν_x ES	D_2O	$2000 \times$ BPB00
hep	ν_x ES	AV	$2000 \times$ BPB00
hep	ν_x ES	H_2O	$2000 \times$ BPB00
^{208}Tl	$\beta - \gamma$ decay	D_2O	0.17 s^{-1}
^{208}Tl	$\beta - \gamma$ decay	AV	0.3 s^{-1}
^{208}Tl	$\beta - \gamma$ decay	H_2O	2.0 s^{-1}
^{214}Bi	$\beta - \gamma$ decay	D_2O	0.17 s^{-1}
^{214}Bi	$\beta - \gamma$ decay	AV	0.3 s^{-1}
^{214}Bi	$\beta - \gamma$ decay	H_2O	2.0 s^{-1}

7.1.6 Failed Monte Carlo Events

On rare occasions events generated in the SNO Monte Carlo code fail due to geometry errors or other numerical problems. This reduces the number of observable events in the Monte Carlo simulations with respect to the solar neutrino flux prediction used to generate those events. The result is that the Monte Carlo prediction for the number of charged-current, neutral-current, and elastic scattering interactions is slightly too low. From high-statistics Monte Carlo simulations we determine that 0.067% of all events are affected by this problem. The efficiency of successful event propagation in the Monte Carlo is $\epsilon_{MC} = (1 - \eta_{MC}) = 0.9933$ and the correction factor used to scale the Monte Carlo predictions is $1/\epsilon_{MC}$.

7.2 Neutrino Cross-Sections

SNO deduces the total integrated flux of solar ^{8}B and *hep* neutrinos from the measurement of the NC interaction rate. The charged-current interaction rate ν_e determines the flux of solar electron neutrinos. Theoretical calculations for the neutrino-deuteron cross-section and neutrino-electron scattering are used to calculate the solar neutrino flux from the measured interaction rates. We review and evaluate the model-dependent variations in the theoretical cross-section calculations and describe our choice of theoretical cross-section.

7.2.1 Charged-Current and Neutral-Current Neutrino Deuteron Cross-Sections

While the ν-e scattering cross-section is readily available from the standard model, estimation of the neutrino-deuteron reaction cross-section requires a detailed structure of two-nucleon systems and their responses to electroweak probes. A number of authors have studied extensively the neutrino-deuterium cross-sections over the past decades. A successful method for describing these responses is to consider one-body impulse approximation terms and two-body exchange current terms acting on non-relativistic nuclear wave functions, with the exchange current derived from a one-boson exchange model.

For the neutrino-deuterium reaction, the first impulse approximation including estimates of all the forbidden terms was done by Ying, Henley and Haxton (YHH) [185]. The latest status of the phenomenological Lagrangian approach which includes the exchange-current effects as well as the impulse approximations terms is described in work by Kubodera and Nozawa (KN) [133]. The KN cross-sections are slightly larger than those of YHH. This difference is mostly due to the absence of the exchange current contributions in YHH. In the analysis of reactor neutrino experiments it was found that the KN calculations agree with the cross-sections measured in the processes $\overline{\nu}_e + d \rightarrow e^+ + n + n$ and $\overline{\nu}_e + d \rightarrow \overline{\nu}_e + p + n$ within the experimental errors of the reactor experiments.

Using a new approach based on effective field theory (EFT), Butler, Chen, and Kong (BCK) [20, 21] have studied the ν-d cross sections for solar neutrino energies. In this approach, one starts with a general effective Lagrangian that contains all possible terms compatible with given symmetries and a given order of expansion. The low-energy coeffi-

cients in the effective Lagrangian cannot be fixed by the symmetry requirements alone and hence need to be treated as parameters to be determined empirically. In [20, 21] the coefficient $L_{1,A}$ of a four-nucleon axial-current counter term enters as an unknown parameter and can be adjusted appropriately such that the KN and YHH calculations agree with the EFT calculation. The optimal value is $L_{1,A} = 6.3$ fm^3 for YHH and $L_{1,A} = 1.0$ fm^3 for KN. The current value used in the SNOMAN Monte Carlo code is $L_{1,A} = 5.6$ fm^3.

The problem associated with the EFT calculation is that $\mathrm{L}_{1,A}$ is an unknown parameter in the EFT Lagrangian and cannot be predicted. It will have to be determined from experiment. However, $L_{1,A}$ cannot be arbitrary and the perturbation is only valid for certain values of $L_{1,A} \sim 5$ fm^3. One can only claim that the EFT calculation is accurate to 3% if $L_{1,A} \sim 5 \pm 1.5$ fm^3. If $L_{1,A}$ were experimentally found to be 10 or 0.1 fm^3 the calculation would be invalid.

A recent calculation by S. Nakamura et al. (NSGK) [147] within the framework of the phenomenological Lagrangian approach complements the EFT calculation in that it does not contain unknown parameters such as $L_{1,A}$. The model and parameters used in this calculation have been tested using many observables. The main improvements over the existing work by YHH and KN are the use of modern nucleon-nucleon (NN) potentials, the use of more accurate nucleon weak-interaction form factors, and the use of the vertex strength that governs the Δ-excitation axial vector exchange derived from the capture reaction, $n + p \rightarrow d + \gamma$. It is found that both approaches agree well for low-energy ν-d cross-sections within a reasonable range for $L_{1,A}$ in the EFT theory, and therefore both cross-section calculations are applicable to solar neutrinos.

In detail, the differences of the NSGK calculation from the previous calculations are as follows: The total ν-d cross-sections are stable within 1% against any changes in the input except for somewhat higher sensitivity to the strength of the axial-vector current. Depending on the normalization of the Δ-excitation axial-current the total cross-section is reduced by ~2-5%. Based on these considerations Nakamura et al. recommend a one-sided uncertainty of -5% which essentially represents the difference between the cross-sections given in YHH and KN. They show [147] that in the ratio of the neutral-current to charged-current cross-section σ_{NC}/σ_{CC} the model dependence is reduced down to 1%.

Exchange currents enhance the Gamow-Teller (GT) transitions. Using the NSGK-YHH differences as a measure of an error may be too conservative. The exchange current Gamow-Teller corrections are uncertain because they are dominated by nucleon resonance diagrams, and the weak N-resonance and strong N-resonance couplings are not well known.

As a final note on the potential model calculations, these calculations agree with each other within 6% but they might still be far off the real numbers due to inherent systematics in the models [164]. Potential model calculations can be extended to A=3 systems, where the known β-decay then can be used to fix the exchange current couplings. The only problem is whether three body terms arise in A=3. Alternatively, $L_{1,A}$ can be measured in muon capture experiments. For a more detailed discussion of current experimental limits on $L_{1,A}$ see Chapter 9.

The size of the model-dependent variation in the different cross-section calculations can be estimated by comparing the best calculations to date. The two calculations by KN [133] and YHH [185] differ by 6% over the range of solar neutrino energies. In the past, people have taken the 6% as an estimate of the uncertainty or the 1σ theoretical error [8]. Using the scaling argument suggested by the Particle Data Group [53] one can derive a value of 3% for the uncertainty on the absolute CC and NC cross-sections. In the ratio of $[CC]\,/\,[NC]$ this uncertainty reduces to 1%.

7.2.2 Neutrino-Electron Elastic Scattering Cross-Section

In contrast to the CC and NC deuteron break-up reactions, ν-e scattering is a Standard Model process and well known. Because of the interest in high-precision solar neutrino measurements the cross-section for ν_e scattering has been recalculated and many higher-order corrections, such as radiative and QED corrections, to the Standard Model process are now being considered. The QED corrections to the scattering process $\nu + e \rightarrow \nu + e$ were studied long ago, but Bahcall et al. performed a detailed investigation of the radiative corrections to the electron recoil spectra and the total cross-sections resulting from scattering with solar neutrinos [7].

On dimensional grounds it is expected that the radiative corrections are of the same

order of magnitude as the fine-structure constant, $\mathcal{O}(\alpha) \sim 1\%$. It is particularly important to know if radiative corrections cause an appreciable energy-dependent modification of the electron recoil spectrum as different MSW solutions predict characteristic modifications to the shape of the electron recoil spectrum. In the discussion of radiative corrections by Bahcall, Kamionkowski, and Sirlin (BKS) [7] one-loop electroweak and QED corrections are included. They conclude that radiative corrections decrease the dominant ν-e scattering cross-sections by about 2%. The shape of the recoil energy spectrum produced by the scattering of ^{8}B solar neutrinos is decreased by about 4% at the highest electron energies. For pp and ^{7}Be neutrinos, the recoil spectra are not affected significantly. In the interpretation of experimental results, an additional correction comes from the effect that the photons produced by the radiative corrections are more strongly peaked in the forward direction than are the Čerenkov photons. This particular effect is not yet taken into account in the SNOMAN Monte Carlo simulations.

The $\mathcal{O}(\alpha)$ QED corrections to the electron recoil spectrum in the process $\nu_l + e \rightarrow \nu_l + e$ and the differential cross-sections have been calculated and evaluated recently by M. Passera [156, 157] (and references therein). In the analysis of neutrino scattering experiments it is necessary to distinguish between these two corrections as it depends on the design of the experiment whether the energy of the recoil electron and a possible accompanying photon can be determined separately or not. In a water Čerenkov detector, the electron and photon may produce indistinguishable signals and the total observed energy may not be the simple sum of E and ω, where ω is the energy of the possible accompanying photon. SNO measures solar neutrinos with energies varying from 3 to 18 MeV. In their analysis M. Passera et al. show that for $\nu = 10$ MeV the QED corrections to the differential cross-sections of both the electron and the possible photon are of the order of $\mathcal{O}(1\%)$. These corrections provide also good approximations of the complete $\mathcal{O}(\alpha)$ QED corrections to the electron spectrum. However, because of the different detection (in)efficiencies for electrons and γ's in water Čerenkov detector a more complicated analysis or Monte Carlo simulation using the double-differential cross-sections may be necessary. For now we assume a 1% error on both the total ES cross-sections as well as the differential ones.

For the neutrino-electron elastic scattering the cross section is decreased by 2% by ra-

diative corrections [7]. This introduces a correction factor of 1.02 into the calculation of the ν flux deduced from the ES interaction rate.

7.2.3 Implementation of Neutrino Cross-Sections in SNOMAN

In our simulations of the neutrino signals in SNO the total and differential neutrino-deuteron cross-section calculated by Butler, Chen, and Kong (BCK) are chosen as the default and compared with the NSGK cross-sections. The BCK calculations are used to simulate the spectra, angular distributions, and final state distributions of the neutrino interactions. They depend on the coupling constant of the axial two-body current, $L_{1,A}$. It fixes the exchange-current counterterm. In SNOMAN $L_{1,A}$ is set to be 5.6 fm^3 so that the BCK cross-sections best model the NSGK cross-sections.

The SNOMAN code uses the total cross-sections to calculate the daily rates of each interaction while the differential cross-sections are used when the Monte Carlo is run to predict the energy and direction of the electron in charged-current reactions and elastic scattering, and the neutron in neutral-current interactions. The total cross-sections for the charged-current and neutral-current interactions are taken from tables provided by theoretical calculations. The cross-sections are calculated analytically at discrete energy values that are relevant for SNO. SNOMAN subsequently interpolates through the tables to estimate the cross-sections for individual neutrino energies.

From SNOMAN calculations we determine that the BCK and NSGK cross-sections agree to 0.5-1%. The neutral-current cross-sections show agreement at the 1% level. Figure 7.4 shows the charged-current and neutral-current total cross-sections as a function of neutrino energy E_ν. A comparison of the CC event rates as predicted in SNOMAN for different cross-section models is shown in Table 7.3. The different values of g_A used in the BCK and NSGK calculations are listed in the same table. It is necessary to account for these model-dependent differences when calculating the solar ν_e and ν_x flux from the measured CC and NC interaction rates. From here on, all interaction rates will be based on the BCK model with $L_{1,A} = 5.6$ fm^3 and normalized to the g_A value of 1.267 as recommended by the PDG [53]. The additional correction to the Monte Carlo prediction is $(1.267/1.26)^2$. The

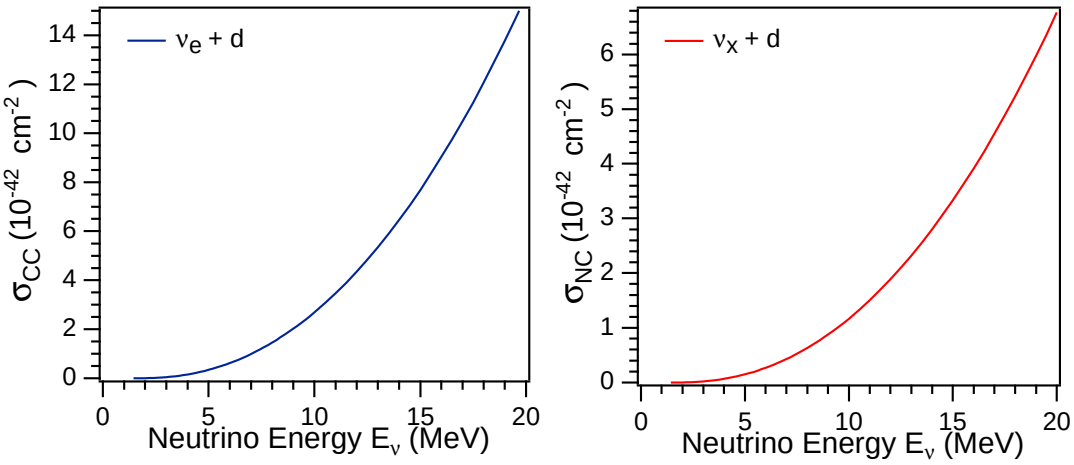

Figure 7.4: Charged-current and neutral-current neutrino-deuteron cross-section calculated by NSGK as a function of neutrino energy, E_ν.

effect is a cross section larger by a factor 1.0111(55).

As a verification of the cross-section implementation in SNOMAN, the yield of charged-current events in SNO has been compared for different neutrino-deuteron cross-sections. Figure 7.5 shows the charged-current interaction rate in BCK per year for the BPB00 standard solar model predictions [11]. At $L_{1,A} = 5.6$ fm^3 there is good agreement between the CC rate calculated by BCK and NSGK. The remaining differences might be due to the values used for g_A. Figure 7.6 shows the recoil electron spectrum from charged-current events generated with the BCK and NSGK model-calculation.

As SNO has the capability to reconstruct both the event vertex as well as the event direction it is important to consider the angular distribution of the final states. The angular distribution of Čerenkov electrons can be used in the identification and characterization of the both the elastic scattering and the charged-current interaction. In case of the charged-current interaction the recoil electron is characterized by a backward angular asymmetry due to the Gamow-Teller matrix element. Naively, one expects the angular distribution to be of the form $F[\cos(\theta)] \propto 1 + \alpha\cos(\theta)$ where $\alpha = -0.341$. The d-wave admixture makes it not pure Gamow-Teller and deviations from $\alpha = -0.341$ are to be expected. Additional

Table 7.3: Charged-current yield above NHIT ≥ 30 for different cross-section models.

Model	R^{CC}/R^{CC}_{BCK} Ratio	g_A	Ref.
NSGK	1.0057	1.254	[147]
BCK, $L_{1,A} = 5.6$	1	1.26	[21]
KN	1.0071		[133]
YHH	0.9605		[185]
Particle Data Group		1.2670(35)	[53]

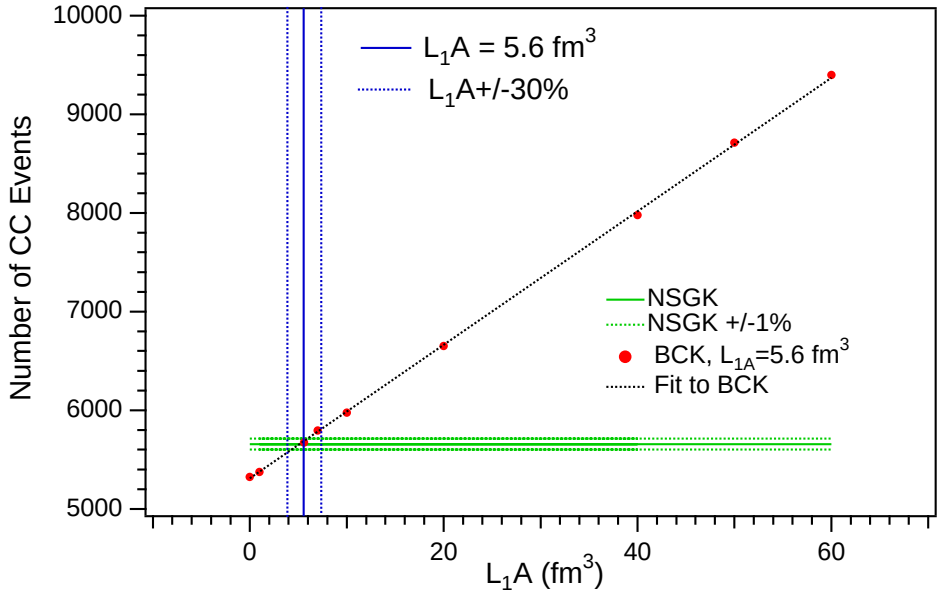

Figure 7.5: Charged-current interaction rate in BCK as a function of $L_{1,A}$ compared to the NSGK calculation.

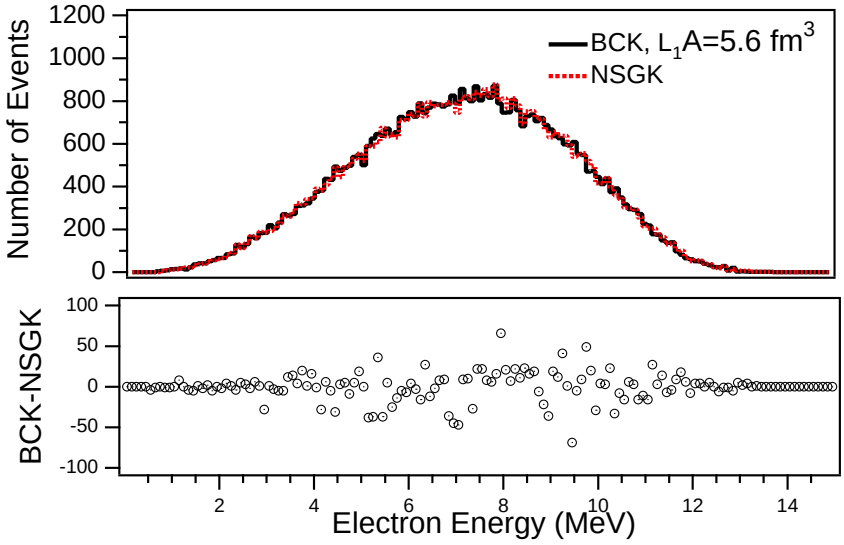

Figure 7.6: Electron recoil energy spectrum of charged-current events generated in SNOMAN with BCK and NSGK cross-sections.

corrections include weak magnetism and recoil corrections. The implementation of the angular distributions in SNOMAN has been verified.

From the BCK implementation in SNOMAN we obtain $\alpha_{BCK} = -0.341$. This is to be compared to $\alpha_{KN} = -0.357$ from Kubodera et al. and - 0.340 from Beacom et al. The agreement between the different calculations is fairly good. Recoil corrections make the angular distribution more forward for both the ν_e and $\overline{\nu}_e$ channels. Weak magnetism has a sign difference for ν_e and $\overline{\nu}_e$. Recoil and weak magnetism nearly cancel for ν_e, but add for $\overline{\nu}_e$.

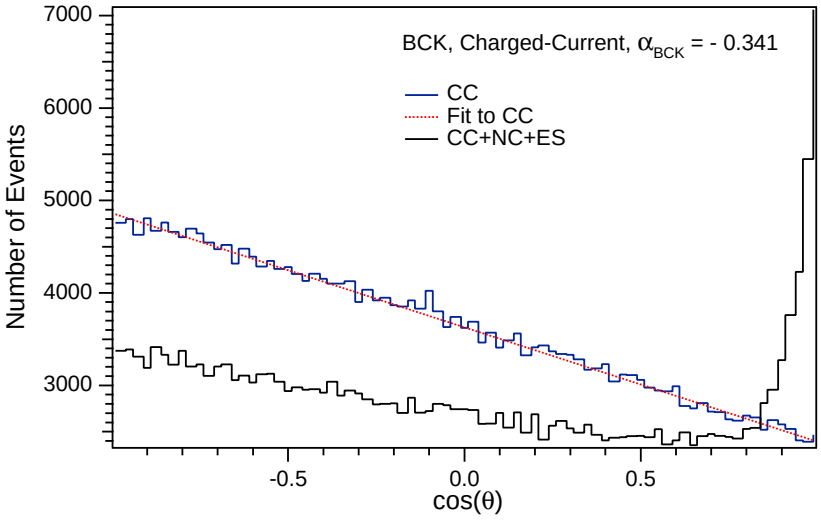

Figure 7.7: Angular distribution of Čerenkov electrons from CC events as calculated by the BCK implementation in SNOMAN. For comparison, we show with a different overall normalization the combined angular distribution of all neutrino signals.

New calculations indicate [74, 134] that radiative corrections and other improvements change the neutrino-deuteron cross-section by as much as 2-3%. Kurylov, Ramsey-Musolf, and Vogel (KMV) calculated the radiative corrections to the NC cross-section to be about 1.5%. In their calculation it is assumed that the Brehmsstrahlung is detected with an electron-equivalent energy 1 MeV smaller than the γ energy. This approximates the situation in SNO very closely. A simulation of the KMV radiative process has been included in SNOMAN and the estimated net effect is an increase of 2% in the cross-section. Radiation from real photons is negligible in the NC case. A new potential model calculation by Nakamura et al. (NSA) [74] finds a neutral-current cross-section that is $\sim 1\%$ higher than NSGK, including some radiative corrections and an updated value of g_A.

It has been recommended to normalize the previous cross-section calculations to the NSA calculation. A summary of all correction factors to the SNO Monte Carlo simulations as they apply to the cross-section calculation has been compiled in [162] and is shown Table 7.4.

In SNOMAN the elastic scattering cross-section is calculated using the same method as Bahcall et al.. Radiative corrections are not taken into account. This is about a 2% effect on the elastic scattering cross-sections. In addition, $\sin^2\theta_W$ of the weak mixing angle in the elastic scattering code is 0.2325 whereas the newest number from the Particle Data Group is 0.23117(16). In the electroweak formalism, the cross-section depends quite sensitively on $\sin^2\theta_W$. A 1% increase in $\sin^2\theta_W(M_Z)$ decrease the ν_e cross-section by 2.7% and increases the $\nu_{\mu,\tau}$ cross-section by 1.8%.

A summary of the model-dependencies of the cross-section calculations as discussed above is given in Table 7.5.

7.2.4 Ratio of the ν_e and $\nu_{\mu,\tau}$ Elastic Scattering Cross-Section

The different interaction potential in ν_e and $\nu_{\mu,\tau}$ scattering yields a different total cross-section for the neutrino-electron scattering of ν_e and $\nu_{\mu,\tau}$. The measurement of the elastic scattering rate of solar neutrinos is a combined measurement of the ν_e and $\nu_{\mu,\tau}$ component of the solar neutrino flux. It is of interest to determine the ratio of the ν_e and $\nu_{\mu,\tau}$ elastic

Table 7.4: Correction factors for the theoretical cross-section models used to normalize all SNOMAN calculations to NSA. All SNOMAN Monte Carlo simulations of CC and NC interactions are performed with BCK.

Model	Theory	g_A	CC Radiative	NC Radiative	ES Radiative
NSGK	0.970	1.0208	1.02	1.015	
NSA	1.000	1.000	1.00	0.995	
BCK, $L_{1,A} = 5.6$	0.976	1.0208	1.02	1.015	
Bahcall et al.					0.98

Table 7.5: Model-dependencies in the cross-section calculation. These estimates are taken as systematic errors in our ν flux measurements.

Cross-section σ	Uncertainty $\Delta\sigma$
CC	3%
NC	3%
$[CC]\,/\,[NC]$	1%
ES	1%

scattering cross-section so that the ratio of ν_e and $\nu_{\mu,\tau}$ in the ES signal can be determined.

The total elastic scattering cross-section for ν_e and ν_μ is shown in Figure 7.8. From the cross-section calculation in SNOMAN we can deduce the elastic scattering cross-section ratio for solar neutrinos by convoluting the neutrino-electron cross-sections, σ_{ES}, with the ^{8}B energy spectrum of solar neutrinos, $\lambda(E_\nu)$, above threshold energy, E_{th}.

$$R^{ES}_{\nu_e/\nu_\mu} = \frac{\int_{E_{th}}^{\infty} \sigma^{ES}_{\nu_e} \lambda(E_\nu)}{\int_{E_{th}}^{\infty} \sigma^{ES}_{\nu_\mu} \lambda(E_\nu)} \tag{7.3}$$

$R^{ES}_{\nu_e/\nu_\mu}$ determines the ratio of the interaction rates of electron and non-electron type neutrinos. If the charged-current and elastic scattering fluxes measured by SNO are different this ratio allows us to determine the $\nu_{e,\mu}$ component in the solar neutrino flux.

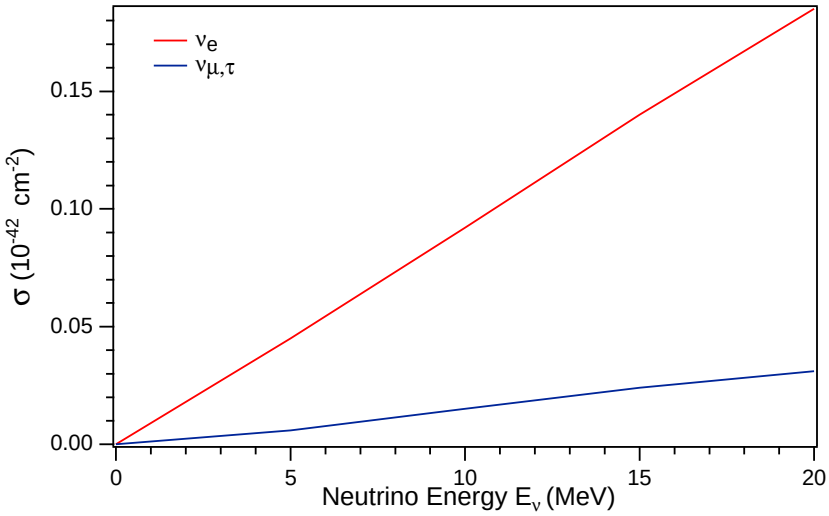

Figure 7.8: Total elastic scattering cross-section of ν_e and $\nu_{\mu,\tau}$ as a function of neutrino energy, E_ν.

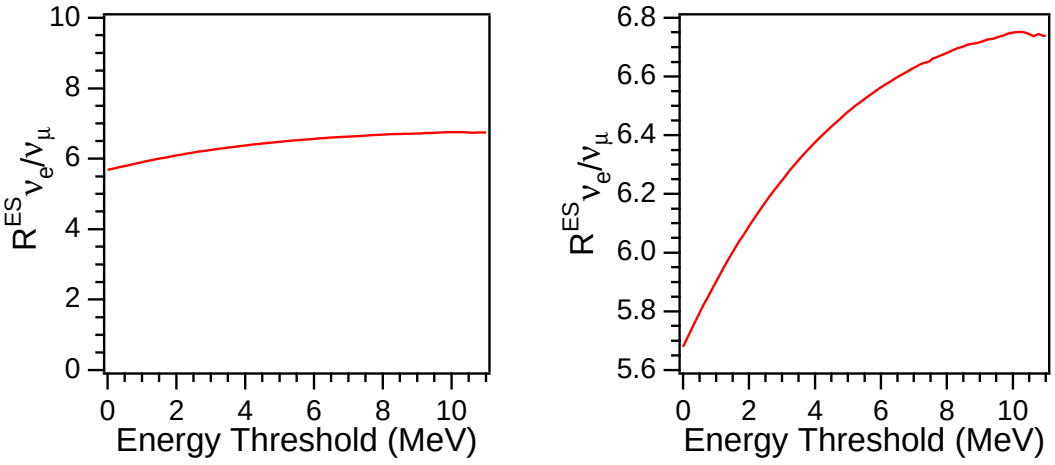

Figure 7.9: Ratio of the integrated cross-sections times the ^{8}B flux above the indicated threshold energy. The left and right panel only differ by the scale of their ordinate.

7.3 Systematics of the Water Target in the SNO Detector

The SNO detector consists of a central target volume of a 1000 t of D_2O surrounded contained in an acrylic vessel and surrounded by several thousand tonnes of ultra-pure H_2O. Neutrinos interact through the charged-current, neutral-current, and elastic scattering interaction with the D_2O. In addition, they scatter elastically off electrons in the H_2O and AV. The rate of solar neutrino interactions observed in SNO depends on the mass of the D_2O target contained in the acrylic vessel. Accounting for the number of deuterons contained in the AV is critical for the measurement of the CC and NC interaction rates. The error on the number of deuterons contained in the acrylic vessel is part of the systematic error on the solar neutrino flux measured in the SNO detector. Values are also given for the number of electrons. In addition, the differences between the ideal spherical geometry of the detector in the Monte-carlo code and the real detector configuration contribute to the uncertainty in SNO's solar neutrino flux measurement. This systematic effect is estimated.

For analyses using SNOMAN's prediction of the number of deuterons a correction is needed to account for the number of deuterons in the detector and the density of the D_2O at the water temperature of 11.5 °C. SNOMAN calculates the number of ^8B and *hep* charged-current events per day for the number of deuterons that SNOMAN assumes are in the neck and acrylic sphere. The events are set to be distributed throughout the neck and acrylic sphere region. The number of target deuterons assumed in the neck and the acrylic sphere is assumed to be 6.023×10^{31}. The volume SNOMAN assumed is for these regions is 9.1834×10^8 so the number density used in SNOMAN is 6.5586×10^{25} deuterons/l.

There are 6.0086×10^{31} deuterons in 1000 t of D_2O. The measured density of D_2O is 1.10555 at 11.5 C. Within a fiducial volume of $R_{fit} \leq 550$ cm the number of events generated is too low by a factor of 1.0128. The correction factor for the entire D_2O volume is 1.00297. This only describes the adjustments to the number of deuterons in the SNO Monte Carlo code. A full discussion of the D_2O target systematics is given below.

7.3.1 Systematics in the Number of Deuterons

The amount of D_2O in the acrylic vessel (AV) is estimated from calculations based on the geometry of the AV. There are a number of factors that need to be considered when estimating how many deuteron targets are present in any given experimental setting:

1. *AV Absorption and Swelling:* There is evidence that acrylic absorbs some small quantity of H_2O and D_2O. That in turn leads to a swelling of the acrylic, which has increased the vessel diameter. The mass of D_2O contained in the vessel is very sensitive to the AV diameter as only a 0.2 inch increase in the radius of the AV leads to a 0.25% increase in the volume contained in the vessel. The AV swelling is by far the largest contribution to the difference between the mass of D_2O shipped underground and the mass calculated from as-built dimensions [39]. In addition, the uncertainty in the change of volume due to swelling is the largest contribution to uncertainties in the calculated mass of D_2O underground. The effect of absorption and swelling has been studied in detail and has been summarized in an internal SNO report by D. Earle [37].

2. *Acrylic and D_2O Temperature:* The temperature of the acrylic affects the D_2O mass. The detector is operated at essentially the maximum D_2O density, with the result that temperature changes do not have a significant effect on D_2O density, but the acrylic vessel diameter increases with increasing temperature.

3. *AV Geometry:* At the time the upper hemisphere of the vessel was complete, and before it was suspended on ropes, the dimensions were surveyed by R. Komar [132]. The mean inner radius was found to be 600.5(6) cm. The vessel is also not a perfect sphere. Acrylic panels at the supports are thicker than the nominal wall. There are also smaller effects for internal piping and at the neck reinforcement. The target calculations in the SNO Monte Carlo code are based on complete spherical symmetry without all details of the AV design.

4. *AV Deformation*: Deformation of the acrylic vessel under normal operating conditions while full of D_2O was studied using finite element analysis. It was found that the

maximum deformation of the spherical vessel occurs at the point where the chimney intersects the spherical shell. The calculations, survey measurements, and monitoring data give no indication for any significant AV deformation [38].

5. *AV Hydrostatic Loading:* This effect is assumed to be negligible.

6. *Isotopic Abundance of D_2O Target in SNOMAN*: Both the geometry and the isotopic abundance used in SNOMAN are not identical to the actual detector target.

7. *Heavy water inventory:* The actual amount of heavy water measured by mass to be present in the vessel.

8. *Compressibility:* The average density of the large mass of D_2O in SNO is slightly higher than that measured in the laboratory.

7.3.2 Estimating the Number of Deuterons in the Acrylic Vessel

The heavy water inventory in the vessel has been calculated in two different ways [144]. The basic source of information is an e-mail sent October 30, 2000, by Ken McFarlane:

"The estimates as put together on Nov 1, 1999 are as follows. The mass of D_2O in the AV is 1,003,497 kg (water and acrylic temperature assumed at 11.5 °C). The mass of D_2O in the neck is 9,053 kg. Most of the non-sphericity is thought to be from the thickened panels at the equator. This decreases the D_2O mass by 611 kg in this region, and has been included in the above value. These estimates are based on physical acrylic survey information, acrylic swelling properties, water temperature information, and a number of calculations. A comparison estimate was also made using the inventory tank surface records, looking at how much was shipped underground, and subtracting quantities used in deuteration, filling storage tanks and process piping. This alternate approach gives a value 1,367 kg lower than the above estimate. One get an some idea of the uncertainty by comparing the two numbers.

All of the above numbers are based on 99.918 % D_2O. The mass numbers include the .092% H_2O. The actual mass also fluctuates by a few hundred kg due to temperature fluctuations."

The phrase "Mass of D_2O in the AV" is ambiguous. When the vessel radius deduced from the measured density and the stated mass is compared with the radius obtained directly by surveying, it becomes clear that Ken meant the spherical part of the vessel, not the total vessel including the neck. Both earlier versions of this report and the SNOMAN code have taken the opposite interpretation, that the mass 1,003,497 kg referred to the total vessel contents. The masses are summarized in Table 7.6.

Table 7.6: SNO heavy water inventory.

Quantity		
Temperature	11.5	°C
Specific gravity [158]	1.10555	
Mean gauge pressure in SNO	0.2	MPa
Isothermal Compressibility	4.59×10^{-4}	MPa^{-1}
Corr. sp. gravity	1.10565	
Vessel radius as surveyed	600.5(6)	cm
Vessel radius in service	600.54(61)	cm
Calculated mass in sphere	1002970	kg
Reported mass [144]	1003497	kg
Reported neck mass [144]	9053	kg
Inventory mass discrepancy	-1367	kg
Net inventory mass	1011183	kg
Sphere inventory mass	1002142	kg
Neck inventory mass	9041	kg
Vessel radius as calculated	600.33	cm

In the first approach, the dimensions of the vessel, modifications from spherical shape, corrections for swelling and distortion, temperature, the measured specific gravity and the compressibility give a calculated mass. Some contraction (about 0.5 cm) occurred in cooling to 11.5 °C: the expansion coefficient of acrylic is between 50 and 90 ppm/C. A further

reduction is caused by the belly plates, which displace 611 kg of heavy water within the sphere [144]. That corresponds to a reduction of 0.12 cm in effective radius. AV swelling, on the other hand, makes the vessel larger by about 0.33(7)% in volume, or 0.66 cm in radius. The net effective radius in service is 600.54(61) cm. The calculated mass of D_2O thus has an uncertainty of about 0.3%, dominated by geometrical uncertainties. The directly weighed inventory mass as an uncertainty of about 0.1%.

The inventory values rather than the density-volume values are used in this document not only because they are more accurate, but also because they are independent of other information and thus may be cross-checked.

The current best estimate of the errors affecting the number of deuterons in SNO are summarized in Table 7.7.

Table 7.7: Input systematic errors in D_2O target calculations.

Systematic Error	Percentage
Uncertainty in D_2O Mass	0.1%
Volume Change due to AV Swelling	$+0.33 \pm 0.07\%$
Volume Change due to AV Deformation	-0.001%
D_2O specific gravity	0.009%
Isotopic Abundance	0.0023%

7.3.3 AV Neck and Chimney

The mass of D_2O in the neck region of the detector has been estimated by volume and density to be about 9,053 kg [144], about 0.9% of the mass contained in the spherical volume [32]. When the inventory mass is used for the total, the difference is assumed to be split proportionally between the neck and the sphere, leading to a slightly smaller mass of 9,041 kg in the neck.

7.3.4 Isotopic Abundance

The number of target deuterons in the SNO detector also depends on the isotopic abundance of the heavy water. The number of deuterons in a heavy water target of mass M is

$$N_D = 2\frac{Mf_D}{2m_D f_D + 2m_H(1-f_D) + m_{17}f_{17} + m_{18}f_{18} + m_{16}(1-f_{17}-f_{18})}, \tag{7.4}$$

where f_D, f_{17}, and f_{18} are the fractional isotopic enrichments of deuterium, ^{17}O, and ^{18}O, respectively, and m_i is the atomic mass of isotope i. In Table 7.6 the abundances and atomic masses are listed.

Table 7.8: Fractional isotopic abundances and masses.

Isotope	Abundance	Mass Excess ΔA, MeV	Mass A, MeV	Mass A, 10^{-27} kg
D	0.999084(23)	13.136	1876.124	3.34449
H	0.000916	7.289	938.783	1.67353
^{16}O	0.99624	-4.737	14899.167	26.5602
^{17}O	0.000485(5)	-0.809	15834.589	28.2277
^{18}O	0.00320(3)	-0.782	16766.110	29.8883
^{23}Na	1	-9.529	21414.833	38.1754
^{35}Cl	0.7577	-29.013	32573.277	58.0671
^{37}Cl	0.2423	-31.762	34433.516	61.3833

Isotopic abundance measurements for deuterium between October 1999 and March 2000 give an average of 99.9176% with a standard deviation of 0.0023 [152]. This average is based on 29 samples processed with the FTIR (Fourier Transform Infrared Spectrometer). The uncertainty on a single measurement with the machine operating in the 99.5% and above range is expected to be about 0.005%. These are % by mass D_2O isotopic values. The conversion from isotopic mass abundance μ_D to fractional abundance f_D is

$$f_D = \mu_D \frac{2m_H + m_{16}}{2(1-\mu_D)m_D + m_{16} + 2\mu_D m_H}, \tag{7.5}$$

with the result that $f_D = 0.999084$. The uncertainty on the isotopic abundance is about 0.01%. The largest uncertainty in the absolute isotopic measurement comes from the accuracy of the standard. The nearest standard was 99.92±0.01% when supplied several years ago [170].

The abundances of the minor oxygen isotopes have been reviewed by Dragowski [33]. The values given are slightly revised from earlier ones used in SNOMAN 4.0186 (0.000487 and 0.00327 for ^{17}O and ^{18}O respectively) and greatly revised from the ones in the SNO NIM paper [105] as a result of new measurements.

Conversion from tabulated mass excesses to mass has been carried out using 931.494013 MeV per atomic mass unit and 1.660539×10^{-27} kg per atomic mass unit, on the ^{12}C scale. The derived value for Avogadro's number is 6.02214×10^{23}.

From Equ. 7.4 and the data in Table 7.8 there are $N_D = 6.0082 \times 10^{31}$ deuterons in 1000 tonnes.

7.3.5 Target Calculations in SNOMAN: Deuterons

SNOMAN 4.0186 uses the figure of 6.023×10^{31} deuterons in the acrylic vessel, including the neck. This quantity should probably have been the number of deuterons in the spherical part alone. SNOMAN takes the spherical part of the vessel volume to be 9.07×10^8 cm^3 (corresponding to a radius of approximately 600.5 cm) and the volume of the neck to be 0.1134×10^8 cm^3, and from 6.023×10^{31} deuterons total it calculates the number of deuterons in the spherical part of the vessel (5.9486×10^{31}). (SNOMAN actually returns 5.9477×10^{31} for the number in the vessel owing to a small inconsistency in the way the correction for the neck volume is made. SNOMAN uses a factor of $(1-V_{\rm neck}/V_{\rm sphere})$ instead of $(1-V_{\rm neck}/V_{\rm total})$ which it does when distributing events, and this will give a slightly different and incorrect number density, but the difference is only 1.5×10^{-4}.) Early versions of the SNOMAN code only simulated neutrino interactions in a spherical D_2O volume rather than including the neck. In SNOMAN 4.0186, the neutrino interactions in the neck region are simulated.

For calculations of rates within a certain fiducial volume defined by a (reconstructed) radius, the actual number of neutrino interactions depends on the number density of deuterons. SNOMAN infers a number density of 6.5585×10^{28} d m^{-3}. The actual number density based on the measured [158] specific gravity at 11.5 °C (1.10555) and the number of deuterons per kg is 6.6429×10^{28} d m^{-3}, larger by a factor 1.01287 than the SNOMAN value. The uncertainty contributed by the D abundance is 0.00002 and by the density is 0.00013. The uncertainty in the inventory does not contribute to this ratio.

The water density is measured on the surface at atmospheric pressure. The isothermal compressibility of water at 20 °C is 4.59×10^{-4} MPa^{-1}. The average gauge pressure in the AV is 0.2 MPa, which means the density is larger by a factor $1 + 9.2 \times 10^{-5}$. The specific gravity increases from 1.10555 to 1.10565.

The heavy water in SNO is degassed but when measured on the surface is (probably) saturated with air. The mole fraction solubilities of nitrogen and oxygen at 1 bar are respectively 1.39×10^{-5} and 2.76×10^{-5}. The volume (density) dependence on dissolved gas content is not known, but the solubilities are small enough to neglect in any case.

7.3.6 Target Calculations in SNOMAN: Electrons

The elastic scattering reaction similarly depends on the volume and density. The number of electrons per mass M of heavy water is given by

$$N_e = 10 \frac{M}{2m_D f_D + 2m_H(1 - f_D) + m_{17} f_{17} + m_{18} f_{18} + m_{16}(1 - f_{17} - f_{18})} \tag{7.6}$$

There are thus 30.0684 x 10^{31} electrons per 1000 tonnes. SNOMAN takes the number of electrons to be exactly 5 times the number of deuterons, *i.e.* 30.115×10^{31} electrons in the acrylic vessel. The dependence on composition is, in fact, very weak. For ES interactions in the whole AV, the number of interactions is 1.00962 that predicted by SNOMAN. Of course, electron interactions do not have a real boundary at the AV, but it is a SNOMAN calculable quantity to compare with expectations from theory.

For ES interactions within a defined fiducial radius, the number of interactions exceeds that given by SNOMAN by a factor 1.01380, which is predominantly the density ratio. The

parameters for both deuterons and electrons are summarized in Table 7.9.

Table 7.9: Target atoms in SNOMAN and actual physical parameters.

Quantity	SNOMAN	Actual	Actual/ SNOMAN	Uncert
Mass in vessel, kg		1011183		
Mass in sphere, kg		1002142		
Mass in neck, kg		9041		
d in vessel, 10^{31}	6.023	6.0754	1.00869	0.00120
d in sphere, 10^{31}	5.9486	6.0210	1.01218	0.00120
d in neck, 10^{31}	0.0744	0.0543	0.73009	
Implicit specific gravity	1.09161	1.10565	1.01287	0.00013
Implicit d dens. 10^{28} m^{-3}	6.5585	6.6429	1.01287	0.00013
Electrons in vessel, 10^{31}	30.1150	30.4046	1.00962	0.00120
Electrons in sphere, 10^{31}	29.7430	30.1328	1.01310	0.00120
Electron density, 10^{28} m^{-3}	32.7927	33.2451	1.01380	0.00013

7.3.7 Spherical (A)Symmetry in the Signal Decomposition

The error in the signal decomposition due to the non-spherical shape of the vessel is assumed to be negligible. As discussed above, there are no indications for any AV deformation [38] that could significantly change the inner volume of the detector or affect the radial distribution of events.

7.3.8 Conclusions

The current best estimate for the mass of D_2O in the AV is $1,002,130 \pm 1,230$ kg. The error in the AV volume is dominated by the swelling of the AV which has been estimated to be about $0.33 \pm 0.07\%$. All other errors related to the AV geometry are small. The current

best estimate of the errors affecting the number of deuterons in SNO are summarized in Table 7.9. Correction factors to bring calculated rates in SNOMAN to the correct values are summarized in Table 7.10.

Table 7.10: Correction factors for D_2O target calculations.

Target	Actual/SNOMAN
D in AV sphere	1.01218
D in FV	1.01287
e in AV sphere	1.01310
e in FV	1.01380
Effective radius	600.33/600.5

7.4 Systematics in the Orientation of the SNO Detector

The orientation of the SNO detector in the SNOMAN Monte Carlo simulations affects the reconstructed direction of neutrino interactions and backgrounds with respect to the Sun. In our analysis the characteristic angular distribution of neutrino interactions will be used to distinguish elastic scattering interactions and to demonstrate that the neutrinos observed at the Sudbury Neutrino Observatory originate in the Sun. Knowing the exact orientation of the detector geometry with respect to the Sun is critical.

The orientation of the SNO detector with respect to true North was determined using a commercial gyrocompass [62]. A correction of 2.49 ± 0.22 (stat.) ± 0.47 (syst.) degrees with respect to the PSUP construction North and INCO/Monenco survey data was determined. The new orientation of the detector is used in all SNOMAN simulations.

To estimate the effect of a possible systematic error in our data analysis the angular distributions of neutrino interactions with the correct and incorrect orientation of the detector were compared. Two data sets with elastic scattering neutrino interactions corresponding to 1 live year of data were generated in the D_2O and the H_2O, one with the correct implementation of true North and the other with a systematic shift of 2.5 degrees. Any error in the true North determination with the gyrocompass will fall within the error estimated from the two different simulations.

A comparison of the elastic scattering peak in the $\cos\theta_\odot$ distributions reveals no discernible difference between the two data sets. The difference is within the statistical error of the distributions.

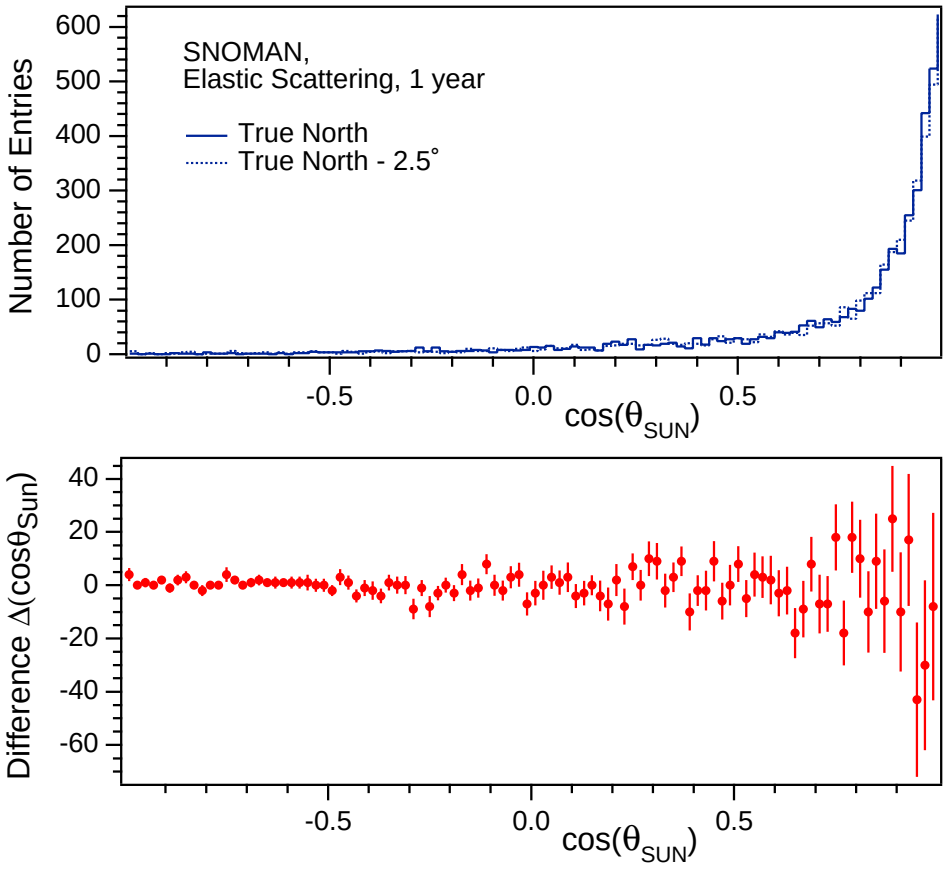

Figure 7.10: Top panel: Reconstructed angular distribution of elastic scattering Monte Carlo events with detector orientations ± 0 and -2.5 degrees off true North. Bottom panel: The difference between the two $\cos\theta_{\odot}$ distributions is consistent with zero.

7.5 Predictions for the Neutrino Event Rate in SNO

With the Monte Carlo inputs described above the event rate of neutrino interactions in the SNO detector is simulated. The event rate above threshold is the integral of the observable interaction rate in the D_2O and H_2O target media over the fiducial volume, R_{FV}, and above threshold, E_0. The observable interaction rate is the product of the true interaction rate, $N_\nu(E,R)$ corrected for the Monte Carlo inefficiency, $1/\epsilon_{MC}$, with the reconstruction efficiency, ϵ_{fit}, and the signal loss, $(1-\eta_{HLC})$, due to the high-level event cuts (HLC).

$$N_\nu^{SNO} = \int_{E_0}^{\infty}\int_{R_{fit}=0}^{R_{FV}} (1-\eta_{HLC})\frac{1}{\epsilon_{MC}}\epsilon_{fit}N_\nu(E,R)dEdR \tag{7.7}$$

Figure 7.11 shows the predicted number of CC, NC, and ES interactions within $R_{fit} \leq$ 600 cm for the BPB00 standard solar model calculations. The same values are tabulated in Table 7.11. To first order we expect the event rate to scale with the fiducial volume. Systematics in the determination of the event location, such as misreconstruction will cause deviations from the $(R_{fit}/R_{AV})^3$ volume scaling.

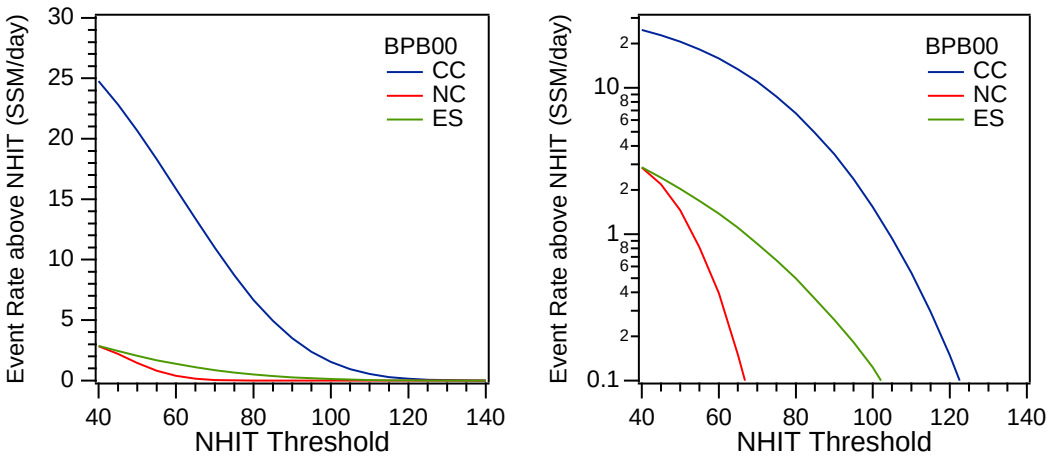

Figure 7.11: Predicted rate of observed neutrino events in SNO for the BPB00 standard solar model calculations. A radial reconstruction cut of $R_{fit} \leq 600$ cm and the high-level event cuts (HLC) are applied.

Table 7.11: Predictions for the neutrino interaction rates in SNO based on the standard solar model calculations by BPB00. A radial reconstruction cut of $R_{fit} \leq 600$ cm and the high-level event cuts (HLC) are applied.

NHIT Threshold	CC (SSM/day)	NC (SSM/day)	ES (SSM/day)
≥40	24.760	2.852	2.867
≥45	22.837	2.190	2.435
≥50	20.661	1.457	2.044
≥55	18.308	0.813	1.683
≥60	15.851	0.395	1.382
≥65	13.362	0.149	1.107
≥70	10.981	0.051	0.858
≥75	8.706	0.011	0.662
≥80	6.670	0.003	0.497
≥85	4.930	0.001	0.361
≥90	3.501	0	0.259
≥95	2.373	0	0.183
≥100	1.531	0	0.122
≥105	0.937	0	0.077
≥110	0.544	0	0.046
≥115	0.294	0	0.026
≥120	0.149	0	0.016
≥125	0.069	0	0.008
≥130	0.032	0	0.004
≥135	0.013	0	0.002
≥140	0.005	0	0.001

CHAPTER 8

CHARACTERISTIC DETECTOR DISTRIBUTIONS OF THE NEUTRINO CANDIDATE EVENT SET

The neutrino candidate event set is characterized by a set of detector distributions which are unique and quite distinctive for the different types of neutrino interactions in the D_2O and H_2O target media of the detector. Given the approximate spherical symmetry of the detector and the well-known position of the Sun with respect to the detector it is natural to consider the following 4 detector distributions:

Radial Distribution: The approximate spherical symmetry of the SNO detector allows one to describe the position dependence of the reconstructed events through their radial distribution. The acrylic vessel of the SNO detector represents a natural boundary between the D_2O and H_2O region of the detector. For convenience all radial event distributions are normalized to the radial position of the AV. With $R_{AV} \approx 600$ cm and R_{fit} being the reconstructed event position in cm we define $R = R_{fit}/600$ as the fractional AV radius. In our analysis of neutrino interaction rates the distribution of interest is R^3 as it normalizes the radial distribution of interaction rates to unit volume. The different radial distributions of events produced in the charged-current (CC), neutral-current (NC), or elastic scattering (ES) interaction can be used in a statistical technique (which we present in Chapter 9) to separate the various components of the candidate event set.

Solar Angle Distribution: The solar angle distribution $\cos\theta_\odot$ describes the relation between the direction of the incident neutrino and the outgoing Čerenkov electron. The type of neutrino interaction (CC, ES, or NC) and its kinematics determine the characteristic shape of the solar angle distribution. The $\cos\theta_\odot$ distribution can be used to distinguish between the charged- or neutral-current process of an event, and uniquely identify neutrinos from the Sun through the forward-peaked distribution of elastic scattering events.

Energy Spectrum: The energy spectrum of neutrino candidate events is derived from

the number of photomultiplier hits, NHIT, of every event. The total energy spectrum is the sum of the energy spectra from the CC, NC, and ES process. At higher energy the spectrum is dominated by charged-current events with a small contribution of elastic scattering interactions. Below $\sim$ 6.5 MeV, or $\sim$ 65 NHIT, there is an additional contribution of events from the neutral-current dissociation of deuterium. While the energy spectrum of CC and ES events can be distorted in the presence of neutrino oscillations the spectrum of NC events is well defined as it is determined by the 6.25-MeV γ-rays from the capture of thermal neutrons on deuterium.

Directionality of Events: The directionality of an event is a useful parameter in the characterization of different event classes. In some cases the event direction allows one to infer the location of events with respect to the central detector. For example, background events from regions external to the central D_2O volume reconstruct predominantly with an inward going event direction while CC interactions are expected to have an isotropic distribution of event directions with respect to the detector's coordinate system. The near-spherical symmetry of the detector suggests the definition of the parameter $\vec{u}.\vec{r}$ that describes the relation between the direction of an event and its reconstructed radial vector. This detector distribution has been studied for various signal and background event classes and may provide additional power in the separation of the neutrino signals. However, it is not yet used in the final analysis.

Solar neutrinos interact with the D_2O target through the charged-current (CC), neutral-current (NC), and elastic scattering (ES) interaction. In addition, electron neutrinos can scatter off the electrons (ES) in the light water volume around the acrylic vessel.

Charged-Current (CC): $\nu_e + d \rightarrow p + p + e^- \; -1.44$ MeV

Neutral-Current (NC): $\nu_x + d \rightarrow p + n + \nu_x \; -2.22$ MeV

Elastic Scattering (ES): $\nu_x + e^- \rightarrow \nu_x + e^-$

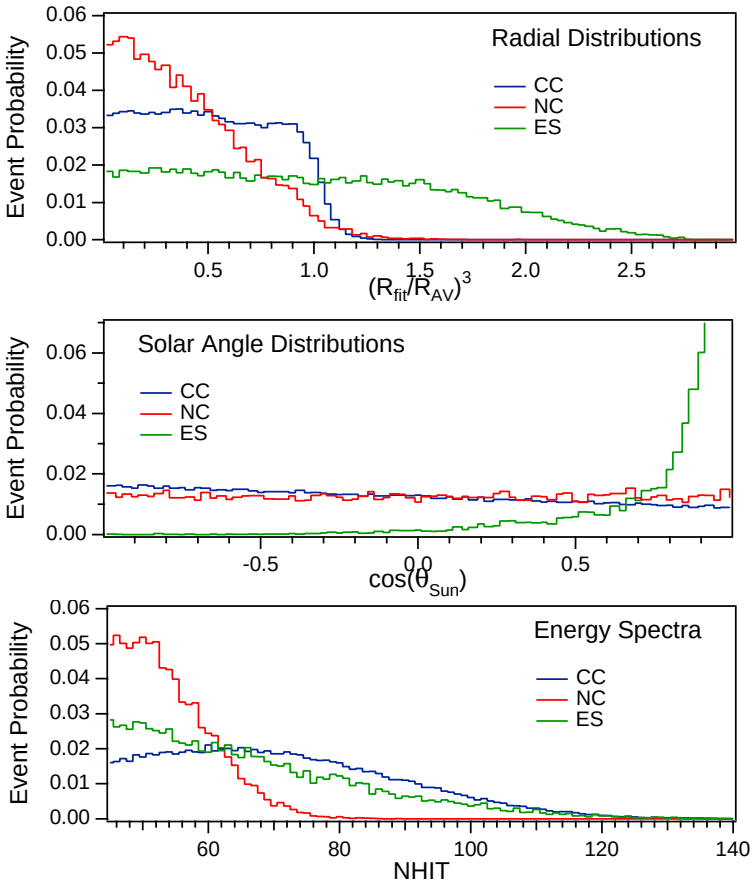

Figure 8.1: Characteristic detector distributions of neutrino signals in SNO as predicted by SNOMAN Monte Carlo simulations. The distributions are normalized to unit area. A threshold cut of NHIT ≥ 45, and the high level event cuts (HLC) are applied.

In this chapter we study and discuss the characteristics event distributions of these three different reactions and and investigate how they can be used to determine the respective interaction rates. In Chapter 9 we will then develop a maximum likelihood technique for the statistical separation and determination of the different neutrino signals using the first three of these characteristic detector distributions, i.e. R^3, $\cos\theta_\odot$, and NHIT. The event distributions shown in Figure 8 are the characteristic detector distributions of neutrino signals in SNO as predicted by SNOMAN Monte Carlo simulations.

In a formal discussion of the characteristic detector distributions we have to distinguish between the fundamental distribution of the neutrino interaction which is determined by the physics of the interaction, the detector response, and the high-level reconstruction of event observables. Neutrino interactions in the SNO detector produce both Čerenkov electrons and γ-rays as event signatures. The electrons and gammas are distributed according to fundamental variables of the interaction. The light from Čerenkov electrons and γ-rays propagates through the various optical media and is detected by an array of photomultipliers. The inefficiency of photon detection in the PMT array and the optical transmission of the various detector media affect the total number of detected photons. The timing and charge information from the photomultipliers allows the characterization and reconstruction of events in energy, position, and direction. It is the reconstructed event observables that determine the characteristic detector distributions. Unless noted otherwise the event distributions shown in this chapter are the reconstructed detector distributions derived from either the data or SNOMAN Monte Carlo simulations.

If α is a fundamental parameter of the interaction (e.g.. the angular distribution), then the underlying event distribution generated by the interaction is:

$$\text{Event Distribution}: \quad N_\nu[\alpha] \quad = N_{CC,NC,ES}[\alpha] \tag{8.1}$$

The efficiency of photon detection and other effects determine the detector response which is described by the total number of detected events as well as their distribution in α. The parameter ϵ^{SNO} parameterizes the efficiency of the SNO detector response.

$$\text{Detector Response}: \quad N_\nu^{SNO}[\alpha] \quad = \epsilon_0^{SNO} N_\nu\left[\epsilon_1^{SNO}\ \alpha\right] \tag{8.2}$$

The event observables of every detected event are then reconstructed to determine the reconstructed detector distribution α' of the fundamental event distribution α.

$$\text{Reconstruction of Event Observables}: \quad N_\nu^{fit}[\alpha'] \quad = \epsilon_0^{fit} N_\nu^{SNO}\left[\epsilon_1^{fit}\ \alpha\right] \tag{8.3}$$

The reconstructed detector distributions discussed in this chapter are the result of these 3 steps:

$$\text{Reconstructed Events}: \quad N_\nu^{SNO,fit}[\alpha] = N_\nu[\alpha] \otimes N_\nu^{SNO}[\alpha] \otimes N_\nu^{fit}[\alpha] \tag{8.4}$$

$$= N_\nu\left[\epsilon_0^{fit}, \epsilon_1^{fit}, \epsilon_0^{SNO}, \epsilon_1^{PMT}, \alpha\right] \tag{8.5}$$

For example, α can be the energy E, the solar angle distribution $\cos\theta_\odot$, or the position $\vec{R}$ of the event. Our ability to distinguish the detector distributions of the CC, NC, and ES neutrino interactions depends on the SNO detector response as well as our ability to reconstruct the "true" event distribution from the event observables.

8.1 Radial Distribution of Neutrino Candidate Events

The radial distribution of events is determined by the specific characteristics of the final state particles, i.e. the electrons produced in the charged-current neutrino-deuteron interaction, the neutrons produced in the neutral-current dissociation of deuterium, and the electron involved in the neutrino-electron scattering.

Charged-Current: CC interactions of ν_e with deuterium only occur in the D_2O. The radial position of the Čerenkov electrons produced in the CC reaction can be reconstructed quite accurately. Therefore, the reconstructed radial distribution of CC event falls off steeply at the edge of the AV. The width of the fall-off is determined by the vertex resolution of reconstructed CC events.

Neutral-Current: The distribution of neutral-current events is governed by the capture distribution of neutrons. Neutrons created in the NC interaction quickly thermalize and diffuse through the entire detector volume before they capture on deuterium or hydrogen, or other nuclei. The neutral-current signal is detected by the capture of the free neutron on deuterium which results in a 6.25 MeV gamma ray. These gamma-ray events display a pronounced radial distribution even though the neutrons themselves are produced uniformly throughout the D_2O. This radial distribution arises because neutrons escape capture on deuterium more readily near the outer edge of the D_2O due to the very long thermal diffusion length in D_2O, and it is the chief means by which Čerenkov events produced by 6.25 MeV gamma rays can be distinguished from CC and ES events of the same energy.

Elastic Scattering: Neutrino-electron elastic scattering occurs in both the D_2O and H_2O. The reconstructed distribution of ES events is expected to be approximately constant per unit volume across the acrylic vessel.

As the SNO detector is approximately spherical it is convenient to display all radial distributions as a cubic function of the radius. This normalizes the event rates to unit volume. For convenience, the radial position coordinate is also normalized to the position of the AV.

$$F(R) = F(R/R_{AV})^3) = F((R/600cm)^3) \tag{8.6}$$

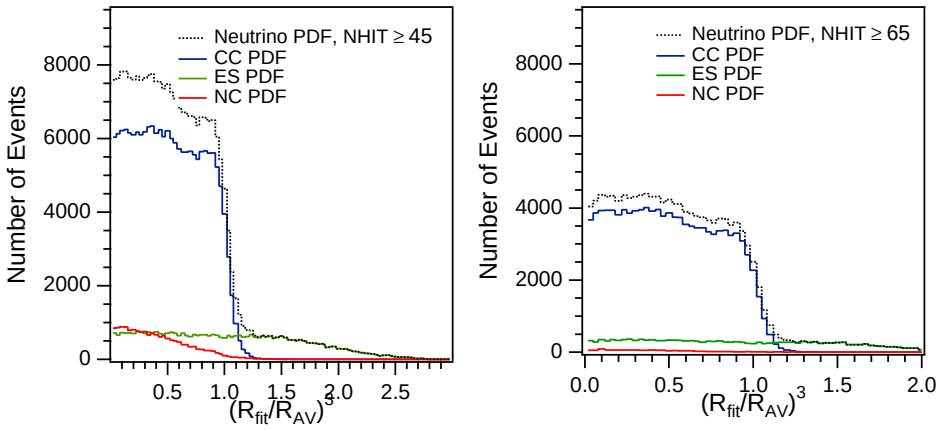

Figure 8.2: Radial distributions of neutrino signals in SNO for NHIT $\geq$ 45 (left panel) and NHIT$\geq$65 (right panel) as predicted by Monte Carlo simulations. A radial cut of $R_{fit} \leq 550$ cm, a threshold cut of NHIT $\geq$ 45, and the high level event cuts (HLC) are applied.

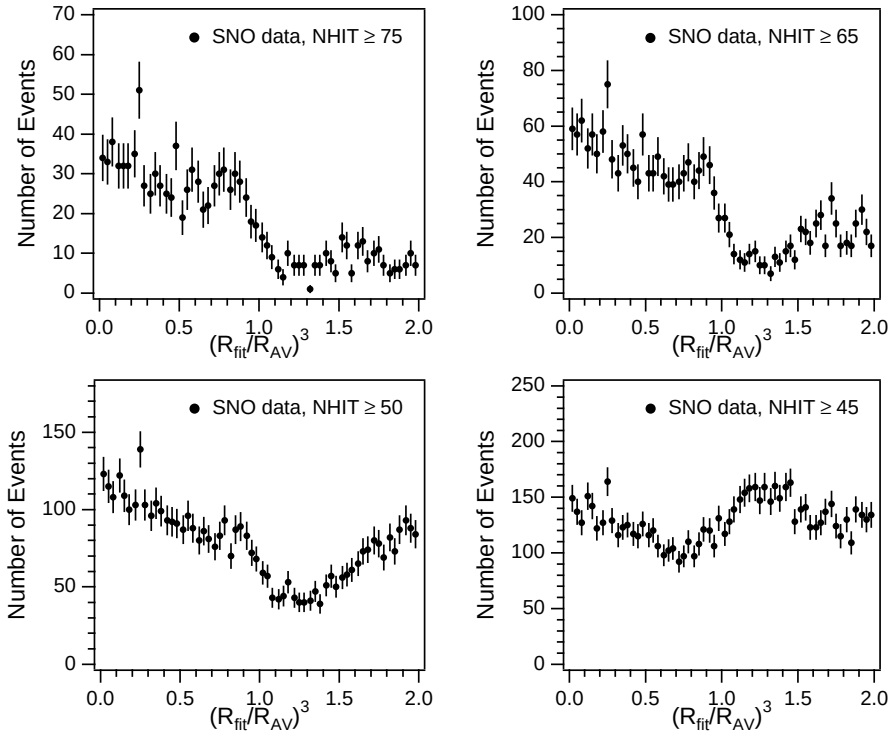

Figure 8.3: Radial distribution of the reduced but otherwise raw SNO data above a threshold of NHIT $\geq$ 45, 50, 65, and 75.

Table 8.1 summarizes the thermal neutron radiative capture cross-sections in millibarns on a variety of nuclei. The cross-section of $^{1}_{1}$H is about 3 orders of magnitudes higher than the neutron cross-section on $^{2}_{1}$H. Neutrons in the outer region of the heavy water volume have a high chance to capture on hydrogen in the AV or in the light water region.

Table 8.1: Thermal neutron capture cross-sections and γ energies. The final column indicates if the energy released by the neutron capture is generally in a cascade.

Nucleus	Cross-Section	Energy (MeV)	Cascade
$^{1}_{1}$H	332	2.2	no
$^{2}_{1}$H	0.519	6.25	no
$^{35}_{17}$Cl	43600	8.9	yes
$^{12}_{6}$C	3.53	4.95	no
$^{13}_{6}$C	1.37	8.18	no
$^{14}_{7}$N	75	10.83	yes
$^{16}_{8}$O	0.19	4.14	2 or 3 γ
$^{40}_{18}$Ar	66	6.1	yes
$_{28}$Ni	2000-5000	7-9	yes
$^{56}_{26}$Fe	2590	7.65	sometimes
$_{30}$Zn	700-900	7-8	yes

8.1.1 Extracting Limits on the Neutrino Interaction Rates from the Radial Event Distribution

The radial distribution of the raw SNO data is quite distinctive and shows clear features of the CC events inside the acrylic vessel and backgrounds in the outer region of the SNO detector. Using nothing but the radial distribution we can make a first estimate of the CC interaction rate in SNO by fitting the radial distribution.

A radial probability distribution function (PDF) of CC events simulated in Monte Carlo is fit to the $(R_{fit}/R_{AV})^3$ distribution of the reduced but otherwise raw data using a maximum likelihood estimator. A fit window between $(R_{fit}/R_{AV})^3$=[0,1.05] is chosen to maximize the sensitivity to the characteristic radial distribution of the CC events in SNO but to minimize the contamination from backgrounds. A threshold of NHIT $\geq$ 65 and 75 is applied to reduce the contribution of neutrons from the NC interaction of neutrinos. As we do not account for the ES contribution in the data the fit results represent upper limits on the CC rate. For comparison, the CC PDF was also fit to a high-statistics Monte Carlo data set consisting of CC, NC, and ES events at standard solar model predictions. This allows us to understand and estimate any systematic bias in the fit. The results are summarized in Table 8.2.

The fit coefficients are given by $[CC_{Data}/CC_{PDF}]$ and $[CC_{MC}/CC_{PDF}]$ respectively. From the studies with the Monte Carlo data set we notice that the fit either underestimates the CC content by $\sim$ 15% for NHIT $\geq$ 65 or overestimates it by $\sim$ 8% for NHIT $\geq$ 75. $[CC_{Data}/CC_{PDF}]'$ is a corrected fit coefficient which is corrected for this systematic bias and for the target corrections, CC_{corr}, discussed in the previous chapter. As there is undoubtedly some ES and NC contribution in the data we consider $[CC_{Data}/CC_{PDF}]$' an upper limit on the CC contribution to the SNO data set.

$$[CC_{Data}/CC_{PDF}]' = [CC_{Data}/CC_{PDF}] \times \frac{CC_{corr}}{CC_{MC}/CC_{PDF}} \tag{8.7}$$

Table 8.2: Results of fitting the radial distribution of the CC PDF to the raw data and to Monte Carlo simulations of neutrino signals.

Threshold	$\left[\frac{CC_{Data}}{CC_{PDF}}\right]$	$\left[\frac{CC_{MC}}{CC_{PDF}}\right]$	C_{corr}	$\left[\frac{CC_{Data}}{CC_{PDF}}'\right]$
NHIT ≥ 65	0.329 ± 0.009	0.851 ± 0.003	0.99	$< 0.379 \pm 0.010$
NHIT ≥ 70	0.404 ± 0.012	1.084 ± 0.004	0.99	$< 0.365 \pm 0.011$
NHIT ≥ 75	0.390 ± 0.013	1.079 ± 0.004	0.99	$< 0.356 \pm 0.010$
NHIT ≥ 80	0.381 ± 0.015	1.080 ± 0.005	0.99	$< 0.346 \pm 0.013$

The weighted mean of these fit results gives

$$\overline{\left[\frac{CC_{Data}}{CC_{PDF}}'\right]} = \frac{1}{\sum_i (1/\sigma_i)} \times \sum_i \left(\left[\frac{CC_{Data}}{CC_{PDF}}'\right]_i / \sigma_i^2 \right) = 0.363 \tag{8.8}$$

Based on this simple study of the radial distribution we expect the flux of solar ν_e to be of the order of or less than 0.36 times the standard solar model prediction.

$$[CC]_{R^3} \leq 0.363 \times \text{SSM} \tag{8.9}$$

Comparing the radial profile of the raw data and the expected event distribution of elastic scattering events we do not expect to place any interesting limits on the ES interaction rate from the radial distribution alone. The statistics of the elastic scattering interaction is limited in the D_2O region of the SNO detector and the radial profile is dominated by CC events. We would expect to see the ES signal free of any CC or NC "background" in the H_2O region. However, backgrounds from the outer region of the detector mask the ES signal in the light water region.

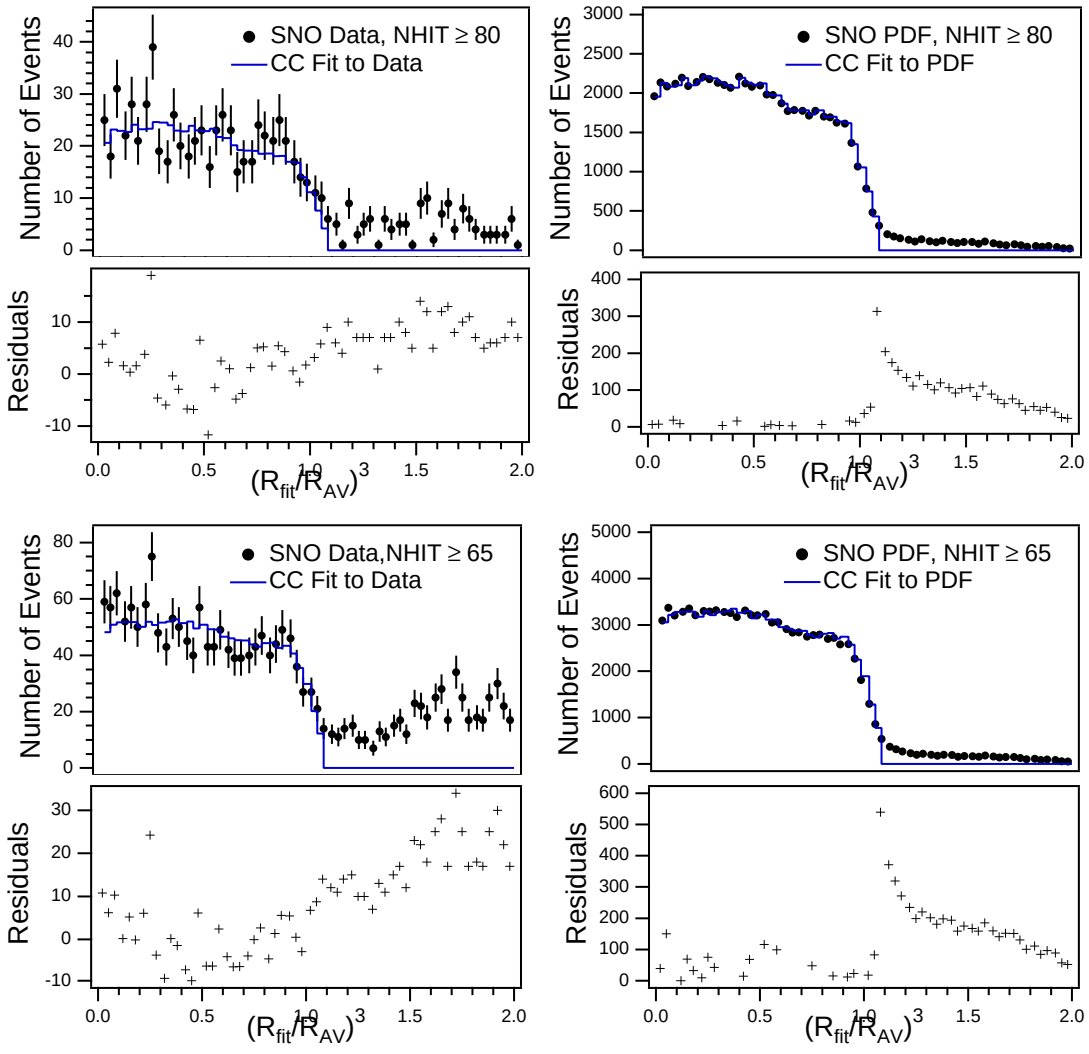

Figure 8.4: Fit of the CC Probability Distribution Function (PDF) to the radial distribution of raw data for NHIT $\geq$ 65 and NHIT $\geq$ 75.

The radial profile of neutron capture events in the D_2O is also quite distinctive. Although neutrons are produced uniformly inside the D_2O the distribution of $^2H(n,\gamma)^3H$ events is characterized by a gradual fall-off towards the acrylic vessel. Although the radial characteristics of the neutron distribution are not as pronounced as the CC event distribution we can attempt to extract an estimate of the neutrons in the raw SNO data set. For this study a lower threshold of NHIT $\geq$ 50, 55, and 60 is selected to increase the statistics of neutron events in the data sample. At the same time the threshold is still high enough so that low-energy backgrounds from ^{214}Bi and ^{208}Tl in the D_2O, AV, and H_2O do not dominate the event statistics.

The NC and CC PDF are now fit to the radial distribution of the data set. The CC contribution to the data set is constrained by the values derived for the high-threshold data set in the section above. The fit results are summarized in Table 8.3.

Table 8.3: Results of fitting the radial distribution of the CC PDF to the raw data and to Monte Carlo simulations of neutrino signals.

Threshold	$\left[\frac{NC_{Data}}{NC_{PDF}}\right]$	$\left[\frac{NC_{MC}}{NC_{PDF}}\right]$	C_{corr}	$\left[\frac{NC_{Data}}{NC_{PDF}}'\right]$
NHIT $\geq$ 45	2.161 ± 0.153	1.721 ± 0.030	0.99	$< 1.266 \pm 0.093$
NHIT $\geq$ 50	2.220 ± 0.182	2.219 ± 0.040	0.99	$< 0.980 \pm 0.081$
NHIT $\geq$ 55	2.182 ± 0.221	2.763 ± 0.066	0.99	$< 0.789 \pm 0.081$
NHIT $\geq$ 60	2.402 ± 0.416	3.947 ± 0.123	0.99	$< 0.609 \pm 0.110$

We find that the results for the fits to the neutron contribution are highly dependent on the threshold. This is not surprising as the statistics of neutron capture events in the data set is limited. From the data we considered in this simple analysis we place the following limit on the neutron contribution to the data in units of the NC flux as predicted in the standard solar model by BPB00 [11].

$$[Neutrons]_{R^3} < 1.27 \times \text{SSM} \tag{8.10}$$

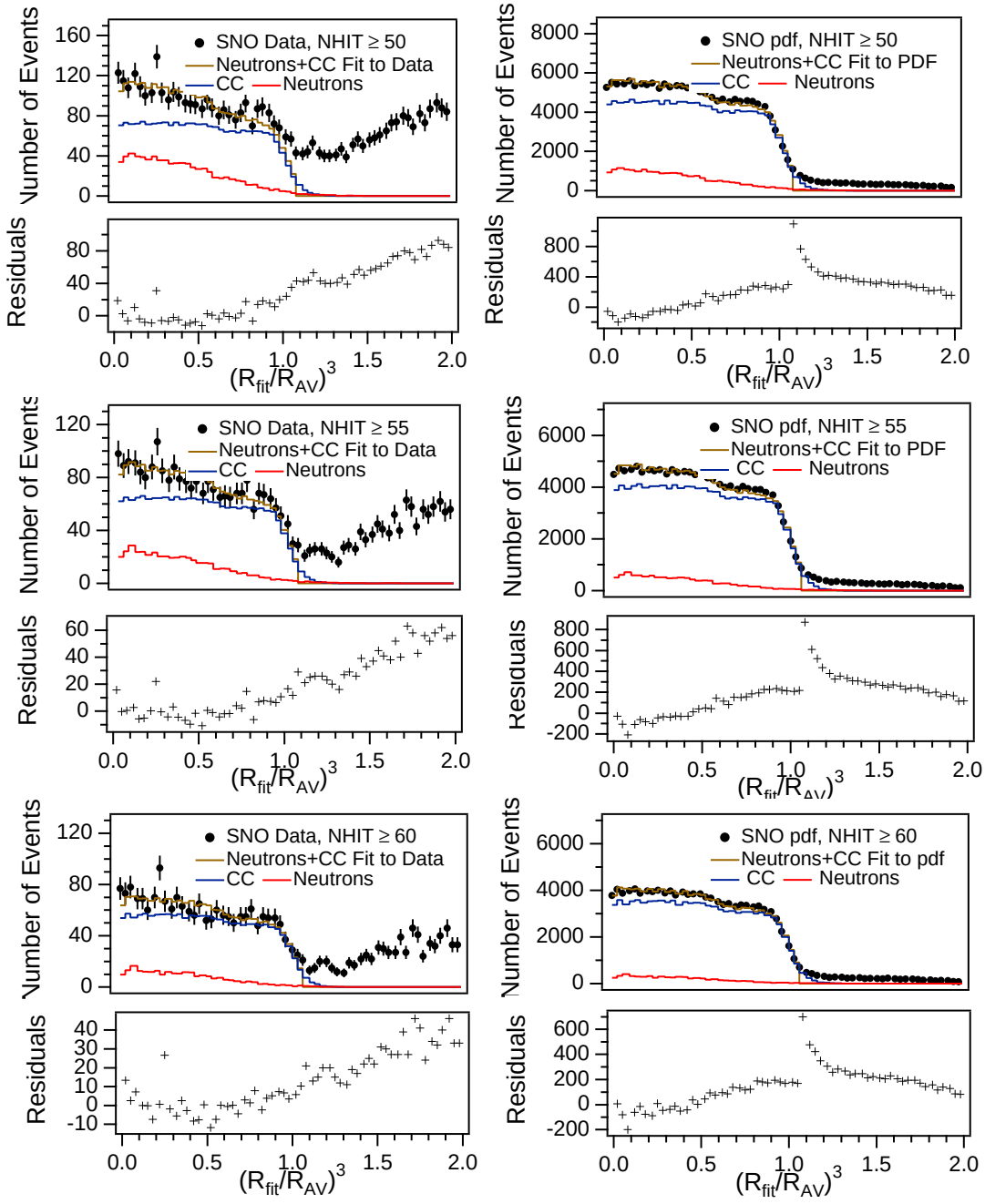

Figure 8.5: Fit of the Probability Distribution Function (PDF) of CC events and neutrons to the radial distribution of raw data for NHIT $\geq$ 50, 55, and 65.

8.1.2 Determining the Position of the Acrylic Vessel From Neutrino Data

As a general verification of the data set and as a test of fitter systematics and fitter pull we can determine the position of the acrylic vessel from the cleaned and reconstructed but otherwise raw data. A Hill equation of the form given below is used to fit the half-point of the radial distribution and to describe the radial fall-off of the reconstructed data near the AV. Using the $(R_{fit}/R_{AV})^3$ distribution of the reconstructed data set the position is determined to within 2%.

$$F(R^3) = A_0 + \frac{(A_1 - A_0)}{1 + (R_{1/2}/R^3)^\beta} \tag{8.11}$$

where A_0 is the coefficient that sets value for F(R) at small R, A_1 sets F(R) value at large R, β sets the rise rate and $R_{1/2}$ is the value of R^3 at which F(R) is at $(A_0 + A_1)/2$.

Some fit results for different NHIT thresholds and fit windows are summarized in Tables 8.4 and 8.5. The NHIT threshold is chosen such that backgrounds do not mask the characteristic radial distribution of charged-current events. The fit results are stable over a wide variety of threshold and fit windows.

The weighted mean of the fit results from Table 8.5 gives

$$\overline{R_{1/2}^{Data}} = \frac{1}{\sum_i (1/\sigma_i)} \times \sum_i (R_{i,1/2}^{Data}/\sigma_i^2) = 1.01 \tag{8.12}$$

Using nothing but the raw data above NHIT ≥ 65 we can determine the position of the AV to about $\sim 2\%$ in R^3 or to about 4 cm in R. The mean of these fits is $(R_{fit}/R_{AV})^3 = 1.01$ with an uncertainty of $\delta(R_{fit}/R_{AV})^3 \approx 0.02$. To summarize, from the radial profile of the candidate event set the position of the acrylic vessel has been determined:

$$R_{AV}^3 = 1.01 \pm 0.02 \tag{8.13}$$

$$R_{AV} = 602 \pm 4 \text{ cm} \tag{8.14}$$

Table 8.4: Half-points $R_{1/2}$ of fits to the R^3_{fit} distribution of the raw data and Monte Carlo simulations for neutrino signals with different NHIT thresholds. The fit window corresponds to $[0.858, 1.188]$ in units of $(R_{fit}/R_{AV})^3$. The choice of fit window is fairly narrow and represents a conservative fit to the half-point.

Threshold	$R^{Data}_{1/2}$	$R^{MC}_{1/2}$
NHIT ≥ 75	0.9741 ± 0.0311	0.9995 ± 0.0028
NHIT ≥ 65	0.9965 ± 0.0166	1.0079 ± 0.0019
NHIT ≥ 55	1.0066 ± 0.0228	1.0072 ± 0.0016

Table 8.5: Half-points $R_{1/2}$ of fits to the R^3_{fit} distribution of the raw data and Monte Carlo simulations for neutrino signals with NHIT ≥ 65.

Fit Range in R^3_{fit}	$R^{Data}_{1/2}$	$R^{MC}_{1/2}$
$[0.726, 1.254]$	1.0155 ± 0.0188	1.0081 ± 0.0024
$[0.759, 1.254]$	1.0086 ± 0.0236	1.0067 ± 0.0021
$[0.792, 1.254]$	1.0191 ± 0.0197	1.0098 ± 0.0016
$[0.825, 1.254]$	1.0086 ± 0.0236	1.0077 ± 0.0020
$[0.858, 1.254]$	0.9924 ± 0.0250	1.0021 ± 0.0019
$[0.759, 1.188]$	1.0091 ± 0.0238	1.0079 ± 0.0020
$[0.759, 1.221]$	1.0086 ± 0.0214	1.0032 ± 0.0021
$[0.759, 1.254]$	1.0109 ± 0.0202	1.0053 ± 0.0023

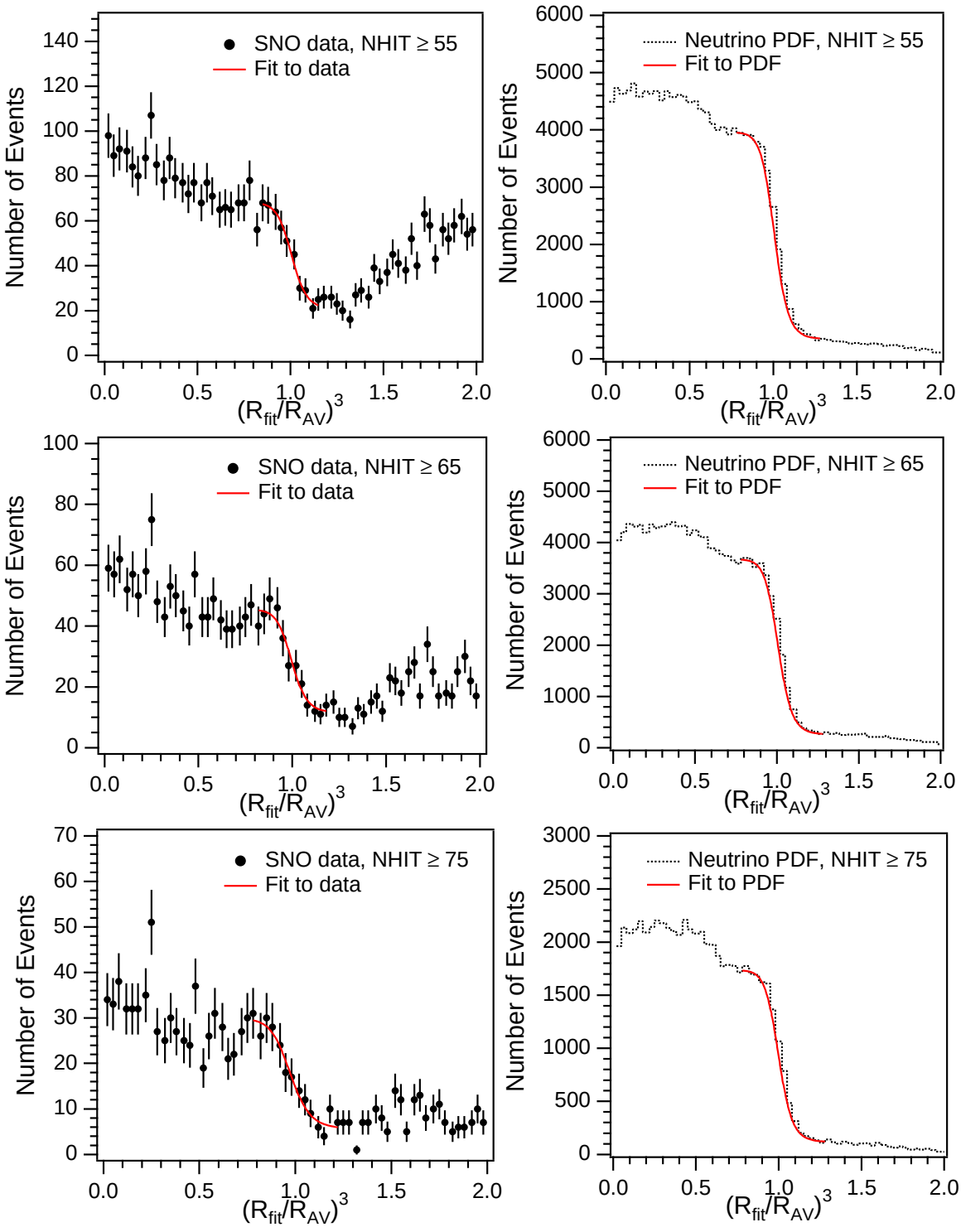

Figure 8.6: Fits to the half-points of the radial distributions of the raw data and the Monte Carlo simulations for different NHIT thresholds.

8.2 Solar Angle Distribution

The solar angle distribution is one of the characteristic detector distributions that can be used to identify solar neutrino interactions.

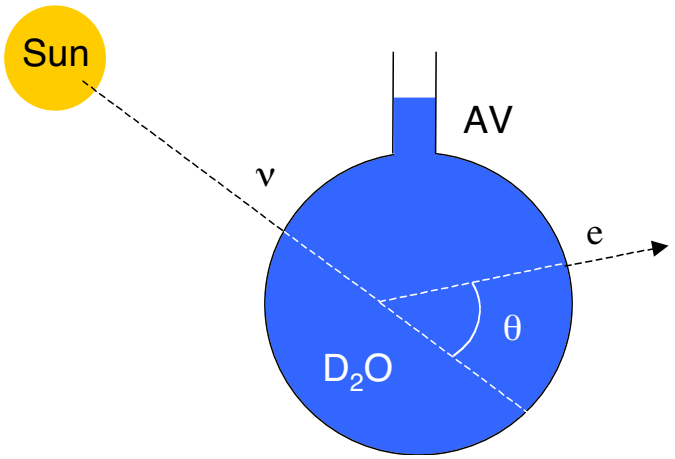

Figure 8.7: The solar angle, $\theta_{\odot}$, of a neutrino interaction describes the angle between the incident neutrino and the outgoing electron.

Elastic Scattering: The elastic scattering reaction provides an unambiguous signature of solar neutrino detection as the initial direction of the electron is sharply peaked away from the Sun. The angular distribution of elastic scattering events can be used to demonstrate that the interactions observed are actually due to neutrinos emitted from the Sun. The half-angle of the cone containing ~90% of the electrons is 14.6 degrees [6]. Being an elastic collision the reaction has no threshold and its differential cross-section follows electroweak theory [174]. The angular distribution of the elastic scattering reaction is forward peaked away from the Sun and can be described approximately by the following form.

$$N^{ES}(\cos\theta_{\odot}) = N_0^{ES} e^{\beta(\cos\theta_{\odot}-1)} \tag{8.15}$$

Charged-Current: The charged-current reaction has a pure Gamow-Teller matrix element resulting in a slightly backward electron angular distribution. The correlation coefficient α is

$\sim -1/3$ in the allowed approximation, appropriate to a pure Gamow-Teller transition with a spin change of 1. With the inclusion of weak magnetism, the correlation becomes slightly larger and weakly energy dependent. This distribution can in principle be used to determine the charged-current interaction rate from the angular distribution and to demonstrate the charged-current events are due to solar neutrinos but the backward asymmetry is rather weak and further weakened by the angular resolution of the direction fit.

$$N^{CC}(\cos\theta_{\odot}) = N_0^{CC}(1 - \alpha\cos\theta_{\odot}) \tag{8.16}$$

Neutral-Current and Backgrounds: Neutral-current interactions and backgrounds are essentially flat in $\cos\theta_{\odot}$. In other words, the solar angle distribution can be used to extract the CC and ES contribution to the data set without knowing anything about the NC part.

$$N^{NC,Bkgd}(\cos\theta_{\odot}) = N^{NC} + N^{Bkgd} \tag{8.17}$$

Figure 8.8 and 8.9 show the Monte Carlo predictions for the solar angle distribution of reconstructed CC, NC, and ES interactions, as well as the solar angle distribution for raw data with NHIT ≥ 45.

One notices that the angular distribution of the data does not fully reproduce the $-1/3$ backward asymmetry predicted in theory. The solar angle distribution of the candidate event set is the convolution of the true angular distribution of the events and the angular resolution of the reconstruction algorithm. This accounts for the differences in the predicted negative angular correlation of CC events and the Monte Carlo simulations shown in Figure 8.8. This convolution is dependent on the energy of an event, NHIT, its original direction, $\cos\theta_{\odot}$, and the underlying distribution, $N(\cos\theta_{\odot})$. It can be written as:

$$N^{Data}(\cos\theta_{\odot}) = F(\cos\theta_{\odot}, NHIT, N(\cos\theta_{\odot})) \tag{8.18}$$

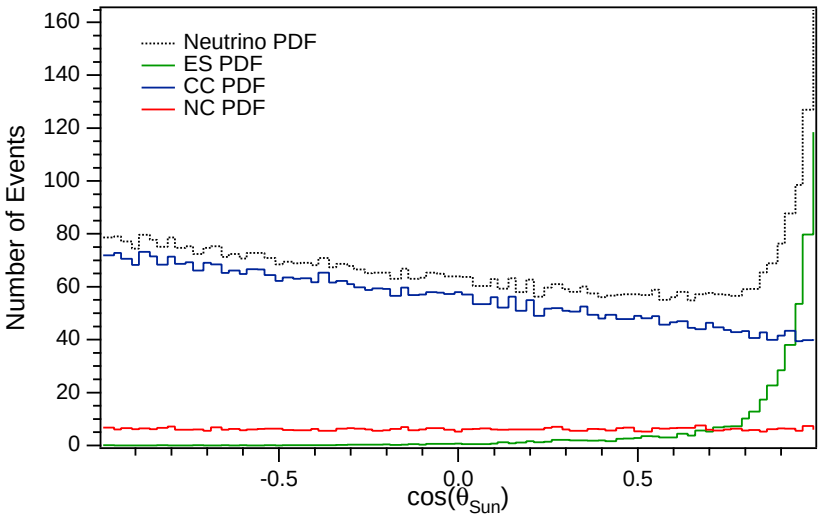

Figure 8.8: Angular distribution of neutrino signals with respect to the direction of the Sun as predicted by Monte Carlo simulations. A radial cut of $R_{fit} \leq 550$ cm, a threshold cut of NHIT ≥ 45, and the high level event cuts (HLC) are applied.

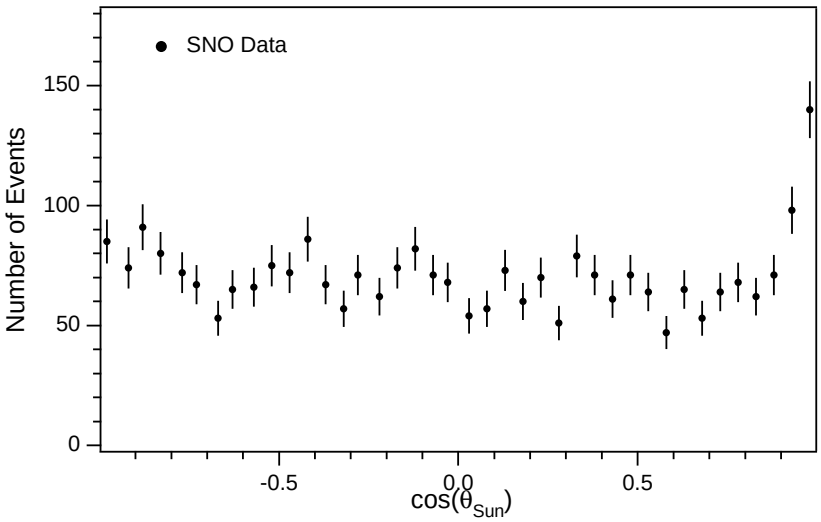

Figure 8.9: Angular distribution of SNO data. The elastic scattering peak is clearly visible. The data also give some indication for the backward angular asymmetry of CC events. A radial cut of $R_{fit} \leq 550$ cm, a threshold cut of NHIT ≥ 45, and the high level event cuts (HLC) are applied.

8.2.1 Determination of Neutrino Interaction Rates from the Characteristic Angular Distribution of Candidate Events

The characteristic angular distribution of events can be used to determine both the magnitude of the charged-current signal as well as the magnitude of the elastic scattering interaction rate. Since instrumental and radioactivity backgrounds are not correlated with the Sun angle it is in principle possible to extract Sun-correlated signals unambiguously. This can be done even if a substantial instrumental, radioactivity, or neutral-current background exists underneath the CC spectrum.The only statistical penalty is the added background. This is the technique used by Kamiokande and Super-Kamiokande to extract the neutrino-electron elastic scattering signal in the presence of a much larger uniform background. It is successful because of the strongly-forward peaked angular distribution of elastic scattering. The presence of an unexpected or poorly determined background introduces a systematic error in the extraction of the charged-current rate based on the radial distribution alone.

Using nothing but the characteristic shape of the elastic-scattering (ES) signal in the solar angle distribution we develop a technique to extract the ES contribution in the data by fitting to the peak amplitude of the ES peak. Fitting the elastic scattering peak in the solar angle distribution of the neutrino data set allows one to extract the elastic-scattering signal with an accuracy of about 12% without performing a full decomposition of the neutrino signals. A parameterization of the solar angle distribution is developed based on SNOMAN Monte Carlo data. This technique is largely insensitive to the systematics of the SNO analysis components as it relies on nothing but the reconstructed event direction with respect to the Sun. The elastic-scattering contribution to the data is determined for various NHIT thresholds and fiducial volumes. We will show that the elastic-scattering signal is constant and consistent with Monte Carlo predictions for a variety of fiducial volumes and NHIT thresholds.

Making additional use of the CC backward asymmetry one can parameterize the solar angle distribution in terms of its contributions from the elastic scattering (ES) and charged-current (CC) interaction and a flat component due to the NC signal and backgrounds. The accuracy of the CC result extracted in this way depends on the theoretical knowledge of

α and the angular resolution of reconstruction. No quantitative statement of the accuracy of α exists but it is likely better than the statistical uncertainties in SNO. At low energies but with the electron still relativistic α is exactly 1/3. At 40 MeV it has risen to about 0.43 due to weak magnetism [153]. Weak magnetism can be calculated via CVC to an accuracy that is probably of the order of 10% or better, which would make the precision in α better than 3%. Forbidden and other recoil-order terms have to be examined. Beacom and Vogel [178] give for the coefficient -0.345. It is more negative than -0.333 because of the weak magnetism contribution. This number is for 10 MeV but it is very flat with energy for neutrinos. The angular distribution predicted by the SNO Monte Carlo code is -0.341 following the prescription by BCK [21] for the neutrino-deuteron cross-section and final state distributions.

8.2.2 Parameterization of the Solar Angle Distribution

The fits to the angular distributions of the three different PDF contributions are parameterized as follows. The functional form of the CC fit function is motivated by the well-known angular distribution of the charged-current interaction. The angular distribution of neutral-current (NC) events is expected to be isotropic. The function describing the angular distribution of elastic scattering events is motivated by fits to Monte Carlo data and based on a parameterization of the SNOMAN PDF's.

$$f_{CC} = CC_0 + CC_1 \cos\theta_\odot \tag{8.19}$$

$$f_{ES} = ES_1 e^{(\alpha \cos\theta_\odot + \beta \cos^4\theta_\odot)} \tag{8.20}$$

$$f_{NC} = NC_0 \tag{8.21}$$

Using this formalism we can then write the fit to the combined PDF consisting of all three interactions as follows:

$$\begin{aligned} f_{PDF} &= (CC_0 + NC_0) + CC_1 \cos\theta_\odot) \quad + ES_1 e^{(\alpha \cos\theta_\odot + \beta \cos^4\theta_\odot)} \\ &= NC_0 + CC_0(1 + \frac{CC_1}{CC_0}\cos\theta_\odot) \quad + ES_1 e^{(\alpha \cos\theta_\odot + \beta \cos^4\theta_\odot))} \end{aligned} \tag{8.22}$$

Or, equivalently:

$$f_{PDF} = PDF_0 + PDF_1(1 + \frac{CC_1}{CC_0}\cos\theta_\odot) + PDF_2 e^{(\alpha\cos\theta_\odot + \beta\cos^4\theta_\odot))} \tag{8.23}$$

with the following equalities:

$$\begin{aligned} PDF_2 &= ES_1 \\ PDF_1 &= CC_0 \\ PDF_0 &= NC_0 \end{aligned}$$

Because of the NHIT dependence of the shape and width of the solar angle peak (Figure 8.10) a NHIT-dependent parameter $\beta(\mathrm{NHIT}_{thresh})$ is used in the fit to the elastic scattering peak. This parameter allows one to fit accurately the solar angle peak for a variety of fiducial volumes and NHIT thresholds. The parameter $\beta(NHIT_{thresh})$ is determined for the PDF distributions with NHIT $\geq$ 45, 55, 65 and linearly interpolated for all NHIT thresholds in between.

$$f_{ES} = ES_1 e^{(\alpha\cos\theta_\odot + \beta(NHIT_{thresh})\cos^4\theta_\odot)} \tag{8.24}$$

$$\tag{8.25}$$

Similarly, the fit to the data can be written as follows, where $\mathrm{CC}_1/\mathrm{CC}_0$, α, and β are determined from Monte Carlo PDF's. The parameters α and β define the functional form of the fit function to the elastic scattering peak.

$$f_{Data} = D_0 + D_1(1 + \frac{CC_1}{CC_0}\cos\theta_\odot) + D_2 e^{(\alpha\cos\theta_\odot + \beta(NHIT_{thresh})\cos^4\theta_\odot))} \tag{8.26}$$

The fit parameters PDF_0, PDF_1, PDF_2, and D_0, D_1, D_2 respectively, are related to the normalization of the ^{8}B flux of solar neutrinos. The contribution of *hep* neutrinos is

negligible in this context. PDF_1 and D_1 are linearly related to the area under the charged-current angular distribution and are therefore a direct measure of the CC interaction rate. The coefficients PDF_2 and D_2 are a measure of the ES rate as they scale with the amplitude of the elastic scattering peak. The amplitude of the elastic scattering peak is defined as follows. ES^{peak}_{PDF} is the amplitude of the PDF as generated in the Monte Carlo. ES^{peak}_{FitPDF} and $ES^{peak}_{FitData}$ are the amplitudes obtained from the fits to the PDF and the neutrino data.

$$\begin{aligned} ES^{peak}_{PDF} &= ES^{peak}_{PDF}|_{\cos\theta_{\odot}=1} \\ ES^{peak}_{FitPDF} &= PDF_2 e^{(\alpha+\beta)} \\ ES^{peak}_{FitData} &= D_2 e^{(\alpha+\beta)} \end{aligned}$$

Taking into account possible systematic biases or inefficiencies in the fit the true amplitude of the elastic scattering peak in the data is then given by:

$$ES^{peak}_{Data} = \frac{ES^{peak}_{PDF}}{ES^{peak}_{FitPDF}}\, ES^{peak}_{FitData} \tag{8.27}$$

$$ES^{peak}_{Data} = \frac{1}{\epsilon_{Fit}}\, ES^{peak}_{FitData} \tag{8.28}$$

The bias of the fit is described by the parameter ϵ_{Fit}.

The livetime-corrected ratios of D_1/PDF_1 and D_2/PDF_2 obtained from fits to the PDF and the data give the relative strengths of the CC and ES signals with respect to the Standard Solar Model (SSM) used in the PDF generation. The NC interaction rate cannot be determined as the isotropic angular distribution of NC events is fully correlated with backgrounds.

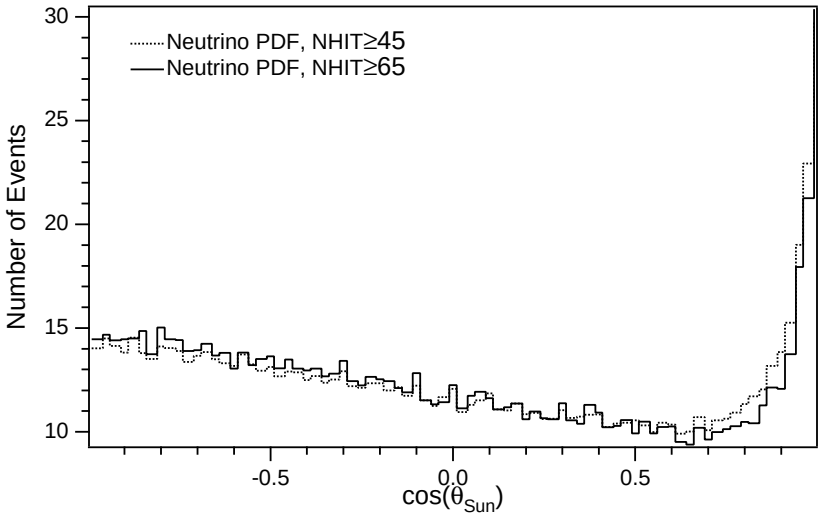

Figure 8.10: NHIT dependence of the probability distribution function (PDF) for the $\cos\theta_{\odot}$distribution of neutrino signals. The distributions are normalized to the same number of total events. A radial cut of $R_{fit} \leq 550$ cm and the high level event cuts (HLC) are applied.

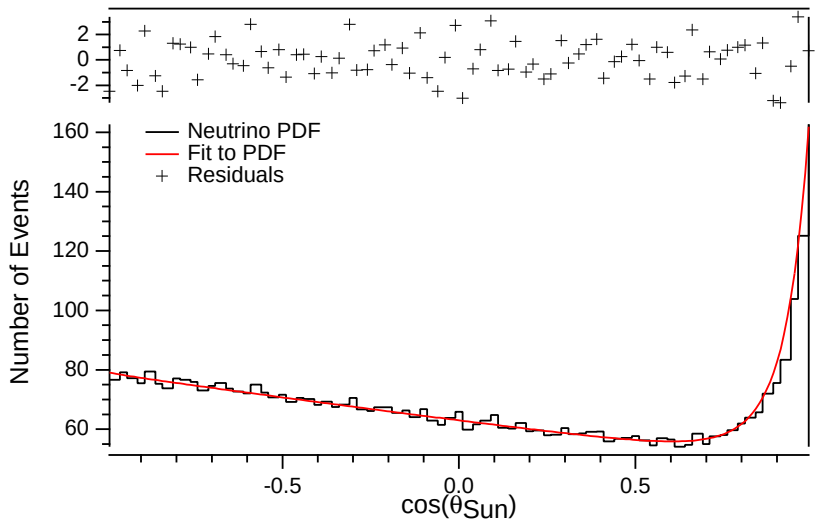

Figure 8.11: Example of a probability distribution function for the $\cos\theta_{\odot}$ distribution of neutrino signals and a parameterized fit function. The excellent agreement between the PDF and the fit function enables us to use the parameterized function instead of the Monte Carlo PDF for all our studies. In this example a threshold cut of NHIT $\geq$ 45, a fiducial volume cut of $R_{fit} \leq$550cm, and the high level event cuts (HLC) are applied.

8.2.3 Determination of Probability Distribution Functions in $\cos\theta_\odot$

The detector response to solar neutrino interactions is simulated using the SNO Monte Carlo code with the inputs described in the previous chapter. From these simulations we derive the probability distribution functions in $\cos\theta_\odot$ for the three types of neutrino interactions: Elastic scattering (ES), the charged-current (CC) reaction, and the neutral-current (NC) interaction.

Using the functional forms given above the solar angle distributions of the individual Monte Carlo PDF's are fitted. Table 8.6 gives the parameters obtained from fits to the individual PDF's with the appropriate reconstruction, NHIT, and high-level cuts. The PDF's were normalized to 1 SSM-yr. The fit results tabulated below are obtained for an NHIT threshold of NHIT $\geq$ 65. The parameter β is specific to this choice. In general, the parameter $\beta(NHIT_{thresh})$ is determined for the PDF distributions with NHIT $\geq$ 45, 55, 65 and linearly interpolated for all NHIT thresholds in between. It can be described by a NHIT-dependent function. The choice of binning does not affect the fit results. In this work, the individual and combined PDF's were binned in equal bins in $\cos\theta_\odot$ between [-1,1]. Improvements are possible by introducing more bins in the region of the elastic scattering peak.

$$\beta(NHIT_{thresh}) = 3.2 + 0.8\frac{(NHIT_{thresh} - 45)}{20} \tag{8.29}$$

Using the values we obtained for the parameterization of the $\cos\theta_\odot$ PDF's we can fit to the angular distribution of the combined PDF's. The results are shown in Table 8.7. These results are stable for different choices of binning.

Table 8.6: Parameterization of the $\cos\theta_{\odot}$ fit function. Fit parameters obtained from the fits to the individual CC, NC, and ES PDF's with NHIT ≥ 65.

Parameter	Fit to PDF 80 Bins	Fit to PDF 40 Bins
NC_0	0.46 ± 0.02	0.91 ± 0.03
CC_0	33.42 ± 0.11	66.85 ± 0.21
CC_1	-9.98 ± 0.20	-19.97 ± 0.37
ES_0	0.16 ± 0.08	0.33 ± 0.20
ES_1	0.098 ± 0.03	0.19 ± 0.10
α	2.64 ± 0.49	2.71 ± 0.75
β	4.04 ± 0.15	4.06 ± 0.23

Table 8.7: Fit parameters obtained from fits to the combined neutrino PDF with NHIT ≥ 65.

Parameter	Fit to PDF 80 Bins	Fit to PDF 40 Bins
PDF_0	2.143 ± 4.45	4.086 ± 8.96
PDF_1	31.928 ± 4.37	64.058 ± 8.79
PDF_2	0.095 ± 0.011	0.198 ± 0.023

8.2.4 Sensitivity of Fit: Signal Correlation, NHIT Dependence, and Fiducial Volume

The sensitivity and systematic bias of this fitting technique are studied using Monte Carlo data sets. There are three primary issues of concern.

- Sensitivity and Bias in Determining the Elastic Scattering Peak:
- Sensitivity to Composition of Data Set: Our ability to extract the CC and ES depends obviously on the backgrounds present in the data. In addition, there are correlation in the extracted ES and CC signals. These signal correlations are studied with Monte Carlo data sets.
- Energy Threshold Dependence: The functional form that describes the elastic scattering peak varies with energy. It is critical to investigate the stability of the ES and CC signal for different NHIT thresholds.
- Fiducial Volume Dependence: As neutrino-electron scattering occurs in both D_2O and H_2O we can investigate the volume dependence of the elastic scattering signal throughout the entire detector. The systematics of the fit to the elastic scattering peak are studied for a wide variety of volumes.

To determine the bias in the fit to the elastic scattering peak we compare the amplitude of the solar angle peak in the Monte Carlo data with the fitted amplitude. We find that the fit routine underestimates systematically the amplitude of the solar angle peak in the PDF by 0.75-2%. The elastic scattering signal obtained from this fit can be corrected for this systematic bias. The average biases in the fit is dependent on NHIT and the fiducial volume:

$$\epsilon_{ES}(NHIT, R_{fit}) = \frac{ES_{fit}(NHIT, R_{fit}))}{ES_{PDF}(NHIT, R_{fit}))} \tag{8.30}$$

The mean fit bias, $\overline{\epsilon_{ES}}$, averaged over all reasonable fiducial volumes for different NHIT thresholds is tabulated in Table 8.8 and shown in Figure 8.12.

The sensitivity of this fitting technique to the neutrino composition of the data can is studied by performing the signal extraction on a Monte Carlo data set with varying amounts of elastic scattering (ES) and charged-current (CC) signal. Figure 8.13 shows the ratio of the fitted signal to the Monte Carlo input signal for CC and ES signal fractions between 10 and 100%. There is essentially no bias in the fitted ES signal for varying amounts of CC. For the CC signal, however, this fitting technique tends to underestimate the CC events contained in the angular distribution of the data. The numerical results from the fit are tabulated in Table 8.9. Based on Monte Carlo data the accuracy with which one can extract the ES signal from the solar angle peak is 9-11% for varying amounts of the CC signal.

Table 8.8: Bias in fitting the elastic scattering peak amplitude.

Threshold	Fit Bias $\overline{\epsilon_{ES}}$
NHIT ≥ 45	0.9925
NHIT ≥ 50	0.9880
NHIT ≥ 55	0.9846
NHIT ≥ 60	0.9841
NHIT ≥ 65	0.9874

Table 8.9: Fit parameters obtained from fits to the combined PDF with varying compositions. Excellent agreement is found between the fitted and predicted contributions for ES and CC. The determination of the isotropic component to the angular distribution is uncertain but always consistent with the Monte Carlo prediction.

Monte Carlo Composition NC / CC / ES	$\frac{PDF_0^{fit}}{PDF_0^{MC}}$	$\frac{PDF_1^{fit}}{PDF_1^{MC}}$	$\frac{PDF_2^{fit}}{PDF_2^{MC}}$
1/1/1	1.000 ± 2.076	1.000 ± 0.137	1.000 ± 0.115
1/0.5/0.5	0.442 ± 0.591	0.500 ± 0.097	0.500 ± 0.082
1/0.36/0.49	0.607 ± 1.278	0.353 ± 0.084	0.489 ± 0.008

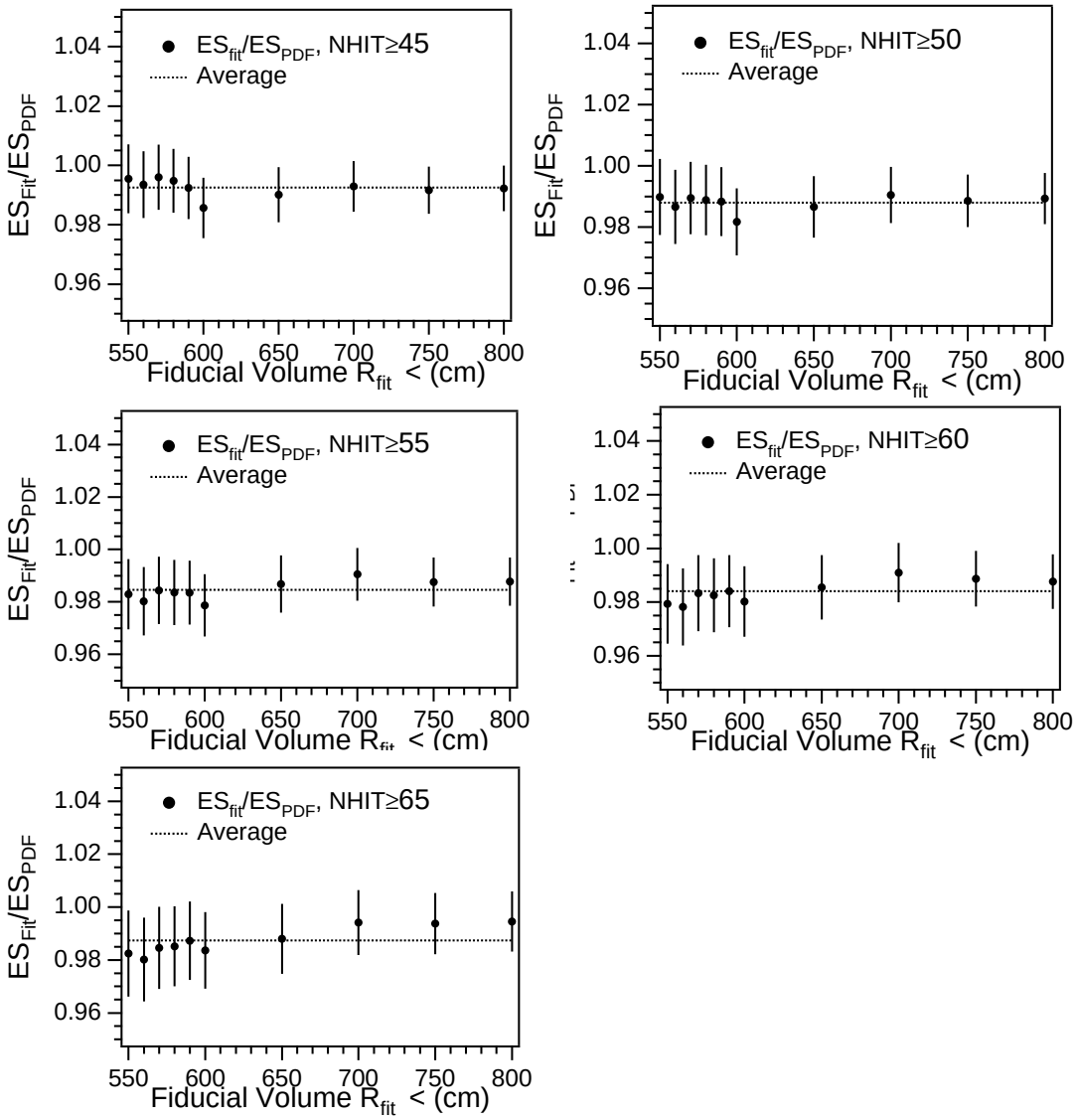

Figure 8.12: Ratio of the fitted amplitude of the ES peak, ES_{fit}, to the ES peak amplitude in the PDF, ES_{PDF}, for different NHIT thresholds.

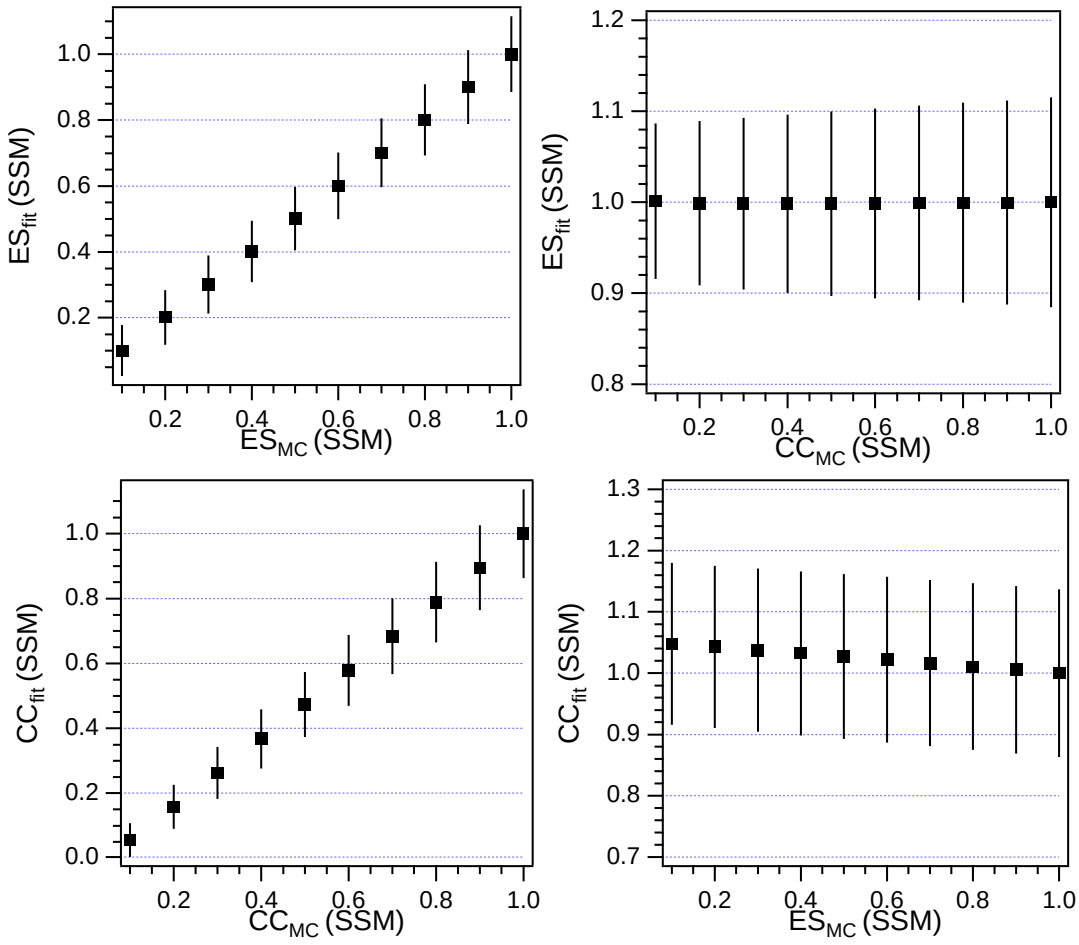

Figure 8.13: Ratio of the fitted CC and ES signals to the input MC input signals for varying amounts of ES and CC.

8.2.5 Determination of the Charged-Current and Elastic Scattering Signal from the Solar Angle Distribution of the Reduced Data Set

The technique developed in the previous sections can be applied to the raw candidate event set. The candidate event set above NHIT $\geq$ 65 and with $R_{fit} \leq 550$ cm is considered. This reduces the isotropic background to the solar angle distribution as well as the isotropic neutron contribution from NC events in the D_2O. The results from the fit are shown in Figure 8.14.

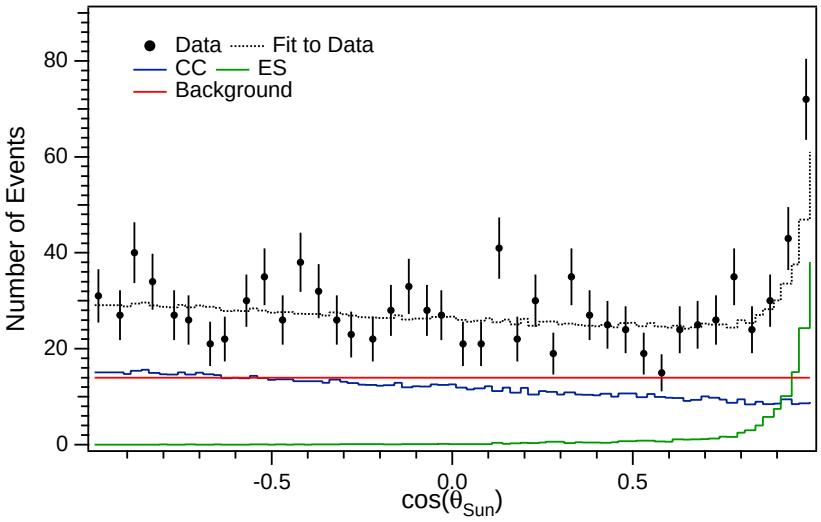

Figure 8.14: Combined fit of the angular distribution of ES and CC events to the data. A radial cut of $R_{fit} \leq 550$ cm, a threshold of NHIT $\geq$ 65, and the high level event cuts (HLC) are applied.

Using nothing but the angular distribution of the candidate event set we obtain the following results in units of the standard solar model prediction by BPB00 [11].

$$[CC]_{\cos\theta_\odot} = 0.360 \pm 0.129 \times \text{SSM} \quad (8.31)$$

$$[ES]_{\cos\theta_\odot} = 0.501 \pm 0.148 \times \text{SSM} \quad (8.32)$$

8.2.6 Neutrino-Electron Elastic Scattering Signal in the D_2O and H_2O

Neutrinos scatter off electrons in D_2O and H_2O. The ES signal is expected to be constant across the acrylic vessel. Using the techniques introduced above we can fit the ES in the solar angle distribution and determine the elastic scattering signal as a function of fiducial volume. The elastic scattering signal is studied for various NHIT thresholds and choices of fiducial volumes in the D_2O and H_2O. In addition to the standard cuts used in the reduction of the raw data set the high-level event cuts (HLC) are applied. We find good agreement across the acrylic vessel.

Figures 8.15 and 8.16 summarize the results of this analysis. The following figures show that the variation of the ES PDF peak amplitude agrees with the fits to the data over a large variety of fiducial volumes. For all energy thresholds considered between NHIT ≥ 45 and 65 the agreement is good within a fiducial volume of $R_{fit} = 600$ cm. At large fiducial volumes, the elastic scattering peak amplitude predicted by the Monte Carlo deviates from the R^3 scaling expected from the D_2O and H_2O target volume because of the PMT concentrator cut-off. This detector effect is predicted by Monte Carlo simulations. The data, however, seems to follow the R^3 scaling more closely. This discrepancy is not fully understood but it may be due to the effects of the optics in the detector region beyond $R = 650 - 700$ cm.

Figure 8.16 shows the fitted number of events in the solar angle peak for various NHIT thresholds and radial shells in the unified data set. It shows the behavior of the fitted ES signal in radial shells of equal width and hence allow us to evaluate possible systematic effects, such as optics, as a function of radius. Good agreement is seen between the fitted ES amplitude from data and Monte Carlo out to the AV. These plots also show the fitted amplitudes of the isotropic and charged-current component in $\cos\theta_\odot$ (NC+CC for PDF and NC+CC+background for data). We find that the characteristic fall-off of the CC+NC component is clearly visible in the PDF while the fitted NC+CC+Background amplitude in the data shows the contribution of backgrounds at low threshold.

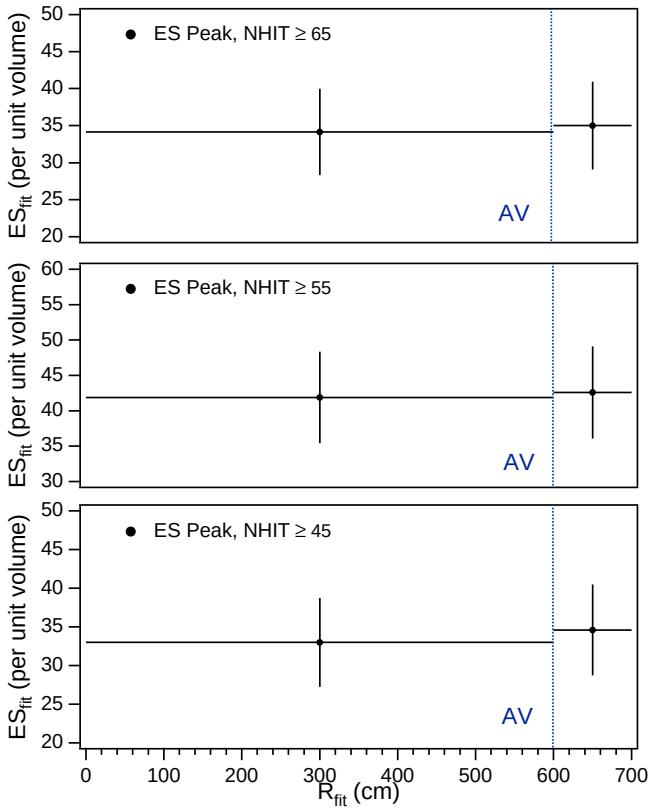

Figure 8.15: Elastic scattering signal inside and outside the AV for $0 \leq R_{fit} \leq 600$ cm and $600 \leq R_{fit} \leq 700$ cm as determined by a fit to the elastic scattering peak. The ES rates are normalized to unit volume. Excellent agreement is found for the ES rates in the D_2O and H_2O within the limited statistics of the data.

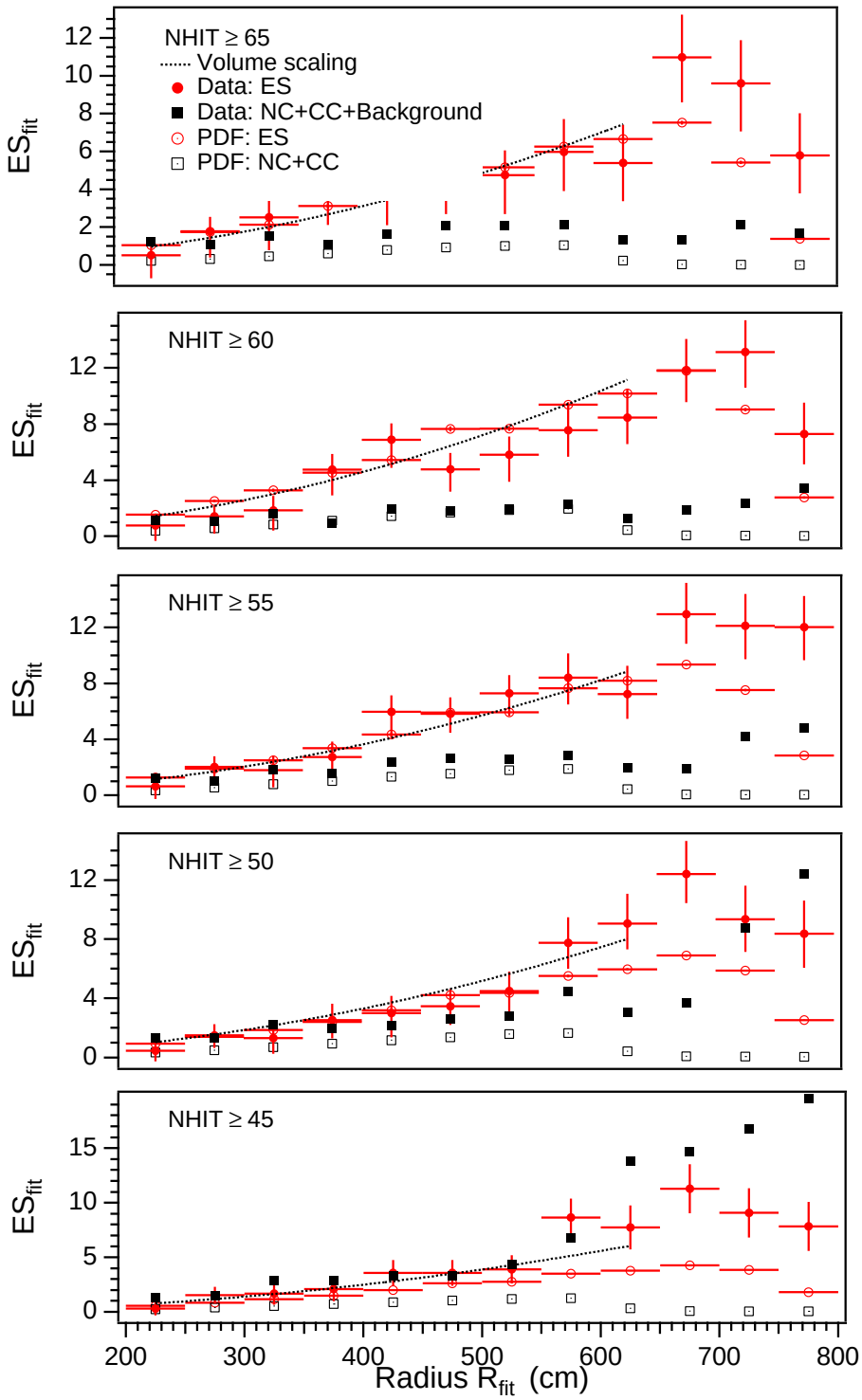

Figure 8.16: Fitted ES peak amplitude for different radial shells with NHIT $\geq 45 - 65$ in the unified data set. In this representation, the predicted volume scaling of ES events goes as R^2.

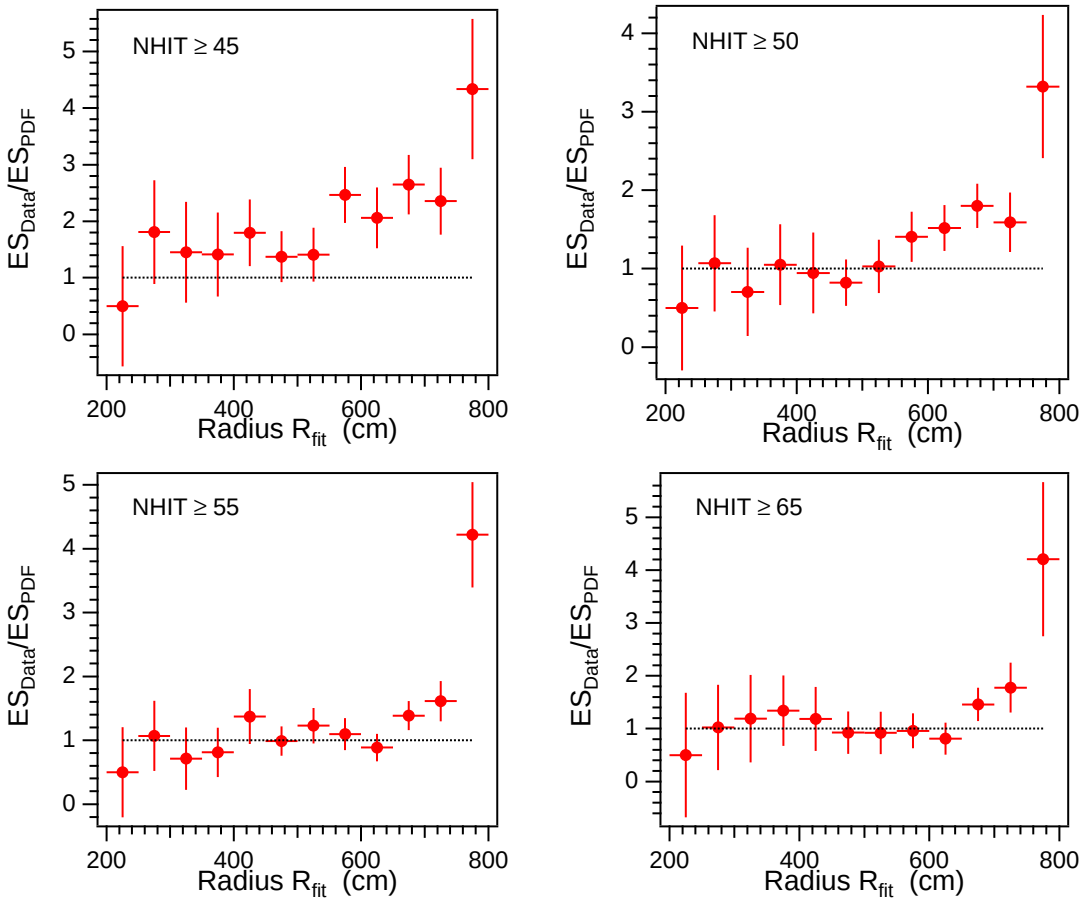

Figure 8.17: Ratio of the ES peak in the data to the PDF for different NHIT thresholds. The PDF is scaled with the flux prediction of $0.5 \times SSM$. For NHIT $\geq$ 65 the deviation from unity at large radii is likely due optical effects that are modeled incorrectly in the Monte Carlo simulations. For NHIT $\geq$ 45, backgrounds in the light water region contribute to the fitted amplitude of the elastic scattering signal at large radii.

8.2.7 Low-Energy Neutrino Events: Observing Solar Neutrinos at Energies below 4 MeV at the Sudbury Neutrino Observatory

The neutrino-electron elastic scattering is very directional, even at low energies. Investigating the characteristic $\cos\theta_\odot$ distribution of the SNO data set at low NHIT we can find indication for solar neutrinos at energies below 4 MeV. Because of the limited statistics of elastic scattering events in SNO the possibilities of quantitative studies are limited. As an analysis of the elastic scattering peak is based on only 2-3 bins near $\cos\theta_\odot = 1$ one may argue that these data points are statistical fluctuations.

Alternatively, we can demonstrate the backward angular correlation of events with $\cos\theta_\odot < 0.75$. No backward asymmetry is expected for low-energy backgrounds or events other than CC neutrino interactions. A weighted straight line fit tests the hypothesis of no angular backward asymmetry. Significant deviations from horizontal are an indication of low energy solar neutrino events.

$$N(\cos\theta_\odot) = N_0(1 + \alpha\cos\theta_\odot) \tag{8.33}$$

Figure 8.19 shows the $\cos\theta_\odot$ distribution of the neutrino data set for NHIT thresholds between $30 \leq NHIT \leq 45$ for a fiducial volume with $R_{fit} \leq 500$ cm. Most sensitivity can be obtained by selecting a fiducial volume in the central volume of the detector. In this region of the detector the backgrounds that underlie the $\cos\theta_\odot$ distribution and can mask the ES signal are lowest. We find evidence for a peak at $\cos\theta_\odot = 1$ in the $\cos\theta_\odot$ distribution and, by fitting the data for $\cos\theta_\odot < 0.75$, we observe a distinct backward asymmetry of the data set. The results of this fit are tabulated in Table 8.10.

In conclusion, based on the angular distribution of events with $\cos\theta_\odot < 0.75$ and evidence for an elastic scattering peak at $\cos\theta_\odot = 1$ we find evidence for solar neutrino interactions at NHIT ≥ 35. This threshold corresponds roughly to an energy threshold of ~ 3.8 MeV.

Table 8.10: Fit results for the angular correlation coefficient, α, of charged-current events. The angular distribution of events with $\cos\theta_{\odot} \leq 0.625$ is significantly backwards above NHIT ≥ 35 and in agreement with Monte Carlo above NHIT ≥ 38.

Threshold	Fiducial Volume	α_{CC}^{Data}	α_{CC}^{MC}
$NHIT \geq 30$	$R_{fit} \leq 500$	-0.096 ± 0.001	-0.235
$NHIT \geq 32$	$R_{fit} \leq 500$	-0.236 ± 0.001	-0.235
$NHIT \geq 35$	$R_{fit} \leq 500$	-0.290 ± 0.001	-0.226
$NHIT \geq 38$	$R_{fit} \leq 500$	-0.275 ± 0.002	-0.244
$NHIT \geq 40$	$R_{fit} \leq 500$	-0.271 ± 0.002	-0.249
$NHIT \geq 45$	$R_{fit} \leq 500$	-0.268 ± 0.001	-0.255

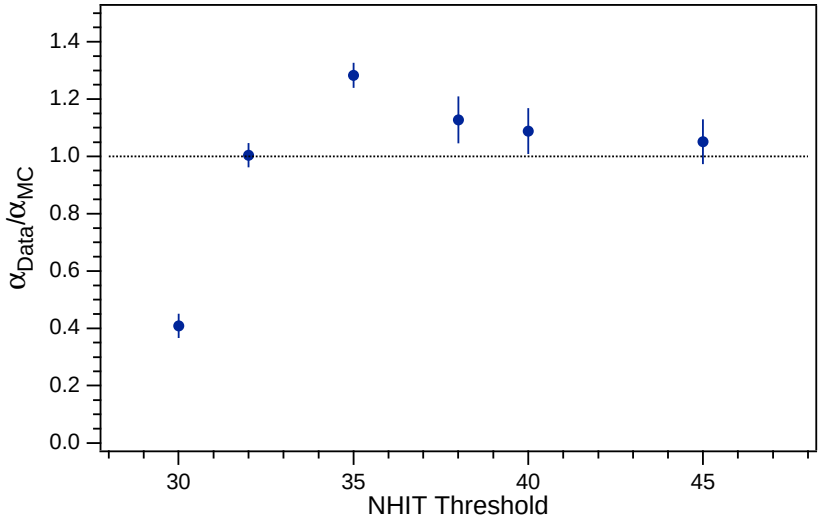

Figure 8.18: Angular distribution of events with $\cos\theta_{\odot} \leq 0.625$ normalized to Monte Carlo predictions for different NHIT thresholds. A radial cut of $R_{fit} \leq 500$ and the high-level event cuts (HLC) are applied.

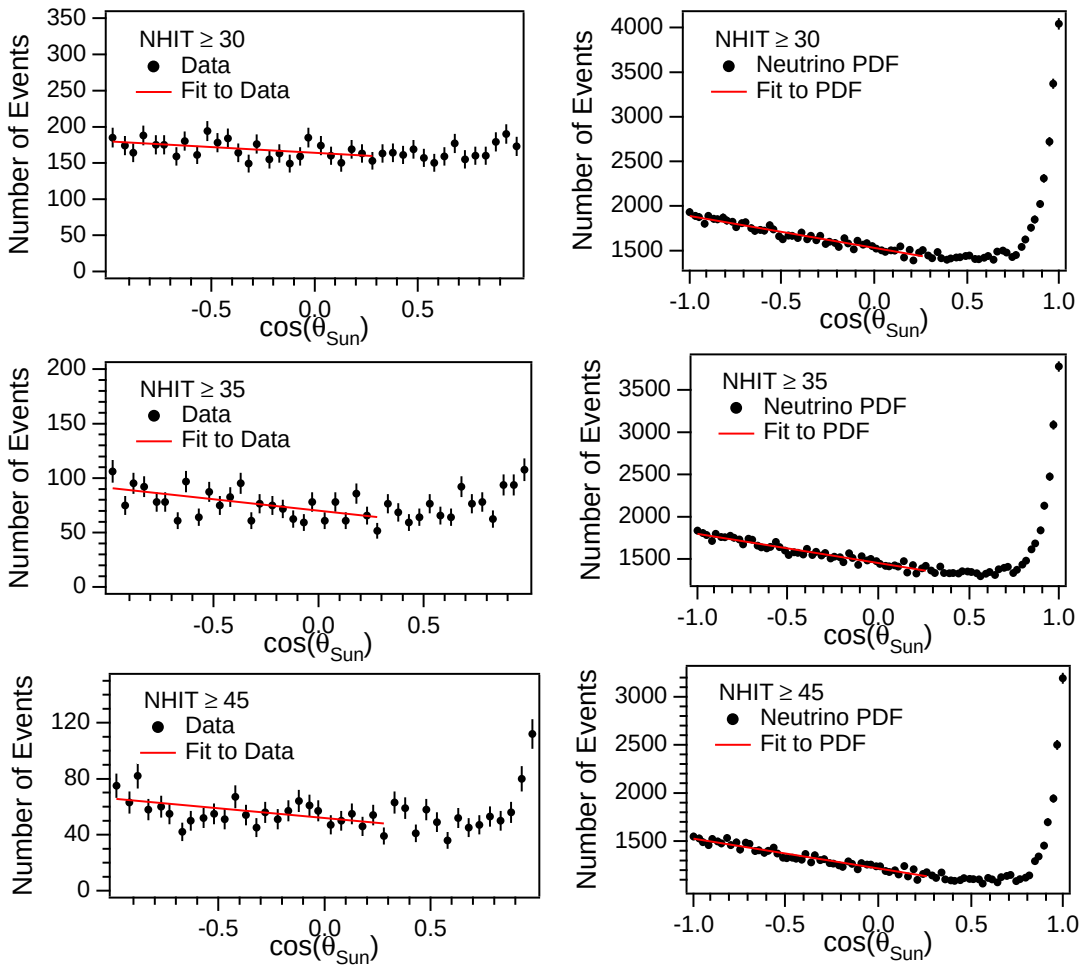

Figure 8.19: Fits to the angular distribution of data (left) and Monte Carlo events (right) with $\cos\theta_{\odot} \leq 0.625$ for different NHIT thresholds. A radial cut of $R_{fit} \leq 500$ and the high-level event cuts (HLC) are applied.

8.3 Event Direction: Inward and Outward Going Events

The parameter $\vec{u}.\vec{r}$ describes the event direction with respect to the radial vector of the reconstructed event. Distributions in $\vec{u}.\vec{r}$ are used to describe the asymmetry between the number of inward and outward going events. It is interesting to consider the $\vec{u}.\vec{r}$ distributions of both neutrino signals and backgrounds in the SNO detector. Charged-current and elastic scattering neutrino interactions in the central D_2O volume of the detector are expected to have a random distribution in $\vec{u}.\vec{r}$. In the spherical approximation of the detector there is no preferred direction for Čerenkov electrons produced in the CC reaction or in the neutrino-electron elastic scattering. Interestingly, Monte Carlo simulations indicate that the capture γ's from the neutral-current interactions appear to be predominantly outward going. Figure 8.20 shows the definition of the $\vec{u}.\vec{r}$ parameter and Figure 8.21 the Monte Carlo distributions of CC, ES, and NC events in $\vec{u}.\vec{r}$.

The tilt in the NC is due to the fact that γ's are produced at the point of capture, and then travel away from that point isotropically. On average, more γ's convert pointing toward the photomultipliers than pointing inwards. While the $\vec{u}.\vec{r}$ distribution is not yet used in the separation of neutrino signals the difference between CC and NC is likely to be as powerful a means of discriminating NC and CC as is the radial distribution. In addition, it is possible to make use of the inward going nature of backgrounds from the outer region of the detector, such as PMT $\beta - \gamma$'s to further discriminate the background contribution to the neutrino signal in the central volume of the SNO detector.

Figure 8.22 shows the $\vec{u}.\vec{r}$ distribution of the SNO data set for various fiducial volumes and NHIT thresholds. The contribution of inward-going background events is clearly visible for low NHIT thresholds.

In summary, the $\vec{u}.\vec{r}$ distribution provides further separation of the NC signal from other neutrino signals as well as discrimination of backgrounds. This parameter is not yet used in the current analysis presented in this thesis.

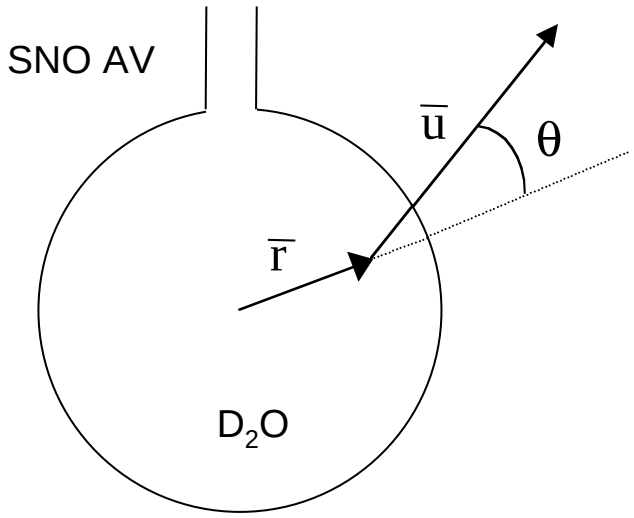

Figure 8.20: Definition of $\vec{u}.\vec{r}$.

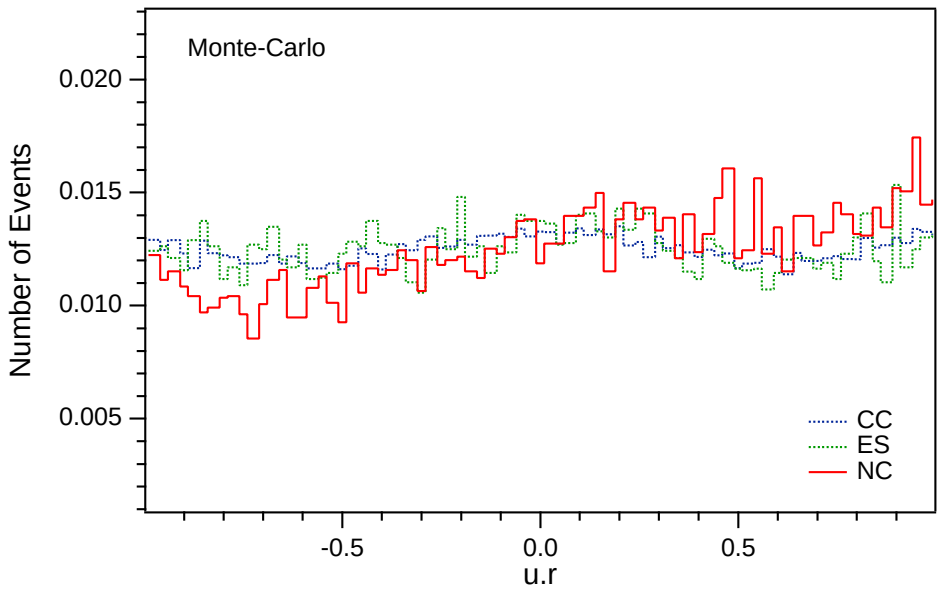

Figure 8.21: $\vec{u}.\vec{r}$ distribution of NC, CC, and ES Monte Carlo events. A threshold of NHIT ≥ 45 and a radial cut of $R_{fit} \leq 600$ cm is applied.

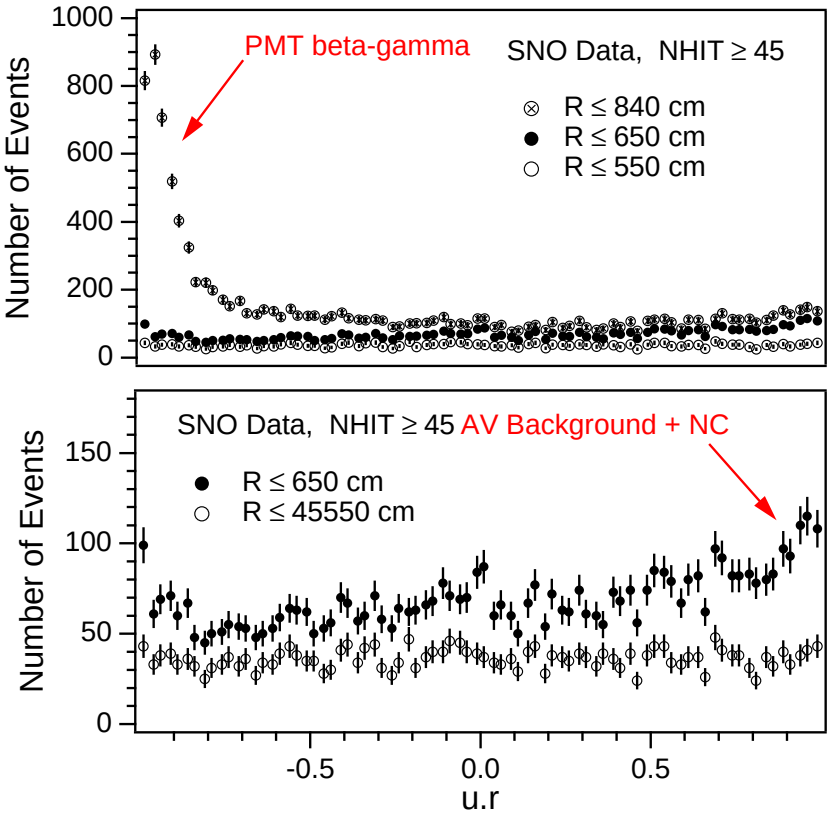

Figure 8.22: $\vec{u}.\vec{r}$ distribution of SNO data for various fiducial volumes and NHIT thresholds. The PMT $\beta - \gamma$ background as well as the AV and NC contribution are clearly visible.

8.4 NHIT and Energy Spectrum

The last of the three characteristic event distributions used is the energy or NHIT spectrum of events. As for the radial and the angular distribution the unique characteristics of the three different types of neutrino interaction with deuterium determine the characteristic shape of the energy spectrum.

Charged-Current: Although strictly referring to the class of weak interaction involving the $W^{\pm}$ the term charged-current interaction (CC) is used in SNO to refer to the breakup of deuterium through electron neutrinos: $p+p+e^{-}$ −1.44 MeV. The protons emerge generally with little energy from the interaction while the electron is emitted with most of the energy of the neutrino minus the Q-value of 1.44 MeV. The yield of Čerenkov photons and the consequent number of PMT hits is closely linear with the electrons' initial energy so long as it is well above the Čerenkov threshold. The charged-current interaction can be used to measure the ν_e spectrum as well as the integral flux of ν_e . The electron neutrinos detected in SNO come from the ^{8}B reaction and the very rare *hep* process. The energy spectrum of the Čerenkov electrons produced in the CC reaction exhibits an energy spectrum that is characteristic of β-decay, with an endpoint energy of $\sim$ 15 MeV.

Neutral-Current: The neutral-current interaction refers to the neutrino-induced breakup of the deuteron. This interaction is equally sensitive to all of the three weak neutrino flavors and so the measurement determines the total solar neutrino flux irrespective of neutrino oscillations involving active flavors. The detection of the neutral-current interaction depends upon the capture of the final-state neutron. After thermalization in the heavy water the neutrons capture on deuterium and emit a characteristic γ signal with an energy of E_γ = 6.25 MeV. The energy spectrum of neutral-current interactions is peaked at this energy with a distribution and width determined by the detector response.

Elastic Scattering: The elastic-scattering of neutrinos is determined by the kinematics of the scattering. The differential cross-section follows electroweak theory [174].

$$\frac{d\sigma}{dE_e} = \frac{2G^2 m_e}{\pi}\left[g_L^2 + g_R^2\left(1-\frac{T_e}{E_\nu}\right)^2 - g_L g_R\left(\frac{m_e\, T_e}{E_\nu^2}\right)\right] \tag{8.34}$$

where $g_L = (\pm\frac{1}{2} + sin^2\theta_W)$ and $g_R = sin^2\theta_W$. The upper sign applies to ν_e scattering and the lower to ν_μ scattering. The cross-section for electron neutrinos is approximately a factor of 7 larger than that for the other weak flavors as the electron flavor has a $W^{\pm}$ channel open to it as well as the Z^0 channel available to all three neutrino types. The cross-section for electron scattering is approximately two orders of magnitude smaller than those of the two reactions on deuterium but it is somewhat compensated for by the fact that there are 5 times as many electrons as deuterons in the D_2O molecule and that electrons are also available in the light water.

Table 8.11 summarizes some of the characteristics of the neutrino interactions in the SNO detector. The data and Monte Carlo predictions for the NHIT spectra of neutrino interactions are shown in Figures 8.23 and 8.24.

Table 8.11: Neutrino interactions in the SNO detector.

Channel	Reaction	Q-Value	σ at ~10 MeV (10^{-42} cm^2)
CC	$\nu_e + d \rightarrow p + p + e^-$	-1.44 MeV	2.7
NC	$\nu_x + d \rightarrow p + n + \nu_x$	-2.22 MeV	1.1
ES	$\nu_x + e^- \rightarrow \nu_x + e^-$	0	0.092

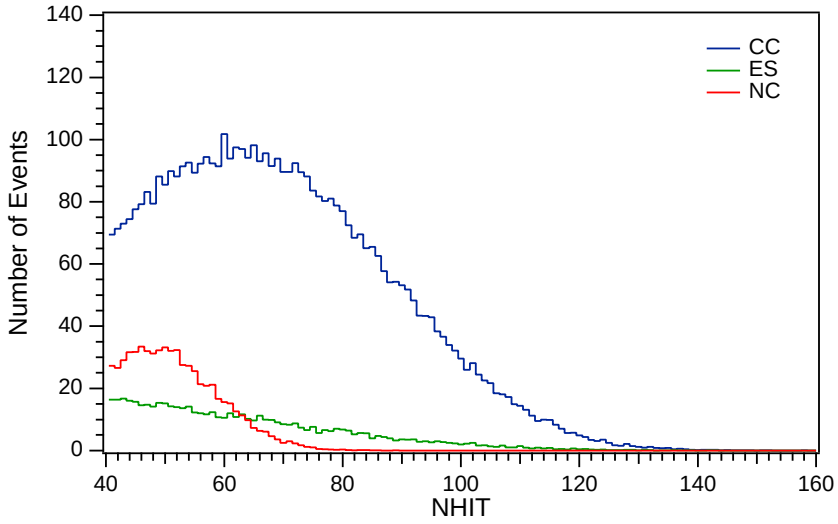

Figure 8.23: NHIT spectrum of Monte Carlo events in the SNO detector. The charged-current spectrum has a rapidly changing shape that makes SNO ideal for the study of the shape of the CC spectrum. The neutral-current spectrum shows a characteristic peak centered at the γ-energy of neutron capture on deuterium. The elastic-scattering signal in SNO is small and has a relatively flat energy spectrum. A radial cut of $R_{fit} \leq 550$ cm, a threshold cut of NHIT ≥ 40, and the high-level event cuts (HLC) are applied.

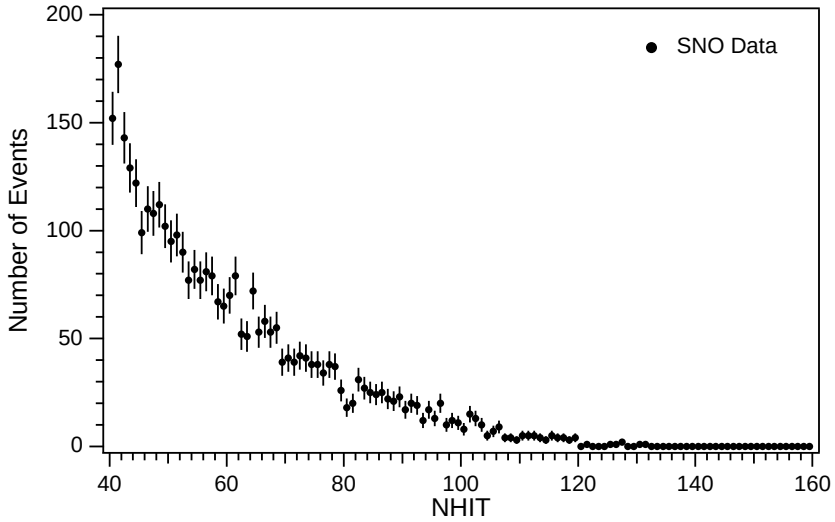

Figure 8.24: NHIT spectrum of the reduced but otherwise raw candidate event set in SNO. A radial cut of $R_{fit} \leq 550$ cm, a threshold cut of NHIT ≥ 40, and the high-level event cuts (HLC) are applied.

8.4.1 Volume- and Time-Dependence of the SNO NHIT Spectrum

Studies of the SNO NHIT spectrum of the reduced but otherwise raw data set show a dip at NHIT $= 80 - 82$, that is a reduced count rate for particular choices of fiducial volume. Figure 8.25 shows the SNO NHIT spectra above NHIT ≥ 65 for different choices of fiducial volume. We find that this spectral feature at NHIT $= 80 - 82$ is most pronounced for data reconstructed within a radius of $R_{fit} \leq 550$ cm from the center of the detector. It is possible that this spectral feature is only a fluctuation in the data set for a particular choice of fiducial volume, reconstruction, and high-level event-quality cuts. In this section we study the volume- and time-dependence of the raw SNO NHIT spectrum and investigate possible systematic effects.

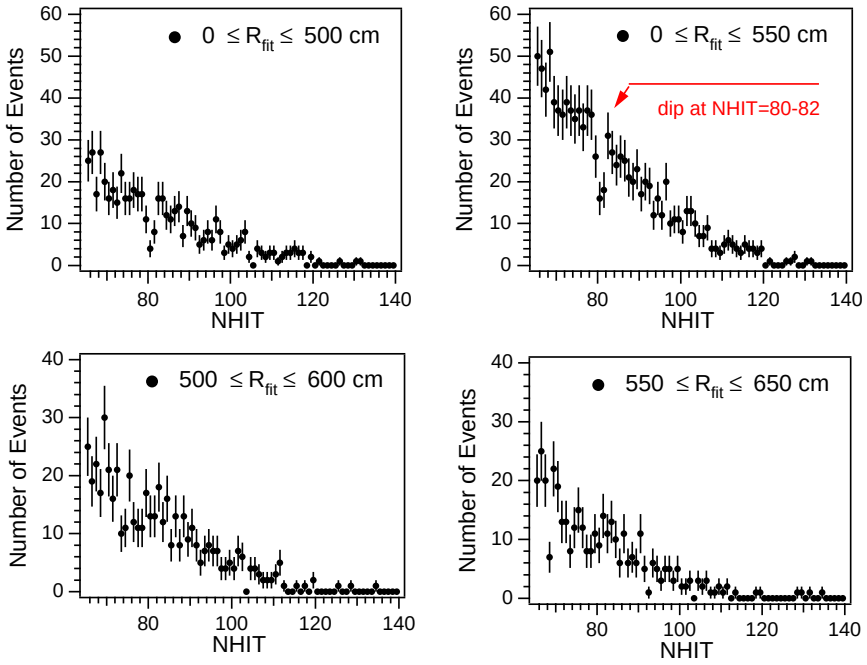

Figure 8.25: Fiducial volume dependence of the dip at NHIT $= 82$ in the SNO Spectrum. The high-level event-quality cuts (HLC) have been applied. It appears that the dip in the spectrum comes from data collected in the central fiducial volume of $R_{fit} \leq 550$ cm (top panels). This feature does not appear in the spectrum of data from the outer regions of the detector (bottom panels).

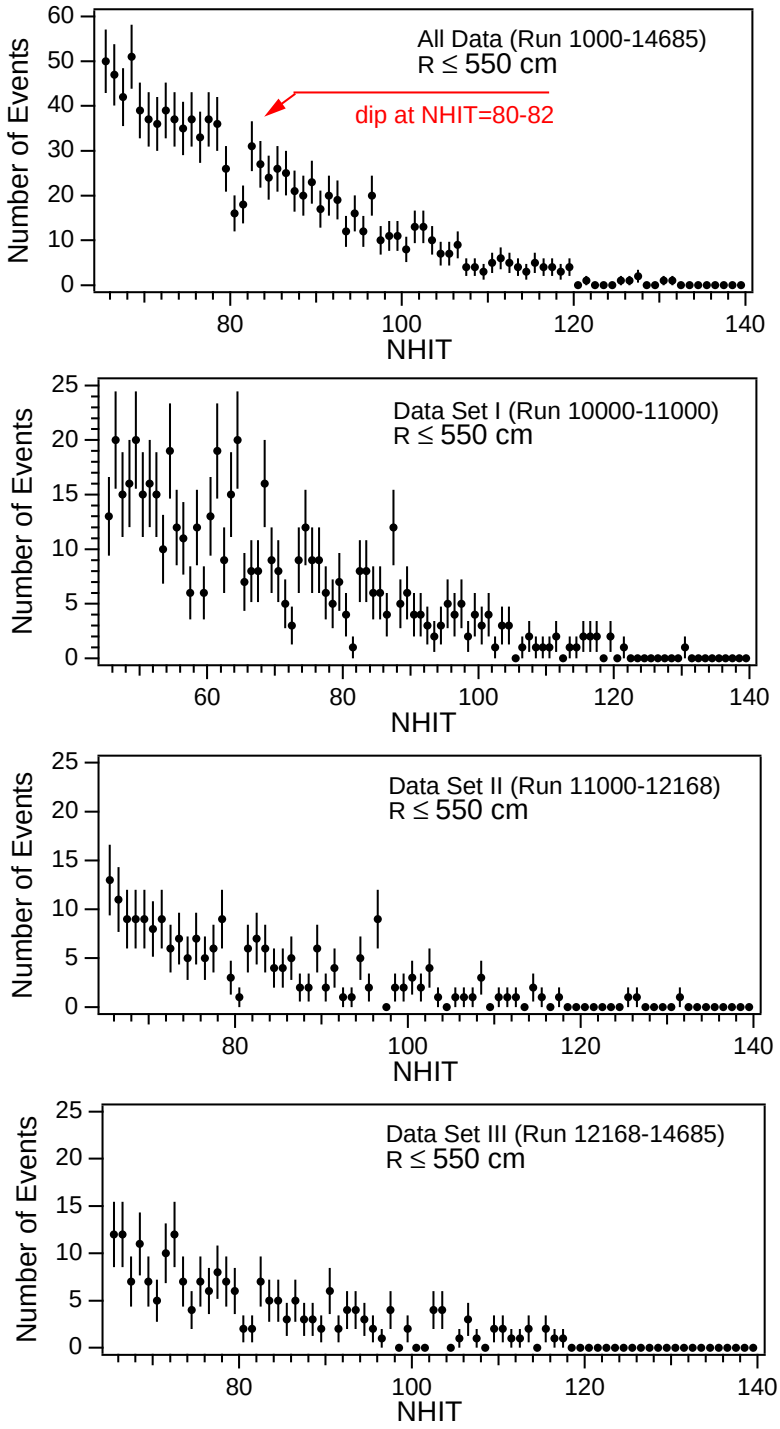

Figure 8.26: Time dependence of the dip in the SNO NHIT spectrum at NHIT $= 80 - 82$. The event count is found to be low in all three data sets I, II, and III.

Possible time variations of the dip at NHIT $= 80 - 82$ over the period of data taking are studied by comparing three different data sets (I, II, III) corresponding to roughly the same livetime over a period of 15 months. Within the statistical limitations of the data set the event count at NHIT $= 80 - 82$ is found to be low in all three data sets. As a result, we conclude that there are no significant long-term, temporal variations in this spectral feature.

In summary, the fiducial volume dependence of this dip indicates that this spectral feature is indeed just a fluctuation in the data set. If this dip in the SNO spectrum were due to an instrumental effect or a new physics effect, such as [23], we would expect to see the same spectral feature in all data from the various detector regions. Transient effects with time scales of the order of weeks or months cannot explain this effect either as there is no significant variation in the three data sets (I, II, III) defined above. Based on the data set under consideration we conclude that there are no obvious systematics effects that affect the shape of the SNO NHIT spectrum.

8.4.2 ^8B Endpoint Fit: Simultaneous Determination of the Energy Scale and Normalization of the ^8B Charged-Current Spectrum:

The charged-current energy spectrum is a β-spectrum with an endpoint energy of ~ 15 MeV. Making use of the characteristic shape of a β-spectrum we can determine the normalization of the CC interaction rate as well as the energy scale from the NHIT spectrum of the raw data. This has two advantages.

1. Calibration source-independent verification of energy scale: Using nothing but the raw data we determine an energy scale without use of any calibration devices. This provides an important verification of the energy response and scale derived in Chapter 6 from ^{16}N calibration data. This technique may also provide an approach to reducing the uncertainty in the CC flux measurement. For a "flux-above-threshold" measurement the energy scale uncertainty turns out to be the single dominant systematic.

2. Measurement of charged-current rate from ^{8}B Spectrum: The NHIT spectrum allows us to determine the CC interaction rate. This measurement of the CC interaction rate is independent of the specific energy threshold of the data set as long as there are no significant contributions from backgrounds or NC events that alter the characteristic spectral shape.

Due to backgrounds SNO cannot measure the entire ^{8}B spectrum. While data is taken at a hardware threshold of $\sim$ 2 MeV the effective analysis threshold is about 5 MeV. Low-energy backgrounds in the D_2O, AV, H_2O, and from the photomultipliers mask the neutrino signal in the low-energy part of the spectrum. Hence only part of the CC spectrum is available for the determination of the CC interaction rate and the solar flux of ν_e. One approach is to determine the number of events above a fixed energy threshold and relate this measurement to the total flux of ν_e.

$$\Phi = \int_0^\infty S(N,E)dE = N\int_0^\infty S(E)dE \tag{8.35}$$

The CC flux derived from this type of "flux-above threshold" analysis is very sensitive to errors in the energy scale. The uncertainty on the threshold propagates directly into the flux measurement. This error is the limiting systematic of the CC measurement in SNO due

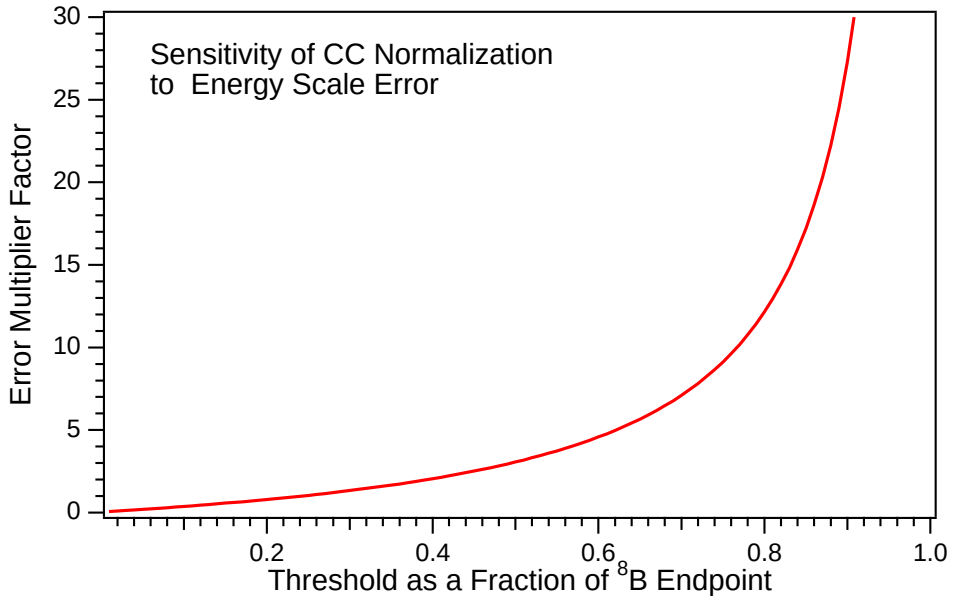

Figure 8.27: Error in the measured charged-current flux due to uncertainties in the energy threshold and scale.

to the rapidly varying CC spectrum. Also, in this analysis approach the CC normalization is ill-defined at the endpoint. Figure 8.27 illustrates how the measurement of the CC rate in SNO depends critically on the energy scale uncertainty.

In the flux-above-threshold analysis, the fractional change in flux is determined by varying the energy scale, $\Delta E \rightarrow \Delta\alpha E$ and the variations in the fitted number of events in the SNO signal extraction, ΔC. The fractional error from the energy scale and from the number of extracted events are propagated into flux changes.

$$(\Delta\phi)^2 = (\frac{d\phi}{dC})^2(\delta C)^2 + (\frac{d\phi}{d\alpha})^2(\delta\alpha)^2 + 2\rho_{\alpha C}(\frac{d\phi}{dC})(\frac{d\phi}{d\alpha})(\Delta\alpha) \tag{8.36}$$

However, the normalization of a spectrum and its energy scale are constrained by an integral equation. The integral of the spectrum is constrained to be the same under change of variables.

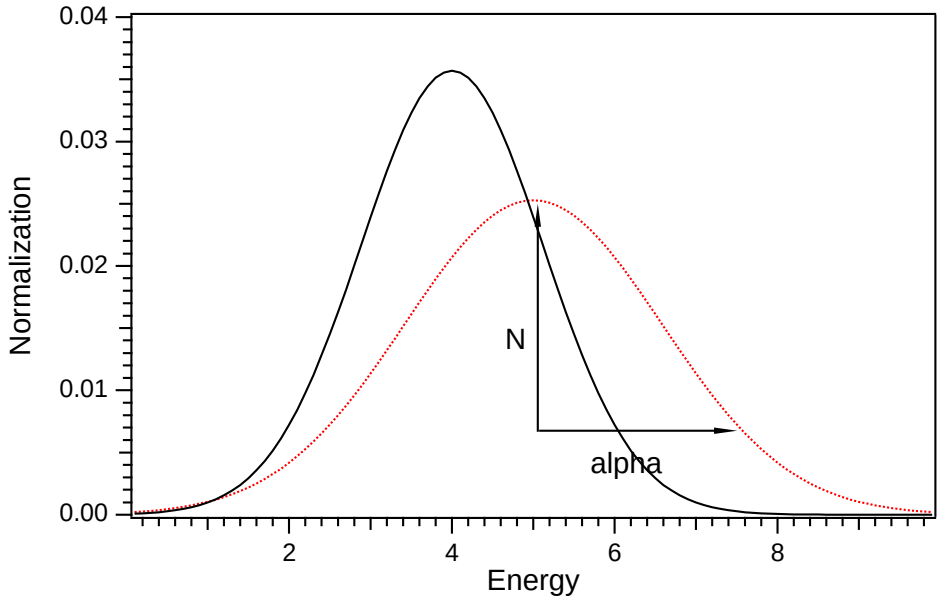

Figure 8.28: Illustration of the relation of energy scale and normalization in the determination of the charged-current interaction rate.

$$\int_0^\infty S(E)dE = \int_0^\infty S(\alpha E)\alpha dE = 1 \tag{8.37}$$

The parameter α describe the energy scale change. The errors on α and N are correlated. $\Delta\alpha \rightarrow \Delta N$. As illustrated in Figure 8.28, a change in energy scale results in an effective change of the normalization of the spectrum. Hence a systematic error in the energy reflects in the normalization of the CC spectrum.

The determination of our energy scale uncertainty comes from a variety of calibration devices that probe the SNO detector response over the energy range of the ^{8}B spectrum. At present SNO has good energy calibration points at the ^{16}N line at 6.13 MeV, the thermal neutron capture line at 6.25 MeV, and beyond the ^{8}B endpoint at 19.8 MeV from the pT source. In addition, calibration data from the ^{8}Li source allows calibration from $\sim 5 - 13$ MeV.

Instead of using a fixed energy threshold and propagating the energy scale uncertainty we

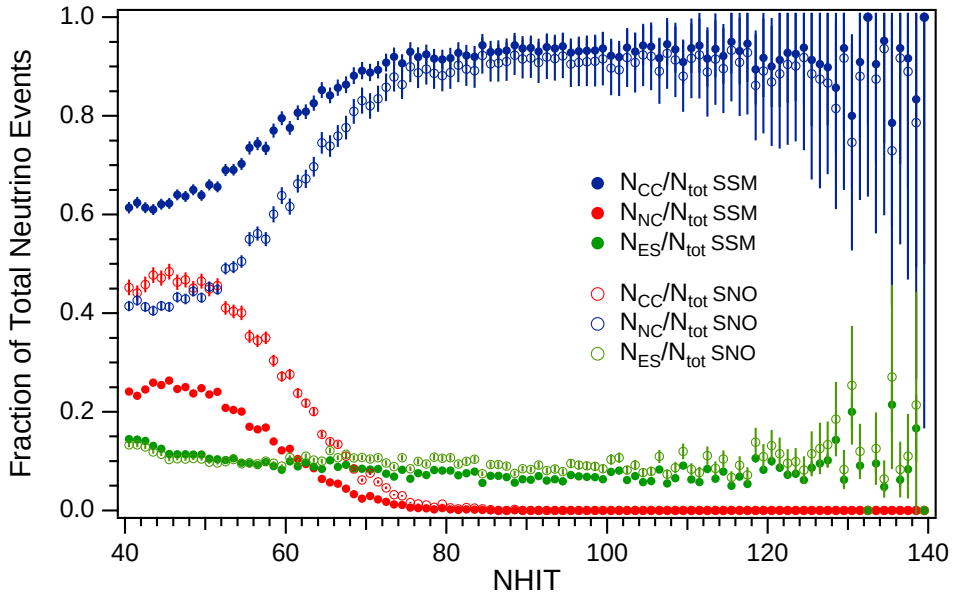

Figure 8.29: CC, NC, and ES contributions to the spectrum as a fraction of the total number of events versus NHIT threshold. Both the SSM predictions (solid circles) and the true composition of the solar ν flux as measured in SNO is shown. In this plot we assume that there are no significant spectral distortions to the CC spectrum. The error bars in this plot are statistical and due to the limited statistics of Monte Carlo events at high NHIT.

can perform a fit to the spectrum and determine the energy scale, α, and normalization,N_{CC}, simultaneously. We fit a probability distribution function for the CC NHIT spectrum to the raw SNO spectrum above a high NHIT threshold. The high NHIT threshold assures that very few neutrons and very little background are contained in our data sample. Figure 8.29 illustrates the ratio of CC, NC, and ES events to the total number of events as a function of NHIT threshold. Predictions according to the standard solar model (SSM) as well as our measurements of the CC and ES signal are shown. Using the CC and ES interaction rates which we determined in the previous sections of the chapter we can scale the SSM predictions to obtain a realistic estimate of the fraction of NC and ES events contained in the data set. According to Figure 8.29, for NHIT $\geq$ 75 the NC contribution to total number of events is expected to be less than 5%.

A maximum likelihood fit with continuos parameterized probability distribution func-

tions allows us to perform the fit over a wide fit window between $75 \leq \text{NHIT} \leq 140$. The energy scale parameter α is determined relative to the energy scale obtained from calibration sources. The ES contribution to the raw SNO data spectrum is fixed with the value determined from the high precision measurement by Super-Kamiokande. A *hep* contribution of $1\times$ SSM of is included in the CC and ES spectrum. The underlying ^{8}B spectrum used in this analysis is an undistorted ^{8}B spectrum from Ortiz et al. In principle, one can use both distorted and undistorted ^{8}B spectra to test a particular neutrino oscillation hypothesis. The analysis approach is illustrated in Figure 8.31. From this analysis we obtain the following results.

$$[CC]_{NHIT} = 0.355 \pm 0.016 \times \text{SSM} \tag{8.38}$$

$$\alpha_{NHIT} = 0.9895 \pm 0.0176 \times \alpha_{N16} \tag{8.39}$$

The results from this analysis are completely consistent with the energy scale and energy scale uncertainty determined by SNO's calibration program. For a comparison of results see Table 8.12. The CC interaction rate is in agreement with the value derived from the radial and solar angle distribution. The systematic error on the CC flux is dominated by the energy scale uncertainty. Fitting the ^{8}B spectrum has the potential to improve SNO's CC flux measurement. It appears that the inherent energy calibration present in the ^{8}B spectrum alleviates the sensitivity of the normalization obtained to energy calibration uncertainties. With this technique one can expect to achieve an effective energy uncertainty of $\mathcal{O}(1\%)$ and an uncertainty in the normalization of the CC flux of $\mathcal{O}(5\%)$.

As the radial and solar angle distribution, the NHIT spectrum is a powerful event distribution that can be used to determine the CC interaction rate with great accuracy.

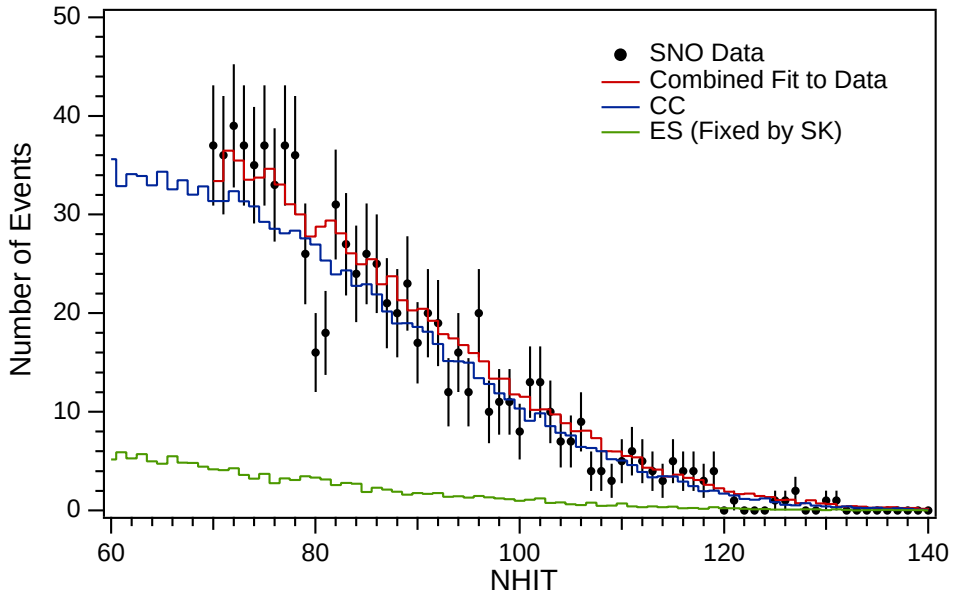

Figure 8.30: Fit of an undistorted CC spectrum with variable normalization and energy scale to the NHIT spectrum of the raw data. The ES contribution in this fit is fixed by the measurement of Super-Kamiokande. A radial cut of $R_{fit} \leq 550$ cm and the high-level event cuts (HLC) are applied to the data.

Table 8.12: Results from the ^{8}B endpoint fit to the energy spectrum and from the analysis and signal extraction presented in the other chapters of this thesis.

Fit Parameter	^{8}B Endpoint Fit	Calibration Sources
Energy Scale α	0.9895 ± 0.0176(stat) ± 0.006(syst)	1 ± 0.006(stat) ± 0.006(syst)
Total Error $\Delta\alpha$	1.7%	1.4%
Normalization N_{CC}	0.355 ± 0.016(stat) ± 0.006(syst)	0.347 ± 0.014(stat)± 0.024(syst)
Total Error ΔN_{CC}	4.7%	8.4%

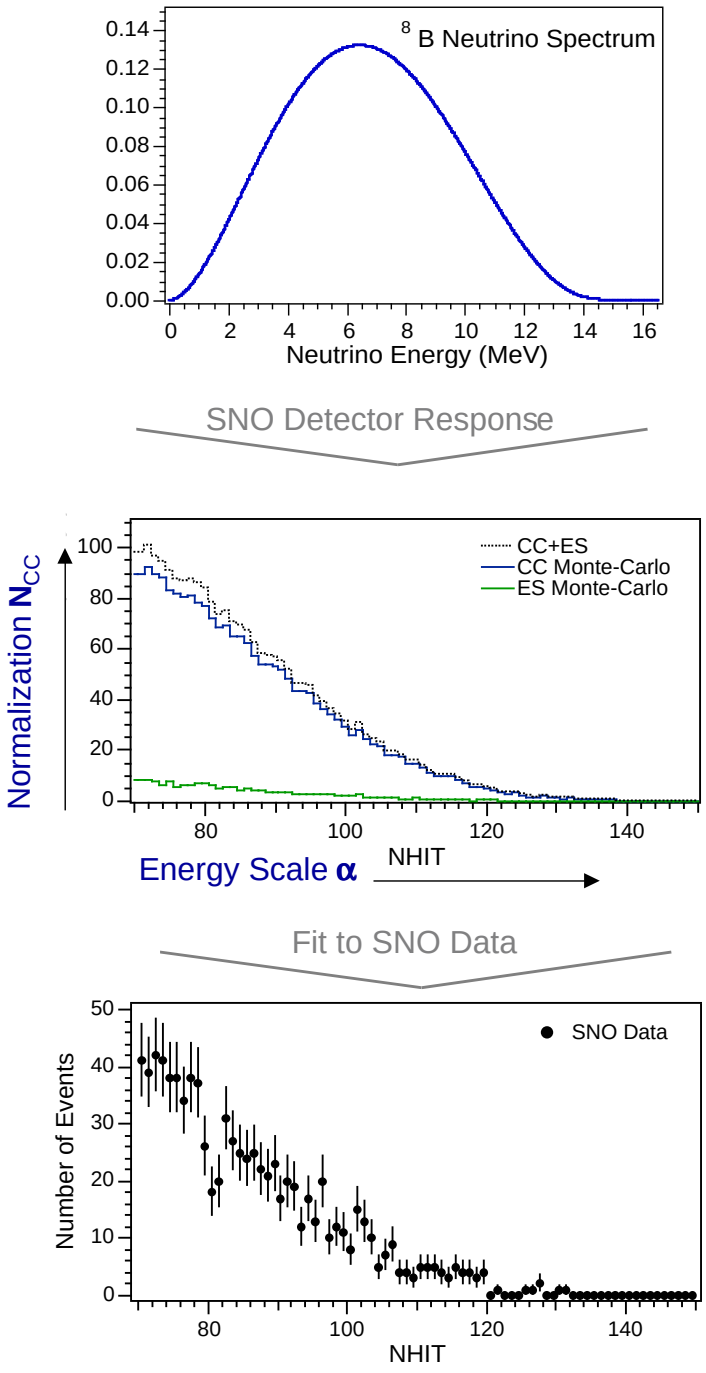

Figure 8.31: Schematic of the 2-parameter fit to the ^{8}B spectrum. The ^{8}B energy spectrum is convolved with the SNO detector response. The predicted Monte Carlo NHIT spectrum is then fit with a varying energy scale and normalization to the SNO data. The ES contribution is fixed by the measurement from Super-Kamiokande.

8.4.3 Systematics of the ^8B Endpoint Fit

As a verification of the results obtained with the ^{8}B endpoint fit some of the systematic behavior of this method have been studied. Both the sensitivity to the fit interval and to artificial energy scale distortions have been investigated.

• Fit Threshold and Interval: We find that the central value of the fitted normalization varies by 3.1% between [0.349 and 0.360] over 8 NHIT. The estimated error on [CC] is ±1.6%. The energy scale parameter α varies by 1.2% between [0.981, 0.993] over 8 NHIT. The estimated error on α is ±0.6%.

• Artificial Energy Scale Distortion: An artificial energy scale distortion was introduced into the data set and the sensitivity of the technique to this systematic errors was determined. It was found that the central value of the energy scale parameter α varies by 7.9% over a artificial 10% energy scale change. The fitted normalization, however, varies only by 2.9% over 10% energy scale change. The fit value for the energy scale α is 0.989±0.018. The results of these systematic studies are shown in Figure 8.32. The variation of the central fit value with NHIT threshold and energy scale can be treated as a systematic uncertainty. The resulting systematic error in the normalization of the CC spectrum is given by:

$$\begin{aligned}\frac{\Delta[CC]}{[CC]} &= \sqrt{\left(\frac{\Delta\alpha}{\alpha}\Delta N_{CC}(\alpha)\right)^2 + \left(\frac{\Delta N_{CC}}{N_{CC}}\right)^2} \\ &= \sqrt{\left(0.006 \times \frac{0.029}{10}\right)^2 + (0.016)^2} = 0.016\end{aligned}$$

The systematic error is estimated to be ± 1.6%. It is obviously dominated by the variation of [CC] with fit threshold. As this error is derived from the maximum variations with NHIT threshold, it is expected to decrease as the statistics of the CC spectrum increases.

Additional checks of this fit method have been performed using data from the ^{8}Li calibration source. The spectrum of the ^{8}B charged-current signal is in very similar to the spectrum obtained with the ^{8}Li calibration source, both in endpoint and shape. ^{8}B and ^{8}Li β-decays are isospin mirrors. Both isotopes decay to the same broad excited state of ^{8}Be which in turn promptly decays to α-particles.

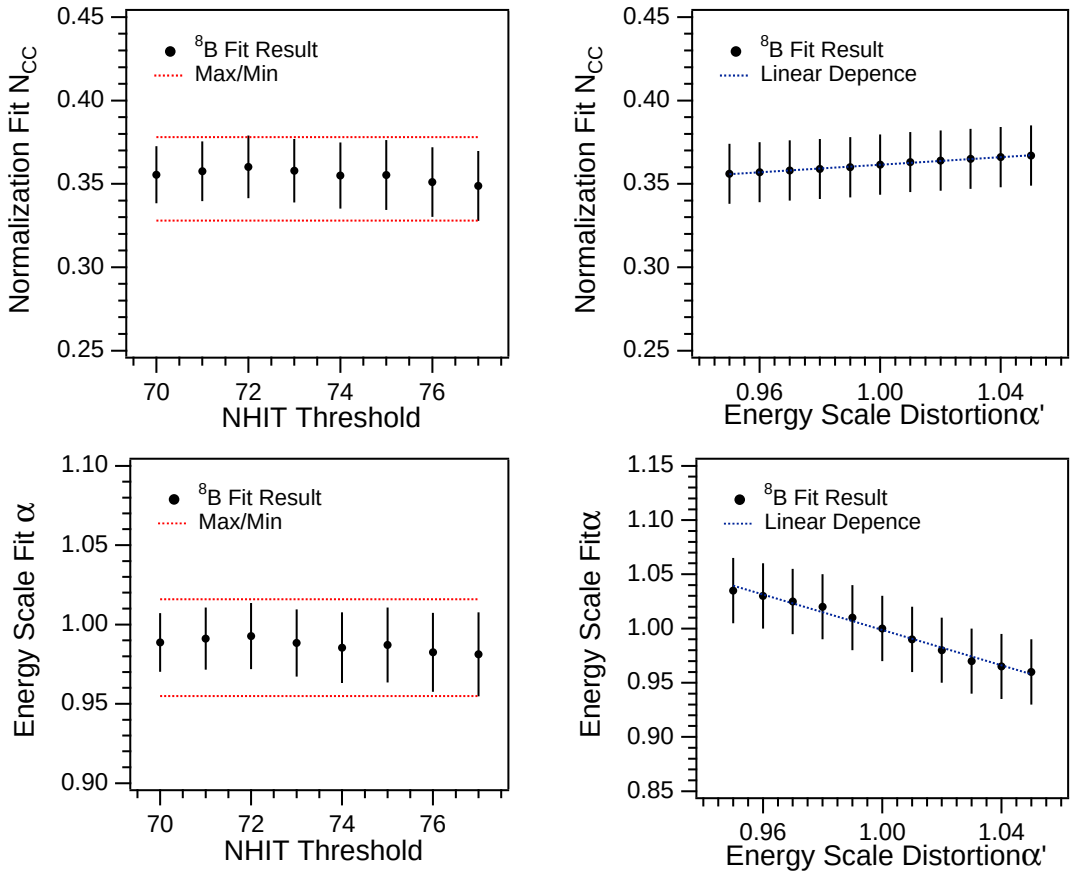

Figure 8.32: Systematics of fitting the ^{8}B β-spectrum.

8.5 Characteristic Event Distributions: Summary

In this chapter we investigated the characteristic distributions of the candidate event set for different energy thresholds and fiducial volumes. In general good agreement was found between the data and the Monte Carlo predictions. First estimates of the CC and ES interaction rates have been obtained by individual fits to the radial, solar angle, and NHIT distribution of the data set. The results obtained from this simple analysis give a first indication of the reduced charged-current interaction rate compared to standard solar model predictions. In units of 5.05×10^6 cm$^-2$ s$^-1$, we obtain:

$$\begin{aligned} [CC]_{R^3} &\leq 0.363 \\ [CC]_{\cos\theta_\odot} &= 0.360 \pm 0.129 \\ [ES]_{\cos\theta_\odot} &= 0.501 \pm 0.148 \\ [CC]_{NHIT} &= 0.355 \pm 0.016 \end{aligned}$$

From a fit of the ^{8}B β-spectrum we determine the energy scale of the neutrino data relative to the energy scale obtained with the ^{16}N calibration source.

$$\alpha_{NHIT} = 0.989 \pm 0.018$$

Various fiducial volumes were studied using the elastic scattering signal in the D_2O and H_2O. Overall, good agreement was found between the data and the Monte Carlo predictions although the statistics of ES events is limited. Within the statistical limitations of the data set the elastic scattering signal is found to be constant across the AV. Solar neutrinos with energies below 4 MeV have been identified in the SNO data in a study of the angular distribution of CC and ES events.

The neutral current interaction rate cannot be determined from the individual characteristic distributions of neutrino event as there are many backgrounds that are correlated with the neutron capture signal from the NC interactions. The determination of backgrounds and a method to determine the neutral-current interaction rate will be discussed in the following chapter.

CHAPTER 9

DETERMINATION OF THE INTERACTION RATES OF SOLAR ^{8}B NEUTRINOS WITH DEUTERIUM

The primary physics goal of this analysis is the measurement of the neutrino interaction rates with deuterium, in particular the measurement of the neutral-current interaction rate of solar ^{8}B neutrinos. The neutral-current interaction rate of solar neutrinos with deuterium can be measured in the pure D_2O phase of SNO using the fact that the observed neutral-current events have a non-uniform spatial distribution throughout the acrylic vessel holding the heavy water.

Solar ^{8}B neutrinos interact with the heavy water target of the SNO through the neutral-current (NC) reaction, the charged-current (CC) reaction, and the neutrino-electron elastic scattering (ES). The neutrons produced by the NC reaction are captured by deuterium to produce tritium plus a 6.25 MeV γ ray and by hydrogen to produce deuterium and a 2.2 MeV γ ray. The capture cross-section on deuterium is about 640 times smaller than on hydrogen. With a heavy water concentration of 99.91% one expects about 37% of the neutron capture to take place on hydrogen and about 10% on oxygen. The 2.2 MeV γ rays from capture on hydrogen will fall into the background wall. The 6.25 MeV γ rays from n-capture on deuterium, however, will be above the background wall.

Because the mean distance for thermal neutrons to travel from creation to absorption in nearly pure D_2O is of the order of several meters there is a high probability that neutrons created near the acrylic vessel will be captured on hydrogen in the AV and the H_2O outside it. As a result, the distribution of neutron captures per unit volume inside the acrylic vessel will be non-uniform, whereas the CC events will be uniformly distributed throughout. The events can be fitted as a function of distance from the center to separate the NC and CC contributions to the signal.

The NC signal in D_2O is obscured by various backgrounds, and the CC and ES neutrino

signals. Th and U in the D_2O, AV, and H_2O are the most important sources of background. These event classes have very different angular distributions that allow the correlation of solar neutrino events with the direction of the Sun. The observation of the characteristic angular distribution of the CC and ES reaction is first evidence for the charged-current and elastic scattering interaction of neutrinos and allows us to determine that neutrinos observed in SNO are of solar origin. Furthermore, the solar angle distribution can be used as an additional tool to separate the NC, CC, and ES components of the neutrino signal.

While the energy spectrum of the charged-current spectrum is unknown in the presence of possible neutrino oscillations or other flavor-changing phenomena the energy spectrum of 6.25-MeV γ rays produced in the NC reaction is well understood and can be calibrated using calibration sources with energies close to the NC peak. Hence, the NC energy spectrum can be used as a constraint in the separation of neutrino signals.

In conclusion, the characteristic volume dependence of the NC reaction, the angular distribution of the CC and ES signal, and the energy constraint of the NC reaction can be used to decompose the data and separate the three different solar neutrino signals. The details of this data decomposition and neutrino signal extraction are described below.

9.1 A Model-Independent Determination of the Solar ^{8}B Neutrino Flux: Analysis Overview

Measurement of the solar neutrino flux requires the identification of neutrino signals and their separation from backgrounds. The analysis approach for the solar neutrino analysis is based on a statistical separation of the NC, CC, ES signals from the background contributions to the data set. The types of event contained in the candidate event set are:

1. *Neutrino Signal:* NC, CC, and ES
2. *Low-Energy Backgrounds:* U, Th in the D_2O, PMT $\beta - \gamma$'s, AV hot spots, etc.
3. *High-Energy Backgrounds:* External backgrounds, muon-induced spallation, etc.
4. *Instrumental Effects:* Pickup, PMT flashers, etc.

The fundamental parameters of every event are:

- Number of hit PMT's: NHIT
- Reconstructed position in detector: $\vec{r} = \vec{r}(R, \theta_{det}, \phi_{det})$
- Direction with respect to Sun: $\vec{u} = \vec{u}(\theta_\odot, \phi_\odot)$
- Time (t)

Formally, the collection of events , $\mathcal{N}$, in the candidate event set can be written as

$$\mathcal{N} \quad = \sum NC + CC + ES + Bkgd = \quad \mathcal{N}(NHIT, r, \theta_{det}, \phi_{det}, \theta_\odot, \phi_\odot, t) \tag{9.1}$$

where the number of events $\mathcal{N}$ is a function of event energy, NHIT, the radial position, r, vertex location with respect to the detector, θ_{det} and ϕ_{det}, and reconstructed direction with respect to the Sun, $\theta_\odot$ and $\phi_\odot$.

A number of different techniques and approaches exist to make the statistical separation of these events. It is important to emphasize that the signal extraction method used for the separation of the neutrino signals and background very much defines the physics potential of the analysis. Conversely, the analysis path depends critically on the goals pursued in this analysis.

9.1.1 Hypotheses in the Solar Neutrino Analysis

There are two possible hypotheses for the solar neutrino analysis at SNO.

1. *Neutrinos do not change flavor:* In the Standard Model Model of particle physics neutrinos are described as massless particles. States prepared in one flavor projection remain that way as neutrinos propagate. With the measurement of the NC and CC interaction rate SNO can make a comparison of the ν_e and ν_x flux and perform a direct test of the flavor change of solar ^{8}B neutrinos. With the measurement of the NC and CC interaction rate SNO is able to give evidence against the flavor-conversion principle independent of the results obtained at other experiments. Under this hypothesis, one can use the predicted shape of the ^{8}B energy spectrum to extract the neutrino signal because the shape is unchanged from laboratory measurements. As long as the inputs to this analysis are consistent with the standard model picture of neutrinos they can be used to test this *null* hypothesis. A discrepancy between standard model predictions and the results obtained in this model-dependent analysis can be used to reject the null hypothesis.

2. *Neutrinos change flavor:* Considering the evidence from many other experiments it is likely that neutrinos undergo flavor change. In this case SNO's measurement of the NC and CC interaction rate may provide evidence for neutrino flavor transformation and also constrain the neutrino oscillation-model parameters. In the case of neutrino flavor changes standard model predictions are no longer valid and we are required to make a *model-independent* analysis. This requires that the signal extraction used to derive the NC and CC measurement result be free of any underlying assumptions. With this approach SNO can make the first model-independent measurement of the total flux of active solar ^{8}B neutrinos.

9.1.2 Characteristics of this Solar Neutrino Analysis

Based on these considerations we require model-independence to be an integral part of this analysis.

1. *Model-Independence:* We derive a model-independent measurement of the CC spectrum and the solar ^{8}B ν flux, free of any assumptions about the underlying ^{8}B spectrum, neutrino flavor changes, or solar models. This may provide evidence for the flavor transformation of solar neutrinos, and is an important test of the predictions of standard solar models. The neutrino interaction rates are determined without any assumptions on the shape of the ^{8}B CC spectrum. This method will be referred to as *unconstrained* signal extraction. The experimental results obtained in this analysis allows us to derive model-independent conclusions on the nature of neutrinos.

Furthermore, we demonstrate that the neutrino interaction rates measured in SNO are independent of the specific threshold and fiducial volume used in the analysis.

1. *Independence of Analysis Threshold and Fiducial Volume:* The results obtained from this analysis are expected to be independent of the specific threshold chosen in the analysis. While some threshold choice may reduce the background contributions to the data analysis of the data with various energy thresholds will give us confidence that the backgrounds are well understood and have been estimated correctly. The same applies to the fiducial volume. With its heavy and light water target SNO can measure neutrino interactions in different detector regions. Studies in various fiducial volumes allow us to map the neutrino signal and backgrounds throughout the entire detector. Some of correlations between the contributions from the NC and the CC signal may also be broken more effectively through the characteristic radial distributions of the signals. With the results obtained from various fiducial volumes it is possible to determine with more confidence the systematic uncertainties on the results obtained form data taken in the central volume of the detector.

9.2 Spectral Decomposition: Separation of the NC, CC, ES Signals and Background Contributions

While neutrino interactions proceed through different types of interactions with different signatures it is not possible to separate CC, NC, and ES events on an event-by-event basis. Particularly in pure D_2O the CC and NC events produce similar-looking event patterns of Čerenkov light. One cannot determine with any certainty whether a given event was produced by a 6.25-MeV γ from neutron capture or by the Čerenkov electron from a CC interaction. Statistical separation methods can be used as the different event classes have statistically distinct properties that can be used to distinguish them from other types of events. The characteristic distributions of neutrino events are described in Chapter 8 of this thesis. Table 9.1 summarizes the characteristics of the known event classes in the SNO detector. In the present analysis only the characteristics of the neutrino signals and the AV and H_2O backgrounds are used. One can imagine extending this analysis to take into account detector asymmetries and effects from localized radioactive backgrounds.

A generalized maximum likelihood method is used to separate the event classes and perform an extraction of the solar neutrino signals. In signal extraction we decompose the NHIT spectrum of the cleaned, but otherwise raw data set, into coarse NHIT spectra for its various signals and background components. The amplitude (or normalization) f_i of the individual components to the data set is then a vector in NHIT space.

$$\begin{aligned} \mathcal{N} &= \sum NC + CC + ES + Bkgd \\ &= \sum_i f_i(NHIT) S_i(NHIT, r, \theta_{det}, \phi_{det}, \theta_\odot, \phi_\odot, t) \end{aligned} \tag{9.2}$$

Assuming spherical symmetry in the detector (and in our signal analysis), the number of free parameters reduces to NHIT. The distribution of events in NHIT is given as a function of a radial parameter, R^3, the reconstructed direction of the event with respect to the Sun, $\cos\theta_\odot$, and time.

$$\mathcal{N} = \sum_i f_i(NHIT) S_i(NHIT, R^3, \cos\theta_\odot, t) \tag{9.3}$$

Table 9.1: Characteristics of the components of the candidate event set. S(R) is the radial source distribution of the event class. S(NHIT) is the corresponding NHIT distribution and $S(\cos\theta_\odot)$ describes the solar angle distribution of events. Only the background contributions from the AV and H_2O are included in the fit. All other backgrounds are treated separately and do not enter the global fit. The function $f(\theta_{detector}\text{-}\theta_\odot)$ is an effective detector coordinate corrected for the zenith angle dependence.

Event Type	S(R)	S(NHIT)	$S(\cos\theta_\odot)$
NC	neutron	$^2H(n,\gamma)^3H$	flat
CC	flat in D_2O, 0 in H_2O	arbitrary	$1+\alpha\cos\theta_\odot$
ES	flat	arbitrary	$f_{ES}(\theta_\odot)$
^{214}Bi	$S(R)_{D2O}=u_1$, $S(R)_{H_2O}=u_2$	U chain	flat
^{208}Tl	$S(R)_{D2O}=v_1$, $S(R)_{AV}=v_2$ $S(R)_{H_2O}=v_3$	Th chain	flat
PMT $\beta-\gamma$	no step at AV	arbitrary, monotonic decrease	flat in $S(\theta_{det}\text{-}\theta_\odot)$ and $S(\phi_{det}\text{-}\phi_\odot)$
PSUP	0 in D_2O, arbitrary in H_2O	monotonic decrease	flat in $S(\theta_{det}\text{-}\theta_\odot)$ and $S(\phi_{det}\text{-}\phi_\odot)$
Cavity Bkgd.	0 in D_2O, arbitrary in H_2O	arbitrary monotonic decrease	flat in $S(\theta_{det}\text{-}\theta_\odot)$ and $S(\phi_{det}\text{-}\phi_\odot)$
HE-γ	0 in D_2O, arbitrary in H_2O	arbitrary	flat in $S(\theta_{det}\text{-}\theta_\odot)$ and $S(\phi_{det}\text{-}\phi_\odot)$
AV hot-spot	R_{AV}	arbitrary	localized in θ_{det}, ϕ_{det}
Muon spallation	flat, step at AV	$^2H(n,\gamma)^3H$	associate with μ, flat in $S(\theta_{det}\text{-}\theta_\odot)$ and $S(\phi_{det}\text{-}\phi_\odot)$
Instrumental Bkgd.	depends on bkgd.	depends on bkgd.	depends on bkgd.

The amplitudes f_i are determined in a generalized maximum likelihood method. The basic procedure of signal extraction is to break the raw NHIT spectrum into separate bins, then to take the R^3 and $\cos\theta_\odot$ distribution for each NHIT bin separately and perform a maximum likelihood fit to the R^3 and $\cos\theta_\odot$ probability distribution functions for each event type. For the best separation of the various signals the known NC NHIT distribution is used to constrain the fit. The distortions to the ES spectrum in case of neutrino oscillations are small and we can safely use the ES NHIT spectrum as an additional constraint to the fit. To take into account possible time variations in the signal and backgrounds the underlying probability distribution functions for the maximum likelihood technique are generated including time variations in the signal and the detector response. In this spectral decomposition the NHIT bins are chosen such that there is roughly an equal number of events in every bin. In this approach a superposition of the individual neutrino and background event distributions is fit to the data. The weighting factors for the components in the fit give the relative proportions for each event type. The maximum likelihood analysis method generalizes this procedure to a simultaneous fit for the distributions of all variables used in the fit. This includes the correlation between variables.

$$\mathcal{N}(NHIT, R^3, \cos\theta_\odot) = \sum_i f_i(NHIT) S_i(NHIT, R^3, \cos\theta_\odot) \tag{9.4}$$

S_i describes the distributions of the number of events for source i in the detector. The amplitude f_i is the fraction of events compared to Monte Carlo predictions. The ^{16}N spectrum is used to constrain this vector for the NC component in the fit.

$$\begin{aligned} \mathcal{N} &= f_{NC}(NHIT) S_{CC}(NHIT) F_i(NHIT, R^3, \cos\theta_\odot) \\ &+ \sum f_{CC}(NHIT) S_{NC}(NHIT) F_i(NHIT, R^3, \cos\theta_\odot) \\ &+ \sum f_{ES}(NHIT) S_{ES}(NHIT) F_i(NHIT, R^3, \cos\theta_\odot) \\ &+ \sum Bkgd \end{aligned} \tag{9.5}$$

The maximum likelihood function is then defined as

$$L = \sum_j \ln \mathcal{N}(NHIT_j, R_j^3, \cos\theta_{\odot j}) - \sum_i f_i \tag{9.6}$$

where we sum over all events (j) in the data sample and over the different event classes (i). The maximum likelihood technique determines the fractional contribution, f_i, of each event class, i, in every NHIT bin. The overall contribution, $\overline{f}_i$, is the weighted average of the contributions in every NHIT bin, α,

$$\overline{f}_i = \frac{1}{\sum_\alpha (1/\sigma_i^\alpha)^2} \sum_\alpha \frac{f_i^\alpha}{(\sigma_i^\alpha)^2} \tag{9.7}$$

The error $\overline{\sigma}_i$ is determined from σ_i and f_i by a simple propagation of errors. The results of this analysis can be shown as a NHIT spectrum of fit parameters with the appropriate errors. The fit value f_i is the solar neutrino signal in units of the underlying probability distribution function (PDF). The Monte Carlo simulations for the PDF are based on standard solar model flux predictions as given BPB00 [11]. Therefore, the neutrino signal is determined as a fraction of standard solar model predictions. However, one should emphasize that this is a convenient but arbitrary choice of units and does not introduce any model-dependence in the analysis! The raw neutrino interaction rates determined in this analysis are still independent of solar models and free of any assumption on the shape of the underlying ^{8}B spectrum. This approach requires no conversion to the actual number of events in the detector and thus circumvents any conceptual problems the maximum likelihood technique would have introduced in the actual counting of integer number of events.

As described in the previous chapters, there are some effects we need to correct for to obtain absolute measurements of the ν_e and ν_x flux. These include the signal loss in data reduction, $(1 - \eta_{Data})$, the loss in Monte Carlo events, $(1 - \eta_{MC})$, corrections to the cross-sections used in the calculation of the standard solar model predictions, X, and a correction for the number of deuterons in the detector, D. For the charged current signal an additional correction, O, for the abundance of ^{17}O and ^{18}O in the detector applies.

$$[CC] = \frac{CC_{SNO}}{CC_{SSM}} = f_{CC} \times \frac{1-\eta_{MC}}{1-\eta_{HLC}} \times O \times D \times X \quad (9.8)$$

$$[NC] = \frac{NC_{SNO}}{NC_{SSM}} = f_{NC} \times \frac{1-\eta_{MC}}{1-\eta_{HLC}} \times O \times D \times X \quad (9.9)$$

$$[ES] = \frac{ES_{SNO}}{ES_{SSM}} = f_{ES} \times \frac{1-\eta_{MC}}{1-\eta_{HLC}} \times E \times X \quad (9.10)$$

The values used in this correction are tabulated in Table 9.2.

Table 9.2: Correction factors used in the determination of the neutrino interaction rates.

Quantity	Parameter	Value	Ref.
Signal Loss in Data Reduction	$(1-\eta_{HLC})$	0.9867	[Chapter 5]
Monte Carlo Signal Loss	$(1-\eta_{MC})$	0.9933	[Chapter 7]
Number of Deuterons ($R_{fit} \leq 550$ cm)	D	0.9874	[Chapter 7]
Number of Deuterons ($R_{fit} \leq 600$ cm)	D	0.9997	[Chapter 7]
Number of Electrons ($R_{fit} \leq 550$ cm)	E	0.9874	[Chapter 7]
Number of Electrons ($R_{fit} \leq 600$ cm)	E	0.9997	[Chapter 7]
Cross-Section + Rad. Corrections	X	0.9841	[Chapter 7]
Oxygen Isotopes	O	0.9921	[Chapter 7]

Once the NC, ES, and background contributions to the data have been determined they can be subtracted from the raw NHIT spectrum to yield a model-independent CC spectrum in NHIT space. Using this analysis approach it is possible to work entirely in NHIT space without having to assign effective energies to every event before the separation of the neutrino signals. The method of unconstrained, model-independent signal extraction is illustrated in Figure 9.1.

To summarize, the probability distribution functions used in this maximum likelihood analysis method are

1. Radial Distribution: $(R_{fit}/R_{AV})^3$
2. Solar Angle Distribution: $\cos\theta_{\odot}$

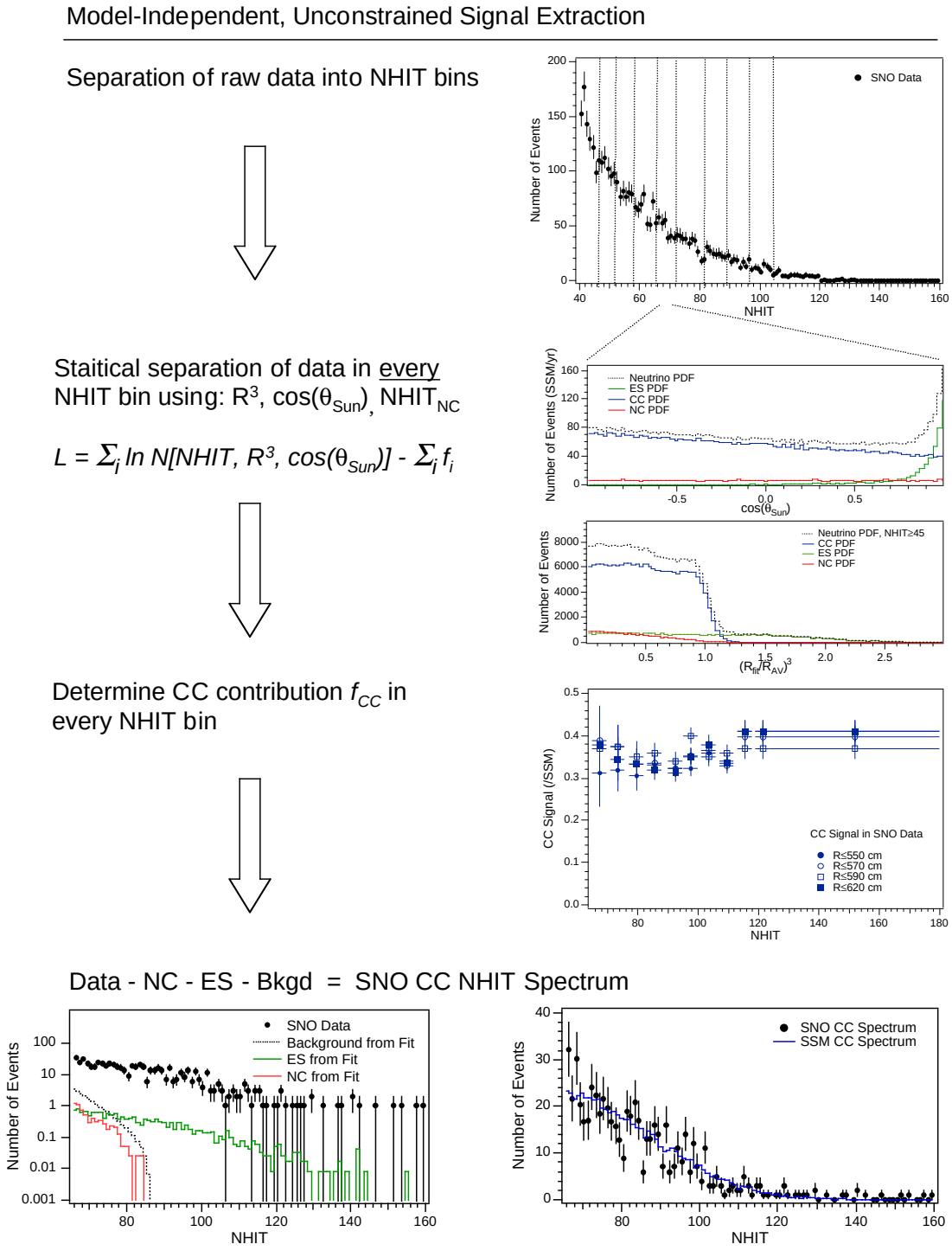

Figure 9.1: Model-independent, unconstrained signal extraction in the SNO solar neutrino analysis.

3. Energy Spectrum: NC and ES shape constrained, CC shape unconstrained

The probability distribution functions S_i used in this maximum likelihood analysis are obtained from Monte Carlo, calibration data, and the time-varying backgrounds in the detector itself. The NC shape and the reconstruction of the NC spectrum is calibrated by comparing ^{16}N calibration data with simulated NC Monte Carlo data at the various ^{16}N source positions. Neutron capture on deuterium releases a γ with an energy of 6.25 MeV and the ^{16}N source produces γ's with an energy of 6.13 MeV through the β-decay of ^{16}N into the excited state of ^{16}O. Calibration runs with the ^{16}N have shown so far that the mean NHIT value for ^{16}N runs is stable within <0.5% after correction for the energy scale drift and that Monte Carlo simulations reproduce the ^{16}N spectrum very well. Figure 9.2 shows the neutral-current NHIT constraint used in this analysis. It is based on ^{16}N calibration data that is volume weighted according to the ^{16}N source positions.

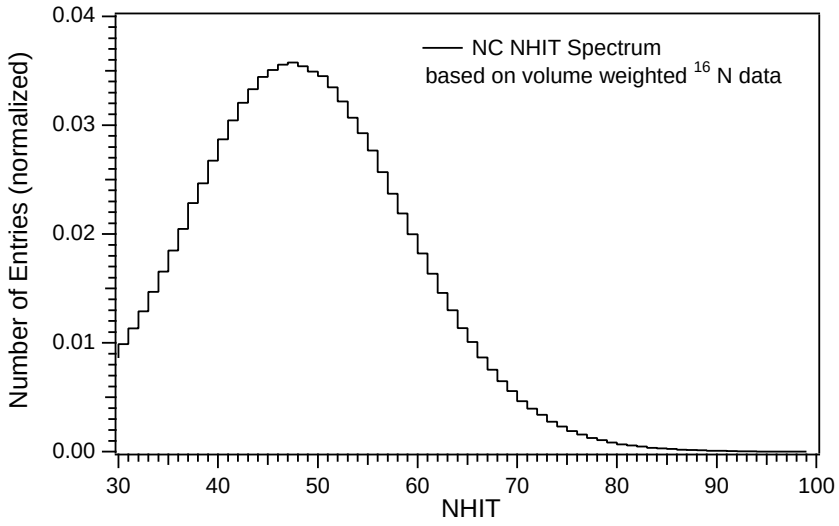

Figure 9.2: NHIT constraint of the neutral-current signal based on volume-weighted ^{16}N calibration data.

An analysis of the NC, CC, and ES signals requires a good understanding of the low- and high-energy backgrounds to the NC signal in D_2O. The principal background contributions come from the H_2O and AV. They can be characterized by their characteristic radial

dependence and energy spectrum and included in the fit. Other backgrounds need to be estimated explicitly. For this analysis we assume that there is some *a priori* knowledge of the backgrounds to constrain the separation of the NC, CC, and ES NHIT spectra. Only the H_2O and AV backgrounds are included in the maximum likelihood analysis.

9.2.1 Systematic Errors in the Maximum Likelihood Spectral Decomposition

A variety of systematic uncertainties contributing to the measurement of neutrino interactions in the SNO detector have been considered. This list includes systematics associated with the overall efficiency of the detector, the cross-section and target uncertainties, the background PDF's, energy scale etc. One can distinguish between those uncertainties that affect the PDF's and data (e.g. reconstruction) or those that will affect the absolute normalization of the neutrino flux or spectrum (e.g. livetime and energy scale).

- *Decomposition Systematics:* Reconstruction, Angular Resolution etc.
- *Systematics of Absolute Normalization:* Livetime, Energy Scale etc.

The uncertainties in the PDF's and the data fall under the category of detector response uncertainties. These systematic errors are propagated through the procedure of spectral decomposition using perturbation functions for event observables. The basic idea of the perturbation function method is to take the Monte Carlo generated event sample and perturb or shift the observables for each event. The shifts for each event are drawn randomly from a distribution of probable shifts. These primary observables include the reconstructed energy, position, and direction. The choice of perturbation functions is constrained by the comparison of data and Monte Carlo for calibration sources, or by comparing the default Monte Carlo to Monte Carlo simulations with varying input parameters. By applying this method to the primary probability distribution functions one can generate secondary probability distribution functions that represent a plausible range of microscopic input parameters. Ideally, one would like to use a single perturbation function which operates within the multidimensional space of the observables and hence incorporates all correlations. Because of the inherent difficulty in finding the correct function, the observables are treated separately for now. In case of energy one shifts the value according to

$$NHIT' = NHIT + \mathcal{R}[f_1(NHIT, \vec{r}, \vec{u})] \tag{9.11}$$

where $\mathcal{R}$ represents a random choice from the distribution of probable shifts. As the entire analysis is performed in NHIT space the shifts must be integer valued. In case of reconstructed position and direction one shifts the values according to

$$\begin{aligned} \vec{r}' &= \vec{r} + \mathcal{R}[f_2(NHIT, \vec{r}, \vec{u})] \\ \vec{u}' &= \vec{u} + \mathcal{R}[f_3(NHIT, \vec{r}, \vec{u})] \end{aligned} \tag{9.12}$$

The PDF's are perturbed based on the systematic errors in the vertex reconstruction and angular resolution of the reconstruction algorithm. The uncertainty in reconstruction is fitted as a smooth function of $\vec{r}$ and an interpolation function is used for the actual perturbation procedure.

9.2.2 Interpretation of the Neutrino Signal in SNO

The decomposition of the data into neutrino signals and backgrounds leads to a number of experimental results. These can be interpreted in in several ways: Model-independent and model-dependent interpretations are possible. Table 9.3 summarizes the basic experimental results obtained in this solar neutrino analysis and the derived quantities.

The experimental results from this work are reported in terms of an NHIT spectrum of charged-current interactions and the raw CC, NC, ES, and *hep* interaction rates. The composition of the solar neutrino flux can then be studied in a model-independent way by comparing the interaction rates measured in SNO. Differences between the NC and CC interaction rates measured in SNO will provide model-independent evidence for the flavor change of solar neutrinos. In principle, the same tests can be performed by comparing the ES and CC rates although the ES rate is statistically limited. Using a $NHIT \rightarrow E$ transformation function based on Monte Carlo we can derive an electron energy spectrum that corresponds most likely to the derived NHIT spectrum.

Table 9.3: Results from a signal decomposition of SNO data. Experimental results as well as model-independent and model-dependent interpretations of these results are obtained.

Type of Result	Quantity
Experimental Results	$CC_{SNO} = [CC]$
	$NC_{SNO} = [NC]$
	$ES_{SNO} = [ES]$
	CC NHIT spectrum
	$hep_{SNO} = [hep]$
Model-Independent	$NC_{SNO} - CC_{SNO}$
	$CC_{SNO} - ES_{SNO}$
Model-Dependent	CC_{SNO}/CC_{SSM}
	ES_{SNO}/ES_{SSM}
	NC_{SNO}/NC_{SSM}

While $[CC], [NC], [ES]$ are reported in standard solar model flux units they are model-independent measurements of the neutrino interaction rates in SNO. Their differences $[NC] - [CC]$ and $[ES] - [CC]$ or the corresponding ratios are also model-independent quantities. However, the comparison of CC_{SNO}, NC_{SNO}, ES_{SNO} to the solar model predictions is a model-dependent interpretation of the agreement or disagreement between the measured neutrino fluxes and predictions based on the currently adopted solar models. An interpretation of SNO's solar neutrino flux measurements in terms of neutrino oscillation parameters or other flavor changing descriptions requires model-dependent assumptions on the type of flavor changing mechanism and the interactions and neutrinos involved.

9.3 Backgrounds in the Determination of Neutrino Signals in SNO

A variety of sources contribute to the backgrounds in SNO. These include a number of low-energy backgrounds such as U and Th in the D_2O and H_2O, as well as high energy backgrounds from external γ-rays, muon-induced spallation products, and a residual contamination of instrumental backgrounds. These backgrounds are part of the neutrino candidate event set and need to be accounted for in the extraction of the neutrino signal.

The spectrum of ^{8}B charged-current events allows the measurement of the CC interaction rate at relatively high energies. The CC spectrum extends to an energy up to ~ 15 MeV which corresponds to an effective of NHIT of $\sim 135 - 140$. In contrast, a measurement of the neutral-current signal in SNO requires a much lower analysis threshold. The peak of the spectrum from NC events is at ~ 45 NHIT. Figure 9.11 shows the NHIT spectra for charged- and neutral-current events in D_2O.

All backgrounds can potentially influence our measurement of the neutral-current interaction rate. The photodisintegration background from the dissociation of deuterium needs to be determined separately as its ^{2}H(n,γ)^{3}He signal is identical to the event signature of neutral-current interactions. The most troublesome background to the measurement of the NC interaction rate is Th and U in the acrylic and the H_2O. Their high energy γ-rays which enter the D_2O clearly do not disintegrate deuterons uniformly over the D_2O volume. The attenuation length is about ~ 25 cm. This provides an extra source of neutrons near the surface of the AV. Many of these neutrons will be captured by hydrogen in the D_2O and in the acrylic, or by light water because they are created near the vessel.

In this analysis we use the fact that in the decomposition of the candidate event set we have some *a priori* knowledge of the backgrounds in the SNO detector. Studies of backgrounds at different energies and over time allow us to describe the background event distributions in the SNO detector with a high degree of accuracy. In our analysis we combine a global fit to the neutrino signals and principal background contributions combined with separate estimates for the internal D_2O background and other external backgrounds.

For the spectral decomposition of the data into neutrino signals and background contributions we derive AV and H_2O background probability distribution functions in $(R_{fit}/R_{AV})^3$,

NHIT, and $\cos\theta_{\odot}$. This is motivated by the fact the radial distribution of the raw SNO data shows clear evidence for backgrounds from the AV and the light water region. See Figure 9.3.

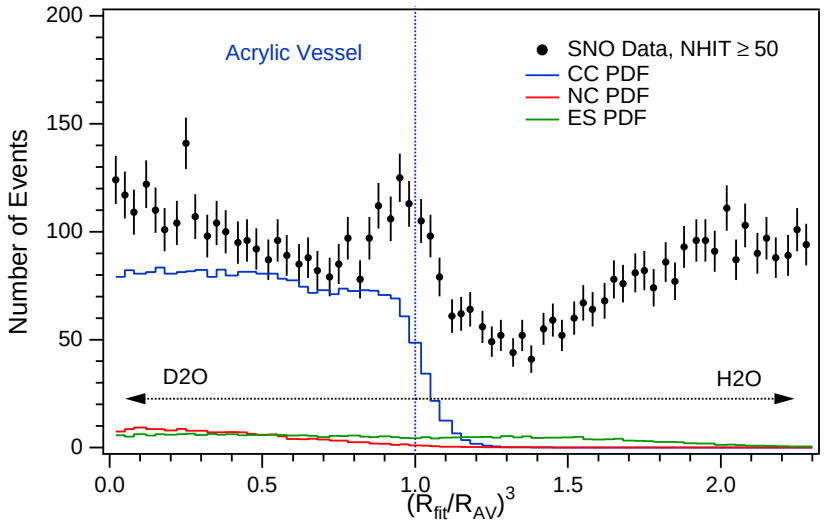

Figure 9.3: AV and H_2O backgrounds in the radial distribution of raw SNO data without the high-level event-quality cuts above NHIT $\geq$ 50. The AV and H_2O backgrounds are clearly visible. Most of these backgrounds are discriminated by the high-level event-quality cuts (HLC). For comparison, Monte Carlo predictions for the NC, CC, and ES signal are shown.

Unlike the internal H_2O backgrounds the internal D_2O backgrounds do not show any characteristic features in $(R_{fit}/R_{AV})^3$. They also shows no directionality in terms of $\vec{u}.\vec{r}$, i.e. the angular distribution between the reconstructed direction, $\vec{u}$, and the reconstructed radial position, $\vec{r}$, of an event. It is therefore impossible to include a probability distribution function for this background in our maximum likelihood fit. The signal of this background is covariant with the neutrino signal and external estimates are needed to determine its contribution to the energy spectrum measured in SNO. All other backgrounds are estimated separately. These include high energy backgrounds, PMT $\beta-\gamma$'s and miscellaneous neutron backgrounds.

9.3.1 Probability Distribution Function for the H_2O Background

One of the independent *signals* we can use to determine the event distribution of backgrounds is their time variation in an energy window that is dominated by backgrounds. At low NHIT backgrounds dominate the total event rate in the detector and neutrino interactions are a very minor contribution to the data. In this section we describe the development of a probability distribution function for the H_2O background based on the variations of this background with time. We consider the difference in the R^3 and NHIT distributions at different instances in time to determine the characteristics distributions of the dominant background component in the H_2O. The NHIT region of interest for this study is in the range of $30 \leq$ NHIT ≤ 40. Figure 9.4 shows the difference in the raw event rates between the background-dominated low-NHIT region and the neutrino signal. For NHIT ≤ 40 the neutrino signal is a very small contribution to the background "wall".

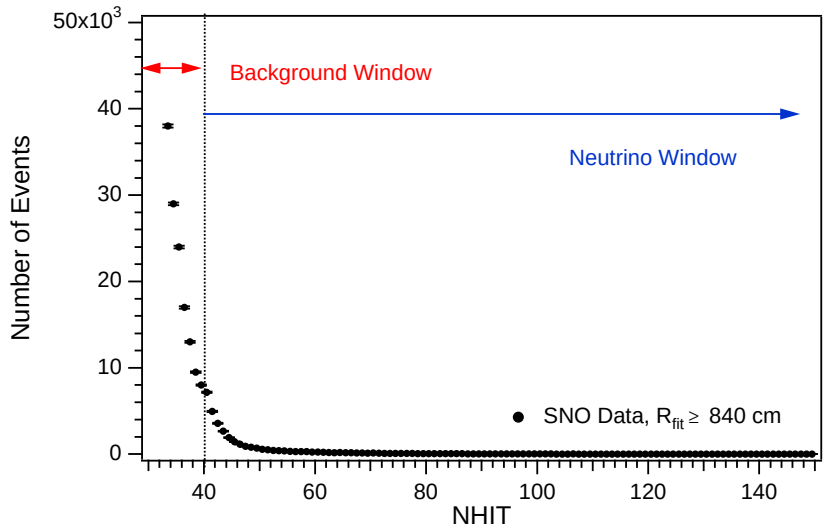

Figure 9.4: NHIT spectrum of raw SNO data above NHIT ≥ 30. For NHIT ≤ 40 the neutrino signal is a very small contribution to the background "wall".

At the start of production data taking on November 2, 1999, a failure of the H_2O degasser over several weeks resulted in increased levels of Rn. The failure of the degasser meant that water with relatively high radon was being pumped back into the region between the PSUP

and AV. The high radon produced noticeably larger numbers of events in the light water. ^{222}Rn decays away with a half-life of 3.825 days. Its presence in the SNO detector provided a unique opportunity to monitor in-situ the detector response to backgrounds. These data can be used for determining the background due to misreconstruction of light water radioactivity. The most important advantage of this method is that the high radon water sampled the entire space between the AV and PSUP in a way a calibration source never can. The natural radon spike has no source geometry and therefore no additional optical complications than those in the detector itself. The high radon levels persisted long enough that the data sampled many varying detector conditions with different rates, different instrumental backgrounds, channel thresholds, etc. One can expect that the detector response is more stable averaged over long periods of time than it is over short tuns typical in the deployment of calibration sources.

Obviously we cannot do any kind of event-by-event separation to learn about the reconstruction or energy distribution of radioactive backgrounds. However, the large number of events during this time allows us to make a statistical separation based on the difference between distributions during the high radon and subsequent low radon data. It is these distributions in which we are interested in the first place.

Comparing high- and low-radon data we derive an empirical probability distribution function (PDF) for the radial distribution of the internal light water backgrounds. The empirical PDF's derived from data are then compared with the Monte Carlo background simulations in the region of interest. In deriving a probability distribution function from the difference in the data we assume that the only difference between the high and low radon data sets is just the increased radon in the light water. All other sources of events in the detector are assumed to be constant so that once distributions of equal livetimes of the data are subtracted the characteristic distributions of pure samples of light water radioactivity are obtained. The distributions obtained from the difference of the high and low radon data can be used in the decomposition of the data to describe the light water backgrounds in the data set. In using these distributions as a probability distribution function in our data set we make the assumption that all light water radioactivity has the same radial distribution as does the radon that was present in the data during November 1999.

Table 9.4: Time periods and run numbers of high- and low-radon data used for the development of the H_2O background PDF.

Month	Radon Content	Run Numbers	Live Time
November 1999	High	10000-10400	1.54039×10^6 s
March 2000	Low	11380-11520	2.68357×10^6 s

The radon in the light water does not only produce events in the light water but events in the heavy water as well. By taking the difference of the high- and low-radon data the effect of misreconstruction is included in this empirical PDF. Also, the additional neutrons created by the γ's entering the D_2O during the high radon period will be included in the estimated background. The same is true for the Compton events produced by the γ's themselves although we expect most of them to be at low NHIT.

By deriving an empirical H_2O background PDF from the high and low radon data we assume that the only difference seen in the number of events is from radon. There is no way of excluding a change in the radioactivity level within the D_2O except to use radioassays of the water. The measurement of the water backgrounds in SNO by means of assays is described in [106]. A more detailed description is forthcoming.

In this study we compare data from the months of November 1999 and March 2000. The data sets used in this study are normalized to their respective livetime. The livetime of the data was determined from the raw livetime of the runs. No corrections for the deadtime due to burst cuts were made. This correction is however small and should not affect the distributions very much. While it may cause some small uncertainty in the comparison of the high and low radon data, the fact that these data sets are compared over a fairly long periods of time is likely to minimize these effects. The run numbers considered in these two months and the corresponding live times are listed in Table 9.4.

Overall good agreement is found between the NHIT and R^3 distributions of ^{214}Bi Monte Carlo events in H_2O and the empirical radon PDF. Figures 9.7 and 9.8 illustrate the agreement. ^{208}Tl in H_2O does not reproduce correctly the R^3 distribution of Radon. We

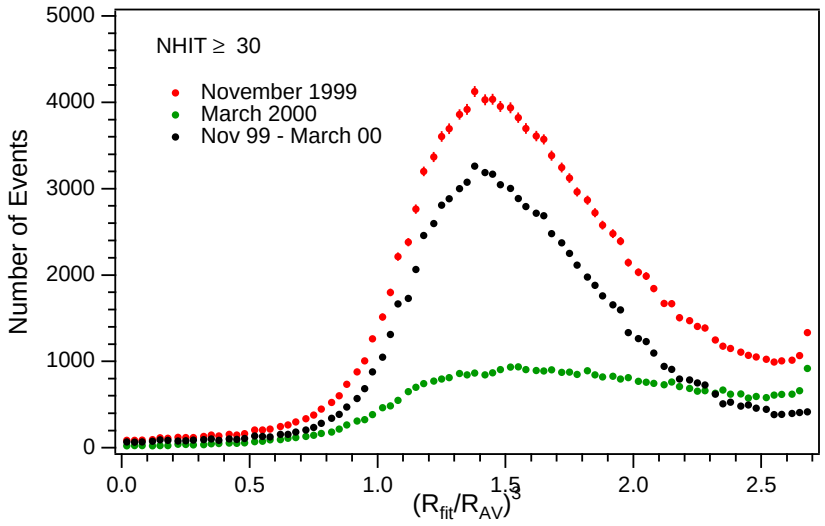

Figure 9.5: Difference between the R^3 distributions of months November 1999 and March 2000 for SNO data with NHIT $\geq$ 30.

conclude that the excess of radon during the high radon period of November 1999 is most likely ^{222}Rn, a daughter of the U chain. Figure 9.9 shows the radial probability distribution function for the H_2O background used in the signal decomposition of the neutrino candidate event set. The statistical error on the high- and low-radon data and the difference between the empirical PDF derived from the high-radon data and the Monte Carlo simulations is taken as an error estimate on R^3 distribution. There are a number of additional systematic effects that need to be taken into consideration. For example, changes in the detector response can clearly mimic an excess of events as the number of events at a given NHIT will change with the detector response at that NHIT. In Chapter 6 we found evidence for a change in the energy scale of the detector. This difference has been included in the systematic error by performing time-dependent simulations of the ^{214}Bi and ^{208}Tl backgrounds in the H_2O.

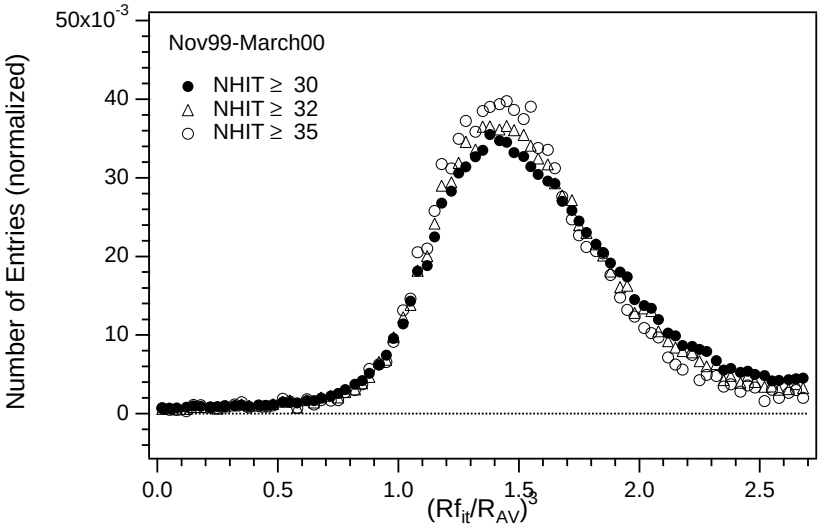

Figure 9.6: Comparison of the difference distributions normalized to unit area. The radial distribution of events are in good agreement in the region of interest ($(R_{fit}/R_{AV})^3 \leq 1.25$) for different NHIT thresholds.

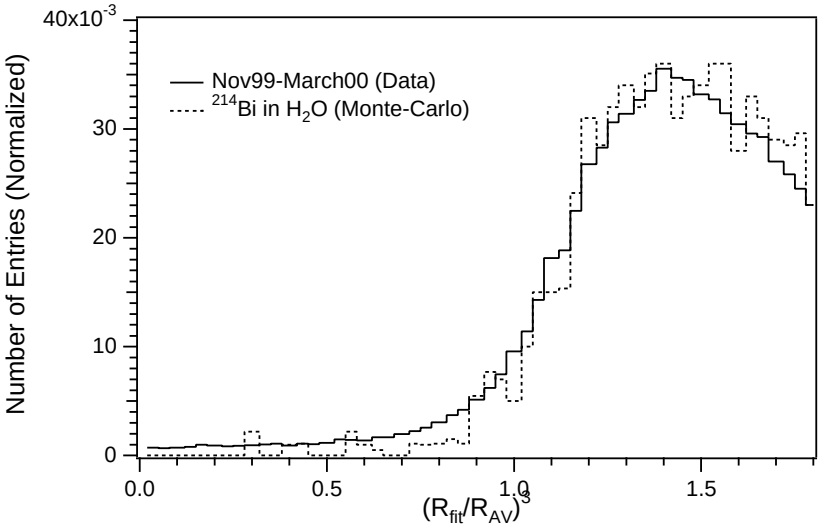

Figure 9.7: Comparison of the R^3 distribution derived from the data with the R^3 distribution expected from ^{214}Bi in H_2O.

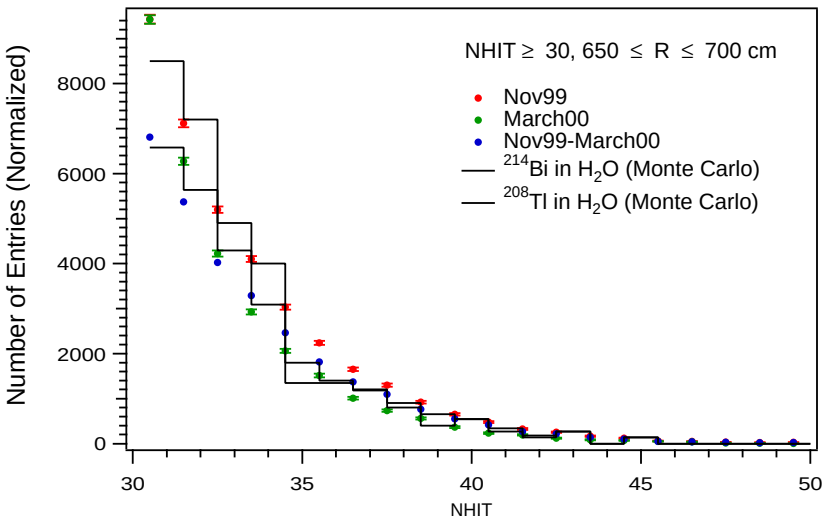

Figure 9.8: Comparison of the NHIT distributions derived from the data with the NHIT distribution expected from ^{214}Bi in H_2O. The NHIT distributions are normalized to allow a shape comparison. The agreement between data and Monte Carlo simulations for ^{214}Bi in H_2O is good.

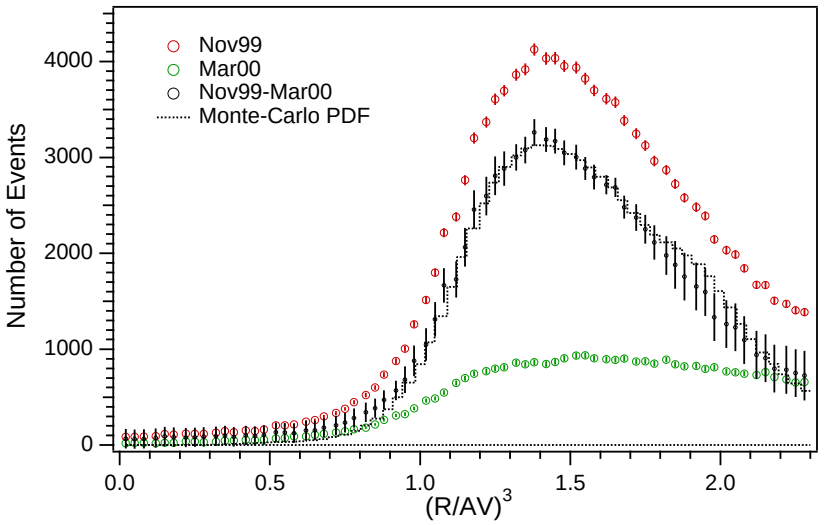

Figure 9.9: Radial probability distribution function (PDF) for the H_2O ^{214}Bi background. The error band includes the statistical error from the subtraction of the data as well as systematic error estimates based on the difference between Monte Carlo and data. The errors shown in this plot are used as uncertainties on the R^3 PDF of the H_2O background in the neutrino signal decomposition.

9.3.2 Probability Distribution Function for the Acrylic Vessel Background

An accurate description of the radial profile of the data requires the contributions from both the H_2O background and the acrylic vessel backgrounds. Backgrounds from the AV will also leak into the D_2O volume and contribute to the event rate in the central volume of the detector. Furthermore, they will be a substantial contribution to the data in fiducial volumes extending beyond $R_{fit} \sim 580$ cm. Assuming that most of the radioactive background from the acrylic vessel is similar to mine dust [1] we simulate the radial profile of the AV backgrounds using ^{208}Tl on the surface and embedded in the AV. The systematic error on the radial profile of the probability distribution function for the AV backgrounds is derived from variations in the Monte Carlo inputs. Figure 9.10 shows the radial profile of both background PDF's used in this analysis.

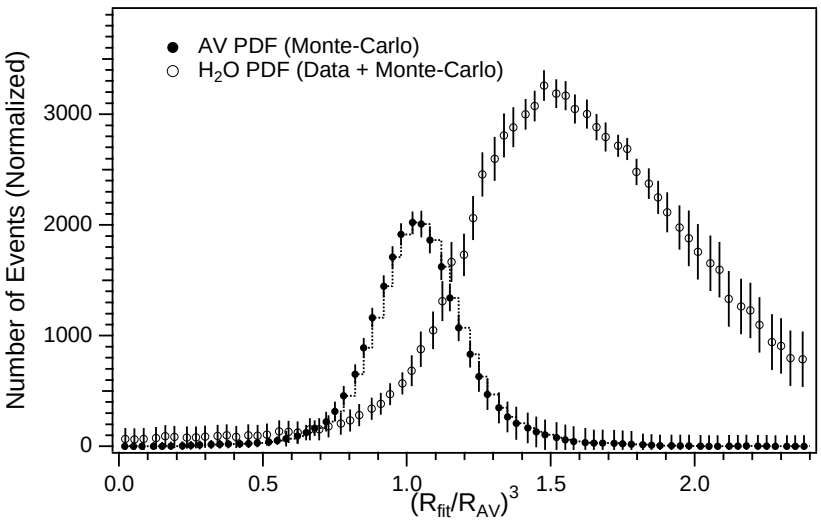

Figure 9.10: Radial probability distribution function (PDF) for the ^{208}Tl AV background. This probability distribution function is based on Monte Carlo simulations. The systematic error on the R^3 distribution is derived from the variations in the ^{208}Tl Monte Carlo simulations. For comparison the ^{214}Bi H_2O background PDF is shown.

[1] The ratio of ^{238}U and ^{232}Th in mine dust is about $\sim 1/3$ [105]. The U and Th concentration in the host rock and concrete liner of the SNO cavity has been measured to be about 1.5 μg of uranium and 4 μg of thorium.

The shape of the radial profile of the AV and H_2O background PDF show similar slopes and we expect to see correlations in the fit to these distributions. The background correlations is not a concern in this analysis as we are mainly interested in determining the neutrino interaction rates. It is reasonable to assume that any backgrounds in the outer region of the detector will be described by a linear combination of these two PDF's. Only the radial profile of the background PDF's is used in the maximum likelihood fit.

$$F_{Bkgd}(R^3) = f_{AV}(NHIT)F_{AV}(R^3) + f_{H_2O}(NHIT)F_{H_2O}(R^3) \tag{9.13}$$

Further improvements to the background probability distribution functions used in the decomposition of the data set and the neutrino signal extraction may come from the use of calibration source data. Neutron and γ calibration source data taken in the light water region of the detector can be used to describe the detector response in the outer regions of the detector and to derive a radial profile for the background distributions.

9.4 Extracting Neutrino Signals in Variable Fiducial Volumes

The signal extraction techniques described above are applied to the data using different fiducial volume cuts between $R_{fit} \leq 550 - 620$ cm and energy thresholds between NHIT $\geq$ $45 - 65$. The data and Monte Carlo PDF's are divided in the characteristic distributions fo R^3 and $\cos\theta_{\odot}$ distributions for a number of NHIT bins. The different contributions to the data are then determined by a maximum likelihood fit. The shapes of the elastic scattering and neutron NHIT distributions were constrained to match the Monte Carlo. The charged-current shape, however, was left unconstrained. The NHIT bin sizes are chosen so that each contains roughly the same number of events from the data. The extracted charged-current and neutral-current interaction rates are found to be in agreement for different fiducial volumes and NHIT thresholds.

The fiducial volumes and NHIT thresholds considered in this analysis are motivated by the goal to determine both the charged-current rate and neutral-current interaction rate. Figure 9.12 shows that the region between R=550-620 cm provides the greatest sensitivity to the radial distribution of the NC and CC signal. Using different NHIT threshold and variable fiducial volumes allows us to do two different types of analyses:

1. *"Background-Free" Measurement of CC Signal*: This analysis selects the cleanest region in the center of the detector to determine the neutrino interaction rates. Residual backgrounds to the neutrino signal are estimated.

2. *Combined Fit to Signal and Backgrounds in Variable Fiducial Volumes:* Using variable fiducial volumes we fit probability distribution functions in R^3, $\cos\theta_{\odot}$, and NHIT to the neutrino signal and the principal backgrounds. Consistency of the fit results demonstrates stability of the neutrino flux measurement with fiducial volume and maps out the backgrounds throughout the detector.

In fact, approach 1 is a limiting case of the more general combined fit to signals and backgrounds. Agreement between two approaches is used to demonstrate the internal consistency of the analysis.

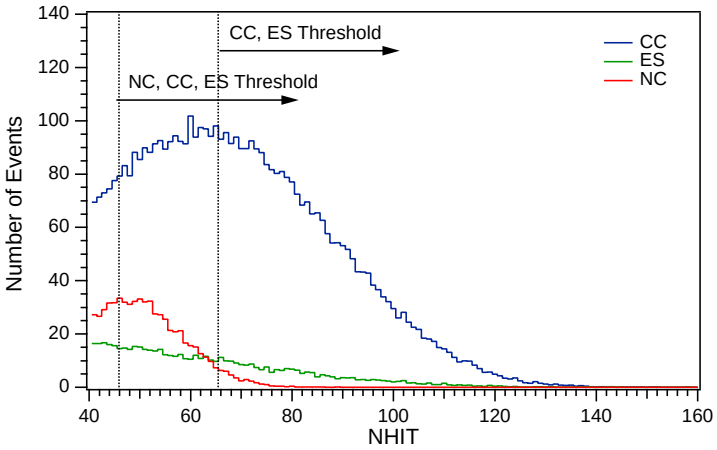

Figure 9.11: NHIT thresholds for the analysis of the CC, ES, and NC signal.

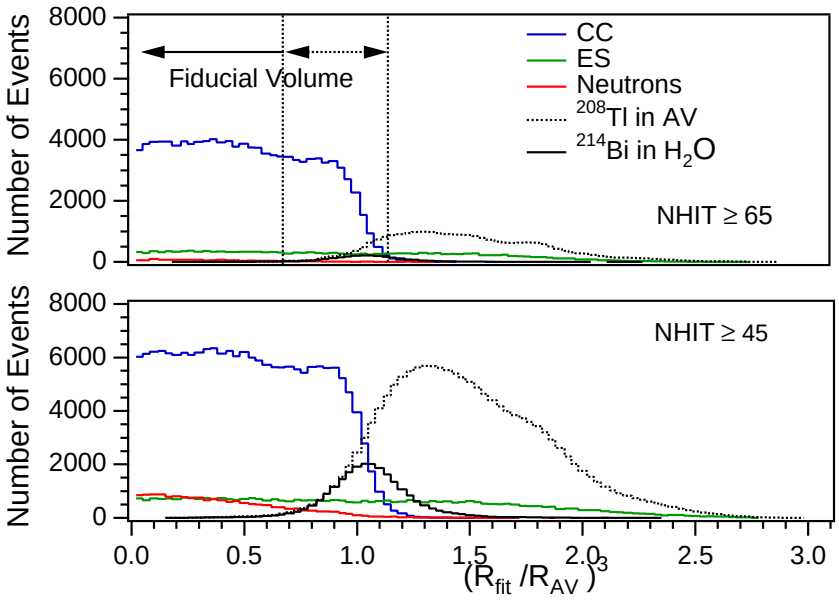

Figure 9.12: Fiducial volumes considered in the analysis of the CC, ES, and NC signal. The radial probability distribution functions of the neutrino signal and main backgrounds are shown for NHIT $\geq$ 45 and NHIT $\geq$ 65.

9.4.1 Determining the CC and ES Interaction Rate at energies above NHIT $\geq$ 65

The charged-current interaction rate in SNO can be determined from data above a high threshold of NHIT ≥ 65. Above that threshold the contributions from the neutron capture signal, including NC interactions, and backgrounds are small. Below we show the results from a spectral decomposition for fiducial volumes between $R_{fit} \leq 550-650$cm. In the maximum likelihood fit to the neutrino signals and the AV and H_2O backgrounds all amplitudes are constrained to be positive definite.

$$\mathcal{N} = \sum F_i(NHIT, R^3, \cos\theta_\odot) + F_{AV}(R^3) + F_{H_2O}(R^3), \quad \mathrm{i} = \mathrm{NC, CC, ES} \tag{9.14}$$

$$L = \sum_j \ln\mathcal{N}(NHIT_j, R_j^3, \cos\theta_{\odot j}) - \sum_i f_i \tag{9.15}$$

The fit results are shown in Figure 9.13 and listed in Table 9.5. The various correction factors which were applied for an analysis within a fiducial volume of $R_{fit} \leq 550$ cm were taken to be valid at larger radii. The only correction factor which should have a radial dependence is the signal loss in data reduction which is small compared to the uncertainty on the fit results. Possible background contributions to the CC and ES signal in this data set have been estimated in a number of different studies. The results are listed in Table 9.6. Figure 9.15 illustrates the composition of the SNO NHIT spectrum above NHIT ≥ 65.

Table 9.5: CC and ES signal in variable fiducial volume analysis above NHIT ≥ 65. All results are in given in units of SSM CC and ES flux predictions.

Fiducial Volume	$[CC]$	$[ES]$
$R_{fit} \leq 550$ cm	0.341 ± 0.020(stat.)	0.492 ± 0.081(stat.)
$R_{fit} \leq 570$ cm	0.336 ± 0.021(stat.)	0.510 ± 0.082(stat.)
$R_{fit} \leq 590$ cm	0.340 ± 0.024(stat.)	0.489 ± 0.078(stat.)
$R_{fit} \leq 620$ cm	0.347 ± 0.032(stat.)	0.513 ± 0.075(stat.)

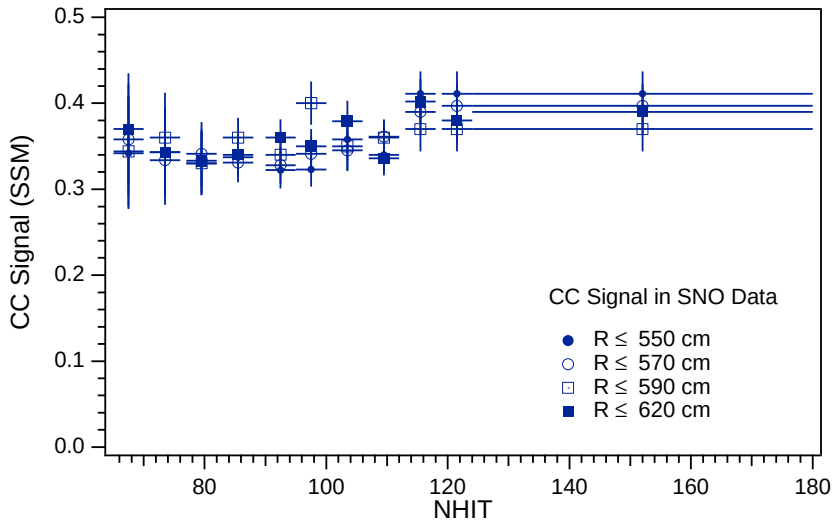

Figure 9.13: CC signal in SNO data from an unconstrained signal extraction for various fiducial volumes above NHIT ≥ 65.

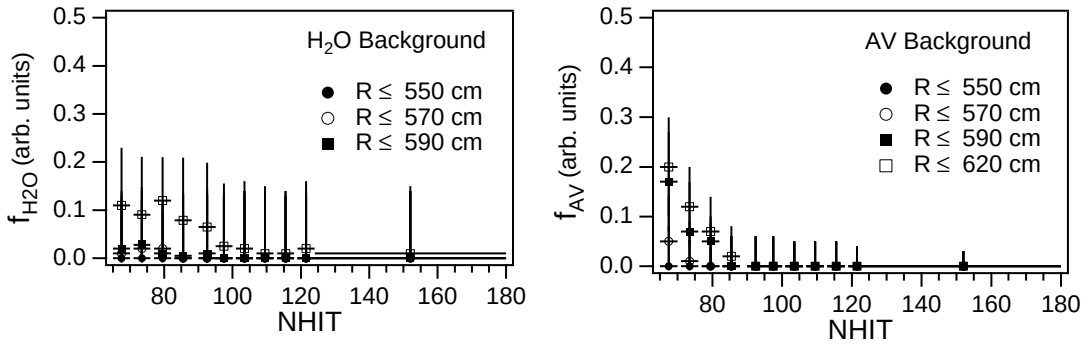

Figure 9.14: Background contributions from the AV and H_2O to the SNO data for various fiducial volumes above NHIT ≥ 65.

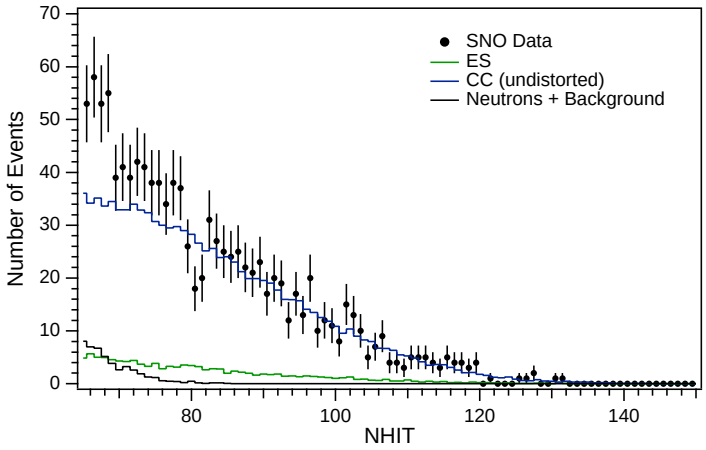

Figure 9.15: SNO NHIT spectrum above NHIT ≥ 65 and the contributions of the CC, ES signal obtained from the unconstrained signal extraction. The true CC spectrum is obtained by subtracting the ES and background contribution from the data. For illustration we indicate the undistorted ^{8}B CC spectrum scaled with the fit result for the CC contribution.

Table 9.6: Estimates of backgrounds and other systematic errors on the CC and ES signal above NHIT ≥ 65 within $R_{fit} \leq 550$cm.

Background	Fractional CC Error	Fractional ES Error	Ref.
High energy γ's	$1^{-0.008}_{+0.000}$	$1^{-0.019}_{+0.000}$	[70]
Low-energy background	$1^{-0.002}_{+0.000}$	$1^{-0.002}_{+0.000}$	[70]
Instrumental background	$1^{-0.002}_{+0.000}$	$1^{-0.006}_{+0.000}$	[70]
Energy Scale	$1^{-0.055}_{+0.065}$	$1^{-0.038}_{+0.055}$	[Chapter 6]
Energy Resolution	$1^{-0.005}_{+0.005}$	$1^{-0.003}_{+0.003}$	[Chapter 6]
Energy Scale Non-Linearity	$1^{-0.005}_{+0.005}$	$1^{-0.005}_{+0.005}$	[Chapter 6]
Vertex accuracy	$1^{-0.031}_{+0.031}$	$1^{-0.033}_{+0.033}$	[Chapter 4]
Vertex Resolution	$1^{-0.007}_{+0.007}$	$1^{-0.004}_{+0.004}$	[Chapter 4]
Trigger Efficiency	$1^{-0.000}_{+0.000}$	$1^{-0.000}_{+0.000}$	[28]
Live time	$1^{-0.001}_{+0.001}$	$1^{-0.001}_{+0.001}$	[Chapter 3]
Cut acceptance	$1^{-0.006}_{+0.007}$	$1^{-0.006}_{+0.007}$	[Chapter 5]
Cross-Section	$1^{-0.030}_{+0.030}$	$1^{-0.010}_{+0.010}$	[Chapter 7]

The systematic errors on the CC and ES fluxes are determined by perturbing the input parameters to the spectral decomposition. Using the data within a fiducial volume of $R_{fit} \leq 550$ cm and above a threshold of NHIT ≥ 65 we obtain

$$[CC]_{NHIT\geq 65} = 1.72 \pm 0.10 \text{ (stat.)} \, {}^{+0.14}_{-0.12} \text{ (syst.)} \times 10^6 \text{cm}^{-2}\text{s}^{-2} \tag{9.16}$$

$$[ES]_{NHIT\geq 65} = 2.48 \pm 0.41 \text{ (stat.)} \, {}^{+0.16}_{-0.14} \text{ (syst.)} \times 10^6 \text{cm}^{-2}\text{s}^{-2} \tag{9.17}$$

9.4.2 Determination of the Neutral-Current Interaction Rate above NHIT ≥ 46

For the measurement of the neutral-current interaction rate we consider data above a threshold of NHIT ≥ 46. This threshold is close to the peak of the NC signal and right at the ^{16}N calibration point. Internal backgrounds as well as external backgrounds need to be taken into consideration. Again, we will perform a spectral decomposition for fiducial volumes between $R_{fit} \leq 550 - 650$ cm. A maximum likelihood fit to the neutrino signals with radial probability distribution functions for the AV and H_2O background is performed. The background amplitudes are constrained to be positive definite.

$$\mathcal{N} = \sum F_i(NHIT, R^3, \cos\theta_\odot) + F_{AV}(R^3) + F_{H_2O}(R^3), \quad \mathrm{i} = \mathrm{NC, CC, ES} \tag{9.18}$$

$$L = \sum_j \ln\mathcal{N}(NHIT_j, R_j^3, \cos\theta_{\odot j}) - \sum_i f_i \tag{9.19}$$

The fit results are shown in Figure 9.16 and listed in Table 9.7. The various correction factors which were applied for an analysis within a fiducial volume of $R_{fit} \leq 550$ cm were taken to be valid at larger radii. The only correction factor which should have a radial dependence is the signal loss in data reduction which is small.

Background contributions to the CC and ES signal in this data set have been estimated in a number of different studies. The results are listed in Table 9.9. Figure 9.18 illustrates the composition of the SNO NHIT spectrum above NHIT ≥ 46.

Table 9.7: Results from a variable fiducial volume analysis above NHIT ≥ 46. The statistical error comes from the maximum likelihood fit. All results are in given in units of 5.05×10^6 cm^{-2} s^{-1}.

Fiducial Volume	$[CC]$	$[ES]$	$[Neutrons]$
$R_{fit} \leq 550$ cm	0.344 ± 0.021 (stat.)	0.483 ± 0.081 (stat.)	1.358 ± 0.298 (stat.)
$R_{fit} \leq 570$ cm	0.341 ± 0.023 (stat.)	0.503 ± 0.093 (stat.)	1.362 ± 0.283 (stat.)
$R_{fit} \leq 590$ cm	0.342 ± 0.024 (stat.)	0.510 ± 0.082 (stat.)	1.355 ± 0.267 (stat.)
$R_{fit} \leq 620$ cm	0.347 ± 0.032 (stat.)	0.513 ± 0.084 (stat.)	1.357 ± 0.312 (stat.)

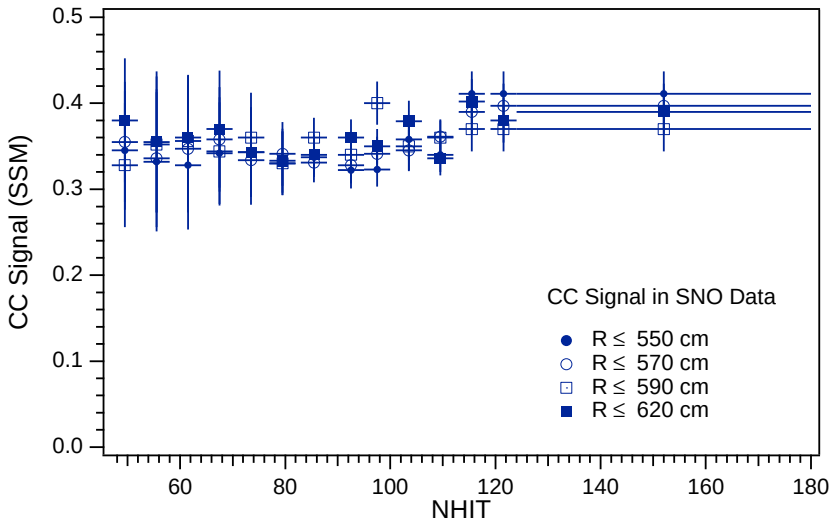

Figure 9.16: CC signal in SNO data from an unconstrained signal extraction for various fiducial volumes above NHIT ≥ 46.

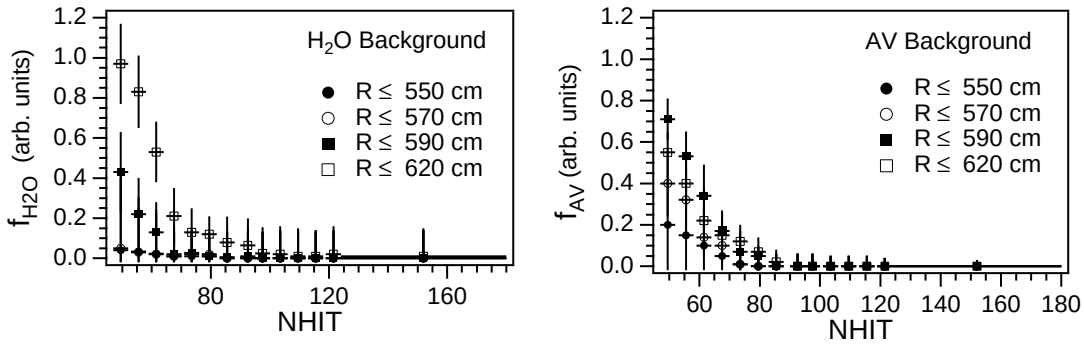

Figure 9.17: Background contributions from the AV and H_2O to the SNO data for various fiducial volumes above NHIT ≥ 46.

The neutron backgrounds to the NC signal from internal D_2O backgrounds have been determined using ex-situ water assays and in an in-situ analysis of low-energy Čerenkov data [106]. The results from these analyses are listed in Table 9.8. They are scaled by the target volume and corrected for the different energy threshold. The average rate of background neutron production from sources in the D_2O region is found to be 1.0 ± 0.2 neutrons/day. The production rate from external sources is 0.6 ± 0.2 neutrons per day. The neutron detection efficiency within the D_2O region is about 14.4% [106]. The total photodisintegration background from internal D_2O backgrounds corresponds to approximately 8.2% of the number of NC neutrons predicted by the standard solar model from ^{8}B neutrinos. The AV and H_2O backgrounds are accounted for by the background probability distribution functions used in the fit. Other sources of free neutrons in the D_2O region are cosmic ray events and atmospheric neutrinos. The number of sub-Čerenkov threshold background events from muons has been estimated. The sum of these backgrounds is subtracted from the total neutron contribution to the data set.

Table 9.8: Estimated neutron and Čerenkov background events in the neutrino data above NHIT ≥ 46.

Source	Events (per year) for NHIT ≥ 45	Fraction of SSM for NHIT ≥ 45
D_2O Photodisintegration	73^{+13}_{-15}	$0.082^{+0.015}_{-0.017}$
H_2O + AV Radioactivity	45^{+13}_{-13}	$0.051^{+0.015}_{-0.015}$
Atmospheric ν	$7^{+1.7}_{-1.7}$	$0.008^{+0.002}_{-0.002}$
Fission	< 1	< 0.001
^{2}H(α,α)pn	$3^{+0.3}_{-0.3}$	$0.003^{+0.00003}_{-0.00003}$
^{17}O$(\alpha$,n)	$\ll 1$	< 0.001
Terrestrial and Reactor $\overline{\nu}$	5	0.006
External Neutrons	$\ll 1$	< 0.001

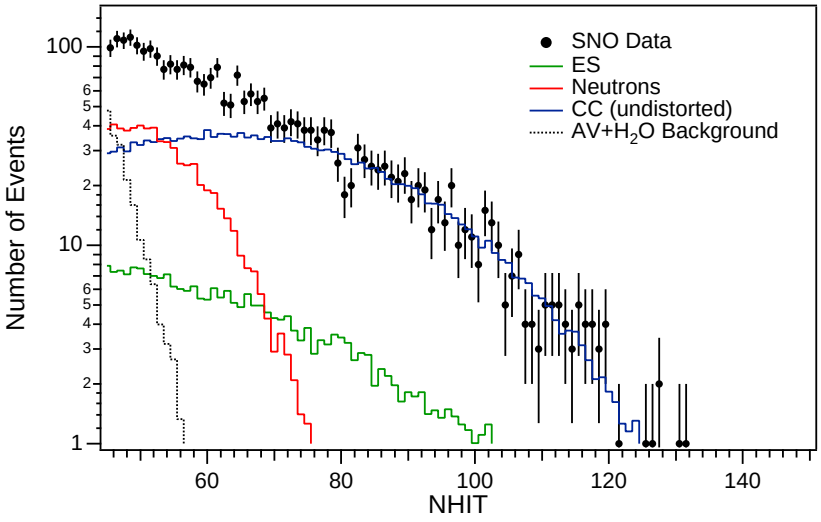

Figure 9.18: SNO NHIT spectrum above NHIT ≥ 46 for $R_{fit} \leq 550$ cm and the contributions of the CC, NC, and ES signal obtained from the unconstrained signal extraction. The true CC spectrum is obtained by subtracting the ES and background contribution from the data. For illustration we indicate the undistorted ^{8}B CC spectrum scaled with the fit result for the CC contribution.

With these background estimates we obtain for NHIT ≥ 46 and $R_{fit} \leq 550$ cm

$$\begin{aligned} [NC] &= [Neutrons] - [Bkgd] \\ &= (1.358 \pm 0.298) - (0.097 \pm 0.018) = 1.261 \pm 0.279 \end{aligned} \tag{9.20}$$

in units of 5.05×10^6 cm^{-2} s^{-1}. To optimize our sensitivity to the neutral-current signal we can consider the result with the smallest statistical error from the fit. With these background estimates we obtain for NHIT ≥ 46 and $R_{fit} \leq 590$ cm

$$\begin{aligned} [NC] &= [Neutrons] - [Bkgd] \\ &= (1.355 \pm 0.267) - (0.097 \pm 0.018) = 1.258 \pm 0.268 \end{aligned} \tag{9.21}$$

in units of 5.05×10^6 cm^{-2} s^{-1}.

The charged-current NHIT spectrum is obtained by subtracting the NC, ES, and background contributions from the measured SNO NHIT spectrum. The background contributions include the AV and H_2O contributions from the fit as well as the neutron background contributions, f_{bkgd}, described above. The neutron PDF is scaled accordingly to account for these additional backgrounds.

$$\begin{aligned} \mathcal{N}_{Data}(NHIT) &= \mathcal{N}_{CC} + \mathcal{N}_{NC} + \mathcal{N}_{ES} + \mathcal{N}_{AV} + \mathcal{N}_{H_2O} \\ \mathcal{N}_{CC}(NHIT) &= \mathcal{N}_{Data}(NHIT) \\ &- f_{ES}F_{ES} - (f_{NC} + f_{Bkgd})F_{NC} - f_{AV}F_{AV} - f_{H_2O}F_{H_2O} \end{aligned} \tag{9.22}$$

Table 9.9: Estimates of backgrounds and other systematic errors on the CC ES, and NC signal above NHIT ≥ 46 within $R_{fit} \leq 590$cm.

Background	CC Error	ES Error	NC Error	Ref.
Low-energy background	in fit to PDF	in fit to PDF	$1^{-0.183}_{+0.207}$	[70]
Instrumental background	$1^{-0.002}_{+0.000}$	$1^{-0.006}_{+0.000}$	$1^{-0.002}_{+0.000}$	[70]
Energy Scale	$1^{-0.055}_{+0.065}$	$1^{-0.038}_{+0.055}$	$1^{-0.076}_{+0.076}$	[Chapter 6]
Energy Resolution	$1^{-0.005}_{+0.005}$	$1^{-0.003}_{+0.003}$	$1^{-0.000}_{+0.005}$	[Chapter 6]
Energy Scale Non-Linearity	$1^{-0.005}_{+0.005}$	$1^{-0.005}_{+0.005}$	$1^{-0.005}_{+0.005}$	[Chapter 6]
Vertex accuracy	$1^{-0.031}_{+0.031}$	$1^{-0.033}_{+0.033}$	$1^{-0.021}_{+0.021}$	[Chapter 4]
Vertex Resolution	$1^{-0.007}_{+0.007}$	$1^{-0.004}_{+0.004}$	$1^{-0.007}_{+0.007}$	[Chapter 4]
Trigger Efficiency	$1^{-0.000}_{+0.000}$	$1^{-0.000}_{+0.000}$	$1^{-0.000}_{+0.000}$	[106]
Live time	$1^{-0.001}_{+0.001}$	$1^{-0.001}_{+0.001}$	$1^{-0.001}_{+0.001}$	[Chapter 3]
Cut acceptance	$1^{-0.006}_{+0.007}$	$1^{-0.006}_{+0.007}$	$1^{-0.006}_{+0.007}$	[Chapter 5]
Neutron Capture	N/A	N/A	$1^{-0.036}_{+0.040}$	[106]
Cross-Section	$1^{-0.030}_{+0.030}$	$1^{-0.010}_{+0.010}$	$1^{-0.030}_{+0.030}$	[Chapter 7]

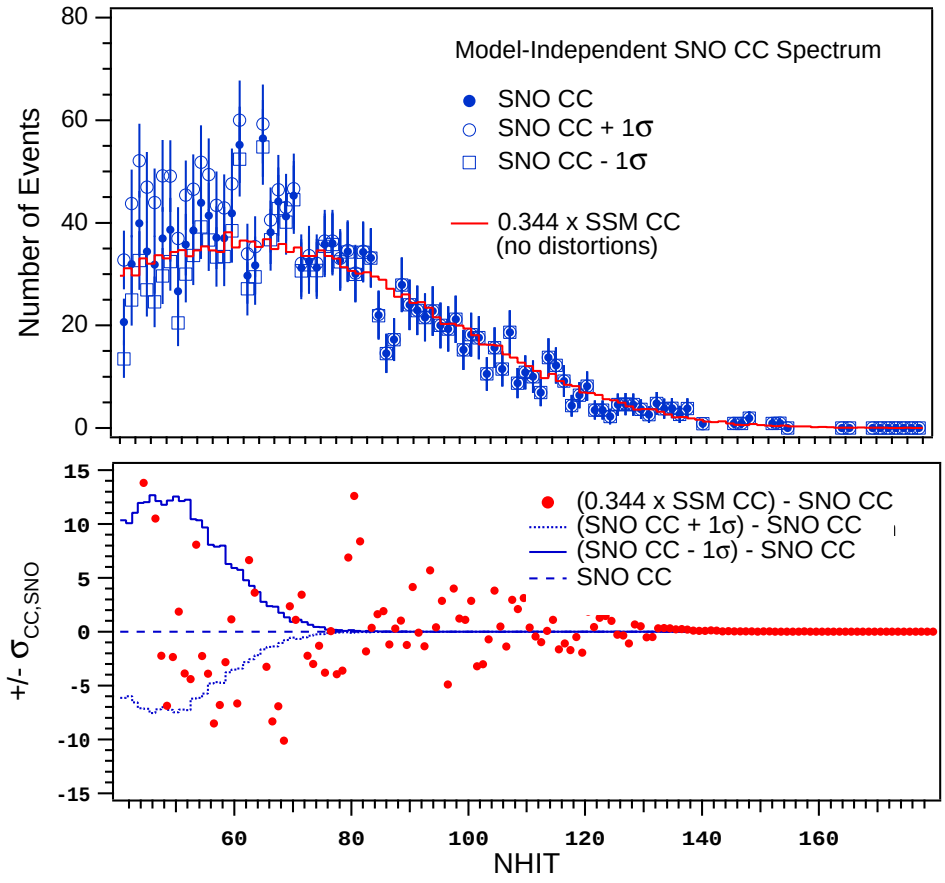

Figure 9.19: CC NHIT spectrum above NHIT $\geq$ 46 for $R_{fit} \leq$ 550 cm as determined in the model-independent unconstrained signal extraction. The lower panel shows the $\pm 1\sigma$ deviations of the experimental CC spectrum and the difference between the experimentally measured CC spectrum and the suppressed but undistorted ^{8}B CC spectrum.

9.4.3 Results from the Spectral Decomposition

Using a model-independent technique of spectral decomposition the neutrino-deuteron interaction rates have been measured for various fiducial volumes and NHIT thresholds. This method involves the use of probability distributions functions in NHIT, R^3, and $\cos\theta_\odot$ for the neutrino signals and radial background probability distribution functions that describe the backgrounds from the acrylic vessel and the H_2O. The results we obtain are consistent for various fiducial volumes and are in good agreement with (and provide independent confirmation of) the measurements derived from data taken in the central volume of the SNO detector. Within a fiducial volume of $R_{fit} \leq 550$ cm and with NHIT ≥ 46 the neutrino interaction rates as determined in the model-independent, ^{8}B shape-unconstrained spectral decomposition are

$$\begin{aligned}
[CC] &= 0.344 \pm 0.021 \text{ (stat.)} \, {}^{+0.025}_{-0.022} \text{ (syst.)} \\
[NC] &= 1.261 \pm 0.279 \text{ (stat.)} \, {}^{+0.117}_{-0.119} \text{ (syst.)} \\
[ES] &= 0.483 \pm 0.081 \text{ (stat.)} \, {}^{+0.031}_{-0.025} \text{ (syst.)}
\end{aligned}$$

in units of 5.05×10^6 cm^{-2} s^{-1}, the Standard Solar Model prediction by Bahcall et al. [11]. The statistical errors are obtained from the fit. The systematic errors are derived from perturbation of the event observables in the spectral decomposition and systematic error estimates of the neutrino flux normalization. The ν_e flux corresponding to the model-independent charged-current spectrum is determined by fitting a standard ^{8}B spectrum to the measured, unconstrained CC spectrum shown in Figure 9.19. Tables 9.10 and 9.11 compare the solar neutrino flux measurements obtained in this work with the final results published by the SNO collaboration. From the results listed in Table 9.7 we find that the unconstrained NC measurement with the smallest statistical error is obtained for a fiducial volume of $R_{fit} \leq 590$ cm.

$$\begin{aligned}
[CC] &= 0.342 \pm 0.024 \text{ (stat.)} \, {}^{+0.025}_{-0.022} \text{ (syst.)} \\
[NC]_{unconst.} &= 1.258 \pm 0.268 \text{ (stat.)} \, {}^{+0.118}_{-0.116} \text{ (syst.)}
\end{aligned}$$

Combining the statistical and systematic errors in quadrature and forming the $[NC] - [CC]$ difference we obtain

$$[NC]_{unconst.} - [CC] = 0.916\ ^{+0.295}_{-0.294} \tag{9.23}$$

The difference between the charged-current and neutral-current interaction rates determined in this way is more than 3.1 σ. With the assumption of the standard ^{8}B beta-decay shape in the spectra decomposition of the data a more precise determination of the NC interaction rate can be made.

$$[NC]_{const.} \quad = \quad 1.012 \pm 0.100\ (\text{stat.})\ ^{+0.095}_{-0.094}\ (\text{syst.}) \tag{9.24}$$

Again, combining the statistical and systematic errors in quadrature and forming the $[NC] - [CC]$ difference we now obtain

$$[NC]_{const.} - [CC] = 0.670\ ^{+0.142}_{-0.141} \tag{9.25}$$

In the CC-shape constrained case, under the assumption of the undistorted, standard ^{8}B energy spectrum, the difference between the NC and the CC flux is 4.79 σ. These results are solar-model independent evidence for the flavor transformation of solar neutrinos.

The measurement of the neutral-current interaction rate is a model-independent measurement of the flux of active solar ^{8}B neutrinos and a critical test of solar model predictions. The measurements of the total active solar ^{8}B flux derived from a constrained and unconstrained spectral decomposition of the data within $R_{fit} \leq 590$ cm and NHIT ≥ 46 are

$$\Phi^{SNO}_{^8B}\ (\text{const.}) = [NC]_{const.} = 5.12 \pm 0.47\ (\text{stat.})\ ^{+0.49}_{-0.48}\ (\text{syst.}) \times 10^6\ \text{cm}^{-2}\text{s}^{-1} \tag{9.26}$$

$$\Phi^{SNO}_{^8B}\ (\text{unconst.}) = [NC]_{unconst.} = 6.35 \pm 1.35\ (\text{stat.})\ ^{+0.60}_{-0.60}\ (\text{syst.}) \times 10^6\ \text{cm}^{-2}\text{s}^{-1} \tag{9.27}$$

Both the CC shape-constrained and unconstrained measurement of the CC flux are in good agreement with the Standard Solar Model predictions of $\Phi^{SNO}_{^8B} = 5.05 \times 10^6\ \text{cm}^{-2}\text{s}^{-1}$ by Bahcall et al. [11].

Table 9.10: Solar neutrino flux measurements at the Sudbury Neutrino Observatory above a $\sim$ 7 MeV analysis threshold for a central fiducial volume of $R_{fit} \leq 550$ cm. All flux measurements are given in units of $\times 10^6$ cm^{-2} s^{-1}. Results from other solar neutrino flux measurements at SNO are reported in [15, 150, 182]. The final results of the SNO collaboration are those reported in the publication from June 2001 [70].

	this work	SNO PRL 2001 [70]
Data Period	Nov 99 - Jan 2002	Nov 99 - Jan 2002
Livetime	240.9 days	240.9 days
Fiducial Volume	$R_{fit} \leq 550$ cm	$R_{fit} \leq 550$ cm
Analysis Threshold	NHIT ≥ 65	$E \geq 6.75$ MeV
Φ_{CC}^{SNO}	1.72 ± 0.10(stat.) $^{+0.14}_{-0.12}$ (syst.)	1.75 ± 0.07(stat.) $^{+0.12}_{-0.11}$(syst.)
Φ_{ES}^{SNO}	2.48 ± 0.41(stat.) $^{+0.16}_{-0.14}$ (syst.)	2.39 ± 0.34(stat.) $^{+0.16}_{-0.14}$(syst.)

Table 9.11: Solar neutrino flux measurements at the Sudbury Neutrino Observatory for a central fiducial volume of $R_{fit} \leq 550$ cm above a ~ 5 MeV analysis threshold. All flux measurements are given in units of $\times 10^6$ cm^{-2} s^{-1}. For the NC measurement two results are given, a constrained (const.) and unconstrained (unconst.) flux measurement. Results from other solar neutrino flux measurements at SNO are reported in [15, 150, 182]. The final results of the SNO collaboration are those reported in the publication from April 2002 [106].

	this work	SNO PRL 2002 [106]
Data Period	Nov 99 - Jan 2002	Nov 99 - May 2002
Livetime	240.9 days	306.4 days
Fiducial Volume	$R_{fit} \leq 550$ cm	$R_{fit} \leq 550$ cm
Analysis Threshold	NHIT ≥ 46	$E \geq 5.0$ MeV
Φ_{CC}^{SNO}	1.74 ± 0.11(stat.) $^{+0.13}_{-0.11}$(syst.)	$1.76\ ^{+0.06}_{-0.05}$(stat.) $^{+0.09}_{-0.09}$(syst.)
Φ_{ES}^{SNO}	2.44 ± 0.41(stat.) $^{+0.16}_{-0.13}$(syst.)	$2.39\ ^{+0.24}_{-0.23}$(stat.) $^{+0.12}_{-0.12}$(syst.)
Φ_{NC}^{SNO} (const.)	5.11 ± 0.50(stat.) $^{+0.48}_{-0.48}$(syst.)	$5.09\ ^{+0.44}_{-0.43}$(stat.) $^{+0.46}_{-0.43}$(syst.)
Φ_{NC}^{SNO} (unconst.)	6.37 ± 1.41(stat.) $^{+0.59}_{-0.60}$(syst.)	$6.42\ ^{+1.57}_{-1.57}$(stat.) $^{+0.55}_{-0.58}$(syst.)

9.5 *Removing the Last Model-Dependence from the SNO Solar Neutrino Flux Measurements: Constraints on the Two-Body Axial Current $L_{1,A}$ in Effective Field Theory from the Solar Neutrino Measurements at SNO and Super–Kamiokande*

The Sudbury Neutrino Observatory and Super–Kamiokande have made precision measurements of the interaction rates of solar neutrinos with their respective target media. The results of the solar neutrino flux analysis at SNO are summarized in Tables 9.10 and 9.11. To deduce the absolute solar neutrino flux from the measured interaction rates theoretical input is needed. The solar neutrino flux measurements reported by these experiments depend on the cross-section calculations for charged-current and neutral-current neutrino-deuteron interactions and the elastic scattering cross-section of neutrinos and electrons. Modern calculations of the neutrino-deuteron cross-sections make use of Effective Field Theory (EFT). These calculations depend on one free parameter: $L_{1,A}$ [21]. (For a discussion of neutrino-deuteron cross-section calculations see Chapter 7 and references therein.) The elastic scattering cross-section of neutrinos is independent of $L_{1,A}$ and well-known. Recently, Jiunn-Wei Chen [25, 163] suggested to make a determination of $L_{1,A}$ using the solar neutrino measurements of the SNO and Super–Kamiokande experiments. The questions we can ask are:

Is it possible to constrain $L_{1,A}$ in a model-independent way from the recent solar neutrino measurements? What are the best values of $\phi_{\nu_e}(^8B)$, $\phi_{\nu_x}(^8B)$, and $L_{1,A}$ that fit the current set of solar neutrino measurements?

A model-independent analysis of the solar neutrino interaction rates measured in the second generation solar neutrino experiments SNO and Super–Kamiokande allow us not only to derive constraints on $L_{1,A}$ but also remove the last model-dependence from the evidence of solar neutrino flavor transformation presented by SNO. At the end of this chapter we will report the significance of evidence for neutrino flavor transformation from the combined results of SNO and Super–Kamiokande and evaluate the joint parameter regions of the solar neutrino fluxes ϕ_{ν_e} and ϕ_{ν_x}, and the parameter $L_{1,A}$.

9.5.1 Solar Neutrino Measurements

Using D_2O and H_2O as their respective target media SNO and Super–Kamiokande have measured the charged-current (CC), neutral-current (NC), and elastic scattering (ES) interaction rates of solar neutrinos. Under the assumption of no spectral distortions in the ^{8}B spectrum the experiments have reported the following flux results in units of $\times 10^6$ cm^{-2} s^{-1}:

$$\phi_{CC}^{SNO} = 1.76\ ^{+0.06}_{-0.05}\ (\text{stat.})\ ^{+0.09}_{-0.09}\ (\text{syst.}) \tag{9.28}$$

$$\phi_{ES}^{SNO} = 2.39\ ^{+0.24}_{-0.23}\ (\text{stat.})\ ^{+0.12}_{-0.12}\ (\text{syst.}) \tag{9.29}$$

$$\phi_{NC}^{SNO} = 5.09\ ^{+0.44}_{-0.43}\ (\text{stat.})\ ^{+0.46}_{-0.43}\ (\text{syst.}) \tag{9.30}$$

$$\phi_{ES}^{SK} = 2.32\ ^{+0.03}_{-0.03}\ (\text{stat.})\ ^{+0.08}_{-0.07}\ (\text{syst.}) \tag{9.31}$$

For comparison, the Standard Solar model prediction [11] for the flux of ^{8}B neutrinos is $\phi_{8B}^{SSM} = 5.05 \times 10^6$ cm^{-2} s^{-1}. These measurements are considered evidence for the flavor transformation of solar neutrinos. It is generally believed that the change of solar neutrinos is caused by the oscillation of massive neutrinos but other mechanisms that explain the observed flavor change have been proposed. Positive evidence for the oscillation of solar neutrinos is yet to be reported. In the case of neutrino oscillations, the shape of the ^{8}B spectrum may be distorted. In a truly model-independent analysis we have to demonstrate that the effect of possible shape distortions is small or can be accounted for. As we will show below, the effect of shape distortions for the Large Mixing Angle solution of solar neutrino oscillations is negligible in the context of this analysis.

The experimentally measured neutrino interaction rates, the neutrino fluxes, and their respective cross-sections are related through equations 9.32 - 9.34. In modern EFT calculations the neutrino-deuteron cross-sections depend on the two-body axial current $L_{1,A}$ while the elastic scattering cross-section is independent of $L_{1,A}$.

$$[CC] = \sigma_{CC}(L_{1,A})\ \Phi_{\nu_e} \tag{9.32}$$

$$[NC] = \sigma_{NC}(L_{1,A})\ (\Phi_{\nu_e} + \Phi_{\nu_\mu} + \Phi_{\nu_\tau}) \tag{9.33}$$

$$[ES] \approx \sigma_{ES}\ \left[\Phi_{\nu_e} + 0.154\ (\Phi_{\nu_\mu} + \Phi_{\nu_\tau})\right] \tag{9.34}$$

9.5.2 $L_{1,A}$ Dependence of the Neutrino-Deuteron Cross-Sections

In the SNO solar neutrino analysis the choice of $L_{1,A}$ is based on the comparison of the cross-section calculations of Nakamura-Sato-Gudkov-Kubodera NSGK [147] and Ando et al. [72] with Butler-Chen-Kong (bck) [21]. To reproduce the calculations of Ando et al. with BCK we correct for the updated values of g_A and G_F and then scale $L_{1,A}$ to match the two different cross-section calculations. We find $L_{1,A} = 4.0$ fm^3.

Simulations with the SNO Monte-Carlo and Analysis code, SNOMAN (version 4_0184), are then used to determine the yield of the neutrino-deuteron interactions as a function of $L_{1,A}$. The $L_{1,A}$ dependence is derived from the predicted number of CC, NC, ES events. A fiducial volume cut of $R_{fit} \leq 550$ cm, the high-level event-quality cuts (HLC), and a threshold cut of NHIT ≥ 45 are applied to the Monte Carlo data. This allows us to determine the $L_{1,A}$ dependence of the CC and NC cross-sections. The ES cross-section is not a function of $L_{1,A}$. Figure 9.20 shows the result of SNOMAN Monte Carlo simulations for the CC yield at different values of $L_{1,A}$, and the resulting fit to the Monte Carlo simulations.

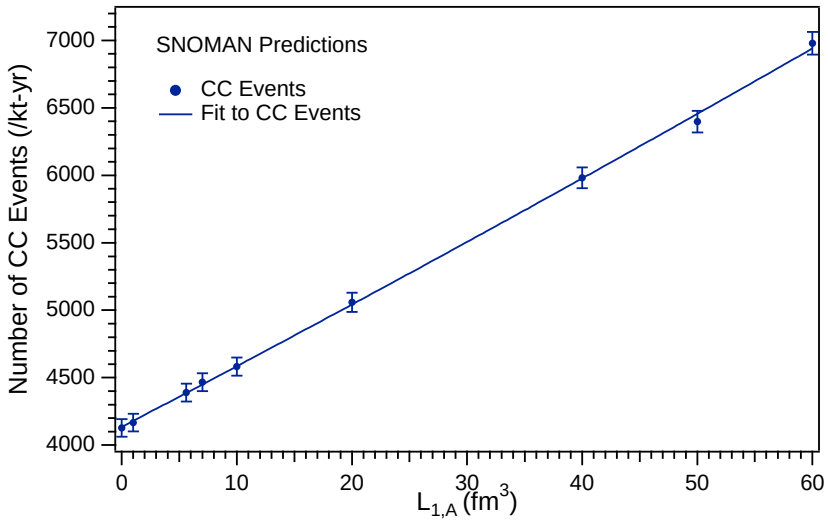

Figure 9.20: SNOMAN Monte Carlo calculations for the yield of CC events in SNO with NHIT ≥ 45 for different values of $L_{1,A}$. A fiducial volume cut of $R_{fit} \leq 550$ cm and the high-level event-quality cuts (HLC) are applied to the Monte Carlo data. In addition to the SNOMAN results we show a fit to the CC yield.

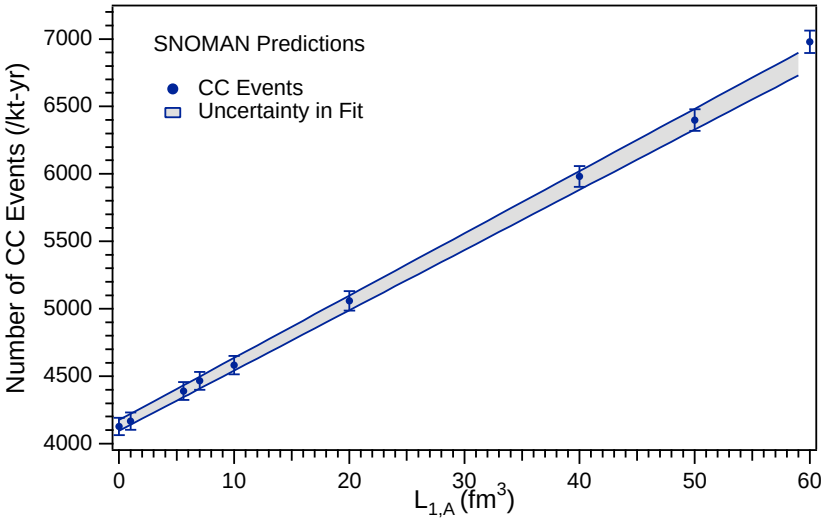

Figure 9.21: SNOMAN Monte Carlo calculations for the yield of CC events in SNO with NHIT ≥ 45 for different values of $L_{1,A}$. The error band is derived from the uncertainty in the fit to the discrete set of Monte Carlo simulations.

From a polynomial fit to the SNOMAN calculations we obtain:

$$N_{CC}(L_{1,A}) = (4135 \pm 39.6) + (44.655 \pm 4.9) \times L_{1,A} \tag{9.35}$$

The non-linear term of the fit is vanishingly small (and an artifact of the numerical calculation). This linear function is a parametrization of the charged-current yield as a function of $L_{1,A}$ as predicted by the cross-section calculation in the SNO Monte Carlo code. The error in the fit describes the statistical uncertainty in the simulation. In the absence of higher-statistics simulations we can define a band that describes the $L_{1,A}$-dependence of the predicted number of CC events. As we will see below, the limited statistics of the SNOMAN simulation is a negligible uncertainty in the determination of $L_{1,A}$.

By normalizing the yield of the interaction rates to 1 at $L_{1,A} = 4.0$ fm^3 we can compare the relative $L_{1,A}$-dependence of the cross-sections. Figure 9.22 shows the yield of the CC, NC, and ES cross-sections as a function of $L_{1,A}$. It has been shown by Butler and Chen [20] that the ratio $[CC]/[NC]$ of the cross-section yields is insensitive to $L_{1,A}$. This implies

that the relative (normalized) $L_{1,a}$-dependence of the CC and NC cross-sections is the same. The yield of the elastic scattering (ES) interaction is independent of $L_{1,A}$.

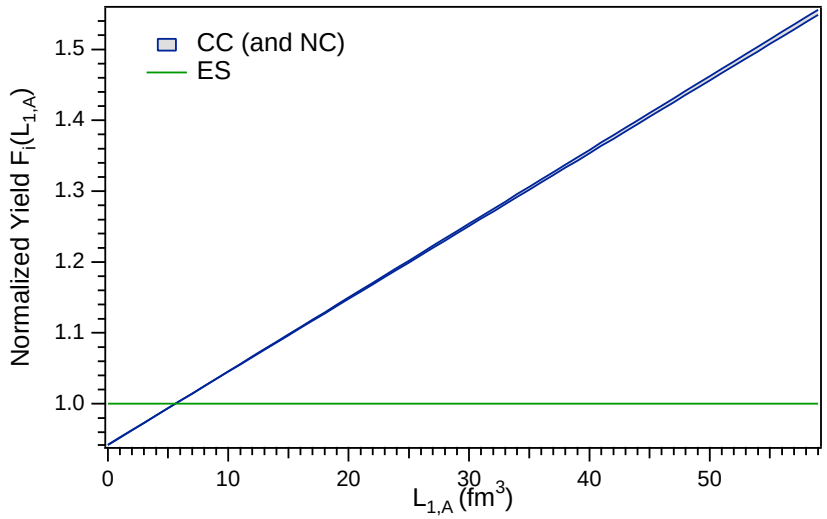

Figure 9.22: $L_{1,A}$ dependence of the normalized yields of the CC, NC, and ES neutrino cross-sections with deuterium as determined by SNOMAN calculations. The horizontal and diagonal bands are parameterizations of the $L_{1,A}$-dependence derived from fits to Monte Carlo simulations at discrete values of $L_{1,A}$. The statistical error in $F_{CC,NC}(L_{1,A})$ from the Monte Carlo calculations is small and a negligible contribution to the uncertainty in the determination of $L_{1,A}$.

We define $F(L_{1,A})$ to be the function that describes the normalized $L_{1,A}$-dependence of the cross-section.

$$F_i(L_{1,A} = 4.0) = 1, \quad i = \mathrm{NC}, \mathrm{CC} \tag{9.36}$$

$$F_{ES}(L_{1,A}) = F_{ES} = 1 \tag{9.37}$$

Introducing $F(L_{1,A})$ we can rewrite the previous equations 9.32 - 9.34 as

$$[CC] = F(L_{1,A})\ \sigma_{CC}\ \Phi_{\nu_e} \tag{9.38}$$

$$[NC] = F(L_{1,A})\ \sigma_{NC}\ (\Phi_{\nu_e} + \Phi_{\nu_\mu} + \Phi_{\nu_\tau}) \tag{9.39}$$

$$[ES] = F_{ES}\ \sigma_{ES}\ \left[\Phi_{\nu_e} + 0.154\ (\Phi_{\nu_\mu} + \Phi_{\nu_\tau})\right] \tag{9.40}$$

9.5.3 Analysis Threshold Dependence of $F(L_{1,A})$ and $L_{1,A}$ Constraints

The constraints we derive on $L_{1,A}$ are expected to be independent of the data set or the analysis threshold used in the SNO analysis. In the analysis presented in Chapter 9 and in [106] a threshold of NHIT $\geq$ 46, or $\sim$ 5 MeV has been chosen. The functional form of $F(L_{1,A})$ which we determined in the previous section is based on Monte Carlo data sets generated with SNOMAN for this particular analysis threshold. The specific $F(L_{1,A})$ function given above corresponds to Monte Carlo data with an NHIT (or energy) threshold of NHIT $\geq$ 45. The same fiducial volume and high-level event-quality cuts which are used in the reduction of the SNO data set are applied to the Monte Carlo data.

It is important to verify that the normalized $L_{1,A}$-dependence $F_i(L_{1,A})$ derived above is independent of the threshold used in the Monte Carlo simulations. Figure 9.23 shows the yield of CC events for different analysis thresholds as a function of $L_{1,A}$. The statistical error bars are the size of the markers and too small to be seen. The results for NHIT $\geq$ 10 are in question because of Monte Carlo threshold effects. The resulting normalized yields are shown in Figure 9.24. The solid line gives $F(L_{1,A})$ for NHIT $\geq$ 45. We find that the $L_{1,A}$-dependencies derived from Monte-Carlo are in good agreement for thresholds between NHIT $\geq$ 45-65. The contribution of the analysis threshold to the uncertainty on $F(L_{1,A})$ is small.

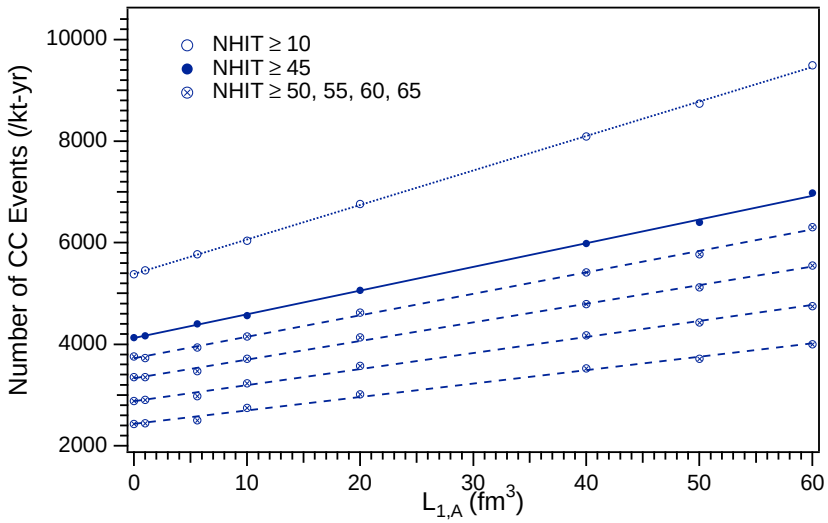

Figure 9.23: Yield of CC events for different analysis thresholds as a function of $L_{1,A}$. The statistical error bars are the size of the markers and too small to be seen. The results for NHIT $\geq$ 10 are in question because of Monte Carlo threshold effects.

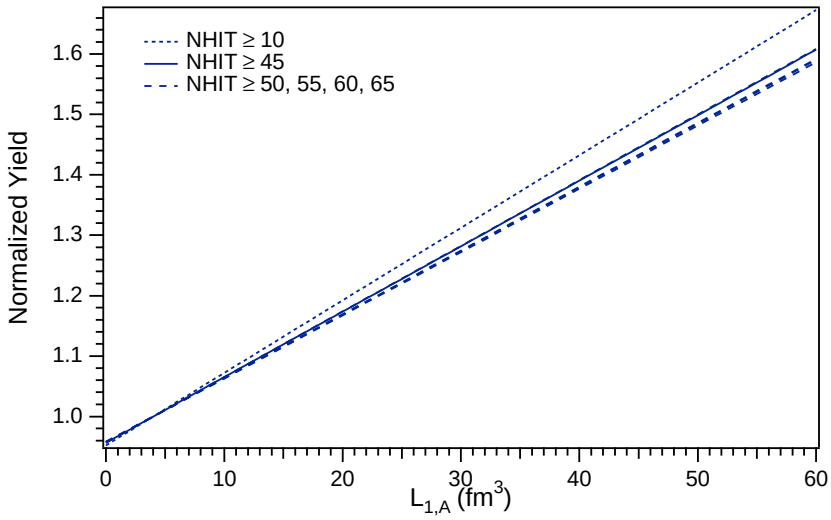

Figure 9.24: $L_{1,A}$ dependence of the normalized yields of the CC neutrino cross-sections with deuterium for different NHIT analysis thresholds. The results for NHIT $\geq$ 10 are in question because of Monte Carlo threshold effects. There is good agreement for the Monte Carlo predictions of $F(L_{1,A})$ for analysis thresholds between NHIT $\geq$ 45-65.

9.5.4 Spectral Distortions in the ^8B Spectrum and their Effect on $L_{1,A}$ Constraints

In the presence of neutrino oscillations the ^{8}B spectrum may be distorted. In this case the simulated yield of the neutrino-deuteron interactions changes and hence the normalized yield $F(L_{1,A})$ may be different. We can treat the effect of spectral distortions as an additional uncertainty on $F(L_{1,A})$ and propagate the error on $F(L_{1,A})$ into the constraints on $L_{1,A}$.

Figure 9.25 shows Monte Carlo calculations of the yield of CC interactions in SNO for a standard ^{8}B spectrum (SSM), a suppressed but otherwise standard ^{8}B spectrum (0.344 $\times$ SSM), and for a LMA-distorted ^{8}B spectrum (LMA). The LMA MSW oscillation parameters chosen in this analysis are $\sin^2 2\theta = 0.78$ and $\Delta m^2 = 5 \times 10^{-5}$ eV^2. Based on these simulations we find (see Figure 9.26) that the variation in the normalized yield $F(L_{1,A})$ is small. However, more detailed studies of all spectral shapes corresponding to the currently allowed oscillation parameters are necessary to quantify this effect more precisely.

For reference, Figure 9.27 shows SNOMAN Monte Carlo predictions for CC spectra in SNO with neutrino energy spectra based on the standard ^{8}B spectrum (SSM), a suppressed ^{8}B spectrum (0.344 $\times$ SSM), and a MSW LMA-distorted ^{8}B spectrum. The suppression factor 0.344 is obtained in an earlier part of this chapter and comes from the analysis of the CC interaction rate of solar ^{8}B neutrinos with deuterium.

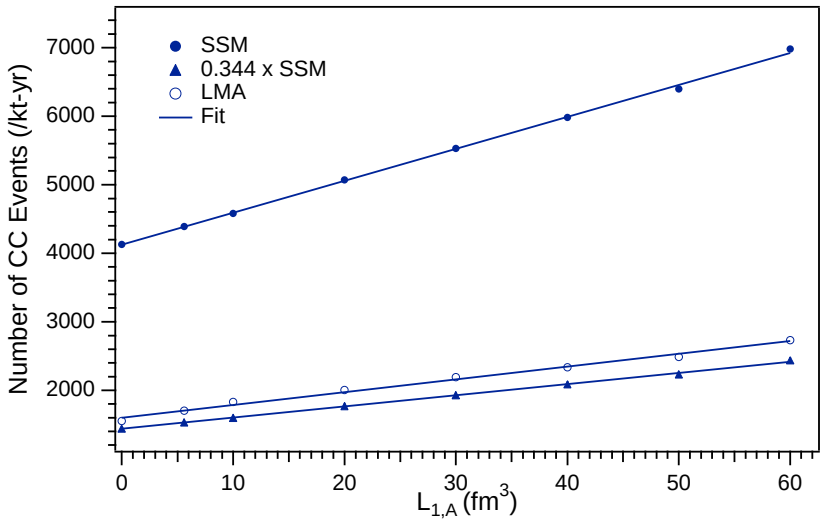

Figure 9.25: Yield of CC events with NHIT ≥ 45 as a function of $L_{1,A}$ for the standard ^{8}B spectrum, a suppressed but otherwise standard ^{8}B spectrum, and the LMA-distorted ^{8}B spectrum. The LMA MSW oscillation parameters chosen in this analysis are $\sin^2 2\theta = 0.78$ and $\Delta m^2 = 5 \times 10^{-5}$ eV^2. The statistical error of the simulation is of the size of the markers and too small to be seen.

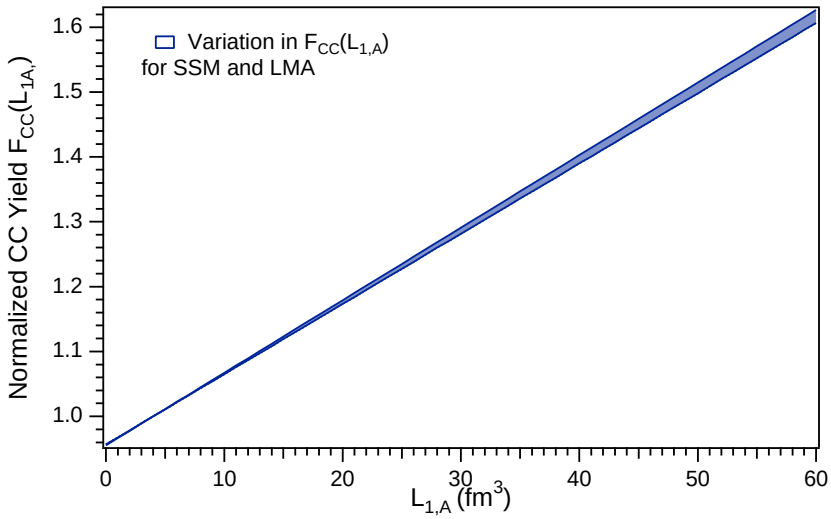

Figure 9.26: Normalized yield of CC events as a function of $L_{1,A}$ for the standard ^{8}B spectrum, a suppressed but otherwise standard ^{8}B spectrum, and the LMA-distorted ^{8}B spectrum. The effect of spectral distortions on the normalized $L_{1,A}$-dependence of the cross-section yield is small.

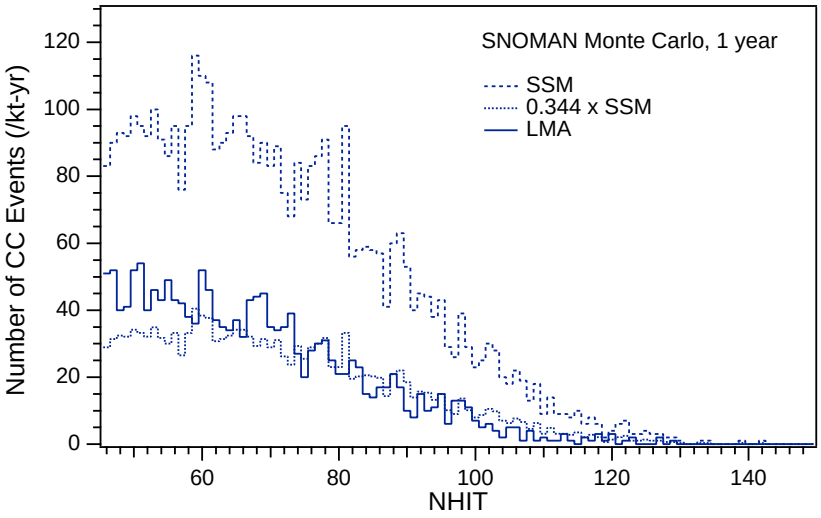

Figure 9.27: SNOMAN Monte Carlo predictions for CC spectra in SNO with neutrino energy spectra based on the standard ^{8}B spectrum (SSM), a suppressed ^{8}B spectrum (0.344 $\times$ SSM), and a MSW LMA-distorted ^{8}B spectrum.

9.5.5 *Model-Independent Determination of Φ_{ν_e}, Φ_{ν_x}, and $L_{1,A}$ from the SNO and Super–Kamiokande Solar Neutrino Flux Measurements*

The characteristic $L_{1,A}$-dependence of the neutrino-deuteron cross-sections allows one to make a model-independent determination of ϕ_{ν_e}, ϕ_{ν_x}, and $L_{1,A}$ from the experimental measurements Φ_{CC}^{SNO}, Φ_{NC}^{SNO}, Φ_{ES}^{SK} alone. We determine Φ_{ν_e}, Φ_{ν_x}, and $L_{1,A}$ simultaneously from a fit to the experimentally measured interaction rates. We rewrite equations 9.38 - 9.40 in terms of Φ_{ν_e}, Φ_{ν_x}, and $L_{1,A}$, eliminating Φ_{ν_μ} and Φ_{ν_τ}.

$$\phi_{CC}^{SNO} = F(L_{1,A})\ \Phi_{\nu_e} \tag{9.41}$$

$$\phi_{NC}^{SNO} = F(L_{1,A})\ \Phi_{\nu_x} \tag{9.42}$$

$$\phi_{ES}^{SK} = \Phi_{\nu_e} + 0.154\ (\Phi_{\nu_x} - \Phi_{\nu_e}) \tag{9.43}$$

with $F(L_{1,A}) = F_{CC}(L_{1,A}) = F_{NC}(L_{1,A})$. We can use the three measurements ϕ_{CC}^{SNO}, ϕ_{NC}^{SNO}, and ϕ_{ES}^{SK} in equations 9.41 - 9.43 and solve for the three unknowns Φ_{ν_e}, Φ_{ν_x}, and $L_{1,A}$. The statistical and systematic errors on the experimental results are combined in quadrature and included in the fit.

As one special case, it is instructive to consider first the $L_{1,A}$ constraints we obtain from the high-statistics Super–Kamiokande ES measurement while assuming the central values for SNO. Figure 9.28 shows the Super–Kamiokande constraint on $L_{1,A}$. With the measurements of Super–Kamiokande and the central values from SNO we can constrain $L_{1,A}$ to be in the range $L_{1,A}^{SK} \approx 4 \pm 3.0$ fm^3. This special case is illustrated in Figure 9.28. In the full model-independent analysis, however, we do not make any assumptions about the measured interaction rates and let Φ_{ν_e}, Φ_{ν_x}, and $L_{1,A}$ vary simultaneously.

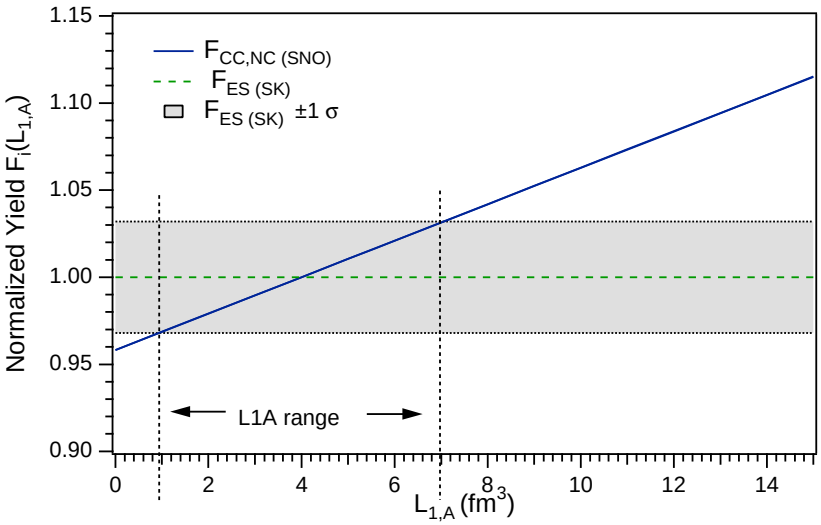

Figure 9.28: Constraints on $L_{1,A}$ from Super–Kamiokande and SNO in an analysis with only 1 variable parameter, assuming the central values for Φ_{CC}^{SNO} and Φ_{NC}^{SNO}.

To understand the effect the experimental solar neutrino flux measurements have on the determination of Φ_{ν_e} , Φ_{ν_x}, and $L_{1,A}$ we first vary the measured interaction rates by $\pm 1\sigma$ individually before we go on to calculate the joint parameter region. Figure 9.29 illustrates the variation of Φ_{ν_e} , Φ_{ν_x}, and $L_{1,A}$ in equations 9.41 - 9.43 as ϕ_{CC}^{SNO}, ϕ_{NC}^{SNO}, and ϕ_{ES}^{SK} are varied by $\pm 1\sigma$ around their central values. In the top panel of Figure 9.29 ϕ_{ES}^{SK} and ϕ_{CC}^{SNO} are kept constant while ϕ_{NC}^{SNO} is varied, and vice versa in the lower plots. The left ordinate gives the neutrino flux in units of $\times$ 10^6 cm^{-2} s^{-1} while the right ordinate gives the $L_{1,A}$ values in fm^3. Table 9.12 summarizes the results of equations 9.41 - 9.43 for specific values of ϕ_{CC}^{SNO}, ϕ_{NC}^{SNO}, and ϕ_{ES}^{SK} and helps with the interpretation of Figure 9.29.

Both the measurements of Super–Kamiokande and SNO are required to constrain $L_{1,A}$. The plots in Figure 9.29 illustrate the fact that it is the relative $L_{1,A}$-dependence of the various neutrino interactions measured in SNO and SK that provide the constraint on $L_{1,A}$. The variation of $L_{1,A}$ with ϕ_{ES}^{SK} is the inverse of the $L_{1,A}$ variation with $\phi_{NC,CC}^{SNO}$. The joint confidence levels and parameter regions of Φ_{ν_e} , Φ_{ν_x}, and $L_{1,A}$ are calculated in Figure 9.30.

Table 9.12: Φ_{ν_e}, Φ_{ν_x}, and $L_{1,A}$ fit values for specific ϕ_{CC}^{SNO}, ϕ_{NC}^{SNO}, and $\phi_{\underline{E}S}^{SK}$ input values. The input values are specified by their deviation σ from the central value $\bar{\phi}$.

ϕ_{CC}^{SNO}	ϕ_{NC}^{SNO}	ϕ_{ES}^{SK}	Φ_{ν_e} ($\times 10^6$ cm^{-2} s^{-1})	Φ_{ν_x} ($\times 10^6$ cm^{-2} s^{-1})	$L_{1,A}$ (fm^3)
± 0	± 0	± 0	1.797	5.196	2.117
$+\sigma$	$+\sigma$	± 0	1.760	5.340	9.682
$-\sigma$	$-\sigma$	± 0	1.840	4.960	-5.448
$-\sigma$	$+\sigma$	± 0	1.681	5.829	2.377
$+\sigma$	$-\sigma$	± 0	1.912	4.559	1.857
± 0	± 0	$+\sigma$	1.863	5.387	-1.105
± 0	± 0	$-\sigma$	1.730	5.004	5.586
$+\sigma$	$+\sigma$	$+\sigma$	1.825	5.594	6.191
$-\sigma$	$-\sigma$	$+\sigma$	1.907	5.142	-8.402
$-\sigma$	$+\sigma$	$+\sigma$	1.743	6.044	-0.854
$+\sigma$	$-\sigma$	$+\sigma$	1.983	4.727	-1.356
$+\sigma$	$+\sigma$	$-\sigma$	1.695	5.197	13.439
$-\sigma$	$-\sigma$	$-\sigma$	1.772	4.777	-2.269
$-\sigma$	$+\sigma$	$-\sigma$	1.619	5.614	5.856
$+\sigma$	$-\sigma$	$-\sigma$	1.842	4.391	5.315

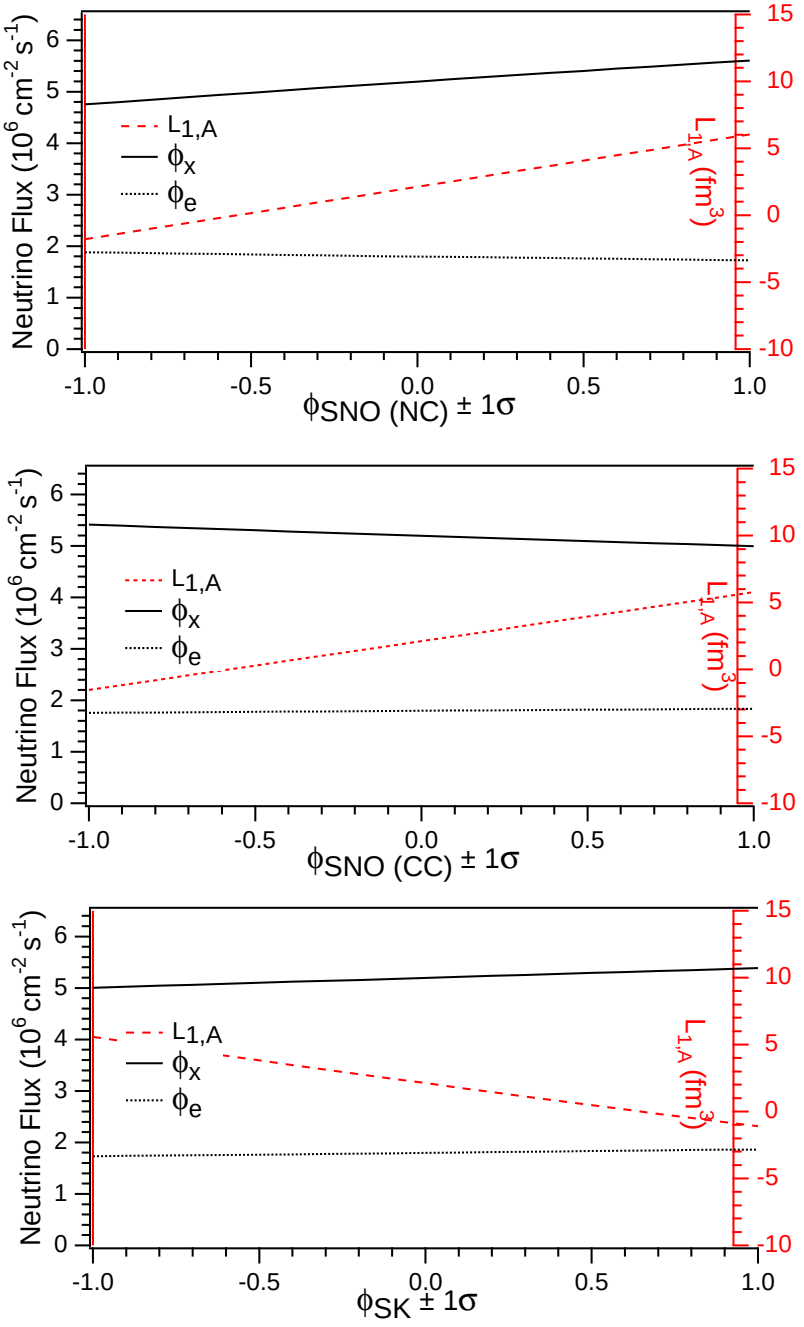

Figure 9.29: Variation of Φ_{ν_e} , Φ_{ν_x}, and $L_{1,A}$ as a function of ϕ_{CC}^{SNO}, ϕ_{NC}^{SNO} and ϕ_{ES}^{SK}, keeping two of the measured fluxes at their central value and varying the third flux measurement in the allowed 1-σ range defined by the experimental result. The left ordinate shows the neutrino flux in units of 10^6 cm^{-2} s^{-1}. The right ordinate gives $L_{1,A}$ in fm^3. These three plots illustrate how $L_{1,A}$, Φ_{ν_e} , and Φ_{ν_x} depend on the experimental measurements ϕ_{CC}^{SNO}, ϕ_{NC}^{SNO} and ϕ_{ES}^{SK}. In a model-independent analysis $L_{1,A}$, Φ_{ν_e} , and Φ_{ν_x} are varied simultaneously. The joint confidence regions of $L_{1,A}$, ϕ_{ν_x}, and ϕ_{ν_e} are calculated in Figure 9.30.

Confidence levels (CL) on $L_{1,A}$, ϕ_{ν_x}, and ϕ_{ν_e} are calculated following the prescription of the Particle Data Group for the evaluation of joint confidence regions. For any unbiased procedure used to estimate k parameters the probability (1-ϵ) that the true value of all k parameters lie within an ellipsoid bounded by a fixed value of $\Delta\chi^2 = \chi^2 - \chi^2_{min}$ can be derived from a χ^2 probability distribution function (PDF) [53]. The allowed values of the parameter $L_{1,A}$ and the physical quantities ϕ_{ν_x} and ϕ_{ν_e} form a 3-dimensional ellipsoid. We can calculate the confidence levels for this object and then use 2-dimensional projections of this ellipsoid to place bounds on ϕ_{ν_e}, ϕ_{ν_x}, and $L_{1,A}$. The $\Delta\chi^2$ corresponding to $(1-\epsilon)$ for joint estimation of $k = 3$ parameters are 3.53 (68.27%), 6.25 (90.00), and 8.03 (95.45%) respectively. These probabilities assume Gaussian errors, unbiased estimators, and that the model represented by equations 9.41 - 9.43 is correct. The results of this parameter estimation are shown in Figure 9.30. The best fit values are indicated by stars.

The upper panel of Figure 9.30 shows clearly that the flux of solar ^{8}B electron neutrinos, ϕ_{ν_e}, is less than the total active ^{8}B neutrino flux, ϕ_{ν_x}, independent of the theoretical parameter $L_{1,A}$. Treating ϕ_{ν_e}, ϕ_{ν_x}, and $L_{1,A}$ as variables removes the last model-dependent assumption from the evidence of neutrino flavor transformation obtained by SNO and Super–Kamiokande and demonstrates in a truly model-independent way the flavor transformation of solar neutrinos. Floating $L_{1,A}$ does not reduce the disparity between ϕ_{ν_e} and ϕ_{ν_x} which are derived from the CC, NC, and ES neutrino interactions measured at SNO and Super–Kamiokande. In fact, the combined analysis of the SNO and Super–Kamiokande results yields that with $L_{1,A}$ as a free parameter ϕ_{ν_e} and ϕ_{ν_x} are incompatible at the 99.99996% CL, compared to 99.9991% based on an analysis of the SNO data alone with fixed $L_{1,A}$.

The lower plot of Figure 9.30 shows the joint confidence regions of $L_{1,A}$ and the total ^{8}B neutrino flux ν_x. We find that $L_{1,A}$ is constrained to be less than ~ 13 fm^3 at the 68% CL. The best fit value is $L_{1,A} = 3.02 \pm 7.40$ fm^3 corresponding to a ^{8}B neutrino flux of $\phi_{\nu_x} = 5.21 \times 10^6$ cm^{-2} s^{-1}.

Figure 9.31 illustrates the prospects for future model-independent constraints on ϕ_{ν_e}, ϕ_{ν_x}, and $L_{1,A}$ from solar neutrino flux measurements. The use of NaCl in the current phase of SNO and the installation of the ^{3}He-filled Neutral Current Detector array will improve SNO's ability to measure ϕ_{ν_e} and ϕ_{ν_x}. The expected accuracy on the NC flux measurement

in the current NaCL+D_2O configuration of SNO is 6-8%. This is a factor of $\sim 1.5-2$ better than the currently published NC measurement. Based on the continued good performance of the SNO detector we expect that the livetime of the available SNO solar neutrino data set will increase by a factor of 3-4 over the life time of the experiment. The independent measurement with the ^{3}He-filled Neutral Current Detector array in the final phase of the SNO experiment will help reduce the NC uncertainty and aid in the separation of the CC and NC signal. (For a detailed discussion of this unique NC detection system see Appendix A.) As illustrated in Figure 9.31, an improvement in the combined statistical and systematic uncertainty in SNO's NC and CC measurement by a factor of 2 would significantly improve the joint confidence regions for ϕ_{ν_e}, ϕ_{ν_x}, and $L_{1,A}$, and constrain $L_{1,A}$ to < 8 fm^3 at the 68% CL.

In summary, a model-independent analysis of the solar neutrino measurements at SNO and Super-Kamiokande shows that the measured ϕ_{ν_e} and ϕ_{ν_x} fluxes are incompatible at the 99.99996% CL. The best fit values are $\phi_{\nu_e}^{SNO+SK} = 1.78 \pm 0.14 \times 10^6$ cm^{-2} s^{-1} and $\phi_{\nu_x}^{SNO+SK} = 5.21 \pm 0.79 \times 10^6$ cm^{-2} s^{-1}. This is unambiguous evidence for the flavor transformation of solar neutrinos. Removing the last model-dependence of SNO's solar neutrino flux measurements, the normalization of the neutrino deuteron cross-sections, does not remove the disparity between the measured ν_e flux and the total active ^{8}B solar neutrino flux. A combined, model-independent analysis of the data from SNO and Super–Kamiokande does in fact strengthen the evidence for neutrino flavor change compared to the results presented by SNO. We can use the solar neutrino measurements from SNO and Super–Kamiokande to place constraints on the parameter $L_{1,A}$ which describes the two-body axial current in effective field theory and normalizes the νd cross-sections. The best fit value is $L_{1,A} = 3.02 \pm 7.40$ fm^3. At the 68% CL $L_{1,A}$ is constrained to be less than ~ 13 fm^3. Until the recent analysis of reactor antineutrino-deuteron breakup reactions [22] this data provided the only direct experimental constraints on the uncertainty in the neutrino-deuteron cross-sections. The analysis of reactor antineutrino-deuteron breakup reactions yields the more precise constraint $L_{1,A}^{reactor} = 3.6 \pm 5.5$ fm^3 [22]. However, the fact that we can derive model-independent constraints on $L_{1,A}$ is a nice example of how the results of the different solar neutrino experiments can be used together to calibrate one of the parameters that

was previously used as a theoretical, model-dependent input to these experiments. In that sense one can say that the modern solar neutrino experiments have become self-calibrating. A reduction of the uncertainty in SNO's CC and CC flux measurements will significantly improve the constraints solar neutrino measurements place on $L_{1,A}$. With the expected accuracy of future measurements at SNO it may be possible to improve the precision on $L_{1,A}$.

9.5.6 Other Constraints on the Two-Body Axial Current $L_{1,A}$

There are other approaches to fixing and constraining $L_{1,A}$ with experimental results: Direct measurements of neutrino-deuteron reactions such as $\overline{\nu}d$ breakup reactions in antineutrino reactor experiments and the proposed measurement of $\nu_e + d \rightarrow e^- + p + p$ constrain the uncertainty in these CC cross-sections to $\mathcal{O}(1\%)$. Combined with higher-order EFT calculations they can be used to calibrate the νd CC and NC cross-sections in SNO to the same accuracy. Furthermore, muonic atom capture ($\mu^- + d \rightarrow \nu_\mu + n + n$) and tritium beta-decay ($^3\mathrm{H} \rightarrow {}^3\mathrm{He} + e^+ + \nu_e$) can be used to fix the two-body current. The calculations used to derive $L_{1,A}$ constraints from these processes claim an accuracy of 1%, but rely on certain theoretical assumptions [22].

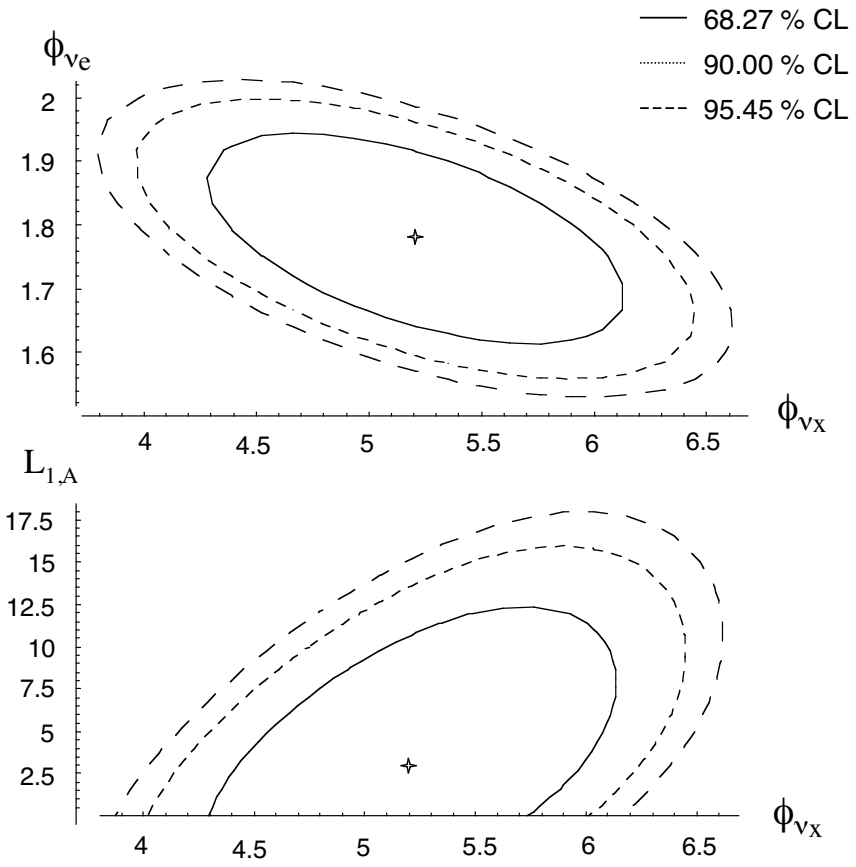

Figure 9.30: Model-independent confidence levels (CL) on $L_{1,A}$, ϕ_{ν_x}, ϕ_{ν_e} from the SNO and Super–Kamiokande solar neutrino flux measurements. The 2-dimensional confidence intervals in ϕ_{ν_e} versus ϕ_{ν_x} and $L_{1,A}$ versus ϕ_{ν_x} are projections of the joint confidence region of $L_{1,A}$, ϕ_{ν_x}, and ϕ_{ν_e}. The stars indicate the best fit points. The upper plot demonstrates that ϕ_{ν_e} is less than ϕ_{ν_x}, independent of the theoretical parameter $L_{1,A}$. This removes the last model-dependent assumption from the evidence of neutrino flavor transformation obtained by SNO and Super–Kamiokande.

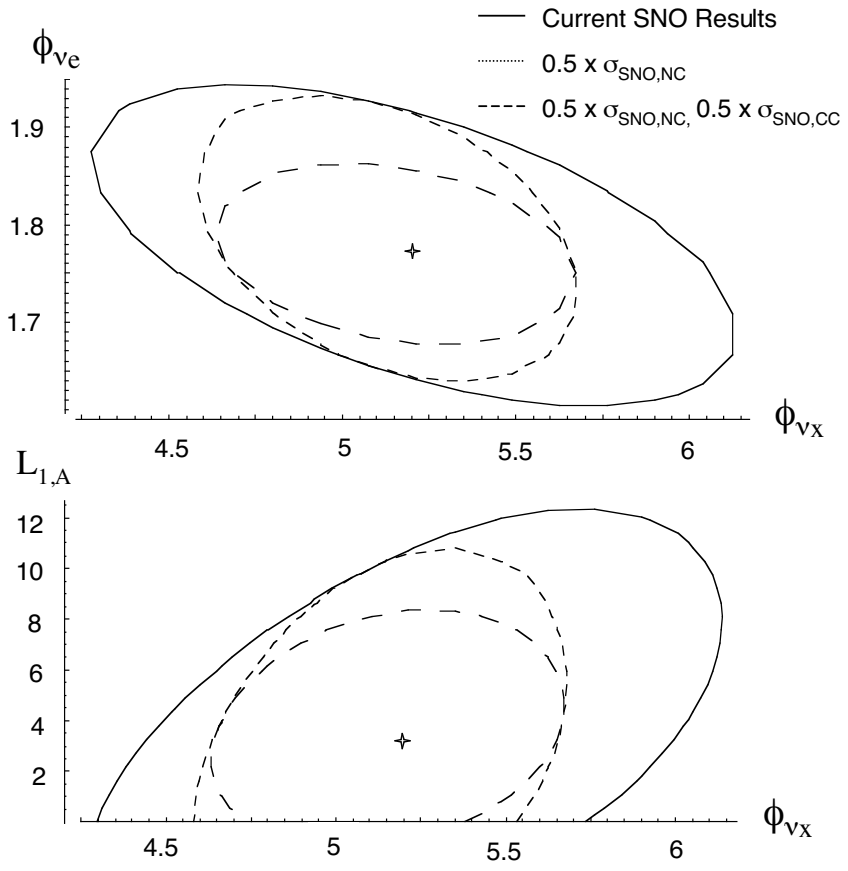

Figure 9.31: Prospects for future model-independent constraints on ϕ_{ν_e}, ϕ_{ν_x}, and $L_{1,A}$ from solar neutrino flux measurements. The confidence regions indicate the current constraints (solid line) and the ones one can obtain if the combined statistical and systematic uncertainties of SNO's NC and CC measurements improve by a factor of 2 (dashed lines).

CHAPTER 10

SEARCH FOR SOLAR *HEP* NEUTRINOS IN THE SUDBURY NEUTRINO OBSERVATORY

The Sudbury Neutrino Observatory (SNO) is designed to measure the flux of solar neutrinos and to determine the shape of the solar neutrino spectrum. Neutrinos from the beta-decay of ^{8}B dominate the solar neutrino spectrum between 5-15 MeV. The shape of the neutrino energy spectrum from a single beta-decaying source is well known and independent of solar physics to an accuracy of 1 part in 10^6. A measurement of the shape of the solar neutrino energy spectrum is a direct test of the minimal electroweak model and can be used to constrain models of neutrino flavor transformation.

Near the ^{8}B endpoint the solar neutrino spectrum is very sensitive to any underlying background, including neutrinos with energies above 15 MeV from other sources than ^{8}B-decay. In a rare branch of the pp-chain in the Sun, ^{3}He and proton fuse forming the reaction $^3\mathrm{He} + p \rightarrow {}^4\mathrm{He} + e^+ + \nu_e$. This *hep* process produces high energy solar neutrinos with an energy of up to 18.77 MeV.

Standard Solar Model calculations [11] predict a *hep* neutrino flux three orders of magnitude smaller than the flux of ^{8}B neutrinos. The *hep* prediction is 9.64×10^3 cm^{-2} s^{-1} compared to 5.05×10^6 cm^{-2} s^{-1} for the much more abundant ^{8}B neutrinos.

Although the *hep* neutrino flux is a negligible contribution to the total neutrino flux measured in SNO it can significantly distort the ^{8}B neutrino spectrum near the endpoint if the *hep* S-factor is much larger than the existing estimates. The SSM predictions of the *hep* flux are based on low-energy cross-section calculations with an S-factor of $S^{SSM}(hep) = (2.3 \pm 1.3) \times 10^{-20}$ keV-b. The rate of the *hep* reaction is so small that it does not affect solar modeling and other solar model predictions. The reliable estimation of the *hep* cross-section has been a long-standing challenge in nuclear physics and a direct measurement of the flux of *hep* neutrinos has not been done. A number of laboratory experiments to measure the

$^3\mathrm{He} + p \rightarrow {}^4\mathrm{He} + e^+ + \nu_e$ process have been suggested [80, 81, 135].

In the past, the Super-Kamiokande experiment measured the spectrum of recoil electrons in the solar-neutrino induced process $\nu + e^- \rightarrow \nu + e^-$. The recoil electron spectrum measured in the Super-Kamiokande experiment is in agreement with the predicted (but suppressed) spectrum in the whole energy range above 5.5 MeV with the possible exception of the highest energy region. At the highest energies there is an excess of events relative to the suppressed Standard Solar Model (SSM) prediction but the large statistical error make the data relatively uncertain. One possible interpretation of the Super–Kamiokande measurement suggested a flux of *hep* neutrinos ≥ 20 times larger than the best theoretical estimate at the time [59]. The measurement of Super-Kamiokande has raised significant theoretical interest in the calculation of the *hep* neutrino flux and new calculations of the *hep* process have become available.

In the first phase of the experiment, SNO has measured the interaction rates of solar neutrinos with pure D_2O. The results deduced from SNO's measurements include the total active flux of ^{8}B neutrinos. It was found to be in good agreement with Standard Solar Model predictions. Low backgrounds and the efficient discrimination of instrumental effects have made it possible to measure the energy spectrum of solar neutrinos from the measurement of the electron spectrum in the process $\nu_e + d \rightarrow e^- + p + p$ above a kinetic energy of 5 MeV [106], or a NHIT threshold of NHIT ≥ 46 (see Chapter 9). The SNO solar neutrino spectrum is now analyzed for the contribution from solar *hep* neutrinos.

Calibration of the solar neutrino energy spectrum in SNO is based on a tagged 6.13-MeV ^{16}N γ-source below the ^{8}B endpoint and 19.8-MeV γ's from a pT source above the ^{8}B endpoint. Besides the somewhat higher energy the event signature of *hep* neutrinos in SNO is identical to the event signature of ^{8}B neutrino interactions. The energy scale derived in Chapter 6 is valid for the entire solar neutrino spectrum including *hep* neutrinos. The effective energy of atmospheric neutrino events and other interactions will have to determined differently and cannot be derived from the set of calibrations described in this work.

Using analysis techniques similar to the ones developed for the measurement of the interaction rates of ^{8}B neutrinos with deuterium (see Chapter 8 and 9) we determine in this

chapter a new upper limit on the flux of *hep* neutrinos in the Sudbury Neutrino Observatory.

The search for *hep* neutrinos is a rare-event search in the high-energy region of the solar neutrino spectrum. SNO's ability to identify *hep* candidate events and to measure the *hep* neutrino flux will depend critically on the identification of backgrounds in the region near the ^{8}B endpoint. The data set under consideration is statistically limited and it is not possible to make an actual measurement of the *hep* flux based on 240.9 live days of data. In this case, the upper limit we can place on the *hep* flux will depend on the residual contamination in the data set.

10.1 Review of Calculations and Predictions of the Solar hep Process

Prior to the analysis of the SNO data we review the theoretical calculations of the S-factor for the solar *hep* process and determine the correction factors for the *hep* neutrino flux relative to the Standard Solar Model predictions of BPB00 [11].

The *hep* process proceeds via a Gamow-Teller transition and is strongly suppressed because the matrix element of the process vanishes in the allowed approximation for the main S-state components of the ^{4}He and ^{3}He wave functions. In addition, there are strong cancellations between different matrix elements of the weak nuclear current. The suppression is great enough that first-forbidden contributions compete with the allowed. Current Standard Solar Model calculations predict a *hep* neutrino flux of $\phi(hep) = 9.64 \times 10^3$ cm^{-2} s^{-1}. The value of $S_0(hep)$ used in Standard Solar Model predictions is the result of a complicated and model-dependent calculation. Independent theoretical and experimental confirmation is required. The astrophysical S-factor at center-of-mass (C.M.) energy, E_{CM}, is defined as

$$S(E) = E\sigma(E)e^{2\pi\eta} \tag{10.1}$$

where $\sigma(E)$ is the *hep* cross-section and η is given by $\eta = \frac{2\alpha}{v_{rel}}$ with α as the fine structure constant and v_{rel} as the relative velocity between p and ^{3}He. The Gamow peak energy at which the reaction is most probable to occur is 10.7 keV.

The reason for the difficulty in making a precise estimation of the *hep* S-factor is multifold. The *hep* reaction is sensitive to (i) small components in the wave functions, in particu-

lar D-state admixtures generated by the tensor interactions, (ii) relativistic corrections and many-body terms in the weak transition operator, and (iii) P-wave capture contributions. Below we summarize the most recent calculations of the *hep* process and determine the correction factors as they apply to the SNO analysis.

10.1.1 Recent Calculations of the Solar hep Process

The most recent work done by Park et al. [77, 78, 155] is based on a combination of the standard nuclear physics approach (SNPA) and heavy-baryon chiral perturbation theory (HBChPT) and builds an improved effective field theory (EFT). This approach exploits the role of the chiral-symmetry scale in short-distance effects encoded in short-range nuclear correlations. HBChPT is used to calculate all transition operators and operators up to $\mathcal{O}(N^3LO)$. The strength of this approach is in the combination of EFT with realistic wave functions obtained in SNPA. The result of this work is a model-independent prediction of $S(hep)$. The calculation of $S_0(hep)$ is governed by $^3S_1$ plus tiny $^1S_0$ and sizeable P-wave contributions. Park et al. also investigate the energy dependence of the S-factor. For all channels other than $^3S_1$, the Λ-dependence is small and less than 2%. Some Λ-dependence remains in $^3S_1$. The error on the calculation of $S_0(hep)$ is estimated from the Λ-dependence in the range between Λ = 500-800 MeV. With this procedure the theoretical uncertainty is reduced to $\sim 20\%$. This EFT approach gives $S_0(hep) = 8.6 \pm 1.3 \times 10^{-20}$ kev-b. The results of this work support the latest SNPA calculation.

Marcucci et al. [138, 64, 63] calculate the astrophysical S-factor for the proton weak capture on ^{3}He based on a standard nuclear physics approach (SNPA) with correlated-hyperspherical-harmonics bound and continuum wave functions corresponding to a realistic Hamiltonian model (AV18/UIX). This model consists of the Argonnne V18 two-nucleon and Urbana-IX three-nucleon interactions. The nuclear weak charge and current operators have vector and axial-vector components that include one- and many-body terms. This calculation includes S- and P-wave capture channels and retains all multipoles connecting these states to the $J^\pi = 0^+$ ground state of ^{4}He. The S-factor is calculated at different center-of-mass energies E_{CM}. The energy dependence of $S_0(hep)$ is found to be weak. At

10 keV the S-factor is 4% larger than at 0 keV. P-wave capture is found to be important, contributing $\sim$ 40% to the total S-factor. The D-wave channel contributions are small. Many-body axial currents are dominant in $^3S_1$ where they reduce the S-factor by a factor of $\sim$ 4. Inclusion of 3-nucleon interactions reduces S(hep) by about 20%. In this modern SNPA approach the S-factor for the *hep* process is calculated to be $S_0(hep) = 9.64 \times 10^{-20}$ keV-b. The results from this work are used in the latest Standard Solar Model predictions by Bahcall et al. [11].

All Standard Solar Models prior to 2000 use the original estimate of $S_0(hep)$ by Schiavilla et al. [167] for the prediction of the *hep* neutrino flux. In this work, P-wave contributions are not included in the calculation of $S_0(hep)$ and the description of the wave functions is based on the variational Monte Carlo (VMC) technique instead of the more accurate CHH. This calculation also does not include $1/m^2$ relativistic corrections in the one-body axial current. By using two different, typical NN-potentials, Schiavilla et al. obtained the following results for the S-factor of the *hep* process (i) $S(hep) = 1.44 \times 10^{-20}$ keV-b and (ii) $S(hep) = 3.14 \times 10^{-20}$ keV-b. The average between these two values $S_0(hep) = 2.3 \times 10^{-20}$ keV-b is used in Standard Solar Model calculations prior to 2000.

10.1.2 Summary of hep Predictions

Tables 10.1 and 10.2 summarize the results of the theoretical calculations as well as the resulting Standard Solar Model predictions for the *hep* neutrino flux. The *hep* flux predictions scale directly with $S_0(hep)$. We update the latest published SSM prediction with the new S-factor obtained from the EFT calculations by Park et al. [78]. The S-factor and *hep* flux prediction for this "BPB00+EFT" model are obtained by scaling the BPB00 predictions with (8.6/9.64). Flux correction factors as they apply to SNOMAN Monte-Carlo simulations based on the BPB98 and BPB00 solar models are listed in Table 10.2.

Table 10.1: The *hep* S-factors as estimated in different theoretical calculations.

Author	Calculation	$S(hep)$ $\times 10^{-20}$ keV-b	E_{CM} (keV)	Ref.
Park	HBChPT+SNPA, $\mathcal{O}(N^3LO)$	8.6 ± 1.3	0 keV	[78, 77]
Marcucci et al.	SNPA, CHH+AV18/UIX	9.64	0 keV	[138, 64]
Marcucci et al.	SNPA, CHH+AV18/UIX	10.1	10 keV	[138, 64]
Schiavilla	SNPA, VMC	2.3	10 keV	[167]
Salpeter et al.	First Estimate	630	0 keV	[166]

Table 10.2: Predictions of the *hep* neutrino flux in different Standard Solar Model calculations. The values for $S(hep)$ correspond to the S-factor at the Gamow-peak of 10.7 keV. The correction factors relative to the BPB00 and BPB98 prediction are given.

Solar Model	$S(hep)$ $\times 10^{-20}$ keV-b	*hep* Flux (10^{10} cm^{-2} s^{-1})	$\frac{SSM}{BPB00}$	$\frac{SSM}{BPB98}$	Ref.
BPB00 + EFT	$9.0\ (1 \pm 0.15)$	$8.3 \times 10^{-7}\ (1 \pm 0.15)$	0.892	3.952	unpublished
BPB00	10.1	9.3×10^{-7}	1.000	4.429	[11]
BPB98	2.3	2.1×10^{-7}	0.226	1.000	[60]

10.2 Characteristic Event Distributions in the Search for hep Neutrinos

The determination of the interaction rates of solar ^{8}B neutrinos in SNO is based on the spectral decomposition of the data based on three different characteristic detector distributions: NHIT, $(R_{fit}/R_{AV})^3$, and $\cos\theta_\odot$. The comparatively high statistics of the ^{8}B neutrino interactions in SNO [1] and the unique characteristics of the CC, NC, and ES processes allow us to not only determine the total number of neutrino interactions but also distinguish between the CC, NC, and ES interactions of ^{8}B neutrinos (see Chapter 9).

The limited statistics of *hep* interactions requires us to pursue a different approach in the search for *hep* neutrinos in SNO. It will not be possible to distinguish between the NC, CC, and ES interactions of *hep* neutrinos. Except for the slightly higher energy the Čerenkov characteristics of *hep* events is the same as the event characteristics of ^{8}B neutrinos. We can only determine the *hep* flux from the number of events near the ^{8}B endpoint where the ^{8}B interactions form a background to the *hep* signal. Two characteristic detector distributions are used in our *hep* analysis:

- *Energy Spectrum:* The radial and the $\cos\theta_\odot$ distribution of ^{8}B and *hep* neutrinos in SNO are expected to be nearly identical (except for energy dependent detector effects). Only the small difference in neutrino energies between the ^{8}B and *hep* process may make it possible for us to identify *hep* neutrinos in SNO. The ^{8}B and *hep* contributions to the data set are determined in a maximum-likelihood fit to the NHIT spectrum of the candidate event set.

- *Radial Distribution:* Besides the energy spectrum, the radial distribution of events $(R_{fit}/R_{AV})^3$ is used in the analysis. For a chosen fiducial volume, the reconstructed radial distribution defines the candidate event set. The accuracy of reconstruction determines the uncertainty on the fiducial volume. Understanding the reconstruction of ^{8}B and *hep* neutrino events is critical to our evaluation of the signal loss in the reduced data set. Different reconstruction algorithms are used to determine the sensitivity of the *hep* candidate event set to reconstruction effects.

---

[1] Compared to the first generation water-based solar neutrino detectors, such as Kamiokande [91], SNO detects about an order of magnitude more ^{8}B neutrinos. The statistics of the ES interaction in SNO is still poor but the CC and NC allow a high-statistics measurement, comparable to ES in Super–Kamiokande.

10.3 High-NHIT Events in the SNO Solar Neutrino Data

The same data set we used for the determination of the interaction rates of ^{8}B neutrinos is used in the search for *hep* neutrinos. It consists of selected neutrino runs taken between November 2, 1999 and January 15, 2001. The livetime of this data set is 240.9 days as calculated in Chapter 3. The data set is reconstructed using the SNO grid fitter (Chapter 4). Details of data taking and the reduction of the raw data set are described in Chapter 3.

The search for *hep* neutrinos is dominated by our ability to identify, characterize, and distinguish higher neutrino interactions from high-NHIT instrumental events and other effects. The term "high-NHIT event" refers usually to events with NHIT $\geq$ 120, that is events that are likely to have energies near or greater than the endpoint energy of the ^{8}B spectrum.

Events with with 65 $\leq$ NHIT $\leq$ 200 are selected for the *hep* candidate event set. The majority of events in this data set will be ^{8}B neutrinos. For all practical purposes the probability of having *hep* events with NHIT $\geq$ 200 is vanishingly small in a data set of 240.9 days of livetime. However, higher-NHIT data with event energies up to NHIT$\leq$ 500 are used to estimate the atmospheric neutrino background and study the event characteristics of high-NHIT events.

Two independent schemes for the removal of instrumentals have been developed in the SNO analysis: The Data Analysis Mask Number (DAMN) and the First, Second, and Third Pass Filter (FiST). The details of these data reduction schemes are described in Chapter 3. As data reduction is such a critical step in our search for *hep* events we compare the data sets obtained in both data reduction schemes on an event-by-event basis.

The standard high-level event-quality cuts used in the SNO solar analysis are the in-time light ratio ITR and the event isotropy θ_{ij}. The standard cut values are ITR $\geq$ 0.55 (CUT1) and 0.75 $\geq \theta_{ij} \geq$ 1.45 (CUT2). For a detailed discussion of these data reduction cuts see Chapter 5. The combination CUT1 $\otimes$ CUT2 is usually referred to as the high-level event-quality cuts (HLC).

10.3.1 Event-By-Event Comparison of High-NHIT Events in the FiST- and DAMN-Reduced Solar Neutrino Data Sets

The comparison of the data reduction techniques is made on an event-by-event basis on a data set with 120 $\leq$ NHIT $\leq$ 300. With the high level θ_{ij} and ITR cuts applied and the muon followers removed, the DAMN-reduced data set above NHIT $\geq$ 120 contains 25 high-NHIT events while 43 events survive the cuts in the FiST-reduced data set. This comparison is largely independent of reconstruction since no reconstruction cuts are applied [2]. We find that the events in the DAMN data set are not a simple subset of the FiST data set. In general, more high-NHIT events are contained in the FiST data set. The events that are unique to either one of the data sets were hand-scanned and classified. Most of the events that are contained in the FiST data set but not DAMN have the AMB and/or Retrigger data reduction bit set. For a definition and description of these data reductions cuts see Chapter 3. The presence of the AMB and retrigger bits indicates that these events may be decay electrons. These events will nearly always fail the retrigger cut as in DAMN this is set to 5 μs, compared to 1 μs for FiST.

The reduction of the solar neutrino data set with the application of individual high-level event-quality cuts is shown in Table 10.3.

Table 10.3: Event sample with NHIT $\leq$ 200 after application of individual high-level event-quality cuts.

Data Set	Cuts	Number of Events
DAMN	NHIT$\geq$65	2675
DAMN	NHIT$\geq$140	92
DAMN	Muon Followers, NHIT$\geq$140	88
DAMN	Muon Followers, NHIT$\geq$140, ITR	40
DAMN	Muon Followers, NHIT$\geq$140, θ_{ij}	24
DAMN	Muon Followers, NHIT$\geq$140, ITR, θ_{ij}	18

[2]Only the high level cut parameters θ_{ij} and ITR depend on the details of the reconstruction algorithms.

10.3.2 Detector Distributions and High-Level Event Quality Cuts

It is interesting to consider the characteristic distributions of high-NHIT events in the solar neutrino event set. In particular, we want to examine the effect of the standard high-level cuts θ_{ij} and ITR (HLC) on the characteristic NHIT and R^3 distributions of events with NHIT ≥ 140. The performance of the high-level event-quality cuts on data sets containing ^{8}B neutrinos has been characterized in great detail in Chapter 5. With a NHIT threshold of NHIT ≥ 140 we are now particularly interested in studying the possible effects of the HLC on *hep* neutrinos.

Figures 10.1 and 10.2 show the NHIT and R^3 distributions of the reduced candidate event set for different high-level event-quality cuts. The R^3 distributions show clearly the presence of AV background events which can be largely discriminated with the θ_{ij} cut. The selected event sample consists of 92 events with NHIT ≥ 140. All events above NHIT ≥ 500 are removed by the ITR cut. The ITR cut also removes misreconstructed events in the NHIT range between $140 \leq$ NHIT ≤ 500. The lower θ_{ij} cut ($\theta_{ij} \geq 0.75$) appears to remove events from the entire NHIT spectrum while the upper θ_{ij} bound $\theta_{ij} \leq 1.45$ removes primarily events from the NHIT region between 140 and 200. With the HLC applied, 18 out of 92 candidate events remain in the event sample above NHIT ≥ 140.

10.3.3 Considerations for the Fiducial Volume: Volume-Dependence of the Candidate Event Set

The number of high-NHIT events in the reduced SNO data set depends strongly on the chosen fiducial volume. Fiducial volume cuts with R_{fit} = 600-840 cm do not significantly affect the NHIT distribution of the event sample. However, a large fraction of high-NHIT events is discriminated by fiducial volume cuts of $R_{fit} \leq 580$ cm and less. This is an indication that these high-NHIT events are backgrounds from the outer region of the detector. As discussed in Chapter 3 and 5, there is a class of non-physics, AV-related backgrounds (called '*Leslie-Heeger*' events) that can cause high-NHIT events with energies in excess of NHIT ≥ 140. The high-NHIT events we see in this reduced data set are the tail of this event class. They cluster on the upper hemisphere of the detector and reconstruct near the

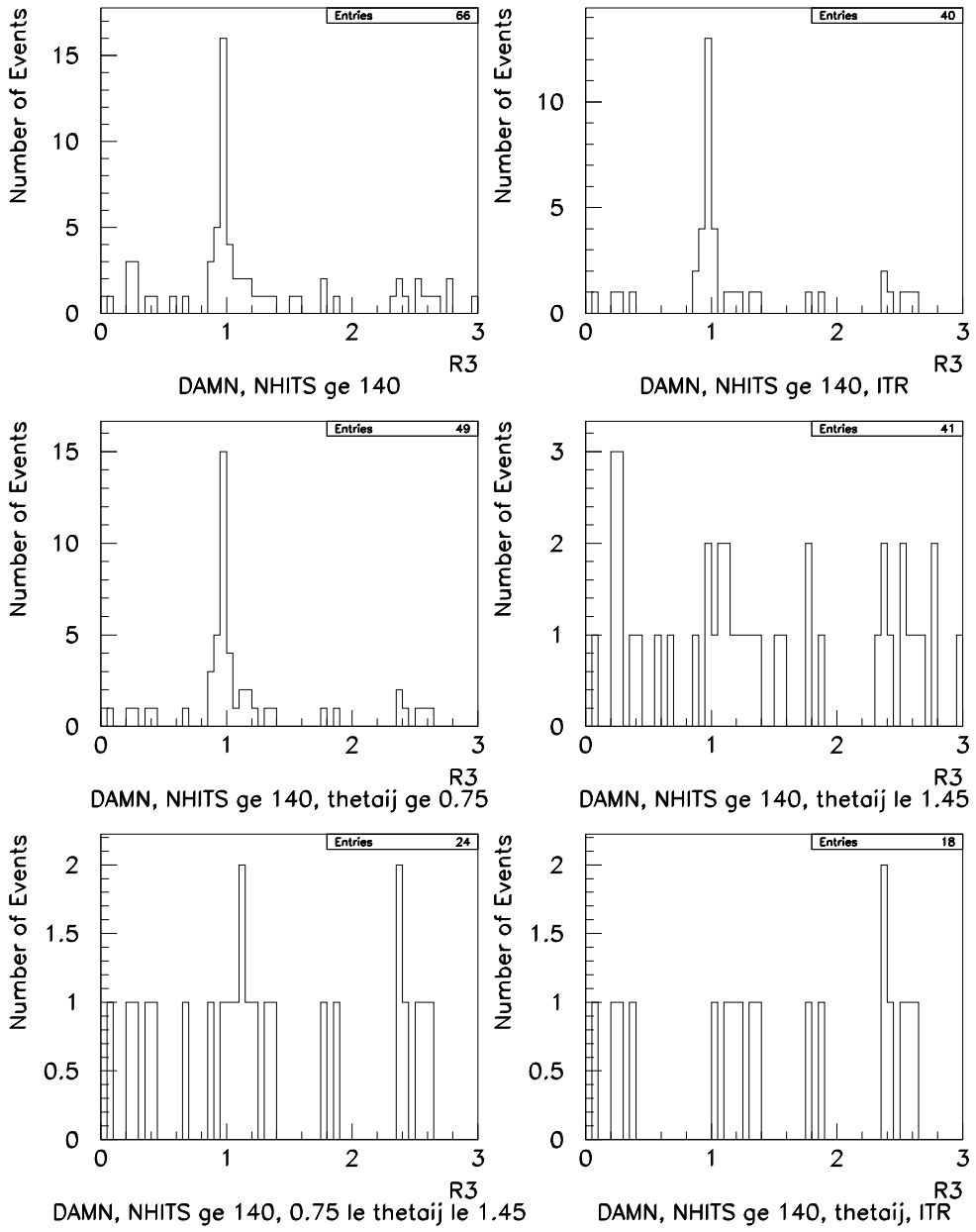

Figure 10.1: R^3 distribution of the selected event sample with different high-level cuts.

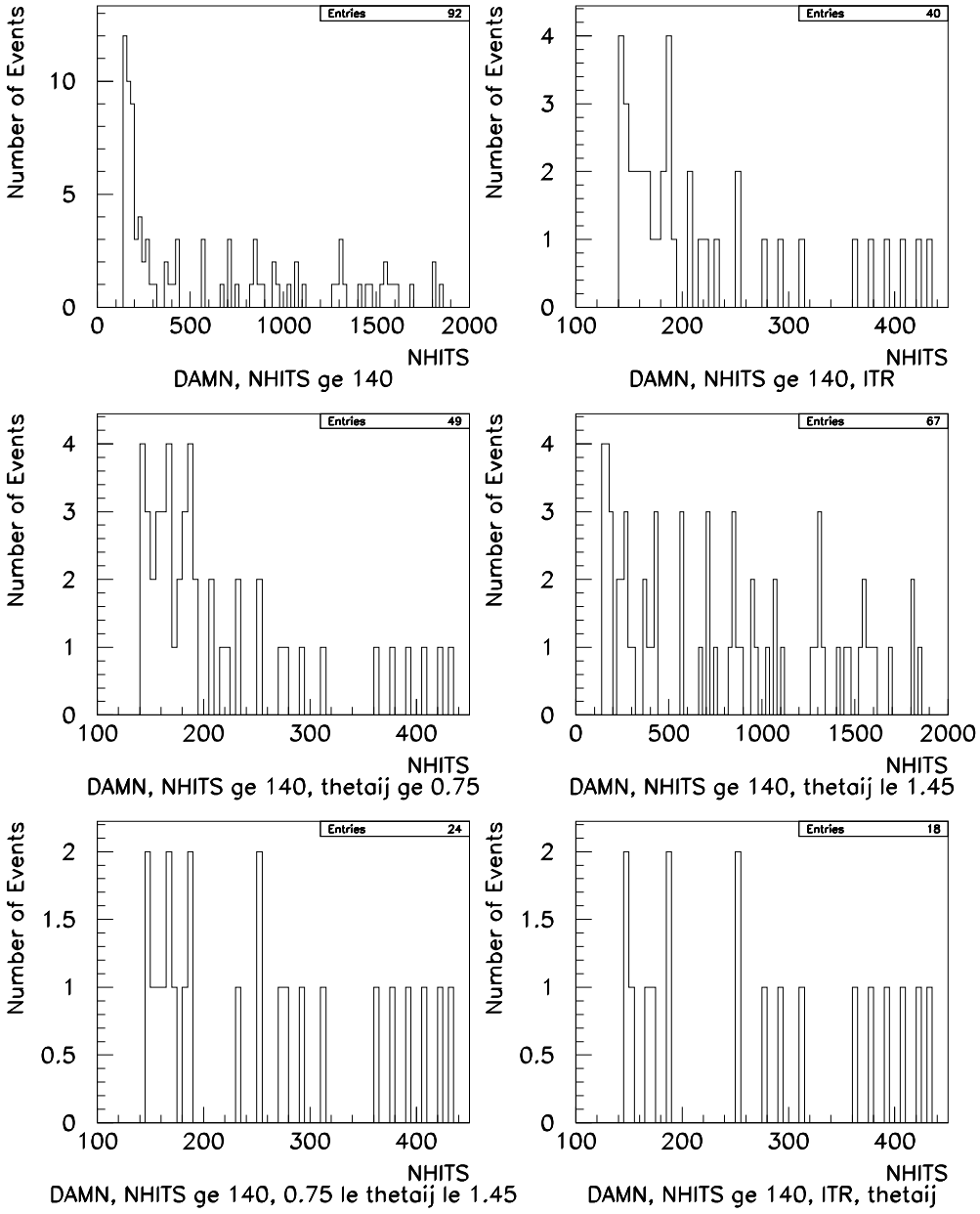

Figure 10.2: NHIT distribution of the selected event sample with different high-level cuts.

AV. Most events near the AV are discriminated by the upper θ_{ij} limit ($\theta_{ij} \geq 1.45$). The ITR cut as well as the lower θ_{ij} limit ($\theta_{ij} \geq 0.75$) do not help significantly in separating this AV-related background.

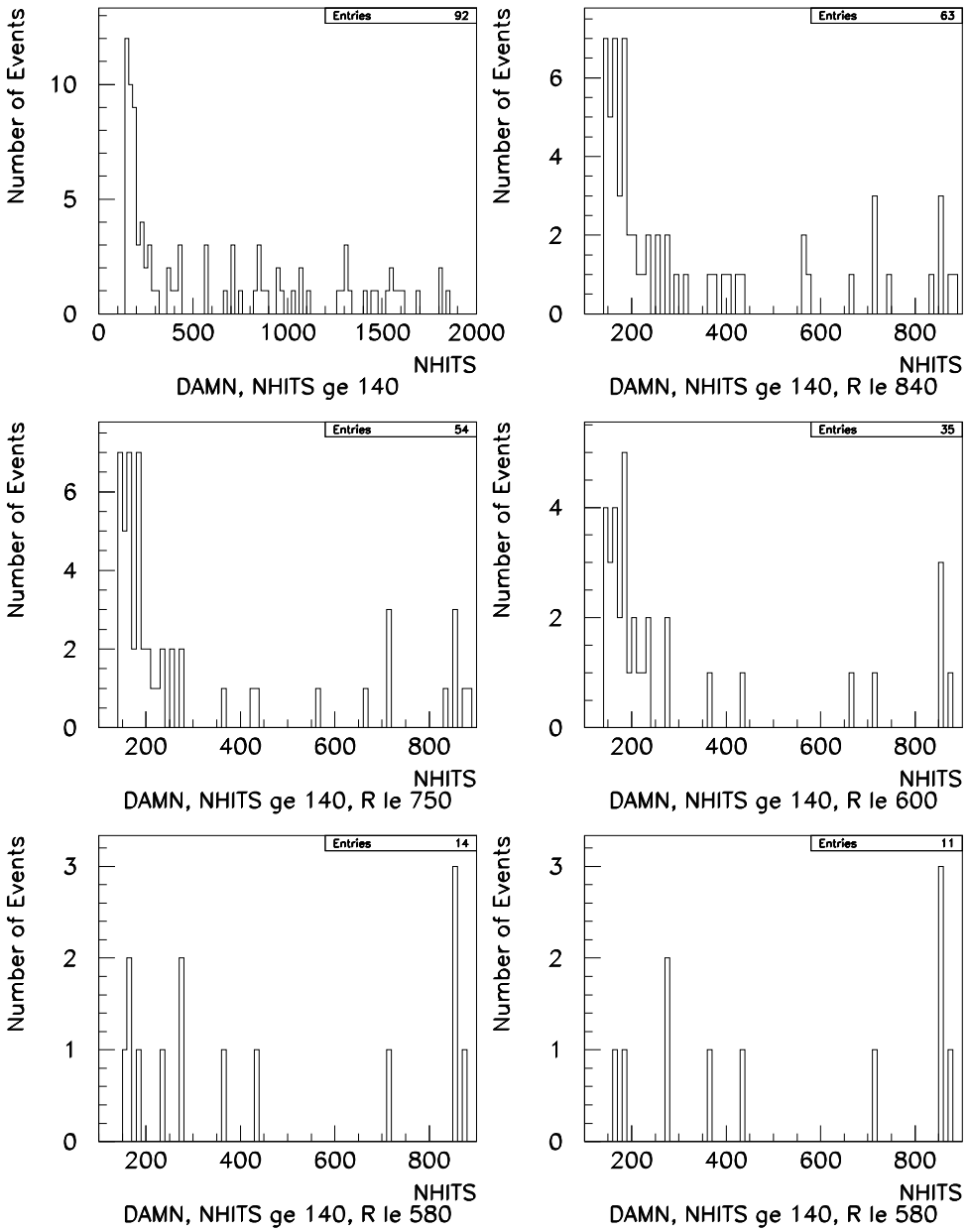

Figure 10.3: NHIT distribution of the selected event sample for different fiducial volume cuts.

10.4 Classification of High-NHIT Events

From the DAMN-reduced data set with 140 $\leq$ NHIT $\leq$ 500 and with the high-level event-quality cuts (HLC) applied we obtain a final sample of 18 high-NHIT events out of 92 high-NHIT events in the raw data set. All events with NHIT $\geq$ 140 are hand-scanned and classified into ring-like and non-ring like events. At such high-NHIT we expect all neutrino interactions to show the Čerenkov ring-like PMT hit pattern while AV-related backgrounds have a more isotropic PMT hit distribution. Events were classified according to three categories:

- CLASS I - *Ring Events:* Any type of single or multi-ring events.
- CLASS II - *Single Ring Events:* Single ring events. Subset of CLASS I.
- CLASS III - *Other Non-Ring Events:* Any other type of event.
  (Mostly '*Leslie-Heeger*' events from the AV background.)

The characteristics and identification of these 18 events are tabulated in Table 10.4. Figure 10.4 shows the reconstructed radius and event classification of these 18 high-NHIT events. The characteristic detector distributions of the single ring and multiple-ring events as well as the non-ring like background events are shown in Figures 10.5- 10.7. Sample events of these 3 different event classes are shown in Figures 10.8- 10.10.

Single and multiple ring events are found to have a fairly broad NHIT distribution. Their NHIT ranges from 140 (the lower NHIT threshold) to several hundred NHIT. The ITR, θ_{ij}, and R^3 distributions of the ring- and multi-ring like events do not reveal any anomalous features. The non-ring like events, however, are very distinct. Their typical NHIT is limited to 140 $\leq$ NHIT $\leq$ 200. The radial distribution shows a peak at $(R_{fit}/R_{AV})^3 = 1$ which means that they reconstruct in the vicinity of the AV. All of the non-ring like events are characterized by large values of θ_{ij} of about 1.5-1.6. About 25% of these events fail the reconstruction with the grid fitter or the θ_{ij} and ITR event classification in SNOMAN, the SNO analysis code.

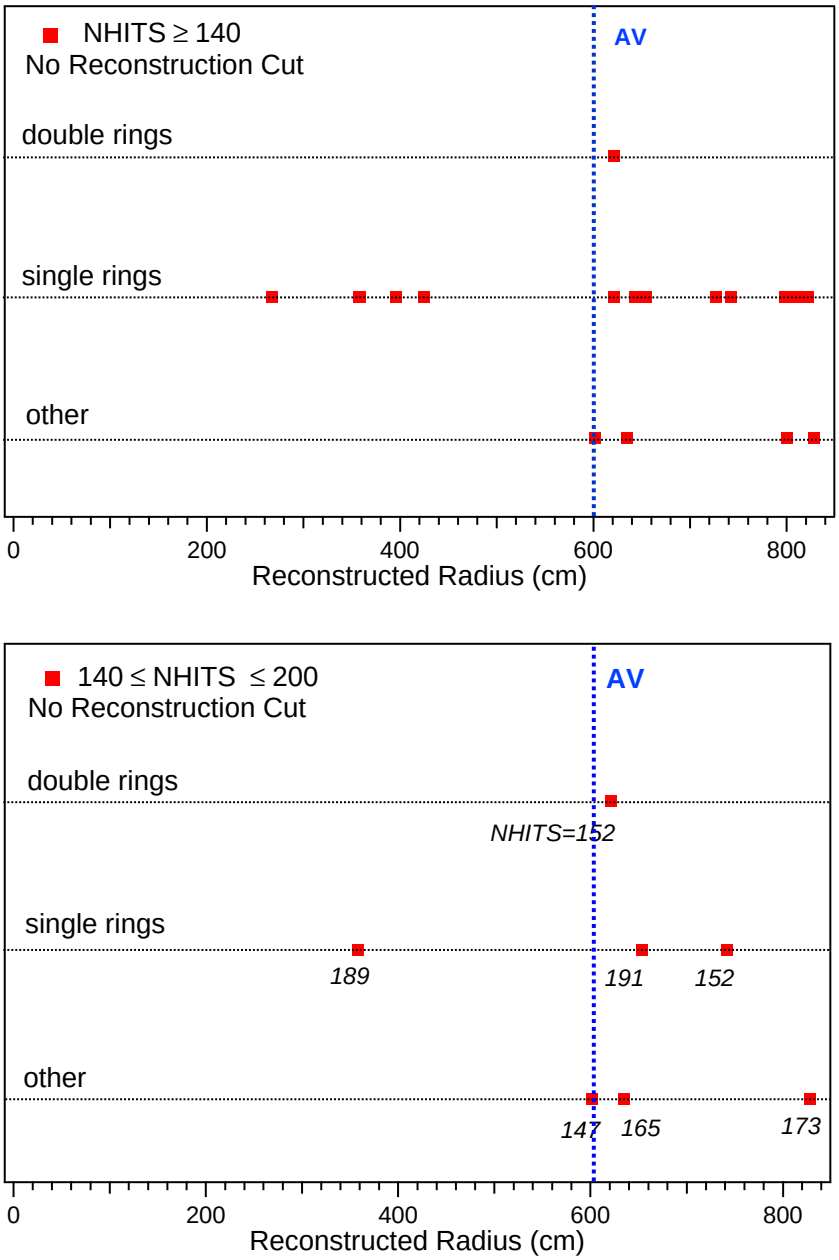

Figure 10.4: Reconstructed radii and event class identification of high-NHIT events that are not cut by HLC. The upper plot shows the entire event sample for NHIT $\geq$ 140. The lower plot shows a reduced event sample in the region of interest for the *hep* analysis, i.e. 140 $\leq$ NHIT $\leq$ 200. The probability of finding *hep* events with NHIT $\geq$ 200 is vanishingly small.

Table 10.4: Final sample of high-NHIT events with 140 $\leq$ NHIT $\leq$ 500 and high-level event-quality cuts (HLC) applied. All events are classified by their hit pattern into ring-like and other events. The identification of one event is ambiguous.

Run Number	Event ID (GTID)	NHIT	R_{fit} (in cm)	Event Type (Hit Pattern)
10040	1292386	424	621	single ring
10133	739417	408	818	single ring
10174	3978543	165	635	other
10686	1512179	147	602	other
10739	4983793	293	822	single ring
10826	616048	278	396	single ring
10885	201257	189	358	single ring
11312	3785302	191	654	single ring
11393	36053	364	267	single ring
11399	3295432	152	621	double ring
11462	763150	255	727	ring?
12082	369546	432	425	single ring
12178	57282	392	800	other
12187	5859843	173	828	other
12576	800789	314	798	single ring
13874	1026915	380	806	single ring
13874	1961526	253	643	single ring
14438	824782	152	742	single ring

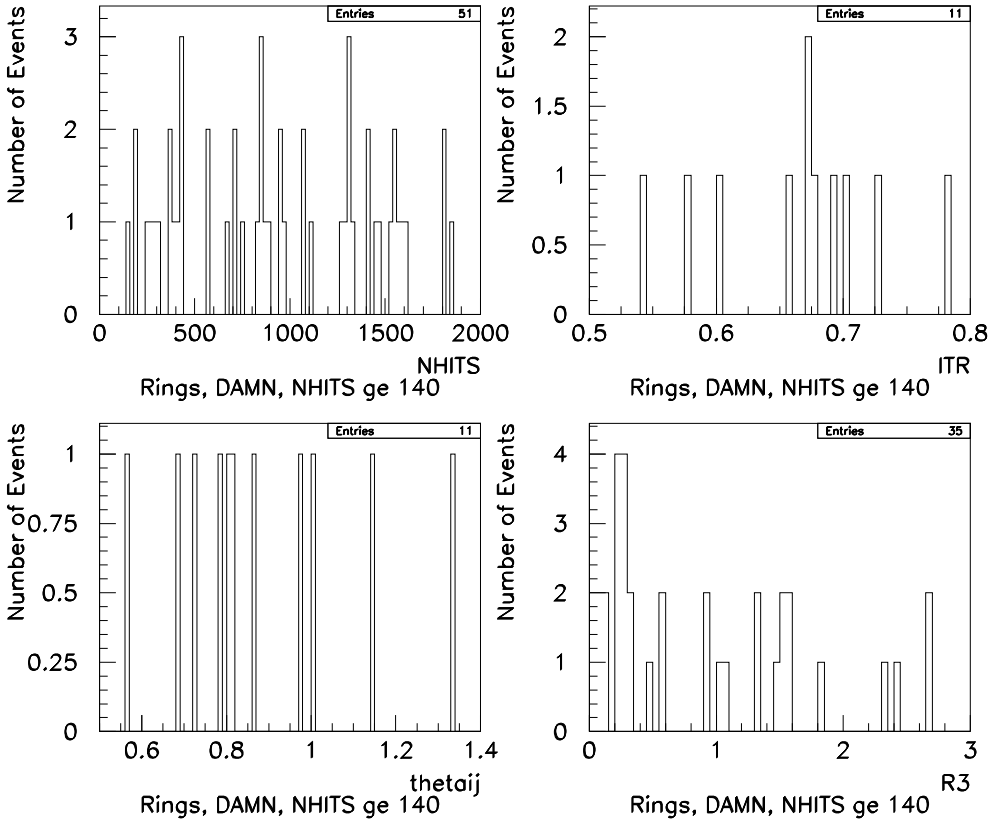

Figure 10.5: Characteristic distributions of high-NHIT ring events.

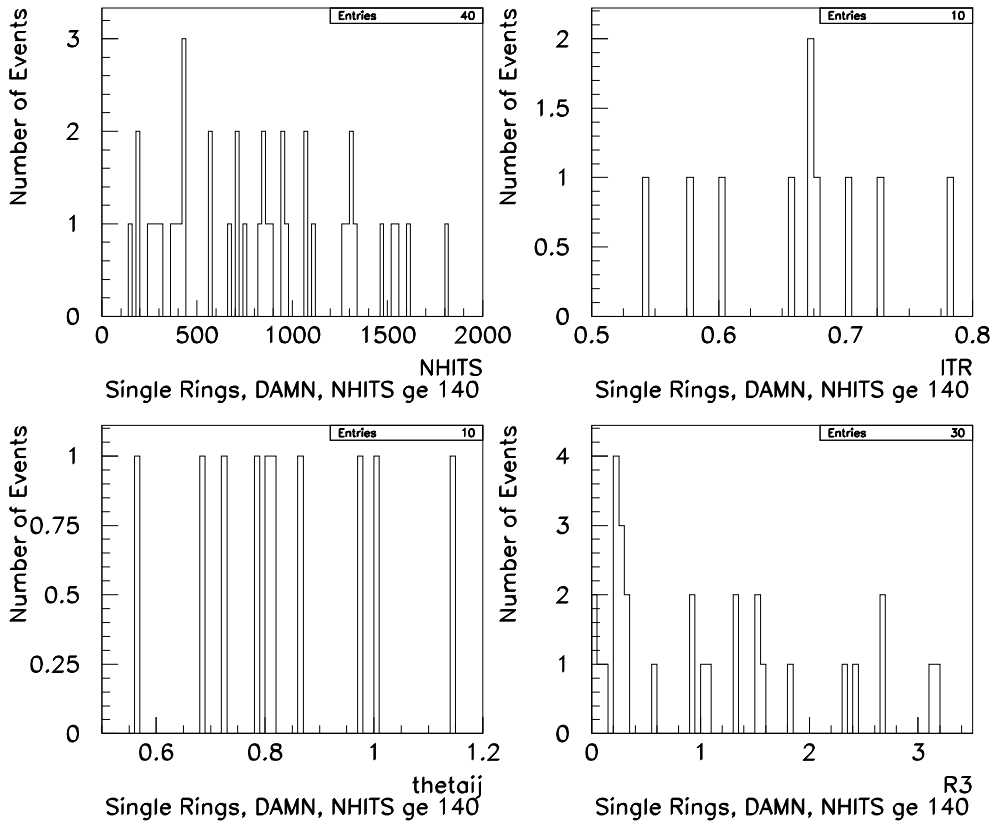

Figure 10.6: Characteristic distributions of high-NHIT single ring events.

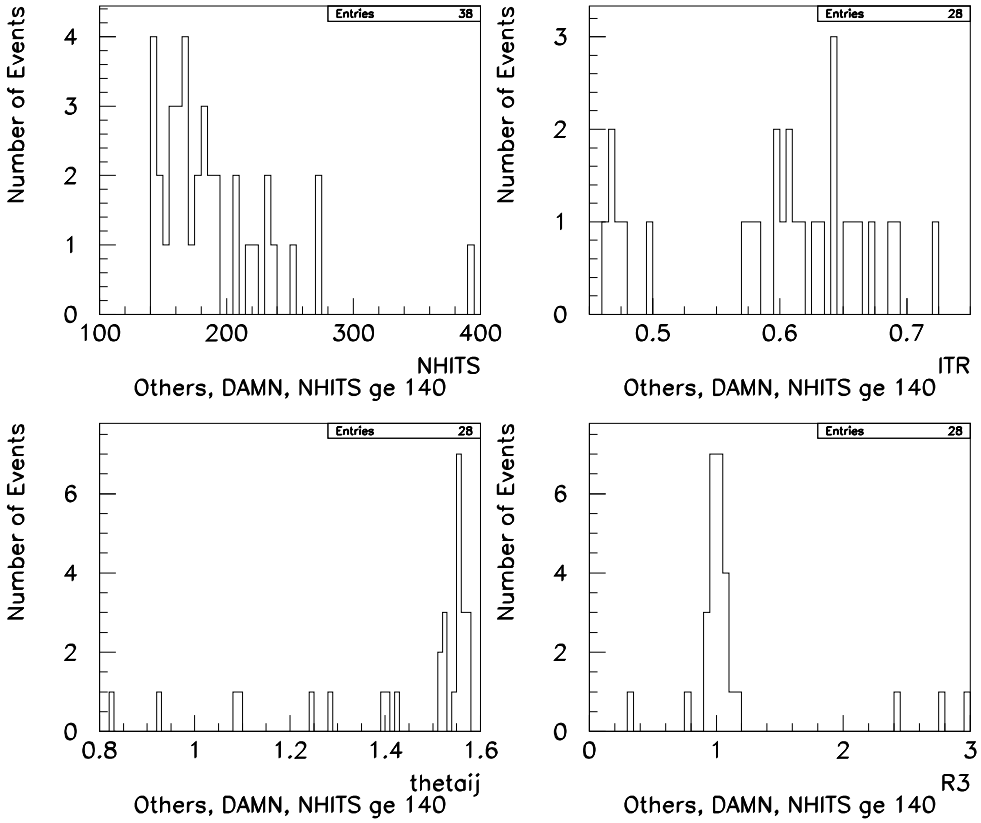

Figure 10.7: Characteristic distributions of non-ring like high-NHIT events.

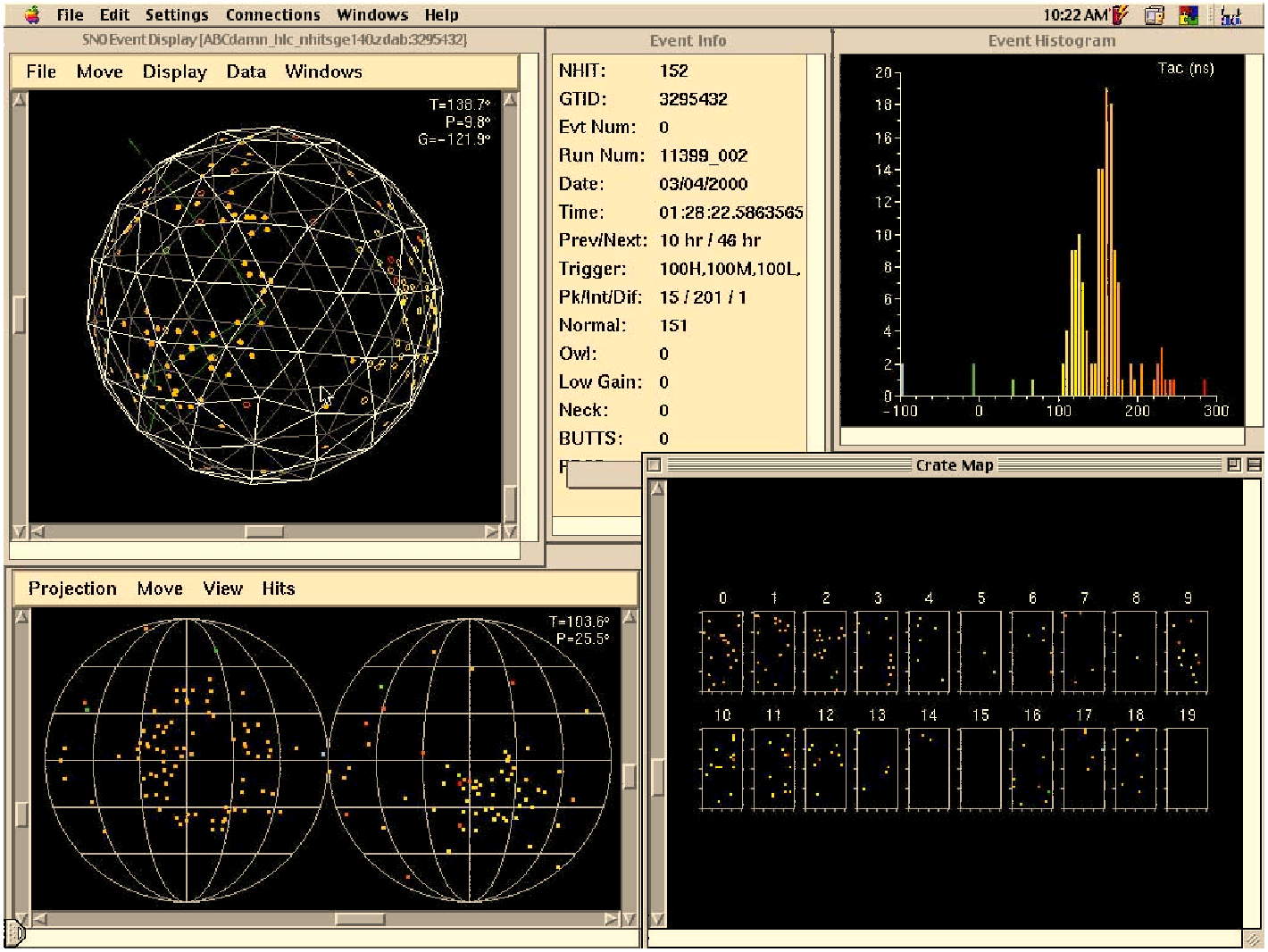

Figure 10.8: Example of a double ring event.

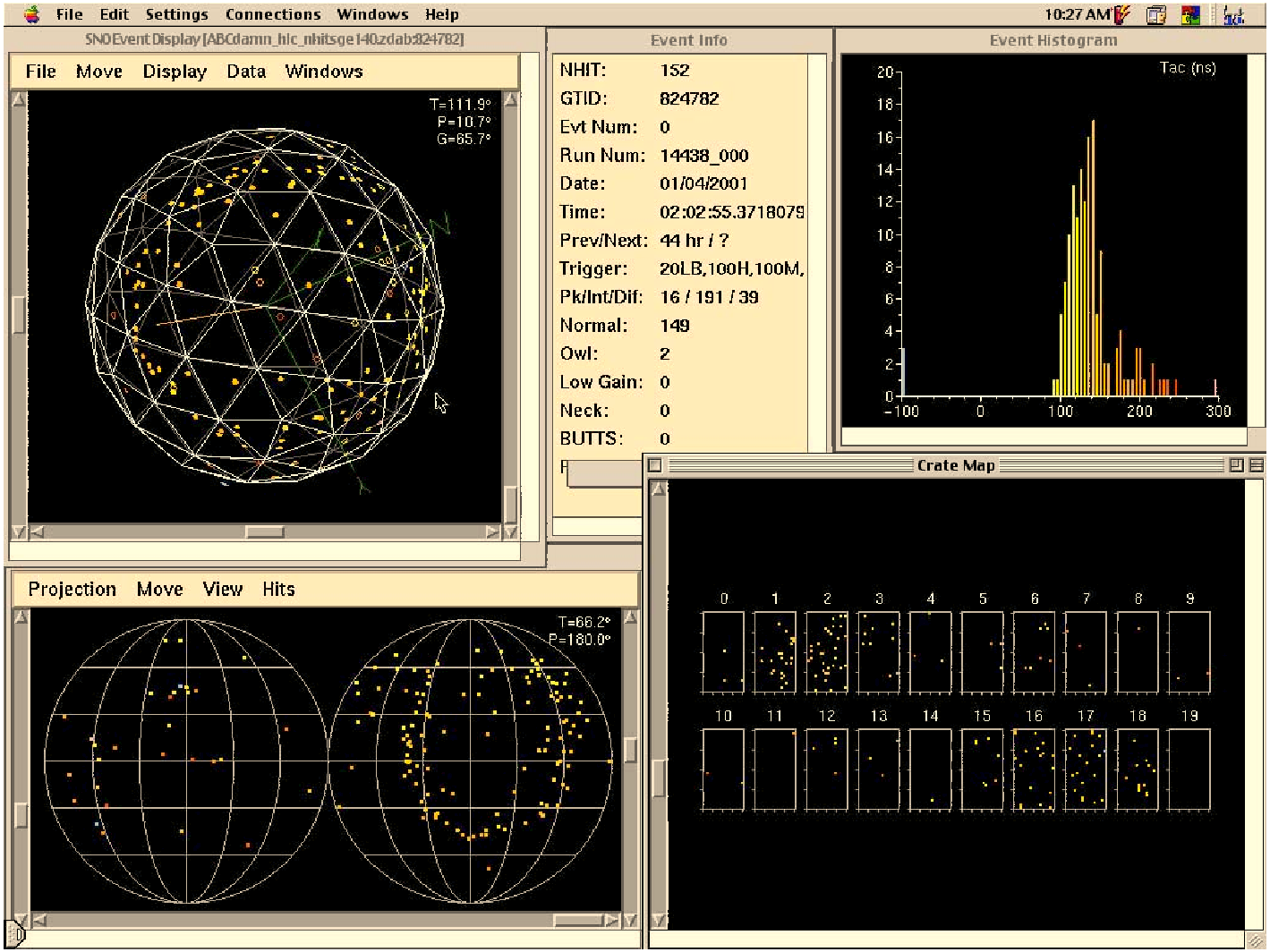

Figure 10.9: Example of a single ring event.

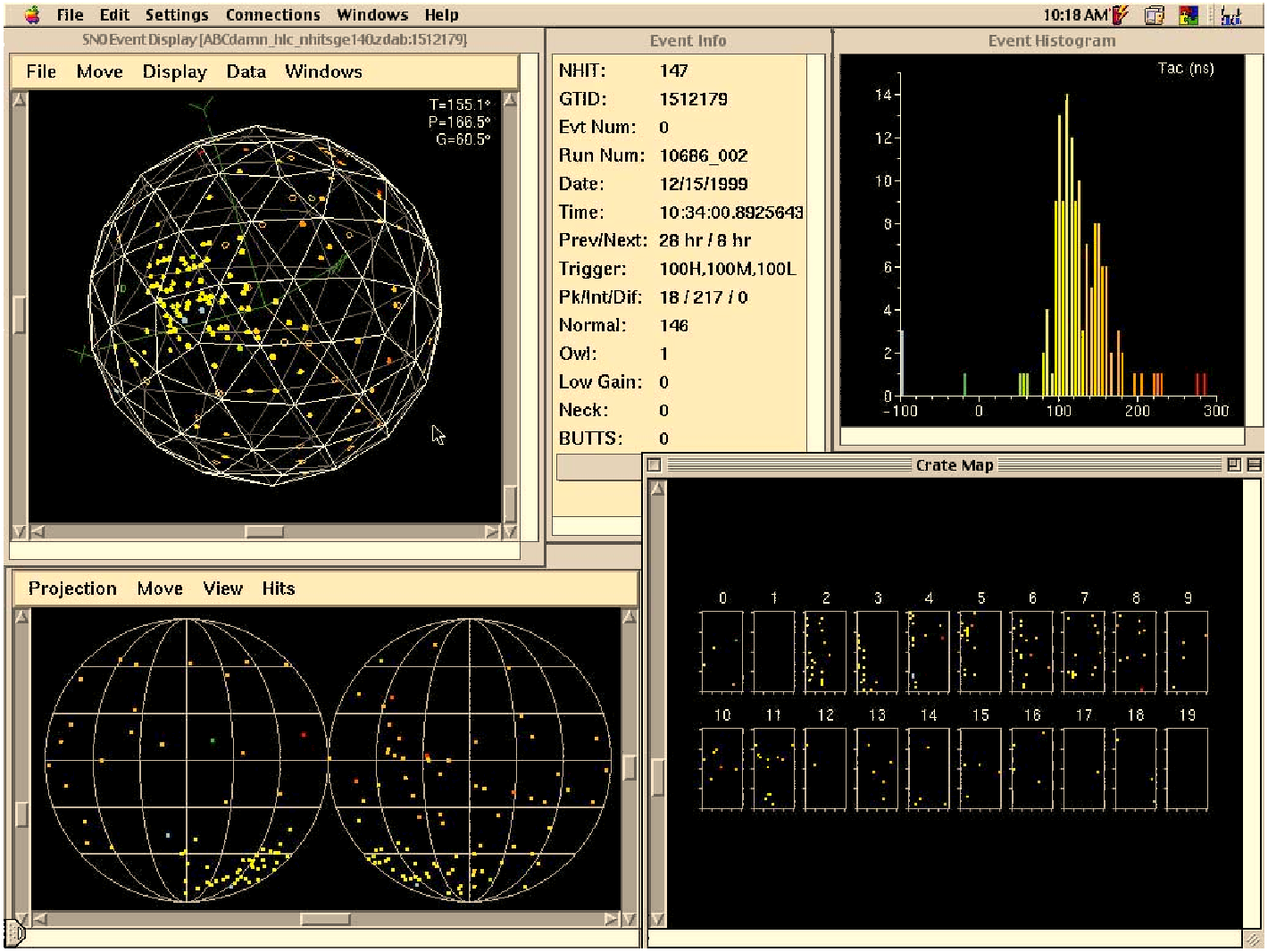

Figure 10.10: Example of a non-ring like event, most probably an AV background event.

10.5 Signal Loss and Event Selection in Data Reduction and Reconstruction

The signal loss in data reduction and reconstruction is one of the systematics in the data analysis we can quantify by means of calibration sources and Monte Carlo simulations and correct for in the final determination of the neutrino signal. As shown in Chapters 4 and 5 the signal loss in our measurement of the ^{8}B interaction rates in SNO is small and of the order of 1-2% depending on the interaction, the analysis threshold, and the fiducial volume. Below we will discuss studies of the *hep* signal loss in data reduction and reconstruction.

10.5.1 Signal Loss in the High-Level Data Reduction

Calibration sources and Monte Carlo studies are used to determine the *hep* signal loss due to ITR and θ_{ij} high-level event-quality cuts. In the energy region of interest for the *hep* analysis, three different calibration sources are available. For a more detailed discussion see Chapter 6.

- (p,t): This is a 19.8 MeV gamma source. The θ_{ij} distribution of high-energy γ's is different from the θ_{ij} distribution of neutrino interactions which makes it difficult to use for studies of the *hep* signal loss. This calibration source, however, does verify the accuracy of the SNOMAN Monte Carlo simulations of the θ_{ij} and ITR distributions at energies comparable to the *hep* neutrino energies.

- ^{8}Li: This source allows one to calibrate the detector response to electrons but it covers only part of the energy window of interest to the *hep* analysis. Statistics of the ^{8}Li data is limited in the high-NHIT region.

- Decay Electrons: The characteristic spectrum of the decay electrons from stopped muons can be used to establish a high-energy calibration point. Statistics is limited and it is difficult to obtain a sufficiently large sample of decay electrons. Results from this work are very preliminary and not described here.

As part of the SNO solar neutrino analysis, the aspect of signal loss and the residual contamination in the data set was studied in great detail in [142]. This work includes signal loss studies on γ and electron calibration data. For reference, we reproduce the final estimates for the signal loss after application of all data reduction and high-level event cuts

developed in [142]. The total signal loss due to all cuts for data within $R_{fit} \leq 550$ cm and above NHIT ≥ 65 is listed in Table 10.5.

Table 10.5: Total signal loss due to all cuts for data inside $R_{fit} \leq 550$ cm and with NHIT $\geq$ 65 as determined in [142].

Signal	Signal Loss (%)	Fractional Loss (η_{HLC})
^{8}B CC	$1.33^{+0.73}_{-0.63}$	$\eta_{CC} = 0.0133^{+0.73}_{-0.63}$
^{8}B NC	$1.33^{+0.78}_{-0.68}$	$\eta_{NC} = 0.0133^{+0.78}_{-0.68}$
^{8}B ES	$1.52^{+0.74}_{-0.64}$	$\eta_{ES} = 0.0152^{+0.74}_{-0.64}$
hep CC+ES	$1.74^{+0.73}_{-0.63}$	$\eta_{hep} = 0.0174^{+0.73}_{-0.63}$

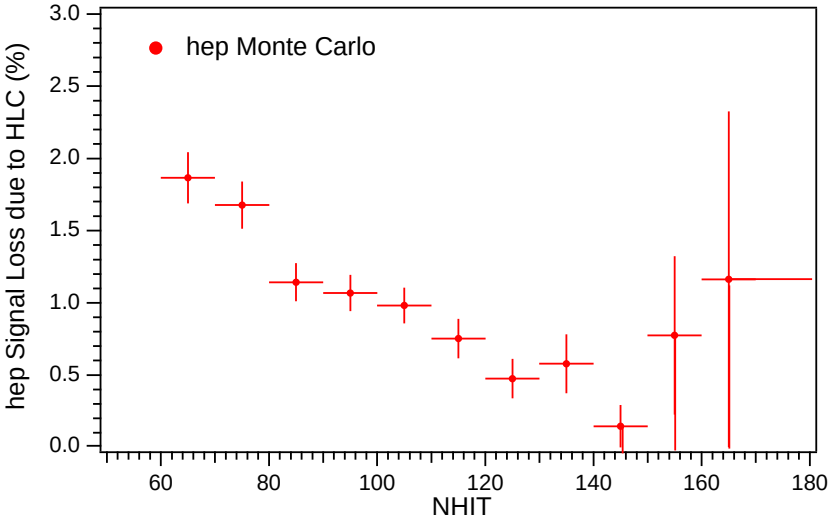

Figure 10.11: *hep* Monte Carlo signal loss due to the high-level event-quality cuts (HLC).

Under the assumption that the Monte Carlo distributions for θ_{ij} and ITR have been verified for electrons at lower energies and for γ's at higher energies the Monte Carlo can be used to estimate the signal loss. We compare the results of Table 10.5 to the signal loss determined from *hep* Monte Carlo simulations and find generally good agreement. We

note that the *hep* signal loss does not dominate the error on the *hep* limit as long as it is reasonably small. In summary, the *hep* signal loss due to the removal of instrumental background and data reduction is estimated to be $\eta_{hep} \approx 0.02$. This signal loss is corrected for in the final analysis of the *hep* contribution to the SNO solar neutrino data set.

10.5.2 Signal Loss in the Reconstruction of High-NHIT Events

The reconstruction of events is not 100% efficient and a very small fraction of events can get lost in the processing of the data set. In our analysis of the ^{8}B signal in SNO we determined the efficiency of reconstruction to be $> 99.97\%$ for neutrino signals and $> 98.9\%$ for low-energy backgrounds. In the context of the *hep* analysis one of the concerns is that a *hep* candidate event may be lost in the inefficiency of reconstruction. Furthermore, we need to verify that the underlying principle of a reconstruction algorithm does not bias the selection of *hep* events.

A number of different reconstruction algorithms have been developed for use in the SNO solar neutrino analysis [150, 15]. It has been found that these reconstruction algorithms show excellent agreement in the vertex reconstruction and angular resolution of ^{8}B neutrino events. The overall signal loss is very small and corrected for in the ^{8}B analysis (Chapter 9). As a verification of the successful reconstruction of high-NHIT events we compare the event set derived from two different reconstruction algorithms, the grid fitter (FTG) and the path fitter (FTP). Both fitters have been used successfully in independent analyses of the SNO ^{8}B neutrino data.

The path fitter is described in detail in [150] and references therein. It differs from the grid fitter in that it tests explicitly for the ring-like Čerenkov characteristics of an event. In addition to the high-level event-quality parameters, θ_{ij} and ITR which are used in all approaches to the SNO data analysis, the path fitter makes use of 2 additional figures of merit. They are derived from the underlying assumptions about the Čerenkov nature of events.

The standard SNO high level cuts (HLC) are

- CUT1: ITR ≥ 0.55
- CUT2: $0.75 \geq \theta_{ij} \geq 1.45$

For the path fitter (FTP) two additional figures of merit (FOM) are used [150]

- CUT3: PHIPRB > 0.0001
- CUT4: A2DPRB $> (4 \times 10^6/\mathrm{NHIT}^6)$

To evaluate the effect of reconstruction on the candidate event set we compare the high-NHIT events in the DAMN-reduced data set for (i) $CUT1 \otimes CUT2$ and (ii) $CUT1 \otimes CUT2 \otimes CUT3 \otimes CUT4$.

In an NHIT region of $120 \leq \mathrm{NHIT} \leq 200$, 21 events remain in the final FTG-reconstructed data after application of HLC. The FTP-reconstructed data set reduced with HLC and FOM contains 17 events. The events in the FTP-reconstructed data set are a simple subset of the FTG-reconstructed data set. Four single and double ring events with NHIT ≥ 151 fail the A2DPRB path fitter figure of merit and are not in the FTP-reconstructed final event sample.

Table 10.6: List of Events contained in the FTG-reconstructed DAMN data set with HLC but not in the event sample reconstructed with FTP and HLC+FOM. The high-level cuts θ_{ij} and ITR (HLC) were applied to both data sets. Within a fiducial volume of $R_{fit} \leq 550$ cm the difference between the two data sets consists of one event at NHIT = 188. The event type is determined from a handscan and visual inspection of the data

Run Number	Event ID (GTID)	NHIT	R_{fit} (in cm)	Event Type
10885	201257	188	358	single ring
11312	3.7853e+06	189	654	single ring
11399	3.29543e+06	151	621	double ring
14438	824782	149	742	single ring

One should note that the event reconstruction methods currently used in the SNO analysis are not designed to deal with the geometry and timing of PMT tube hits in multiple

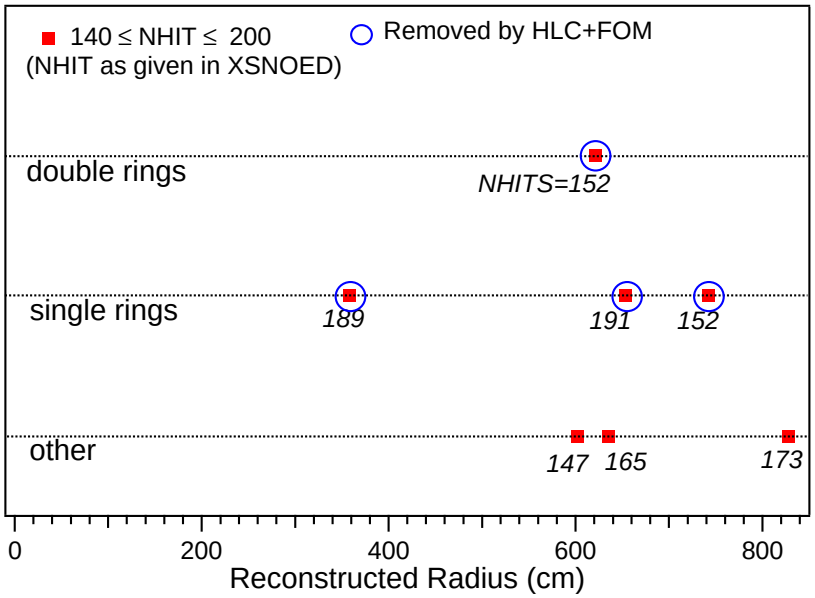

Figure 10.12: Event identification and reconstructed radii in the FTG-reconstructed data set for 140 ≤ NHIT ≤ 200. The four events removed by the FTP figure of merit (FOM) A2DPRB in the FTP-reconstructed data set are circled in blue.

ring events. Hence, we do not expect the reconstructed vertex of the double-ring event in Table 10.6 to be correct. A fiducial volume cut based on the reconstructed radial position of this double-ring event cannot be applied. However, we discard this event from the *hep* candidate set based on the assumption that a *hep* CC, NC, or ES neutrino interaction will not produce a double ring pattern in the PMT hit display. The events that are discarded in the reconstruction with the path fitter (FTG) will successfully reconstruct with the grid fitter but in any case be eliminated by the fiducial volume cut. The events in question reconstruct outside the acrylic vessel.

In summary, two independent reconstruction techniques yield an identical set of high-NHIT events for the *hep* candidate event set.

10.6 Candidate Event Set for the hep Analysis

Using the unified DAMN-reduced data set with the standard high-level data reduction cuts we find 18 events with NHIT $\geq$ 140 and 7 events with 140 $\leq$ NHIT $\leq$ 200. See Figure 10.12. Out of these 7 events, one single ring event with an NHIT of 189 is reconstructed inside the AV in the D_2O volume. Within $R_{fit} \leq 630$ we find 5 events, one double ring event, two single ring events, and two non-ring like events. The single ring events have high NHIT and are unlikely to be *hep* candidates. The non-ring like events belong most probably to the group of '*Leslie-Heeger*' events. They are the high-NHIT tail of some AV-related background. It is unlikely that any one of the events within $R_{fit} \leq 630$ cm is a *hep* neutrino interaction. However, in the absence of techniques to uniquely identify lowest-energy atmospheric neutrinos and to discriminate the AV backgrounds effectively it seems appropriate to choose a conservative fiducial volume of $R_{fit} \leq 550$ cm.

Figure 10.13 shows the NHIT spectrum of the solar neutrino candidate events set after application of all high-level event-quality cuts and within a fiducial volume of $R_{fit} \leq 550$ cm. For the *hep* analysis we consider data in the NHIT region between 65 and 200.

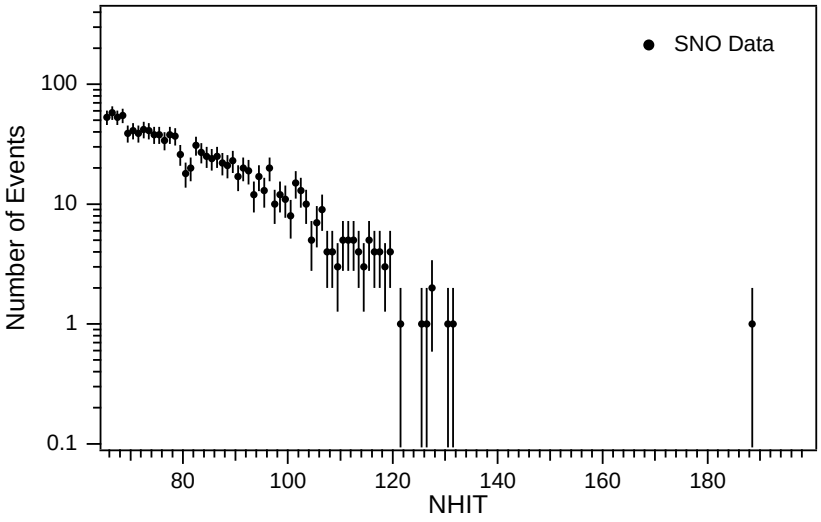

Figure 10.13: NHIT spectrum of SNO data for $R_{fit} \leq 550$ cm and 65 $\leq$ NHIT $\leq$ 200. The high-level event-quality cuts (HLC) are applied.

For the chosen fiducial volume and data reduction cuts the SNO data shows very few events above NHIT $\geq$ 120. This shows that the possible backgrounds from atmospheric neutrino interactions or from AV-related backgrounds must be small. With this data we will only be able to set an upper limit on the flux of *hep* neutrinos from the Sun. More data from a larger data set or an extended fiducial volume will be needed to make a measurement of the *hep* neutrino flux.

10.7 Backgrounds in the hep Analysis

Studies of the reduced but otherwise raw data set have shown that non-physics high-NHIT events form the principal background to the *hep* signal. They belong to some AV-related background and have an energy distribution that extends up to NHIT $\sim$ 200. No other significant instrumental high-NHIT background is found in the characteristic NHIT and R^3 distributions of the DAMN-reduced data set. Above the ^{8}B endpoint, high energy backgrounds and instrumental backgrounds are estimated to contribute less than 0.8% and 0.5% to the measured interaction rate [28]. The physics background from atmospheric neutrino-induced interactions is estimated to be small in comparison. An estimate of the atmospheric neutrino background is presented below.

10.7.1 Leakage of AV-Related Background Events into the Fiducial Volume

In this section we estimate the leakage of the AV background events into the signal box defined by the high-level event-quality cuts θ_{ij} and ITR. The goal is to estimate the residual contamination of AV background events in the candidate event set. Most of the AV-related background events can be discriminated using a θ_{ij} cut of $\theta_{ij} \geq 1.45$.

The reconstructed positions of the high-θ_{ij} background events show that these events occur predominantly in the upper hemisphere around the neck of the detector. The clustering of these events and possible correlations with the repairs and bonds in the acrylic vessel have been examined in detail by A.W. Poon and others [159]. Figure 10.14 shows the clustering of the AV background in scatter plots of θ_{ij} versus R^3. The AV background is clearly distinguishable for various NHIT cuts. Figures 10.15 and 10.16 illustrate the effect of a

fiducial volume cut on the reduced data set. For $R_{fit} \leq 550$ cm there is essentially no background with $\theta_{ij} \geq 1.45$ in the data. When we increase the fiducial volume to $R_{fit} \leq 600$ cm a significant number of high-θ_{ij} background events underlie the neutrino data in the NHIT region between 140 and 200.

By taking a high-NHIT event sample from the DAMN data with appropriate reconstruction cuts we obtain an almost pure sample of AV-related '*Leslie-Heeger*' events. This event sample can be used to estimate an upper limit of the leakage of these backgrounds events into the signal box defined by $0.75 \leq \theta_{ij} \leq 1.45$ and ITR ≥ 0.55. The sample of background events is selected by applying the following cuts: ITR ≥ 0.55 AND $\theta_{ij} \geq 0.75$ AND $580 \leq R_{fit} \leq 620$ cm. The fraction of events cut by $0.75 \leq \theta_{ij} \leq 1.45$ for different NHIT windows is given in Table 10.7. The average fraction of AV background events leaking into the signal window $0.75 \leq \theta_{ij} \leq 1.45$ is $\leq 12.5\%$. With a fiducial volume cut of $R_{fit} \leq 550$ cm this background contamination is expected to be much less in the actual actual candidate event set. The limited statistics of the available data do not allow us to perform a complete bifurcated analysis of these high-θ_{ij} '*Leslie-Heeger*' events.

Table 10.7: Fraction of potential high-θ_{ij} AV background events leaking through the $\theta_{ij} \leq 1.45$ cut into the signal window $0.75 \leq \theta_{ij} \leq 1.45$.

NHIT Window	Events with $\theta_{ij} \geq 0.75$	Events with $0.75 \leq \theta_{ij} \leq 1.45$	Leakage of AV Events (%)
120-200	24	3	$\leq$12.5%
120-130	4	1	$\leq$ 25%
130-140	6	2	$\leq$ 33.4%
140-200	16	1	$\leq$ 6.25%
130-200	20	3	$\leq$15%

Finally, we should point out that the upper limit on the *hep* contribution to the data set will be determined from a maximum likelihood fit to the NHIT spectrum of the data. A $\sim 10\%$ uncertainty on the number of background events will have a small effect on the

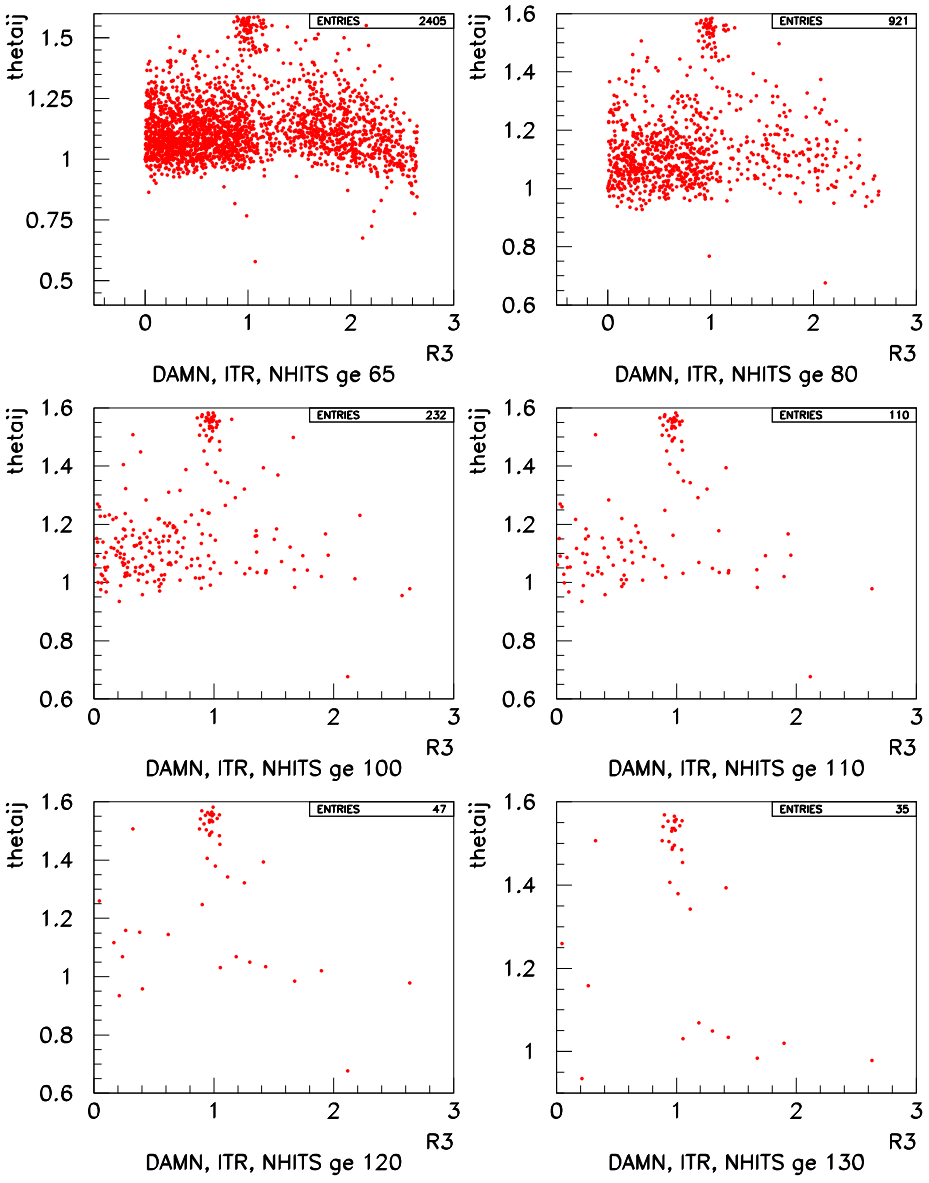

Figure 10.14: Plots of θ_{ij} versus R^3 reveal the parameter region that characterizes AV-related background events. These events are clearly distinguishable for various NHIT cuts.

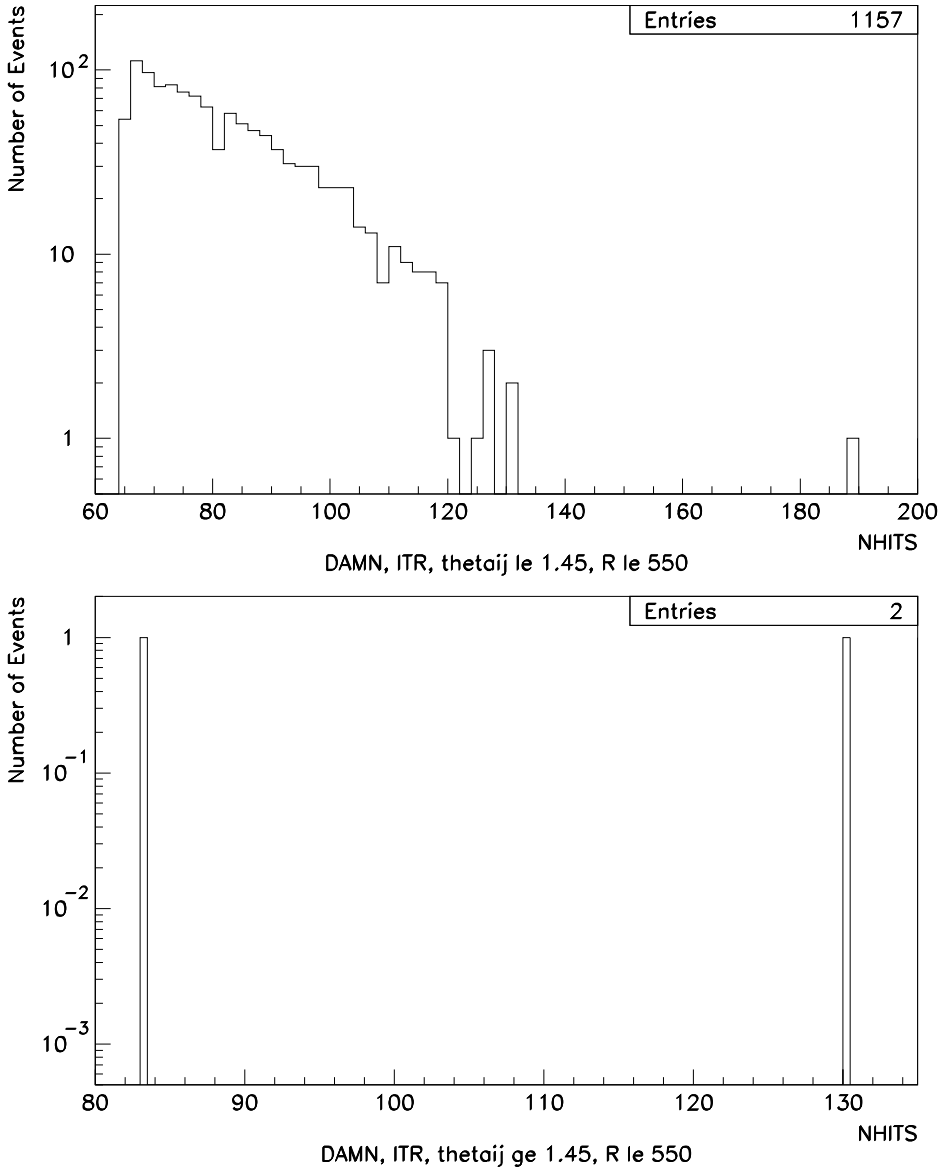

Figure 10.15: NHIT distributions of the DAMN-reduced data set with $R_{fit} \leq 550$ cm for all events with $\theta_{ij} \leq 1.45$ (upper plot) and $\theta_{ij} \geq 1.45$ (lower plot). There is essentially no background to the *hep* signal in the NHIT window of interest.

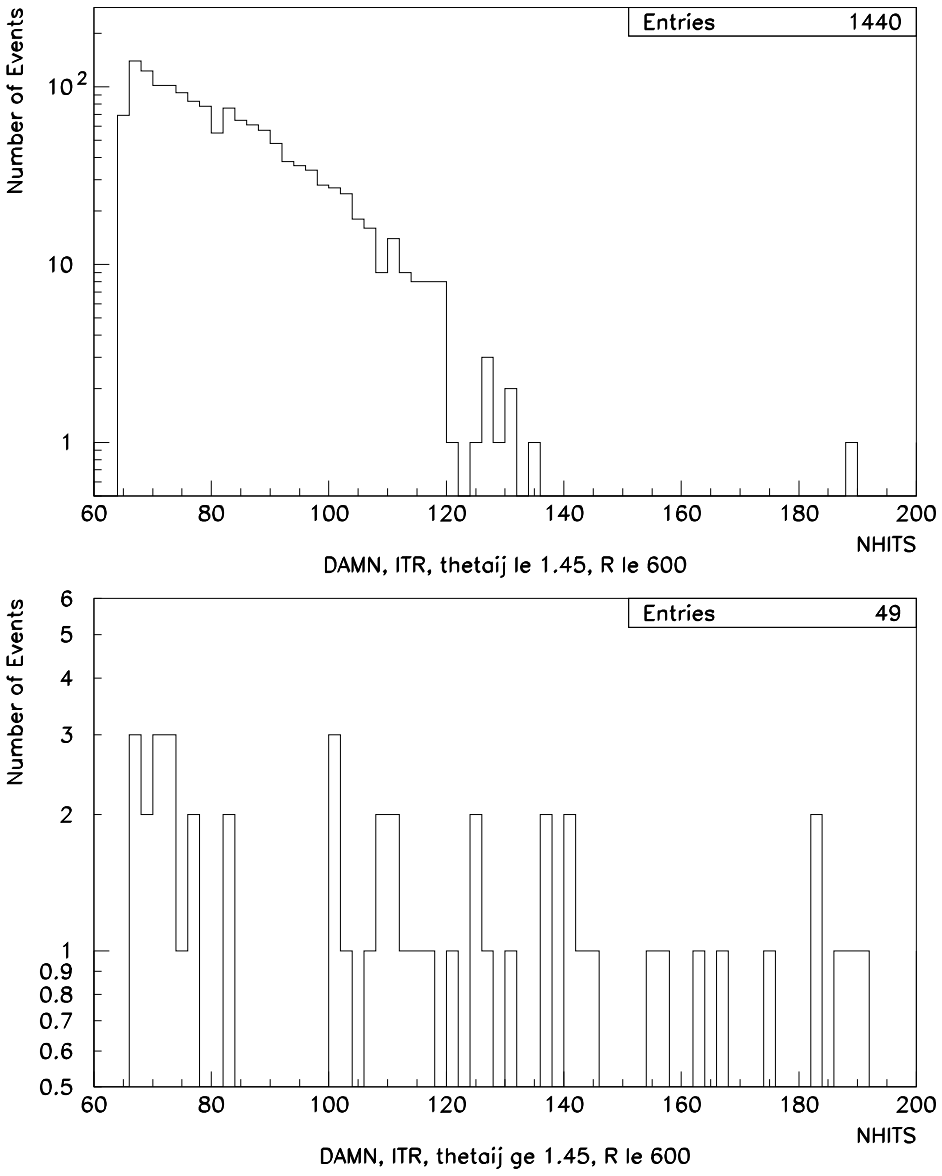

Figure 10.16: NHIT distributions of the DAMN-reduced data set with $R_{fit} \leq 600$ cm for all events with $\theta_{ij} \leq 1.45$ (upper plot) and $\theta_{ij} \geq 1.45$ (lower plot). The lower plot shows the AV-related background to the *hep* signal.

upper *hep* limit derived from a statistically limited but clean data set.

10.7.2 Atmospheric Neutrino-Induced Backgrounds in the Solar Energy Range

Atmospheric neutrino-induced interaction in SNO can contaminate the solar neutrino signal and form a background to the ^{8}B and *hep* signal. There are two principal ways in which this could happen. Low-energy electrons from ν_e , $\overline{\nu}_e$ can cause a signal that is identical to the Čerenkov electrons from solar neutrino interactions. In addition, we can have interactions of ν_μ and $\overline{\nu}_\mu$ of higher energies than 15 MeV producing muons which yield the same amount of Čerenkov light as solar neutrino-induced electrons. Finally, there may be decays of undetected sub-threshold muons either directly from cosmic rays or from atmospheric neutrino interactions.

The solar neutrino background from these interactions has been studied in detail [179, 180]. The estimates for the atmospheric neutrino-induced background to the solar neutrino signal from this work are summarized in Table 10.8. In summary, the total number of atmospheric neutrino-induced background events is ~ 1 /kt-yr or 0.1% of the data set and vanishingly small compared to the possible backgrounds from the AV.

As a verification of this estimate we have handscanned the high-NHIT data in the range between $70 \leq$ NHIT ≤ 500. From the number of single ring events we can extrapolate under the solar neutrino signal and obtain 1.7 /kt-yr. The upper limit is a one-sided error calculation. From the data alone one could set an upper limit on the atmospheric neutrino induced background of ≤ 0.3 /kt-yr or $\leq 0.3\%$ which is in good agreement with the combined estimates of Table 10.8.

Table 10.8: Summary of low-energy atmospheric neutrino induced backgrounds following estimates by C. Waltham et al. [179, 180].

Interaction	Number of Events
ν_μ quasi-elastic	0.3
silent μ decay	0.07
$\nu - p$ NC	0.1
ν inelastic NC	≤ 0.5

10.8 Determining the Contribution of hep Neutrinos to the Solar Neutrino Data at the Sudbury Neutrino Observatory

In close analogy to the ^{8}B endpoint analysis described in Chapter 8 the contribution of *hep* neutrinos to the solar neutrino data in SNO can be determined from a maximum likelihood fit to the NHIT spectrum of the candidate event set. NHIT probability distribution functions (PDF's) of ^8B and *hep* neutrinos derived from SNOMAN Monte Carlo simulations are fit to the NHIT spectrum of the reduced but otherwise raw data.

The NHIT spectra of the ^{8}B and *hep* neutrino interaction rates in SNO as predicted by Standard Solar Models are shown in Figure 10.17. The allowed approximation is made in calculating the *hep* spectrum shape. The number of ^{8}B interactions above NHIT > 140 is small and the number of expected *hep* events in the region between $140 >$ NHIT > 200 is of the order of a few at best. Above NHIT ≥ 200 the number of expected *hep* events is vanishingly small.

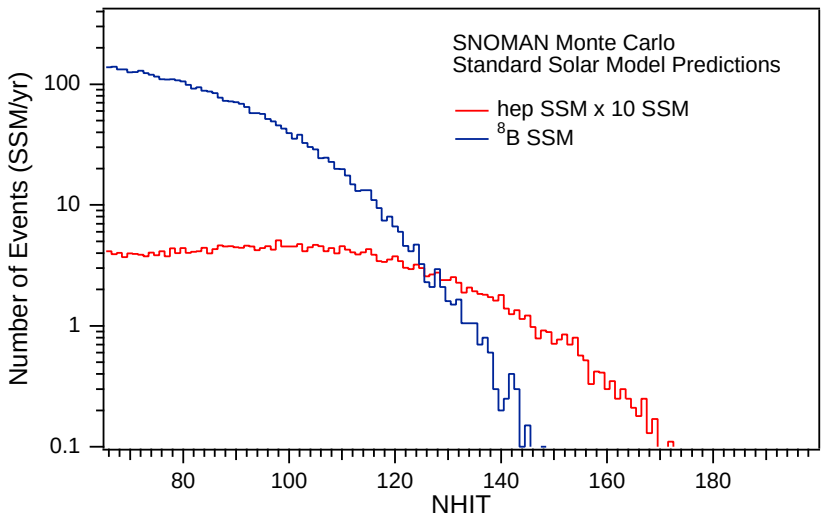

Figure 10.17: ^{8}B and *hep* NHIT spectra for Standard Solar Model predictions of the neutrino interaction rates in SNO. This includes CC, NC, and ES interactions. In Chapter 9 it was determined that the ν_e ^{8}B flux is suppressed by a factor of ~ 0.342 relative to Standard Solar Model predictions of the total ^{8}B flux.

This maximum likelihood analysis is performed with both a fixed and a free-floating ^{8}B amplitude. In contrast to the ^{8}B endpoint fit from Chapter 8, the energy scale of the probability distribution functions used in the *hep* analysis is kept constant. Formally, we can write the NHIT spectrum of the data as the sum of the ^{8}B and *hep* contribution

$$N^{SNO}\left[NHIT\right] = f_{8B} \times N_{8B}^{PDF}\left[NHIT\right] + f_{hep} \times N_{hep}^{PDF}\left[NHIT\right] \tag{10.2}$$

where f_{8B} and f_{hep} are the fit parameters determined from the maximum likelihood analysis of the spectrum. The parameters of the fit are determined for different NHIT thresholds to determine the stability of the fit. Figures 10.18 and 10.19 illustrate that the results are mostly constant and do not change significantly with the choice of a particular analysis threshold.

Figure 10.18 shows the 99% confidence level on the ^{8}B contribution to the SNO solar neutrino spectrum as determined in a 2-parameter maximum likelihood fit (red band). In a 1-parameter fit to the *hep* contribution alone the ^{8}B amplitude is fixed at the value (0.342 $\times$ SSM) determined in the unconstrained spectral decomposition (black dashed line).

Figure 10.19 shows the 95%, 99%, and 99.9% confidence level on the *hep* contribution to the SNO solar neutrino data. The red lines give the upper limits for a free-floating ^{8}B amplitude while the black lines give the *hep* upper limit for a fixed ^{8}B contribution of 0.342$\times$ SSM. The fact that the hep upper limit decreases with NHIT threshold in case of a fixed ^{8}B contribution is an indication of slight spectral distortions. Comparing the suppressed ^{8}B spectrum and the LMA spectrum shown in Figure 9.27 we see that this is what we would expected for a LMA-distorted spectrum. The structure in the fit results at NHIT $\sim$ 80 is due to the dip in the original NHIT spectrum of the SNO data.

The NHIT spectrum of the data reveals one event at NHIT=189. It turns out that the fit results for the ^{8}B and *hep* contribution to the data are very similar independent of whether the event at NHIT=189 is included or not. This is expected as the probability of finding a *hep* or ^{8}B event at such high NHIT is small. This event might be a rare *hep* interaction or an atmospheric neutrino event. Further analysis is necessary to determine the nature of this event.

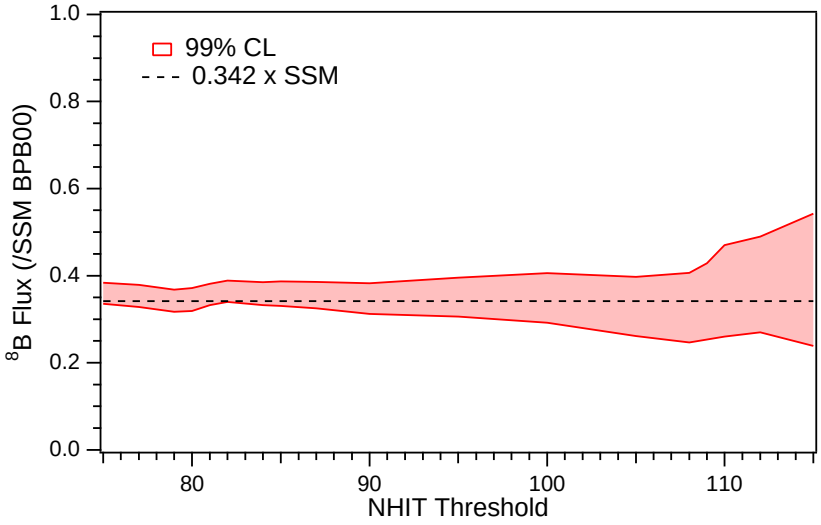

Figure 10.18: 99% confidence level on the ^{8}B contribution to the SNO solar neutrino spectrum as determined in a 2-parameter maximum likelihood fit (red band). In a 1-parameter fit to the *hep* contribution alone the ^{8}B amplitude is fixed at the value (0.342 × SSM) determined in the unconstrained spectral decomposition (black dashed line).

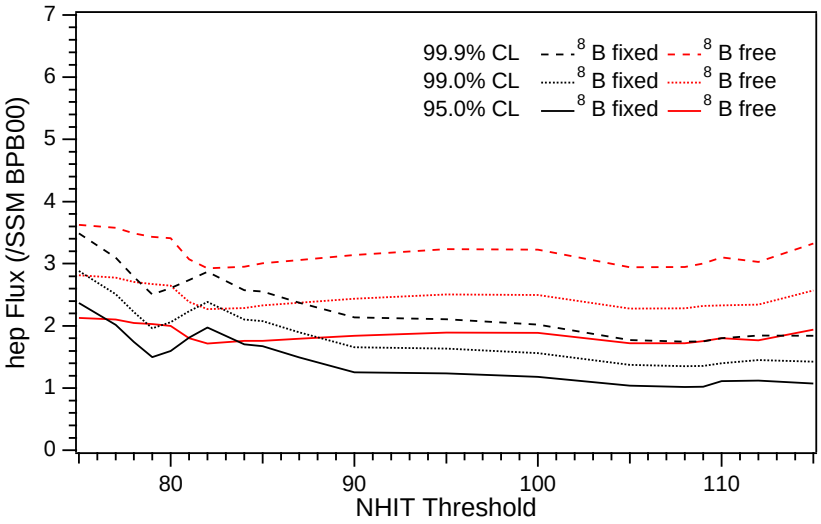

Figure 10.19: 95%, 99%, and 99.9% confidence level on the *hep* contribution to the SNO solar neutrino data. The red lines give the upper limits for a free-floating ^{8}B amplitude while the black lines give the *hep* upper limit for a fixed ^{8}B contribution of 0.342× SSM. The structure at NHIT ∼ 80 is due to the dip in the original NHIT spectrum.

The final result is based on the fit above NHIT $\geq$ 95 as this analysis threshold or fit interval gives a conservative estimate of the confidence interval. The *hep* contribution to the SNO data was determined in a fit of the ^{8}B and *hep* probability distribution functions to the NHIT spectrum of the SNO data. A 2-component maximum likelihood analysis of the SNO spectrum yields a *hep* limit of $\Phi_{hep}^{SNO} < 1.7 \times 10^4$ cm^{-2} s^{-1} at the 95% C.L. with a fit value of 0.351 ± 0.026 for the ^{8}B charged-current component. This *hep* limit corresponds to approximately 1.89 $\times \phi_{hep}^{SSM}$, roughly twice the Standard Solar Model prediction [11]. The ^{8}B component determined in this analysis is in excellent agreement with the ^{8}B ν_e flux of $0.342 \times \phi_{8B}^{SSM}$ determined in the model-independent analysis in Chapter 9. With the ^{8}B contribution fixed at $0.342 \times \phi_{8B}^{SSM}$, we obtain an upper *hep* limit of $\Phi_{hep}^{SNO} < 1.1 \times 10^4$ cm^{-2} s^{-1} at 95% C.L..

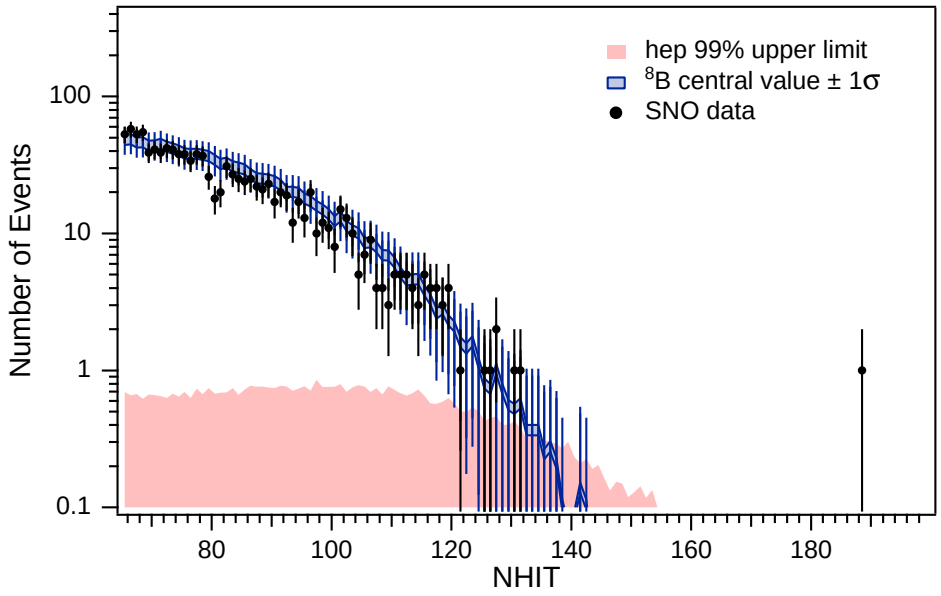

Figure 10.20: 99% confidence regions of the *hep* and ^{8}B signal in the SNO data derived from a 2-component maximum likelihood analysis of the NHIT spectrum.

CHAPTER 11

CONCLUSIONS

For more than 30 years, experiments have measured solar neutrinos produced in the thermonuclear fusion reactions that power the Sun. Data from these solar neutrino experiments were found to be incompatible with the predictions of solar models. More precisely, the flux of neutrinos detected on Earth was less than expected, and the relative intensities of the sources of neutrinos in the Sun were incompatible with those predicted by solar models. This was known as the Solar Neutrino Problem. By the mid-1990s the data were beginning to suggest that one could not even in principle adjust solar models sufficiently to account for the effects. Novel properties of neutrinos seemed to be called for. With the recent measurements of the Sudbury Neutrino Observatory (SNO), it has finally become possible to test the solar model predictions and the particle properties of neutrinos independently.

Here we summarize the main results of our measurement of the interaction rates of solar ^{8}B and *hep* neutrinos with deuterium in the Sudbury Neutrino Observatory and discuss their implications for particle physics, astrophysics, and cosmology.

11.1 Solving the Solar Neutrino Problem: Direct Evidence for the Flavor Transformation of Solar Neutrinos

In common with all previous solar neutrino experiments [48, 91, 113, 104, 85, 86], SNO observes a reduced flux of ν_e from the Sun [70, 106]. The fraction of the SNO charged-current ^{8}B flux of that predicted by Standard Solar Models (SSM) as determined in this work is 0.342 ± 0.024 (stat.) $^{+0.025}_{-0.022}$ (syst.) for a SSM prediction of 5.05×10^6 cm^{-2} s^{-1}. The elastic scattering flux measured by SNO is consistent with the high-precision measurement performed at Super-Kamiokande [113], a light water Čerenkov detector located in Kamioka, Japan. The total flux of active ^{8}B neutrinos is the sum of the electron and non-electron flavors and is measured by the neutral-current disintegration of deuterium to

be 1.258 ± 0.268 (stat.) $^{+0.118}_{-0.116}$ (syst.) times the Standard Solar Model prediction [11], or 6.35 ± 1.35 (stat.) $^{+0.60}_{-0.60}$ (syst.) $\times 10^6$ cm^{-2} s^{-1}, without assumptions about the charged-current shape of the ^{8}B spectrum.

A comparison of the charged-current (CC) and neutral-current (NC) interaction rates is used to test the hypothesis of neutrino flavor transformation. The charged-current reaction on deuterium is sensitive exclusively to ν_e while the neutral-current interaction rate is equally sensitive to ν_μ and ν_τ, as well as ν_e. Anti-electron neutrinos can contribute to the neutral-current signal through the $\overline{\nu}_e + d \rightarrow e^+ + n + n$ process. An analysis of Super–Kamiokande's solar neutrino data [176] for a possible contribution of $\overline{\nu}_e$ sets a limit on the flux of solar $\overline{\nu}_e$ of less than 1.8×10^{-5} cm^{-2} s^{-1} at the 95% C.L.. This is less than 2.9% of the total neutral-current signal measured in SNO or less than 3.6% of the ^{8}B flux predicted by Standard Solar Models [1]. We conclude that $\nu_e \rightarrow \overline{\nu}_e$ oscillations cannot explain the solar neutrino flux measurements at SNO. Under the assumption of no spectral distortions in the CC spectrum the difference between the CC and NC interaction rates derived in this work is 4.8 σ, or more than 5.3 σ in the published SNO results [106]. This is clear evidence for the non-electron flavor component of the solar neutrino flux. Without the constraint on the CC spectrum we make a model-independent determination of the ^{8}B flux. The ν_e flux corresponding to the model-independent charged-current spectrum is determined by fitting a standard ^{8}B spectrum to the measured, unconstrained CC spectrum. The difference between the charged-current and neutral-current interaction rates determined in this way is more than 3.1 σ. The measured total flux of solar ^{8}B neutrinos is in good agreement with solar model predictions. For a summary of the SNO neutrino flux measurements from the D_2O phase see Figure 11.1.

The ratios of the charged-current to neutral-current interaction rates determined in a model-dependent (^{8}B shape constrained) and model-independent analysis (^{8}B shape unconstrained) are given below. The results of this work are derived from 240.9 live days of D_2O data while the published SNO analysis is based on 306.4 days of data.

---

[1] A detailed analysis of the $\overline{\nu}$ signal at SNO is underway and expected to yield roughly an order of magnitude greater sensitivity to the solar $\overline{\nu}_e$ flux [154].

$$[CC/NC]^{\rm SNO}_{\rm const.} = 0.346\ ^{+0.048}_{-0.046} \quad (11.1)$$

$$[CC/NC]^{\rm SNO}_{\rm unconst.} = 0.274\ ^{+0.073}_{-0.073} \quad (11.2)$$

$$[CC/NC]^{\rm (this\ work)}_{\rm const.} = 0.341\ ^{+0.057}_{-0.055} \quad (11.3)$$

$$[CC/NC]^{\rm (this\ work)}_{\rm unconst.} = 0.273\ ^{+0.071}_{-0.070} \quad (11.4)$$

While the non-Gaussian errors in the $[CC/NC]$ ratios complicate the interpretation the ratios $[CC/NC]$ illustrate clearly the difference between the solar ν_e flux and the total active ^{8}B ν flux from the Sun. We note that the total ^{8}B neutrino flux deduced in June 2001 from SNO's measurement of the charged-current interaction and Super–Kamiokande's measurement of the elastic scattering of ^{8}B neutrinos is in excellent agreement with the neutral-current measurement obtained in this work. This measurement is the first model-independent evidence for the flavor transformation of solar neutrinos. The total ^{8}B flux measurement agrees well with Standard Solar Model predictions.

The measurements at the Sudbury Neutrino Observatory show that the neutrino flux produced in the $^8{\rm B} \rightarrow {}^8{\rm Be}^* + {\rm e}^+ + \nu_e$ beta-decay reaction in the Sun contains a significant non-electron type component when measured on Earth. About 2/3 of the active solar neutrino flux consists of flavors other than ν_e. Neutrino flavor transformation is found to be the solution to the Solar Neutrino Problem.

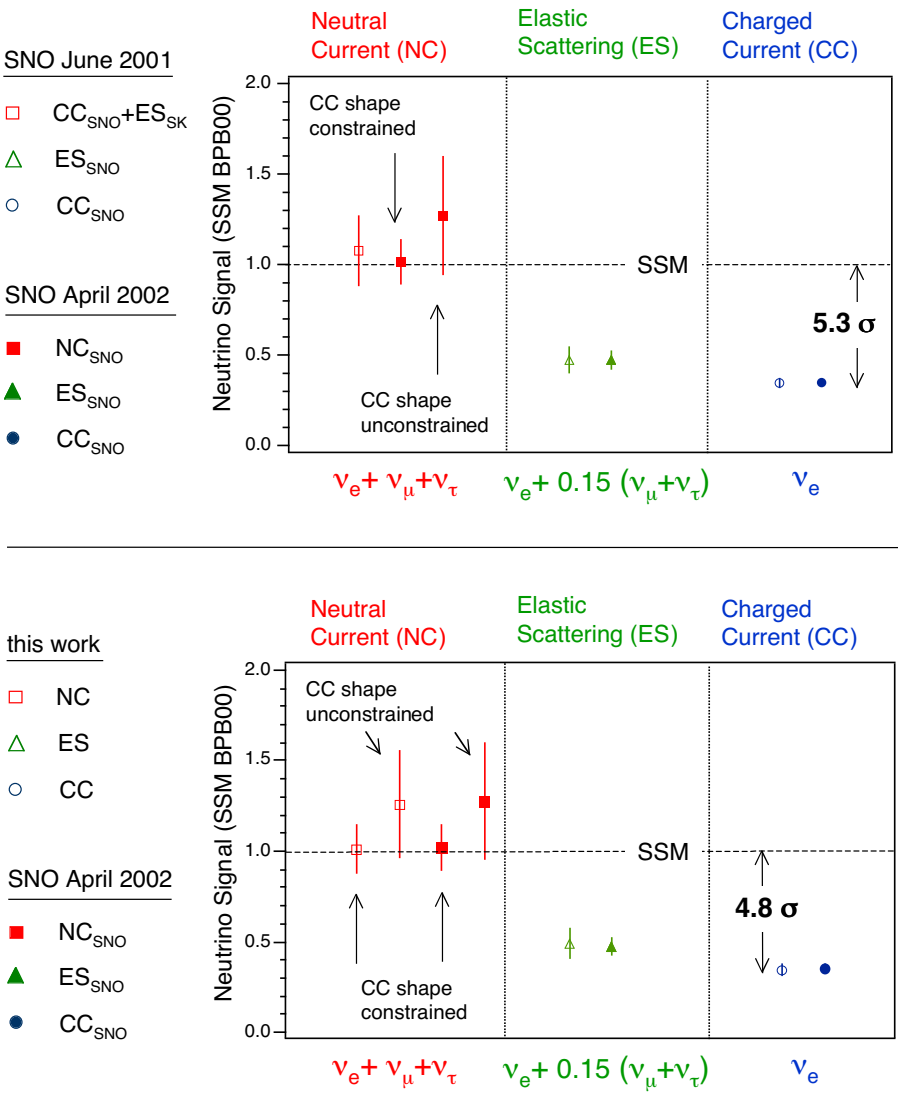

Figure 11.1: Summary of SNO's published solar neutrino flux measurements from the D_2O phase [70, 106] (upper plot). The difference between the measured neutral-current and the charged-current interaction rate in SNO is evidence for the flavor conversion of solar neutrinos. The lower plot shows a comparison of the solar neutrino flux measurements of this work to the published solar neutrino flux measurements from the D_2O phase [70, 106].

11.2 Testing the Predictions of Standard Solar Models: Model-Independent Measurement of the ^{8}B Flux and the CC Spectrum

For the first time, it has become possible for a solar neutrino experiment to measure both the electron and non-electron component of the solar ^{8}B neutrino flux independently. In this thesis we developed techniques for the model-independent measurement of the flux of solar ^{8}B neutrinos and for the determination of the CC spectrum and interaction rate. Our measurement of the total ^{8}B neutrino flux, $\Phi_{8B} = 6.37 \pm 1.41$ (stat.) $^{+0.59}_{-0.60}$ (syst.) $\times$ 10^6 cm^{-2} s^{-1}, is in good agreement with Standard Solar Model predictions of $\Phi_{8B}^{SSM} = 5.05 \times 10^6$ cm^{-2} s^{-1} [11]. Under the assumption of the standard ^{8}B spectral shape the measurement of the total ^{8}B flux becomes more precise and the agreement with Standard Solar Model predictions is excellent.

The charged-current spectrum obtained from the model-independent spectral decomposition of the data is shown in Figure 11.2. This figure shows SNO's CC spectrum with its $\pm 1\sigma$ uncertainties arising mainly from the NC contribution that has been removed and an undistorted standard ^{8}B CC spectrum (scaled to 0.344 $\times$ SSM) for comparison. This spectrum represents the true, experimental CC spectrum as it is derived without assuming a particular spectral shape. Within the statistical limitation of the data there is good agreement between this spectrum and the shape of the standard ^{8}B spectrum. Spectral distortions in the CC electron spectrum due to neutrino oscillations are therefore relatively small. We note the small excess of events in the low-energy region of the spectrum and the apparent suppression in the high-energy region relative to the standard ^{8}B spectrum. This may be a first hint of spectral distortions. This observation would be consistent with the kind of spectral distortions we expect from the Large Mixing Angle (LMA) solution of solar neutrino oscillation.

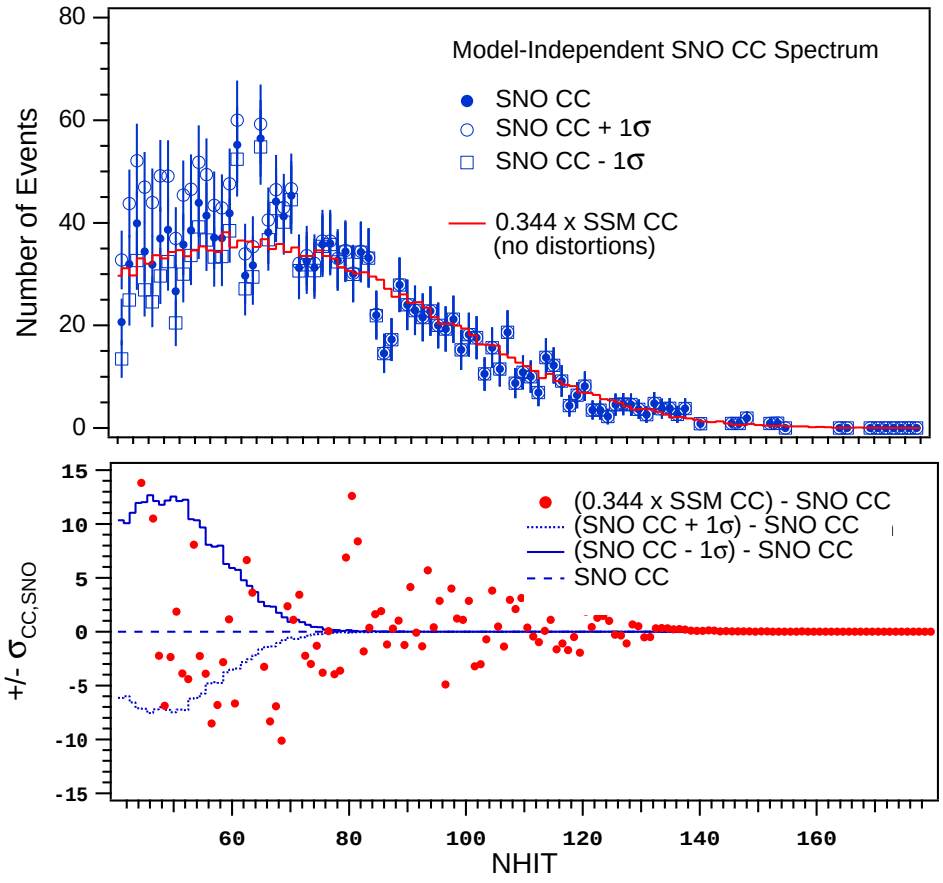

Figure 11.2: CC NHIT spectrum above NHIT ≥ 46 and with $R_{fit} \leq 550$ cm as determined in the model-independent, unconstrained spectral decomposition. The lower panel shows the $\pm 1\sigma$ deviations of the experimental CC spectrum and the difference between the experimentally measured CC spectrum and the suppressed but undistorted ^{8}B CC spectrum.

11.3 Removing the Theoretical Cross-Section Dependence from the SNO Solar Neutrino Flux Measurements: Model-Independent Determination of Φ_{ν_e} and Φ_{ν_x}, and Experimental Constraints on the Two-Body Axial Current $L_{1,A}$ from SNO and Super-Kamiokande

The Sudbury Neutrino Observatory and Super–Kamiokande have made precision measurements of the interaction rates of solar neutrinos. To deduce the solar neutrino flux from the measured interaction rates theoretical input is needed. The solar neutrino flux reported by these experiments depends on the cross-section calculations for charged-current and neutral-current neutrino-deuteron interactions and the elastic scattering cross-section of neutrinos and electrons. Modern calculations of the neutrino-deuteron cross-sections make use of Effective Field Theory (EFT). In Effective Field Theory the dominant uncertainties in all neutrino-deuteron reactions can be expressed through a single, common, isovector axial two-body current parameterized by $L_{1,A}$ [21]. The elastic scattering cross-section of neutrinos is independent of $L_{1,A}$ and well-known. Using the solar neutrino flux measurements from SNO and Super–Kamiokande it has become possible to constrain $L_{1,A}$ in a model-independent way. In this analysis we can determine the best values of ϕ_{ν_e} , ϕ_{ν_x}, and $L_{1,A}$ that fit the current set of solar neutrino measurements. This in turn provides direct experimental constraints on the two-body axial currents parameterized by $L_{1,A}$. Until the recent analysis of reactor antineutrino-deuteron breakup reactions [22] this datum provided the only direct experimental constraints on the neutrino-deuteron cross-sections.

A model-independent analysis of the solar neutrino measurements at SNO and Super-Kamiokande shows that the measured ϕ_{ν_e} and ϕ_{ν_x} fluxes are different at the 99.99996% CL. The best fit values are $\phi_{\nu_e}^{SNO+SK} = 1.78 \pm 0.14 \times 10^6$ cm^{-2} s^{-1} and $\phi_{\nu_x}^{SNO+SK} = 5.21 \pm 0.79 \times 10^6$ cm^{-2} s^{-1}. This is unambiguous evidence for the flavor transformation of solar neutrinos. Removing the last model-dependence of SNO's solar neutrino flux measurements, the normalization of the neutrino deuteron cross-sections, does not remove the difference between the measured ν_e flux and the total active ^{8}B solar neutrino flux (see Figure 11.3). A combined, model-independent analysis of the data from SNO and Super–Kamiokande

does in fact strengthen the evidence for neutrino flavor change compared to the results presented by SNO. We can use the solar neutrino measurements from SNO and Super–Kamiokande to place constraints on the parameter $L_{1,A}$ which describes the two-body axial current in effective field theory and normalizes the νd cross-sections. The best fit value is $L_{1,A} = 3.02 \pm 7.40$ fm^3.

The analysis of reactor antineutrino-deuteron breakup reactions yields the more precise constraint $L_{1,A}^{reactor} = 3.6 \pm 5.5$ fm^3 [22], in excellent agreement. The fact that we can derive model-independent constraints on $L_{1,A}$ is a nice example of how the results of the different solar neutrino experiments can be used together to calibrate one of the nuclear-physics parameters that was previously available only as a theoretical, model-dependent input to these experiments. In that sense one can say that the modern solar neutrino experiments have become self-calibrating. A reduction of the uncertainty in SNO's CC and CC flux measurements will significantly improve the constraints solar neutrino measurements place on $L_{1,A}$. With the expected accuracy of future measurements at SNO it may be possible to improve the precision on $L_{1,A}$ substantially.

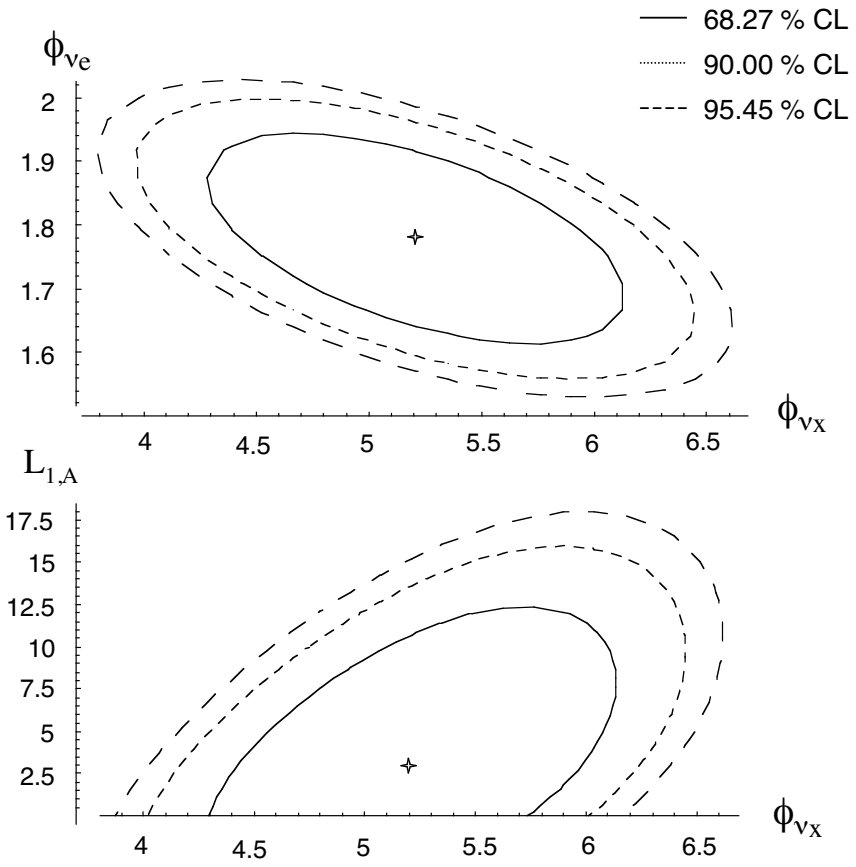

Figure 11.3: Model-independent confidence levels (CL) on $L_{1,A}$, ϕ_{ν_x}, ϕ_{ν_e} from the SNO and Super–Kamiokande solar neutrino flux measurements. The 2-dimensional confidence intervals in ϕ_{ν_e} versus ϕ_{ν_x} and $L_{1,A}$ versus ϕ_{ν_x} are projections of the joint confidence region of $L_{1,A}$, ϕ_{ν_x}, and ϕ_{ν_e}. The stars indicate the best fit points. The upper plot demonstrates that ϕ_{ν_e} is less than ϕ_{ν_x}, independent of the theoretical parameter $L_{1,A}$. This removes the last model-dependent assumption from the evidence of neutrino flavor transformation obtained by SNO and Super–Kamiokande.

11.4 Constraining the Mixing Parameters of Solar Neutrinos: Evidence for Large Mixing between Leptons

From SNO's measurement of the flux of ^{8}B neutrinos as well as the energy spectrum we can infer general constraints on the mixing of active and sterile species, and, under the hypothesis of 2-ν mixing, allowed values for neutrino oscillation parameters. The difference between the interaction rates (normalized to the Standard Solar Model predictions) disfavors the oscillations of ν_e to sterile neutrinos alone, which would lead to a reduced flux of electron neutrinos but equal fluxes measured in all reaction channels. Sterile neutrinos might be, for example, right-handed neutrinos or left-handed antineutrinos which do not interact through Standard Model interactions. On the other hand, the different interaction rates are consistent with oscillation of ν_e into active ν_μ and ν_τ. SNO's result is consistent with both the hypothesis that electron neutrinos from the Sun oscillate into other active flavors, and with the Standard Solar Model prediction for the total number of neutrinos released in the solar fusion reactions.

Under the assumption of effective 2-ν mixing between active species we can determine the allowed space of neutrino oscillation parameters. For simplicity, only the total energy spectra (NC+CC+ES) broken up into day and night data sets were used in the MSW oscillation analysis. The radial R and direction $\cos\theta_\odot$ information was omitted. There are 3 free parameters in the fit: The total ^{8}B flux, the difference Δm^2 between the squared masses of the two neutrino mass eigenstates, and the mixing angle θ. In this particular analysis the flux of higher energy neutrinos from the solar *hep* reaction was fixed at 9.3×10^3 cm^{-2} s^{-1}.

Figure 11.4 shows allowed mixing parameter regions using only SNO data with no additional experimental constraints or inputs from solar models. Figure 11.5 shows the allowed regions of the MSW parameter space determined by a global χ^2-fit to the data from all available solar neutrino experiments, combined with input on the *pp*, *pep*, and ^{7}Be neutrino fluxes from solar model calculations. The star indicates the best fit. This global analysis strongly favors the large-mixing-angle (LMA) solution and mixing angles θ with $\tan^2\theta < 1$.

In the MSW model the survival probability of solar neutrinos depends on $\sin^2 2\theta$ and

$\Delta m^2 = m_2^2 - m_1^2$. In this formalism solutions with $\theta > \pi/4$ are equivalent to solutions with $\Delta m^2 < 0$. Solutions of the global analysis with $\tan^2\theta < 1$ imply $m_1 < m_2$. We find that the electron neutrino is predominantly composed of the lighter mass eigenstate.

A comparison of the allowed MSW parameter space derived from separate day and night energy spectra and the averaged energy spectrum shows no significant difference. The $[CC]\,/\,[NC]$ ratio measured at SNO which constrains the parameter space in θ can be deduced from the measured energy spectrum, while the mass difference Δm^2 can be determined from the Day/Night difference of the ^{8}B neutrino flux, and low-energy solar neutrino experiments. The most stringent limits on Δm^2 currently come from a global fit including the low-energy solar neutrino experiments.

With the measurements of the neutral-current and charged-current interaction rates at the Sudbury Neutrino Observatory it has become possible to identify one region of neutrino oscillation parameter space that is strongly favored by all experiments: The Large Mixing Angle (LMA) solution. From the 2-ν analysis described above a unique set of oscillation parameters $\Delta m^2_{\rm solar}$ and θ_{12} has been determined [106]. The following parameters describe the oscillation behavior of solar ν_e into ν_μ and ν_τ. The uncertainties correspond to the 68% confidence level. The best fit points are given in parentheses.

$$\Delta m^2_{\rm solar} = 5.0\ ^{+4.5}_{-1.1} \times 10^{-5}{\rm eV}^2 \tag{11.5}$$

$$\theta_{12} = 30.3\ ^{+8.8}_{-3.5}\ ^\circ \tag{11.6}$$

Matter enhancement of neutrino oscillations can lead to neutrino flavor transformation not only in the Sun but also in the Earth. Under certain conditions the MSW model predicts significant flavor change for neutrinos during their passage through the Earth. Neutrino flavor transformation effects in the Earth can be detected by studying the diurnal time variation of the solar neutrino flux. The solar neutrino oscillation parameters determined above constrain the expected day-night variation of the solar neutrino flux measured in the Sudbury Neutrino Observatory. With the best fit values from the global analysis ($\Delta m^2 = 5.0 \times 10^{-5}$ and $\tan^2\theta = 0.34$) the expected day-night asymmetry of the solar ν_e flux is 6^{+2}_{-4} %. This is in good agreement with the measured day-night flux asymmetry [107, 172]

in SNO.

$$\mathcal{A}_{CC}\,[LMA] = 6.4^{+1.5}_{-5.2}\ \% \tag{11.7}$$

In summary, the measurements of the solar neutrino flux at SNO have provided direct evidence for the flavor conversion of solar neutrinos. Mechanisms that cause neutrino flavor conversion require massive neutrinos. Together with the oscillation signature in atmospheric neutrino experiment, these results are strong evidence for mixing in the lepton sector and new physics beyond the Standard Model. Unlike the quark sector where the CKM mixing angles are small, fits to the solar and atmospheric neutrino data indicate that the lepton sector exhibits large mixing. However, while the atmospheric mixing is maximal the mixing of solar neutrinos is not.

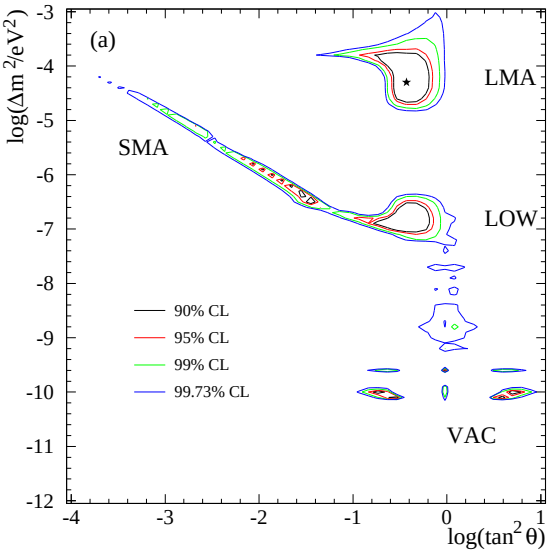

Figure 11.4: Allowed regions of the MSW parameter space determined by a χ^2-analysis of the SNO data [107].

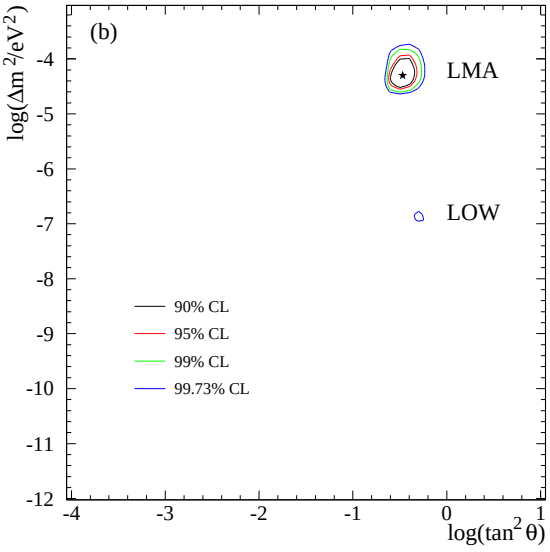

Figure 11.5: Allowed regions of the MSW parameter space determined by a χ^2-fit in a global analysis of all experimental solar neutrino data [107]. The strongest constraints from SNO on the neutrino mixing parameters come from the ratio of the CC and NC interaction rates $[CC]\,/\,[NC]$. The measured diurnal variation of the solar neutrino flux has a small effect on the presently allowed parameter space.

11.5 *Searching for hep* Neutrinos in the Sudbury Neutrino Observatory: A New Limit on the Neutrino Flux from the Solar $^3\mathrm{He} + p$ Process

Neutrinos from the beta decay of ^{8}B dominate the solar neutrino spectrum measured in SNO. The shape of the neutrino energy spectrum from a single beta-decaying source is well known and independent of solar physics to an accuracy of 1 part in 10^6. A measurement of the shape of the solar neutrino energy spectrum is a direct test of the minimal electroweak model and can be used to constrain models of neutrino flavor transformation.

Near the ^{8}B endpoint the solar neutrino spectrum is very sensitive to any underlying background, including neutrinos with energies above 15 MeV from other sources than ^{8}B-decay. In a rare branch of the pp-chain in the Sun, ^{3}He and proton fuse forming the reaction $^3\mathrm{He} + p \rightarrow {}^4\mathrm{He} + e^+ + \nu_e$. This *hep* process produces high energy solar neutrinos with an energy of up to 18.77 MeV.

Standard Solar Model calculations predict a *hep* neutrino flux three orders of magnitude smaller than the flux of ^{8}B neutrinos. Although the *hep* neutrino flux is a negligible contribution to the total neutrino flux measured in SNO it can significantly distort the ^{8}B neutrino spectrum near the endpoint especially if the *hep* S-factor is much larger than the existing estimates. The reliable estimation of the *hep* cross-section has been a long-standing challenge in nuclear physics. Using the same data as for the determination of the interaction rates of ^{8}B neutrinos we have determined a new upper limit on the flux of *hep* neutrinos from the Sun.

The *hep* contribution to the SNO data was determined in a fit of the ^{8}B and *hep* probability distribution functions to the NHIT spectrum of the SNO data. A 2-component maximum likelihood analysis of the SNO spectrum yields a *hep* limit of $\Phi_{hep}^{SNO} < 1.7 \times 10^4$ cm^{-2} s^{-1} at the 95% C.L. with a fit value of 0.351 ± 0.026 for the ^{8}B charged-current component. This *hep* limit corresponds to approximately $1.89 \times \phi_{hep}^{SSM}$, roughly twice the Standard Solar Model prediction [11]. The ^{8}B component determined in this analysis is in excellent agreement with the ^{8}B ν_e flux of $0.342 \times \phi_{8B}^{SSM}$ determined in the model-independent analysis in Chapter 9. With the ^{8}B contribution fixed at $0.342 \times \phi_{8B}^{SSM}$, we obtain an upper *hep* limit of $\Phi_{hep}^{SNO} < 1.1 \times 10^4$ cm^{-2} s^{-1} at the 95% C.L..

11.6 Concluding the First Phase of SNO: Current and Future Measurements of the SNO Experiment

Using data from the first phase of the SNO experiment we have measured the interaction rates of solar ^{8}B neutrinos with deuterium. From the measured flux of ν_e and $\nu_{\mu,\tau}$ unambiguous evidence for the flavor transformation of solar neutrinos has been obtained. These results have shown that the long-standing Solar Neutrino Problem was caused by new physics. It was found that massive and mixed neutrinos provide a coherent explanation of the current results. The results from SNO are an indication of physics beyond the Standard Model of particle physics.

Future data from SNO will provide many more interesting measurements on solar and non-solar neutrino topics. The use of NaCl in combination with D_2O in the second phase of the SNO experiment enhances the detection efficiency of the neutral-current signal and allows SNO to make an even better NC measurement, as well as new measurements of the other ^{8}B interaction rates. Based on our systematics studies for the current ^{8}B neutrino flux measurement we expect to reduce the total uncertainty on the measured NC signal in the D_2O+NaCl configuration from 13% to $\sim$ 8%. In the final phase of the SNO experiment the flux of solar ^{8}B neutrinos will be measured with a novel detection system based on a discrete array of ^{3}He-filled proportional counters. In this phase of the experiment the NC interaction will be detected through ^{3}He(n,p)^{3}H with the neutron capture in the array of ^{3}He-counters. It is expected that this detection system will improve the SNO's sensitivity to Day/Night variations in the solar neutrino flux and spectral distortions in the ^{8}B neutrino energy spectrum. The total ^{8}B flux will be measured with a similar precision as in the current D_2O+NaCl configuration. The appendices to this work describe in detail the design and construction as well as the status of the SNO Neutral Current Detector project.

11.7 Constructing the U_{MNSP} Neutrino Mixing Matrix: Constraints from Current Neutrino Oscillation Experiments

The recent results of the SNO experiment together with the atmospheric neutrino measurements can be interpreted in terms of matter-enhanced neutrino oscillation. In a MSW neutrino mixing scheme with 3 active Dirac neutrinos the results of the atmospheric and solar neutrino experiments are explained by the effective 2-ν mixing between the two dominant mass eigenstates involved in the oscillation of either the solar or atmospheric neutrinos. In this framework the solar neutrino flux measurements of the Sudbury Neutrino Observatory constrain the oscillation parameters of solar neutrinos to the Large Mixing Angle (LMA) region. In contrast to atmospheric neutrinos, the mixing angle of solar neutrinos is found to be large but not maximal. Having established one allowed solution for the oscillation of solar neutrinos we can now write down unique values for the U_{MNSP} neutrino mixing matrix elements that describe the $\nu_e \rightarrow \nu_{\mu,\tau}$ mixing of solar neutrinos. Additional Majorana phases have no effect on the results presented below. The best fit values derived from a global analysis of all solar neutrino experiments are

$$\Delta m^2_{\rm solar} = 5.0 \times 10^{-5}{\rm eV}^2 \tag{11.8}$$

$$\theta_{12} = 30.3^\circ \tag{11.9}$$

The precise measurements of Super–Kamiokande determine the U_{MNSP} elements for the $\nu_\mu \rightarrow \nu_\tau$ mixing of atmospheric neutrinos. The experimental results reported in [112] give

$$\Delta m^2_{\rm atm} = 3.2 \times 10^{-3}{\rm eV}^2 \tag{11.10}$$

$$\theta_{23} = 45.0^\circ \tag{11.11}$$

The measurements of the CHOOZ [65] reactor neutrino experiment combined with the results from Super–Kamiokande yield an upper limit of $\tan^2\theta_{13} < 0.03$ at the 90% confidence level. These experimental constraints on U_{e3} imply that $\cos\theta_{13}$ is approximately ~ 1. New experiments are necessary to determine U_{e3} and $\sin\theta_{13}$. The actual value of U_{e3} determines

$\sin\theta_{13}$ and the prospect of seeing CP violation in the neutrino sector will depend on U_{e3} not vanishing.

As shown in Chapter 2, the mixing matrix for Dirac neutrinos in the presence of one CP-violating phase δ_D can be written as

$$U_{MNSP} = \begin{pmatrix} U_{e1} & U_{e2} & U_{e3} \\ U_{\mu 1} & U_{\mu 2} & U_{\mu 3} \\ U_{\tau 1} & U_{\tau 2} & U_{\tau 3} \end{pmatrix} \tag{11.12}$$

$$= \underbrace{\begin{pmatrix} 1 & 0 & 0 \\ 0 & c_{23} & s_{23} \\ 0 & -s_{23} & c_{23} \end{pmatrix}}_{\text{atmospheric } \nu} \underbrace{\begin{pmatrix} c_{13} & 0 & s_{13}e^{-i\delta_D} \\ 0 & 1 & 0 \\ -s_{13}e^{i\delta_D} & 0 & c_{13} \end{pmatrix}}_{\text{reactor/accelerator } \nu} \underbrace{\begin{pmatrix} c_{12} & s_{12} & 0 \\ -s_{12} & c_{12} & 0 \\ 0 & 0 & 1 \end{pmatrix}}_{\text{solar } \nu} \tag{11.13}$$

where $c_{12} = \cos\theta_{12}$, $c_{13} = \cos\theta_{13}$, $c_{23} = \cos\theta_{23}$, $s_{12} = \sin\theta_{12}$, $s_{13} = \sin\theta_{13}$, and $s_{23} = \sin\theta_{23}$. For the first time it has become possible to find unique numerical values for (almost) all elements in the U_{MNSP} neutrino mixing matrix. With the experimental results listed above we obtain

$$U_{MNSP} = \overbrace{\begin{pmatrix} 1 & 0 & 0 \\ 0 & \frac{1}{\sqrt{2}} & \frac{1}{\sqrt{2}} \\ 0 & \frac{-1}{\sqrt{2}} & \frac{1}{\sqrt{2}} \end{pmatrix}}^{\text{Super}-\text{Kamiokande}} \overbrace{\begin{pmatrix} \sim 1 & 0 & s_{13}e^{-i\delta_D} \\ 0 & 1 & 0 \\ -s_{13}e^{i\delta_D} & 0 & \sim 1 \end{pmatrix}}^{\text{Chooz}} \overbrace{\begin{pmatrix} 0.86 & 0.51 & 0 \\ -0.51 & 0.86 & 0 \\ 0 & 0 & 1 \end{pmatrix}}^{\text{LMA}} \tag{11.14}$$

11.8 Constraining the Mass of Fermions: New Limits on Neutrino Masses from Oscillation Experiments

The neutrino flux measurements from SNO and Super–Kamiokande constrain the allowed mass values for neutrinos. Assuming that the oscillation of massive neutrinos explains both the evidence for the electron neutrino flavor change presented here and the atmospheric neutrino data of the Super–Kamiokande collaboration, two separate splittings of the squares of the neutrino mass eigenvalues are indicated: 5×10^{-5} eV^2 for the solar sector and $\sim 3.2 \times 10^{-3}$ eV^2 for atmospheric neutrinos. Together with the direct kinematic mass measurements of tritium beta-decay experiments [53, 50], these results limit the sum of mass eigenvalues of active neutrinos to $0.05 < \sum_{m_{1,2,3}} < 6.6$ in the case of only 3 light ν mass states. Neutrino scenarios with 3 light Dirac and 3 Majorana states are, however, possible. See Chapter 2. Figure 11.6 shows the fermion masses and neutrino mass limits. From the global MSW analysis of the solar neutrino experiments we find $m_{\nu_2} > m_{\nu_1}$. The ordering of m_{ν_3} with respect to $m_{\nu_{1,2}}$ is still undetermined and both a normal and inverted mass hierarchy are presently allowed.

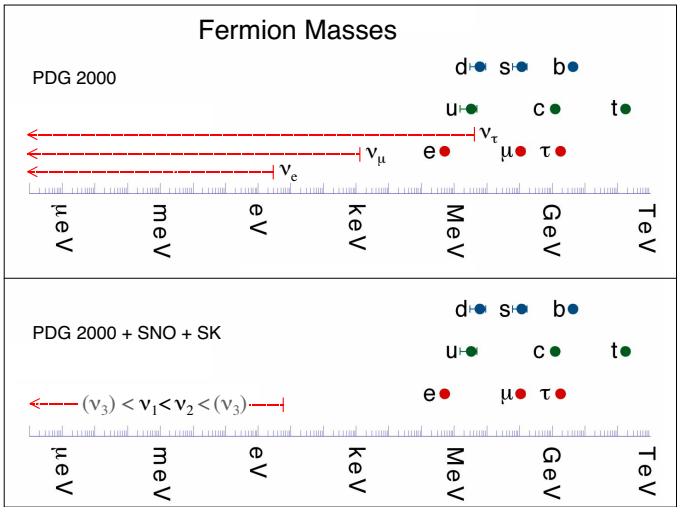

Figure 11.6: Fermion masses and neutrino mass limits based on PDG2000 [53] with and without the results from the SNO and Super–Kamiokande neutrino oscillation experiments [106, 112].

11.9 Cosmological Implications of Massive Neutrinos and Large Mixing

11.9.1 Constraints on the Lepton and $\nu - \overline{\nu}$ Asymmetries in the Universe

The observational success of Big Bang Nucleosynthesis is one of the main components of standard cosmology. If one assumes three standard neutrino flavors, then the only free parameter is the baryon to photon ratio n_B/n_γ which is found to be 5×10^{-10}. The baryon-antibaryon asymmetry remains a mystery and might hold an important clue for understanding the Universe at temperatures at least as high as the electroweak scale. In contrast to the baryons, which annihilate readily with antibaryons, we expect the lepton and antilepton numbers to be close to their primordial values. Even models that allow $\Delta L \neq 0$ generally conserve $B - L$, the difference between the baryon and lepton numbers. If it is both conserved and zero, the lepton asymmetry is $n_L/n_\gamma \approx n_B/n_\gamma \simeq 5 \times 10^{-10}$ as well. However, in certain models the lepton asymmetry can be much larger [2, 24]. It is of interest to constrain the lepton-antilepton asymmetry with experimental results.

Given constraints on charge asymmetry, any large lepton asymmetry would have to be hidden in the neutrino sector. In the Big Bang neutrinos and antineutrinos are expected to be in chemical equilibrium until they decouple at a temperature of $T \sim 2$ MeV. The recent results from solar and atmospheric neutrino experiments give strong indication of large mixing in the lepton sector. In the case of near bi-maximal mixing for the neutrino mixing matrix significant flavor transformation between $\nu - \overline{\nu}$ asymmetries can occur in the early Universe [137]. It has been suggested that large mixing angles may transfer large asymmetries in L_μ and L_τ to L_e well before beta-equilibrium freezeout at $T \simeq 1$ MeV. The almost complete transformation of asymmetries in $\nu_\mu - \overline{\nu}_\mu$ or $\nu_\tau - \overline{\nu}_\tau$ to $\nu_e - \overline{\nu}_e$ is an inescapable consequence of the near bi-maximal mixing framework and provides the strongest limit on the total lepton number of the Universe. The experimental observation of large neutrino mixing in the Super–Kamiokande and SNO experiment allows one to reduce the uncertainty in the lepton number of the Universe by up to two orders of magnitude [1]:

$$|L_e| \leq 0.03 \text{ and } |L_\mu + L_\tau| \leq 0.4 \tag{11.15}$$

11.9.2 Massive Neutrinos as Particle Dark Matter

Numerous observations have obtained evidence for the existence of dark matter and energy in the Universe. Using a variety of methods including gravitational lensing, virial analysis, and X-rays from intracluster gas it is found that the matter density is significantly greater than can be accounted for by the baryon density allowed by Big Bang nucleosynthesis and the measured primordial abundance of deuterium and other light elements. From the large discrepancy between measurements of cluster dynamics and the baryon abundance it is likely that the bulk of dark matter is non-baryonic, and possibly of some exotic form. The relatively early formation of small-scale structures in the Universe allows us to infer that the bulk of the non-baryonic dark matter must be cold [177, 165, 14]. Hot dark matter, such as neutrinos, damps structure formation until the universe is very large.

In the search for the unseen matter, particle dark matter candidates are looked for in schemes beyond the Standard Model. Particle physicists have suggested a number of candidates for non-baryonic dark matter: massive neutrinos, axions, and supersymmetric relics. Many dark matter candidates are potentially detectable by the current generation of dark matter experiments. Attractive candidates for non-baryonic dark matter are slow thermal relics born in an early phase of the Universe. These so-called WIMPS (weakly interactive massive particles) arise in supersymmetric models independently from cosmological considerations. Supersymmetric extensions of the Standard Model indicate that weakly interacting particles created at the electroweak symmetry breaking scale could have survived until the present day with a matter density of the right order of magnitude if they carry a conserved new quantum number. The naturalness of producing the correct density makes these weakly interacting massive particles (WIMPS) the currently most favored candidates for non-baryonic dark matter. Supersymmetric theories have a rich phenomenology for dark matter, but interesting candidates may also be found in theories that do not involve supersymmetry.

Light massive neutrinos are the simplest extension to the Standard Model. With the mounting evidence for neutrino mass, one might think of neutrinos as the nonbaryonic dark matter. Among the non-supersymmetric candidates, the massive neutrino and the

axion are the most direct possibilities. In the Standard Big Bang model, copious numbers of neutrinos were produced in the early Universe. Approximately 12 billion years ago, the Universe was hot and compact creating particles in pairs at temperatures far above currently available particle accelerator energies. The Universe today is thought to be filled with 1.7 K thermal neutrino radiation, the neutrino complement to the thermal radiation background. If neutrinos are massive these primordial neutrinos can comprise a fraction of the hot dark matter and make a contribution to the total energy density of the Universe.

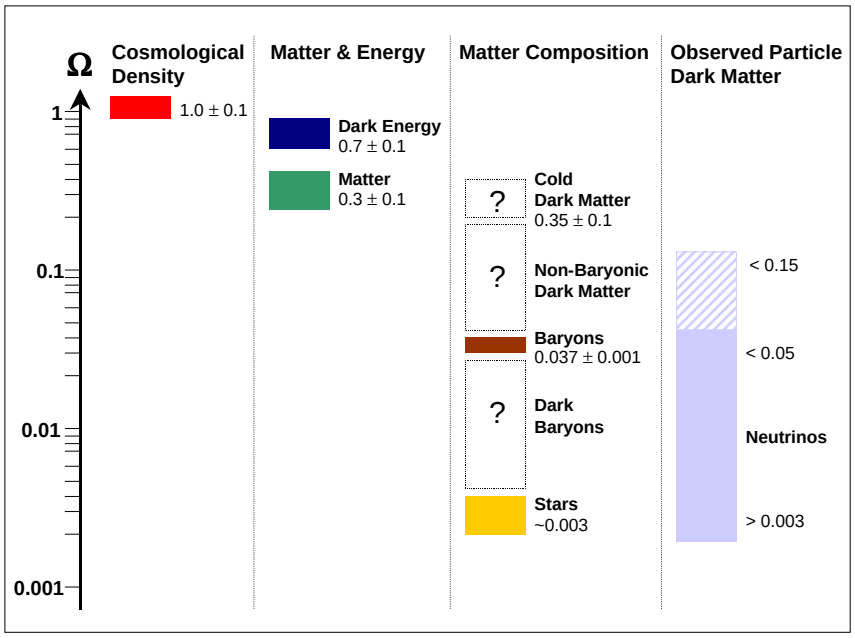

Figure 11.7: Composition of the cosmological constant Ω. Neutrino oscillation experiments have provided evidence for massive neutrinos and hence established neutrinos as a particle dark matter component with $\Omega_\nu < 0.15$. Massive neutrinos are the first directly observed component of hot dark matter. Observational constraints from structure formation limit the contribution of neutrinos to $\Omega_\nu \sim 0.05$. Neutrinos contribute as much as stars to the cosmological density but they cannot explain the dark side of the Universe.

With the results from SNO and Super–Kamiokande [70, 112] we have obtained unambiguous evidence for the flavor conversion of neutrinos and hence for massive neutrinos. The observation of massive neutrinos has shown that non-baryonic dark matter is multi-

component. For the first time experiments have obtained direct evidence for one of the particle components of dark matter. The improving results from neutrino oscillation experiments allow us to define the contribution of primordial neutrinos to hot dark matter. Assuming that the oscillation of massive neutrinos explains both the evidence for the solar neutrino flavor conversion found in SNO and the atmospheric neutrino data of the Super–Kamiokande collaboration, then the results of the tritium beta-decay experiments [53] limit the sum of mass eigenvalues of active neutrinos to be between 0.05 and 6.6 eV, corresponding to a constraint of $0.003 < \Omega_\nu < 0.15$ for the contribution to the critical density of the Universe. Neutrinos account for as much matter as luminous stars but it is very likely they cannot contribute more than $\Omega_\nu \sim 0.05$ in order not to spoil the process of structure formation. Contrast in the structure would be erased by relativistic neutrino streaming until quite late. Neutrinos have to be mixed in with cold non-baryonic dark matter or seeded by topological defects. In our Universe massive neutrinos are only present as a subdominant component to dark matter. While the detection of massive neutrinos has shown us clear signs of new fundamental physics the dark components of the Universe still remain unexplained.

11.10 Outlook on Future Results in Neutrino Physics

The evidence for neutrino mass appears very strong. With the observation of neutrino flavor transformation the Standard Model which was established in the late 1970s and has withstood all experimental tests, has finally been found to be incomplete. To incorporate neutrino mass into the theory and to explain why it is so small requires changes to the Standard Model. Extra dimensions or other new phenomena may be the explanation. A suite of new neutrino experiments such as terrestrial oscillation experiments, rare event searches in double-beta decay, and direct kinematical experiments will continue to measure the mass of neutrinos and determine their mixing parameters with increasing accuracy. They will gather more information about the particle nature of neutrinos and provide clues about their role in astrophysics and cosmology. We may find that neutrinos are their own antiparticles. With Majorana neutrinos it would be possible to explain the excess of matter in the Universe as slight differences in the probabilities of the decays into matter and antimatter. In this case we would have to abandon the distinction between matter and antimatter for neutrinos and find a model that explains their curious role in the family of fundamental particles.

BIBLIOGRAPHY

[1] K.N. Abazajian, J.F. Beacom, and N.F. Bell. *LANL arXive*, astro-ph/0203442, 2002.

[2] I. Affleck and M. Dine. *Nucl. Phys. B*, 249:361, 1985.

[3] Q.R. Ahmad. *Muon Correlated Background at the Sudbury Neutrino Observatory*. Ph.D. Thesis, Brown University, USA, 2002.

[4] J.F. Amsbaugh. *CHIME Mechanical Integrity Load Tests. SNO Internal Report*, September 1999.

[5] F.T. Avignone. *Phys. Rev. C*, 34:666, 1986.

[6] J.N. Bahcall. *Rev. Mod. Phys.*, 59(2):505, 1987.

[7] J.N. Bahcall, M. Kamionkowski, and A. Sirlin. *Phys. Rev. D*, 51:6146, 1995.

[8] J.N. Bahcall, P.I. Krastev, and A.Y. Smirnov. *Phys. Rev. D*, 62(93004), 2000.

[9] J.N. Bahcall, E. Lisi, D.E. Alburger, L.D. Braeckeler, S. Freedman, and J. Napolitano. *Phys. Rev. C*, 54:411, 1996.

[10] J.N. Bahcall and J.P. Ostriker, editors. *Unsolved Problems in Astrophysics*. Princeton University Press, 1997.

[11] J.N. Bahcall, M.H. Pinsonneault, and S. Basu. *Astrophys. J.*, 555:990, 2001.

[12] R.J. Barlow. *Statistics*. John Wiley & Sons, 1989.

[13] P.C. Bergbush. *Measurement of the Decay of* $K^+ \rightarrow \pi^+ + \nu\overline{\nu}$. Ph.D. Thesis, University of British Columbia, Canada, 2000.

[14] L. Bergstroem. *Rep. Prog. Phys.*, 63:793, 2000.

[15] M.G. Boulay. *Direct Evidence for Weak Flavor Mixing with the Sudbury Neutrino Observatory.* Ph.D. Thesis, Queen's University, Canada., 2001.

[16] S.J. Brice. *Monte Carlo and Analysis Techniques for the Sudbury Neutrino Observatory.* Ph.D. Thesis, Oxford University, UK, 1996.

[17] M.C. Browne. *Preparation for Deployment of the Neutral Current Detectors for the Sudbury Neutrino Observatory.* Ph.D. Thesis, North Carolina State University, USA, 1999.

[18] A.S. Brun, S. Turck-Chièze, and P. Morel. *Astrophys. J.*, 506:913, 1998.

[19] A.S. Brun, S. Turck-Chièze, and J.P. Zahn. *Astrophys. J.*, 525:1032, 1999.

[20] M. Butler and J.-W. Chen. *LANL arXive*, nucl-th/9905059, 1999.

[21] M. Butler, J.-W. Chen, and X. Kong. *Phys. Rev. C*, 63(035501), 2001.

[22] M. Butler, J.-W. Chen, and P. Vogel. *LANL arXive*, nucl-th/0206026, 2002.

[23] D.O. Caldwell, R.N. Mohapatra, and S.J. Yellin. *Phys. Rev. D*, 64:073001, 2001.

[24] A. Casas, W.Y. Cheng, and G. Gelmini. *Nucl. Phys. B*, 538:297, 1999.

[25] J.-W. Chen. *private communication*, May 2002.

[26] X. Chen. *Monte Carlo Simulations and Analyses of Backgrounds in the Sudbury Neutrino Observatory.* Ph.D. Thesis, Oxford University, UK, 1997.

[27] E.D. Church, K. Eitel, G.B. Mills, and M. Steidl. *LANL arXive*, hep-ex/0203023, 2002.

[28] SNO Collaboration. *Analysis for First Solar Neutrino Paper. SNO Internal Report*, June 2001.

[29] SNO Reconstruction Committee. *Comparison of Fitters for SNO. SNO Internal Report*, 2002.

[30] M.G. Danikas. *IEEE Trans. Dielectrics and Electrical Insulation*, 4(6):863, 1997.

[31] M.G. Danikas and G. Adamidis. *Electrical Engineering*, 80(2):105, 1997.

[32] P. Doe. *private communication*, September 2000.

[33] M. Dragowsky. *SNO Internal Report*, May 2001.

[34] C.A. Duba. *Title TBA*. Ph.D. Thesis, University of Washington, USA, 2002.

[35] V.M. Dubovik and V.E. Kuznetsov. *Int. J. Mod. Phys. A*, 13:5257, 1998.

[36] J.A. Dunmore and R.G.H. Robertson. *SNO Technical Report*, SNO-STR-98-025, 2002.

[37] E.D. Earle. *Tests on the Swelling of Acrylic. SNO Internal Report*, December 1999.

[38] E.D. Earle. *private communication*, October 2000.

[39] E.D. Earle. *AV Swelling. SNO Internal Report*, March 2000.

[40] S.R. Elliott. *private communication*, 1997.

[41] S.R. Elliott. *private communication*, April 1999.

[42] S.R. Elliott and P. Vogel. *LANL arXive*, hep-ph/0202264, 2002.

[43] A. Hime et al. *Gas Handling and Diagnostic Procedures for Neutral-Current Detectors in SNO. SNO Internal Report*, 1998.

[44] A.W.P. Poon et al. *Nucl. Instr. Meth. A*, 452:115, 2000.

[45] A.W.P. Poon et al. *Systematic Studies of the LBNL Data Cleaning Cuts. SNO Internal Report*, April 2000.

[46] A.W.P. Poon et al. *Systematic Studies of the LBNL Data Cleaning Cuts II. SNO Internal Report*, May 2000.

[47] B. Armbruster et al. *LANL arXive*, hep-ex/0203021, 2002.

[48] B.T. Cleveland et al. *Astrophys. J.*, 496:505, 1998.

[49] C. Ortiz et al. *Phys. Rev. Lett.*, 2000.

[50] C. Weinheimer et al. *Neutrino 2002, XXth International Conference on Neutrino Physics and Astrophysics*, May 2002.

[51] C.E. Aalseth et al. *LANL arXive*, hep-ex/0202018, 2002.

[52] Childers et al. *Composite Signal Decomposition. IEEE Trans. Audio Electroacoustics*, AU-18:472, 1970.

[53] D.E. Groom et al. *The European Physical Journal*, C15:1, 2000.

[54] E.W. Beier et al. *Performance of the Electronics for the Sudbury Neutrino Observatory. IEEE Nuclear Science Symposium Conference Record*, 2:872, 1998.

[55] F. James et al. *MINUIT - Function Minimization and Error Analysis. CERN Program Library*, D506, 1998.

[56] H. Albrecht et al. *Z. Phys. C*, 56:339, 1992.

[57] I. Kitani et al. *IEEE Proc.*, 1:282, 1994.

[58] J.F. Briesmeister et al. *MCNP - A General Monte Carlo N-Particle Transport Code.* Technical Report, LANL Radiation Schielding Center. 1997.

[59] J.N. Bahcall et al. *LANL arXive*, hep-ph/9807525, 1998.

[60] J.N. Bahcall et al. *Phys. Lett. B*, 478:208, 1998.

[61] K.M. Heeger et al. *IEEE Trans. Nucl. Sci*, 47:1829, 2000.

[62] K.T. Lesko et al. *True North of the SNO Detector. SNO Internal Report*, June 2000.

[63] L.E. Marcucci et al. *LANL arXive*, nucl-th/0003065, 2000.

[64] L.E. Marcucci et al. *Phys. Rev. C*, 63(015801), 2001.

[65] M. Apollonio et al. *Phys. Lett. B*, 466:415, 1999.

[66] M.R. Dragowsky et al. *Neutron Efficiency from the ^{252}Cf Sources for SNO. SNO Internal Report*, 1997.

[67] M.R. Dragowsky et al. *LANL arXive*, nucl-ex/0109011, 2001.

[68] N.J. Tagg et al. *LANL arXive*, nucl-ex/0202024, 2002.

[69] Oppenheim et al. *Nonlinear Filtering of Multiplied and Convolved Signals.* 56:1264, 1968.

[70] Q.R. Ahmad et al. and (SNO Collaboration). *Phys. Rev. Lett.*, 87(073101), June 2001.

[71] R. Hazama et al. *The Design of the SNO NCD Resistive Cable-End Couplers. SNO Internal Report*, May 2000.

[72] S. Ando et al. *LANL arXive*, nucl-th/0206001, 2002.

[73] S. Brice et al. *Sacrifice and Contamination in SNO Data Cleaning Cuts. SNO Internal Report*, November 2000.

[74] S. Nakamura et al. *LANL arXive*, nucl-th/0201062v3, 2002.

[75] S. Turck-Chièze et al. *Astrophys. J. Lett.*, 555:L69, 2001.

[76] Takenaka et al. *J. Nucl. Science Techn.*, 32(4):295, 1995.

[77] T.S. Park et al. *LANL arXive*, nucl-th/0108050, 2001.

[78] T.S. Park et al. *LANL arXive*, nucl-th/0110084, 2001.

[79] Uritani et al. *J. Nucl. Science Techn.*, 32(8):719, 1995.

[80] W.M. Alberico et al. *LANL arXive*, hep-ph/0002029, 2000.

[81] W.M. Alberico et al. *LANL arXive*, hep-ph/0001245, 2000.

[82] K. Kodama et al. (DONUT Collaboration). *Phys. Lett. B*, 504:218, 2001.

[83] C. Berger et al. (Frejus Collaboration). *Nucl. Instr. Meth. A*, 262:463, 1987.

[84] K. Daum et al. (Frejus Collaboration). *Z. Phys. C*, 66:417, 1995.

[85] T.A. Kirsten et al. (GALLEX and GNO Collaboration). *Nucl. Phys. B (Proc. Suppl.)*, 77:26, 1999.

[86] M. Altman et al. (GNO Collaboration). *Phys. Lett. B*, 490:16, 2000.

[87] R. Becker-Szendy et al. (IMB Collaboration). *Phys. Rev. Lett.*, 69:1010, 1992.

[88] R. Becker-Szendy et al. (IMB Collaboration). *Nucl. Instr. Meth. A*, 324:363, 1993.

[89] R. Clark et al. (IMB Collaboration). *Phys. Rev. Lett.*, 79:345, 1997.

[90] W. Gajewski et al. (IMB Collaboration). *Nucl. Phys. A (Proc. Suppl.)*, 28:10164, 1992.

[91] Y. Suzuki et al. (Kamikoande Collaboration). *Nucl. Phys. B (Proc. Suppl.)*, 38:54, 1995.

[92] M. Koshiba et al. (Kamiokande Collaboration). *Nuova Cimento*, C9:141, 1986.

[93] S. Hatakeyama et al. (Kamiokande Collaboration). *Phys. Rev. Lett.*, 81:2016, 1998.

[94] Y. Fukuda et al. (Kamiokande Collaboration). *Phys. Lett. B*, 335:237, 1994.

[95] Y. Fukuda et al. (Kamiokande Collaboration). *LANL arXive*, hep-ex/9706008, 1997.

[96] M. Sung et al (LSND Collaboration). *Int. J. Mod. Phys. A*, 16S1B:752, 2001.

[97] C. De Marzo et al. (MACRO Collaboration). *Nuova Cimento*, C9:281, 1986.

[98] Giorgio Giacomelli et al. (MACRO Collaboration). *LANL arXive*, hep-ex/0110021, 2001.

[99] M. Ambrosio et al. (MACRO Collaboration). *Phys. Lett. B*, 434:451, 1998.

[100] M. Spurio et al. (MACRO Collaboration). *Nucl. Phys. A*, 663:779, 2000.

[101] R. Stefanski et al. (MiniBooNE Collaboration). *Nucl. Phys. B (Proc. Suppl.)*, 110:420, 2002.

[102] G. Battistoni et al. (NUSEX Collaboration). *Ann Phys*, 245:277, 1986.

[103] M. Aglietta et al. (NUSEX Collaboration). *Europhys. Lett.*, 8:611, 1989.

[104] J.N. Abdurshitov et al. (SAGE Collaboration). *LANL arXive*, astro-ph/0204245, 2002.

[105] J. Boger et al. (SNO Collaboration). *Nucl. Instr. Meth. A*, 449:172, 2000.

[106] Q.R. Ahmad et al. (SNO Collaboration). *LANL arXive*, nucl-ex/0204008, 2002.

[107] Q.R. Ahmad et al. (SNO Collaboration). *LANL arXive*, nucl-ex/0204009, 2002.

[108] Q.R. Ahmad et al. (SNO Collaboration). *To be published*, (2002).

[109] J. Thron et al (Soudan-2 Collaboration). *Nucl. Instr. Meth. A*, 283:642, 1989.

[110] Sanchez et al. (Soudan-2 Collaboration). *Int. J. Mod. Phys. A*, 16S1B:727, 2001.

[111] W.W.M. Allison et al. (Soudan 2 Collaboration). *Phys. Lett. B*, 449:137, 1999.

[112] S. Fukuda et al. (Super-Kamiokande Collaboration). *Phys. Rev. Lett.*, 85:3999, 2000.

[113] S. Fukuda et al. (Super-Kamiokande Collaboration). *LANL arXive*, hep-ex/0103032, 2001.

[114] T. Futagami et al. (Super-Kamiokande Collaboration). *Phys. Rev. Lett.*, 82:5194, 1999.

[115] Y. Farzan and A.Yu. Smirnov. *LANL arXive*, hep-ph/0201105, 2002.

[116] S. Fostner, I. Levine, and H. Lee. *Measurement of Radon in the SNO Detector. SNO Internal Report*, April 2000.

[117] M. Gell-Mann, P. Ramond, and R. Slansky. *Supergravity.* North Holland, 1997.

[118] C. Giunti. *Mod. Phys Lett. A*, 16:2363, 2001.

[119] C. Giunti. *LANL arXive*, hep-ph/0205014, 2002.

[120] C. Giunti. *LANL arXive*, hep-ph/0202063, 2002.

[121] SNO NCD Group. *SNO NCD Construction Procedures. SNO Internal Report*, 1999.

[122] A. Hallin. *Cross-Talk Studies in the SNO Detector. SNO Internal Report*, 2001.

[123] E.D. Hallman. *private communication*, March 2000.

[124] N. Hata and P. Langacker. *Phys. Rev. D*, 49:420, 1995.

[125] K.M. Heeger and R.G.H. Robertson. *Phys. Rev. Lett.*, 77:3270, 1996.

[126] K.M. Heeger and R.G.H. Robertson. *Prog. Part. Nucl. Phys.*, 40:135, 1998.

[127] A. Hime. *private communication*, 1996.

[128] C. Jillings. *The Electron-Scattering Reaction in the Sudbury Neutrino Observatory.* Ph.D. Thesis, Queen's University, Canada, 1999.

[129] Kemerait and Childers. *Signal Detection and Extraction by Cepstrum Techniques. IEEE Trans. Information Theory*, 6:745, 1972.

[130] H.V. Klapdor-Kleingrothaus, A. Dietz, H.L. Harney, and I.V. Krivosheina. *Mod. Phys Lett. A*, 16:2409, 2001.

[131] J.R. Klein, M. Neubauer, F. Mitch Newcomer, and R. Van Berg. *The SNO Trigger System. SNO Technical Report*, SNO-STR-97-35, 1997.

[132] R. Komar. *The Shape of the Upper Half of the Acrylic Vessel Prior to Hanging it on Ropes. SNO Technical Report*, SNO-STR-98-003, 1997.

[133] K. Kubodera and S. Nozawa. *Int. J. Mod. Phys. E*, 3:101, 1994.

[134] A. Kurylov, M.J. Ramsey-Musolf, and P. Vogel. *Phys. Rev. C*, 65(055501), 2002.

[135] Nuclear Physics Laboratory. *Proposal for a Grant for Experimental Nuclear Physics.* University of Washington, June 1999.

[136] M.D. Lay. *Creation and Detection of Cherenkov Light in the Sudbury Neutrino Observatory.* Ph.D. Thesis, Oxford University, UK, 1994.

[137] C. Lunardini and A.Y. Smirnov. *Phys. Rev. D*, 62:073006, 2001.

[138] L.E. Marcucci. *LANL arXive*, nucl-th/0009066, 2000.

[139] A.D. Marino. *Studies on Leslie Events. SNO Internal Report*, March 14 2002.

[140] M. Maris and S.T. Petcov. *LANL arXive*, hep-ph/0201087, 2002.

[141] C. J. Martoff and P. D. Lewin. *COSMO–A program to estimate spallation radioactivity produced in a pure substance by exposure to cosmic-radiation on the Earth. Comp. Phys. Comm.*, 72:96, 1992.

[142] N.K. McCauley. *Producing a Background Free Data Set for Measurement of the Charge Current Flux and Day-Night Aymmetry at the Sudbury Neutrino Observatory.* Ph.D. Thesis, Oxford University, UK, 2001.

[143] S.D McDonald. *Studies of the Sudbury Neutrino Observatory detector and sonoluminescence using a sonoluminescent source.* Ph.D. Thesis, University of Pennsylvania, USA, 1999.

[144] K. McFarlane. *private communication*, October 2000.

[145] S.P. Mikheyev and A. Yu Smirnov. *Sov. J. Nucl. Phys.*, 42:913, 1985.

[146] B. Moffat. *Optical Calibration of the Sudbury Neutrino Observatory.* Ph.D. Thesis, Queen's University, Canada, 2001.

[147] S. Nakamura, T. Sato, V. Gudkov, and K. Kubodera. *Phys. Rev. C*, 63(034617), 2001.

[148] W.W. Nazaroff and A.V. Nero. *Radon and its Decay Products in Indoor Air.* Wiley, New York, 1989.

[149] W.R. Nelson, H. Hirayama, and D.W.O Rogers. *The EGS4 code system.* Technical Report, SLAC. 1985.

[150] M. Neubauer. *Evidence for Electron Neutrino Flavor Change through Measurement of the ^8B Solar Neutrino Flavor Content at the Sudbury Neutrino Observatory.* Ph.D. Thesis, University of Pennsylvania, USA, 2001.

[151] M.S. Neubauer and J.R. Klein. *Measurement of the SNO Trigger Efficiency. SNO Internal Report*, 2000.

[152] A.J. Noble. *private communication*, November 2000.

[153] J.S. O'Connel. *Neutrino Disintegration of the Deuteron at LAMPF Energies. Technical Report*, 1973.

[154] J. Orrell. *private communication*, May 2002.

[155] T.S. Park. *LANL arXive*, nucl-th/0005069, 2000.

[156] M. Passera. *Phys. Rev. D*, 64(113002), 2001.

[157] M. Passera. *LANL arXive*, hep-ph/0102212, 2001.

[158] J. Pilon. *Density of NaCl in D_2O solutions. SNO Internal Report*, March 2001.

[159] A.W.P. Poon. *Backgrounds and Light from the Acrylic Vessel. SNO Internal Report*, 2001.

[160] R.G.H. Robertson. *Leakchecking of Blind Welds. SNO Internal Report*, 1998.

[161] R.G.H. Robertson. *private communication*, February 2002.

[162] R.G.H. Robertson. *Radiative Corrections to the Neutrino-Deuteron Cross Sections. SNO Internal Report*, April 2002.

[163] R.G.H. Robertson and P. Vogel. *private communication*, May 2002.

[164] G. Rupak. *private communication*, May 2001.

[165] B. Sadoulet. *Rev. Mod. Phys.*, 71:S197, 1999.

[166] E.E. Salpeter. *Phys. Rev.*, 88:547, 1952.

[167] R. Schiavilla. *Phys. Rev. C*, 45:2628, 1992.

[168] M. Shiozawa. *Nucl. Instr. Meth. A*, 433:307, 1999.

[169] V.S. Shirley, editor. *Table of Isotopes*. Wiley-Interscience, 1996.

[170] D. Sinclair. *private communication*, November 2000.

[171] M.W.E. Smith. *Aluminum Contamination of Nickel Tubes Used in NCD Construction. SNO Internal Report*, 1997.

[172] M.W.E. Smith. *Title TBA*. Ph.D. Thesis, University of Washington, USA, 2002.

[173] T.D. Steiger. *private communication*, 1998.

[174] G. t'Hooft. *Phys. Lett. B*, 37:195, 1971.

[175] P.T. Thornewell. *Detectors for the Sudbury Neutrino Observatory*. Ph.D. Thesis, Oxford University, UK, 1998.

[176] E. Torrente-Lujan. *Nucl. Phys. B*, 87:504, 2000.

[177] M.S. Turner. *Phys. Rep.*, 33:619, 2000.

[178] P. Vogel and J.F. Beacom. *Phys. Rev. D*, 60(053003), 1999.

[179] C.E. Waltham. *Estimate of Neutral Current Atmospheric Neutrino Background. SNO Internal Report*, 2001.

[180] C.E. Waltham and C. Nally. *Atmospheric Neutrino Backgrounds to the Solar Neutrino Signal in SNO. SNO Internal Report*, 2001.

[181] C.E. Waltham and A.W.P. Poon. *private communication*, 1997.

[182] P. Wittich. *First Measurement of the Flux of Solar Neutrinos from the Sun at the Sudbury Neutrino Observatory.* Ph.D. Thesis, University of Pennsylvania, USA, 2000.

[183] L. Wolfenstein. *Phys. Rev. D*, 17:2369, 1978.

[184] T. Yanagida. *Prog. Theor. Phys.*, 64:1103, 1980.

[185] S. Ying, W.C. Haxton, and E.M. Henley. *Phys. Rev. C*, 45:1992, 1982.

APPENDIX A

DESIGN CHARACTERISTICS OF THE SNO NEUTRAL CURRENT DETECTOR ARRAY

Both the measurement of the neutral-current interaction rate as well as the detection of antineutrinos in SNO rely on the signature of a neutron produced in the neutrino interaction with deuterium. The detection of a free neutron is the signal that a neutral-current (NC) interaction of a neutrino with deuterium has occurred, while the detection of a neutron (or two neutrons) in coincidence with a positron indicates a $\overline{\nu}_e$ interaction.

$$\nu_x + d \rightarrow n + p + \nu_x - 2.22 \text{ MeV} \tag{A.1}$$

$$\overline{\nu}_e + d \rightarrow n + n + e^+ - 4.03 \text{ MeV} \tag{A.2}$$

The neutrons produced in the neutral-current or charged-current break-up of the deuteron thermalize and wander through the D_2O for tens of milliseconds before being absorbed because of the effective capture cross-section of about 1.5 mb per molecule. A number of possible strategies for detecting neutrons can be devised. One such strategy involves the addition of a chloride salt to the D_2O. In this method neutrons thermalize in the heavy water and capture predominantly on ^{35}Cl. When a neutron captures on 75% abundant ^{35}Cl, it emits 8.6 MeV in γ rays, which mainly Compton scatter.

$$^{35}\text{Cl} + n \rightarrow {}^{36}\text{Cl} + \Sigma\gamma + 8.6 \text{ MeV} \tag{A.3}$$

The resulting Čerenkov radiation emitted by the electron can be detected by the PMT array in the same way CC events are detected, and the Čerenkov-light patterns produced by γ rays distinguished from those of electrons on the basis of their greater isotropy.

Alternatively, neutrons can be detected with high efficiency in separate neutron detectors. The choice of neutron capture target nucleus is in practice confined to those with large

cross-sections, such as ^{3}He, ^{6}Li, ^{10}B, and ^{155,157}Gd. Besides ^{3}He proportional counters, ^{3}He scintillators and Gd foil counters were considered as possible neutron detection schemes in SNO.

Since heavy water is an excellent moderator with low absorption of thermal neutrons, it is possible to detect the free neutron by placing a sparse array of proportional counters filled with a neutron-absorbing gas such as ^{3}He in the heavy water. An array of such detectors constructed of highly purified materials, has been designed for SNO. In this way, the NC and CC events can be recorded separately and distinguished on an event-by-event basis. Event-by-event sorting makes optimum use of available statistics, and optimizes the measurement and interpretation of sparse and transient signals, such as neutrinos from a distant supernova. Furthermore, it allows the simultaneous determination of neutron-producing neutrino interactions and light-emitting radioactive backgrounds. Thermal neutrons can be detected by the reaction

$$^{3}\mathrm{He} + \mathrm{n} \rightarrow \mathrm{p} + {}^{3}\mathrm{H} + 764 \text{ keV} \tag{A.4}$$

which takes advantage of an enormous cross section, 5330 b. Neutron capture deposits 764 keV of energy in the gas, creating about 30,000 ion pairs that can be detected readily with or even without avalanche multiplication at the central wire. The neutron production rate in SNO is expected to be about 4520 neutrons per year (12.8 neutrons/day) based on the BPB00 predictions, and the measurement of the ^{8}B flux in the Sudbury Neutrino Observatory. The design of an array of ^{3}He proportional counters for SNO poses unusual problems. The neutron signal must not be overwhelmed by backgrounds from naturally occurring radioactivity in construction materials, nor can substances be allowed to leach significantly into the heavy water and interfere with water purification. Helium permeates readily through many otherwise acceptable materials. The counters are to survive under water at absolute pressures up to 3.18 atm for 10 years or more, placing stringent demands on detector longevity and stability. A counter array with high neutron efficiency is needed, but not at the cost of significantly obscuring the Čerenkov light from CC events. These conditions severely constrain detector design, the materials employed in constructing the

detector array, and the methods of handling and deployment. Proportional counters are devices inherently capable of extremely low-background performance since the active medium is a gas and can, in most cases, be readily purified. The background floor is set by cosmic rays, radioactivity in construction materials, and spurious pulses originating from sources other than ionizing radiation.

Despite these technical challenges the advantages of a discrete neutron detection scheme in SNO are compelling:

1. Event-by-event Detection of NC Events: With the proposed array of ^{3}He proportional counters the neutral- and charged-current interactions of neutrinos with deuterium can be recorded separately and distinguished event-by-event.

2. Model-Independent Measurement of Active Solar ^{8}B Flux: Under the assumption that the backgrounds to the NC signal can be determined from Čerenkov techniques and radioassays the measurement of the neutral-current interaction rate with the Neutral Current Detector array is a model-independent determination of the ^{8}B flux above the threshold for the NC interaction.

3. Enhanced Signal Decomposition: The NC, CC, and ES signals are usually separated based on their characteristic radial and solar angle distributions as well as their energy spectrum. During the D_2O phase it was found that the CC and NC signals can be separated by fitting to these distributions but the differences between the CC and NC distributions are small enough to cause substantial correlations between the two. The measurement with the NCD array can be used to break those correlations and constrain the neutron signal in SNO. In addition, the NCD array acts as a neutron poison in that it captures a significant fraction of the neutrons and hence removes a large fraction of the ^{2}H(n,γ)^{3}H signal underlying the spectrum from the charged-current reaction.

4. Spectral Analysis: By means of the separate and largely uncorrelated NC and CC measurements with the NCD and PMT array it is possible to make the best possible determination of the CC spectrum and search for spectral distortions.

5. Temporal Variations: Time variations in the NC flux can be followed simultaneously

in the NC and CC channels on the timescale of milliseconds to years. This allows the study of SN burst signals as well as secular variations in the NC rate due to the Earth's orbital eccentricity.

6. Simultaneous Determination of Signal and Background: All signals and backgrounds can be determined at the same time, and there is no need to compare and subtract data taken at different times and under different conditions.

7. Independent Systematics: Measuring the NC interaction rate by means of the neutron capture on dissolved NaCl as well as the neutron detection in ^{3}He-filled proportional counters allows the determination of the total active solar neutrino flux with two independent techniques. This provides an independent check on the systematics of each measurement.

8. High Efficiency: The duty factor for full-efficiency NC detection is essentially 100% and the possibility of missing NC data from a supernova or any other interesting event is low.

9. Supernova Physics: Event-by-event NC detection offers the prospect of determining a ν_μ or ν_τ mass if a supernova should occur.

The installation of the ^{3}He counters in SNO would benefit almost every physics capability of the detector. This appendix gives an overview of the design characteristics and specifications of the ^{3}He counters that have been built for the SNO Neutral-Current Detector array.

A.1 Physical Dimensions and Characteristics of NCD Array

The Neutral Current Detector array for SNO consists of a total of 300 tubular ^{3}He-filled proportional counters that make up approximately 775 m active detector length. The ^{3}He-filled Neutral-Current Detectors to be deployed in SNO have an internal diameter of 5.08 cm, and are manufactured in lengths of 200, 227, 250, 272, and 300 cm. An upper limit is set by the dimensions of the cage in the INCO shaft No. 9, which permits an object 3.7 m long to be brought down. They are filled with a gas mixture containing ^{3}He and CF_4, and deployed in long strings in the heavy water. The individual counters are organized end-to-end in 96 strings anchored to the bottom of the acrylic vessel on a square lattice with a 1-m spacing. The buoyancy of the ^{3}He detectors make the arrangement of the array vertical.

Every NCD string is made up of 2 to 5 individual ^{3}He-filled proportional counters and varies in length between $\sim 4 - 11$ m to fill the spherical volume of the SNO detector efficiently. As a check against internal backgrounds 5% of the array are filled with ^{4}He. The active length of each NCD is 13 cm less than the mechanical length. The important physical parameters of the detectors are summarized in Table A.2. Signals are read out from each NCD string through cables connected to the top of the NCD strings. This arrangement is illustrated in Figure A.1. In 1000 tons of 99.92% enriched heavy water, 46.4% capture efficiency [1] can be obtained with a counter array containing only 600 g of ^{3}He. In the presence of the NCD array there is a 12.8% neutron capture probability in deuterium that produces 6.25 MeV γ's and a 1.3% probability for neutrons to capture on Ni with the production of 9 MeV γ's.

Figure A.2 shows the main features of a string of Neutral-Current Detectors.

[1] The ^{17}O abundance in D_2O is assumed to be 0.055%.

Table A.1: Some characteristics of the Neutral Current Detector array.

Characteristic Quantity	NCD Array	Pure D_2O
Total Length of NCD Array	∼775 m	
Number of NCD Strings	96	
Number of Counters per NCD String	2-5	
NCD Neutron Capture Efficiency	46.4%	
Neutron Capture Efficiency on D	12.8%	25%
Mean Time to Neutron Capture	16 ms	4 ms
Mean Distance to Capture	110 cm	48 cm
Photon Absorption	12%	

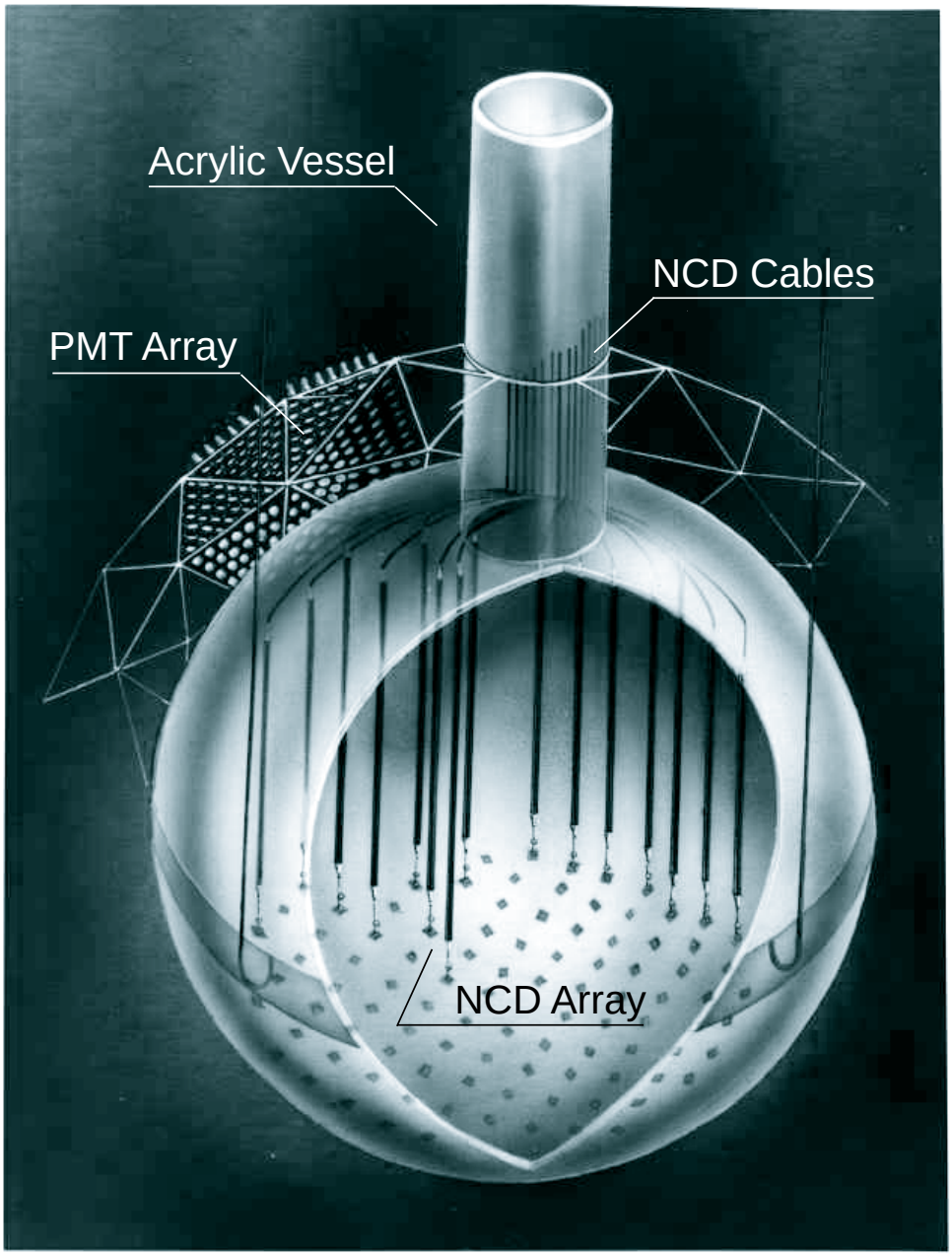

Figure A.1: Artist's illustration of the NCD array in the SNO detector.

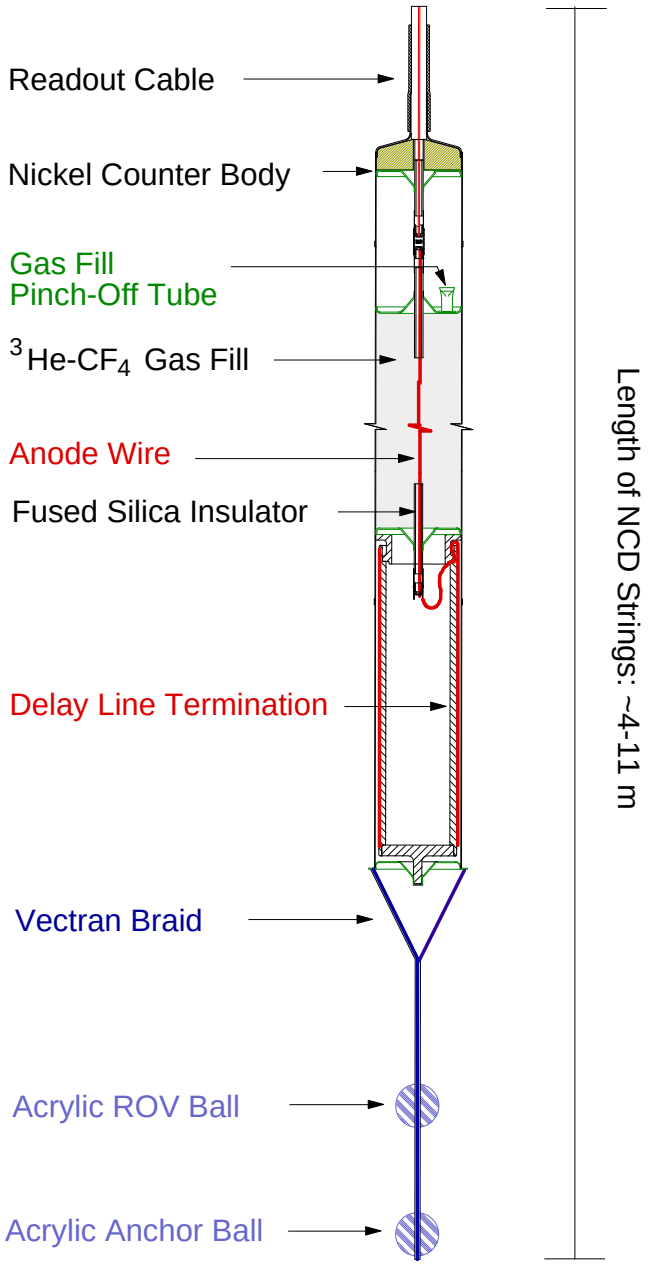

Figure A.2: Schematic of a ^{3}He-filled Neutral-Current Detector (NCD) string. A remotely operated vehicle (ROV) will be used to attach the end of the NCD detector string to the bottom of the acrylic vessel. Most technical NCD figures in this appendix are adapted from technical drawings by T. Steiger, T. Burrit, G. Harper, J. Amsbaugh, and A.W.P. Poon.

A.2 Counter Bodies and Endcaps

The material used for the counter bodies is chosen to satisfy a number of requirements, including gas fill pressure, yield strengths, elective safety margins, and other mechanical considerations. In addition, the stringent radiopurity requirements of the NCD array need to be met. The fact that He permeates amorphous materials such as plastic and glass suggests the use of metal walls or metal-coated walls. CVD Ni obtained by chemical vapor deposition satisfies all criteria and is the material of choice.

The CVD nickel tubing used for the SNO Neutral-Current detectors must be able to withstand one atmosphere external pressure while being pumped out in preparation for filling and must have a safety margin against collapse under external pressures up to 3.5 atm at the greatest depth in SNO. At the same time the total amount of Ni used in the NCD array is to be minimized to maximize the counter efficiency and to minimize radioactive backgrounds. Based on the properties of CVD Ni the collapse pressure of the counters has been calculated. Calculations yield that a wall thickness of 0.01295 inches is required to withstand 14.73 psi. Mechanical collapse tests indicate that the effective wall thicknesses obtained from the collapse pressures are slightly less than the mechanically measured values. This is probably a manifestation of the surface roughness. Therefore minimum wall thickness of $0.015^{+0.003}_{-0.000}$ is used as a specification for the NCD counter bodies. This includes a 2-fold safety margin against collapse under evacuation and under external pressure. The margin against rupture from the internal pressure is much higher, a factor of 10.

The end of each counter is closed by an endcap consisting of a CVD nickel body with a silica tube as an electrical feedthrough. The design of the endcaps and electrical feedthroughs were optimized following mechanical as well as as electrical considerations. Both the strength of the endcap, the soldering of the silica feedthrough into the endcaps and the uniformity of the electrical field in the end region of the proportional counter were taken into account.

Endcap bodies are made by Mirotech, Inc. on polished stainless steel mandrels. They are welded into the tubes with a Lumonics 50-W Nd-YAG laser welder. Insulators are Heraeus-Amersil Suprasil T-21 synthetic fused-silica tubes. The conical relief at the center

of the endcap serves both to strengthen it against pressure distortions and to shape the electric field near the end so as to minimize axial gain variations.

The central insulating feedthroughs are pure at the level of about 10 ppt Th and U. They are internally coated with a layer of pyrolytic graphite at anode potential to eliminate electric fields inside them. They extend 2.5 cm into the gas volume to act as field tubes and prevent multiplication of electrons from regions where the electric field is distorted. It also minimizes surface microdischarge leakage. A silica-nickel seal is highly mismatched, so the design places the silica under compressive stress at working temperatures to take advantage of the high compressive strength of that material. Techniques were developed in collaboration with IJ Research (Santa Ana), Inc. to metallize the seals and solder them with a 96.5:3.5 eutectic Sn:Ag alloy. Cr-Ni bands are RF sputtered on the outside for solder seals.

Fused silica is quite permeable to He, but the small cross-section of the silica and the added metallization reduce the loss to negligible levels. Making a metal seal between nickel and silica is difficult owing to the mismatch in thermal-expansion coefficients. The seal design makes use of a small-diameter (5-mm) silica tube which is metallized with Cr and Ni layers and soldered through the endcap and sleeve with SnAg alloy solder. As the joints cool, the nickel contracts more than the silica, compressing the joints. Fused silica is extremely strong under compression, and the nickel yields without breaking the silica.

The endcap feedthroughs are sealed with copper endplugs machined from oxygen-free high-conductivity copper alloy C10100. This material is characterized by high thermal and electrical conductivity (101% IACS [2]) as well as high ductility. Some of the characteristics of C10100 are listed in Table A.4.

A pinch-off tube is used to make the required gas seal on the NCD counters. The pinch-off tubes are machined from C10100 copper. Figure A.4 shows the parts of NCD endcaps. Assembly of the endcaps is carried out in a Class-100 cleanroom. For reference,

[2]The conductivity of copper is expressed in units of a percentage of IACS (International Annealed Copper Standard). This standard is based on an annealed copper wire having a density of 8.89 g/cm^3, 1 meter long, weighing 1 gram, with a resistance of 0.15328 ohms. This standard was assigned the value 100 at 200 °C (680 °F). The higher the % IACS, the more conductive the material is. It is not uncommon for commercially pure copper products to have IACS conductivity values greater than 100 because of improved processing techniques which have been developed since the adoption of the standard in 1913.

the important mechanical parameters of the detectors are summarized in Table A.2. The mechanical properties of CVD nickel are summarized in Table A.3.

Table A.2: Nominal physical parameters of the Neutral Current Detectors.

Number of Production Counters	300
Counter Lengths *	200, 250, 300 cm
Internal Diameter of Counters	5.08 cm
Total Production Length CVD Nickel Tube	775.20 m
Total Gas-Fill Length Endcap-to-Endcap	745.55 m
Total Active Length Field-Tube Extension	728.55 m
Counter Volume	2.027 l/m
Wall Thickness	$0.036\ ^{+0.012}_{-0.000}$ cm
Nominal Thickness	0.0381 cm (0.015 in)
Counter Surface Area	0.1596 m^2/m
Mass of Ni in NCD Array	416790 gm (not counting endcaps)
Volume of nickel	46819.8 m^2 μm

* A few counters were made in lengths of 227 and 272 cm.

Table A.3: Mechanical properties of CVD nickel (courtesy Mirotech, Ltd.)

Weight of CVD nickel	510 gm/m
Density of CVD nickel	8.902 gm/cm^3 = 8.902 gm/(m$^2\mu$m)
Specific Gravity	8.871
Yield Strength $\|\|$	440 MPa
Yield Strength $\perp$	600 MPa
Ultimate Tensile Strength	$\sim$ 640 MPa (1 MPa = 144.6 psi)
Elongation	$\sim$ 25%
Modulus of Elasticity for CVD Ni	178 GPa (25.8 Mpsi)
(Modulus of Elasticity for Standard Ni)	210 GPa (30.5 Mpsi)
Hardness (Rockwell)	10-20
Residual Stress (surface)	30-60 MPa tensile
Coefficient of Thermal Expansion	13.1×10^{-6} K^{-1}
Thermal Conductivity	88 W m^{-1} K^{-1}

Table A.4: Characteristics of copper alloy C10100 used in the NCD counters.

Properties	Nominal Value
Chemical Composition by Weight	
Copper	99.99%
Phosphorus	0.0003%
Tellurium	0.0010%
Density	27.68 g/cm^3
Thermal Conductivity	32.6 Watts/m °K
Electrical Conductivity	101% IACS

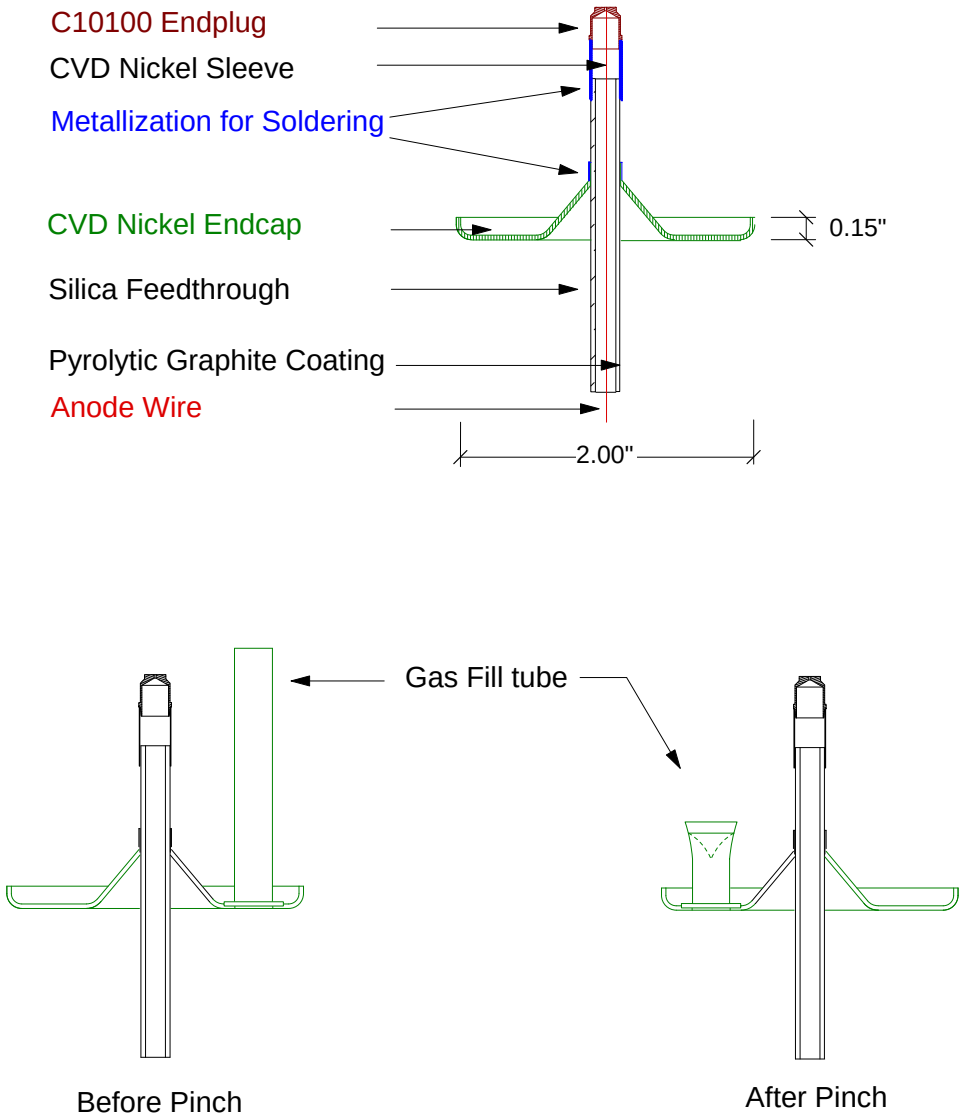

Figure A.3: Endcaps for the counter bodies of the Neutral Current Detectors.

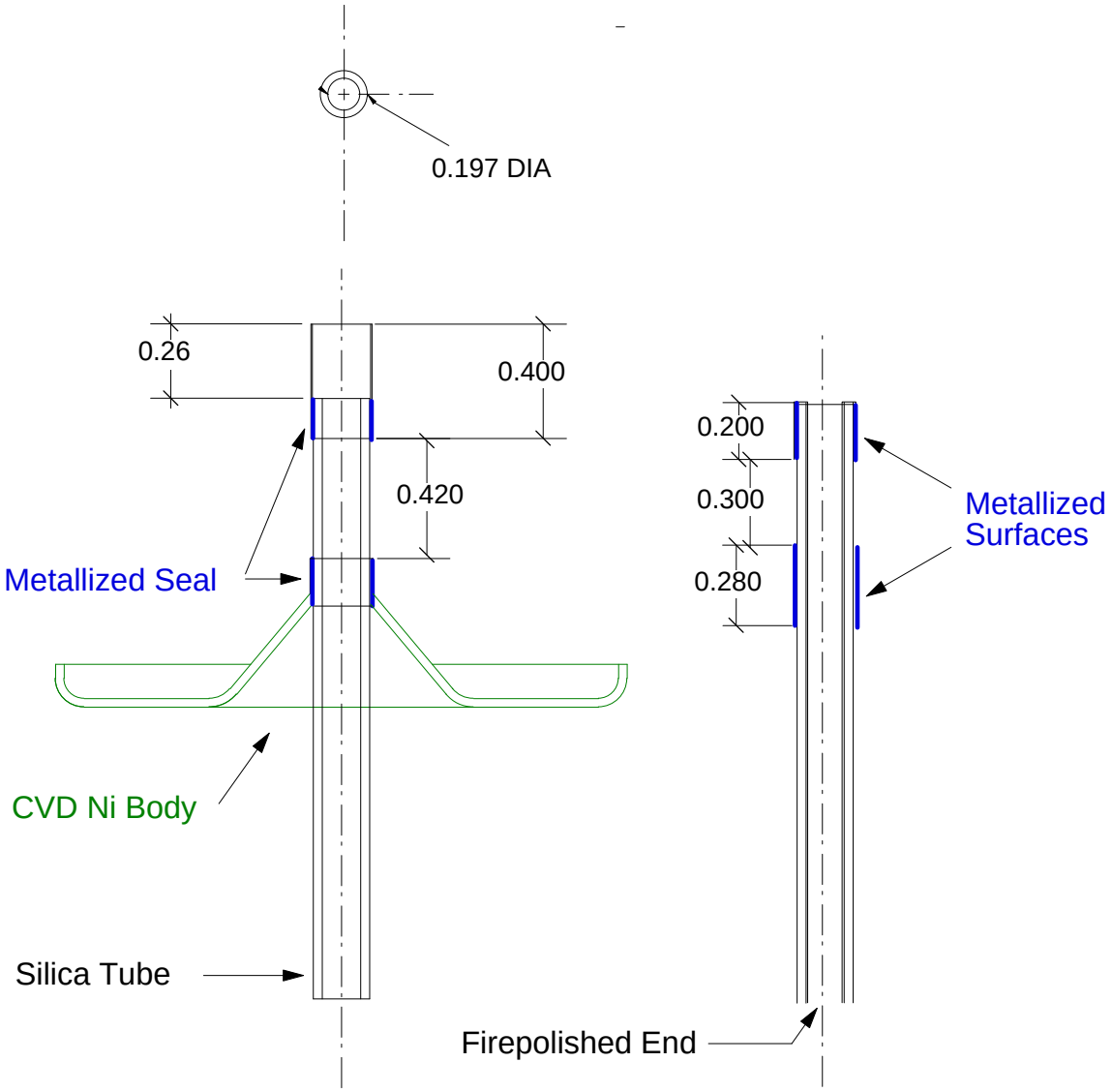

Figure A.4: Assembly of NCD endcaps.

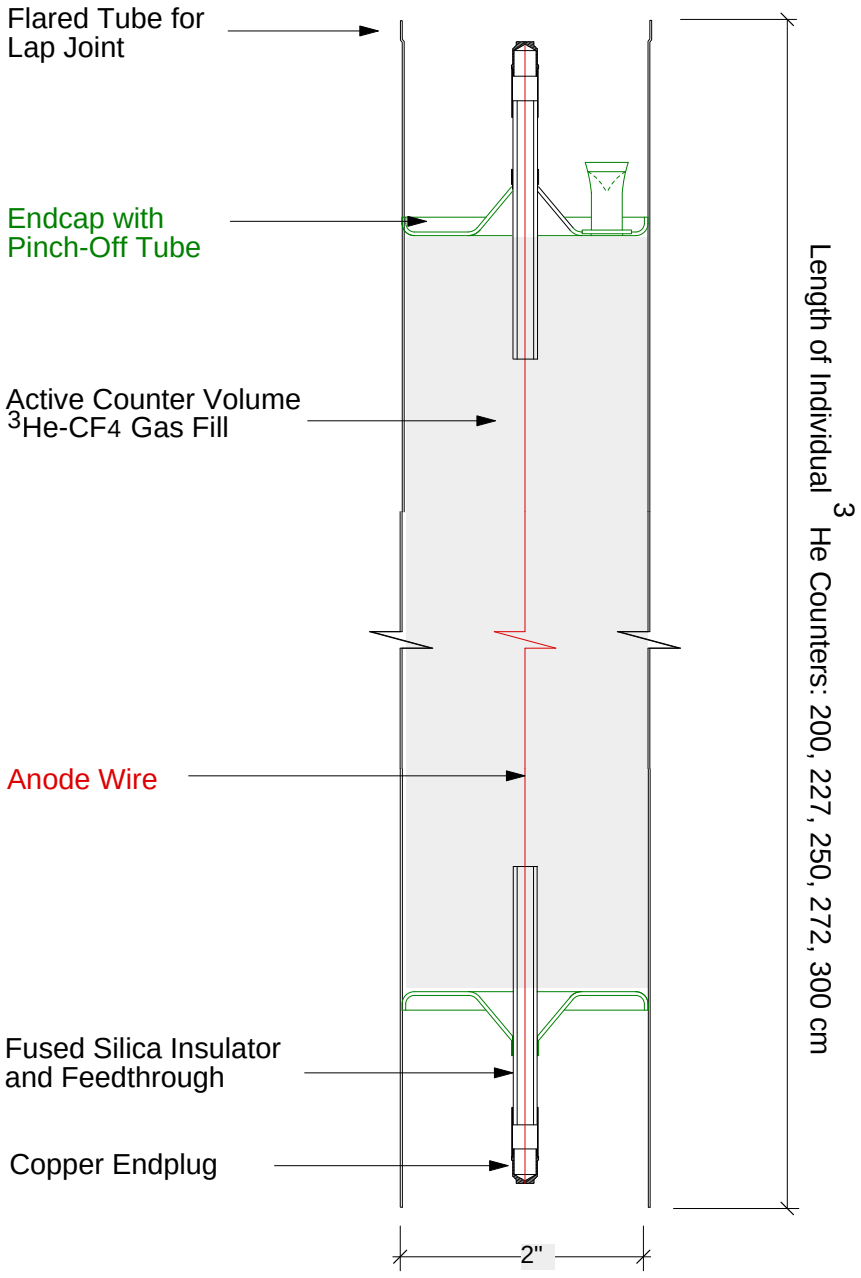

Figure A.5: Individual Neutral Current Detector.

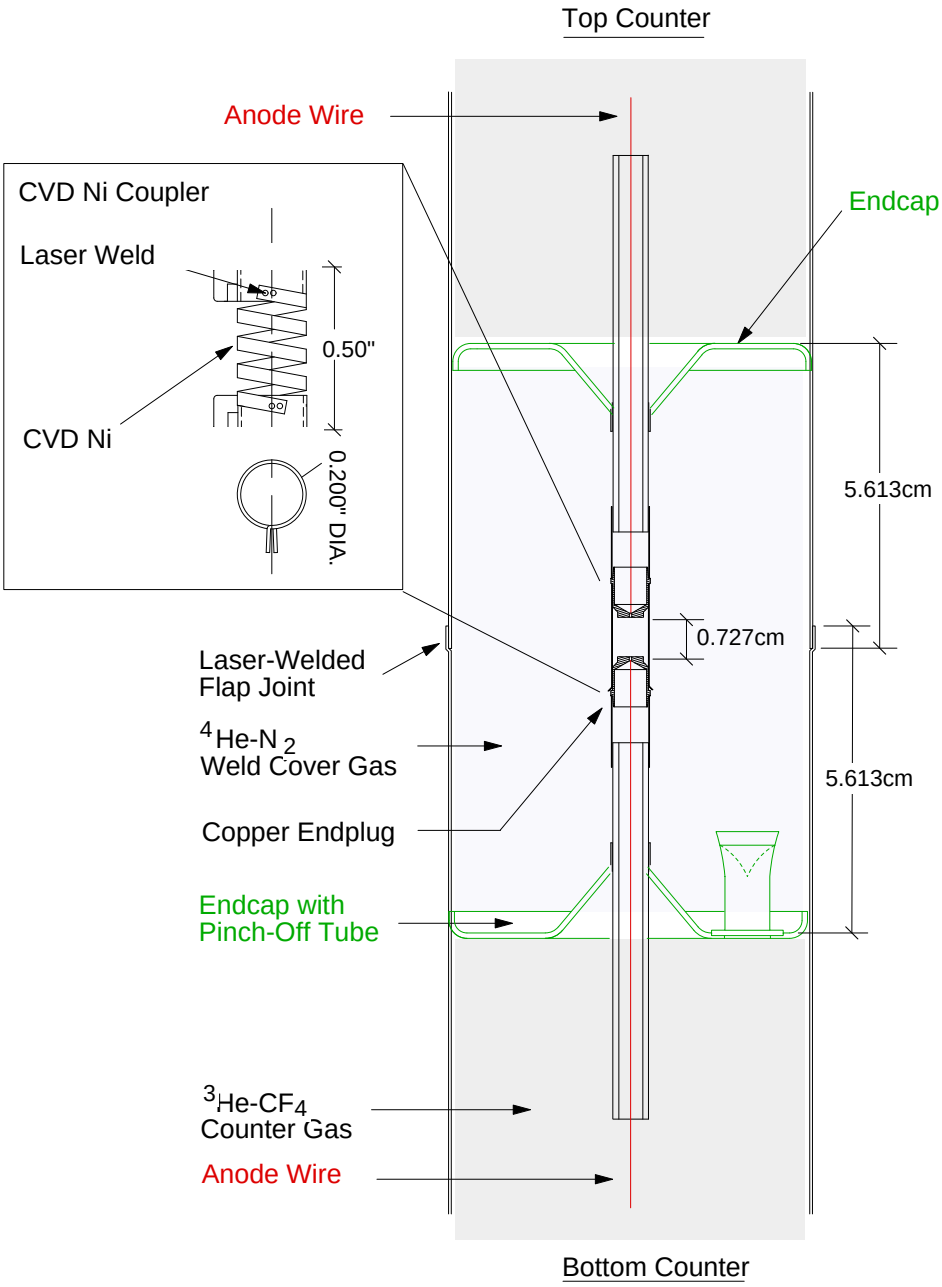

Figure A.6: Connection with CVD Ni coupler between individual counters in a NCD string.

A.3 Gas Fill

The gas pressure used in a NCD counter is a compromise between the need to obtain good capture probability and the low drift speeds, poor signal-to-noise, high operating voltage, and low space-charge saturation threshold that characterize high-pressure proportional counters. Furthermore, these counters are designed to withstand the external pressure of the heavy water medium at the depth of the bottom of the acrylic vessel.

The counter part of the NCD strings ends 35 cm above the bottom of the acrylic vessel. At this point the absolute pressure is that due to a column of D_2O of height 17.65 m plus 1.3 atm of air pressure, for a total of 3.18 atm. The counter, when evacuated before filling, experiences a net compressive pressure of 1 atm. To be assured of withstanding the external pressure these thin-walled counters need to contain an internal pressure of more than 2.18 atm.

At partial ^{3}He pressures above 1/3 atm the counters have essentially 100% capture efficiency. The capture efficiency increases only slowly with increasing ^{3}He pressure. Increasing the partial ^{3}He pressure from 1 atm to 3 changes the total capture efficiency by 10%. The performance of detectors as a function gas fill parameters has been studied [43] with the conclusion that a total operating pressure of 2.5 atm of 85:15 He:CF_4 by volume is an optimum.

To fill the 775 m-long array of Neutral Current Detectors requires $\sim 6 \times 10^3$ STP liters of ^{3}He. The ^{3}He gas was obtained was obtained from Westinghouse Savannah River Company through Los Alamos National Laboratory. The ^{3}He gas, which is recovered from the decay of tritium, contains a residual activity of ~ 1 mCi/liter (about 0.3 ppm). Tritium decays deposit, on average, 6 keV in the gas. At the delivered contamination level of 1 mCi/liter there would be 4.4×10^8 tritium decays/s in each 2-m detector segment. Using a purification procedure during the gas fill this rate is reduced to $\sim 10^3$ s^{-1}, which represents a 1% probability for an event to occur in an assumed 10-μs integration time for neutron-capture signals. The T/^{3}He atom ratio in the gas is $\leq 8 \times 10^{-7}$ and it is reduced to 1.8×10^{-12} (4.8×10^{10} atoms per STP liter) using purification techniques before use in the NCD counters.

When neutron capture occurs close to the wall of the counter, either the proton or the triton may strike the wall before the end of its range, causing "wall effect" events that leave less than 764 keV in the gas. The lowest energy deposited in the gas is 191 keV, when the proton loses all its energy in the wall.

For pure ^{3}He at high pressure the triton or the proton strikes the wall in about 31% of all the captures. Wall effect can be diminished with the addition to the gas of another component that contributes stopping power but not neutron absorption. The detector "wall effect" is to first order independent of ^{3}He pressure, and depends only on the pressure and stopping power of inert additives. The wall effect drops with the addition of another gas, because the ratio of neutron capture distance to charged-particle range increases. The range R (length units) in the mixture is

$$\frac{1}{R} = \frac{P_{CF4}}{R_{CF4}} + \frac{P_{He}}{R_{He}} \tag{A.5}$$

where the quantities P_x are the proportions by volume of the component gases.

The detector gas gain, G, relates the energy to produce an ion pair, γ, in a gas counter to the total energy of an event, E:

$$q = \frac{EG}{\omega} \tag{A.6}$$

As shown in [43], the gas gain (G) can be parameterized according to the prescription of Diethorn:

$$\begin{aligned} ln(G) &= \frac{V}{V_0} \ln\left(\frac{V}{V_t}\right), \text{ where} \\ V_t &= P\ a\ K\ \ln(b/a) \\ V_0 &= \Delta V\ \frac{\ln(b/a)}{\ln(2)} \end{aligned} \tag{A.7}$$

in terms of the operating voltage, V, the threshold for multiplication, V_t, an effective scattering potential P, the anode wire radius, a, and the cathode wall radius, b.

The Diethorn parameters K and ΔV are functions of the gas mixture. Consequently, for the two-component (He-CF_4) gas-mixture relevant for SNO-NCDs, these parameters can be empirically determined as functions of the CF_4 fraction only.

Usable gas gains are limited on the low side by deteriorating signal-to-noise ratios, and on the high side by space-charge effects that worsen the resolution for high-charge-density tracks such as α particles. Space-charge broadening begins to set in around $\gamma = 20$ for 5.4-MeV alphas in the gas selected, 2.5 atm of 85:15 He:CF_4. It is independent of the diameter of the anode wire, but depends somewhat on gas mixture and pressure. Experimental work shows that to obtain adequate signal-to-noise ratios with neutron events, a gas gain of about 100 is required. Off-line corrections for pulse-height defect can be made to some extent by making use of the fact that the tracks most affected by space charge are those aligned almost perpendicular to the wire. Such tracks produce longer pulses as the charge drifts in. However, the correction is not unambiguous because the particle type is not known in advance and because tracks perpendicular to the wire have pulse durations that depend on the distance of closest approach of the projected track to the wire, and the location of the end of the track.

Table A.5: Characteristics of NCD gas fill.

Gas Mixture	^{3}He-CF_4 (85:15)
Gas Fill Pressure	2.5 atm (1900 Torr)
He Partial Pressure	2.125 atm (1615 Torr)
CF_4 Partial Pressure	0.375 atm (285 Torr)
Operating Voltage	1835 V
Gas Gain	$\sim$ 100

Assembly of NCD counters into strings involves welding several counters in a string and 96 cable ends to detectors. Each of these welds is a blind weld that must be shown to be sound at the level of 10^{-7} std cc/s. A technique for leakchecking blind welds has been designed [160] that allows to test with sufficient sensitivity the counter-to-counter welds.

All welds will be made with a mixture of 75% He and 25% N_2 as a cover gas. The He-rich gas is trapped inside the blind volume in order to identify a leak outside. The N_2 is added to assure acceptable high voltage performance of the gas inside the endcap spaces.

A.4 Electrical Characteristics

The electrical characteristics of the NCD strings are determined by a number of critical components. These include the anode wire, the NCD cable-end couplers, delay lines, and readout cables.

A.4.1 Anode Wire

The strongest constraints on the specifications of the anode wire come from the electrical requirements. Copper is usually a choice because of its high purity, mechanical properties, and good electrical conductivity. Mechanical and radioactivity considerations permit wire diameters ranging from a low of ∼25 μm (mechanical constraint) to a high of ∼250 μm (radioactivity constraint). The electrical requirements limit this range to 25-50 μm. A smaller wire attenuates the signal too much while a larger one requires too high an applied voltage leading to spurious pulses and an increased background. The choice of wire diameter depends on a number of factors:

1. Voltage at which the desired gain is obtained.
2. Resistive losses for transmission of signal.
3. Ease of construction and wire uniformity.

Operation at high voltages is undesirable because the tendency for surface leakage across insulators to produce spurious microdischarge pulses rises rapidly with voltage. Thus minimizing this voltage is important for minimizing the background. The result for the wire is that a smaller diameter wire is favored. The applied voltage coupled with the diameter of the anode wire determines the overall gas gain of the detector. The NCD design goal is ∼100 for the gas gain. With a gas mixture of 85% He, 15% CF_4 at a total pressure of 2.5 atm, an anode voltage of 1835 V for a 25 μm diameter wire and 2200 V for a 50 μm wire is needed to obtain a gas gain of ∼100 in a 5-cm diameter counter.

The resistivity of the wire has a strong influence on the resulting amplitude of the signal pulses and the signal to noise ratio. At low frequencies, there is a roughly linear dependence of resistance with the cross section of the wire. At higher frequencies thinner wires degrade the pulse proportionally faster than thicker wires. Signals in a 25 μm wire are attenuated

over 53% at low frequency while the signal in 50 μm wire is attenuated only 18%. The higher frequency components are attenuated even more. Thus a larger diameter wire is favored in order to obtain the maximum signal to noise, and to minimize frequency dependence in the analysis of event-position.

Our conclusion upon considering pulse propagation effects is that the material from which the anode wire is made must have the lowest resistance possible and thus the wire should have as large a diameter as feasible. Copper and silver are good choices for the anode wire. They both have low resistivity of 17.0 nΩm for Cu versus 16.0 nΩm for Ag. The specific DC resistance of pure copper wire of 25 and 50 μm diameter is 32 and 8 Ω per meter. The resistance increases with frequency due to skin effect.

The best compromise for the NCDs is 50-μm diameter hard-drawn copper. Copper is a material that is sufficiently free of radioactivity to be used in this application. CVD Ni, a very pure material, is ruled out because nickel is ferromagnetic and exhibits high skin-effect losses.

The copper anode wire of diameter 50 μm is low in radioactivity and ohmic losses. At 1835 V the gas gain is approximately 100. For higher gas gains positive-ion space charge at the wire causes the avalanche multiplication to depend increasingly on track orientation. The wire was obtained from California Fine Wire on special low-radioactivity spools made out of polyethylene. A total amount of approximately 14.5 g of copper is used for the NCD array with an overall length of 800 m.

Copper C10100 has been chosen as the baseline material in part because it is normally very clean. As shown in Table A.4, C10100 is 99.99% copper with limits in ppm for several other elements. Work related to double beta decay experiments has shown that C10100 has the following typical activity levels: < 0.03 dpm/kg ^{208}Tl (40 ppt), < 0.05 dpm/kg ^{214}Bi (200 ppt) and < 0.5 dpm/Kg ^{40}K (30 ppt) [40].

Anode wire consisting of 50 μm diameter C10100 contributes substantially less to the background than the Ni bodies. It contributes a factor of 19 less alpha particles and 1000 less neutrons than the Ni. C10100 is a suitable material for the anode wire in the NCD counters with respect to radioactivity and its mechanical properties.

Table A.6: Characteristics of the NCD anode wire in the NCD array.

Material	C10100
Wire Diameter	0.005 cm
Resistance	32 Ω/m (for 0.0025 cm wire)
Total Mass in Array	14.5 g

A.4.2 Resistive Counter Couplers

A resistive coupler is used to match the impedance of the NCD counters with the impedance of the NCD readout cable. The NCD resistive couplers connect the NCD detector strings which are an open-ended line with 416 Ω impedance to a 91-Ω coaxial cable. The radiopurity constraints, high voltage requirements, and its electrical properties make this coupler unique in comparison to conventional resistors. A Stableohm wound-wire coupler has been designed to meet these requirements [71].

This resistive coupler consists of a wire resistor in coil shape. The resistive wire is wound about a Teflon tube in opposing directions to avoid self-inductance by cancellation of magnetic fields. The use of Teflon assure radioactive cleanliness and high dielectric strength. A schematic of the coupler is shown in Figure A.7.

Table A.7: Characteristics of NCD cable-end couplers.

Characteristics of NCD Resistive Coupler	
Resistance	375 Ω
Wire Diameter	0.0010 in
Wire Spacing	0.025 in
Loop Length	0.5707 in
Inductance	0.024 μH

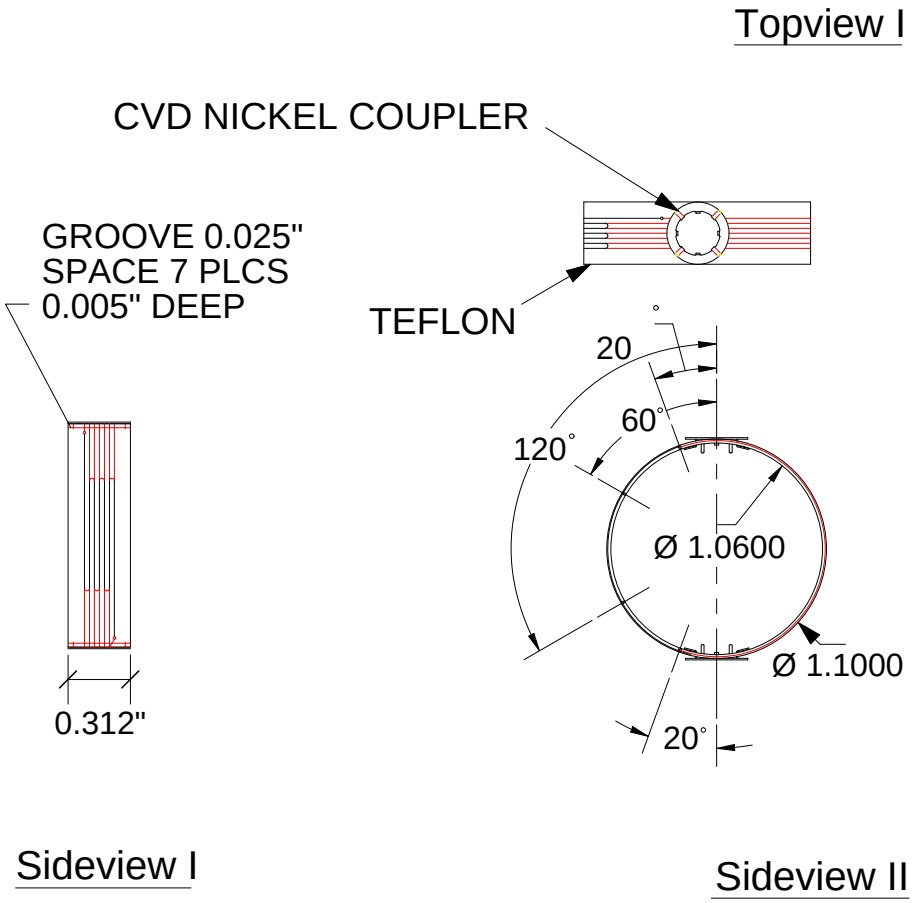

Figure A.7: Schematic drawing of the NCD resistive cable coupler.

A.4.3 Delay Lines

The bottom of each string is terminated with a 30 ns open-ended 415 Ω delay line to facilitate position readout by pulse-reflection timing. The impedance of the delay line is matched to the impedance of the proportional counters. The delay line consists of a planar circuit board mounted on a cylindrical acrylic core in the end of each NCD string. The circuit boards are etched onto 2 mil (5.08×10^{-3} cm) copper-clad Kapton. The board is not tinned or coated but left to as bar copper. This design allows to obtain the required delay and minimizes high-voltage induced microdischarges and other effects. The characteristic physical and electrical properties of the NCD delay line are summarized in Tables A.8 and A.9.

Table A.8: Physical characteristics of the NCD delay line.

Physical Characteristics of the NCD Delay Lines	
Conductor Width (in)	0.010
Conductor spacing (in)	0.020
Loop length (in)	5.40
Loop spacing (in)	0.04
Annular gap (in)	0.085
Circumference (in)	5.75
Total Length (in)	7.00
Number of traces	350.00
Total trace length (m)	48.0
Trace Thickness (oz/cu ft)	2
Density of Cu (oz/cu ft)	8870
Trace Thickness (in)	0.0027
Mass of Acrylic Core	136.40 g

Table A.9: Electrical characteristics of the NCD delay line.

Electrical Characteristics of the NCD Delay Lines	
Loop Inductance (nH)	67.53
Dielectric constant	1.00
L per cm (nH)	797.58
C per cm (pF)	4.69
C_{tot} (pF)	83.47
Z_0 (Ω)	412.17
Delay (ns/cm)	1.94
Total Delay-Round Trip (ns)	68.81
Resistivity of Cu (mΩ-cm)	1.77
Total Resistance (Ω)	49

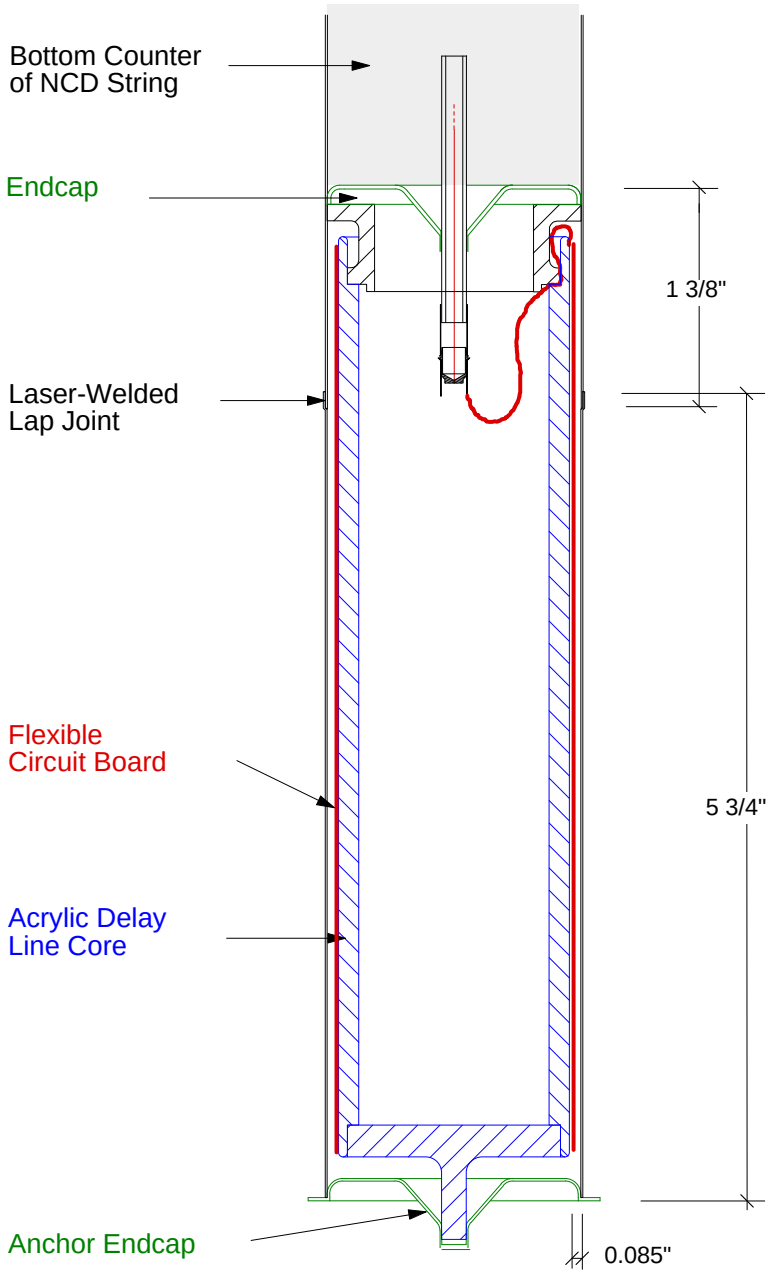

Figure A.8: Assembly of a Neutral Current Detector delay line.

A.4.4 Readout Cables

Cables ranging in lengths from 8 to 14 m connect the NCD strings to the preamplifiers that are situated on the deck of the SNO cavity. To maximize the signal coupled from the detector into the preamplifier and minimize reflections, the cable is matched to the detector characteristic impedance through a resistive coupler. The cable is custom made by South Bay Cable (Idyllwild, CA) to comply with the stringent requirements for use in the SNO detector.

Water Immersion: Cables are rated for long-term (5-10 years) underwater use without significant degradation of electrical properties.

Radiopurity: The experimental conditions in which the cable will be used require that the amount of uranium and thorium in the entire length of cable be less than 1750 parts per trillion by weight (ppt) and 150 ppt, respectively.

Acceptable Materials: To aid in the compliance with the radio- purity requirements, only the following materials may are used in the cables: copper with no tinning or coatings, polyethylene with no colorings, and a water blocking compound.

The characteristics of the NCD readout cable are summarized in Table A.10.

Table A.10: Characteristics of the NCD readout cables.

Impedance	91 Ω
Type	Coaxial
Voltage Rating	3 kV
Outer Diameter	< 0.350 in (including tolerances)
Specific Gravity	< 1
Shield Coverage	100%
Minimum Bend Radius	< 3 in

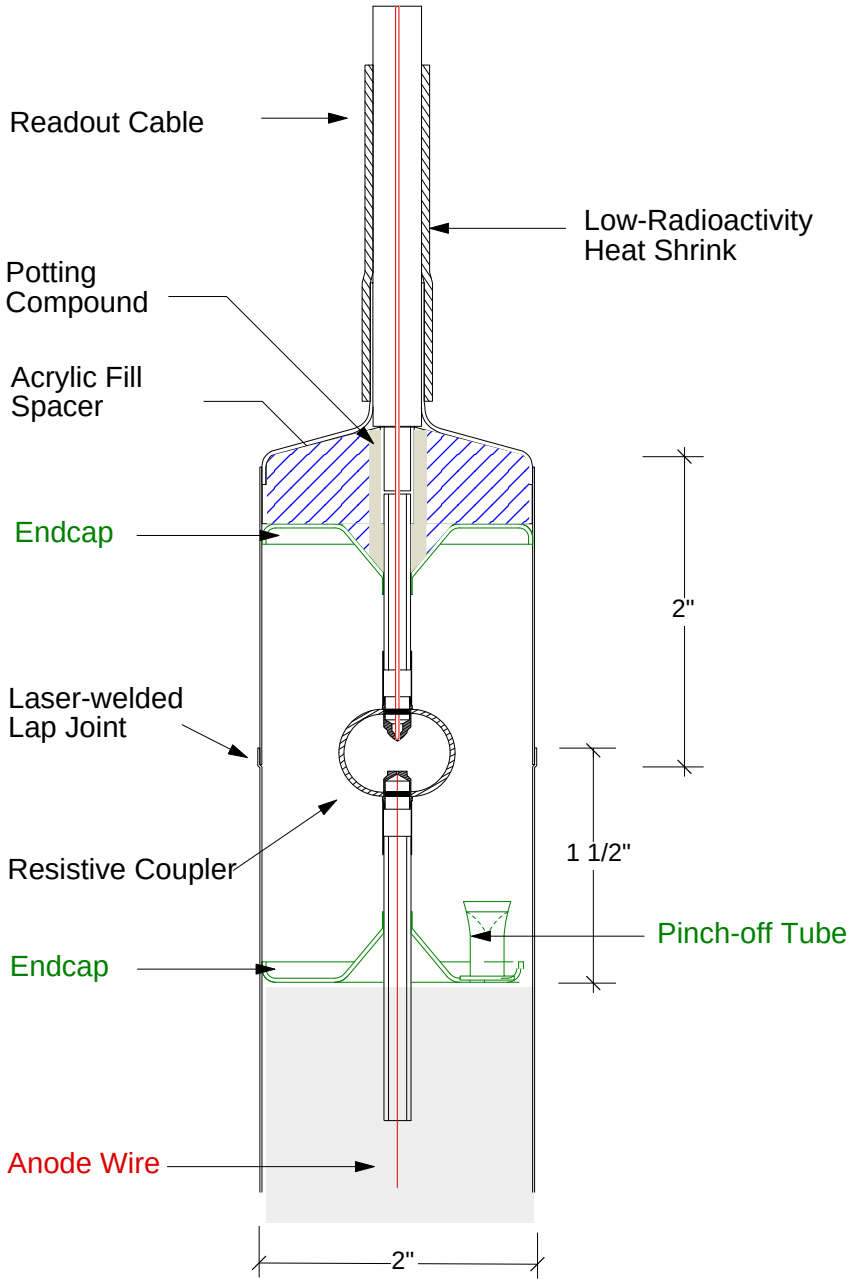

Figure A.9: Schematic of the single-ended readout of the NCD strings.

A.5 Characteristics of a Neutral Current Detector Signal

Charged particles slowing down in a gas deposit energy in part by creating electron-ion pairs (i.p.). Typically, one ion pair is produced for every 20-30 eV of loss. In a proportional counter, the electrons, which are much more mobile than the ions, are accelerated toward the anode where the electric fields are high, and avalanche multiplication can occur very close to the wire. In the usual mode of operation, the total charge collected is converted to a voltage in a charge-sensitive (integrating) preamplifier, and gives a measure of the energy deposited in the gas initially.

More information than just the total charge is actually available, however, and will be used in the ^{3}He counters. The primary ionization from a track will drift in and be multiplied over a period of time that depends on the track orientation and the drift velocity which is a property of the gas mixture. Thus the ionization density projected onto a plane perpendicular to the wire can be deduced from the current profile of the pulse. This information reveals a great deal about the event that created the track.

An example of this principle is shown in Fig. A.10. In this case alpha particles of ~ 5 MeV enter the volume of a proportional counter directed toward the center wire. Near the end of the track, the ionization density for α particles becomes highest (the "Bragg peak"), and that part of the track arrives first at the wire. One then sees a sharp initial maximum in the electron current, followed by a period of decreasing current terminating after 1.5 μs when the most distant ionization reaches the wire. The signal shown is the output of a current preamplifier. For the proposed NC detector array, current signals will be digitized and recorded in order to derive the ionization characteristics of each event. The total energy deposited can be derived from the integral of the distribution.

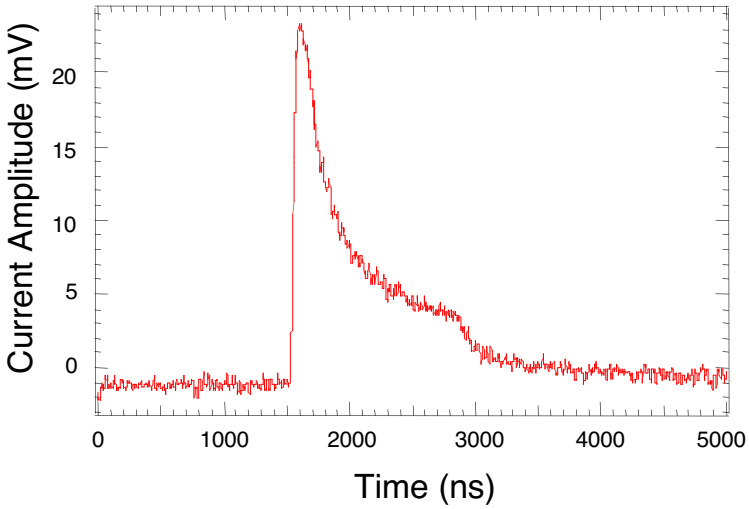

Figure A.10: Current pulse from 5-MeV α in a proportional counter.

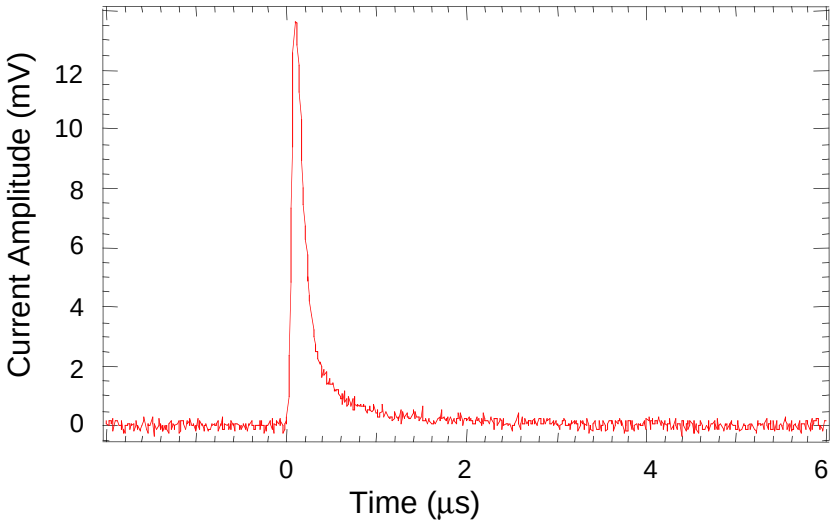

Figure A.11: Neutron capture in NCD: p+t event parallel to anode wire.

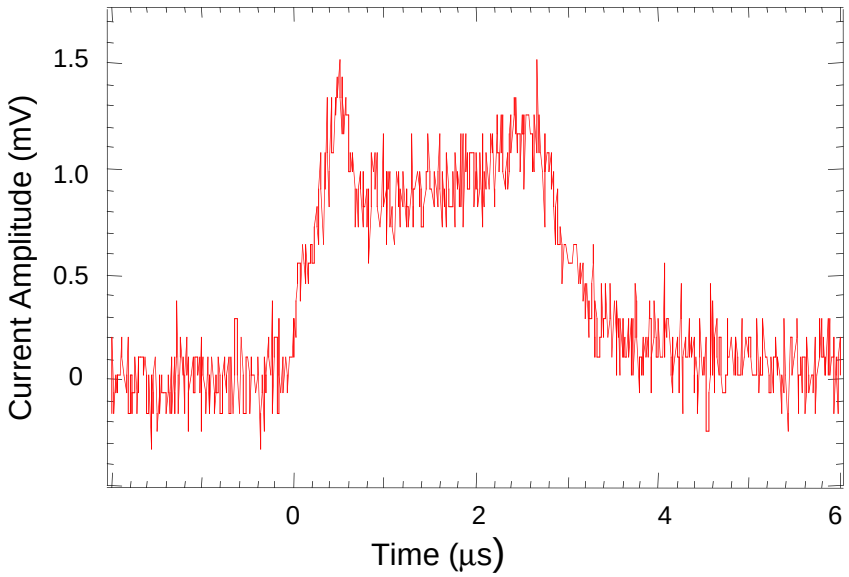

Figure A.12: Neutron capture in NCD: p+t event perpendicular to anode wire.

A.5.1 Event Topology

Thermal neutron capture on ^{3}He produces an anti-parallel proton (573 keV) and triton (191 keV) with a full energy of 764 keV. ^{3}He(n,p)t events fill the proportional counter volume with all possible track orientations relative to the anode wire. The largest surface area exposed to the gas in a proportional chamber is that of the cathode wall. The greatest threat from natural radioactivity in the counter material results from α-particles entering the gas from the cathode wall. The track length for a fully contained $t+p$ event is generally $\sim$3 times longer than that of an α-particle of the same energy. Consequently, a significant subset of neutron capture events will yield pulses that are longer in duration than the longest possible α-pulse. The electron drift velocity is smallest at the cathode wall where the electric field is weakest. Hence, the longest α-pulse corresponds to the case where an alpha track originates at the cathode wall and points perpendicular to the anode wire.

The wall effect, wherein a proton or a triton strikes the counter wall before the end of its range, accounts for the continuum of points to the left of the main 764-keV peak.

A.5.2 Energy Range

The ^{3}He(n,p)t window is defined by a full energy peak at 764 keV with a continuum below this peak that extends down to the proton edge at 191 keV. Accounting for finite energy resolution the NCD counters are required to be sensitive to energies from $\sim$150 keV to 850 keV. A lower energy threshold of $\sim$100 keV is needed to extract the spectrum associated with Compton electrons and β-particles. Backgrounds form the decay chain of U and Th emit α-particles with an energy up to 8.8 MeV. Hence, the energy range of interest in the NCD counters ranges from a low energy threshold of 0.1 MeV up to a maximum of 8.8 MeV.

A.5.3 Pulse Duration

Pulse duration or width is defined as the time it takes for electrons to drift into the avalanche region. The pulse width is thus the difference in time taken for electrons to drift from that point of the track farthest from the wire relative to the point of the track closest to the wire. The maximum drift time is thus the time it takes an electron to drift from the cathode wall

to the anode wire. For a gas mixture containing 2.5 atm He:CF_4=85:15 this drift time is ~ 3.6 μs when operating the detector at 1700 V and using a 25-μm anode wire diameter. The ranges of α particles less than 5.5 MeV and ^{3}He(n,p)t events are less than the counter radius. For 2.5 atm He:CF_4=85:15 alpha tracks above $\sim$ 5.5 MeV will begin to cross the anode wire when they point perpendicularly to the anode wire from the cathode wall. Beyond this energy the α-pulses will evolve with the maximum pulse duration of ~ 3.6 μs.

A.5.4 Current Pulses and Readout

The current associated with a given event depends on the event type , track location and orientation, gas fill, and operating voltage. The different types of events include ^{3}He(n,p)t reactions, αs, Compton electrons and β's. The detailed ionization pulse shape conveys information about what caused it, whether it be a neutron capture, a background α, or a spurious pulse. This information is more difficult to extract when the initial ionization track is nearly parallel to the anode wire, because the total pulse length becomes very short.

The current arriving at the wire is proportional to rate at which primary ionization drifts in:

$$i(t,r) = \frac{dE}{dx}\frac{dx}{dr}q\frac{\gamma}{\omega}\left(\frac{dt_d(r)}{dr}\right)^{-1} \tag{A.8}$$

where $\frac{dE}{dx}$ is the specific energy loss along the track, $\frac{dx}{dr}$ describes the geometrical orientation of the track with respect to the wire, q is the charge on the electron, γ is the gas gain, ω is the energy required to create one ion pair, and $\frac{dt_d(r)}{dr}$ is the reciprocal of the effective radius-dependent drift velocity. The smallest current is produced by protons at the wall pointed toward the wire. At a gain of 100 the current is 130 nA.

A fundamental, physical lower limit to the pulse length is set by lateral straggling. For tracks parallel to the wire lateral straggling of the primary ionization causes a finite arrival duration for the ionization. The lateral straggling limits the current even when tracks are nominally parallel to the wire. Taking the standard deviation lateral straggling distance as a measure of the dimensions of the charge packet, the peak current (for alpha particles at the wall, parallel to the wall) is estimated to be 29 μA.

Lateral straggling for 191-keV tritons then dictates a minimum standard deviation of approximately 33 ns, which sets the limit to the bandwidth of information that can be usefully extracted from pulse profiles. Electronic effects should, if possible, be kept below this level. Inductively-wound 410-Ω cable initially considered for this application exhibits a risetime of 100-120 ns over 15 m, but standard coaxial cable contributes negligibly to the risetime. For low-noise current preamplifiers tested to date, risetimes in the range 20-40 ns can be obtained. Digitizing sample rates in the range 2.5 to 10 ns have been used on typical data without apparent loss of information.

Preamplifier and cable risetimes limit the peak current if they are too long. A 10 to 20-ns risetime matches the lateral straggling for the fastest pulse. The 0.25-ns response time of the preamplifier smears the ideal current profile of the measured track but the characteristic shape is still apparent and may be compared with the α tracks. In order to record the detailed structure of pulses having a dynamic range of at least 150, and to allow some information to be obtained about pulses that fall outside that range (e.g. Compton events), logarithmic amplifiers are used before digitization. A more detailed discussion of the specifications of the electronics for the Neutral Current Detector array is given elsewhere. [34].

The current and charge profiles of the pulse both contain all the information initially present in the ionization trail, differing formally only by a simple mathematical transformation. The fundamental noise limits are similar in current- and charge-readout methods, setting aside small differences of the order of 10% associated with departures from the optimum shaping function in charge readout. However, when the signals are digitized before analysis, significant differences in the performance of charge and current amplifiers appear. With current readout, very short pulses will not be integrated very accurately digitally because the pulse lasts only a few sample bin widths, but with charge readout, if subtle features at the leading edge of a pulse must be discerned, the dynamic range within a single pulse becomes acute, and differentiation of the signal introduces digitization noise. Tests with both current and charge preamplifiers have shown that it is quite difficult to extract high-quality ion-track profiles from the charge signals, and that current readout is a more convenient method.

Table A.11 summarizes the basic quantities that characterize events in the NCD proportional counters. In Table A.12 the relevant quantities for different ionizing particles are summarized. Also included for reference are the effective energy losses for electrons and for minimum-ionizing particles (M.I.) that leave at least 100 keV in the detector after crossing a diameter.

Table A.11: Characteristics of the NCD signals.

Energy Range	0.1-8.8 MeV
Maximum Drift Time	3.6 μ s
Current	30 nA - 25 μA

Table A.12: Range, initial differential energy loss and lateral straggling for protons, tritons and alphas in 85:15 $HeCF_4$ at 2.5 atm total pressure.

Ion	Energy keV	Range mm	$\frac{dE}{dx}$ keV/mm	Lat. Strag. σ, mm	Energy/σ keV/mm
p	576	4.9	83	0.23	2504
t	191	1.7	145	0.16	1194
α	191	0.89	315	0.12	1592
α	9000	44	126	0.74	12162
e	100	50	2	-	-
M.I.	23	50	0.5	-	-

A.5.5 Single-Ended Position Readout by Reflection

Position information is desired in order to reconstruct the radial distribution of events from NC interactions and from the acrylic-vessel background, as well as to establish connections

between Čerenkov events and related neutrons. The latter would be particularly important in the detection of $\overline{\nu}_e$ interactions from a supernova or, possibly, from the Sun. Two-dimensional position coordinates are automatically delivered by the grid layout of detectors. The z-position can be obtained from the proportional counter signal. Since the mean distance to capture is 113 cm the position resolution requirements are not demanding.

Single-ended readout from the top end is used for the NCD array in SNO to minimize the introduction of backgrounds and interference with Čerenkov light. A variety of position encoding techniques have been developed for gas counters. [79, 76, 52, 129, 69]. One approach is to leave the remote end of the counter string unterminated (open) and to measure the time delay between current arriving directly at the preamp input and that reflected from the open end. Since the line is open, the low-frequency noise performance is determined by parallel noise alone, and is much improved. Moreover, the full signal charge is collected from an open line, which further improves the signal-to-noise ratio.

In this scheme the line is terminated at one end by the preamp in $Z_0 = 415\ \Omega$. The other end is left open. The DC resistance is typically small and of the order of 8 Ω/m for a 0.005-cm diameter copper wire. The signal contains a broad spectrum of frequencies, but there will be a notch in the response at $\lambda/4$, $3\lambda/4$, etc. and a peak at $\lambda/2$, $3\lambda/2$, etc. Hence the position of the pulse can be determined in an open line by Fourier analysis of the pulse. A wide variety of other techniques, discussed elsewhere, have been used in conjunction with and in place of Fourier analysis. Pulses can be decomposed into the direct and reflected part, but since line delays are in general ~ 40 ns one-way, the reflection arrives long before the end of the prompt pulse (μs in duration) and it may be difficult to distinguish the reflection from structure in the ionization current or noise.

A small section of delay line at the bottom of the detector chain is needed to allow reflections for events at the physical lower end of the counters.

APPENDIX B

BACKGROUNDS TO THE NEUTRON SIGNAL IN THE NEUTRAL CURRENT DETECTOR ARRAY

In this appendix we give an overview of the backgrounds that contribute to the signals detected in the ^{3}He-filled Neutral-Current Detector array. These include background signals in the proportional counters as well as neutron-producing backgrounds in the heavy water target of the SNO detector. Preliminary estimates of the internal and external backgrounds are presented.

B.1 Proportional Counter Signals

Neutrons from the NC interaction of neutrinos with the D_2O thermalize and then capture via ^{3}He(n,p)^{3}H in the proportional counters. They produce a 573 keV proton and a 191 keV triton that leave ionization tracks in the proportional counters. A number of different backgrounds contribute to the overall event rate detected in the counters.

The principal background to the ^{3}He(n,p)^{3}H reaction originates from natural alpha emitters embedded in or adhering to the wall of the counter, because degraded alphas can emerge into the gas with an energy between 191 and 764 keV. About 1000-10000 alpha particles per day are expected from the decay chains of ^{232}Th and ^{238}U. They enter the detection volume from the wall of the proportional counters and create a continuous background that underlies the ^{3}He(n,p)^{3}H peak. Pulse shape analysis of the digitized proportional counter signals can be used to distinguish between neutron capture, alphas, and other ionization events. Compton electrons, photoelectrons, and β's tend to be less serious a problem because, in detectors of the dimensions normally used, extensive multiple scattering must occur before such processes can deposit enough energy in the gas to mimic a neutron event. The hadronic component of cosmic rays can be a significant background when secondary alphas and protons are ejected from nuclei in the wall of the counter to enter the gas. Minimum

ionizing particles are not an appreciable problem.

The ^{3}He gas contains tritium that is of concern if the concentration is high enough to lead to random coincidences and to pileup of tritium decay pulses. ^{3}H decays deposit an average of 6 keV/event in the proportional counters. Low temperature purification techniques are used to reduce ^{3}H in the ^{3}He-fill gas. The sensitivity of the ^{3}He counters and their stringent background criteria make it essential to minimize all spurious pulses including signals induced by high voltage. The phenomenon of microscopic surface discharges and techniques for their reduction have been described elsewhere [61]. Gamma rays with an energy greater than 2.2 MeV contribute to the photodisintegration background.

For experiments conducted deep underground the main source of background in ^{3}He counters is therefore the natural alpha emitters. In the particular case of SNO, a second concern is gammas above the breakup threshold of the deuteron, 2.22 MeV. Photodisintegration of the deuteron liberates a free neutron that is indistinguishable from a neutral-current neutrino process. Again, both Th and U must be controlled because of the high-energy gammas emitted near the bottom of both decay chains (2.62 MeV from ^{208}Tl, and 2.44 MeV from ^{214}Bi). In addition, cosmogenic activities induced when construction materials were on the Earth's surface can be of concern, but only one, ^{56}Co, has a long half-life of 78 days.

Table B.1: Neutral-Current signal and neutron backgrounds in the NCD counters.

	Event	Counter Signature	Background Control
Signal	^{3}He + n $\rightarrow$ p + ^{3}H	573 keV p + 191 keV t ionization tracks	
Backgrounds	Photodisintegration, $E_\gamma \geq 2.2$ MeV	573 keV p + 191 keV t ionization tracks	Radioassay of components, In-situ measurement of counters
	^{56}Co Photodisintegration		Cooldown time
	Tritium in ^{3}He gas	6 keV pile-up pulses	^{3}He purification
	High-voltage microdischarge	Discharge signal	High-voltage testing
	Surface α's from ^{210}Po	α pulse	Electrochemical surface treatment, Pulse shape analysis
	Bulk α's from ^{238}U, ^{232}Th	α pulse	Pulse shape analysis
	e^-, γ scattering		Negligible

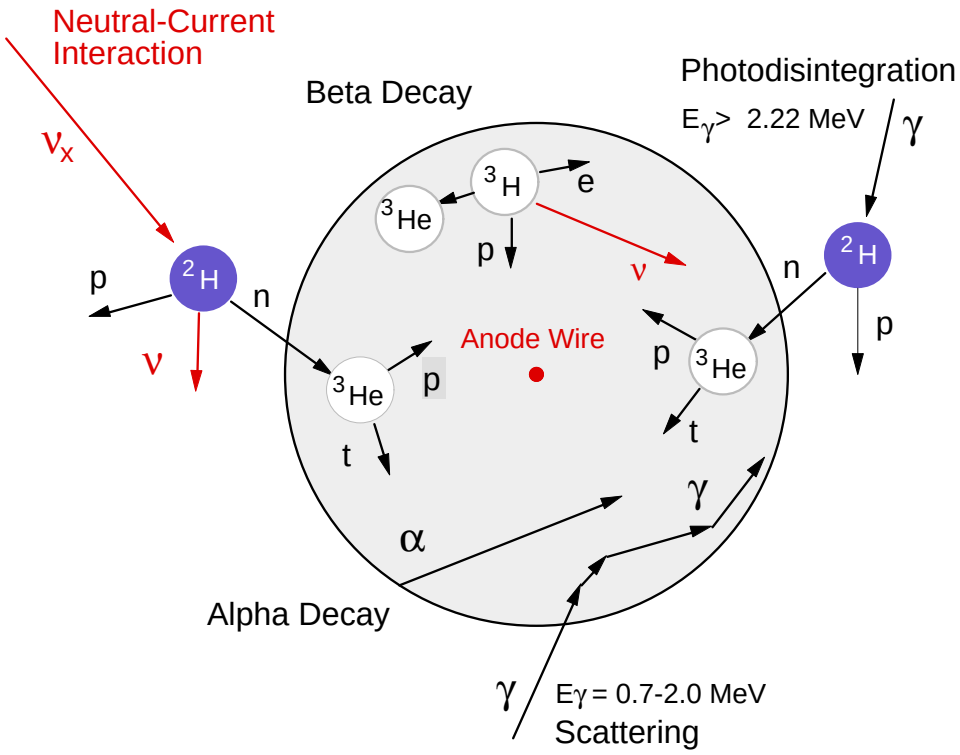

Figure B.1: Schematic of NCD cross-section with proportional counter events. Illustration of the detection of the neutral-current neutrino interaction (red) with deuterium (blue) and backgrounds (black).

B.1.1 Alpha Activity from Radon Surface Contamination

Radon is ubiquitous in air, being present at the level of typically 1 pCi/l (37 Bq/m^3) in indoor air and about a third of that level outside. Radon isotopes and their daughters are all too short-lived to be of much concern for neutral-current detector construction, with one exception, ^{210}Pb from ^{222}Rn decay. This 22-year activity accumulates on surfaces exposed to radon-laden air, and represents a background. The low-energy β-decay of ^{210}Pb leads to 5-day ^{210}Bi, which, in turn, decays via a 1.2-MeV β to 138-day ^{210}Po. The 5.3-MeV α from ^{210}Po produces in a proportional counter a peak with a continuum tail that underlies the 764-keV neutron line.

There exists an extensive radiologically-motivated literature on the fate of radon daughters, although ^{210}Pb and its daughters receive scant attention owing to its long half-life, which makes it irrelevant as a health hazard. Much of this work is summarized in [148]. When ^{222}Rn reaches equilibrium in a space, the concentration is supported against decay and ventilation losses by emanation from construction materials and the ground. Radon daughters can migrate directly to a surface and be deposited, or they can with much higher probability attach themselves to airborne particulates, which then migrate more slowly, but eventually themselves deposit on surfaces.

Surface deposition of the shorter-lived radon progeny has been studied both experimentally and theoretically. To first order, the naive expectation that every radon decay eventually leads to a surface-fixed daughter is borne out. Ventilation from the enclosed volume is the only means of escape.

It can be calculated [173] that in equilibrium with ^{222}Rn, 50% of 20-minute ^{214}Bi is fixed on surfaces, another 27% is attached to airborne particles, none remains free (atomic), and the remaining 23% has been removed by ventilation (taken to be 0.55 air changes per hour in a space with V/S in the range 0.25 to 0.5 m). The calculation was not continued explicitly down to ^{210}Pb, but, from the ^{214}Bi results, between 50 and 75% of the lead will be fixed on surfaces.

One can calculate the surface α activity as follows. If the deposited fraction is ϵ_d, the specific activity of ^{222}Rn is A_{Rn} Bq/m^3, the room volume is V m^3, and the room surface

area is S m^2, then the rate at which daughter atoms are deposited per m^2 is:

$$R_s = \eta_d A_{Rn} \frac{V}{S} \tag{B.1}$$

The surface activity A_s after a time t (short compared to the daughter halflife) for an activity with decay constant λ is:

$$A_s = Q_s \lambda t/2 \tag{B.2}$$

The factor 1/2 reflects the fraction of decays directed outward from the surface. Choosing $\epsilon_d = 0.6$, $A_{Rn} = 37$ Bq/m^3, V/S = 0.5 m (empty room $3 \times 3 \times 4$ m), then the surface activity reaches 1 $m^{-2}d^{-1}$ after 40 min.

B.2 Neutron Background to the Neutral-Current Signal

Neutrons entering the inner volume of the SNO detector or produced by secondary interactions inside the detector are a background to the neutral-current signal in SNO. While these backgrounds have very different sources they can be summarized in terms of the total number of neutrons produced in the detector. Determination of the photodisintegration and all external backgrounds is essential for an accurate measurement of the NC interaction rate with the NCD array. According to the standard model prediction BPB00 [11] the expected neutral-current signal rate in the SNO detector is $\sim$ 4520 n/yr.

B.2.1 Photodisintegration from Internal D_2O, AV, and H_2O Backgrounds

Gamma rays above the deuteron binding energy can break the deuteron in the heavy water apart and produce neutrons that are indistinguishable from the NC signal. In the SNO detector the main sources of the photodisintegration background are ^{238}U and ^{232}Th in the water, gammas from photomultipliers, and (α, p) and (α, n) reactions on the PMT's and their support structure.

It has been estimated that the photodisintegration background contributes an estimated 368 n/yr to the internal D_2O backgrounds. The neutron background due to spallation reactions with cosmic rays muons (about 5400 n/yr) can be completely discriminated by the Čerenkov signal associated with each muon. Reactor and terrestrial $\overline{\nu}_e$ do not contribute more than 28 n/yr. A complete summary of the internal neutron background estimates are given in Table B.2. The total detector-internal background to the NC signal is estimated to be less than 520 n/yr [36].

For reference, 3.7 μg of Th or 29 μg of U (in equilibrium with their daughters) in the heavy water would produce 365 neutrons per year by photodisintegration. These quantities set a standard also for anything that might be deployed in the heavy water, such as proportional counters. In particular, the construction material must be free of Th at the level of 12 ppt (ppt = parts in 1012 by weight) to equal that level.

Table B.2: Neutron production in the SNO detector D_2O volume. Table reproduced from [36].

Internal D_2O Backgrounds	Rate	Unit	Expected y^{-1}
$^2H(\gamma,n)^2H$: ^{208}Tl [Th]	95.5	n μg^{-1} yr^{-1}	167 (54)
$^2H(\gamma,n)^2H$: ^{214}Bi [U]	12.2	n μg^{-1} yr^{-1}	$\leq$1
$^2H(\gamma,n)^2H$: ^{214}Bi [^{222}Rn]	12.2	n μg^{-1} U yr^{-1}	201 (34)
Fission [U]	0.43	n μg^{-1} U yr^{-1}	0
$^2H(\alpha,\alpha n)^1H$ [Th]	1.9	n μg^{-1} yr^{-1}	3
$^2H(\alpha,\alpha n)^1H$ [^{222}Rn]	0.8	n μg^{-1} U yr^{-1}	13(2)
$^{17}O(\alpha,n)^2H$: ^{208}Tl [Th]	0.008	n μg^{-1} yr^{-1}	0
$^{17}(\alpha,n)^2H$: ^{208}Tl [Th]	0.021	n μg^{-1} U yr^{-1}	0.3
Muons	5900	n	0
Atmospheric ν	108	n	108
$\overline{\nu}_e$ ccp	0.4	n	0.4
$\overline{\nu}_e$ ccd	11	n	11
$\overline{\nu}_e$ ccd	16	n	16
Total			520

B.2.2 Photodisintegration Backgrounds from the NCD Array

Decay products of ^{238}U, ^{223}Th, and cosmogenically activated ^{56}Co in the nickel bodies of the Neutral- Current Detectors add to the photodisintegration background. Čerenkov light from associated gammas and radioassay techniques can be used to estimate these backgrounds. Results from radioassays indicate that the neutron background from the NCD array will contribute about 130 neutrons/year in the main detector volume, i.e. about 2.8% of the expected neutrons from the NC interaction.

Very few materials are known to be radiopure to such a degree. In no small measure, this is a result of the difficulty in finding diagnostic techniques that are sufficiently sensitive. Available methods include:

a) Direct gamma or alpha counting

b) Mass spectrometry

c) Neutron activation analysis (followed if necessary by radiochemical separations)

Direct counting methods do not, as a rule, have sufficient sensitivity without some form of preconcentration. A notable exception is the stringent limits set on the purity of shielding and construction materials by double β-decay experiments. Such experiments with large-volume Ge detectors and long counting intervals set limits at the few-ppt level.

B.2.3 Cosmogenic Production of Radio-Isotopes in Nickel

Radiopure counter components for the NCD array can be made through chemical vapor deposition of Ni. However, any exposure to cosmic ray neutrons produces activity from spallation products. Gamma rays emitted in the decay of cosmogenically activated isotopes can contribute to the photodisintegration background to the neutral-current signal. ^{56}Co is the only isotope that has many gammas above 2.224 MeV and a significantly long half-life of 78 days. A total of 31% of ^{56}Co decays result in γ's with $E_\gamma \geq 2.224$ MeV [175]. The ^{56}Co isotope is formed in (n,p n) reactions on Ni.

$$^{58}\mathrm{Ni} + \mathrm{n} \rightarrow \mathrm{p} + 2\mathrm{n} + ^{56}\mathrm{Co} \tag{B.3}$$

$$^{60}\mathrm{Ni} + \mathrm{n} \rightarrow \mathrm{p} + 4\mathrm{n} + ^{56}\mathrm{Co} \tag{B.4}$$

The ^{56}Co nucleus then decays to an excited state of ^{56}Fe which then de-excites by gamma cascade to its ground state.

$$^{56}\mathrm{Co} \rightarrow ^{56}\ \mathrm{Fe}^{*} + \Sigma\gamma \tag{B.5}$$

The energy distribution of all significant γ's with an energy of $E_\gamma \geq 2.0$ MeV is shown in Table B.3. The γ's can either Compton scatter from the electrons in the D_2O or photodisintegrate the deuteron. The cross-sections for the photoelectric effect and pair production are so small that their contributions can be ignored.

As the CVD process ensures that no ^{56}Co is present in the nickel at the time of manufacture, then the decay rate for an isotope which has a half life of $t_{1/2}$ and has been exposed to cosmic rays for a period t_s is given by

$$R(t_s) = R_0(1 - e^{-t_s ln2/t_{1/2}}) \tag{B.6}$$

where R_0 is the equilibrium decay rate (R_0=24.22 decays/day/kg). If the Ni counters are stored underground for a time t_u then the decay rate is reduced by the normal decay

$$R(t_s, t_u) = R_0(1 - e^{-t_s ln2/t_{1/2}})e^{-t_u ln2/t_{1/2}} \tag{B.7}$$

Monte-Carlo simulations with the gamma decay scheme and the photodisintegration cross section of deuterium predict a yield of 1 neutron per 1140 ^{56}Co decays. Hence 400 kilograms of Ni at saturation would produce an initial background of 14.4 neutrons per day in the heavy water [175]. The saturation activity for ^{56}Co from Cu at sea level has been measured to be 0.006 dis/min-kg [5]. Calculations with COSMO [141] [1] predict 0.0084 dis/min-kg.

[1] COSMO is a program to estimate spallation radioactivity produced in a pure substance by exposure to cosmic-radiation on the Earth.

This cosmogenic component to the photodisintegration background is reduced by storing the detectors underground after construction and allowing them to "cool" for a period before installation. Considering that most of the counters for the NCD array have been underground since June 2001 (and longer) the expected background from cosmogenically activated ^{56}Co is < 0.6 neutrons/day.

Table B.3: Gamma energies in the decay of ^{56}Co.

Photon Energy (MeV)	Probability of Decay
2.2763	1.1176×10^{-3}
2.3736	7.7220×10^{-4}
2.5229	6.3780×10^{-4}
2.5984	1.6634×10^{-1}
2.6574	1.7300×10^{-4}
2.9598	7.2200×10^{-5}
3.0102	9.9988×10^{-3}
3.2023	3.0400×10^{-2}
3.2536	7.4300×10^{-2}
3.2733	1.7600×10^{-2}
3.3696	1.1260×10^{-4}
3.4526	8.5750×10^{-3}
3.5480	1.8000×10^{-4}
3.6006	1.5000×10^{-4}
3.6116	5.7000×10^{-5}

B.3 Background Control and Discrimination

This section summarizes some of the background studies that have been performed to date to characterize the performance of the NCD array during its construction phase. Further information on the internal NCD background can be obtain from studying the alpha activity in the NCD array after gas fill and during cooldown underground. First results of this work have been reported in [17].

B.3.1 Neutron Activation Analysis of CVD Ni

The radioassay techniques that are used to verify low levels of U and Th contamination are alpha counting, and radiochemical separation and counting of neutron-activation products, both of which have sufficient sensitivity to reach the 1 pg/g level. At that level, the photodisintegration background rate from the NCD array would be 0.1 neutrons per day, less than 1% of the SSM NC rate.

With the use of automated sample handling and gamma-ray measurement with solid-state detectors it is generally possible to simultaneously measure more than thirty elements in most sample types without chemical processing. The application of purely instrumental procedures is commonly called instrumental neutron activation analysis (INAA) and is one of NAA's most important advantages over other analytical techniques. If chemical separations are done to samples after irradiation to remove interferences or to concentrate the radioisotope of interest, the technique is called radiochemical neutron activation analysis (RNAA).

Radiochemical neutron activation analysis is used when greater sensitivities are required than are provided by INAA. In this method, radiochemical separations on the irradiated material are conducted to isolate an element or class of elements and gamma-ray spectrometry is performed on the separated fraction. Separations enhance sensitivity by eliminating interferences and reducing background count-rates. For some applications, detection limits can be improved by up to three orders of magnitude as compared with INAA.

Radiochemical neutron-activation analysis (RNAA) was used to analyze parts of CVD Ni tubing for Th and U. Samples were clipped off, sealed in Suprasil T-21 fused silica tubes,

and shipped to either the Missouri University Research Reactor (MURR) or the University of Illinois Triga Reactor (UITR) for irradiation. These reactors have fluences of 5×10^{13} n $cm^{-2}s^{-1}$ (MURR) and 8×10^{12} n $cm^{-2}s^{-1}$ (UITR) respectively. Tests were carried out to assure that there was no contamination introduced from the cutters, and flux monitors were included in each irradiation group to permit quantitative relation of the Pa and Np fractions measured to the Th and U in the samples. The results from this analysis are summarized in Table B.4.

Table B.4: Results from a radiochemical neutron activation analysis (RNAA) on various nickel tube samples. Data compiled by S.R. Elliott.

Sample	Date	U, pg/g	Th, pg/g	Reactor	Etch
Tube "NiP"	4/96	-	15(1)	UITR	10% HNO_3 20 min
Tube "NiP"	4/96	≤ 1.1	≤ 3.3	UITR	hot 30% HNO_3 2.5 min
5 tube samples	6/96	-	22.6(16)	MURR	no etch
tube	6/96	-	23.2(14)	MURR	10% HNO_3 20 min
5 tube samples	6/96	-	10.7(9)	MURR	50% HNO_3 1.75 min
5 tube samples	6/96	-	≤ 1.5	MURR	50% HNO_3 + 0.2 M HF 0.75 min
Tube T58	8/96	-	6.3(12)	MURR	control: no etch
Tube T44	8/96	-	7.0(9)	MURR	control: no etch
Tube T58	8/96	-	2.4(6)	MURR	0.02M EDTA, 70° C, 20 min
Tube T44	8/96	-	2.4(6)	MURR	0.02M EDTA, 70° C, 20 min
Tube T58	8/96	-	≤ 1.0	MURR	50% HNO_3 + 0.2 M HF, 1 min
Tube T44	8/96	-	≤ 0.8	MURR	50% HNO_3 + 0.2 M HF, 1 min
Tube T58	8/96	-	3.6(9)	MURR	0.02M EDTA, 25° C, 41 h
Tube T44	8/96	-	2.9(9)	MURR	0.02M EDTA, 25° C, 41 h
Tube T58	8/96	-	2.7(3)	MURR	0.02M EDTA, 70° C, 3.5 h
Tube T58	8/96	-	≤ 0.8	MURR	0.02M EDTA, 70° C, 3.5 h, 50% HNO_3 1 min

B.3.2 Radioassay of NCD Counter Components

Photodisintegration background from NCD array requires separate determination and subtraction. The photodisintegration background from the individual NCD detector components prior to their assembly has been determined through radioassay techniques. The results from this work [41] are summarized in Table B.5.

Uncertainty in the measurement determines the upper limit of the results. Estimates are conservative upper limits, some parts made out of cleaner materials. One should note that the contribution from ^{238}U is not included. 0.53 μg Th produces 1% SSM photodisintegration neutrons for BPB98 ($\sim$ 5000 n/yr).

In calculating the radioassay numbers one distinguishes between uniform contributions in the main detector volume ($\sim$180 n/year) and additional near vessel contributions ($\sim$190 n/year).

Table B.5 summarizes preliminary results. The contribution from ^{238}U is not included.

Table B.5: Neutron background estimates from radioassay. Data compiled by S.R. Elliott.

Component	Contained Mass Th (in μg)	Effective Mass Th (in μg)	% SSM (BPB00)
Uniform Contributions			
Counters	0.5 $\pm$ 0.4	<0.9	<1.8
Endcaps	0.1 $\pm$ 0.9	<1.0	<2.0
Near AV Contributions			
Delay Lines	0.2 $\pm$ 1.9	<0.5	<1.0
Wet-end connectors	-0.4 $\pm$ 0.6	<0.1	<0.2
Cable	2.5 $\pm$ 3.0	<1.4	<2.8
Total		<2.0	<4.0

B.3.3 Tritium Background

The ^{3}He gas which is used to fill the counters contains a small amount of tritium, about 0.5 mCi/l. The contaminating tritium is in the form of HTO, as well as some free hydrogen. This contamination is reduced to 5 nCi/l or less by passage through a charcoal-loaded cold trap and by recirculation through an SAES, Inc., St101 getter. The heated getter removes much of the free hydrogen and water vapor. This is followed by a pass through a cooled charcoal trap to remove any additional water vapor. The gas is re-circulated for three hours using a bellows pump. At that level, random coincidences and pileup of tritium decay pulses are no longer a concern in the energy regime of interest. Some detectors, about 5% of the total by length, are filled with ^{4}He:CF_4 to provide a check on backgrounds.

The above purification scheme has been established as providing the required tritium level specification of less than 2.7 nCi/STP-liter. After fabrication each NCD is checked for tritium. The tritium level for each detector is measured by looking at its low energy spectrum. Operated at 2225 V, the signal is passed through a charge integrating preamp, followed by an Ortec 855 variable gain amplifier, and finally into an Ortec ADC. The gain of the 855 is adjusted to study the 2-25 keV energy range. A 10-min run provides ample statistics and the spectrum is integrated to give an approximate measure of the tritium contamination.

The most significant background to the measurement of tritium contamination is from cosmic rays as these measurements were done at sea level. Assuming a constant flux of cosmic rays, they must contribute less than an equivalent 0.04 nCi/STP liter to the measurements, as this is the lowest rate obtained for any counter. Knowing that the cosmic ray flux only adds to the result, we can be satisfied in knowing that our measurements provide an upper limit to the tritium contamination above 2 keV.

Dead time is a potential systematic in this measurement. Its effect was shown to be less than 1%. Also, the integration over energy is not done from zero but rather from some threshold energy. This threshold energy is approximately 2 keV. To find the total tritium contamination, one would need to correct for the missed events from 0-2 keV. These events contribute less than about 10% of the total tritium decays. They also play a less significant

role in pileup, contributing little to a summation of pulses.

In addition to building ^{3}He detectors, some NCD counters are filled with ^{4}He. This allows the study of alpha backgrounds in the NCD array in the absence of ^{3}He(n,p)t signals. The same gas system is used to fill both types of counters and this allows for the ^{4}He counters to also become contaminated with tritium. The tritium, in the form of water vapor, can adhere to the stainless steel walls of the gas system and then be flushed out during a ^{4}He fill. The tritium measurements on 6 ^{4}He counters are shown in Figure B.3.

The large variation in results reflects the variation in tritium contamination of the gas system. Contamination, once picked up, is hard to remove as the ^{4}He has only a single pass through a heated getter. Heating the system under vacuum can help reduce the cross contamination of ^{4}He counters. Some counters were given a temporary ^{4}He fill before being given their final ^{3}He. In conclusion, the NCD counters are typically much cleaner than the specified 2.7 nCi/STP-liter of tritium.

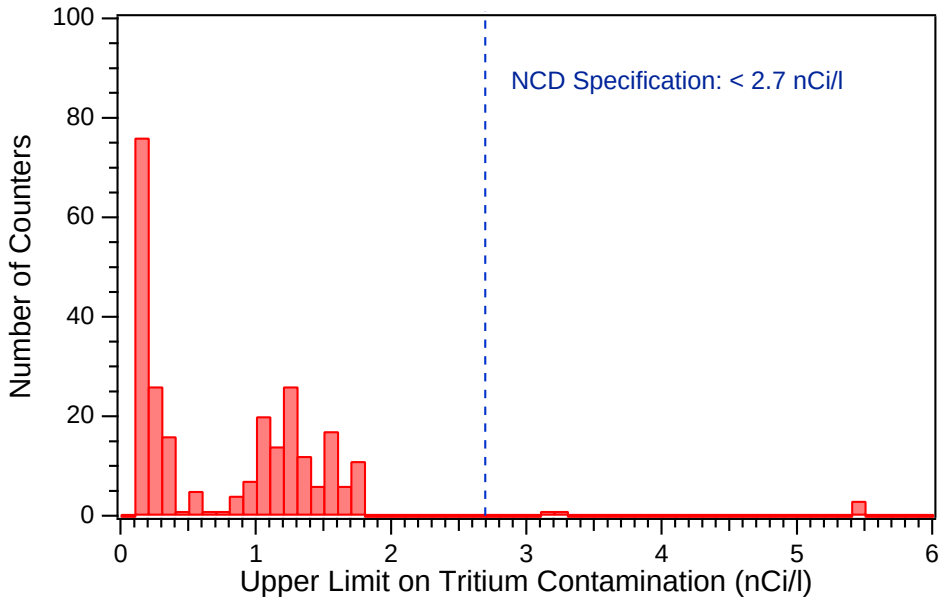

Figure B.2: Tritium contamination in the ^{3}He-fill gas of 255 Neutral-Current Detectors as of September 29, 2000.

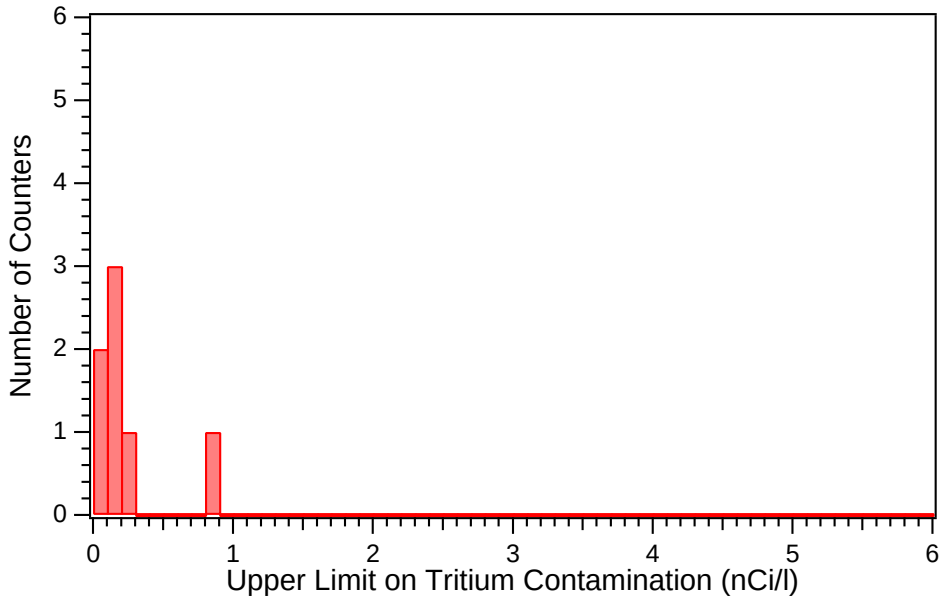

Figure B.3: Tritium contamination in 6 ^{4}He-filled Neutral-Current Detectors.

Table B.6: Leaching properties of the NCD background test source (CHIME).

Sample	μg ^{232}Th from ^{212}Po	μg ^{238}U from ^{214}Po	μg ^{238}U from ^{226}Ra
NCD Test Source	0.26	0.035	0.037
Background	0.057	0.0044	0.0032

B.3.4 In-Situ NCD Background Test: First Deployment of Neutral-Current Detectors into the D_2O

To verify the cleanliness of the final counters after fabrication and assembly a Construction Hardware In-Situ Monitoring Experiment (CHIME) is performed prior to the array's installation in SNO. Observation of Čerenkov light from the CHIME background source allows one to check for unexpected backgrounds. The CHIME source consists of seven close-packed Neutral- Current Detectors. The construction materials and procedures are identical to those in the NCD array. The CHIME is negative buoyant and was deployed along the central vertical axis of the SNO detector using a specifically designed winding mechanism. In September 2000 the CHIME was deployed into the central volume of the SNO detector. During a 70 hrs-long engineering run no unexpected backgrounds were found. The Čerenkov signal in the appropriate energy region from the NCD background test source was found to be the same within statistics as the Čerenkov signal from D_2O itself.

An additional test run would be required for a measurement of the NCD-related photodisintegration background. The details of this NCD background test experiment are described in Appendices E - F.

B.3.5 Emanation of ^{3}He-filled Neutral Current Detectors

In preparation for the first deployment of the NCD background test source (CHIME) a leaching test of the Neutral Current Detectors was performed to determine the leaving properties of the NCDs in ultrapure D_2O. The results are summarized in Table B.6. Details can be found in Appendix F.

The upper limits at 95% CL correspond to 0.26 μg ^{232}Th and 0.035 μg ^{238}U, or less than 1% SSM neutrons.

B.3.6 NCD Surface Contamination During Underground Storage

Average dusts contain approximately 7% iron by weight. The iron content of dust samples is also strongly correlated with the thorium level of the dust which produces the most serious background γ-ray. Tape lift measurements from the surface of the NCD counters, analyzed with an X-ray fluorescence (XRF) system, have been used to verify the surface cleanliness of the Neutral Current Detectors. The analysis procedures and the results from the NCD tape lifts measurements are described in detail in Section F.2.3. The main results are summarized in Table F.10. The tape lift measurements indicate that Ni is apparently lifted from the surface of the counters. This is probably a reasonable result given surface texture. No evidence for significant dust contamination was found.

Table B.7: Results from the NCD tape lifts.

Tape	Element	Tape Lift Measurement
Sample No. 1027	mine dust	0.00 $\pm$ 0.04 μg/cm^2
	Zn	0.003 $\pm$ 0.003 μg/cm^2
	Ni	7520 counts (net)/20 min. $\rightarrow$ 0.15 μg/cm^2
Sample No. 1028	mine dust	0.22 $\pm$ 0.04 μg/cm^2
	Zn	0.012 $\pm$ 0.003 μg/cm^2
	Ni	12380 counts (net)/20 min. $\rightarrow$ 0.25 μg/cm^2

B.4 Electronic Event Identification and Background Discrimination

While the photodisintegration background to the NC signal cannot be discriminated and has to be determined separately the NCD-internal backgrounds can be discriminated on an event-by-event basis through detailed analysis of the digitized proportional counter signal.

The difference in range between α and $t + p$ tracks allows a means of background discrimination based on the pulse duration at each energy. In general, however, $t + p$ pulses will be shortened by virtue of their orientation with respect to the anode wire. When the current pulses become of shorter duration than the longest α-pulses, simple pulse duration is not sufficient to discriminate. The basic concept for discriminating background events from ^{3}He(n,p)t events is demonstrated in Figure B.5 where a scatter plot in the pulse-duration (risetime of charge) *vs* energy plane for analysis of charge integrated pulses is shown.

^{3}He(n,p)t events are confined to a plane defined by the solid red boundary in Figure B.5. Events produced by Compton electrons are also shown but are completely discriminated from the ^{3}He(n,p)t window. Specifically, experimental results indicate that of 4322 Compton electron induced events above the electronic threshold at 100 keV, only one is found in the ^{3}He(n,p)t window. As a result, the probability that a Compton or β particle contaminates the region of interest is less than $\sim 5 \times 10^{-4}$. Also shown in Figure B.5 is a solid curve intersecting the ^{3}He(n,p)t window which represents an energy-dependent upper bound on the pulse duration of alpha particle tracks originating in the cathode wall. The region above this curve represents a "background-free" region for ^{3}He(n,p)t events [127] and contains 45% of detected neutron events. (The fact that the total efficiency of the array for neutron capture is also 45% is a coincidence.) The energy histogram of events is shown in Figure B.4. The α-distribution presents a continuum under the ^{3}He(n,p)t spectrum when information from the integrated energy only is obtained. In the latter case, one is forced to rely on statistical methods and knowledge of the underlying energy distributions to determine the relative contributions of neutron capture events *vs* α-particles from backgrounds.

It is the difference in track length for $p + t$ events relative to α-particles that yields the background-free region in Figure B.5. It is clear, however, that further discrimination could be obtained by exploiting the information contained in the pulse shape. The event

topology is preserved in the current profile and techniques to exploit this information by direct analysis of digitized current pulses are under development.

More than 50% of the neutron events are completely free of α background when the time information is invoked. And, as mentioned above, background rejection for short tracks may also be improved by differentiating between the rather distinctive characteristics of neutron and alpha events. The signal and the background occupy overlapping but different regions of the two-parameter space, and may be extracted with little correlation between them. It may readily be shown that the uncertainty in the total neutron rate N_n under these conditions is given approximately by

$$\sigma_n^2 = N_n(1 + \frac{N_\alpha}{N_n + N_\alpha}) \tag{B.8}$$

where N_α is the total α rate in the region being analyzed. This expression behaves very mildly when alpha rates go to infinity, tending (not surprisingly) to the statistics of half the neutron data, i.e. that part of the data that is free of alpha background.

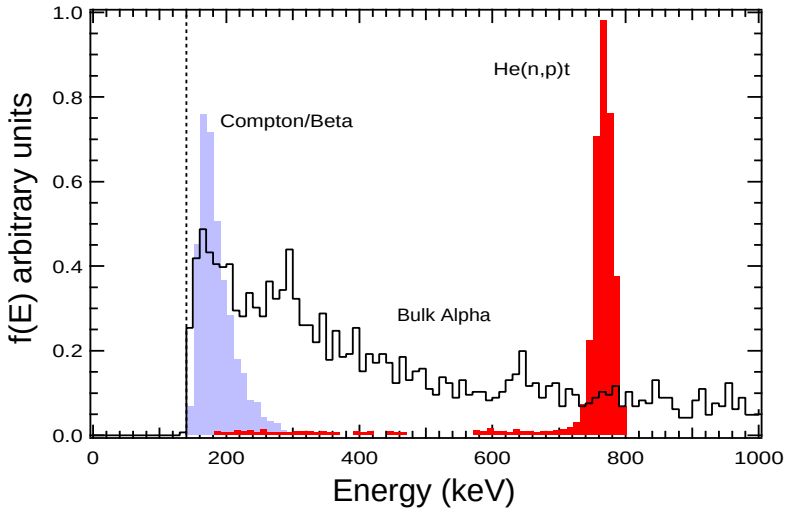

Figure B.4: Energy spectrum of signal and background events in the NCD counters. Figure courtesy of A. Hime, Los Alamos National Laboratory.

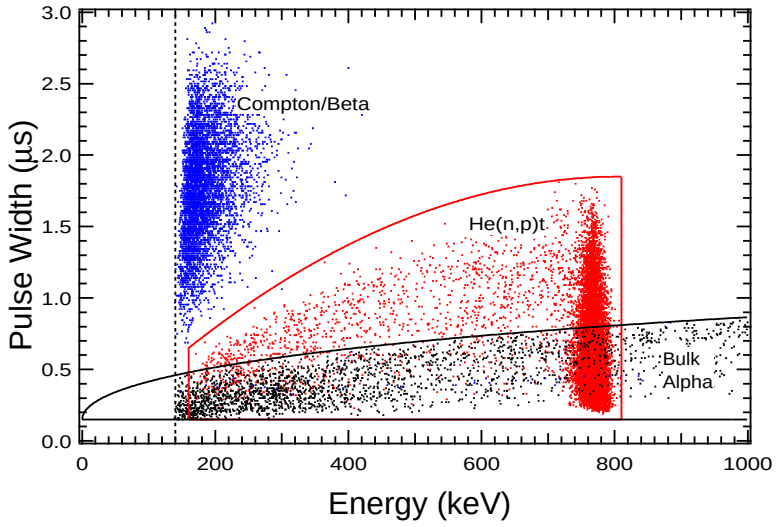

Figure B.5: Pulse width of signal and background events in the NCD counters. Figure courtesy of A. Hime, Los Alamos National Laboratory.

APPENDIX C

DECAY SCHEMES OF ^{238}U, ^{232}TH, ^{40}K, AND ^{56}CO.

Natural radioactivity is a background to the signal of neutrinos in SNO. It can mask both the Čerenkov signature of neutrinos as well as the detection of neutrons from the neutral-current interaction of neutrinos in the Neutral Current Detector array.

Many radioactive isotopes are known that could either produces enough Čerenkov light that could mimic the signature of Čerenkov electrons in SNO's water Čerenkov detector or contribute to the photodisintegration neutron background detected in the array of ^{3}He-filled proportional counters. It has been pointed out [161] that only few isotopes have both substantial decay energies and long lives to be of concern. The argument that limits the number of possible background is that the weak interaction will allow energetic decays to occur sufficiently quickly that after some days or certainly years high-energy β emitters are gone. The exceptions are activities that are supported by chains. U and Th are the most important ones as they can photodisintegrate the deuteron. Other examples are ^{32}Si-^{32}P and ^{68}Ge-^{68}Ga. It has also been pointed out that highly forbidden transitions may lengthen the halflives. These cases tend to occur around closed shells where the density of states is low and the likelihood of a big mismatch in spin increases (e.g. ^{40}K, ^{56}Co, ^{60}Co). Other examples, very rare, are high-spin isomeric states.

The significance of U and Th as a background to the water Čerenkov signal has been discussed in Section B. The background contributions to the neutron signal from both the internal U and Th background as well as the ^{40}K and ^{56}Co backgrounds are also tabulated in Section B. This appendix gives the detailed decay schemes of ^{238}U, ^{232}Th, ^{40}K, and ^{56}Co.

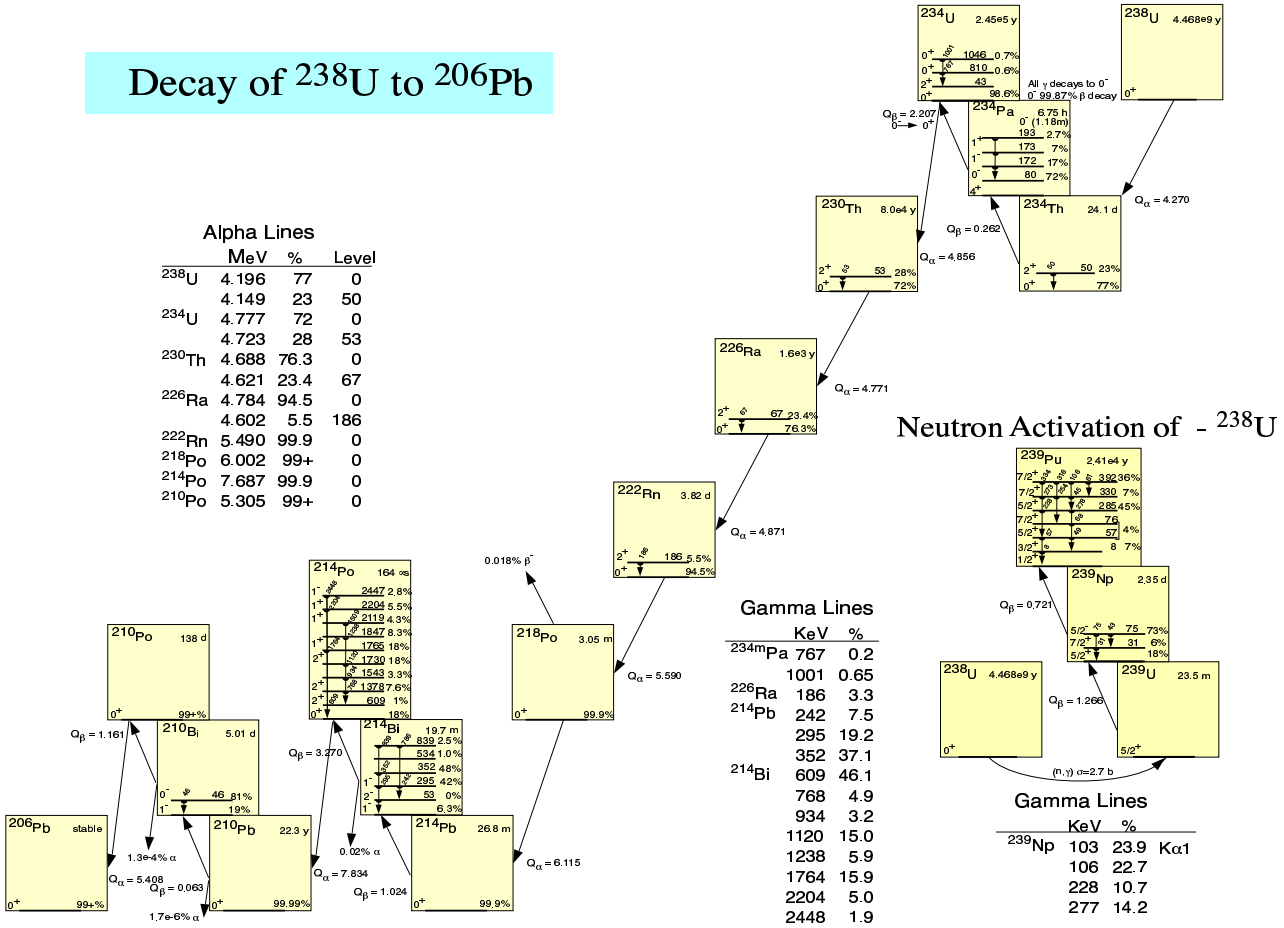

Figure C.1: Decay chain of ^{238}U $\rightarrow$ ^{206}Pb. Courtesy of Los Alamos National Laboratory.

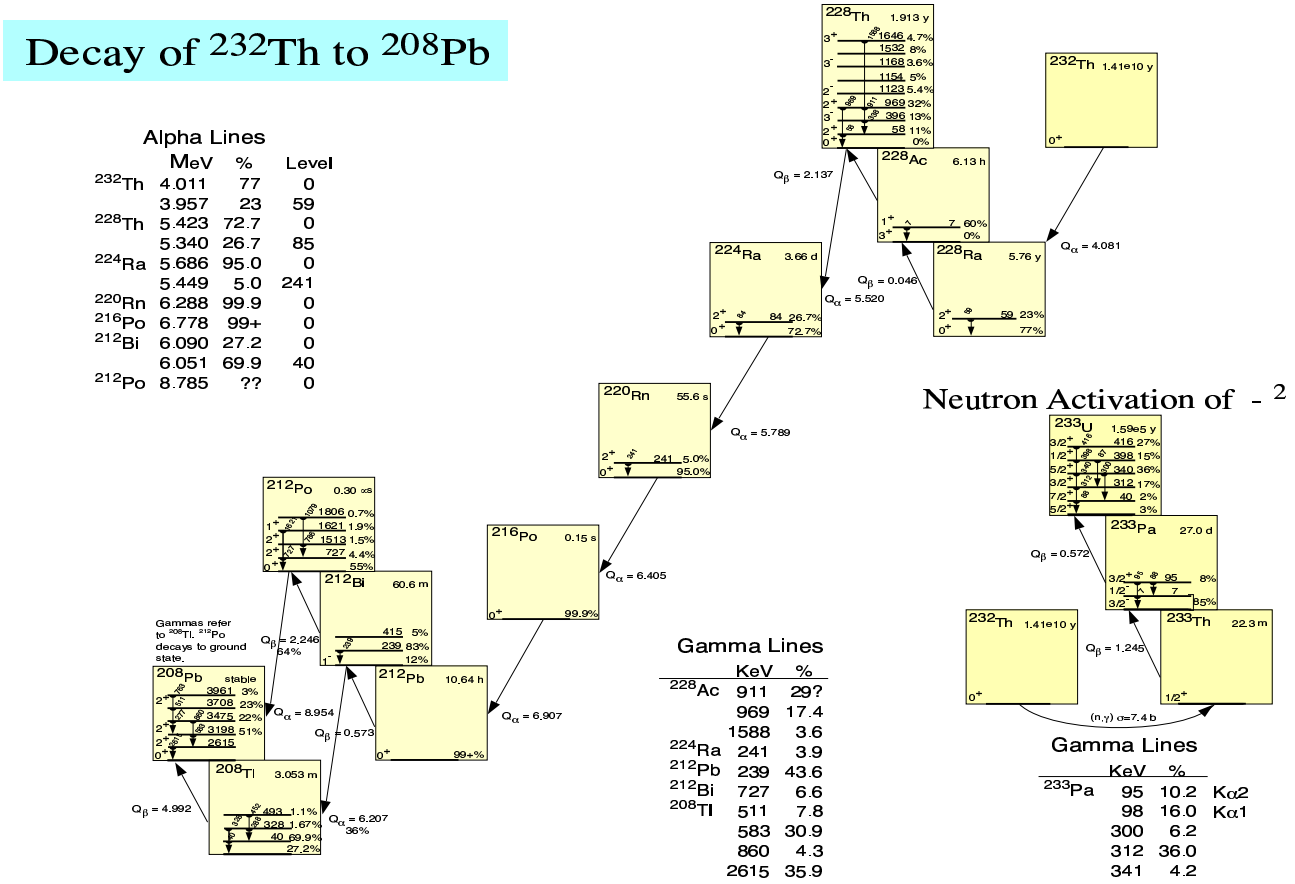

Figure C.2: Decay chain of ^{232}U $\rightarrow$ ^{208}Pb. Courtesy of Los Alamos National Laboratory.

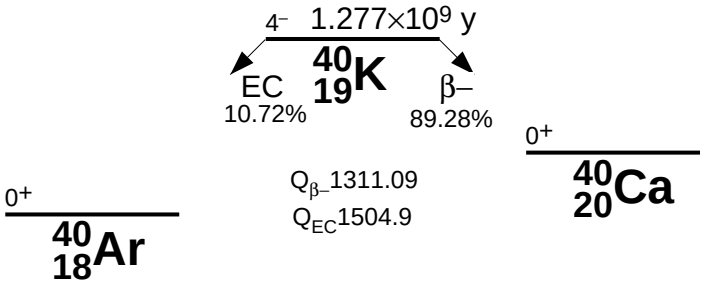

Figure C.3: Decay scheme of ^{40}K.

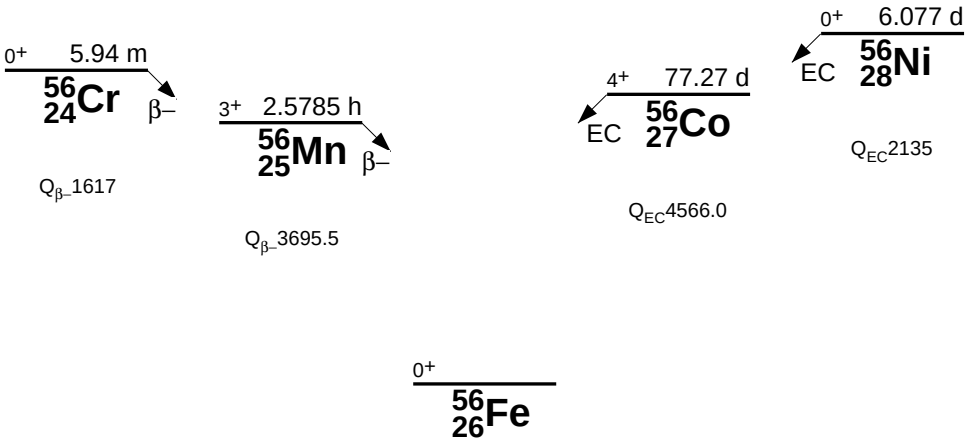

Figure C.4: Decay scheme of ^{56}Co.

C.1 Useful Numbers for the Calculation of U and Th Backgrounds

Table C.1 is a compilation of some useful numbers for the calculation of U and Th backgrounds.

Table C.1: Some useful numbers for background calculations. Properties and constants for U and Th in equilibrium.

1 AMU	1.66054×10^{-24}gm
Mass of Th	232.0381 amu = 3.85309×10^{-22} gm
Number of Th atoms per ppt	1.0817×10^{15} (whole array)
Half life of Th	1.405×10^{10} yr
Decay rate of Th	4.93343×10^{-11} yr^{-1}
Number of Th decays per year	53364.9 yr^{-1}
Branch to Parent	0.36
1 ppt Th	19,212 ^{208}Tl decays
Mass of U	238.029 amu = 3.95257×10^{-22} gm
Number of U atoms per ppt	$1{,}0545 \times 10^{15}$ (whole array)
Half life of U	4.468×10^{9} yr
Decay rate of U	1.55136×10^{-10} yr^{-1}
Number of U decays per year	63588.0 yr^{-1}
Branch to Parent	0.99979
1 ppt U	63588.0 ^{214}Bi yr^{-1}

APPENDIX D

CONSTRUCTION OF ^{3}HE-FILLED PROPORTIONAL COUNTERS FOR THE SNO NEUTRAL CURRENT DETECTOR ARRAY

This appendix describes the construction of the ^{3}He-filled proportional counters and gives an overview of the activities we were involved in. These include (a) receiving and preparation of detector components, (b) fabrication of the Neutral Current Detectors, and (c) the acceptance tests of detectors. The development and fabrication of the NCD electronics, the NCD data acquisition system, and the commissioning and deployment of the NCD array will be described elsewhere [34, 172].

The Neutral-Current Detectors are built in a joint effort by Los Alamos National Laboratory, the University of Washington in Seattle, and Lawrence Berkeley National Laboratory. The assembly of the proportional counters takes place in a Class-100 cleanroom facility at the University of Washington. Major components of the counters were produced by Mirotech (Toronto), Inc. (now CVD Manufacturing), IJ Research (Santa Ana), Inc., California Fine Wire (Grover Beach), and South Bay Cable (Idyllwild).

One of the major considerations during counter fabrication is the reduction of backgrounds from the materials of the NCD components themselves, from environmental influences, and from the fabrication process. The physics considerations concerning backgrounds in the NCD array are discussed in Appendix B. The techniques used to reduce and eliminate these backgrounds are described below.

D.1 Fabrication of Ultra-Pure Counter Bodies

D.1.1 Chemical Vapor Deposition of Nickel

Parts required for the NCD counters are made by chemical vapor deposition (CVD). CVD tubing is made from thermolysis of $Ni(CO)_4$ vapor at the surface of 2-inch diameter anodized aluminum mandrels heated to 2153 °C. The end material of this process is usually referred to as CVD nickel. The precursor to this process is high toxic and only three companies in world equipped to handle it INCO, Mirotech, Toronto, and BIRL/Northwestern University, Evanston. INCO uses it for purification. The cylindrical bodies and endcaps for the NCD array are made of ultrapure nickel fabricated at Mirotech (Toronto), Inc.

The CVD process involves the heating of nickel to approximately 100 °C at which temperature it combines with CO to form a nickel carbonyl ($Ni(CO)_4$). At this temperature only a few elements form carbonyls, resulting in a nickel vapor of higher purity than the original nickel stock. The vapor temperature is then increased approximately 200 °C at which point the Ni carbonyl cracks, allowing only Ni to plate out onto an aluminum mandrel at an average rate of 0.75 mm/hr. When the desired thickness is achieved, the process is stopped and the system is cooled with liquid nitrogen, allowing the two materials to separate. Thus one can prepare pure deposits of Ni by chemical vapor deposition (CVD) from the carbonyl. The forward reaction occurs at 100 °C, and the reverse reaction at 200 °C. Very few elements form carbonyls, and none reversibly in this temperature range.

$$Ni + 4CO \rightarrow Ni\ (CO)_4 \tag{D.1}$$

A limited number of elements (Pb, Ra, Th, and U not among them) react with CO to form carbonyls, and the metals formed by chemical vapor deposition (CVD) from this precursor can be expected to be free of the most troublesome radioisotopes. The elements that go through carbonyl process are Cr, Fe, Ni, Co, Cu, Mo, and W. Uranium, Thorium, Ra, and lead, however, are left behind. The nickel deposit has properties very similar to conventional metallurgical products. Nickel is the strongest material in pure, elemental form besides tungsten. It is also a relatively inert metal and is therefore ideally suited as

a fabrication material for the NCD array. The CVD process results in very low U and Th contamination (1-2 ppt Th). Vapor-deposited nickel is a structural material with low alpha activity. Radiochemical neutron activation analysis has shown Th levels in the bulk material of order 10^{12} (1 ppt) by weight or less.

CVD Ni tubing is made on Al mandrels while the CVD nickel for the endcaps is deposited on machined stainless steel endcap forms. The body of each proportional counter is a 5.08 cm ID chemical-vapor deposited (CVD) nickel tube. The CVD surface against the mandrel is an accurate replica and appears shiny. Free CVD Ni surfaces are matte and dark and have about 13% reflectivity [181]. Imperfections in the anodizing of the mandrel map into raised patches or splotches on the inside nickel surface. When separation occurs, some material is also taken from the mandrel, causing the imperfections to worsen. As additional tubes are made on a given mandrel, the surface splotch density increases and the appearance of the tubes deteriorates. Of considerable concern is that these splotches may be harboring high concentrations of Al, a material known to contain Thorium at the 1-10 ppm level. Since the nickel is required to be $<$ 10 ppt Th contamination from Al becomes a concern at the 1-10 ppm level.

Some of the problems that were encountered during the production were pinholes in the tubing and aluminum splotches on the inside of the nickel CVD tubes from the mandrel. Many of the raw CVD tubes contained fragments of Al which originated from the deposition mandrel. However, studies of the depth profile of this Al indicated that it resided within approximately 13 microns of the surface. Thus by etching away 26 microns of material, the radioactivity could be removed. The problem is the Rn-daughter ^{210}Po which cannot be removed by etching because it plates out. An electropolishing technique, which keeps the radioactivity in solution, has been implemented in tandem with a final acid etch to produce tubes of sufficient cleanliness.

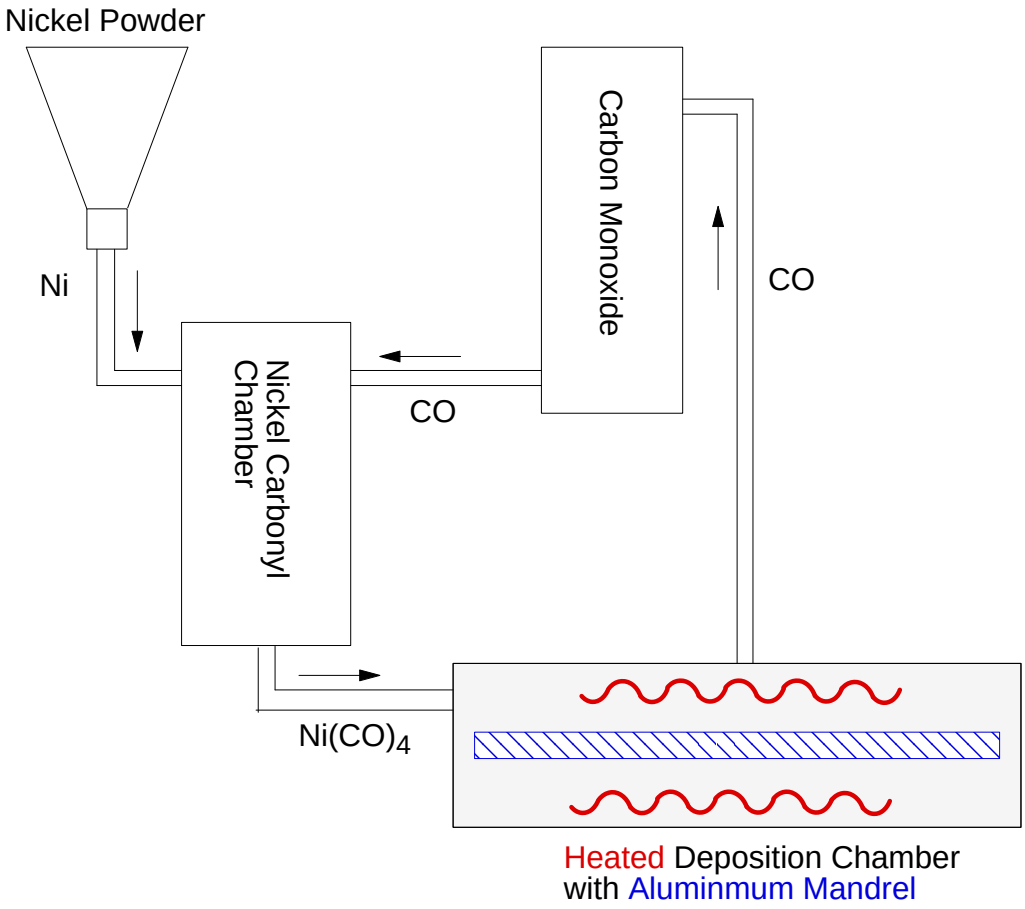

Figure D.1: Schematic of the chemical vapor deposition (CVD) of nickel.

D.2 Preparation of Counter Bodies

The Ni CVD tubes are produced by MiroTech, Inc.. in Toronto and shipped to the NCD production facility at the University of Washington in Seattle. Prior to use in the fabrication process the tubes undergo extensive quality control checks and preparation.

The inside and outside surfaces of each tube are inspected visually for loose particles, cracks, and nodules. The physical properties of each tube such as length, diameter, wall thickness, roundness and straightness are recorded for quality control purposes. Before further processing the raw tubes are first cut to 2 meter length by removing both ends. CVD Ni samples from the ends are retained in a nylon bag and used for radioassays. All tubes are stored in nylon bags to minimize the exposure to Radon. As part of the quality control process the tubes are leak checked using a flat neoprene disk plug to blank off tube ends. This permits leak checking up to the edge of the tube. A helium-filled jacket is used to leak check each tube. The location of leaks is determined by spraying a continuous flow of helium along the tube. The neoprene stoppers are usually given at least 2 hours before re-use as they will have absorbed helium. Leaks and pinholes in the CVD Ni tubes are removed by either shortening the tube or laserwelding them shut in the cleanroom. To avoid contamination from the leak checking procedure the ends of each tube at and beyond O-ring are cut. A digital imaging technique is used to determine and document the Al splotch density at the ends of each tube.

Before the tubes are cut into pieces of appropriate lengths the tubing is electropolished to remove surface contaminants (see Section D.3). After electropolishing the tubes are cut, swaged, flared, and deburred. Five different tube lengths of 200, 100, 50, 16.13, 5.59 cm are used in the construction process. All except the 5.59cm pieces are flared and set after being cut to size. The dimensions of the flared and straight ends are 2.036" ID, and 2.036" OD respectively. The straight end flare will be variable depending on the tube thickness. Most tubes will have to be compressed at the endcap weld location to ensure tight fit of the endcaps during the counter fabrication process. The flared ends will point up in the array. The final mass of each CVD Ni tube is recorded upon receipt and after electropolish and etching.

The electropolishing and etching process removes surface debris stripped off the mandrel during the fabrication process and also removes surface contaminants. Trace amounts of electronegative contaminants such as oxygen and water degrade severely the performance of the gas in a sealed counter. Consequently, counter surfaces are electropolished, acid-etched, baked under vacuum, and purged with boiled-off N_2 prior to gas fill.

D.3 Surface Contaminants on the NCD Counter Bodies

Stringent purity requirements for the NCD Array make it necessary to avoid or remove any surface contaminants from the NCD components during the fabrication and assembly process. Any radioactive contamination of the NCD components can either cause internal α backgrounds or external γ backgrounds that contribute to the photodisintegration of deuterium.

The isotopes of particular concern are ^{238}U and ^{232}Th. The decay chains of each include γ's that can dissociate the deuteron and add to the neutron rate. For example, 0.5 μg of ^{232}Th in the entire NCD array would result in a $\sim$ 1% neutron background to the SSM NC interaction rate. By comparison, the same amount of ^{232}Th in D_2O itself accounts for an estimated 10% SSM. Furthermore, γs can also produce Čerenkovsignals and contribute to the backgrounds measured with the PMT array. The sources of ^{238}U and ^{232}Th are bulk CVD nickel, splotches of Al_20_3, dust, and water impurities.

The main α background comes from ^{210}Po. This background contributes to the signals recorded in the NCD array. Untreated, α rates would swamp the NCD data and could produce false neutron signals due to the effect of pulse shape distortions at the end of each counter.

D.3.1 Radon Contamination of CVD Ni Tubes

During counter assembly care was taken to prevent radon daughter contamination from being a concern. The radon level in the cleanroom at the University of Washington where the detector fabrication takes place was measured to be <0.25 pCi/l. To further reduce the exposure to Rn all counter tubes and endcaps are stored in heat-sealed nylon cleanroom bags after the etch. Nylon has been found to be remarkably impermeable to Rn. The air exposure of all etched NCD components is monitored and recorded. It is minimized by flushing cleanroom air out of all storage bags with boiloff nitrogen.

Before fabrication of the counters most of the Ni tubes were stored in an underground location at Index, Washington, to reduce cosmogenic activation. The air at that location contained very high level of Rn above the maximum reading of a Rn monitor. As a re-

sult, counters constructed from these tubes had very high ^{210}Po-alpha decay rates of ∼800 $\alpha/m^2/day$. The noble metal Po adheres very strongly to Ni and plates out on Ni in acidic solutions. Hence electropolishing is the only technique that can be used to remove Po. Electropolishing which keeps the radioactivity in solution reduces the tubes to this level from an initial rate of 10^5 $\alpha/m^2/day$. With systematic studies of the electropolishing procedure the background reduction could eventually be improved and typical alpha rates of about ∼100 $\alpha/m^2/day$ were obtained.

To test the effect of radon contamination in NCD counters a CVD Ni tube was exposed to room air with a measured radon content of 1 pCi/l for 48 hr, and was then assembled as one half of a 80-cm NCD test counter, with the other, unexposed half acting as a control. The measured rate of ^{210}Po alphas was in good agreement with that expected on the basis of the foregoing calculation. It is mysterious, however, that the Po does not appear to be supported by its grandparent, ^{210}Pb which has a half-life of 22 years, but decays away with the 138-day half-life of ^{210}Po. Evidently Po is sufficiently mobile that it remains in equilibrium with airborne radon, even though the Pb is undoubtedly fixed to surfaces.

D.3.2 Aluminum Contamination of Ni CVD Tubes

During the quality control on the Ni CVD tubes splotches of Al were found on the inside of the raw tubes. The Al splotches are from the surface of the Al mandrel on which the Ni CVD tubes are produced. Th and U occur in Al typically at the 10 ppm level and are a significant concern for internal backgrounds to the counters.

The Al contamination of the Ni tubes was studied using SEM (Scanning Electron Microscopy) and ICP mass spectroscopy (Inductively Coupled Plasma Mass Spectroscopy). SEM is used to imagine the splotches. Elemental abundances can be determined from the scattered x-rays, averaged over a depth of approximately 2 μm. The sensitivity of this technique is of the order of 0.5%. A more sensitive technique is required to address the issue of Al contamination quantitatively. ICPMS works by vaporizing a fluid sample and drawing it into a plasma torch. After the sample is ionized, it is accelerated and electrostatically steered, so to identify the various mass components.

Using SEM it was found that the Ni test samples contained Al oxide, which is expected because the mandrel was anodized. In addition, traces of Si, S, Cl, Ca were found. They appear to be associated with the Al oxide. Seeking a higher sensitivity for Al, the concentration of Al was determined using ICPMS. In principle, one could measure both the Al and nickel intensities on the ICPMS, dividing to give their ratio. As the Al/Ni ratio is usually very small a different approach was taken and the nickel content was determined by weight before and after the etch.

The results of these studies showed that the Al content falls off with depth. A summary of the results obtain by [171] is shown in Figure D.2. Based on these results a procedure was implemented for electropolishing the inner surface to a depth of approximately 20 μm. This is followed by a 10 min etch which removes an additional 2 μm from each side, thus removing a total of approximately 22 μm of material from the inner surface. The resulting total contamination of Al is estimated to be less than 1 ppt. The effectiveness of this procedure in removingthe Po activity of the Ni CVD tubing is shown below in Figure D.4.

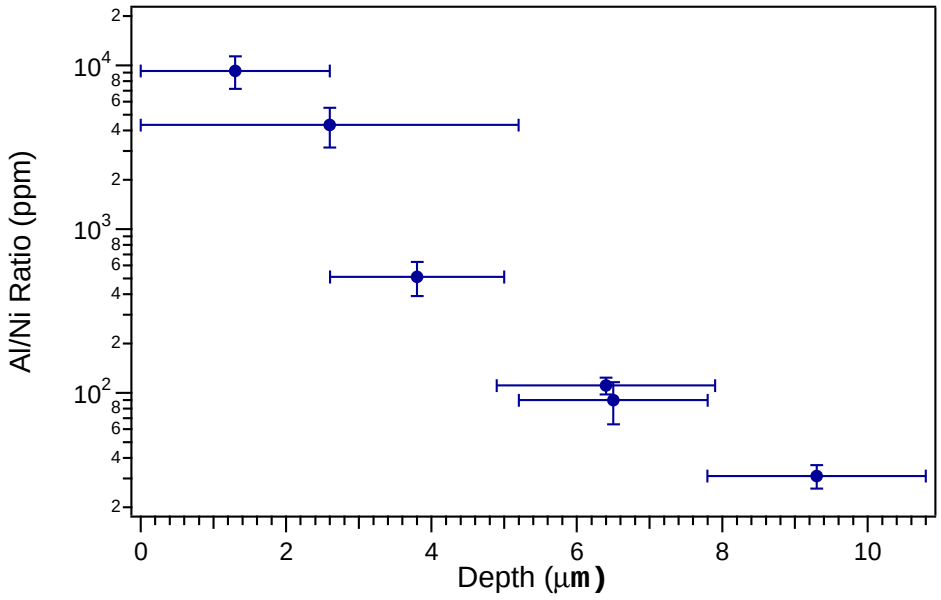

Figure D.2: Ratio of Al/Ni versus depth inside the Ni CVD tubing before electrochemical cleansing.

D.3.3 Contamination from Handling and Assembly

The nickel that comprises the bulk of the fabricated parts (tubing, endcap bodies, sleeves, seal plugs, and couplers) is very pure owing to the chemical selectivity of the process used to produce $Ni(CO)_4$ and subsequently decomposes into metallic nickel. However, surfaces of these parts can become contaminated through handling, air exposure, and contact with mandrels on which they are made. To mitigate the need for extreme care in handling and for special mandrel materials, the surfaces are electropolished and etched to leave only pure nickel immediately before the parts are assembled.

In addition, all tools that come in contact with counter parts are made from stainless steel. It is also insured that all construction lubricants, solder fluxes, and other materials used during counter assembly have a high radiopurity so any left-over residue would not be a concern.

D.4 Removal of Surface Contaminants I: Electropolishing of CVD Nickel Tubes

The CVD Ni tubes are electropolished to remove ^{222}Rn daughters, specifically ^{210}Po, which has a 138-day half-life and decays via a 5.3 MeV α. The electropolish and subsequent acid etch also remove Al and Al oxide. Po adheres to Ni very well and was introduced during the underground storage of the tubes at Index, Washington. The etching is designed to remove the Al oxide from the mandrel. The tubes are first etched and polished then rinsed and vacuum baked as the final preparation procedures.

D.4.1 Electropolishing

Electropolishing is the electrolytic removal of metal in a highly ionic solution by means of an electrical potential and current. The work piece is immersed in a liquid medium (electrolyte) and subjected to direct current. The metal part is made anodic and a metal cathode, usually 316L stainless steel or copper, is used. The direct current then flows from the anode, which becomes polarized, allowing the metal ions to diffuse through the liquid to the cathode, removing metal at a controlled rate. The process is essentially the reverse of electroplating. During electroplating, metal ions are deposited from the solution onto the work piece while during electropolishing the work piece itself is dissolved adding metal ions to the solution.

The amount of metal removed depends on the specific bath, temperature, current density, and the particular material being electropolished. Generally, on stainless steel, 0.005 in. is removed in 1,500 amp-minutes per square foot. The amount of change to the metal is highly dependent upon the metal itself and how it has been processed up to the point where it is electropolished. Other factors, such as the geometry of the work piece, affect the distribution of the current and, consequently, have an important bearing upon the amount of metal removed in local areas.

Electropolishing can be used to simply remove the surface of metals or enhance it. In the case of stainless steel alloys, and important effect is caused by differences in the rates of removal of the components of the alloy. For example, iron and nickel atoms are more easily extracted from the crystal lattice than are chromium atoms. The electropolishing process

removes the iron and nickel preferentially, leaving an enhanced surface layer consisting of corrosion-resistant chromium oxide.

Electropolishing removes surface metal in a unidirectional pattern that is both stress- and occlusion-free, microscopically smooth, and often highly reflective. Plus, improved corrosion resistance and passivity are achieved on many ferrous and non-ferrous alloys. Deburring is accomplished quickly. The current density is higher on the burr while oxygen shields the valleys, enabling the constant exposure of the burr tip. Electropolishing act like a stress-relief anneal by removing Hydrogen from the surface. In general the following components are used in the electropolishing process:

1. *Electropolishing Tank:* Polypropylene usually 3/4 to 1 inch thick. Withstands temperatures of 180 - 190 °F.

2. *Cathode:* The material that is connected to the negative end of the rectifier that accepts the metal ions from the work piece. The cathode is usually made out of metal and is shaped in such a way as to provide even current densities to the surface of the work piece.

3. *Agitation:* Mechanical agitation is the optimum method, which brings fresh solution to the part surface for faster electropolishing. Other agitation methods are stainless steel mixer, filter-pump, or separate pump.

4. *Temperature:* Most electropolishing solutions must be heated and cooled during the operating period. Heating can be accomplished by heater tapes. Passive cooling through a water rinse is usually sufficient.

Only three process steps are required to electropolish most metal surfaces. After some metal preparation and cleaning the work piece is electropolished and rinsed to stop the process. Post-rinse treatment may follow.

D.4.2 Electropolishing CVD Ni Tubes for NCD Counters

The schematics of the electropolishing installation used in the NCD production facility at the University of Washington is shown in Figure D.3. The cylinder of the external polisher is stainless steel 304 seamless with a 3.00" outer diameter (OD). The other components are PVC and high density polypropylene. The anode is made of a 1 inch diameter Ni 270. Seals are Teflon or buna-n O-ring and silicone.

The outside of the CVD Ni tubes is electropolished by inserting the raw Ni tube into a stainless steel tube of 5" inner diameter and filling the space between the two tubes with acid. The acid is heated through the outer stainless steel tube through the application of heater tapes. The ends of the electropolisher tube are sealed with electrodes and silicon plugs.

For polishing the inside of the CVD Ni tubes, the interior electrode, an aluminum tube roughly an inch in diameter, is lowered all the way through the NCD Ni tube. The ends are sealed and acid is pumped in to fill the volume between the two. The exterior electrodes are fastened to the NCD tube's outside using spring-loaded couplers. The electrode tube contains a closed circuit water pipe circulating heated water. This heats the electrode, and in turn the acid.

To stop the electropolishing process the Ni tubes are directly exposed to deionized water at room temperature after the acid solution has been transferred into storage tanks. Double rinses with deionized water at room temperature easily cool the tubes.

During the electropolishing process we found evidence for circulation and agitation of the acid. Running 310 to 620 amps through the solution caused significant liquid motion and agitation. The temperature rarely got above 150 °F, so the acid never boiled but bubbles were visible during the entire electropolishing process. We assume that the acid is well mixed during the entire electropolishing process.

The concentration of nickel in solution was measured during the electropolishing process with a colorimeter by shining an LED through clear polypropylene tubing.

During the rinsing stage the current was sustained to keep elements in solution from plating out. It was found that the critical variables for the electropolishing process are the

temperature at etch and the current that goes through the workpiece. The acid was heated with tube in place. The etching during the heating process was negligible. To insure the mechanical stability and integrity of all tubes during the following assembly process 1010 g was the minimum mass requirement for CVD Ni tubes post etching. For CVD Ni tubes the change in wall thickness due to surface removal can be calculated by dividing the mass removed in g by 2.84 g/μm.

The electropolishing sequence for NCD CVD Ni tubes is summarized in Table D.1. Typical parameters of the electropolishing process are given in Table D.2. The acid used in the NCD electropolisher is 1 M H_2SO_4. In this setup the acid is transferred from storage tanks to the electropolisher using air pressure.

In the NCD fabrication the external surface of the raw CVD Ni tubes is polished first, followed by two rinses with deionized water. After rinsing, the tubes are taken to the interior polish. After completion of the polishing process the tubes are rinsed and dried in a low-dust environment. The weight of each tube is recorded after the electropolishing to determine the mass removal.

Table D.1: Sequence of steps in the NCD electropolishing process.

Step	Electropolish	Acid Used
I	external	recycled acid from internal polish
II	internal	recycled from previous tube
III	internal	fresh, unused sulfuric acid

Table D.2: Parameters of NCD electropolishing process.

Tank Used for Polish	A (exterior polish)	B (interior polish)	C (interior polish)
Current	310 A	620	620
Acid	H_2SO_4, 1 M	H_2SO_4	H_2SO_4
Pre-heat Temperature	130 ± 10 °F	130 ± 10 °F	130 ± 10 °F
	54.5 ± 5.5 °C	54.5 ± 5.5 °C	54.5 ± 5.5 °C
Mass Removal	5 g (0.9 g/l)	42.6 g (10.1 g/l)	14.2 g (3.4 g/l)
	2 μm	15 μm	5 μm
Run Time	45 sec	2-3 min (heated)	2-3 min (heated)
		7 min (cold)	7 min (cold)
Sensor Technique	light sensor	colorimeter	colorimeter

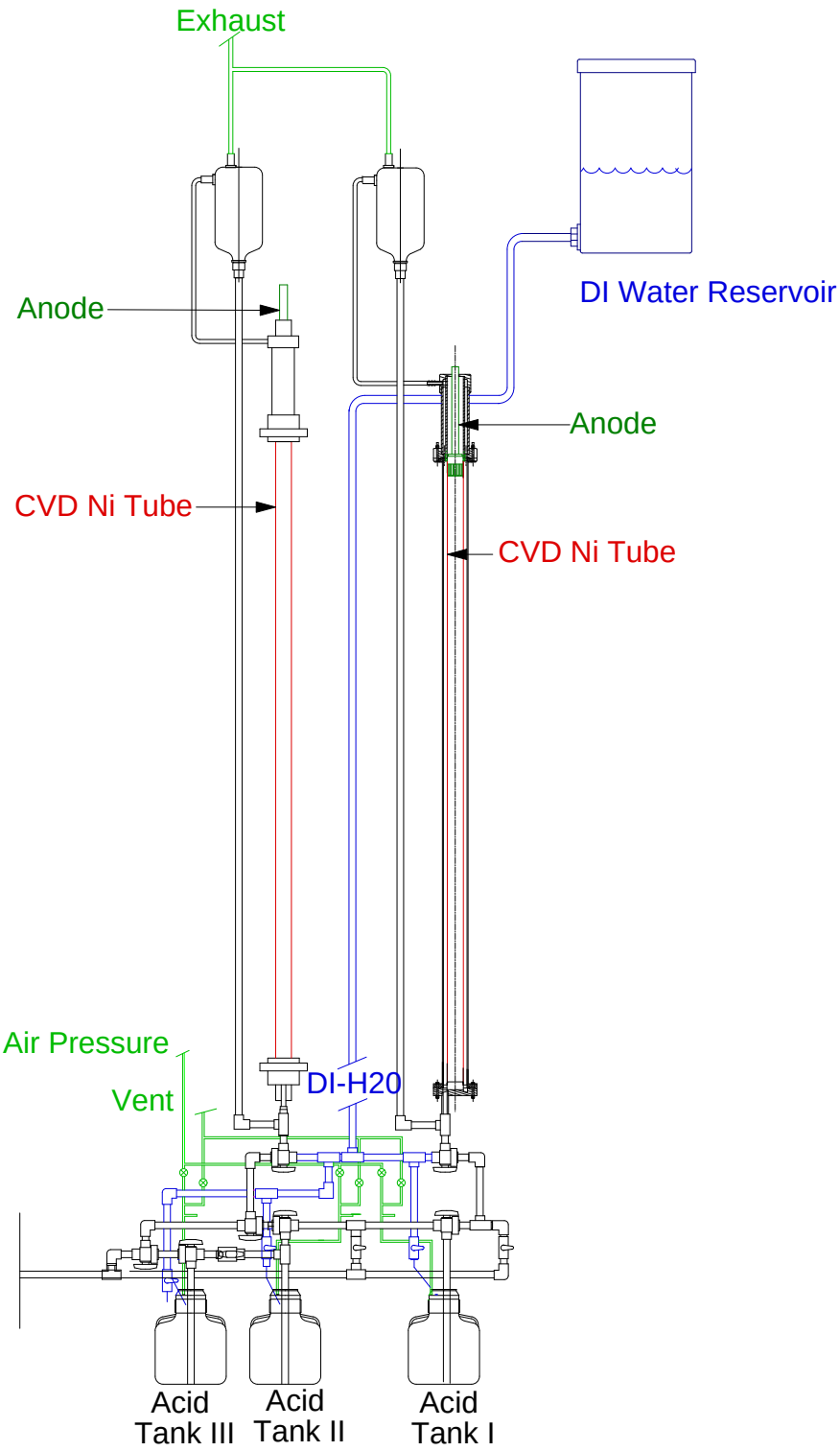

Figure D.3: Schematic of the electropolisher used during the NCD fabrication process.

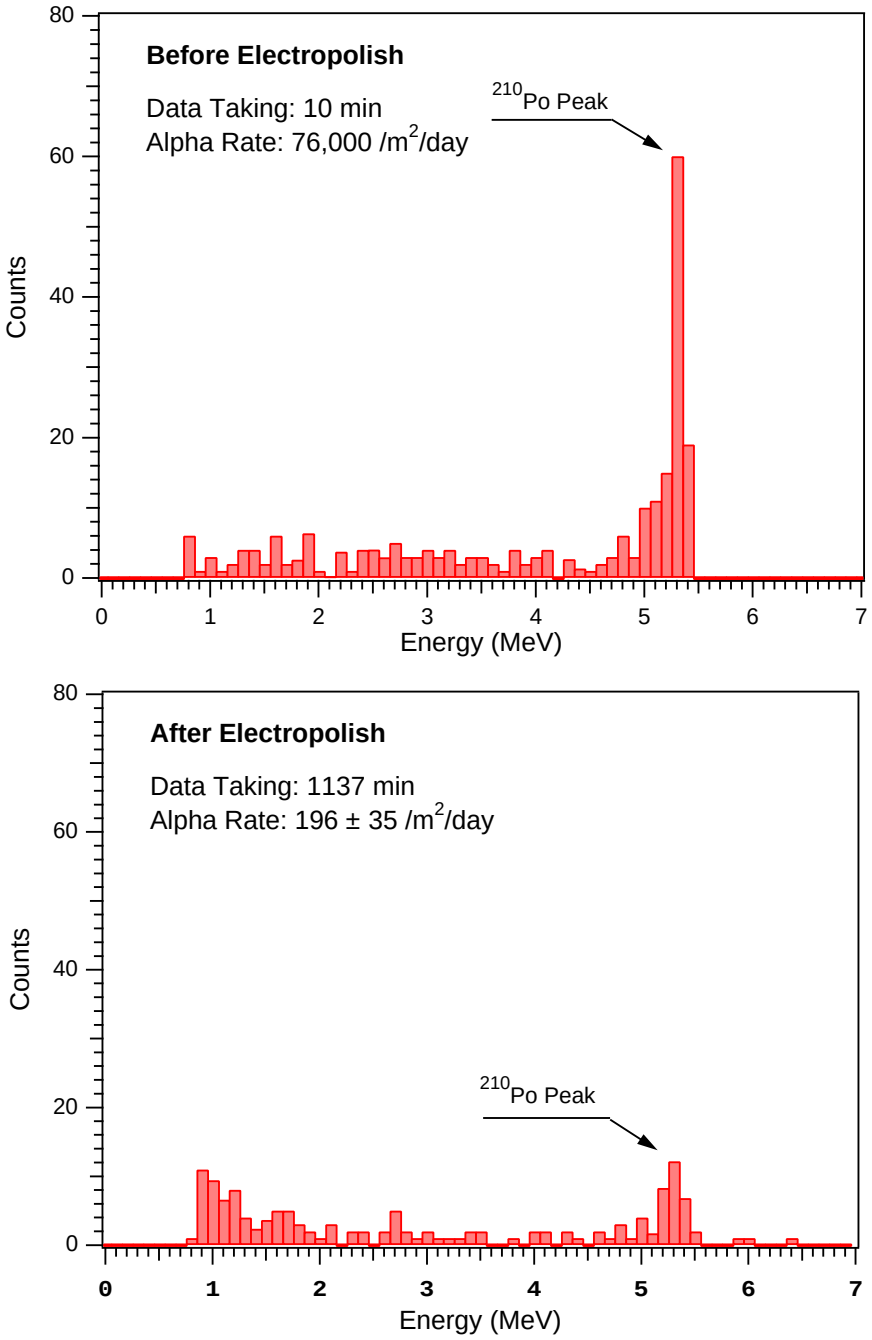

Figure D.4: Alpha spectrum of Ni CVD tubing before and after the electropolishing process. Before the treatment the peak of ^{210}Po is clearly visible in the spectrum. The estimate of the α rate is based on the energy window between 5.0-5.5 MeV.

D.5 Removal of Surface Contaminants II: Etching of CVD Nickel Tubes

During assembly of the detectors, all CVD Ni parts are etched to remove any surface contamination from radon daughters, tool impregnation and dust. To mitigate the need for extreme care in handling and for special mandrel materials, the surfaces were etched away to leave only pure nickel immediately before the parts are assembled into finished detectors. Special care was taken to insure that contamination does not occur after the etch step.

During the etching process the tubes are soaked in room temperature $HN0_3$ and HF for 10 min, then rinsed and transferred to the cleanroom. The etch tank has 4 different compartments that can be drained individually to waste removal tanks. The following acids are used in the electropolishing and etching procedure: HNO_3 (68-70% redistilled HNO_3), H_2SO_4 (50% redistilled H_2SO_4), HF (48% redistilled HF). The composition of the etch and rinse baths is summarized in Table D.3.

Tubes are mounted horizontally on an etch frame. The etch baths are agitated with the tube frame while tubes are in each acid and rinse bath to insure uniform etching. The etch time in the primary bath is about $\sim$10 min at room temperature (72 °F).This removes about 2 microns of material. The etch time is $\sim$1 min in the secondary etch bath, and both the primary and secondary rinse bathes. After each etch bath the parts are rinsed in 18 MΩ-cm deionized water purified by reverse osmosis. The tubes are then transported into the cleanroom to be baked. The amount of Ni which was removed during the etch procedure is determined by weighing the tube after it has been baked. The two acid etch baths are replaced after the equivalent of 30 m of tubing have been etched. The first two rinse baths are changed every 10-12 m of tube etched. When the baths are changed the first rinse bath has a Ni concentration of $\sim$29 ppm. The second rinse bath has a Ni concentration of $\sim$ 0.38 ppm. The tubes are etched at room temperature (72 °F). To account for variations in the room temperature the etch time is corrected for by the temperature of solution.

The biggest uncertainty in the mass removal from the CVD nickel tubes during electropolishing and etching is human error. During the etching process the uncertainty in 6 g comes mainly from the etch time in the primary etch bath. The maximum error is estimated to be about 20%. The goal of the electropolishing process is to remove about 60 g.

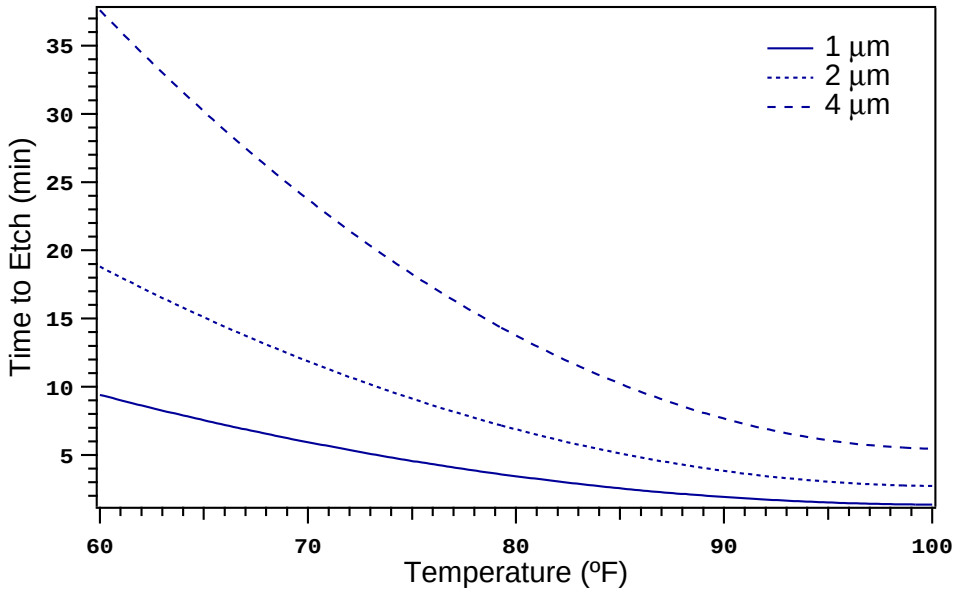

Figure D.5: Time to etch for various thicknesses of CVD Ni.

However, it was found that sometimes 49 g or 53 g were removed. Therefore, we estimate the uncertainty in 60 g mass removal to be about 20%.

Before the tubes are transferred to the laser welding station for assembly they are baked out in a 24 hrs-long pump and bake cycle at 150 C. During bakeout they are pumped to a pressure below 10^{-9} Pa with a hydrocarbon-free turbomolecular pump. After the bakeout the tubes are sealed in nylon sleeves under nitrogen. The air exposure between the etch and storage is recorded. The weight difference of a 200 cm long nickel tube between wet and air dry is about 20 g. It is estimated that $\sim$1 g of water and other gases in the Ni are removed during bakeout.

Table D.3: Etch and rinse bath compositions.

Tank 1	etch tank 1	49.1 l of 18-MΩ water + 15.4 l of "GFS" nitric acid + 0.46 l of "GFS" HF acid; (strongest solution, HF so that heavy ions stay in solution)
Tank 2	etch tank 2	62 l of 18-MΩ water + 3.25 l of "GFS" nitric acid (more dilute nitric acid, no HF)
Tank 3	rinse tank 1	65 l of 18-MΩ water, 3 cc acetic acid
Tank 4	rinse tank 2	65 l of 18-MΩ water, 3 cc acetic acid

Table D.4: CVD Ni mass removal during NCD tube preparation.

Process	Target Mass Removal	Estimated Uncertainty
Electropolishing	60 g	20%
External polisher	5 g	
1st Internal	25 g	
2nd internal	30 g	
Etching	6 g	20%
Total	66 g	20%

D.5.1 Reducing Water Contamination: Deionized Water Filtration

During polishing and etching the tubes are rinsed with several hundred liters of water. U and Th dissolve in water as irons or iron complexes. Hence a deionizing water filtration system is used to purify the building water before mixing the acids and rinsing the tubes. It was found that the characteristics of the water as supplied by the physical plant at the University of Washington change with seasons. It is possible that dissolved solids, organics, bacteria, or colloidal silica contribute to the varying water quality.

D.6 Fabrication and Preparation of Endcaps

D.6.1 Assembly of Endcaps

Endcaps blanks produced by Mirotech, Inc. are converted by precision machining to the final specifications. The final endcaps are inspected, degreased, etched, rinsed, dried before being shipped to IJ Research where the endcap bodies and feedthroughs are assembled. At IJ Research, Inc. the silica tubes are soldered into the endcap body. The feedthroughs consist of Suprasil fused silica which is cut and firepolished. IJ metallizes inner diameter with pyrolytic graphite coat (to conductive level only). Cr-Ni bands are RF sputtered on outside for solder seals. The amounts of Cr and Ni used during this process are listed in Table D.5. The air exposure of each endcap is monitored to track the radon exposure. The endcaps are cleaned in DI water and isopropyl alcohol, followed by an air dry. The integrity of the assembled endcap is tested in a 2-lb push and He leak tester. During shipment and transit the temperature of the endcaps is always recorded using tell-tale thermometers.

Table D.5: Estimated usage of Cr and Ni in endcap assembly.

Metallization of Silica Feedthroughs	
Cr 0.48" × ∼1000 Å layer on outer	0.14 mg (0.1 gm/array)
Ni 0.48" × ∼5000 Å layer on outer	0.85 mg (0.6 gm/array)

D.6.2 Removal and Control of Endcap Contamination

Any metallization on the firepolished end of the quartz tubes resulting from the RF sputtering at IJ Research is removed by acid etching to prevent radioactivity from being located in an extremely sensitive spot in the NCD counters. Backgrounds and spurious pulses originating at the end of the counters can mimic p+t signals from a ^{3}He(n,p)^{3}H reaction. The etch solution consists of 1 part each water, HF, and HNO_3. Etching time is about 20 min at 37 °C. This process etches 0.275" up the quartz. When etch is completed, quartz is rinsed

with DI water both in and out of quartz tube and dipped in alcohol to remove water. The piece is allowed to air dry.

Endcap sleeves are also produced by chemical vapor deposition on aluminum mandrels. They are cut to length while still on the mandrel, then the mandrel is dissolved out in hot NaOH. The sleeves are acid-etched to remove the surface and pretinned by using copper-tip iron in Ar atmosphere.

After receipt at the University of Washington the endcaps are visually inspected for solder quality (blobs, voids), straightness of sleeve, overall cleanliness, voids in carbon coat, metallization on firepolished end, "chalk-like" residue on solder joints, "grunge" on quartz in conductor gap. Each endcap is weighed and its dimensional quality is checked with a jig. The length of the quartz tube that will extend into counter is measured and recorded. An etch procedure is used to remove any metallization from firepolished end. A drill-driven stainless steel brush is used to clean quartz between conductors. Residue on soldered surfaces due to flux are removed with a small hand-held stainless steel brush. A lint-free Q-tip moistened with alcohol is used to remove any excess particles produced by brushes. If an endcap has a seal hole a copper pinch-off tube is attached. Pinch-off tubes are prepared by annealing, etching, and pretinning.

To remove any air deposited contaminants before and endcaps is assembled into a completed counter body the internal-end of the quartz tube is dipped in 5% nitric acid. The quartz tube is lightly scrubbed with lint free cloth and isopropanol. It was noticed that the cleanliness of the quartz tube is critical for its microdischarge behavior. The endcaps are dipped in alcohol to remove water and allowed to air dry. The endcaps are then loaded into a Phototron rack and put into a pump and bake at 10^{-4} Torr for warm bake for 3-4 hrs. Air exposure is monitored and recorded during the entire process. Following the Phototron treatment a leak check is performed on the endcaps. Performing the leak check at this point ensures that any alcohol has been removed from any potential leaks. As a final QA check, the endcaps undergo a microdischarge test. Each endcap weighs about 13 g.

D.6.3 Radiochemical Neutron Activation Analysis of Endcap Bodies

The radiopurity of the CVD Ni bodies of the NCD endcaps is checked using neutron activation analysis of endcap samples. The results are summarized in Table D.6.

Table D.6: Radiochemical neutron activation analysis of the endcap CVD Ni bodies.

Sample	Date	U, pg/g	Th, pg/g	Reactor	Etch
Endcap	4/96	-	8(1)	UITR	10% HNO_3 20 min
Endcap	4/96	≤ 4.3	≤ 3.5	UITR	hot 30% HNO_3 2.5 min
Endcap EC908	6/96	≤ 3.7	5.2(6)	MURR	No Etch
Endcap EC808	6/96	≤ 1.8	5.7(7)	MURR	10% HNO_3 20 min
Endcap EC402	6/96	≤ 1.3	5.2(6)	MURR	50% HNO_3 1.75 min
Endcap EC109	6/96	≤ 5.3	3.8(5)	MURR	50% HNO_3 + 0.2 M HF 0.75
Endcap EC402	6/96	≤ 1.3	4.3(5)	MURR	10% HNO_3 + 0.2 M HF 20 min
Endcap EC109	6/96	1.7(5)	5.3(5)	MURR	710% HNO_3 + 0.4 M HF 20 min
Endcap EC908	6/96	-	6.7(11)	MURR	20% HNO_3 + 0.2 M HF 20 min

D.7 High-Voltage Microdischarge Test of Endcaps, Delay Lines, and Preamplifiers

The sensitivity of the Neutral Current Detectors and their stringent background criteria make it essential to minimize all spurious pulses including signals induced by high voltage. A number of sources that cause noise pulses due to high voltage microdischarges have been identified. A variety of methods is used to reduce or eliminate them:

- *Noise generated in or picked up from HV power supplies:* Filtering is used at the preamp HV input.

- *Leakage or discharge in cables or at HV connectors:* Connectors can be treated with conductive compounds on the electrically conducting inner surfaces and insulating compounds on the outer surfaces, to inhibit leakage currents and breakdown. It was found that silicone grease usually helps. All connections are carefully cleaned and handled in a clean manner to maintain cleanliness.

- *Leakage currents in HV standoff capacitors:* Use Mylar HV capacitors (Southern Electronics Corp.), which have low intrinsic leakage currents, low inductance, and low microdischarge rates.

- *Breakdown in the proportional counter:* Care was exercised in counter construction to eliminate possible sources of breakdown such as sharp points, roughness of the electroplated surfaces, lint, dust, etc.

- *Microscopic surface discharges in counter components*

The microdischarge on counter components has been investigated in great detail. The results of this study have been published in [61] and are summarized below. Studies have shown that this discharge effect occurs mainly at interfaces and in microscopic voids between dielectric surfaces, on contaminated surfaces, and on surfaces with imperfections. Because of its occurrence in various materials and environments, microdischarge is a concern for

all low-background detectors that operate under high voltage. In this section we discuss the phenomenon of surface microdischarge induced by high voltage, and techniques for the reduction and discrimination of such breakdowns in ultra-low background proportional counters.

D.7.1 High-Voltage Testing

Prior to the assembly of the Neutral Current Detectors all critical construction components of the proportional counters undergo testing for microdischarge. The individual components are placed in a specially constructed high voltage test setup and elevated to 2400 V. Each component is monitored for high voltage breakdown and any such breakdown or discharge event is digitized for later review. Components that show a high microdischarge rate are not used in the construction of counters. Once a detector has been assembled, the entire counter is microdischarge tested again at 2400 V, well above the typical operating voltage of 1835 V. All events are digitized and recorded. Any detector that exhibits more than 3 microdischarge events in a 12-hour test period is disassembled and repaired. This limit is high compared to the expected rate of neutron capture events in the proportional counters. However, pulse shape analysis techniques will be used to discriminate microdischarge events efficiently

D.7.2 Critical Detector Components

All detector components that are at the interface between high voltage potentials and ground are tested for high voltage stability. A schematic of a ^{3}He proportional counter and its critical components are shown in Figure A.2. In particular, the fused-silica insulators at the end of the counters have undergone extensive high voltage studies. Most results of this work are based on experiments with the insulating silica feedthroughs. Not shown in Figure A.2 is the readout electronics of the proportional counters. It consists of low-noise current mode preamplifiers AC coupled to the detector supplied with high voltage through a filter network. It is found that foil capacitors used in the preamplifiers differ widely in microdischarge performance and have to be chosen carefully. Their high-voltage performance and micro

discharge characteristics is probably due to gaps in contiguity between sections of conductors and conductors and dielectrics. Good results have been obtained with metallized Mylar foil capacitors from Southern Electronics Company (SEC) [6]. Some ceramic capacitors have been found to show signs of high-voltage noise resembling microdischarge. Microdischarge in capacitors is different from that in insulators and conductors in that one sees a step in voltage and a duration characteristic of circuit time constants

D.7.3 Results of Endcap and Delay Line Microdischarge Tests

Based on extensive endcap testing with a specially designed test setup the following typical results are obtained for production endcaps. The high voltage test is conducted in a nitrogen atmosphere to reduce the air and Rn exposure during the hours-long tests. Usually, before the microdischarge test the endcaps are conditioned for 1 hour at 2.5 kV and then tested at 2.4 kV. The nominal operating voltage for the Neutral Current Detectors is 1835 V. When the endcaps are first brought to voltage microdischarge rates of several Hz are seen which decrease very rapidly. The initial breakdown rates can be explained by surface contamination due to dust and other loose particles. The trigger level for the microdischarge test is -10 mV, which corresponds to 0.8 μA at the preamp input.

Table D.7: High voltage microdischarge (μD) test results for NCD endcaps.

Test Piece	Total hrs	No. of μD *	μD Limit at 95.% C.L.	Events/yr	μD Limit/yr at 95% C.L.
non-Au EC	1991.5	8	<14.44	35.2	63.6
Au EC	771	2	<6.30	22.7	71.6
empty test cells	2857	14	<21.8	42.9	66.9

* μD = microdischarge

Between tests the high voltage test setup and all preamplifiers are kept at high voltage at all times, except when the EC or DL box is being loaded or unloaded. This assures the cables and preamps remain conditioned and do not contribute many pulses. The times

between micro discharge tests is be used to determine accurately the number of background noise and microdischarge pulses.

Only a few delay lines have been tested so far. For the ones that were tested it was critical to clean them before any microdischarge test using special lint-free cleanroom wipes. It was found that the delay line assembly was particularly sensitive to surface dust and contamination. The acrylic counter and cable-end couplers are tested in similar manner as the endcaps and delay lines.

D.7.4 High Voltage Microdischarge

A number of authors have studied the phenomenon of high-voltage induced breakdown and microscopic discharge in the past [57, 30, 31]. Most of these studies, however, investigated discharge as a breakdown phenomenon through dielectrics and dielectric gaps. This work suggests that microdischarge occurs in small voids, especially at interfaces between dielectrics, and between dielectrics and conductors. Experimental evidence suggests that microdischarge depends strongly on the material of the insulating surface, and on its surrounding gas environment. It is shown that gaps of the order of 100 micrometers or less are one of the main causes for microdischarges.

Event Topology of Microdischarges

During the development and construction of the ^{3}He proportional counters the phenomenon of microdischarges has been observed in a wide variety of components. It is found that the event topology of microdischarges is largely independent of the geometry or the specifics of the component. Only the integrated charge varies from event to event when circuit parameters are similar. Various types of microdischarge pulses have been observed. Unlike gas ionization events, they are characterized by a sharply rising and falling edge. They do not show the ion tail that is typical of gas ionization events which show the characteristic tail of positive ion drift. The amplitude of these pulses varies significantly but is typically a few mA into 75 Ohm. The width of microdischarge events studied in this work is less than 30 nanoseconds. It is limited by the bandwidth of the electronics. The integrated charge

is small, of the order of a few femtocoulombs, and is sometimes followed by fluctuations in the baseline of the proportional counter signal. Two types of microdischarge can be distinguished: Microdischarges of type I are characterized by the sharp rising leading edge and a drop in the baseline after the event. An example is shown in Figure D.6. The baseline shift may be associated with a change in the circuit capacitance or the leakage current. Type II microdischarge events feature an oscillatory ringing after the event and no shift in the baseline. Figure D.6 shows a typical example. A very small microdischarge event of type I or II is also shown. In this case the microdischarge is masked almost entirely by the baseline noise. This example illustrates the wide range of amplitudes of microdischarge events. In Figures D.6 the circuit transconductance is 12 V/μA.

A Microdischarge Event Generator

First observation of high-voltage induced microdischarge was made during the high voltage testing of individual proportional counter components. In an experimental program investigating a different effect, the shape of ionization pulses near the ends of counters, Pyrex tubes with cylindrical stainless steel inserts were tested as insulating feedthroughs for the Neutral Current Detectors. It is found that this geometry is a reliable microdischarge event generator which can be used to study the characteristics of high-voltage induced microscopic breakdown. A detailed description of our microdischarge studies can be found in [61].

Microdischarge: A Surface Phenomenon

Systematic studies with the microdischarge event generator show that microdischarges occur in narrow gaps between dielectrics or dielectrics and conductors. The phenomenon of high-voltage induced microdischarges was found to be a surface interface problem. In the cases studied here surface tracking or dielectric breakdown is less likely. We hypothesize that the fundamental cause for microdischarges is the incongruence between surface charge distributions established by the electric field and surface resistivity. In the cases investigated here the causes of microdischarge are the following: Small gaps between interfaces, mobile particles and contaminants, and static surface charge. Microscopic gaps between surfaces

frequently occur in cables and connectors. In these situations microscopic high-voltage breakdown occurs at the dielectric-dielectric and dielectric-conductor interfaces. The cleanliness of dielectric surfaces affects significantly the high voltage characteristics of materials. Additional cleaning and one-time conditioning at high voltage can remove dust particles and other contaminants which contribute to the breakdown of proportional counter components. The establishment of an equilibrium charge distribution on surfaces when the potentials are time-varying often leads to transient microdischarge noise that decreases with time over a period of seconds to minutes. This effect is often seen during slow high-voltage ramp-up procedures.

D.7.5 Techniques for the Reduction and Elimination of Microdischarges

Based on these results a variety of techniques for the reduction of microdischarges on dielectric surfaces have been developed. Most important is the design and selection of high-voltage components. They determine the microdischarge characteristic of any proportional counter. Components are designed to avoid narrow dielectric gaps, such as voids at the interface between conducting and insulating surfaces. Surface treatment and high voltage conditioning are most commonly used to minimize microdischarges after the construction and assembly process. Before the Neutral Current Detectors are operated they are conditioned for one hour at an elevated voltage to improve their high voltage characteristics and stability. Extensive tests show that the rate of spurious signals can be reduced by orders of magnitude if the detector components are conditioned at a voltage 10-50% higher than the operating voltage. The high voltage conditioning presumably removes all mobile contaminants and dust particles from the surface of the dielectrics and establishes an equilibrium charge distribution. Thorough cleaning of high voltage components avoids any discharges due to mobile particles. Also, the application of a silicone grease between the dielectric surfaces closes the voids between surfaces and greatly reduces microdischarge. A number of methods are currently being investigated for the online and offline analysis and identification of these pulses. Event discrimination techniques make use of the unique characteristics of high-voltage microdischarge. The extremely short rise and fall time and small integrated

charge of these pulses are two characteristic features. Besides standard pulse shape analysis techniques, advanced algorithms are being developed for the identification and discrimination of these events. Based on preliminary pulse shape analysis work we expect to be able to reject microdischarges with almost 100% efficiency.

D.7.6 Conclusions and Results

This work indicates that high-voltage induced microdischarge is a surface phenomenon. Experimental evidence suggests that the phenomenon of microdischarge, as observed and described in this work, is not so much a tracking problem but caused by discontinuities in the surface charge distribution. Various types of microdischarges have been observed and characterized. Techniques for the effective reduction of spurious signals have been developed and microdischarges have been greatly reduced in the ^{3}He proportional counters for the Sudbury Neutrino Observatory.

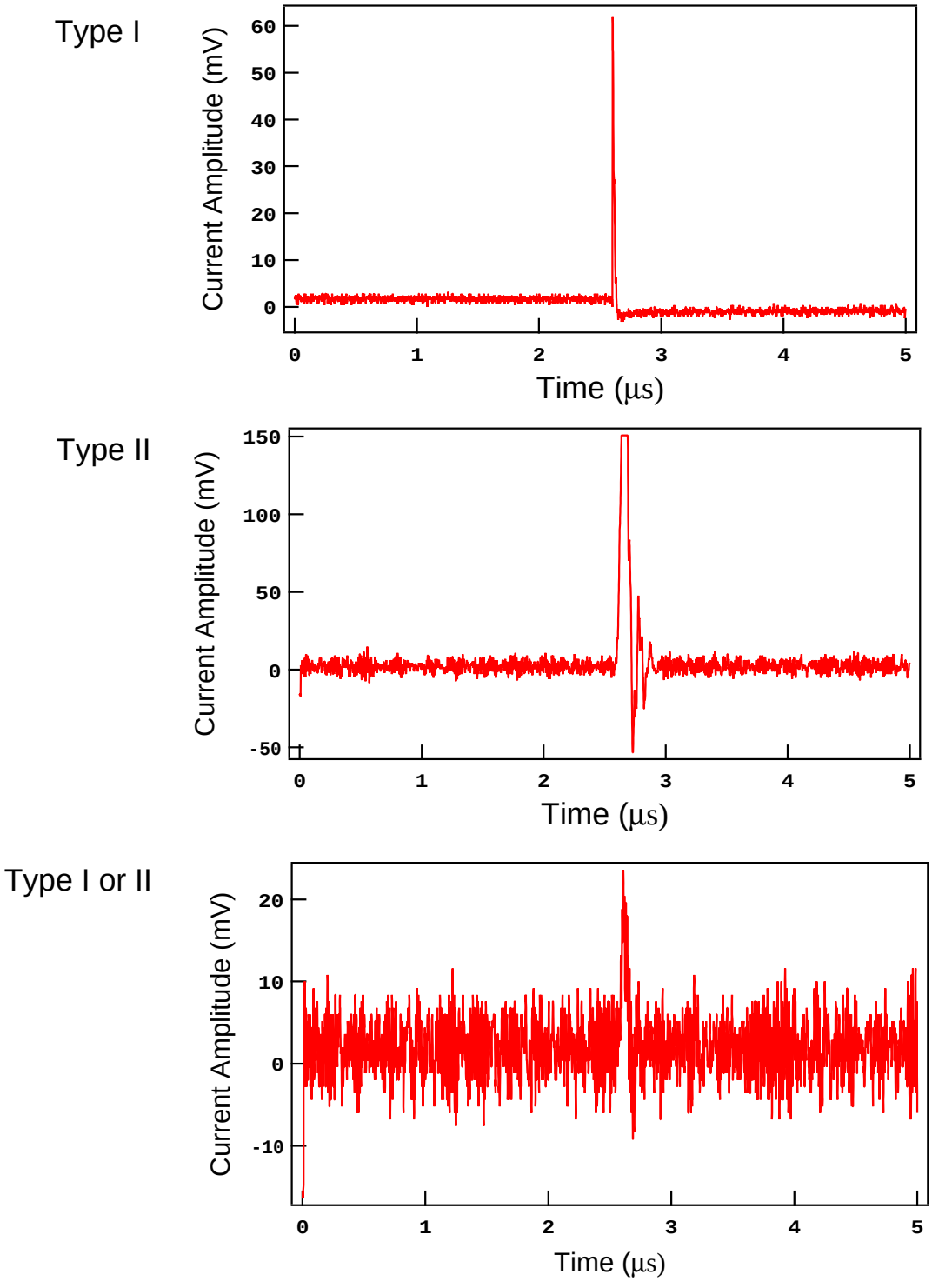

Figure D.6: NCD microdischarge events.

D.8 Assembly of the ^{3}He-filled NCD Counters

Once the individual counter components have been prepared and have passed quality assurance a proportional counter is assembled.

The anode wire is installed by feeding a length through the endcaps before they are welded in place, and then drawing a fresh length through an ultrasonic bath, tensioning it and soldering. In the event of failure of a wire, the counter can be restrung in the vertical position after some painstaking alignment. To permit this repair, a section of the assembly cleanroom has been provided with a 5-m ceiling.

The solder used is 99.99% pure SnAg 96.5:3.5 alloy, a true eutectic with a melting point of 221 °C It has a 0.015 inch diameter and is supplied by Indium Corp. of America, and radioassayed before use. The flux for most parts is Indium Corp. Flux No.4, which contains proprietary ingredients in a vehicle of isopropyl alcohol, and is radioassayed before use. The soldering of the anode wire to the Cu endplug uses Rosin flux due to the difficulty of flux removal at this stage.

The counters are filled according to the NCD gas fill procedure.

Once the CVD Ni proportional counters are welded together and filled with gas they are sealed. The requirements on this seal are very stringent. Any leak in the seal will not only allow gas to escape–possibly affecting the gain of the detector—but will also allow impurities to enter the counter. Electronegative impurities such as O_2 will absorb electrons from the ionization tracks thereby degrading the signal strength and the resolution. In order for the detectors to work properly such impurities must be kept well below the ppm level. Another adverse effect of a leak in the seal is that the "dead" volume between the counters may become filled with ^{3}He and act as a neutron sink, reducing the overall efficiency of the detector. The counters for the NCD array have been designed for a nominal livetime of 10 years.

A pinch-off tube is used to make the required seal. The advantage of the pinch-off tube is that it is extremely simple and is a well-tested technique. The counter is filled through a thin tube attached to one endcap and when the desired pressure is reached the tube is crimped with an air-pressured tool to make the seal. Copper is the material of choice for

the portion of the tube which is crimped. They are degreased, annealed, and etched before use.

D.9 Status of NCD Construction

An array of 293 ^{3}He-filled, ultra-pure background counters has been built for installation in SNO. During fabrication and assembly extreme care has been taken to assure the cleanliness of the detectors. Unique fabrication and assembly procedures were utilized to minimize the backgrounds for every component during the assembly procedure. The counters are now characterized and run underground during their cooldown period. While radioassays of the individual counter components indicate that the photodisintegration background will be less than $\sim 4\%$ of the SSM the cleanliness of fabrication can only be tested in-situ by deploying some Neutral-Current Detectors into the heavy water volume in SNO. A NCD *Construction Hardware-In Situ Monitoring Experiment* named CHIME was designed to perform this test. The design and execution of this NCD background test experiment is described in the following Appendix.

Table D.8: Typical NCD counter characteristics after construction.

Detector Mass of Complete Counter (200 cm long)	$\sim$ 1100 g
Resistance of Anode Wire	$\sim$ 17-18 Ω
Average Al Splotch Density of Tubes	10-20%
Microdischarge Rate	$<$ 3 counts/day
Air Exposure of CVD Ni Tubes	5-10 hrs
Air exposure of CVD Endcaps	$\sim$ 12 hrs
Neutron Gain at 1600 V (^{241}Am)	$\sim$ 58
Neutron Resolution at 1600 V	3.6-4%
Operating Voltage	1835 V
Detector Gas Gain	$\sim$ 100
Tritium Content	$<$ 0.2 nCi/l
Whole Body Leak Rate	0.1-1 $\times$ 10^{-7} cc/s
Above-Ground α Rate from ^{210}Po (in 5-5.5 MeV window)	15-30 $\pm$ 5 counts/day

APPENDIX E

DESIGN AND CONSTRUCTION OF A NCD BACKGROUND TEST SOURCE

Ultra-low background ^{3}He proportional counters will be used in the final phase of the SNO experiment to detect neutrons from the neutral-current interaction rate of solar neutrinos. Since the binding energy of the deuteron is only 2.2 MeV, gamma rays from natural decay chains in the proportional counters may photodisintegrate the deuteron and thus cause a neutron background to the neutral-current signal. This poses stringent limits on the radiopurity requirements for the NCD counters.

The Neutral Current Detector array consists of 775 m of ^{3}He proportional counters arranged in 96 strings with 300 counters. The counter bodies are made of about 450 kg of ultra-pure CVD nickel which contains natural Uranium and Thorium at about the 1-2 ppt level. The photodisintegration gammas are produced in the decay chains of ^{232}Th and ^{238}U, and in the decay of cosmogenically produced ^{56}Co.

$$^{208}\mathrm{Tl} \rightarrow ^{208}\mathrm{Pb}, \mathrm{E}_\gamma = 2.615 \text{ MeV}$$
$$^{214}\mathrm{Bi} \rightarrow ^{214}\mathrm{Po}, \mathrm{E}_\gamma = 2.445 \text{ MeV}$$
$$^{56}\mathrm{Co} \rightarrow ^{56}\mathrm{Fe}, \mathrm{E}_\gamma > 2.224 \text{ MeV}$$

An *in-situ* background measurement of the construction materials used in the Neutral Current Detector (NCD) array has been performed prior to its deployment in SNO. This measurement allows us to determine an upper limit on the activity of ^{232}Th in the Neutral Current Detectors and the expected photodisintegration background from the NCD array. This appendix describes the design of this *Construction Hardware In Situ Monitoring Experiment* (CHIME). It measures the NCD originated background in the presence of the internal D_20 background prior to the deployment of the entire NCD array.

Seven individual NCD counters arranged in a close-packed configuration are deployed as a background test source in the SNO detector. The construction materials and procedures used for the CHIME counters are essentially identical to those in the real NCD array. The difference is that the CHIME counters are not active. They are not made to be active neutron counters because of the additional background associated with the readout cable. The background due to radioisotopes in the readout cable would completely mask the photodisintegration background due to the proportional counters themselves. When the NCD array is installed in SNO the backgrounds associated with the NCD readout cables are not expected to be a significant problem since the NCD cables do not extend much into the main detector volume and connect to the top end of the neutral-current detector strings near the chimney of the acrylic vessel. The CHIME measurement with the NCD background test source ensures the cleanliness of the Neutral Current Detector components and their assembly procedure prior to the deployment of the NCD array in SNO.

E.1 Construction and Assembly of NCD Background Test Source

The NCD background test source is made of seven identical CHIME counters. Each CHIME counter is similar to a string of 2 proportional counters in the NCD array. Figure E.1 shows the schematic of a CHIME counter, while Figure E.2 illustrates the close-packed configuration of the NCD background test source.

Each CHIME counter consists of two 2"-diameter CVD nickel tubes of lengths 9.4" and 34.7" laser-welded together. The total length of each CHIME counter is 45.1". These tubes are electropolished, chemically cleansed, and baked in the manner described in Appendix D prior to the construction of the individual counters. Two 0.5" holes, separated by 180 degrees, are drilled in the long Ni tube as indicated in Figure E.1. These two holes serve as a pressure relief once the counters are submerged in the heavy water during the *in-situ* measurement. Since the lower sections of the CHIME counters will be open to the D_2O they do not have to be leak tight. Pinholes were not repaired in these sections.

The inner volume of each CHIME counter is enclosed between the endcaps EC2 and EC5. It is filled with ^{4}He according to the gas fill procedures [43] for Neutral Current

Detectors and then evacuated to simulate counter handling during gas fill. The endcaps EC3 form a normal counter-to-counter coupling, with the only exception that the anode wire feedthrough holes in the copper endplugs are not sealed in these two endcaps. The endcaps that seal the inner volume of the CHIME the two welds are required to be vacuum leak tight to 10^{-5} std cc/s. In comparison, the standard constraint for leak rates in Neutral Current Detectors is 10^{-9} std cc/s [121].

The use of porous nickel tubes in the construction of the CHIME makes it necessary to consider the leak rate constraints for the CHIME. The two cases of heavy water getting into the counters and counter gas leaving the counter volumes need to be considered. According to [160] an interspace leak rate of 10^{-7} std cc/s will result in condensed water after 10 years in SNO. The CHIME does not need to be electrically sound so water is less of an issue. If the CHIME spends 2 months in SNO (upper limit), and we scale the result from the leak test by the ratio of times this leads to a limit of 10^{-5} std cc/s. However, this is a very conservative limit since even a gram of water would not matter in the CHIME. The condensed water criterion [160] considers droplets and therefore it has been assumed that a leak rate even one order of magnitude greater than this would be acceptable. Therefore, we chose 10^{-4} std cc/s as the leak rate constraint in the construction of the CHIME. A total leak rate of 10^{-4} std cc/s is considered to be acceptable and hence for each CHIME counter the leak rate needs to be less than 10^{-5} std cc/s.

The space between EC3 and EC2 is filled with ^{4}He to simulate the NCD gas fill procedure. At the end the counters are evacuated to prevent any gas from leaking into the SNO detector. Exiting ^{4}He gas is only a problem if it ends up in the phototubes. In any case, the amount would be miniscule. At 10^{-4} cc/s and after 2 months, one has about 40 cc of gas. Dispersed into the cavity, this amount would represent 10^{-3} of the natural atmospheric abundance of He.

The anode wire in the normal NCD counter is not strung in the CHIME counter. It is placed inside the enclosed volume instead. Because of the physical constraint on the length of the enclosed volume in the CHIME counter, EC4 has a shortened quartz tube. These endcaps were selected from our inventory of endcaps that have quartz tubes damaged during the endcap production and handling processes. These four enclosed endcaps (EC2, EC3,

and EC4) are laser-welded to the short Ni tube. The primary purpose of these welds is to hold the four endcaps in place and are not necessarily leaktight.

Since the CHIME counters are not active the criteria for the quality assurance of some counter components are less stringent. Components are chosen from the NCD inventory to meet all specifications and requirements of the CHIME design. They would not necessarily meet all of the QA criteria for NCD components. Amongst these components are endcaps that do not pass the high voltage tests and counter tubes that show signs of pinholes and do not meet the standard specifications for leak rates.

The seven CHIME counters are assembled in a closed-packed configuration with an outer diameter of 6.6". They are held together by CVD nickel rings that connect the seven counters at the top through the holes on the outer ring in the anchor endcaps EC1 and at the bottom of the CHIME tubes through additional holes of the same diameter. The cotter pins and chicane links are made from CVD nickel wires that have been sheared from 1/32" CVD material. These CVD wires are bent into cotter pins and chicane link pins. Typically, widths range from 0.040-0.065". Each CHIME counter in the assembly is connected to its neighboring counter by four nickel pins, one at the bottom of the CHIME assembly and three at the top of the CHIME assembly. Two different types of CVD nickel pins are used to hold the counter assembly together. The strengths of these cotter pins and chicane links have been tested in a load test [4]. Tests indicate that the strength of the nickel pins used in the CHIME assembly exceeds 40 pounds. The CVD nickel rings are the same as the ones used in the assembly of the NCD anchors and a NCD production component.

Vectran loops across the top of the central CHIME counter serve as attachment points for the deployment rope and backup line. The Vectran sling that serves as the attachment to the deployment line is attached to the holes in the endcap of the central CHIME counter. The attachment loop for the backup line is attached in exactly the same way to the holes in two outer endcaps.

The mass of each counter is about 715 g, and the CHIME septet was measured to have a mass of 4947 g.

E.1.1 Tube Assignments and Preparations

For construction of the NCD background test source 4 CVD Ni tubes were selected according to the NCD splotch density requirements specified in [121]. These tubes were electropolished in July 1998 following standard procedures [121]. Since then, the procedures for electropolishing raw tubes were optimized and changed according to the cleanliness of the raw tubes, mostly because it became necessary to remove surface contamination from radon on tubes that were stored at an underground storage facility in Index, Washington. The tubes that were selected for the construction of CHIME were never stored there and thus did not have this problem. Detailed and extensive studies of our electropolishing procedures have shown that during the entire NCD construction process the completed Neutral Current Detectors meet the same stringent cleanliness requirements.

For the construction of the CHIME counters tubes were selected that showed a high number of pinholes in the body of the tube. Since the CHIME counters are not active this will not affect the performance of the counters in the CHIME experiment. There is also no hypothesis that correlates a bulk or surface alpha activity with pin holes in the nickel tubes. The interpretation of CHIME data will rely on this assumption.

With regards to their aluminum splotch density [1] tubes with an average splotch density of 10% were chosen. This corresponds to the average measured splotch density and allows us to represent the whole NCD array most accurately. Table E.1 lists the tube assignments and splotch densities for the CHIME counters.

E.1.2 CHIME Endcaps

Endcaps used in the CHIME counters passed most of the same quality control checks as components for the NCD array. Details are described in Appendix D and [121]. Some components that were sufficient for the construction of the CHIME counters did not meet all specifications for the Neutral Current Detectors. This includes endcaps failing the high voltage tests and our requirements for microdischarges as well as endcaps with leaks, ranging

[1] During the removal of a CVD nickel tube from its Al mandrel splotches of Al from the surface of the mandrel sometimes remain on the inside of the nickel tube.

Table E.1: Tube assignments and splotch density of the NCD background test source CHIME.

CHIME Counter	Tube IDs	Splotch Density of Tubes
X1-112-1	T179	7%
X2-112-1	T316, T179	10%, 7%
X3-112-1	T318, T316	22.3%, 10%
X4-112-1	T322, T316	0%, 10%
X5-112-1	T322, T318	0%, 22.3%
X6-112-1	T322, T318	0%, 22.3%
X7-112-1	T322	0%, 22.3%

from pinholes at the level of 10^{-7} cc/s or less to visible voids. Since the CHIME counters are not active this does not affect the performance of the CHIME counters in the proposed background measurement. Leak tight endcaps were used for the placement at position EC2. Standard copper gas fill tubes are attached to endcaps EC3. They are used to fill the counters with ^{4}He gas, pinched-off, and then detached. Filling the space between EC3 and EC2 with ^{4}He simulates the gas fill procedure.

E.1.3 Irregularities During Construction of the NCD Background Test Source

This section describes miscellaneous irregularities that occurred during construction of the CHIME and may have caused additional backgrounds in the CHIME counters. The handling of the CHIME components during construction was mostly but not always according to standard NCD procedures because of the CHIME dimensions. They required non-standard handling tools and procedures. For example, the anode wire was not strung as usual in the CHIME counters. Instead 4 meters of copper wire and 1 endplug were put into all the CHIME counters except for counter X1. It contains two Cu endplugs, no wire, and a broken quartz piece. Broken quartz pieces may have been put into the other CHIME counters if one of the endcaps broke its quartz during production. The small parts contained in the

sealed volume of the CHIME counters are listed in the Table E.2.

Table E.2: Small parts in CHIME counters.

CHIME Counter ID	Small Parts in Counter Volume
X1-112-1	2 Cu endplugs, broken quartz
X2-112-1	1 Cu endplug, 4m wire
X3-112-1	1 Cu endplug, 4m wire
X4-112-1	1 Cu endplug, 4m wire
X5-112-1	1 Cu endplug, 4m wire
X6-112-1	1 Cu endplug, 4m wire
X7-112-1	1 Cu endplug, 4m wire

Laboratory air is a concern for the exposure of the NCD and CHIME construction materials to Rn. In addition, laboratory air is a source of particulate matter. While most of the construction is done under clean room conditions some of the components for the CHIME counters were exposed to laboratory air during construction. Counters X1-112-1 and X3-112-1 were brought out of the clean room for a short period time to be cut and flared for repair. This was mainly because of the increased complexity associated with the construction of CHIME and some of its non-standard assembly procedures. It is estimated that the air exposure of the CHIME counters exceeds the air exposure of standard Neutral Current Detectors by a factor of 2.

When the counters were assembled, holes in the welds occurred due to misplacement of the ECs. During a repair phase a second laser weld was placed over these holes to close them.

Due to the complexity and non-standard dimensions of the CHIME counters some minor problems were encountered during the construction and assembly of the CHIME. Given the repairs and construction irregularities we encountered during the assembly of CHIME we expect that any measurement we make will represent an upper limit on the photodisintegration background from the actual NCD array.

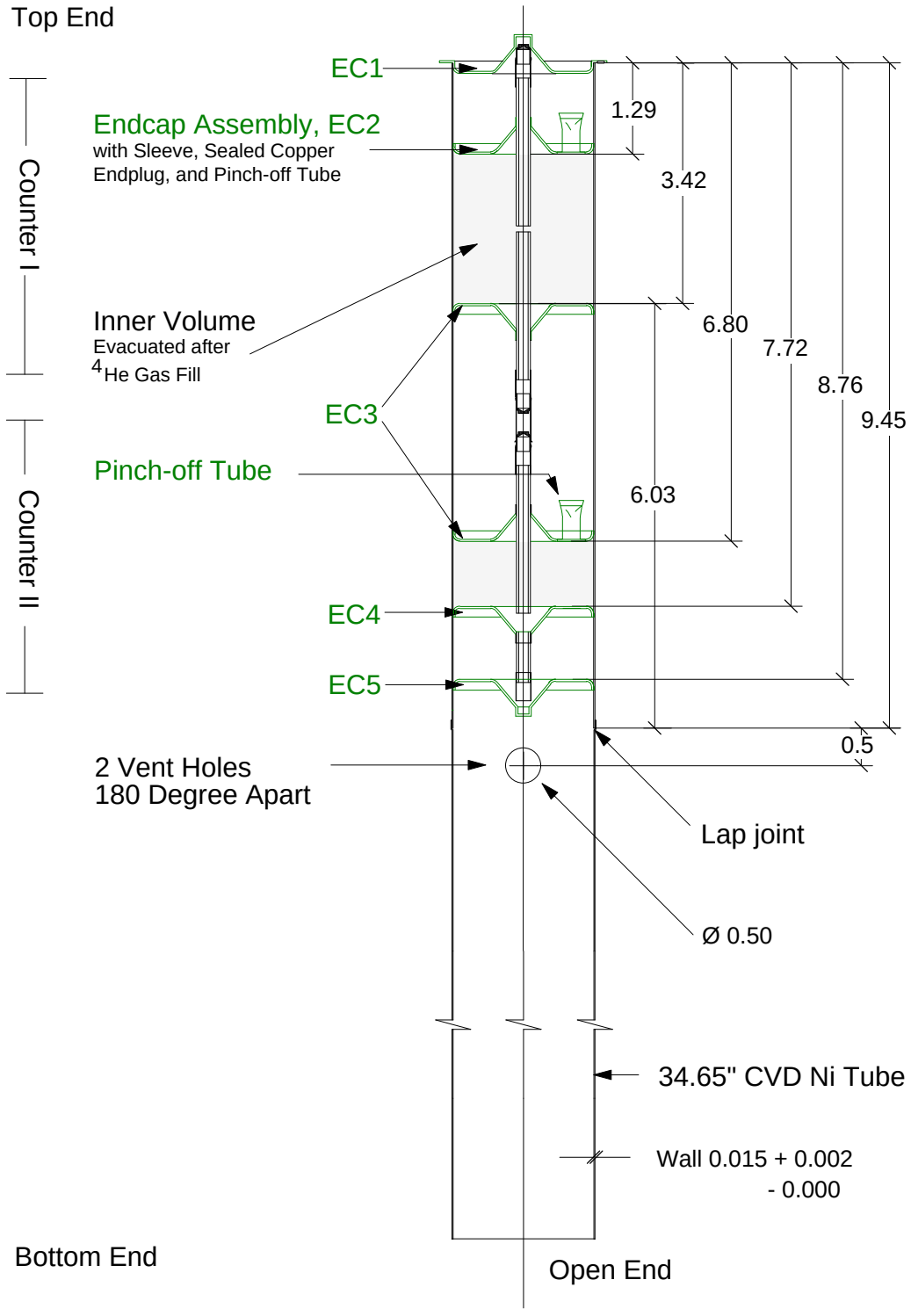

Figure E.1: Schematic drawing of a NCD CHIME counter.

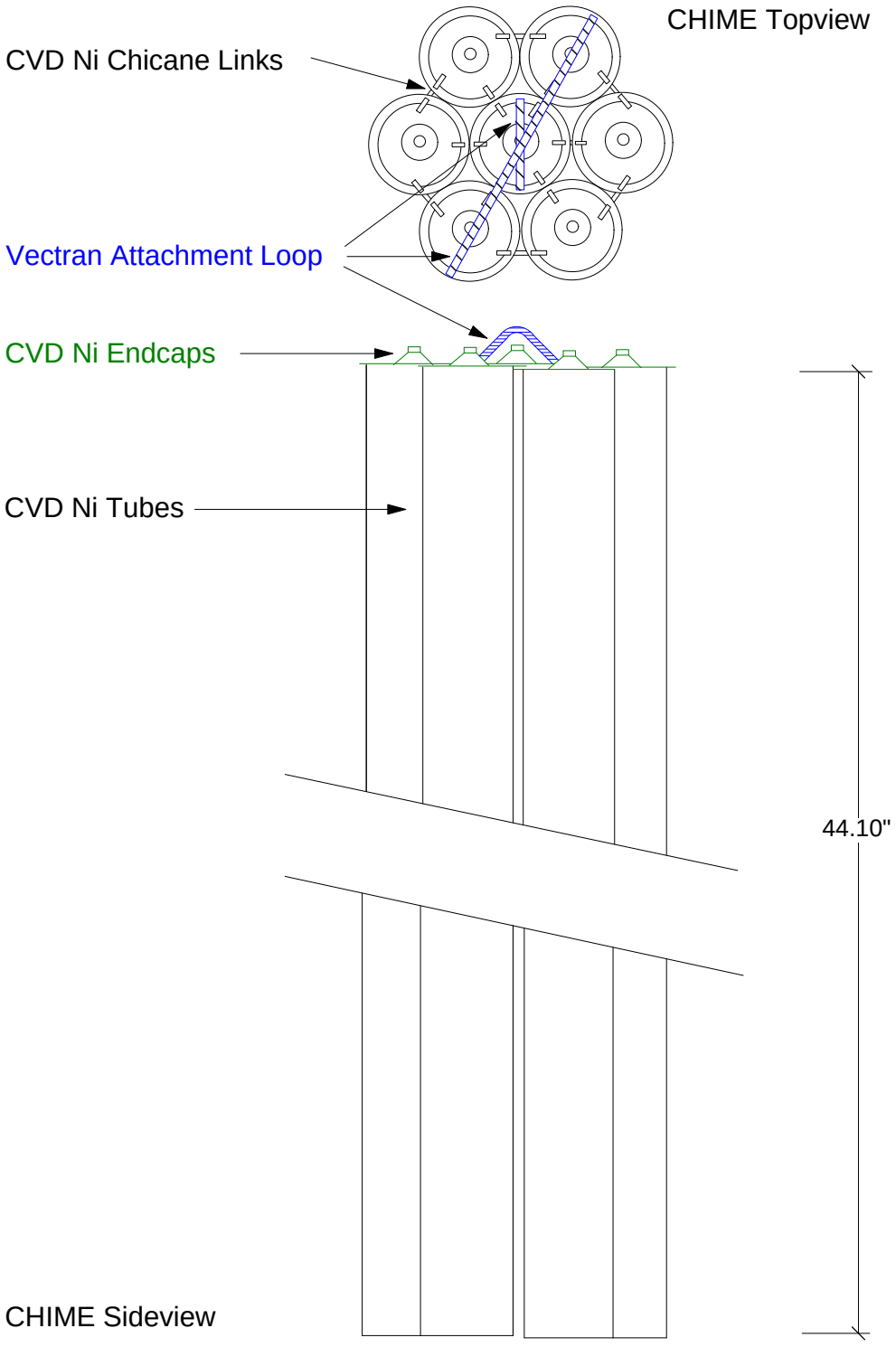

Figure E.2: Schematic of NCD background test source. Close-packed assembly of seven NCD CHIME counters.

E.2 Deployment of the NCD Background Test Source

E.2.1 Deployment Mechanism

The septet of CHIME counters is negative buoyant and can be deployed as a background test source along the central axis of SNO using a simple winding mechanism. The mass of the CHIME septet is 4947 g, and its free fall weight is 9% over its buoyancy in heavy water. Vectran loops are attached to the endcaps of the CHIME counters to serve as attachment points.

Because of its cleanliness only Vectran rope can be used to deploy the CHIME. Both a deployment and backup line are used to assure safe deployment of the NCD CHIME in the SNO detector. The 1/16-inch Vectran braided twine is attached to the winding drum through 0.081-inch holes and tied off with a figure-8 knot. The lower end of the deployment line is tied with a figure-8 knot to a Vectran attachment sling since any metal connection might shave Vectran fibers off the deployment rope. The CHIME counters are connected to each other at multiple points and the nickel rings used in the CHIME assembly are strong enough to make any failure very unlikely.

The standard source umbilical for SNO calibration sources is too radioactive for deployment of the CHIME and cannot be used as a deployment or backup device. For this measurement the umbilical is replaced with a Vectran line and the source deployment hardware is replaced with the CHIME winding hardware which mounts directly on the top of the existing 48" source deployment tube. Deployment of the CHIME follows closely the procedures for handling and deploying standard SNO calibration sources. While the CHIME is deployed it is not be possible to deploy other calibration sources. Use of the CHIME deployment hardware prevents light, laboratory air or debris from entering the detector.

The CHIME deployment hardware consists of a source tube for the 10" diameter port of the SNO Universal Interface and a winding mechanism for the deployment and backup line. The deployment and backup lines for the CHIME are both run on one winding drum along the central axis. This assures that the CHIME hangs vertically even if one of the lines fails. For redundancy each line will connect to independent attachments points. The attachment loop of the deployment line connects to the center CHIME counter while the loop of the

backup line connects to two of the outer counters of the CHIME assembly. The design of the CHIME attachment points is based on the design of the NCD anchors. Load tests have been performed to confirm the strength of the CHIME attachment points. A figure-8 knot will be used to connect the deployment and backup line to the two independent Vectran loops which attach to different parts of the CHIME.

The CHIME rope winder is operated manually with a crank set. A mechanical stop prevents the CHIME deployment line to unwind from the rope winder in case of an emergency or operator failure.

The position of the CHIME in the SNO detector is determined by means of a mechanical turn counter. The accuracy obtained with this method is good enough compared to the accuracy in the reconstructed position of γ's or β-γ's. A series of deployment tests was performed to determine the accuracy of the position calibration. With a gear ratio of 20:1 the turn counter allows accurate positioning of the CHIME. The reading of the turn counter can be calibrated in 2 positions: When the CHIME is in its top position inside the source tube and when the CHIME is in its lowest position, i.e. when the Vectran lines are fully unwound. Any position of the CHIME with respect to the acrylic vessel between these two points is inferred. The elasticity of the 1/16" Vectran line is well known and has been measured. Using the elasticity of the deployment line and measuring the top and bottom position of the CHIME allows the determination of the CHIME's z-position to better than 10 cm. Usually, the CHIME is positioned by lowering it to the lowest possible and raising it into the center position. By starting from the lowest position systematic errors associated with the turn counter system and the winding mechanism will be minimized. This is sufficient for any background measurement with the CHIME. The x-y position of the CHIME with respect to the acrylic vessel is determined by the central axis of the 10" access port which is close but not exactly at the center of the SNO detector.

For a safe retrieval of the CHIME it is critical to know the exact z-position of the CHIME. Therefore, a second, redundant indicator has been installed inside the source tube. An electrical feed-through with two probes attaches to the side port of the source tube and gives a signal when the two probes are shortened. When the CHIME is back in its top position it touches the ends of the electrical feed-through and shortens the circuit. The

electrical feed-through makes a vacuum tight connection with the port. This indicator is completely independent of the turn counter and gives a signal when the CHIME is raised back to its top position in the source tube. This allows one to determine unambiguously when it is safe to close the 10" gate valve.

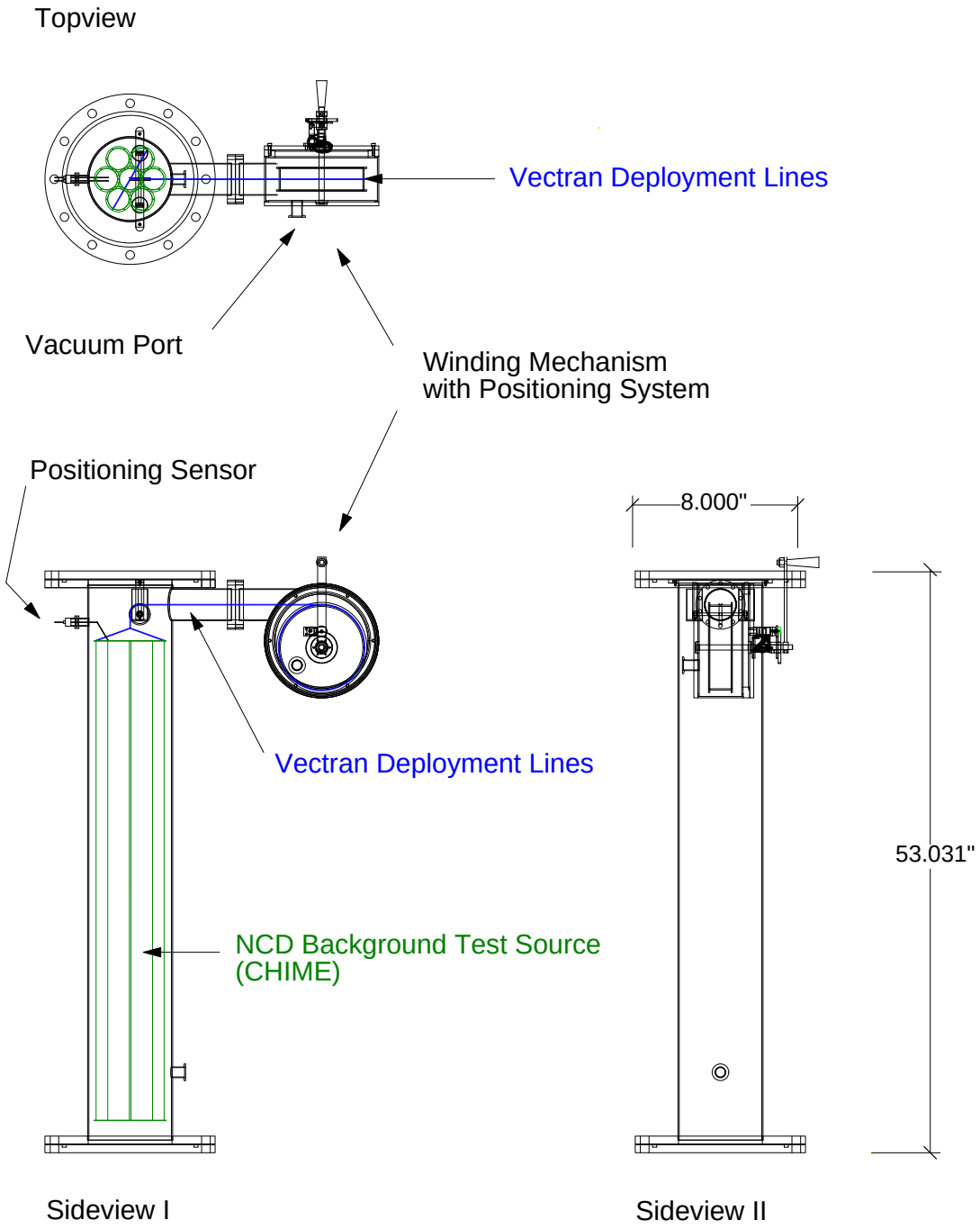

Figure E.3: CHIME deployment mechanism consisting of a cylindrical source tube and a winding drum.

E.2.2 CHIME Vacuum and Pump System

The CHIME deployment hardware is designed to be light and vacuum tight and optimized to reduce the introduction of radon into the SNO detector. Gas ports on the side of the winding drum and the source tube allow the deployment hardware to be evacuated and purged with nitrogen.

The CHIME vacuum system connects the housing of the winding drum and the lower end of the source tube of the CHIME deployment hardware to the DCR vacuum line and to the nitrogen supply system. See Figure E.4. The CHIME vacuum system was designed to allow the source tube to be pumped and purged with boiled-off nitrogen before every CHIME deployment. To minimize the amount of radon leaking into the cover gas volume the CHIME hardware is designed to be vacuum tight. Using a standard leak detector the inner volume of the CHIME deployment mechanism was pumped down and the source tube and winding drum were leak tested. The CHIME deployment hardware was pumped down to a pressure of 5×10^{-3} mb. No leaks were detected at the level of 5×10^{-8} mb l/s.

The design of the source tube also allows for the possibility of storing the CHIME under nitrogen in the source tube prior to its deployment so that the radon activity can decay away. The half life of ^{222}Rn is 3.8 days.

To minimize the radon introduced into the cover gas system during the CHIME deployment the deployment hardware was designed such that it can be easily pumped and purged. Two 1/4" quick-swage gas ports are used to connect to the standard nitrogen lines in the underground SNO lab. As the system is purged with positive pressure of nitrogen during the CHIME deployment procedure the vacuum components are designed to handle positive pressures up to 12 psi. The CHIME source tube is welded at the top and the bottom to 10" flanges. It was estimated that a pressure difference of 20 psi adds 650 psi of simple axial stress to the weld between the tube and the top and bottom flanges. Similarly, the same pressure difference adds 880 psi to the welds in the reel housing. For reference, the typical yield strength for fully annealed SST 304 is 30-35 kpsi.

Manufacturers of vacuum components do not recommend the application of positive pressures on KF-25 fittings. All KF-25 O-rings used in the vacuum system are made of

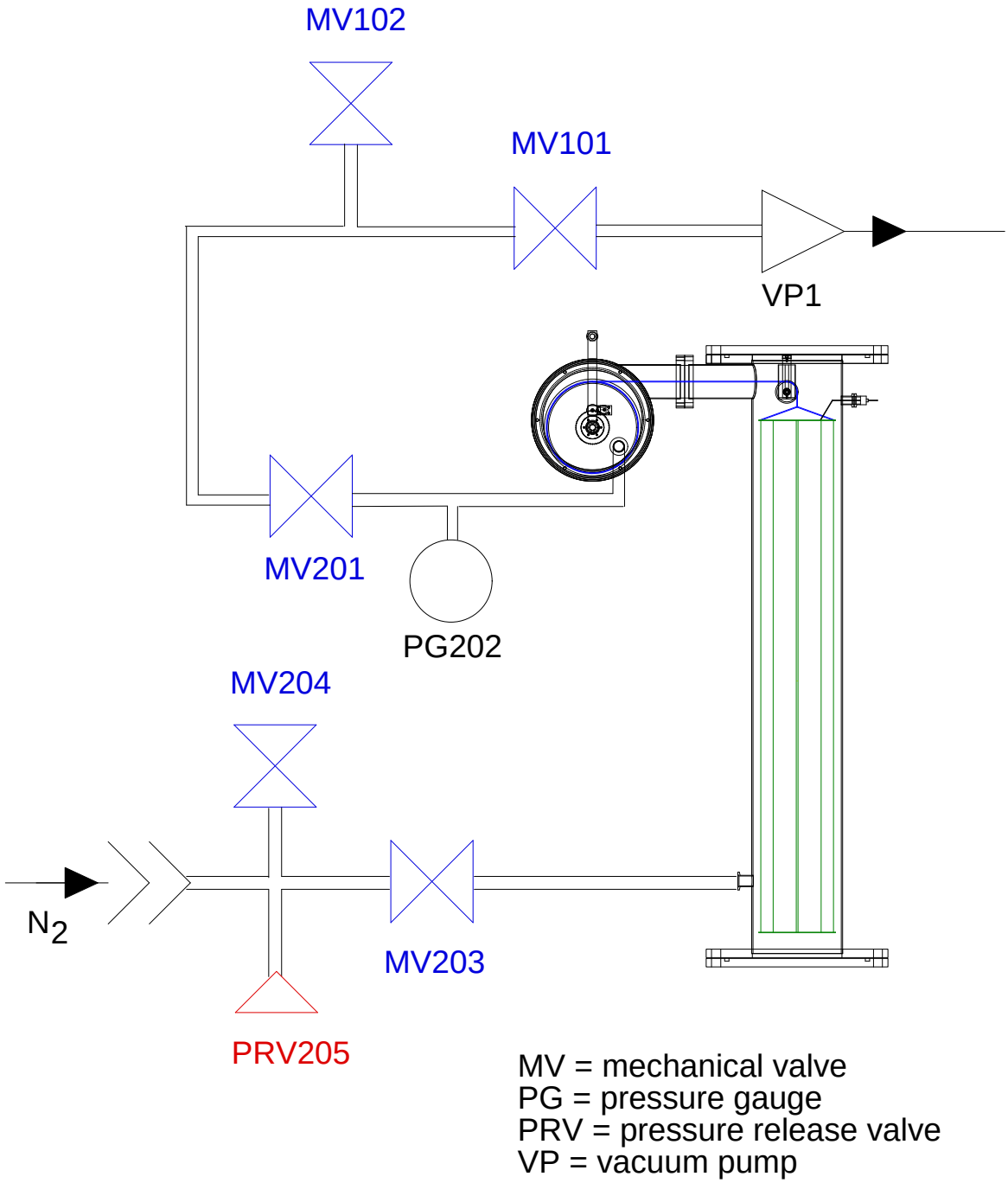

Figure E.4: Vacuum system for the CHIME deployment hardware.

Viton and were purchased from MDC Vacuum Components Corp. To get an estimate of the pressure rating for a KF-25 centering ring the Viton O-rings were tested in a water pressure test setup. A new dry clean Viton O-ring used with polished flanges fails at 11-14 psi. Using a sand blasted flange the highest pressure was 20 psi. Under a pressure of >20 psi the O-ring extruded quickly. The test setup could not hold 5 psi for longer than a few minutes. Therefore, we avoided over-pressurizing the system to more than 3 psi. To protect the CHIME deployment system against high pressures a relief valve with a cracking pressure of 3 psi was added to the CHIME vacuum system.

E.2.3 Radon Contamination During the CHIME Deployment

During the deployment of the CHIME the inner volume of the CHIME deployment hardware is opened to the detector and the air or gas that is contained in the CHIME deployment mechanism will be released into the SNO cover gas system, i.e. into the D_2O vapor space. To minimize the radon introduced into the cover gas system it is planned to pump and purge the source tube several times with boiled-off nitrogen. One can also mount the deployment hardware and the CHIME several days before the actual deployment and let the radon decay away. The CHIME vacuum system for the pump and purge is described in the previous section.

In the worst case, the inner volume of the CHIME deployment hardware would be filled with laboratory mine air. The inner volume of the deployment mechanism consists of the source tube volume, the air space in the winding mechanism, and the connecting tube between the winding drum and the source tube. The volume is estimated to be 0.05 m^3 (see Table E.3). In comparison, the volume of the D_2O vapor space is about 6.7 m^3.

The current levels of Rn in the SNO detector are described in detail in [116]. To estimate the worst possible impact of the CHIME deployment on the SNO detector we use the highest radon levels measured in the laboratory air and the lowest radon levels measured in the D_2O cover gas system.

The highest radon levels measured in the laboratory air in March 2000 were about 90,000 atoms/l. In the worst case the CHIME deployment would introduce about 4279860 atoms

Table E.3: Inner volume of the CHIME deployment hardware and D_2O vapor space.

Region	Volume (in m^3)
CHIME source tube	0.0408
CHIME winding mechanism	0.00601
connecting tube	0.000744
Total inner volume of CHIME hardware	0.047554
D_2O vapor space	6.7

of radon into the cover gas system. The lowest Rn measurement in the D_2O cover gas was 10 atoms/l in March 2000. This corresponds to about 670000 atoms in the entire D_2O cover gas system. If the CHIME were deployed without pumping and purging the source tube the radon levels in the D_2O cover gas system would be increased by a factor of 6.4. With the purging of the source tube prior to the CHIME deployment we expect that the increase in the radon level will be negligible.

E.3 Underground Storage of NCD Background Test Source

E.3.1 Storage and Handling Underground

Before and after deployment the CHIME is stored underground in the NCD cooldown rack. The procedures for handling the CHIME underground are similar to those for receiving and handling NCD's underground. The CHIME is sealed in a nylon bag under nitrogen to prevent contamination through radon contaminants from air. During deployment standard calibration source procedures are followed. In order to allow the cosmogenically produced ^{56}Co to decay, the CHIME must be stored underground for at least 3 months. It was placed on the 6,800' level on December 20, 1998.

The ^3He proportional counters are made by the chemical vapor deposition of nickel from nickel carbonyl, $Ni(CO)_4$. This produces almost pure nickel with almost no uranium

or thorium. However, although the counters can be produced with very low activity any exposure to cosmic ray neutrons produces activity from spallation products. ^{56}Co can be formed as a spallation product of nickel with cosmic ray neutrons through ^{58}Ni(n,p2n)^{56}Co and ^{60}Ni(n,p4n)^{56}Co. As of June, 2002, none of this 78-day activity should remain.

E.3.2 Underground Storage

The NCD background test source was brought to underground storage on December 20, 1998. It is contained in a nylon bag and sealed under nitrogen to minimize its exposure to laboratory air. In November 1999 the CHIME was leached in ultra-pure water and tested for radon emanation. After the radon emanation test it was rinsed with ultra-pure water and re-sealed in its nylon bag. Since then the nylon bag was opened twice for tape lift measurements. The CHIME was handled with clean room gloves at all times.

APPENDIX F

MEASUREMENT OF THE NCD EMANATION AND SURFACE CONTAMINATION

Prior to the deployment of the Neutral Current Detectors their surface contamination and leaching properties are to be determined. Using the NCD background test source (CHIME) a first study of surface contaminants and contamination from leaching has been performed. The Radon emanation test of the NCD background test source was performed with Geoff Miller from Los Alamos National Laboratory in the clean-room environment of the Sudbury Neutrino Observatory. The results from the CHIME leach test and XRF tape lift studies on the NCD counter bodies and the associated deployment hardware are discussed.

F.1 Radon Emanation Leach Test of NCD Background Test Source

A Radon emanation test has been conducted on the NCD background test source prior to its deployment. In a Teflon system ultrapure water is circulated over the CHIME assembly and through a trap containing a cation exchange resin. In such a system the detection limits for ^{228}Th and ^{226}Ra are about 5000 atoms (5 disintegrations/day) and 2×10^6 atoms (2.5 dpd) respectively. The overall detector burden for these species is about 2×10^5 atoms ^{228}Th (210 dpd) and 2×10^9 atoms ^{226}Ra (2100 dpd). These are the amounts that would be in secular equilibrium with 0.6 μg ^{232}Th and 2 μg ^{238}U respectively. The detection limits correspond to approximately 3 times the standard deviation of the background count rate in the alpha energy range of interest.

F.1.1 Leach Test System

The trap used for all leach work consists of a 50 mm cylindrical PTFE housing filled with approximately 45 ml of the cation exchanger AGMP-50, 50-100 mesh. This resin was

selected because of its superior flow properties and its very high affinity for Ra and Th. A 25 mm PTFE filter supported by a PTFE screen holds up the resin column while a 100 mm polypropylene filter is used above the resin to distribute fluid pressure. Prior to assembly of a trap, all traces of Ra and Th are removed from the resin by treatment with 6 M HNO_3 and 6 M H_2SO_4 followed by repeated washing with high purity H_2O.

The CHIME tank consists of a vertically oriented 51" long segment of 8" o.d. (6.75" i.d.) schedule 80 polyethylene (PE) pipe fitted at both ends with PE cover plates. One cover plate has two threaded penetrations through which the leach water is cycled. Through one of these holes a flexible PTFE tube extends nearly to the bottom of the tank. Leach water is withdrawn through this tube and returned to the tank via the other hole in the top. This ensures that the tank contents remain reasonably well mixed.

F.1.2 Leach Test Procedure

In the NCD CHIME emanation test ^{223}Ra is used as a tracer in the test volume. During circulation of ultrapure water in the leach tank Ra is trapped on a clean and blanked cation exchange resin. Upon completion of a leach, the trap is taken into a class-100 clean room and Ra stripped from the resin with 6 M HNO_3. The resulting solution is evaporated to a small volume in a Teflon beaker and the Ra co-precipitated as nitrate with Ra-free Pb carrier. The lead is then removed as a weakly associated chloro complex by anion exchange in dilute HCl. Purification of Ra from Ba, Sr, and any remaining Pb is achieved by cation exchange on a very fine resin in dilute HCl. Finally, the Ra is electrodeposited onto a blank Pt wafer disk from an isopropanol solution containing small amounts of HNO_3 and HCl as electrolyte. The Pt wafer is then alpha counted.

The ^{223}Ra tracer for this work is obtained from ^{227}Th which comes from a 0.1 microcurie sample of ^{227}Ac. ^{223}Ra is diluted and then alpha counted to standardize the tracer. An activity of about 100 dpd is used in each of the leach tests. The half life of ^{223}Ra is 11.4 days. Possible concerns about contamination of the tracer with ^{232}Th are addressed by the preparation of blank samples. The reagent blanks associated with the extraction and purification of ^{227}Th yield upper limits to the ^{232}Th contents of 30-50 nanograms per

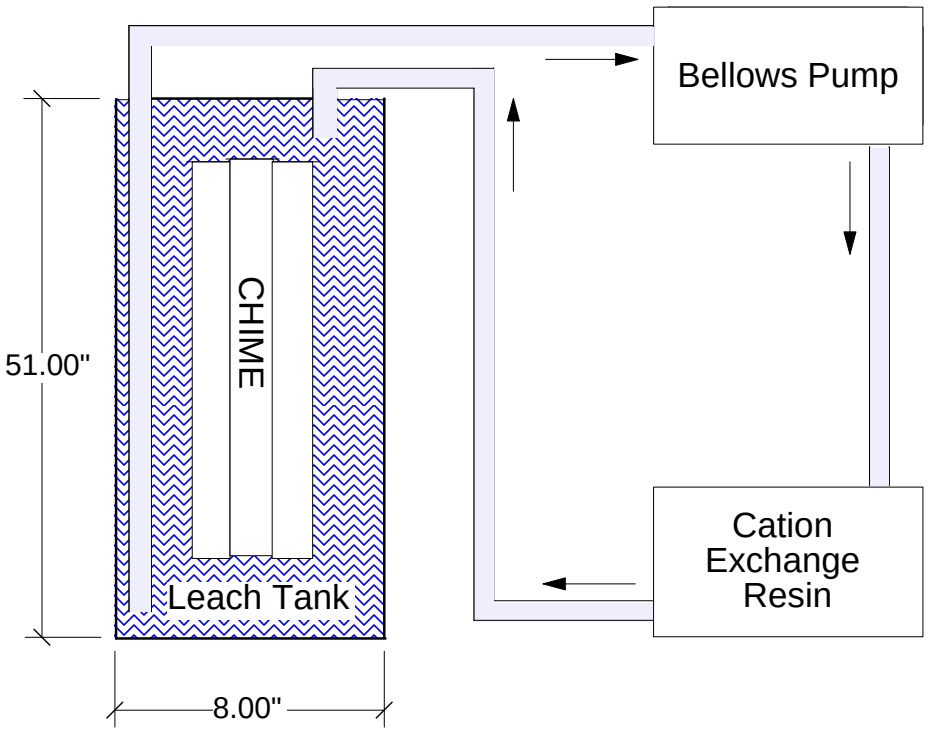

Figure F.1: Schematic of the CHIME leach test setup.

microcurie of ^{227}Th. All of the 500 dpd of ^{223}Ra will therefore contain no more than 5-8 femtograms of Th. This is eight order of magnitudes lower than the amount of Th needed to cause a photodisintegration background of 1% of the SSM NC neutron production rate in SNO. Upper limits on the Th and U contents of ^{223}Ra preparations can also be set by examination of alpha spectra from leach tests. The results are not as sensitive but in agreement.

F.1.3 Leaching System Background Results

In summer 1999, tests of the CHIME leaching systems were conducted in order to evaluate system Ra backgrounds. All conditions were identical to those which are used for leaching the CHIME assembly in Sudbury. Although a prior CHIME tank leach involving added ^{227}Th resulted in high tracer recovery (65%), other studies have shown that surface-bound

Th does not leach into pure water. However, these same studies indicated that Ra resulting from decay of surface-bound Th will diffuse into solution. Hence, current leach studies have focused entirely upon Ra.

The α spectrum of the processed CHIME Ra sample is given in Figure F.2. Obviously the principal peaks in the spectrum are due to the ^{223}Ra tracer. These are listed in Table F.1. Tracer recovery for the ROV sample was 52.1%. Important analytical peaks are listed in Table F.2, and are indicated in the spectrum as well.

Table F.1: Alpha particles associated with ^{223}Ra.

Nuclide	α Energy (MeV)	Branching Ratio (per decay)
^{215}Po	7.386	1.00
^{219}Rn	6.819	0.81
^{211}Bi	6.623	0.84
^{219}Rn	6.553	0.12
^{211}Bi	6.279	0.16
^{223}Ra	5.716	0.53
^{223}Ra	5.607	0.24

Table F.2: Important analytical α peaks.

Nuclide	α Energy (MeV)	Branching Ratio (per Th, U decay)	Series
^{212}Po	8.784	0.6406	^{232}Th
^{214}Po	7.687	1.00	^{238}U
^{226}Ra	4.784	0.945	^{238}U
^{216}Po	6.778	1.00 (strong tracer interference)	^{232}Th

The α spectrum of the processed CHIME Ra sample is given in Figure F.2. The spectrum of the blank disk used to prepare the sample is given as Figure F.3. Figure F.4 is a second

Table F.3: Parameters pertaining to the CHIME system background leach test.

H_2O volume	30 l
Flow rate through trap	300 ml/min (393 l cycled through the trap)
Duration of leach	0.910 d
Flaming of disk (daughter removal)	1.821 d from end of leach (EOL)
Count start	1.842 d from end of leach (EOL)
Count length	7.042 d
Tracer added	163.7 dpd ^{223}Ra (decay corrected to count mid-time)
Detector efficiency	0.2860

count of the CHIME sample begun 8.89 days after the leach using a different detector (ϵ = 0.2466, count length 6147 min).

Final results for Th and U from the CHIME blank runs are given in Table F.4 below. Values are given as ^{232}Th and ^{238}U equivalent masses assuming secular steady state decay within each series. The data show that the measured limits are about 0.05 μg ^{232}Th and 0.015 μg ^{238}U. These are somewhat higher than the previously calculated detection limits of 0.014 and 0.002 (for Th and U) based upon counter backgrounds and counting statistics.

The positive signals that are observed are not due to the Pt disks or counting chambers that were employed. They arise from the leach hardware and reagents used to process the samples. The α spectra show discernible peaks for ^{212}Po and ^{214}Po providing visual confirmation of a very small but detectable reagent/processing blank. However, even with our small reagent blank levels, the detection limits we are able to establish for Th and U are well below (by a factor of 10 for Th and 100 for U) the levels necessary to produce a signal of 1% of the SSM NC neutron production rate in SNO. This is evident from the detector burdens listed in Table F.4. Reliable assessment of superficial Th/U on the CHIME array and ROV will therefore be obtained via this leach method.

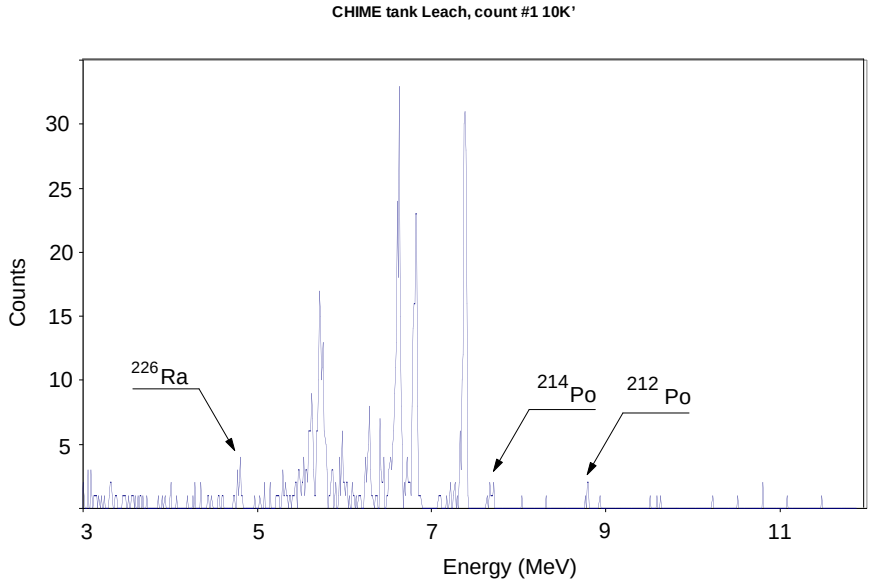

Figure F.2: α spectrum of the processed Ra sample from the CHIME leach tank. This sample was counted for 10,000 min.

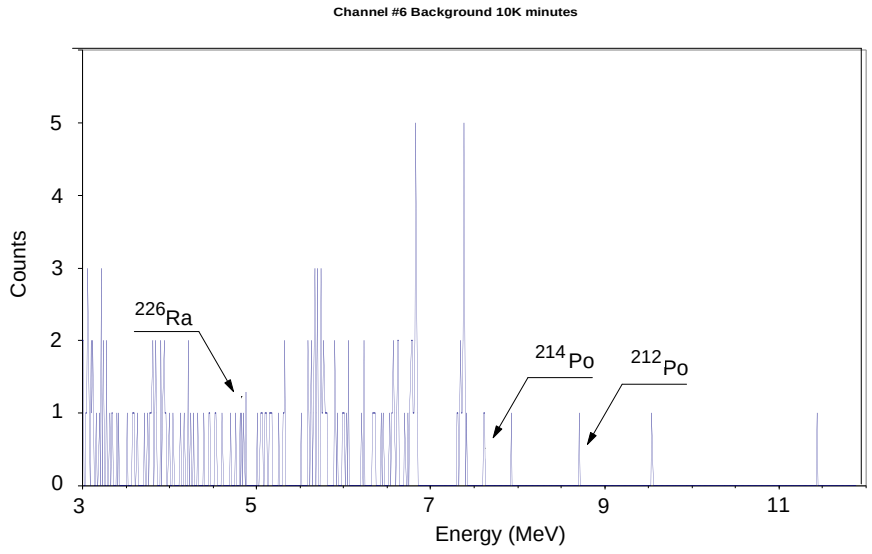

Figure F.3: Alpha spectrum of the blank disk used to prepare the sample. This sample was counted for 10,000 min.

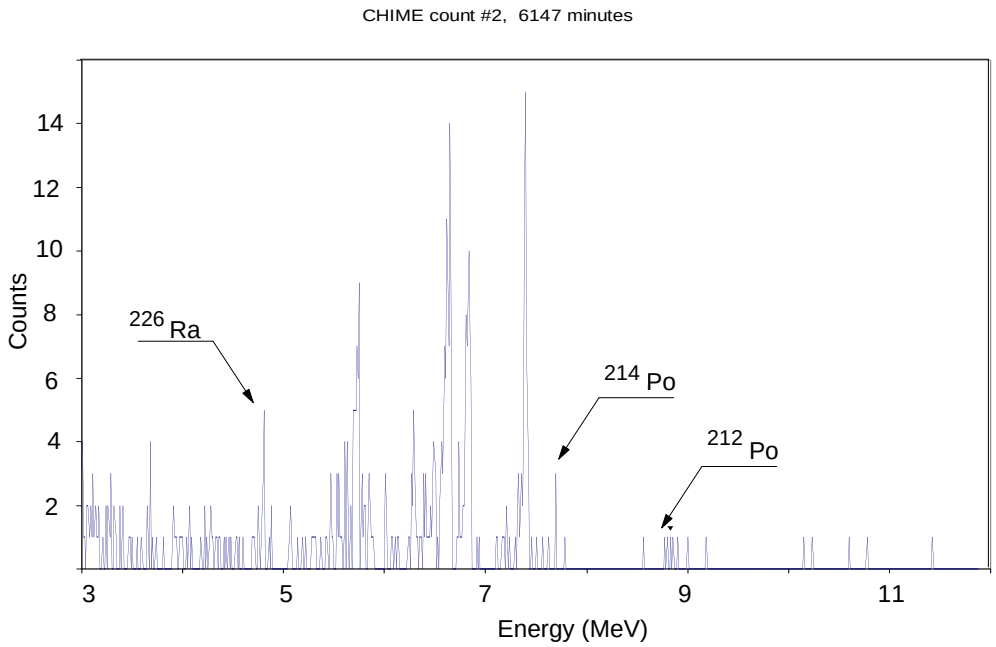

Figure F.4: Second count of the CHIME sample begun 8.89 days after the leach using a different detector. This sample was counted for 6147 min.

F.1.4 Analysis of Alpha Counting Data

Since samples are traced with known amounts of ^{223}Ra, the ^{226}Ra and ^{224}Ra activities present on the sample disk would ideally be readily determined by simple ratio to a suitable tracer peak. However, because of decay and the need to monitor progeny of the species of interest, corrections to the data must be made.

Because of the short half-life of ^{224}Ra, samples must be counted as soon as possible after leaching. Also, since long count times are necessary to achieve the sensitivity for Th required by SNO, decay of ^{224}Ra during a count must be accounted for. Conversion of the "mean" activity, M, observed during a count (i.e. total counts/count length) to the "instantaneous" rate at the beginning of the count, is done via the factor "k":

$$k = \lambda t/(1 - e^{-\lambda t}) \tag{F.1}$$

where t is the count length and λ is the decay constant for ^{224}Ra (0.1894 d^{-1}). This

Table F.4: Results for Th and U the CHIME leach background tests.

System	mg Th (from ^{212}Po)	mg U (from ^{214}Po)	mg U (from ^{226}Ra)
CHIME (1st count)	0.05 0.03	0.015 0.006	0.008 0.003
CHIME (2nd count)	0.2 0.2	0.007 0.005	0.010 0.010
Detector burden	0.6	2	

correction is significant for long count times. For example, k for a 10,000 minute count (6.944 d) is 1.798.

^{212}Po is the nuclide actually used to quantify ^{224}Ra. It is generally at secular steady state with regard to Ra in leaching work, however only 64.06% of ^{224}Ra decays yield ^{212}Po. This further lessens sensitivity for Th. If ^{224}Ra and ^{212}Po are not decaying at steady state, correction for this can be made in the same way ^{226}Ra/^{214}Po "disequilibrium" is handled (see below).

^{214}Po is the nuclide monitored in lieu of its great (x3) grandparent ^{226}Ra. Because of intervening 3.825-day ^{222}Ra, these two do not decay at steady state on the time scale of interest in leaching work. The ratio of the ^{214}Po activity to the ^{226}Ra activity, averaged over the length of a count, is given as R_c :

$$R_c = (R_2 t_2 - R_1 t_1)/(t_2 - t_1) \tag{F.2}$$

where $R = 1 - 1/k$ and t_1 and t_2 are the elapsed times between flaming of samples and start of count. The discs upon which the samples are electrodeposited are heated to red heat "flame" in order to fix the Ra activity on the surface and to remove all daughter activities. This therefore marks the start of ingrowth of ^{222}Rn from ^{226}Ra. Therefore, t_1 represents the ingrowth period prior to a count, and t_2 is equal to t_1 plus the count length. The magnitude of the correction afforded by R_c can be significant. For example, for a 10,000 min count, started immediately after a sample is flamed, $R_c = 0.546$.

F.1.5 Results from the CHIME Leach Test

The CHIME unit was checked for "leachable" Ra in early November of 1999. A closed 17 cm i.d. $\times$ 120 cm polyethylene tube, filled with 26 liters of high purity H_2O was used as the leaching vessel. All wetted parts were of PTFE with the exception of the tank and the trapping medium. The trap contained 45 ml of a "macroporous" cation resin having a styrene/divinylbenzene backbone with sulfonic acid active sites (Bio-Rad AGMP-50, 50-100 mesh). Prior to leaching the CHIME assembly a background run was done. Specially purified ^{223}Ra tracer was used in each run. Table F.5 summarizes the leach parameters employed. Table F.6 gives experimental results expressed as ^{232}Th and ^{238}U equivalents.

Table F.5: Leach conditions during during the CHIME emanation test. The activity is given in disintegrations per day (dpd).

Sample	Leach duration (min.)	H_2O flow (ml/min)	^{223}Ra added (dpd)
Background	250	345	43
CHIME	950	305	108

Table F.6: Results in μg equivalents of ^{232}Th and ^{238}U. All values are upper limits at the 95% confidence level.

Sample	^{232}Th (^{212}Po)	^{238}U (^{214}Po)	^{238}U (^{226}Ra)	Tracer Recovery
Background	0.057	0.0044	0.0032	82.5%
CHIME	0.26	.035	0.037	8.1%

The poor tracer recovery associated with the CHIME sample is due to physical loss of the sample in processing. It is interesting to note that, in leach tests run at LANL involving the CHIME tank and the ROV tank, low but detectable levels of ^{214}Po, ^{212}Po, and ^{226}Ra were seen. No analytical peaks for these nuclides were noted in either of the Sudbury samples

despite the high tracer recovery noted for the background sample. Because none of the blank disks (upon which samples were mounted) showed any activity, and since the same reagents were used to process all of the samples (from both LANL and Sudbury), the water used as leach medium is apparently the source of the signals observed in the tests at Los Alamos. The water used for the Sudbury samples measured 15-18 MΩ-cm and was tapped from the light water processing loop immediately prior to being returned to the cavity. The H_2O for the leach tests conducted in Los Alamos was measured at 18 MΩ-cm and came directly from a milli-Q ion exchange system.

F.2 Analysis of NCD and CHIME Surface Contamination

F.2.1 X-Ray Fluorescence Monitoring Technique and Equipment

Studies of dust in the mine areas outside the SNO laboratory have shown that on average the dusts contain approximately 7% iron by weight. This iron content of individual dust samples is also strongly correlated with the thorium level of the dust which produces the most serious background γ-ray. X-ray fluorescence (XRF) measurements of iron in surface dust samples can be used to detect the presence of mine dust with sufficient sensitivity to monitor the surface cleanliness of the detector components. No other technique for routine monitoring of small dust samples appears to have comparable sensitivity.

The X-ray fluorescence spectrometer used for these measurements was initially developed for air pollution sample analysis at Lawrence Berkeley National Laboratory. Shown schematically in Figure F.5, the unit utilizes a 10 W molybdenum target x-ray generator (E_γ=17.5 keV), a silicon (Li) surface barrier detector cooled by liquid nitrogen and a sample chamber which accepts 3.2 cm diameter polypropylene or tape disc samples. The x-ray beam has a diameter of about 1.5 cm. The compact size of the unit enabled it to be installed underground in the SNO laboratory so that dust samples could be analyzed immediately. Standard samples containing 5 to 10 μg Fe per cm^2 are used to monitor the sensitivity of the spectrometer during each sampling run. The spectrometer has a signal of 3.1 counts/sec in the Fe, K_α x-ray region for a thin sample containing 1 μg/cm^2 of typical mine dust (0.07 μg/cm^2 Fe). For a 10 minute counting period, a minimum detection limit of 0.05 μg/cm^2 equivalent (7% Fe) dust can be reached. A typical X-ray spectrum for one of the CHIME tape lifts is shown in Figure F.6. Analysis is carried out by integrating the counts in a region of interest for the element concerned and subtracting a blank sample background.

F.2.2 Surface Cleanliness of the SNO Acrylic Vessel

During the construction phase of SNO the XRF system was primarily used to monitor the cleanliness of the laboratory and to check for dust contamination on the surfaces of the acrylic vessel. The SNO laboratory is operated under cleanroom conditions with an average air particle level of class 2500 (particles per cubic foot greater than 0.5 μm in diameter).

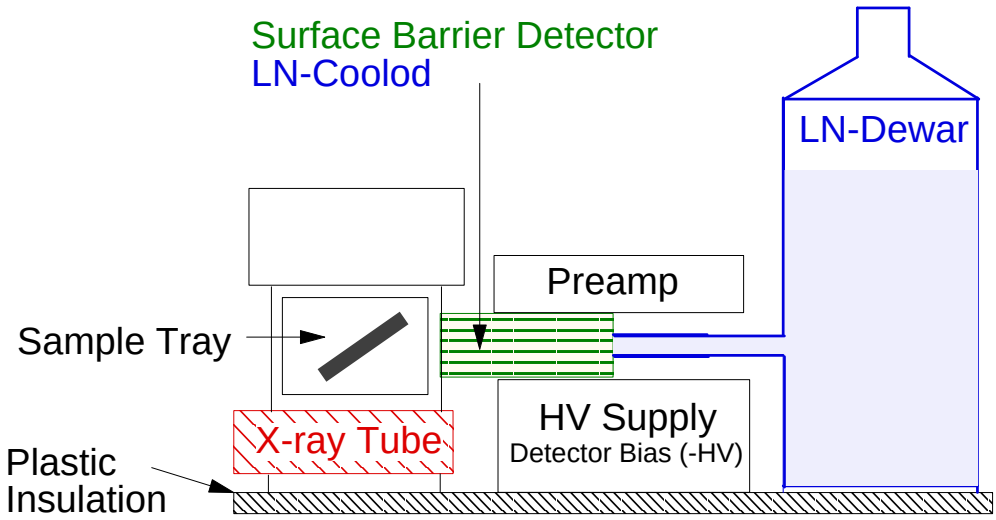

Figure F.5: Schematic of the SNO X-ray fluorescence (XRF) system.

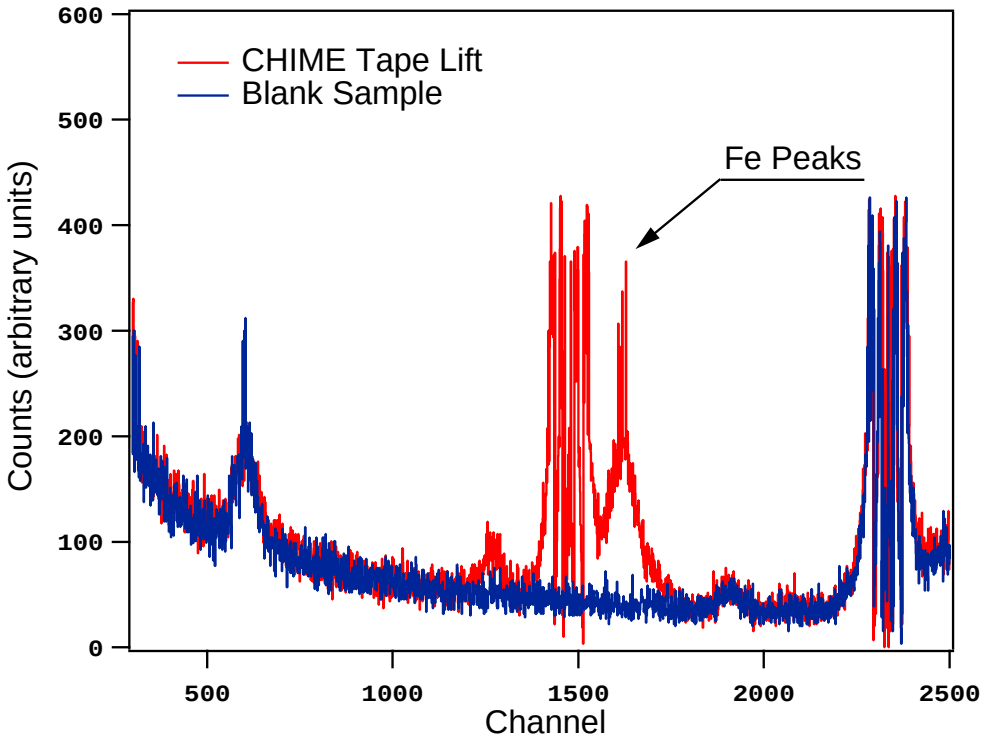

Figure F.6: XRF spectrum of CHIME tape lift.

These conditions are established and maintained through 6 air handler units with 2 mesh filters followed by a final high efficiency HEPA filtration. In the cavity, air is recirculated at about 6 changes per hour using a combination of the air handler and portable recirculating units on the construction platform. About 20% of supply air is brought in from the mine, trough a separate air handler. The geodesic PMT structure was assembled by bonding 1.5 m $\times$ 2 m acrylic panels on site. For comparable background contributions, the purity of the acrylic (exceeding target levels of 5 ppt (5×10^{-12}g/g) in uranium, thorium and decay products) and of the water (3×10^{-15}g/g Th) must be matched by surface dust levels below 0.1 μg/cm^2 equivalent. The acrylic vessel was constructed by bonding individual panels in place under clean conditions to prevent any dust from being incorporated into the bond. An extensive fine cleaning program and monitoring program for the completed vessel surface was setup prior to the fill with heavy water. Numerous locations on the interior and exterior surface of the vessel were checked for cleanliness by applying and removing a low Fe clear tape disc to the surface 5 times on adjacent regions. Surface dust is efficiently removed by this process and can be analyzed through XRF examination of the disc sample. For reference, some typical AV tape lifts results are given in Table F.7. These results were made available by D. Hallman [123].

F.2.3 Tape Lifts of the External CHIME Surfaces

XRF tape lift measurements taken from the external surface of the NCD background test source (CHIME) and a few select NCD counters are used to verify the surface cleanliness of the Neutral Current Detectors. In this section we discuss the results from the CHIME tape lifts. The results from the NCD tape lifts are summarized in Section F.2.4.

Blank tapes were counted for Fe before the CHIME tape lifts were taken. The difference between the blank counts and the CHIME counts was taken to be the Fe signal from dust. The result for each individual tape was averaged with the dust levels measured in adjacent areas. The net Zn signal was determined by comparing the Zn counts for the blank tape and for the tape after the lift. The Ni K$_\beta$ contribution (6% of net Ni K$_l$ peak) was subtracted to derive the Zn level. The Zn level is the number quoted in the initial report. The Ni levels

Table F.7: XRF tape lift results from typical acrylic vessel surfaces. The counts of the XRF system and their equivalent dust levels are given.

Tape Lift	Fe Count /20 min	Zn Count /20 min	Equiv. Dust Fe μg/cm^2	Equiv. Dust Zn μg/cm^2	Dust Level μg/cm^2
34 AV lifts (interior)			0.0067 ± 0.0394	0.0058 ± 0.0056	0.0125
35 AV lifts (exterior)			0.029 ± 0.0344	0.0062 ± 0.0052	0.035
20 AV lifts (rope grooves)	59 ± 142	357 ± 366	0.016 ± 0.0384	0.0059 ± 0.0060	0.025
69 AV lifts (ext./int.)	67 ± 143	400 ± 361	0.018	0.0066	0.025

were derived assuming the same X-ray efficiency as for Fe.

The tape lifts measurements were performed on December 21, 1999. After warming up the XRF setup for about an hour the dead time was measured to be $< 10\%$. Six blank tapes were prepared (no. 1060-1065). The average Fe and Zn for the blank tapes no.1060, 1062, 1064 was measured to be: 4275 ± 28 for Fe and 3381 ± 44 for Zn. All tapes were counted for 1200 s. A Fe signal of 370 counts is equivalent to 0.1 μg/cm^2 of mine dust assuming 7% Fe.

Four tape lifts were taken at various positions on the outside surface of the CHIME. The nylon bags of the CHIME were opened at the ends and slid off to access the top and bottom end of the CHIME. The CHIME and the nylon bags were handled with gloves throughout. There was no contact with the CHIME except by the sticky tape and the AL rings that suspend the sticky tape (This was only discovered later in my discussion with Doug. Acrylic rings will be used for any future CHIME or NCD tape lifts.). The nylon bags always covered more than 90% of the CHIME counter.

- *Sample no.1 (CH1060):* was taken from flat areas of the outer ring of the top endcaps

Table F.8: Results from the CHIME tape lift assuming same efficiency for Ni x-rays as for Fe.

Signal	CH1060	CH1061	CH1062	CH1063
mine dust equivalent	0.0088 μg/cm^2	0.46 μg/cm^2	0.13 μg/cm^2	0.17 μg/cm^2
Zn	0.0051 μg/cm^2	0.017 μg/cm^2	0.0059 μg/cm^2	0.027 μg/cm^2
Ni	0.18 μg/cm^2	0.86 μg/cm^2	0.27 μg/cm^2	0.37 μg/cm^2

of the CHIME. Note that the glove came in contact with the sticky side of the tape. The result from this tape lift might be questionable.

- *Sample no.2 (CH1061):* was taken from the outer cylindrical walls, 2" down from the closed end. One lift was taken per tube for 5 tubes.

- *Sample no.3 (CH1062):* was taken from the edge of the tubes at the open end. Could not get inside the tubes. This tape lift was taken at about 10 places.

- *Sample no.4 (CH1063):* was taken from the outer cylindrical walls, 2" up from the open end. One lift was taken per tube for 5 tubes.

The results from this set of tape lifts are summarized in Table F.8. The average of all samples shows a 0.21 μg/cm^2 mine dust equivalent (7% Fe).

In summary, the performance of the XRF and the backgrounds were acceptable. The tape lift analysis can therefore be consider to be OK. As Table F.8 indicates, the Zn levels are negligible. The correlation between the Ni levels and dust is understandable since Ni indicates the degree of tape contact with surface. Some lift locations were difficult to get to. In these cases the tape contact is questionable. The average CHIME (Fe) dust level is about 0.2 μg/cm^2. This is about twice the limit criterion for the acrylic vessel but well below the requirements of < 0.5 μg/cm^2 for calibration devices. Considering the storage conditions of the CHIME (sealed double nylon bags) it is difficult to interpret this as mine dust.

The results from the CHIME tape lift indicate that the correlation between Ni and Fe is essentially perfect. This raises the question of possible systematics. The Fe and Ni peaks are not very far apart and the actual Fe amounts are about 30 times smaller than Ni. The fluorescent yield for Fe is 20% smaller than for Ni and the sensitivity threshold of this technique is uncertain.

Usually, the data is analyzed by setting windows around the places where peaks are expected and subtracting the corresponding region of a blank and not by fitting peaks and backgrounds to the spectrum. This makes us suspicious that the relatively strong Ni peak (30 x stronger) has low-energy tails that extend under the region of the Fe peak. This technique, which does not require the actual presence of a peak, will give erroneous results when an intense peak is present elsewhere close by in the spectrum.

Therefore, we believe that the "Fe" signal is just the tail of the Ni. If the levels are as interpreted, however, the total activity implied for the array is about 0.1 mg of Th, or about 10 n/y.

Additional CHIME tape lifts were taken from the CHIME Tubing: Data from X-ray fluorescence measurements on the SNO spectrometer, on tape lift samples from the CHIME assembly are summarized below. Tapes 1027, 1028 were prepared and measured on July 21, 1999, while tapes 1060 to 1063 were made and analyzed on December 21, 1999. The measurements for 1061b were made on the same 1061 tape on August 8, 2000. Tape 1052 was used to check the surface of a 1 inch length of Ni tubing from tube T441, on August 8, 2000.

We note the following observations in the data: The Fe counts seen in several samples (1061, 1063) are clearly peaks and not just a continuos background change. The repeat measurement of 1061 shows good consistency with the earlier data. The Zn levels are negligible in all tape lifts. Equivalent dust levels are based on the assumption that mine dust contains 7% Fe. The Ni backgrounds were estimated from blank tape data, and the mass/cm^2 values are based on an assumption of the same efficiency for X-ray fluorescence for Ni as for Zn. There is a variation in the Ni/dust ratio, and data suggests that the partial correlation is due to the fact that some lifts were easier to make and captured both more NI as well as Fe. The higher Fe and dust levels could have resulted from contamination during

the time of the lifts. The lifts made on the test tubing (1052) show that the presence of a Fe peak is not always associated with the Ni signal.

F.2.4 Tape Lifts of the External NCD Surfaces

On August 30, 1999, tape lifts were taken from the ends of two different NCD counters. The procedure for getting the tape lifts was to push the nylon bag back, take four separate lifts on one tape from the region of the counter immediately down stream of the test end cap connector with the SHV connector. The reason for using this position is that it is near the end of the counter that probably has been handled more and exposed to mine are while further in has seen less handling. I didn't want to take samples from the actual end cap connector with the SHV since these are handled all the time to connect and disconnect counters.

The results have been corrected for a 4 lift sample versus the standard 5 lifts (for which 370 counts/20 min. in the Fe peak corresponds to 0.1 μg/cm^2 mine dust). Tape No. 1027 (CH1027_07.21) was a 4 lift sample from counter housing No.5 (Counter A8). Tape No. 1028 (CH1028_07.21) was a 4 lift sample from counter housing No.3 (NCD counter N2).

The nickel is apparently lifted from the surface by the tape - probably a reasonable result given surface texture. There is no evidence of tape adhesive disappearing from the samples, but a more definitive test would be to look at the Ni surface with a hand microscope and/or to weigh the tape samples before and after the lifts.

The results suggest no dust problem with counter housing No. 5 and a slight problem with mine dust for no. 3 - preferably mine dust is < 0.1 μg/cm^2. The fact that more nickel was lifted from housing No. 3 might be related to a change in surface texture, or a more efficient lift set. The Zn result is of no concern.

Witness plates have been installed in some of the deck and deck clean room areas for the shutdown, to check on the level of deposition. In general, previous measurements in the cavity suggest a deposition rate in the general deck area of several tenths of a μg/cm^2 per month, with the level in the clean room being less than a tenth of a μg/cm^2 per month. These numbers can be taken as a guide regarding expected surface cleanliness during the

cooldown period.

We suspect that the outer surface of the Neutral Current Detectors is sufficiently rough that the efficiency of dust pickup by the tape must be uncertain.

F.2.5 Tape lifts on CHIME Deployment Hardware

On August 3, 2000, 4 tape lifts on the stainless steel CHIME deployment hardware were taken. The tapes were counted for 20 min in the XRF setup on August 8, 2000. The results are summarized in Table F.11. In addition to the tape lifts from the stainless steel a tape lift taken from the rag that used to clean the CHIME source tube was counted as well. A detailed description of the CHIME deployment hardware can be found in Appendix E.

In general, the results are consistent with small amounts of stainless steel, containing predominantly Fe, Cr, and Ni. There is no evidence of extra Fe, that could be associated with mine dust. A limit on extra Fe counts appears to be near 500 counts for the first four samples corresponding to a maximum equivalent mine dust of about 0.13 μg/cm^2). The large counts for the source tube cleaning rag reflect the larger particles deposited on the tape sample. Particles appear to have typical stainless steel composition. The ratio in the last row of the table is based on the assumption of the same efficiency for x-ray fluorescence for the three metals.

Table F.9: X-ray fluorescence data (counts per 20 min) for CHIME tape lift samples.

Tape No.	1027	1028	1060	1061a	1061b	1062	1063	1052
Fe count			4513	6252	6202	4864	5045	4262
blank			4303	4275	4275	4247	4275	4213
Net Fe			210	1977	1927	617	770	49
Fe-bkgd			441	1390	1116	345	470	-375
Avg Net Fe			326	1684	1670	481	620	50
Equivalent dust (μg/cm^2)	0.0 ± 0.04	0.22 ± 0.04	0.088	0.46	0.46	0.13	0.17	0.013
Zn count			4298	7439	7502	4742	6309	3478
blank			3356	3381	3381	3425	3381	2975
Net Zn			942	4058	4121	1317	2928	503
-Ni K_β cont			-650	-3050	-3050	-970	-1323	-500
Zn			300	1000	1070	350	1600	0
Zn level (μg/cm^2)	0.003	0.012	0.0051	0.017	0.018	0.0059	0.027	0
Ni count			13735	53387	45094	19153	25047	7690
blank			3000	3000	3000	3000	3000	3952
Net Ni	7520	12380	10735	50387	42094	16153	22047	3738
Ni level (μg/cm^2)	0.15	0.25	0.18	0.86	0.72	0.27	0.37	0.17
Ni/dust	38	1.1	2.05	1.87	1.57	2.08	2.18	13

Table F.10: Results from the NCD tape lifts assuming same efficiency for Ni x-rays as for Fe.

Tape	Element	Tape Lift Measurement
Tape 1027	Mine dust	0.00 ± 0.04 μg/cm^2
	Zn	0.003 ± 0.003 μg/cm^2
	Ni	7520 counts (net)/20 min. $\rightarrow$ 0.15 μg/cm^2
Tape 1028	Mine dust	0.22 ± 0.04 μg/cm^2
	Zn	0.012 ± 0.003 μg/cm^2
	Ni	12380 counts (net)/20 min. $\rightarrow$ 0.25 μg/cm^2

Table F.11: Tape lift results from CHIME deployment hardware.

Tape Number	CH1056	CH1057	CH1058	CH1059	CH1049
Lift No.	1	2	3	4	source tube rag
Net Fe Counts	2600	13150	3000	5700	396K
Net Cr Counts	1000	6500	1500	2600	255K
Net Ni Counts	1000	1500	500	1000	54K
Fe/Cr/Ni %		61/31/8			57/35/8

VITA

Karsten M. Heeger earned a Doctor of Philosophy in Physics at the University of Washington in 2002. He was a graduate student under Prof. R.G.H. Robertson and worked as a member of the Sudbury Neutrino Observatory on measuring the solar neutrino flux and the flavor mixing of neutrinos. His current research interests include the properties of neutrinos, neutrino astrophysics, and weak interactions.

During his graduate education he earned a Master of Arts (M.A.) from Oxford University, England, and a Master of Science (M.Sc.) in Physics from the University of Washington in Seattle. He graduated with honors (B.A. Hons) from Oxford University in 1995.

As a graduate student at the University of Washington he received the Mellam Fellowship (2000), the Dahlstrom prize (2000), and the Karrer Memorial Scholarship (1996). He was awarded several academic distinctions at Oxford University. Between 1992-1997 he was a scholar of the German National Scholarship Foundation.

Since 1993 he has been involved in various professional organizations. He is an elected member (MInstP) of the British Institute of Physics (2001), and graduate member of the European Physical Society, the German Physical Society, and the Institute of Electrical and Electronics Engineers.

He enjoys skiing and playing the violin.